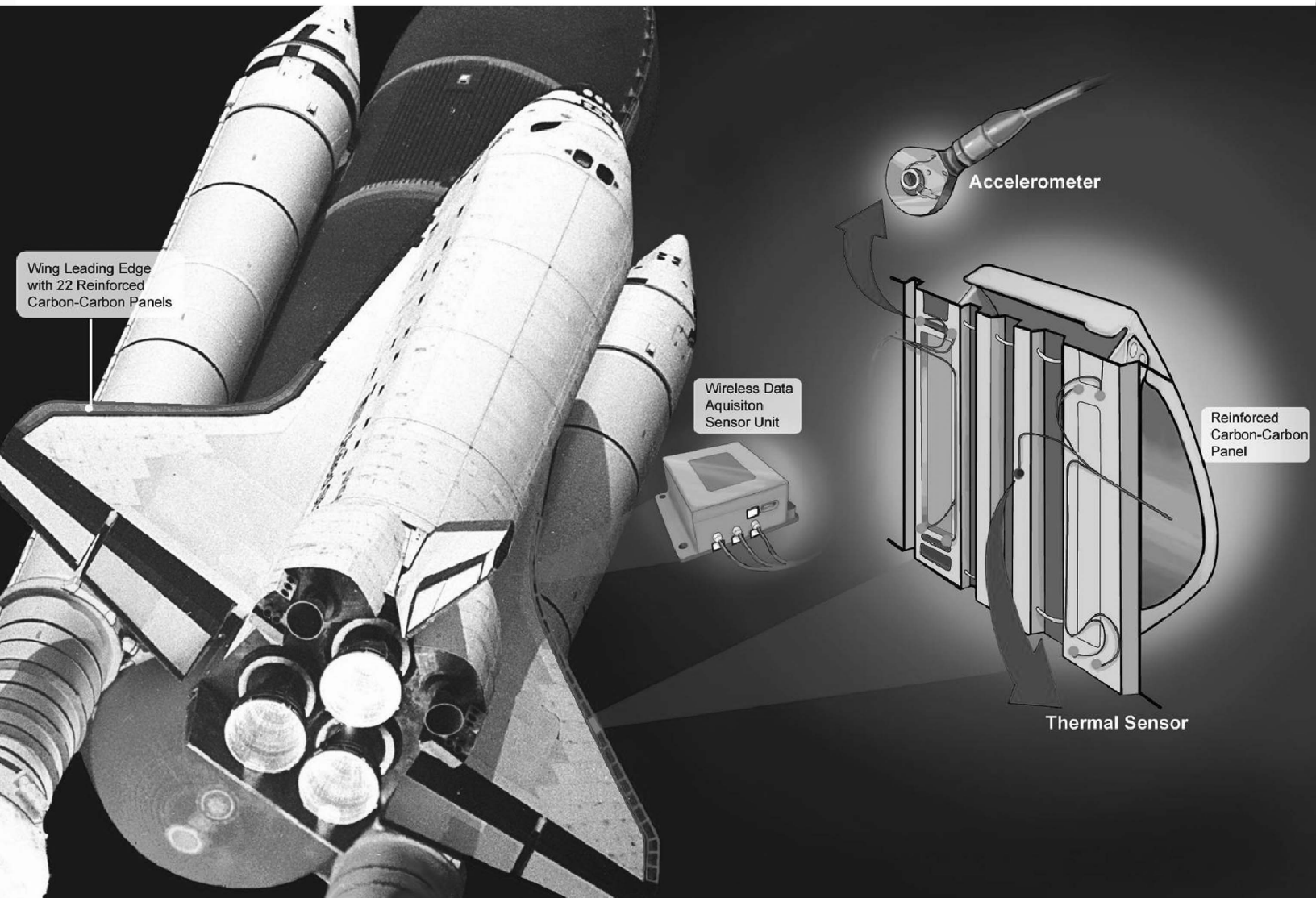


An International
Forum For
The AE Science
and Technology

JOURNAL OF ACOUSTIC EMISSION

Vol.23/January-December 2005



Monitoring Space Shuttle Leading Edges

Endorsed by
AEWG
and
EWGAE

Published by
Acoustic Emission Group
Encino, CA USA

JOURNAL OF ACOUSTIC EMISSION

VOLUME 23, 2005

VIEWING AN ARTICLE ON CD-ROM

You need a software that can read a pdf-file. Two folders are provided for Windows 95/98/ME/2000/XP and for Macintosh. Each contains Adobe Acrobat Reader® Installer for respective OS. Install one first before going further. You can also download the latest version from www.adobe.com. Use of Adobe Acrobat ® (not provided) allows one to utilize the Search function. This gives the power to search for a name or a word in the entire volume and is highly recommended.

PDF Files: Contents are listed below. Individual papers have file names of **23-xxx.pdf**, with xxx as their first page number.

ISSN 0730-0050

Copyright©2005 Acoustic Emission Group

Coden JACEDO

CONTENTS

23-001	EFFECTS OF NOISE ON LAMB-MODE ACOUSTIC-EMISSION ARRIVAL TIMES DETERMINED BY WAVELET TRANSFORM <i>M. A. HAMSTAD and A. O'GALLAGHER</i>	1
23-025	ACOUSTIC EMISSION TECHNIQUE FOR DETECTING DAMAGE AND MECHANISMS OF FRACTURE IN A KNITTED FABRIC REINFORCED COMPOSITE <i>CARLOS R. RIOS, STEVE L. OGIN, CONSTANTINA LEKAKOU and K. H. LEONG</i>	25
23-037	QUANTITATIVE DAMAGE ESTIMATION OF CONCRETE CORE BASED ON AE RATE PROCESS ANALYSIS <i>WILLIAM PROSSER, ERIC MADARAS, GEORGE STUDOR, and MICHAEL GORMAN</i>	37
23-047	MOMENT TENSORS OF IN-PLANE WAVES ANALYZED BY SIGMA-2D <i>MASAYASU OHTSU, KENTARO OHNO and MARVIN A. HAMSTAD</i>	47
23-064	DEVELOPMENT OF AN OPTICAL MICRO AE SENSOR WITH AN AUTOMATIC TUNING SYSTEM <i>HIROSHI ASANUMA, HIRONOBU OHISHI, and HIROAKI NIITSUMA</i>	64
23-072	DEVELOPMENT OF STABILIZED AND HIGH SENSITIVE OPTICAL FIBER ACOUSTIC EMISSION SYSTEM AND ITS APPLICATION <i>HIDEO CHO, RYOUHEI ARAI and MIKIO TAKEMOTO</i>	72
23-081	HIGH PRECISION GEOPHONE CALIBRATION <i>MASAHIRO KAMATA</i>	81
23-091	DEVELOPMENT OF HEAT-RESISTANT OPTICAL FIBER AE SENSOR <i>PORNTHAP CHIVAVIBUL, HIROYUKI FUKUTOMI,</i>	

	<i>SHIN TAKAHASHI and YUICHI MACHIJIMA</i>	91
23-096	DAMAGE DETECTION SYSTEM FOR STRUCTURES WITH SMART AE SENSORS	
	<i>TAKAHITO YANASE and SEI IKEGAYA</i>	96
23-102	HIERARCHICAL FRACTURE PROCESS IN BRITTLE ROCKS BY MEANS OF HIGH-SPEED MONITORING OF AE HYPOCENTER	
	XINGLIN LEI, OSAMU NISHIZAWA, ANDRE MOURA and TAKASHI SATOH	102
23-113	MEASUREMENT OF HYDRAULICALLY ACTIVATED SUBSURFACE FRACTURE SYSTEM IN GEOTHERMAL RESERVOIR BY USING ACOUSTIC EMISSION MULTIPLET-CLUSTERING ANALYSIS	
	<i>HIROKAZU MORIYA, HIROAKI NIITSUMA and ROY BARIA</i>	113
23-119	A MODELING METHOD ON FRACTAL DISTRIBUTION OF CRACKS IN ROCKS USING AE MONITORING	
	YOSHINORI WATANABE, KEN-ICHI ITAKURA, KAZUHIKO SATO, YOSHIAKI FUJII, RAO BALUSU, HUA GUO and XUN LUO	119
23-129	INTERPRETATION OF RESERVOIR CREATION PROCESS AT COOPER BASIN, AUSTRALIA BY ACOUSTIC EMISSION	
	YUSUKE KUMANO, HIROKAZU MORIYA, HIROSHI ASANUMA, NOBUKAZU SOMA, HIDESHI KAIEDA, KAZUHIKO TEZUKA, DOONE WYBORN and HIROAKI NIITSUMA	129
23-136	MICROMECHANICS OF CORROSION CRACKING IN CONCRETE BY AE-SIGMA	
	FARID A. K. M. UDDIN and MASAYASU OHTSU	136
23-142	EVALUATION OF PARAMETER DEPENDENCIES OF AE ACCOMPANYING SLIDING ALONG A ROUGH SIMULATED FRACTURE	
	<i>KATSUMI NEMOTO, HIROKAZU MORIYA and HIROAKI NIITSUMA</i>	142
23-150	AE CHARACTERIZATION OF THERMAL SHOCK CRACK GROWTH BEHAVIOR IN ALUMINA CERAMICS BY DISC-ON-ROD TEST	
	HUICHI WAKAYAMA, SATOSHI KOBAYASHI and TOSHIYA WADA	150
23-156	FATIGUE DAMAGE PROGRESSION IN PLASTICS DURING CYCLIC BALL INDENTATION	
	AKIO YONEZU, TAKAYASU HIRAKAWA, TAKESHI OGAWA and MIKIO TAKEMOTO	156
23-164	EVALUATION OF FATIGUE DAMAGE FOR FRM WITH AE METHOD	
	<i>MASANORI TAKUMA and NOBORU SHINKE</i>	164
23-173	ACOUSTIC EMISSION BEHAVIOR OF FAILURE PROCESSES OF GLASS-FIBER LAMINATES UNDER COMPLEX STATE OF LOADING	
	<i>JERZY SCHMIDT, IRENEUSZ BARAN and KANJI ONO</i>	173
23-181	ROLLING CONTACT FATIGUE DAMAGE OF WC-Co CERMET SPRAYED COATING AND ITS AE ANALYSIS	
	<i>JUNICHI UCHIDA, TAKESHI OGAWA, MIKIO TAKEMOTO</i> <i>YOSHIFUMI KOBAYASHI and YOSHIO HARADA</i>	181
23-189	BORON EFFECTS ON AE EVENT RATE PEAKS DURING TENSILE DEFORMATION OF Ni ₃ Al INTERMETALLIC COMPOUND	
	<i>K. YOSHIDA, Y. MASUI, T. NAGAMACHI and H. NISHINO</i>	189

23-196	AE AND ELECTROCHEMICAL NOISE ANALYSIS FOR FRACTURE STUDY OF HARD SURFACE FILM <i>AKIO YONEZU, HIDEO CHO, TAKESHI OGAWA and MIKIO TAKEMOTO</i>	196
23-206	THE ORIGIN OF CONTINUOUS EMISSIONS <i>KANJI ONO, HIDEO CHO and M. TAKUMA</i>	206
23-215	PRECURSOR OF HYDROIGEN INDUCED GLASS LINING CHIPPING BY AE MONITORING <i>KOHEI MURAKAMI and MIKIO TAKEMOTO</i>	215
23-224	REAL-TIME EXECUTING SOURCE LOCATION SYSTEM APPLICABLE TO ANISOTROPIC THIN STRUCTURES <i>YU KUROKAWA, YOSHIHIRO MIZUTANI and MASAMI MAYUZUMI</i>	224
23-233	INVESTIGATION ON AE SIGNAL/NOISE PROCESSING IN CORROSION DAMAGE EVALUATION OF TANK BOTTOM <i>ZHENGWANG LI, SHIGENORI YUYAMA, MINORU YAMADA, KAZUYOSHI SEKINE, SHIGEO KITSUKAWA, HIROAKI MARUYAMA and SHIGEO KONNO</i>	233
23-243	EXAMINATION OF AE WAVE PROPAGATION ROUTES IN A SMALL MODEL TANK <i>HIDEYUKI NAKAMURA, TAKAHIRO ARAKAWA, MINORU YAMADA</i>	243
23-249	INTEGRITY EVALUATION OF GLASS-FIBER REINFORCED PLASTIC VESSELS BY LAMB WAVE AE ANALYSIS <i>TAKASHI FUTATSUGI</i>	249
23-260	EVALUATION OF REINFORCEMENT IN DAMAGED RAILWAY CONCRETE PIERS BY MEANS OF ACOUSTIC EMISSION <i>TOMOKI SHIOTANI, YASUHIRO NAKANISHI, KEISUKE IWAKI, XIU LUO HIROSHI HAYA</i>	260
23-272	WATER-LEAK EVALUATION OF EXISTING PIPELINE BY ACOUSTIC EMISSION <i>TETSUYA SUZUKI, YUKIFUMI IKEDA, YUICHI TOMODA and MASAYASU OHTSU</i>	272
23-277	ACOUSTIC EMISSION FOR FATIGUE DAMAGE DETECTION OF STAINLESS STEEL BELLOWS <i>KOJI KAGAYAMA, AKIO YONEZU, HIDEO CHO, TAKESHI OGAWA, and MIKIO TAKEMOTO</i>	277
23-285	PLASTIC REGION BOLT TIGHTENING CONTROLLED BY ACOUSTIC EMISSION MONITORING <i>TADASHI ONISHI, YOSHIHIRO MIZUTANI and MASAMI MAYUZUMI</i>	285
23-292	ACOUSTIC EMISSION BEHAVIORS OF RECOVERY FOR Mg ALLOY AT ROOM TEMPERATURE <i>Y. P. LI and M. ENOKI</i>	292
23-299	AN ACOUSTIC EMISSION TEST SYSTEM FOR AIRLINE STEEL OXYGEN CYLINDERS: SYSTEM DESIGN AND TEST PROGRAM <i>ALAN G. BEATTIE</i>	299
23-310	DEVELOPMENT OF IN-SITU MONITORING SYSTEM FOR SINTERING OF CERAMICS USING LASER AE TECHNIQUE <i>S. NISHINOIRI and M. ENOKI</i>	310

23-318	PATTERN RECOGNITION TECHNIQUES FOR ACOUSTIC EMISSION BASED CONDITION ASSESSMENT OF UNFIRED PRESSURE VESSELS <i>ATHANASIOS ANASTASOPOULOS</i>	318
23-331	THE ACOUSTIC EMISSION HALON 1301 FIRE EXTINGUISHER BOTTLE TESTER: RESULTS OF TESTS ON 649 BOTTLES <i>ALAN G. BEATTIE and D. D. THORNTON</i>	331

Contents23.pdf	Contents of Volume 23 (2005)	I-1 - I-4
AuIndex23.pdf	Authors Index of Volume 23	I-5
AUeAddress.pdf	Authors e-mail addresses	I-6
AusNotes.pdf	Policy/Author's Notes/Meeting Calendar/ Subscription Information	I-7 - I-9

JAE Index Folder* Cumulative Indices of J. of Acoustic Emission, 1982 - 2005

* indicates the availability in CD-ROM only.

Photograph credit: CD-ROM label and Cover drawing from NASA, courtesy of Dr. William H. Prosser.

Volume 23 (2005) AUTHORS INDEX

A. ANASTASOPOULOS	23-318	T. NAGAMACHI	23-189
RYOUEI ARAI	23-072	HIDEYUKI NAKAMURA	23-243
TAKAHIRO ARAKAWA	23-243	YASUHIRO NAKANISHI	23-260
HIROSHI ASANUMA	23-064, 23-129	KATSUMI NEMOTO	23-142
		HIROAKI NIITSUMA	23-064, 23-113, 23-129, 23-142
RAO BALUSU	23-119	H. NISHINO	23-189
IRENEUSZ BARAN	23-173	S. NISHINOIRI	23-310
ROY BARIA	23-113	OSAMU NISHIZAWA	23-102
ALAN G. BEATTIE	23-299, 23-331		
		A. O'GALLAGHER	23-001
PORNTHEP CHIVAVIBUL	23-091	TAKESHI OGAWA	23-156, 23-196, 23-181, 23-277
HIDEO CHO	23-072, 23-196, 23-206, 23-277	STEVE L. OGIN	23-025
M. ENOKI	23-292, 23-310	HIRONOBU OHISHI	23-064
YOSHIAKI FUJII	23-119	KENTARO OHNO	23-047
HIROYUKI FUKUTOMI	23-091	MASAYASU OHTSU	23-047, 23-136, 23-272
TAKASHI FUTATSUGI	23-249	TADASHI ONISHI	23-285
		KANJI ONO	23-173, 23-206
MICHAEL GORMAN	23-037	WILLIAM PROSSER	23-037
HUA GUO	23-119	CARLOS R. RIOS	23-025
M. A. HAMSTAD	23-001, 23-047		
YOSHIO HARADA	23-181	KAZUHIKO SATO	23-119
HIROSHI HAYA	23-260	TAKASHI SATOH	23-102
TAKAYASU HIRAKAWA	23-156	JERZY SCHMIDT	23-173
		KAZUYOSHI SEKINE	23-233
YUKIFUMI IKEDA	23-272	NOBORU SHINKE	23-164
SEI IKEGAYA	23-096	TOMOKI SHIOTANI	23-260
KEN-ICHI ITAKURA	23-119	NOBUKAZU SOMA	23-129
KEISUKE IWAKI	23-260	GEORGE STUDOR	23-037
		TETSUYA SUZUKI	23-272
KOJI KAGAYAMA	23-277	SHIN TAKAHASHI	23-091
HIDESHI KAIEDA	23-129	MIKIO TAKEMOTO	23-072, 23-156, 23-196, 23-181, 23-215, 23-277
MASAHIRO KAMATA	23-081	MASANORI TAKUMA	23-164, 23-206
SHIGEO KITSUKAWA	23-233	KAZUHIKO TEZUKA	23-129
SATOSHI KOBAYASHI	23-150	D. D. THORNTON	23-331
YOSHIFUMI KOBAYASHI	23-181	YUICHI TOMODA	23-272
SHIGEO KONNO	23-233		
YUSUKE KUMANO	23-129	JUNICHI UCHIDA	23-181
YU KUROKAWA	23-224	FARID A. K. M. UDDIN	23-136
XINGLIN LEI	23-102	TOSHIYA WADA	23-150
CONSTANTINA LEKAKOU	23-025	SHUICHI WAKAYAMA	23-150
K. H. LEONG	23-025	YOSHINORI WATANABE	23-119
XIU LUO	23-260	DOONE WYBORN	23-129
XUN LUO	23-119		
Y. P. LI	23-292	MINORU YAMADA	23-233, 23-243
ZHENGWANG LI	23-233	TAKAHITO YANASE	23-096
		AKIO YONEZU	23-156, 23-196, 23-277
YUICHI MACHIJIMA	23-091	K. YOSHIDA	23-189
ERIC MADARAS	23-037	SHIGENORI YUYAMA	23-233
HIROAKI MARUYAMA	23-233		
Y. MASUI	23-189		
MASAMI MAYUZUMI	23-224, 23-285		
YOSHIHIRO MIZUTANI	23-224, 23-285		
HIROKAZU MORIYA	23-113, 23-129, 23-142		
ANDRE MOURA	23-102		
KOHEI MURAKAMI	23-215		

e-Mail Addresses of Selected Authors

Hiroshi Asanuma	asanuma@ni2.kankyo.tohoku.ac.jp
Anastasopoulos Athanasios	nassos@envirocoustics.gr
Alan Beattie	agbeattie@worldnet.att.net
Hideo Cho	cho@me.aoyama.ac.jp
Manabu Enoki	enoki@rme.mm.t.u-tokyo.ac.jp
Takashi Futatsugi	takashi_futatsugi@ajinomoto.com
M.A. Hamstad	mhamstad@du.edu
Ken-ichi Itakura	itakura@epsilon2.csse.muroran-it.ac.jp
Masahiro Kamata	kamata@fuchinobe.oilfield.slb.com
Yusuke Kumano	kumano@ni2.kankyo.tohoku.ac.jp
Xinglin Lei	xinglin-lei@aist.go.jp
Yoshihiro Mizutani	ymizutan@mes.titech.ac.jp
Hirokazu Moriya	hirokazu@ni2.kankyo.tohoku.ac.jp
Hideyuki Nakamura	hideyuki_nakamura@iic.ihc.co.jp
Katsumi Nemoto	nemoto@geo.kankyo.tohoku.ac.jp
Masayasu Ohtsu	ohtsu@gpo.kumamoto-u.ac.jp
Kanji Ono	ono@ucla.edu
Rolando Rios Soberanis	rolando@cicy.mx
Jerzy Schmidt	schmidt@iod.krakow.pl
Tomoki Shiotani	Tomoki_Shiotani@tobishima.co.jp
Shin Takahashi	shin.takahashi@nifty.com
M. Takemoto	takemoto@me.aoyama.ac.jp
M. Takuma	t940081@ipcku.kansai-u.ac.jp
Shuichi Wakayama	wakayama@ecomp.metro-u.ac.jp
Takahito Yanase	yanase@just-ltd.co.jp
A. Yonezu	akioyonezu@gmail.com
Kenichi Yoshida	yoshida@me.tokushima-u.ac.jp
Shigenori YUYAMA	yuyama@pacjapan.com

JOURNAL OF ACOUSTIC EMISSION

Editor: Kanji Ono

Associate Editors: A. G. Beattie, T. F. Drouillard, M. Ohtsu and W. H. Prosser

1. Aims and Scope of the Journal

Journal of Acoustic Emission is an international journal designed to be of broad interest and use to both researcher and practitioner of acoustic emission. It will publish original contributions of all aspects of research and significant engineering advances in the sciences and applications of acoustic emission. The journal will also publish reviews, the abstracts of papers presented at meetings, technical notes, communications and summaries of reports. Current news of interest to the acoustic emission communities, announcements of future conferences and working group meetings and new products will also be included.

Journal of Acoustic Emission includes the following classes of subject matters;

A. Research Articles: Manuscripts should represent completed original work embodying the results of extensive investigation. These will be judged for scientific and technical merit.

B. Applications: Articles must present significant advances in the engineering applications of acoustic emission. Material will be subject to reviews for adequate description of procedures, substantial database and objective interpretation.

C. Technical Notes and Communications: These allow publications of short items of current interest, new or improved experimental techniques and procedures, discussion of published articles and relevant applications.

D. AE Literature section will collect the titles and abstracts of papers published elsewhere and those presented at meetings and conferences. Reports and programs of conferences and symposia will also be presented.

E. AE Program and Data Files: Original program files and data files that can be read by others and analyzed will be distributed in CD-ROM.

Reviews, Tutorial Articles and Special Contributions will address the subjects of general interest. Nontechnical part will cover book reviews, significant personal and technical accomplishments, current news and new products.

2. Endorsement

Acoustic Emission Working Group (AEWG), European Working Group on Acoustic Emission (EWGAE), Committee on Acoustic Emission from Reinforced Composites (CARP), and Acoustic Emission Working Group of India have endorsed the publication of Journal of Acoustic Emission.

3. Governing Body

The Editor and Associate Editors will implement the editorial policies described above. The Editorial Board will advise the editors on any major change. The Editor, Professor Kanji Ono, has the general responsibility for all the matters. Associate Editors assist the review processes as lead reviewers. Mr. Thomas F. Drouillard is

responsible for the AE Literature section. The members of the Editorial Board are selected for their knowledge and experience on AE and will advise and assist the editors on the publication policies and other aspects. The Board presently includes the following members:

A. A. Anastassopoulos	(Greece)
F.C. Beall	(USA)
J. Bohse	(Germany)
P. Cole	(UK)
L. Golaski	(Poland)
M.A. Hamstad	(USA)
H.R. Hardy, Jr.	(USA)
K. M. Holford	(UK)
O.Y. Kwon	(Korea)
J.C. Lenain	(France)
P. Mazal	(Czech Republic)
S.L. McBride	(Canada)
A.A. Pollock	(USA)
F. Rauscher	(Austria)
I. Roman	(Israel)
Tomoki Shiotani	(Japan)
M. Takemoto	(Japan)
P. Tscheliesnig	(Austria)
H. Vallen	(Germany)
M. Wevers	(Belgium)
B.R.A. Wood	(Australia)

4. Publication

Journal of Acoustic Emission is published annually in CD-ROM by Acoustic Emission Group, PMB 409, 4924 Balboa Blvd, Encino, CA 91316. It may also be reached at 6531 Boelter Hall, University of California, Los Angeles, California 90095-1595 (USA). tel. 310-825-5233. FAX 818-990-1686. e-mail: kanjiono@gmail.com

5. Subscription

Subscription should be sent to Acoustic Emission Group. Annual rate for 2006 is US \$111.00 including CD-ROM delivery, by priority mail in the U.S. and by air for Canada and elsewhere. For additional print copy, add \$40. Overseas orders must be paid in US currencies with a check drawn on a US bank. Inquire for individual (with institutional order) and bookseller discounts.

6. Advertisement

No advertisement will be accepted, but announcements for books, training courses and future meetings on AE will be included without charge.

Notes for Contributors

1. General

The Journal will publish contributions from all parts of the world and manuscripts for publication should be submitted to the Editor. Send to:

Professor Kanji Ono, Editor - JAE
6531 Boelter Hall, MSE Dept.
University of California
Los Angeles, California 90095-1595 USA
FAX (1) 818-990-1686
e-mail: ono@ucla.edu

Authors of any AE related publications are encouraged to send a copy for inclusion in the AE Literature section to:

Mr. T.F. Drouillard, Associate Editor - JAE
11791 Spruce Canyon Circle
Golden, Colorado 80403 USA

Only papers not previously published will be accepted. Authors must agree to transfer the copyright to the Journal and not to publish elsewhere, the same paper submitted to and accepted by the Journal. A paper is acceptable if it is a revision of a governmental or organizational report, or if it is based on a paper published with limited distribution.

Compilation of annotated data files will be accepted for inclusion in CD-ROM distribution, so that others can share in their analysis for research as well as training. ASCII or widely accepted data formats will be required.

The language of the Journal is English. All papers should be written concisely and clearly.

2. Page Charges

No page charge is levied. One copy of CD-ROM will be supplied to the authors free of charge.

3. Manuscript for Review

Manuscripts for review need only to be typed legibly; preferably, double-spaced on only one side of the page with wide margins. The title should be brief. An abstract of 100-200 words is needed for Research and Applications articles. Except for short communications, descriptive heading should be used to divide the paper into its component parts. Use the International System of Units (SI).

References to published literature should be quoted in the text citing authors and the year of publication. These are to

be grouped together at the end of the paper in alphabetical and chronological order. Journal references should be arranged as below. Titles for journal or book articles are helpful for readers, but may be omitted.

H.L. Dunegan, D.O. Harris and C.A. Tatro (1968), Eng. Fract. Mech., 1, 105-122.

Y. Krampfner, A. Kawamoto, K. Ono and A.T. Green (1975), "Acoustic Emission Characteristics of Cu Alloys under Low-Cycle Fatigue Conditions," NASA CR-134766, University of California, Los Angeles and Acoustic Emission Tech. Corp., Sacramento, April.

A.E. Lord, Jr. (1975), Physical Acoustics: Principles and Methods, vol. 11, eds. W. P. Mason and R. N. Thurston, Academic Press, New York, pp. 289-353.

Abbreviations of journal titles should follow those used in the ASM Metals Abstracts. In every case, authors' initials, appropriate volume and page numbers should be included. The title of the cited journal reference is optional.

Illustrations and tables should be planned to fit a single page width (6.5"). For the reviewing processes, these need not be of high quality, but submit glossy prints or equivalent electronic files with the final manuscript. Lines and letters should be legible.

4. Review

All manuscripts will be judged by qualified reviewer(s). Each paper is reviewed by one of the editors and may be sent for review by members of the Editorial Board. The Board member may seek another independent review. In case of disputes, the author may request other reviewers.

5. Electronic Media

This Journal will be primarily distributed electronically by CD-ROM. In order to expedite processing and minimize errors, the authors are requested to submit electronic files or floppy disk copy of the paper. We can read Macintosh and IBM PC formats. On the INTERNET, you can send an MS Word file to "ono@ucla.edu".

6. Color Illustration

We can process color illustration needed to enhance the technical content of an article. With the new format, authors are encouraged to use them.

MEETING CALENDAR:

The 49th Meeting of AEWG

The next meeting of AEWG will be at University of California, Berkeley on June 19-21, 2006, organized by Professor Frank Beall. The primer will be held on June 19, 2006 organized by Professor Dave Dornfeld on Acoustic Emission Monitoring of Precision Machining. Registration forms, as well as hotel information regarding this conference, can be found at:

<http://www.cecs.pdx.edu/~nordsr/AEWG/aewg-49.htm>

IAES18, The 18th International AE Symposium

The IAES-18 will be held in Tokyo on July 25-27, 2006. The venue will be Aoyama Gakuin University at Sagamihara. It is sponsored by Japan Society for Non-Destructive Inspection. Professor Mikio Takemoto is the organizer.

<http://www.me.aoyama.ac.jp/IAES/>

EWGAE2006

27th European Conference on Acoustic Emission Testing will be held September 20-22, 2006, in Cardiff, Wales, UK. The meeting is sponsored by EWGAE and Cardiff University. Dr. Karen M. Holford is the organizer. Meeting details can be seen at

<http://www.ewgae.com/>

2006/2007 SUBSCRIPTION RATE

Base rate (CD-ROM) for one year	\$ 103.00
Add Postage of	
U.S. - Priority rate	\$ 8.00
All others - Air mail rate	\$ 8.00
CD-ROM + printed copy, US Media mail: add	\$ 40.00
Print copy only with priority/air shipping	\$140.00
For countries without Global Priority Service,	\$160.00

Payment must be in U.S. dollars drawn on a U.S. bank. Bank transfer accepted at
California Bank and Trust, San Fernando Valley Office (Account No. 080-03416470)
16140 Ventura Blvd, Encino, CA 91436 USA

Back issues available; Inquiry and all orders should be sent to (or Fax 1-818-990-1686):
Acoustic Emission Group
PMB 409, 4924 Balboa Blvd. Encino, CA 91316 USA

For inquiry through Internet, use the following address: kanjiono@gmail.com
Editor-Publisher Kanji Ono Tel. (818) 430-5152
Publication Date of This Issue (Volume 23): 28 February 2006.

EFFECTS OF NOISE ON LAMB-MODE ACOUSTIC-EMISSION ARRIVAL TIMES DETERMINED BY WAVELET TRANSFORM^{#,∞}

M. A. HAMSTAD^{1,2} and A. O'GALLAGHER¹

¹) National Institute of Standards and Technology, Materials Reliability Division (853) 325 Broadway, Boulder, CO 80305-3328 USA. ²) University of Denver, School of Engineering and Computer Science, Department of Engineering, Denver, CO 80208, USA.

Abstract

Precise acoustic emission (AE) signal arrival times of the fundamental Lamb modes can be obtained from the arrival time of the peak wavelet transform (WT) magnitude at a particular frequency of interest. Since these arrival times are not determined from a fixed threshold, they are not affected by dispersion, attenuation and source amplitude. They also correspond to a single group velocity and lead to source location results more accurate than those obtained by traditional AE location calculations based on threshold-based arrival times. In this research, noise-free finite-element modeled (FEM) AE signals were combined with experimental wideband electronic noise to form noisy signals. Since the noise-free signal was available, the changes in the WT-based arrival times from noise-free to noise-altered signals could be quantitatively evaluated. Several signal-to-noise (S/N) ratios were examined in a statistical fashion for three important types of AE sources at three propagation distances and at different radiation angles. The arrival times determined by WTs were obtained for the two different frequency-mode combinations (A_0 at 60 kHz and S_0 at 522 kHz) that represent the most energetic portions of the signals in a large 4.7 mm thick aluminum plate. From the arrival times, statistical calculations of linear source location were also studied to evaluate errors in location accuracy caused by noise. Even at S/N ratios as low as 1 to 1, the location error was 2 % or less for a large majority of the cases. The errors in arrival time were also examined using two alternative time-frequency analysis approaches to obtain the arrival times. One algorithm (Choi-Williams) provided significantly improved results for the noisy signals.

Keywords: Acoustic emission modeling, Finite element modeling, Source location, Wavelet transform, Wideband acoustic emission.

[#]Contribution of the U.S. National Institute of Standards and Technology; not subject to copyright in the United States. [∞]Trade names are included only for complete scientific/technical description; endorsement is neither intended nor implied.

1. Introduction

Previous publications [1, 2] have demonstrated the use of wavelet transform (WT) results to extract accurate acoustic emission (AE) signal arrival times in plate structures. This technique determines arrival times that are independent of threshold, source amplitude, attenuation based on geometric spreading, radiation direction and signal dispersion based on propagation distance. Further, the arrival times correspond to a single group velocity (Lamb waves) of an energetic mode-frequency combination in the signal. A wideband AE signal database for several buried-dipole-type sources in a thin aluminum plate was used for these demonstrations. This database was a subset of a broader database that was generated using a validated finite element modeling

code [3-5]. The level of numerical noise in the AE signals obtained from the code is less by approximately three orders of magnitude than the typical out-of-plane displacement signal levels produced by the code.

Since real AE signals normally have significant electronic noise that is superimposed on the AE source-based signal, the purpose of the research reported here was to determine the effects of electronic (sensor/preamplifier-based) noise on the accuracy of WT-based arrival times. The finite element model results are ideal for such a study since the noise-free signals are available. This situation is not the case with experimental AE signals. Further, with experimental signals the exact location of the source is unknown, while for the finite-element signals the precise locations of the source and pseudo sensor(s) are known.

2. Finite Element Modeled AE Signal Database

The signal database used in the research reported here has been described in previous publications [1, 2, 6 and 7]. To provide a ready reference to key information, certain aspects are summarized here. The signals were generated by finite-element modeling (FEM) in an aluminum plate (1 m x 1 m x 4.7 mm). The AE signals represent the out-of-plane top-surface displacement as recorded by a perfect flat-with-frequency point-contact sensor. The AE signals were modeled for three in-plane propagation distances (60 mm, 120 mm and 180 mm from the source epicenter) and seven in-plane radiation angles (0° [x-direction], 12° , 22.5° , 45° , 67.5° , 78° , and 90° [y-direction]). All the FEM signals were numerically processed with a 40 kHz (four-pole Butterworth) high-pass filter followed by resampling from 44.6 ns/point to 0.1 μ s/point. The AE signals were based on a 1.5 μ s source rise time, and they were examined out to 150 μ s after the source operation time. This procedure avoids the plate edge reflections, which appear well after the direct signals.

Table 1 provides pertinent information on the buried dipole-type AE sources used for a detailed examination of the effects of electronic sensor/preamplifier noise. Initially the study focused on data at a propagation distance of 180 mm and a radiation direction of 0° . The six FEM cases described in the table were selected based upon the desire to include AE signal cases with the following features. First, an AE signal where its primary energy (as evaluated by a WT) was in the low frequency region of the fundamental antisymmetric Lamb mode. Second, a case where the primary signal energy was in the high frequency portion of the fundamental symmetric Lamb mode. Third, a case where the primary-signal energy was approximately equally distributed between these two portions of the fundamental modes. And fourth, additional cases so that each of the three selected source types was represented at two source depths. The source types selected were an in-plane dipole (aligned in the 0° direction), a microcrack initiation (with the primary dipole in the 0° direction), and a shear (without a moment) about the y-axis with the shear directions at 45° to the x and z axes. Previous research [1, 7] had identified the primary WT signal energy for this plate and these AE sources to be at the mode and key frequency combinations of A_0 at 60 kHz and S_0 at 522 kHz. Table 1 specifies the dominant mode and frequency combination(s) for each case of source type and source depth. The table also provides the relevant average group velocities [1, 7] and the ratio of the WT peak magnitudes (for each case) of the two mode and frequency combinations.

Table 1 Description of the source cases examined. [1, 7]

Case number	Source (depth in mm)	WT-based high intensity mode(s) and freq., kHz	Average group velocity, mm/ μ s	Ratio of noise-free WT peak magnitudes (A_0 at 60)/ S_0 at 522 and (reciprocal)
9034	Shear w/o moment (0.783)	A_0 at 60	2.5	5.6 (0.18)
9004	Micro-crack initiation (1.41)	A_0 at 60	2.5	4.1 (0.24)
2793	In-plane dipole (1.723)	A_0 at 60	2.5	1.3 (0.77)
9002	Micro-crack initiation (2.037)	A_0 at 60 S_0 at 522	2.5 1.8	1 (1) 1 (1)
9030	Shear w/o moment (2.037)	S_0 at 522	1.8	0.41 (2.3)
2791	In-plane dipole (2.35)	S_0 at 522	1.8	No A_0 mode

3. Wavelet Transform Information

The WT results were obtained using the AGU-Vallen Wavelet freeware [8], with the key parameter settings being: maximum frequency = 700 kHz; frequency resolution = 3 kHz and wavelet size = 600 samples. The Wavelet Time Range Setting for the number of samples (i.e., points) was 1500. Thus, the signal was analyzed from the source operation time out to 150 μ s. This allowed the full-direct-arrival signal to be transformed. The software automatically determines the arrival times of the peak WT magnitude at selected frequencies (for a 3-kHz wide band, starting at the selected frequencies of 60 and 522 kHz). The resolution of the arrival times was taken at 0.1 μ s to correspond to the time resolution of the resampled FEM-based signals. The correspondence of the determined arrival times with the fundamental Lamb modes was facilitated by the software option that superimposed the group velocity curves on the WT results.

4. Description of Noise Signals and Creation of Modeled AE Signals plus Noise

To make the study of the effect of electronic noise as realistic as possible, the noise signals were obtained from a wideband high sensitivity conical sensor developed at NIST-Boulder [9, 10]. The noise signals were recorded at a preamplifier gain of 55 dB with the sensor coupled only to air and protected by soft foam from any airborne signals. A total of ten noise signals were available. Each signal had been digitized by a 12-bit waveform recorder with a sampling interval of 0.1 μ s per point, which corresponded to the resampled FEM signals. Each signal was about 16000 points in length, which resulted in the ten signals representing a total of about 16 ms of noise. The typical crest factor of the signals was 4.2. A typical time domain and Fast Fourier Transform (FFT) from one of these ten signals is shown in Fig. 1. The slightly smoothed FFT was calculated after the signals had been numerically bandpass filtered (six-pole Butterworth) from 40 kHz to 1.2 MHz. This filter was used to make all the noise signals more representative of the frequency range of the FEM signals. After modifying the noise signal amplitudes (so they were less than the FEM signal amplitudes) and changing the units to picometers, the signals were examined to determine their consistency. First, the peak magnitudes for the 10 noise signals were determined. The mean peak magnitude was found to be 0.63 pm with a dispersion of 10 % and a range of 0.54 to 0.73 pm. Thus, the different noise signals were considered to be relatively uniform in their peak signal magnitudes.

Figure 2 shows the WT result of about an 800 μ s portion of a typical noise signal. Figure 3 demonstrates typical plots of the noise WT magnitude versus time at each of the two key

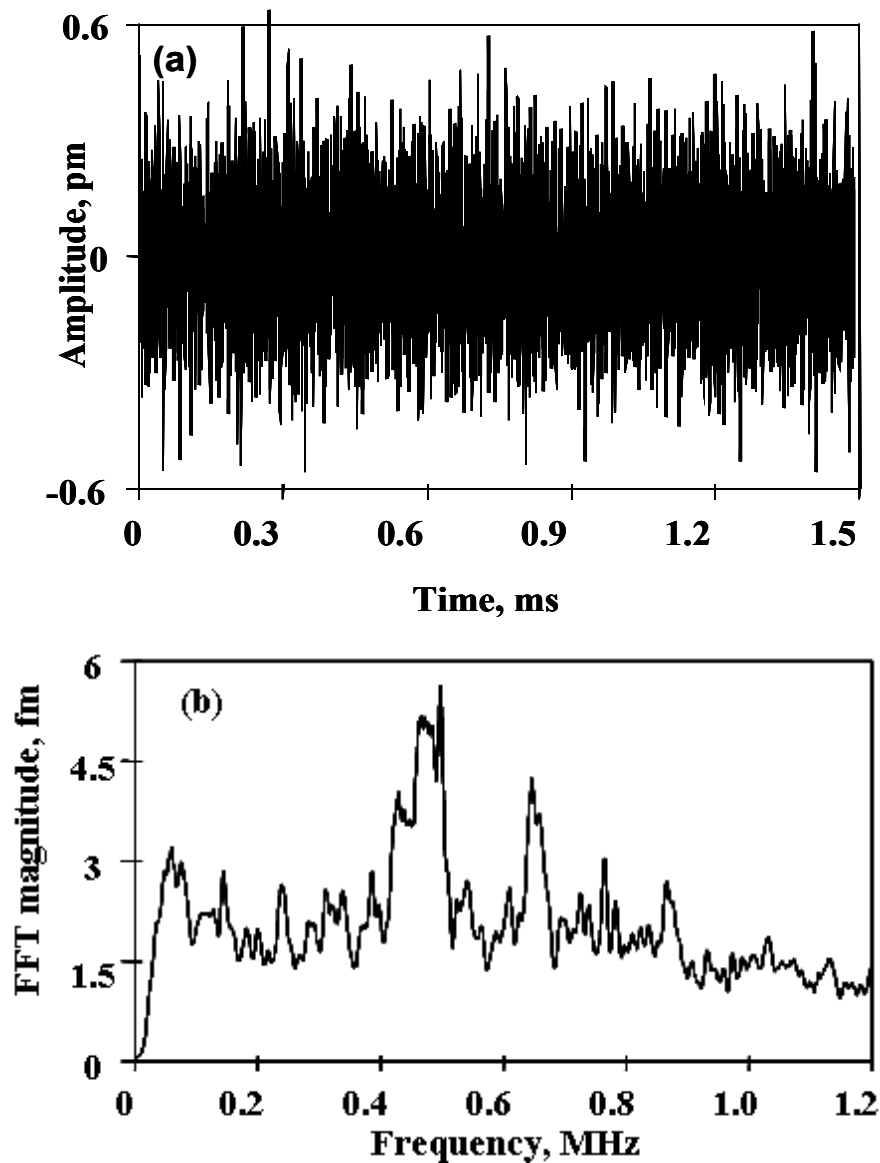


Fig. 1 Time domain (a) and FFT (b) of a typical noise signal (after a gain of 55 dB) of 16384 points at $0.1 \mu\text{s}/\text{point}$.

frequencies. It is clear from this figure that the WT magnitude versus time varies over a wide range for each of the two key frequencies. The figure also shows that the number of fluctuations of the WT magnitudes increases with increasing frequency (likely a characteristic of the WT used in this research). Further, the WT magnitude variations in Fig. 3 indicate that, when noise is added to the FEM-generated AE signals, the WT peak magnitudes of the signal plus noise (S+N) could experience noise-induced modifications. Since, for real-world AE signals, the amplitudes of the WTs of the underlying noise signal at the times of mode arrivals would be a random and unpredictable condition, a statistical study of noise effects on arrival times was necessary.

To form a suitable noise database for a statistical study, a total of 50 different noise segments, each nominally $160 \mu\text{s}$ in length, was extracted (after the filtering and amplitude change, as described above) from the modified database of ten noise signals. A S+N database was then constructed for the selected FEM cases (source type and depth) of interest. For each case the same 50 noise signals were added to the FEM-based (noise-free) AE signal to form a database of

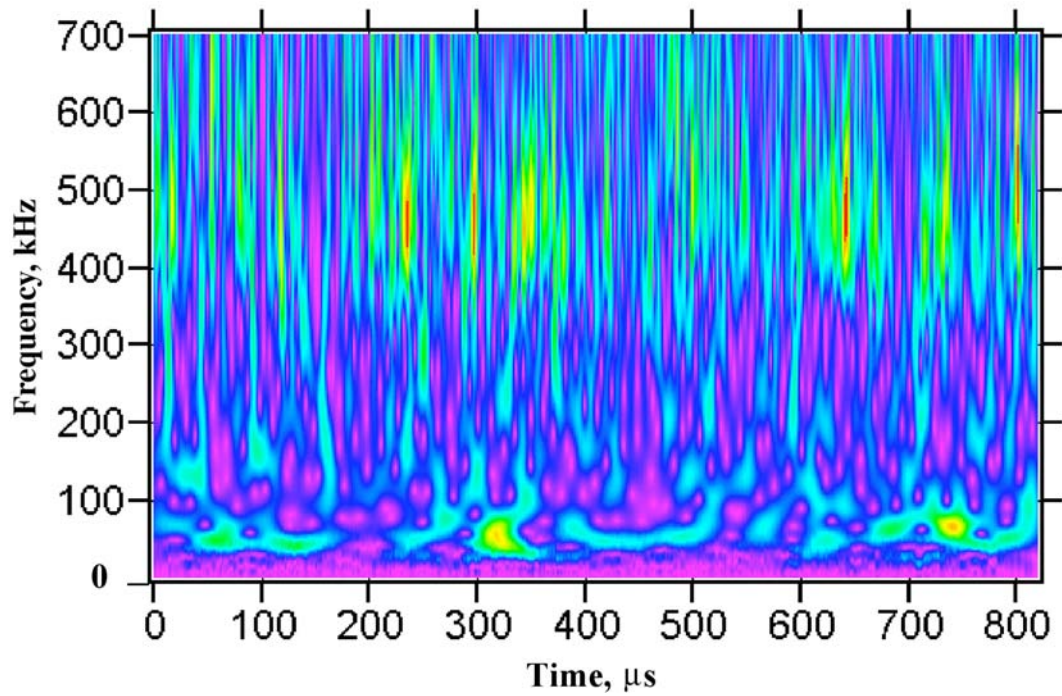


Fig. 2 Wavelet transform of a 819.2 μs portion of a typical noise signal. Color (maximum is red) or contrast shows WT intensity

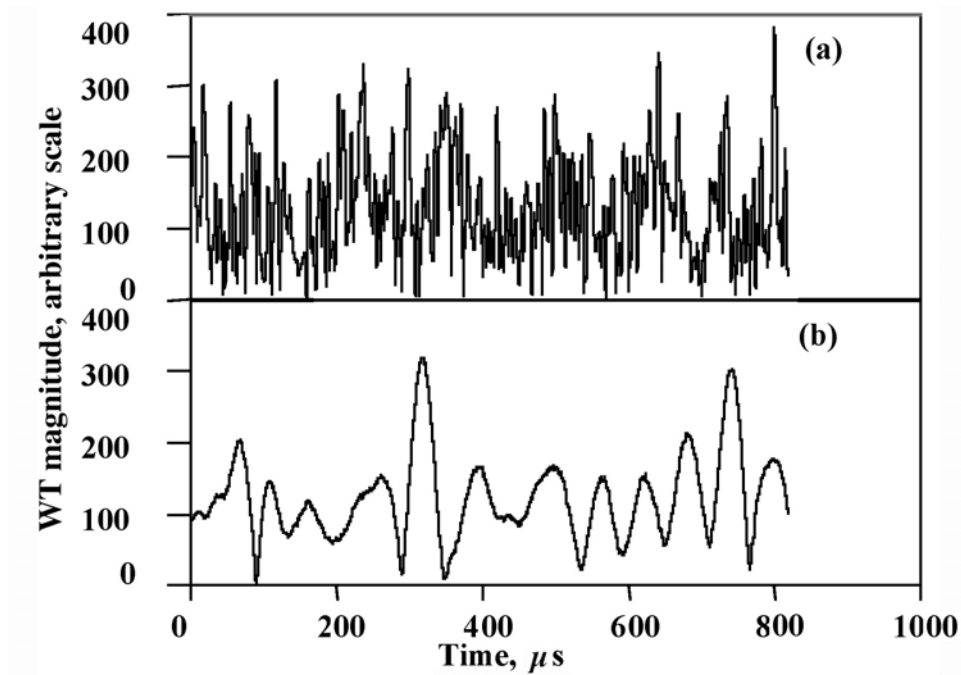


Fig. 3 Magnitude of wavelet transformation (a) at 522 kHz and (b) at 60 kHz versus time for a typical 819.2 μs noise signal.

50 S+N signals. Before adding the noise signals they were multiplied by a factor to obtain a certain S/N ratio. This S/N ratio was based on the peak amplitude of each noise-free FEM signal and the mean peak amplitude (0.63 pm) representative of all the noise signals. The 50 S+N signals were called a “set” of S+N signals for a given FEM signal case. In order to be able to directly track the effects of different S/N ratios applied to the same FEM-based noise-free signals,

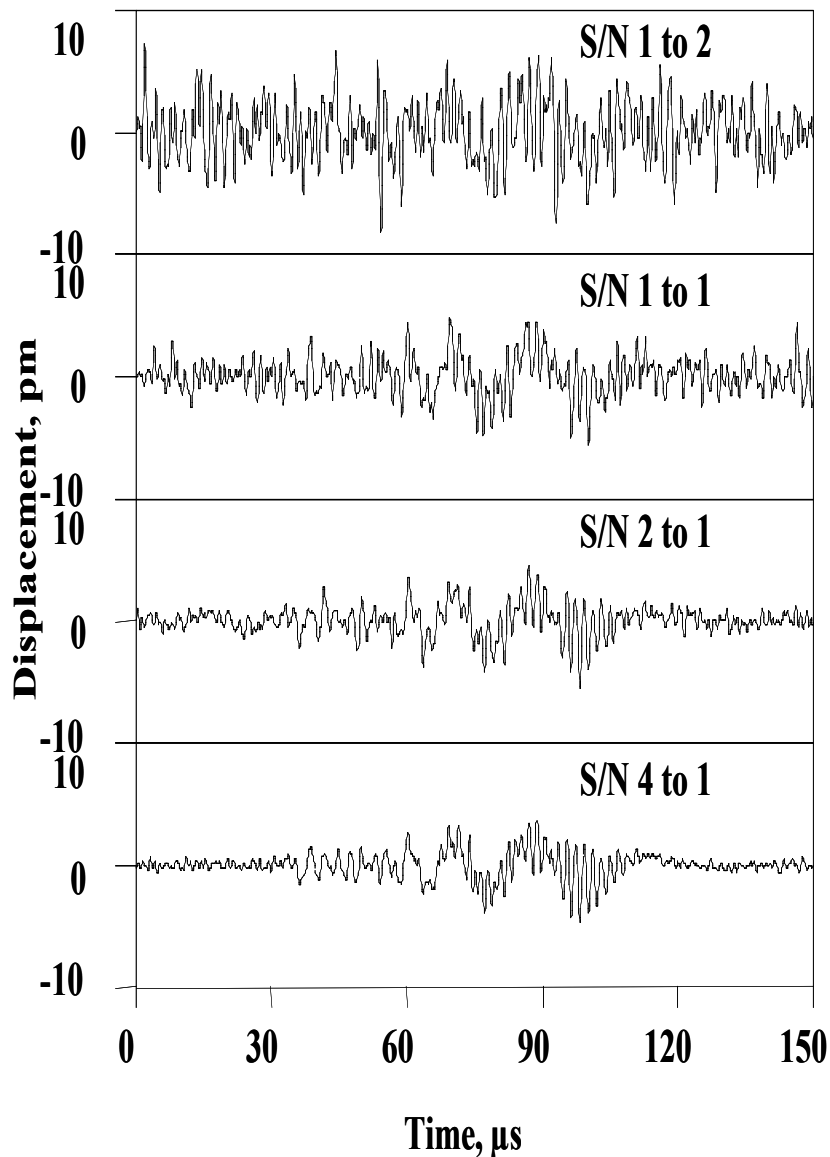


Fig. 4 Typical examples of S+N signals for case 2793 at four different S/N ratios.

the same sequence of noise signals (multiplied by a different factor to create a different S/N ratio) was added respectively to the noise-free signal to form each “set” of S+N signals. WTs of the S+N signals were then carried out for each case for the different S/N ratios, and the appropriate arrival times were obtained. Figure 4 shows examples of the S+N signals for case 2793 at four different S/N ratios.

5. Effects of Electronic Noise on WT-Determined S+N Signal Arrival Times (at a propagation distance of 180 mm in the zero-degree radiation direction)

For each case (AE source type, source depth and S/N ratio), a total of 50 arrival times at the mode and frequency combination(s) (shown in Table 1) was obtained from the WT results. The 50 arrival times represent the effect of the random variation in the noise. Table 2 shows a statistical characterization of the arrival times as a function of the S/N ratio for one source type and depth (case 2793; see Fig. 4). The table provides the average arrival time, maximum time, minimum time and sample standard deviation (SD), as well as the noise-free arrival time. Even

Table 2 Statistical characterization of 50 arrival times for the in-plane dipole source (case 2793) as a function of the S/N ratio for 180 mm propagation distance and at 0° radiation direction.

S/N Ratio	Avg., μs	Max., μs	Min., μs	SD, μs	Noise-free time, μs
1 to 2	81.2	113.7	73.6	8.2	78.2
1 to 1	77.4	80.7	73.8	1.6	78.2
2 to 1	77.9	78.8	75.6	0.8	78.2
4 to 1	78.2	78.4	77.7	0.1	78.2

Table 3 The average and standard deviation (50 samples) of the arrival times for all the cases in Table 1 for 180 mm propagation distance at 0° radiation direction.

Case number and frequency, kHz	Avg. arrival time and SD, μs with S/N at 1 to 2	Avg. arrival time and SD, μs with S/N at 1 to 1	Noise-free arrival time, μs
9034 (60)	77.4 (2.2)	77.5 (1.1)	77.9
9004 (60)	77.4 (1.9)	77.6 (1.0)	78.0
2793 (60)	81.2 (8.2)	77.4 (1.57)	78.2
9002 (60)	78.4 (13)	77.5 (1.9)	78.2
9002 (522)	87.7 (28)	98.1 (4.2)	98.2
9030 (522)	94.2 (15)	98.1 (1.63)	98.0
2791 (522)	92.6 (17)	98.7 (1.55)	98.0

at an S/N ratio of 1 to 1, the maximum and minimum times of 80.7 μs and 73.8 μs are not large deviations from the noise-free value of 78.2 μs . To justify the conclusion that these maximum and minimum times are not large, a threshold-based determination of possible arrival times was made for the relevant noise-free signal. Since the threshold method depends on the actual threshold used, a range of thresholds was used (equivalent to varying AE source signal amplitudes with a fixed threshold). The range of arrival times determined was from 32.9 μs to 75.2 μs . This range of 42.3 μs is clearly much larger than the WT-based range of 6.3 μs at the 1 to 1 S/N ratio. We note again that the WT method is independent of threshold. Thus the threshold-based method would likely lead to significant location errors compared to the WT approach.

Table 3 shows the average and sample standard deviations (SDs) of the arrival times for all the cases (listed in Table 1) at two S/N ratios (1 to 2 and 1 to 1). The results at two additional S/N ratios (2 to 1 and 4 to 1) were nearly identical to the noise-free values as is illustrated for one case in Table 2. Thus those results are not shown here. Compared to the noise-free arrival times, the average values are quite close to the noise-free values, even at an S/N ratio of 1 to 2.

6. Discussion of Above Results

In subsequent discussions, the evaluation of the magnitude of noise-based arrival time errors was based on comparisons of the sample SDs. The decision to use this measure arose from the observation that smaller SDs indicated that the arrival times were tightly grouped around the mean values. As Table 3 shows, the mean values at an S/N ratio of 1 to 1 were all very near the noise-free arrival times. We assert that the smaller the SDs, the smaller the range of noise-induced arrival time errors and the smaller the subsequent location errors.

Examination of the results in Table 3 leads to the interesting observation that the SDs are the largest for case 9002 for each of the two key frequencies and for each S/N ratio. As can be seen in Table 1, the FEM-based noise-free signal for this case exhibited significant energy (in the WT magnitude results) at both key frequency and mode combinations. This observation implies that when the noise-free AE signal energy is significant in more than one mode, then errors in WT-based arrival times will be greater than when the signal energy is predominantly in a portion of a single mode. This conclusion is consistent with the fact that when the FEM displacement signal amplitude is determined by two modes, the WT peaks from those individual modes will be smaller relative to the WT magnitudes of the noise as compared to the case where the FEM signal is significantly dominated by a single frequency/mode. This conclusion is also consistent with the fact that the S/N ratio was related to the time domain, while the WT-based results come from a time *and* frequency domain.

An important question relates as to whether the type of source changes the accuracy of WT-based arrival times when noisy signals are examined. If the information in the last column in Table 1 is considered in relation to the SDs of the arrival times (see Table 3) at an S/N ratio of 1 to 1, there is a correlation. In particular, the greater the dominance of the noise-free peak WT magnitude of the dominant frequency/mode combination, the smaller the SDs. The converse applies the smaller the dominance. As with case 9002 above, this result is related to the fact that the S/N ratio is from the time domain, and the arrival times are from the frequency/time domain. Hence at a certain S/N ratio, strong single-mode dominance means that a greater proportion of the WT magnitude comes from the source-based signal relative to the WT magnitude contribution from the noise. The WT contribution from the noise does not depend on the source type, while that from the source-based signal can be from one or two modes. Thus, it is not the source type, but the magnitude of the modal dominance in the displacement signal, that is significant. Previously published work [2, 6] has shown that the modal dominance is directly related to the depth of the point source below the plate surface, and that the source type typically has only a minor effect on the relative magnitudes of the modes generated.

When the frequency dependence of the results in Table 3 was examined at the S/N ratio of 1 to 2, it is found that the SDs were the largest for the cases where the 522 kHz/ S_0 mode dominates. This conclusion was not surprising considering the typical FFT spectrum of the noise demonstrated in Fig. 2. The figure shows a region of higher noise near this frequency. To quantify the WT magnitude difference of noise between the two frequency bands (3 kHz wide) the 50 noise signals were studied. The WT peak magnitudes at both 60 and 522 kHz were obtained over a signal length of 150 μ s. The average (for 50 samples) WT peak values at each frequency were obtained and their ratio was found. The average 522 kHz WT peak magnitude was found to be 1.6 times the average for the 60 kHz WT peak. This result implies that the peak regions of the noise spectrum can be used to predict the frequencies where the noise will likely result in the largest errors in WT-determined arrival times.

7. Effects of Radiation Angle (at a propagation distance of 180 mm)

To specifically examine the effects of radiation angle on the accuracy of WT-based arrival times for signals with noise, it was decided to ignore changes in signal amplitudes as the radiation angle changed from zero to 90 degrees. Thus the S/N ratios (for this examination) were calculated based on the signal peak amplitude in the specific radiation direction under consideration. Hence, the arrival time errors at radiation angles other than zero could be directly compared

at the same S/N ratio with the results for the zero-degree radiation direction. Only three cases were chosen to examine the effects of radiation angle. This decision was based on the fact that in the previous section all the trends were apparent within the results for cases 9002, 9004 and 9030 (selected from Table 1).

In review, case 9002 provided a case where both frequency and mode combinations were significant. And cases 9004 and 9030 provided examples where the 60 kHz/A₀ and 522 kHz/S₀ combinations respectively had a strong dominance. The S/N ratio considered was limited to 1 to 1 since in the above section the major trends were apparent at this ratio. In addition, to compare with the above section results, the propagation distance was limited to 180 mm.

Table 4 The standard deviation (50 samples) of the arrival times at two different angles for 180 mm propagation distance and an S/N ratio of 1 to 1.

Case number and (frequency, kHz)	SD, μ s at zero deg.	Ratio: noise-free WT peak at indicated freq./alt. freq. value at 0°	SD, μ s at 45°	Ratio: noise-free WT peak at indicated freq./alt. freq. value at 45°	SD, μ s at 67.5°	Ratio: noise-free WT peak at indicated freq./alt. freq. value at 67.5°
9004 (60)	0.99	4.1	-----	-----	0.96	33
9002 (60)	1.9	1.01	1.3	1.5	-----	-----
9002 (522)	4.2	0.99	12	0.68	-----	-----
9030 (522)	1.6	2.3	-----	-----	1.7	3.2

Table 4 shows the arrival time sample SD results at angles greater than 0° for 50 samples at an S/N ratio of 1 to 1 along with the results at the 0° angle to allow a direct comparison. The results indicate that the SD at the larger angle is about the same as the value at the zero-degree radiation angle when a strong dominance of one mode and frequency combination is present. But in case 9002, where both combinations had significant magnitudes, the SD results differed at the larger angle compared to those at the 0° angle. In particular the arrival time errors had a higher SD at 45° compared to the SD at 0° for the 522 kHz/S₀ mode, while the arrival time errors had a lower SD at 45° for the 60 kHz/A₀ mode compared to the 0° direction. This observation is consistent with the discussion in the previous section about the effect of the level of dominance of the frequency/mode combinations. When the noise-free WT peak magnitude ratio of 60 kHz/A₀ over 522 kHz/S₀ was calculated, the ratio at 0° was 1, and at 45° it was 1.5 (see Table 4). Thus, due to the source radiation characteristics, the 60 kHz/A₀ mode content of the signal increases at the larger radiation angle, while the 522 kHz/S₀ mode content decreases. Hence the noise has a smaller effect on the arrival error results for the 60 kHz/A₀ mode, and the converse applies for the 522 kHz/S₀ mode at the larger radiation angle. These results indicate that, as a general conclusion, the dependence (at a certain S/N ratio) of arrival time errors on radiation angle will again depend on the level of dominance of the dominant frequency and mode combination as the radiation angle varies.

8. Effects of Propagation Distance (in the zero-degree radiation direction)

Since it is well known that the amplitude of AE signals falls off with increasing propagation distance, the same philosophy used for the radiation angle study was used in the examination of

the effect of propagation distance. Namely, the noise levels were adjusted such that at each propagation distance the actual S/N ratio was the same. Hence, direct comparisons at the same S/N ratio could be made at the different distances. For all of the cases in Table 1 the arrival times at the 60 and 120 mm propagation distances (0° radiation direction) were determined from the WT-based technique at two S/N ratios: 1 to 2 and 1 to 1. As before, it is most insightful to make comparisons using the SDs of the arrival times that were determined for the 50 trials for each case. Table 5 shows the SDs for an S/N ratio of 1 to 1 at these two distances along with the previously documented results from 180 mm (Table 3).

Table 5 The standard deviation (50 samples) of the arrival times at three different propagation distances for the 0° propagation direction and S/N of 1 to 1.

Case number and (frequency, kHz)	SD, μ s at 60 mm and rank* ()	SD, μ s at 120 mm and rank* ()	SD, μ s at 180 mm and rank* ()
9034 (60)	1.5 (4)	1.0 (2)	1.1 (2)
9004 (60)	1.6 (5)	0.74 (1)	0.99 (1)
2793 (60)	3.0 (6)	1.51 (5)	1.57 (4)
9002 (60)	5.8 (7)	5.3 (7)	1.9 (6)
9002 (522)	1.3 (3)	3.0 (6)	4.2 (7)
9030 (522)	0.84 (1)	1.45 (4)	1.63 (5)
2791 (522)	0.97 (2)	1.2 (3)	1.55 (3)

*Lowest S/N is rank (1)

Table 6 Ratios of noise-free WT peak magnitudes (dominant magnitude in the numerator) at the two key frequencies as a function of propagation distance in 0° direction.

Case number	At 60 mm, dominant frequency (kHz) shown	At 120 mm, dominant frequency (kHz) shown	At 180 mm, dominant frequency (kHz) shown
9034	4.3 (60)	5.0 (60)	5.6 (60)
9004	3.1 (60)	3.4 (60)	4.1 (60)
2793	1.0 (522)	1.2 (60)	1.3 (60)
9002	1.3 (522)	1.1 (522)	1.0 (60)
9030	3.0 (522)	2.5 (522)	2.4 (522)
2791	N.A.*(522)	N.A.*(522)	N.A.*(522)

* No A_0 mode present

To facilitate the discussion of the effects of propagation distance on the SDs, the results in Table 5 at each distance have been numerically ranked from the best (1) with the lowest SD to the worst (7) with the largest SD. In order to try to “break” ties, extra decimal places have been shown in some cases. Clearly the order changes at the 1 to 1 S/N ratio as the propagation distance changes. Some general trends in Table 5 can be associated with the relative level of dominance of the modes. Table 6 shows how the ratios of the two WT peak magnitudes of the noise-free signals varied for the different source cases and propagation distances along the 0° direction. When the 60 kHz/ A_0 mode dominates, the ratio is (60 kHz/ A_0 mode magnitude)/(522 kHz/ S_0 mode magnitude). For each case, the changes in the ratios only show the effect of the propagation distance. Table 6 clearly shows the relative peak WT magnitudes for the 522 kHz/ S_0 mode fall off with increasing propagation distance (Cases 9002 and 9034). In contrast, Cases 9034 and 9004 show the relative 60 kHz/ A_0 mode peak WT magnitudes increasing with distance. A proposed cause for this effect will be discussed in the next section.

Based on the results in Table 6, we note that the ranking in Table 5 (at a certain propagation distance) of the best to worst SD for each frequency and mode generally correlates with the amount of relative dominance of that frequency/mode regardless of the propagation distance. For example at 60 mm, the best SD for case 9034 has a strong dominance for the 60 kHz/ A_0 mode (4.3, see Table 6), and the worst SD for case 9002 is actually dominated by the 522 kHz/ S_0 mode (1.3, see Table 6). Table 6 also provides a reason for the SD ranking (in Table 5) changing with the propagation distance. The increase in 60 kHz/ A_0 mode dominance (see Table 6) with increasing distance correlates with the observation that at the larger propagation distances the 60 kHz/ A_0 mode generally has the best SDs, except for one case (we ignore case 9002 since both modes have about the same peak magnitude). The results for case (2791) rank as one of the best at all the propagation distances due to the fact that the dominance of the 522 kHz/ S_0 mode is very strong since there is no A_0 mode for this midplane source.

A question arises, why are the 522 kHz/ S_0 mode results the best at the 60 mm distance even though there are two 60 kHz/ A_0 cases (9034 and 9004) with strong dominance? The answer to this question is likely due to the “spreading in time” of the WT results at lower frequencies. The “spreading in time” terminology refers to the signal at a specific time contributing to the WT magnitudes over a range in time about that specific time. This characteristic at lower frequencies is illustrated in Fig. 5. In this figure the input signal to the WT is a Dirac delta function. Thus we suggest the 60 kHz/ A_0 mode WT peak magnitude arrival time has larger errors since the WT peak magnitude in that case reflects a wider time-range of the noise signal (see Fig. 5). In contrast, the 522 kHz/ S_0 mode WT magnitude does not have the same range of arrival time errors because the WT peak magnitude at that frequency does not result from as wide a time range of the noise signal. At the longer propagation distances, the drop in the dominance of the 522 kHz/ S_0 mode is evidently sufficient to allow the higher magnitude noise in the region of 522 kHz (see Fig. 2) to increase the SDs. This results in the 60 kHz/ A_0 mode SDs being generally the lowest at the longer distances.

9. Relative Fall-off of the 522 kHz/ S_0 Mode with Increased Propagation Distance

The 522 kHz/ S_0 mode falls-off at a faster rate than the 60 kHz/ A_0 mode with increasing propagation distance as is shown in Table 6. Since the finite element modeling results did not incorporate the available frequency-based attenuation with propagation distance, the source of this frequency/mode fall-off is of interest. Since the frequency band is only 3 kHz wide in the WT computation, there should not be much dispersion with increasing propagation distance. To check this assumption, the profile of the WT magnitude (at each of the two frequencies) as a function of time was plotted for one of the cases (case 9002, noise-free signal) at the three propagation distances. The normalized results in Fig. 6 show some potential dispersion for the 522 kHz/ S_0 mode. For example, at 60 % of the peak magnitude of the 522 kHz profile (in the largest magnitude peak region) the width of the profile increases by 50 % as the propagation distance increases from 60 mm to 180 mm. On the other hand, the change of width over those propagation distances at this level was not perceptible for the 60 kHz mode. It is suspected that this fall-off can be attributed to the following observations. In the 522 kHz region of the S_0 mode, the group velocity curve makes nearly a “U-turn” (see Fig. 1 in reference 1) in the group velocity direction over a limited range of frequency change. Thus a range of frequencies in this region have about the same group velocity. This feature, in combination with the characteristic of the WT described next, likely causes this attenuation.

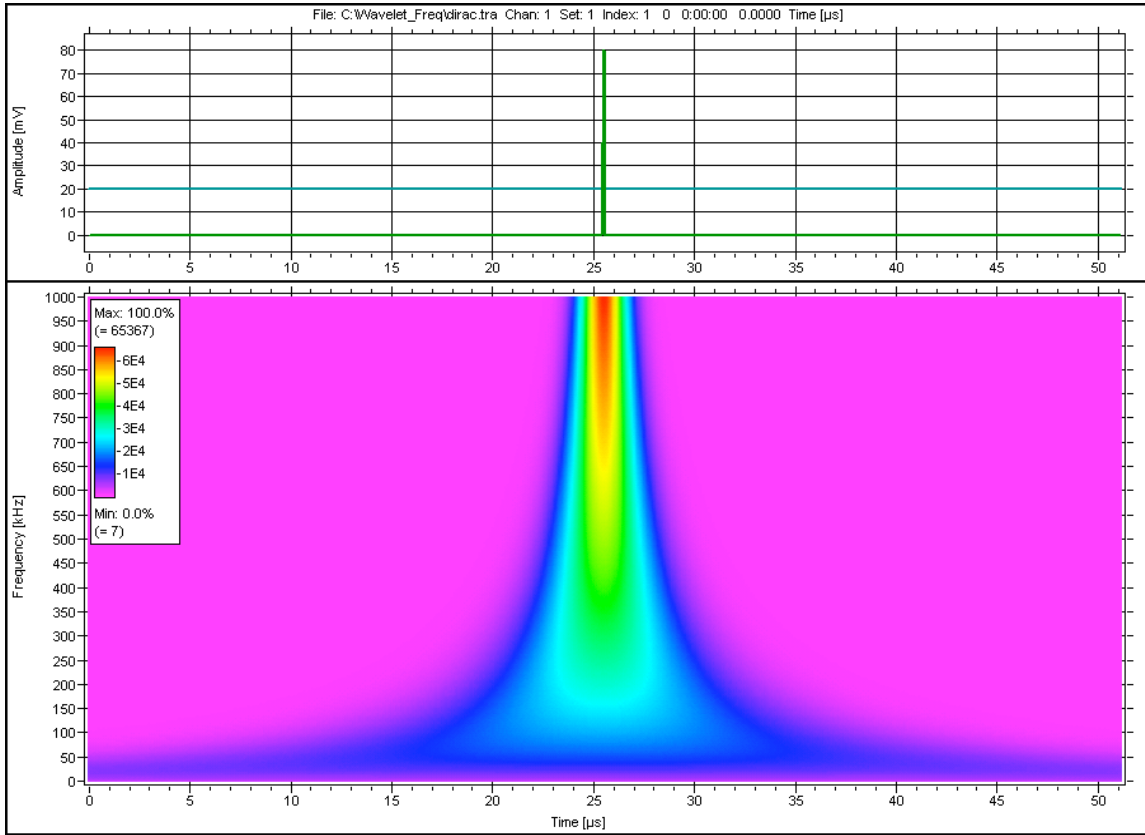


Fig. 5 WT result with input signal of a Dirac delta function (amplitude in mV) as shown in the upper time domain. Vertical frequency scale of WT result (lower part of figure) from 0 to 1 MHz and time scale of both plots 0 to 51.2 μ s. Color or contrast shows the WT magnitude.

Figure 7 shows that the WT used in this research has the characteristic of its magnitude “spreading in frequency” at higher frequencies. This “spreading in frequency” means that the signal at a specific frequency contributes to the WT magnitudes over a range of frequencies about the specific frequency. This effect does not appear in Fig. 7 at lower frequencies. The WT shown in Fig. 7 was created from a time-domain signal that was made up of a sinusoidal signal that has a change in frequency from 60 kHz to 522 kHz, as is shown in the top portion of the figure. The two sinusoidal portions of the time-domain signal had equal amplitudes, yet the WT result has significantly lower peak magnitude (only about 36 % of the 60 kHz value), with obvious “spreading in frequency” for the sinusoidal portion of the signal at the single frequency of 522 kHz. Thus it seems likely that the combination of the “spread in frequency” and the “U-turn” results in the “attenuation” of the 522 kHz/ S_0 WT peak magnitude with increasing propagation distance. Thus the supposed dispersion-based “attenuation” is really related to the characteristics of the WT used in this research in combination with the shape of the group velocity curves in a particular region.

10. Location Errors versus S/N Ratio

The statistical properties discussed above do not directly address the important issue raised by the potential for noise to alter WT-based signal arrival times. The central issue concerns the effect of arrival time errors on the accuracy of the calculated AE source location. To address this question, a decision was made to focus on linear location. This choice was based on a desire to

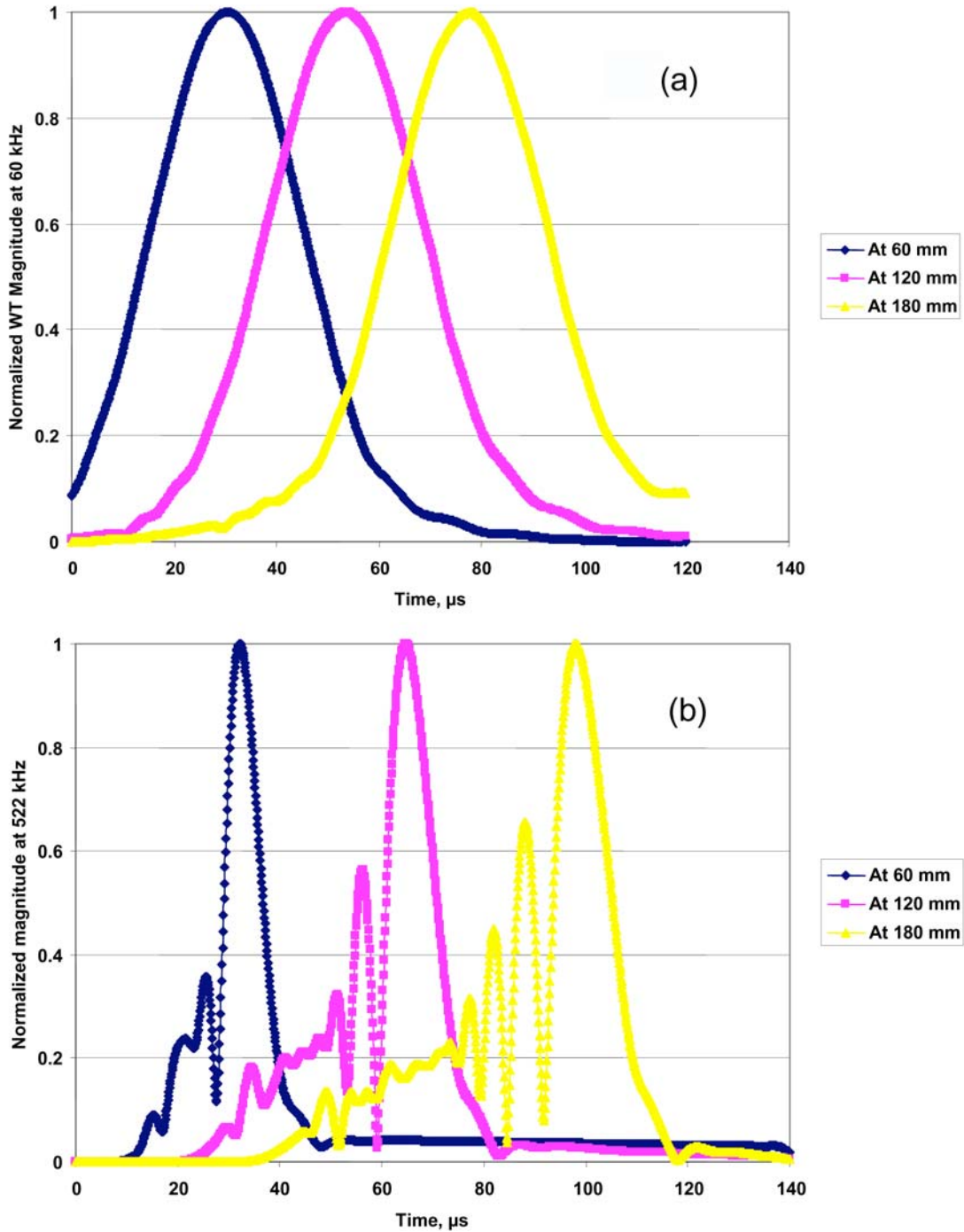


Fig. 6(a) Profile of WT magnitude at 60 kHz versus time and (b) profile of WT magnitude at 522 kHz versus time, both for case 9004.

remove any dependence of the location error-analysis results on the particular computational scheme used for two-dimensional location calculations. Figure 8 shows a schematic of the linear location geometry and the notation used in this paper. Straightforward manipulation of the governing equations leads to the following:

$$d_1 = 0.5 [d - c_g (t_2 - t_1)], \quad (1)$$

$$d_2 = 0.5 [d + c_g (t_2 - t_1)], \quad (2)$$

$$d = d_1 + d_2, \quad (3)$$

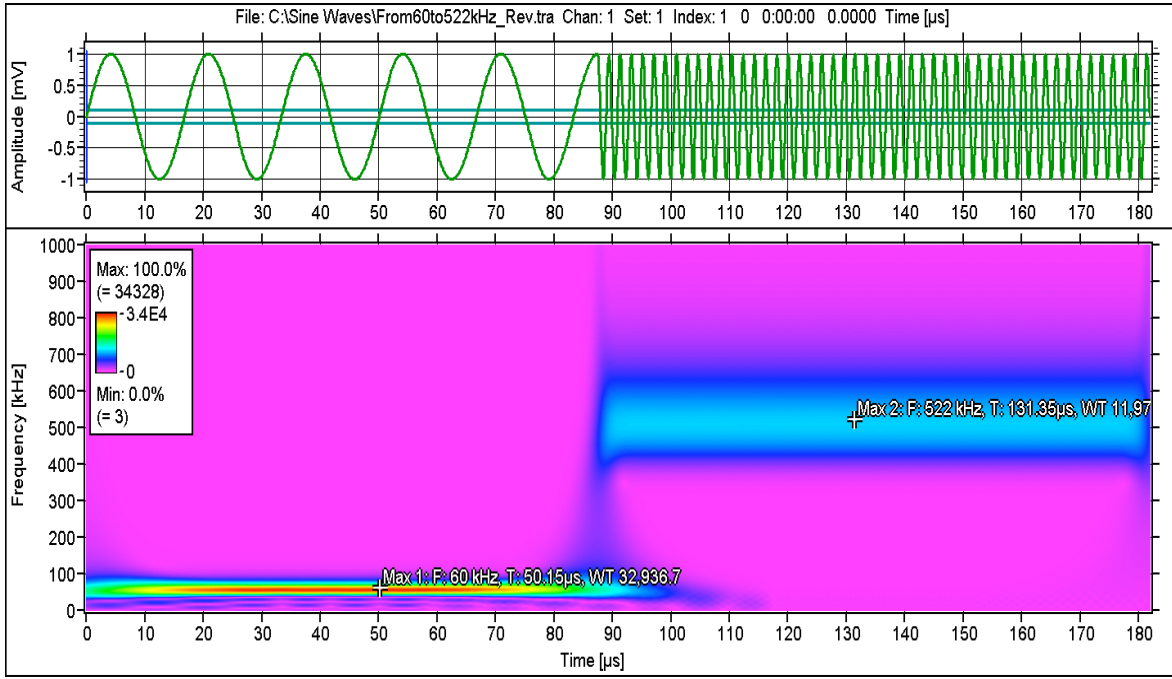


Fig. 7 Signal and WT of the signal. Signal is 60 kHz sine wave followed by 522 kHz sine wave of same amplitude. WT maximum magnitudes of 32,937 and 11,970 for 60 kHz, and 522 kHz portions of WT.

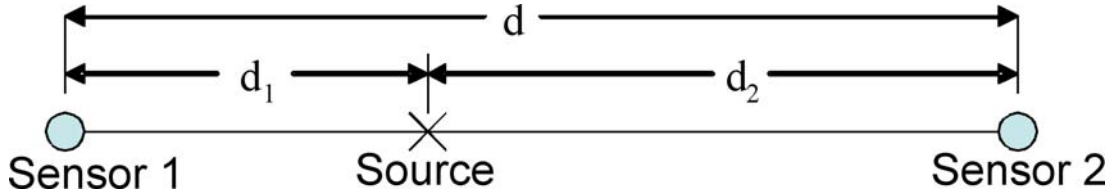


Fig. 8 Geometry for linear location equations.

where c_g is the appropriate group velocity, d is the sensor spacing, d_1 is the distance from the first hit sensor to the source location, and d_2 is the distance from the second hit sensor. The values t_1 and t_2 are the respective arrival times. To allow the analysis to focus directly on arrival time errors due to the addition of noise, it was decided to consider geometry where the source was equally spaced between the two sensors. With this approach, when two different S+N signals (associated with the same noise-free case) are used to calculate a location, the location error will be directly due to noise-altered arrival times. When noise is present, equations (1) and (2) can be rewritten (with italics to denote the values when noise is present) as:

$$d_1 = 0.5 [d - c_g (\pm e)], \quad (4)$$

$$d_2 = 0.5 [d + c_g (\pm e)], \quad (5)$$

where $e = |t_1 - t_2| > 0$ is the arrival *time-difference* error. On an absolute value basis the percent location errors in d_1 and d_2 values are equal, and this error is given by

$$\text{percent error} = [(c_g \cdot e) / d] \times 100 \%. \quad (6)$$

To form databases of time differences for each case (source type, depth and S/N ratio) the 50 arrival times obtained from each “set” were used in the following fashion. The absolute value differences of the first arrival time and each of the subsequent 49 values was determined.

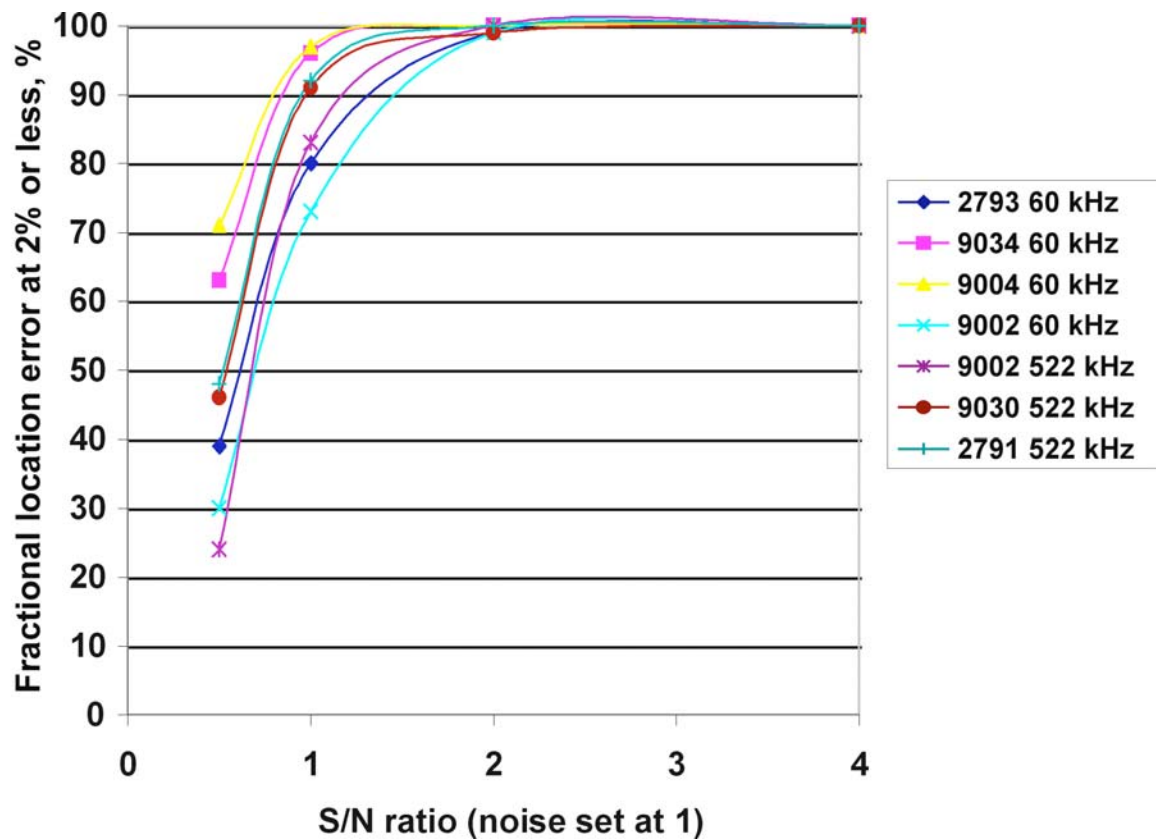


Fig. 9 Fraction (%) of the 1225 calculated locations with an error of 2 % or less as a function of the S/N ratio for all cases (source type and depth).

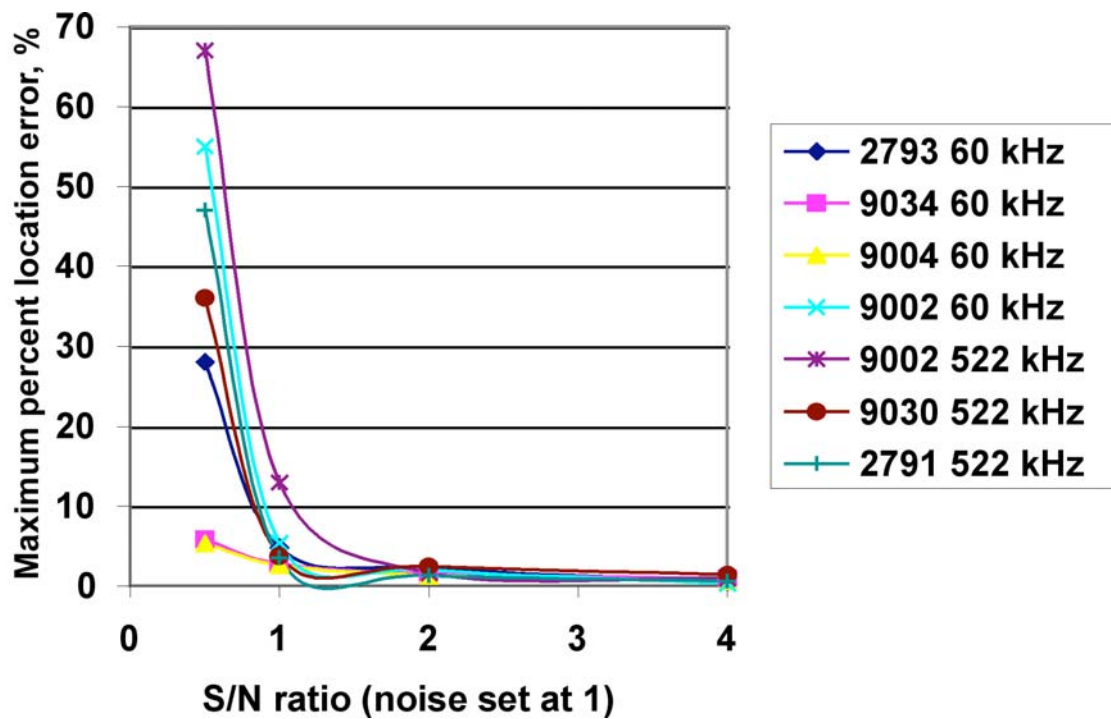


Fig. 10 Maximum location error (%) for the 1225 calculated locations for all cases as a function of the S/N ratio (Note that the dip in the curves between S/N ratios of 1 to 2 is an artifact of the plotting routine).

Then the absolute value differences of the second arrival time and each of the subsequent 48 values were determined. This process was continued in a similar fashion so that a total of 1225 arrival time differences were obtained for each case. These differences correspond to the e values in equation (6). By use of equation (6), the location errors were determined for each of the 1225 arrival time differences. Figure 9 shows as a function of the S/N ratio, the percentage of the 1225 trials for each case when the location error was 2 % or less based upon the sensor spacing (360 mm) for a nominal propagation distance of 180 mm in the zero-degree direction. In addition, Fig. 10 illustrates the maximum location error found in the 1225 trials for each case as a function of the S/N ratios.

The data illustrated in Fig. 9 demonstrates that even with an S/N ratio of 1 to 1, at least 73 % of the 1225 location calculations for each case resulted in a location error that was 2 % or less. Further, Fig. 10 shows the maximum location error for the 1225 location calculations for each case was 13 % or less. To appreciate these results, it should be pointed out that a typical fixed-threshold AE system would not even trigger on any of these signals because the required low threshold would trigger on multiple noise spikes. Hence, the technique used here could be of value for an AE acquisition system that records continuously.

At a 2 to 1 S/N ratio, Fig. 9 shows that at least 99 % of the 1225 location calculations for each case would have location errors of 2 % or less. Figure 10 also shows the maximum location errors would be 2.4 % or less. With an S/N ratio of 2 to 1, a fixed-threshold AE system would likely trigger on real AE signals instead of noise spikes. And for a source equidistant between the sensors, the location errors would not be great. The reason is that the factors of geometric attenuation, dispersion, and variations in source amplitude would be the same for the signal at both sensors. But for a fixed-threshold system, when the source is not equidistant from all the sensors, the above three factors would typically result in relatively large location errors compared to the 2 % location error limit used in this research. On the other hand, the WT-based determination of arrival times would not be affected by the above three factors.

11. Discussion of Location Error Results at a 180-mm Propagation Distance

To better appreciate just how good the above location results are the following facts must be considered. The noise level was taken at the average peak value of the original set of ten noise signals. If it had been set at the peak value (0.73 pm) of the ten signals, then the S/N ratios of 1 to 1 and 2 to 1 would have been 0.86 to 1 and 1.73 to 1. Even these S/N ratios are conservative values from the view of a typical AE experimentalist, since the peak was that for only about 16 ms of noise signal data.

The analysis presented in equations (1) through (6) predicts that the error in the location should depend linearly on the group velocity, c_g . Clearly Figs. 9 and 10 do not support that conclusion. The lower group velocity of 1.8 mm/ μ s for 522 kHz/ S_0 does not give the expected better results. This lack of dependence on c_g is likely due to the previously discussed high noise-signal energy in the region of the 522 kHz frequency. This higher noise was evidently sufficient to overcome the expected dependence on c_g .

For further discussion of the location results, it makes the most sense to focus on the fraction of the 1225 trials that resulted in location errors of 2 % or less. The reason for this focus is that these results represent the average results over many trials. In contrast, the results of the

maximum location error represent only the worst case out of the 1225 trials for each source case and S/N ratio.

With this focus, we can examine in more detail the cases that give the best and worst results for the fraction of trials with location errors of 2 % or less. In each case it will be shown that the same facts apply that explained the general trends of the ordering of the results by SDs of the arrival times for these cases. Hence these discussions will not be as detailed as they were in the discussions of arrival times.

If the order of the best (highest fraction with small location errors) to worst results in Fig. 9 (at 0° , 180 mm and S/N ratios of 1 to 2 and 1 to 1) is examined, the best results are for the cases with a strong dominance of the 60 kHz/ A_0 mode (9004 and 9034) trailed by the results for the strong dominance of the 522 kHz/ S_0 mode (2791 and 9030). The reasons for the cases with strong single mode dominance being best were already described in the discussion of arrival time results. In addition this ordering of the results relates to the “attenuation”, as discussed previously, of the 522 kHz/ S_0 mode with propagation distance. This attenuation increases the dominance of the 60 kHz/ A_0 mode at a propagation distance of 180 mm. The worst location error results are for the cases (9002 and 2793) where both frequency/mode combinations are significant in the noise-free signals. In these cases, as previously described, neither mode overpowers the noise. The case (2791), which has a strong dominance of the 522 kHz/ S_0 mode, is not among the best due to the extra noise in the vicinity of that frequency.

12. Location Error Effects of Propagation Distance and Radiation Angle

To examine the effect of propagation distance on source location errors, one must consider Fig. 11. This figure shows the fraction of trials with errors in location less than or equal to 2 % at the propagation distances of 60, 120, and 180 mm for S/N ratios of 1 to 1 and 2 to 1. The first observation is that the percentage of the 1225 trials with small location errors increases with increasing propagation distance. This result is not unexpected since the calculation of the location error has the sensor spacing in the denominator. Thus, with similar SDs of the arrival times at the different distances, the larger denominator will result in a smaller fractional error at the longer distances.

The second observation is that the ranking of best to worst location accuracy changes with propagation distance. These changes follow the same pattern that was observed for the dependence of the arrival time errors on propagation distance. The general explanation of this behavior follows exactly the previous explanation given for the ranking in arrival time errors. These factors are the greater “attenuation” of the 522 kHz/ S_0 mode as compared to the 60 kHz/ A_0 mode with increasing propagation distance; the characteristic of the noise signal having increased noise in the vicinity of the 522 kHz frequency; and the “spreading in time” of the WT magnitudes at low frequencies versus higher frequencies.

Table 7 shows the location errors for the three cases used for the study of the effects of the radiation direction on arrival times at the S/N ratio of 1 to 1. If the order of the best (highest percentage of trials with a location error of 2 % or less) to worst location errors are examined, then the results for cases 9004 and 9030 show little change with the change in radiation angle since the primary frequency/mode combination has a strong dominance at both angles (see Table 7). As before, however, for arrival time errors for case 9002, the rankings of location error accuracy change with the changes in the radiation angle. The change is due to the radiation pattern of the

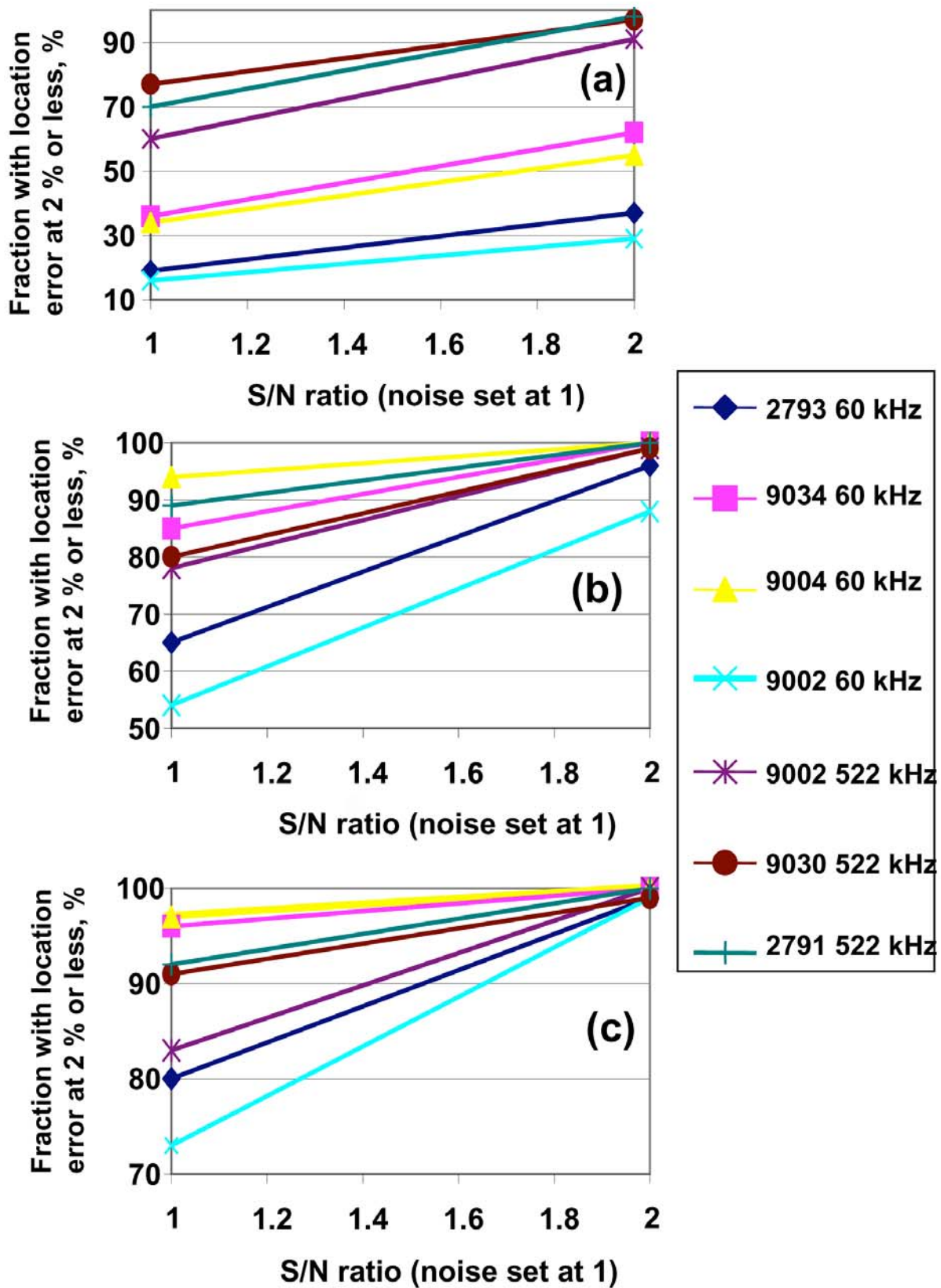


Fig. 11 Fraction of the 1225 calculated locations with an error of 2 % or less at S/N ratios of 1 to 1 and 2 to 1 for all cases (source type and depth) at propagation distances of (a) 60 mm, (b) 120 mm and (c) 180 mm.

two modes not being the same and both modes being significant in the signal. The result is that 9002 (60 kHz/ A_0) has a higher fraction with low location error at 45°, since that mode becomes more dominant at 45° versus 0°. And the opposite is the case for 9002 (522 kHz/ S_0), since the effect of the radiation pattern reduces the dominance of that mode at 45° versus 0°.

Table 7 The percentage of the 1225 time differences with a location error $\leq 2\%$ at two different radiation angles for 180 mm propagation distance and an S/N ratio of 1 to 1.

Case number and (frequency, kHz)	% of trials with location error $\leq 2\%$ at 0°.	Ratio: noise-free WT peak at indicated freq./alt. freq. value at zero deg.	% of trials with location error $\leq 2\%$ at 45°	Ratio: noise-free WT peak at indicated freq./alt. freq. value at 0°.	% of trials with location error $\leq 2\%$ at 67.5°	Ratio: noise-free WT peak at indicated freq./alt. freq. value at 67.5°.
9004 (60)	97	4.1	-----	-----	97	33
9002 (60)	73	1.01	91	1.5	-----	-----
9002 (522)	83	0.99	62	0.68	-----	-----
9030 (522)	91	2.3	-----	-----	91	3.2

13. Alternate Joint Time-Frequency Analysis Algorithms

Since time-frequency analysis results can be dependent on the particular algorithm used [see reference 11 for a discussion of various techniques], this research also examined the errors in mode arrival times determined when noise is present by the use of alternate (relative to the WT) joint time-frequency analysis algorithms. We choose to use the Adaptive Spectrogram and the Choi-Williams Distribution (spectrogram) in their LabVIEW™ implementations and compared their results with those obtained from the WT. The joint time-frequency analysis (JTFA) algorithms provide the instantaneous power spectrum over time [12]. A number of these JTFA algorithms were available. After using these on some of the FEM-based signals, it was decided to focus on two of them. These were the Easy Adaptive Spectrogram (ADS) and the Easy Choi-Williams Distribution (CWD). The results from either of these can be displayed in a plot of frequency versus time with the colors representing the intensity of the signal energy at the time and frequency values. Figure 12 shows for case 9002 that the JTFA results are qualitatively very similar to the WT results.

In this research both the ADS and CWD results were calculated so as to maintain the 0.1 μ s resolution of the original time-domain signals. The frequency resolution could be selected based only on powers of two applied over the range of zero to 5 MHz (based presumably on the Nyquist frequency for the time-domain signals). This led to the choice of a frequency resolution of either 1.22 kHz or 2.44 kHz. To be as consistent as possible with the WT nominal resolution of 3 kHz, the 2.44 kHz resolution was chosen. The ADS results were calculated with the “no-zoom” implementation, the number of terms parameter set at two and the mode parameter selection of “chirplet”. In all other aspects the Easy ADS and CWD implementations were used with the default settings. Also one other selection was made, namely the intensity of the JTFA results was multiplied by 10^{26} to be able to obtain intensity results with larger numbers. These larger numbers were more convenient to use.

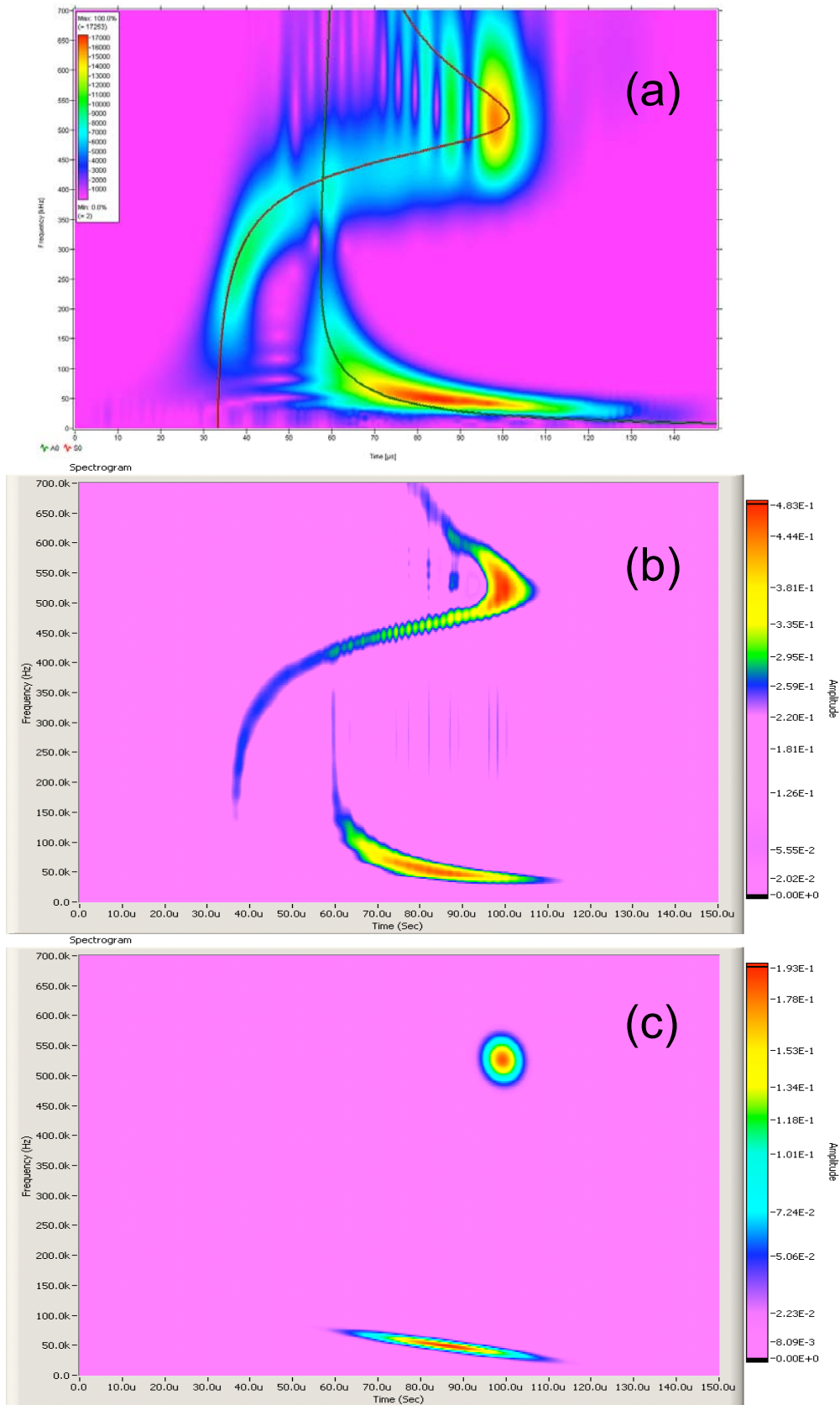


Fig. 12 Spectrograms of WT (a), CWD (b) and ADS (c) for case 9002. Scaling of 0 to 700 kHz vertical and 0 to 150 μ s horizontal. Note that non-linear amplitude (color or contrast) scales were used in (b) and (c) to better show the two modes.

14. Comparison of Results with the JTFA and the WT for Noise-free Signals

To create a comparison of the WT with the two selected JTFA spectrograms, the noise-free signals were used for three key cases (9004, 9002 and 9030) in Table 1. The arrival times of the peak magnitudes of the JTFA frequency bands nearest the 60 and 522 kHz values were determined for the dominant frequency/mode in each case for the 0° radiation direction and a propagation distance of 180 mm. The nominal frequency bands over which the peak spectrogram magnitudes were determined were (a) WT at 60 to 63 kHz and 522 to 525 kHz and (b) ADS and CWD at 61 to 63.5 kHz and 522.5 to 524.9 kHz. Table 8 shows the results for the noise-free signals compared to the previously determined WT results. As can be seen from the table, the arrival time results are very similar. Thus the peak magnitudes of the key frequencies in the JTFA spectrograms do in fact correspond to the Lamb mode arrivals as was seen for the WT. The table also shows the level of dominance of the primary frequency/mode as determined by the peak magnitude ratios for each case. It is of interest to note that the levels of dominance were generally considerably higher for the CWD and ADS than for the WT.

Table 8 Comparison of noise-free arrival times and relative dominance of the modes for the wavelet transform (WT), Choi-Williams (CWD) distribution and Adaptive (ADS) spectrogram at a propagation distance of 180 mm and direction of 0°.

Case number and (frequency, kHz) of arrival time	WT noise-free arrival time, μ s	Ratio: noise-free WT dominant peak /alt. mode value	CWD noise-free arrival time, μ s	Ratio: noise-free CWD dominant peak /alt. mode value	ADS noise-free arrival time, μ s	Ratio: noise-free ADS dominant peak /alt. mode value
9004 (60)	78.0	4.1 (60)*	77.3	14 (60)*	75.6	13 (60)*
9002 (60)	78.2	1 (60)*	77.2	1.1 (522)*	75.3	1.3 (522)*
9002 (522)	98.2	1 (60)*	100.0	1.1 (522)*	99.1	1.3 (522)*
9030 (522)	98.0	2.3 (522)*	99.8	6.2 (522)*	99.2	7.8 (522)*

* Most dominant frequency in kHz

15. Comparison of Arrival Time Results with the JTFAs and the WT

To compare the different spectrogram approaches when noise was present, the three cases from the previous section at a propagation distance of 180 mm and the zero-degree propagation direction were used. As before, case 9004 was used since it has a strong dominance of the 60 kHz/A₀ mode. Case 2791 was used since it has a strong dominance of the 522 kHz/S₀ mode. And case 9002 was used since both of the above modes have a significant presence. As was done with the WT, the arrival times were calculated for 50 S+N signals of each of the three cases. Table 9 shows the average arrival times and sample SDs of the peak magnitude determined arrival times for each of the cases at S/N ratios of 1 to 2 and 1 to 1. It should also be recalled that Table 8 shows the level of dominance of the peak mode for each case of the noise-noise signals.

As before, the focus of the relative performance of the different approaches was based on the SDs. Clearly the CWD approach resulted in the lowest SDs followed by the WT and trailed by the ADS. The better performance of the CWD was especially apparent for the S/N ratio of 1 to 2 for cases 9002 and 9030, where the SD with the CWD was substantially lower than that for the

Table 9 Comparison of average arrival times and their SDs (from 50 samples) at S/N ratios of 1 to 2 and 1 to 1 for the Wavelet transform, Choi-Williams distribution and Adaptive spectrogram at a propagation distance of 180 mm and direction of 0°.

Case number and (frequency*, kHz)	WT 1 to 2, Average and (SD), μs	CWD 1 to 2, Average and (SD), μs	ADS 1 to 2, Average and (SD), μs	WT 1 to 1, Average and (SD), μs	CWD 1 to 1, Average and (SD), μs	ADS 1 to 1, Average and (SD), μs
9004 (60)	77.4 (1.9)	77.4 (1.7)	74.1 (8.1)	77.6 (1)	77.4 (0.72)	74 (6.1)
9002 (60)	78.4 (13)	80.5 (8.8)	60.5 (36)	77.5 (1.9)	77.5 (1.6)	74.9 (20)
9002 (522)	87.7 (28)	92.7 (18.7)	82 (37)	98.1 (4.2)	100 (1.5)	95.5 (13)
9030 (522)	94.2 (15)	100.4 (9)	84.7 (32)	98.1 (1.6)	99.3 (1.4)	99 (1.2)

* Most dominant frequency except for 9002 where both frequencies are significant.

WT. For example, for case 9002 for the 60 kHz/ A_0 mode the SD dropped from 13 μs with the WT to 8.8 μs with the CWD, and for the 522 kHz/ S_0 mode the drop was from 28 μs to 19 μs . The SDs at the 1 to 1 S/N ratio were still better with the CWD than with the WT, but the relative improvement was not as large.

16. Conclusions

These direct conclusions are based on the following key conditions: a large 4.7 mm thick aluminum plate; nominal wave propagation distances of 60, 120 and 180 mm; the use of a particular WT; experimental electronic noise from a particular wideband sensor/preamplifier; noise-free signals from finite element modeling that simulates perfect point contact sensors; and the particular six cases of source types and source depths examined in detail.

- Due to the variations in random-noise signals as a function of time, a statistical study of noise-induced errors was necessary.
- At S/N ratios of 1 to 1 and 2 to 1 and a propagation distance of 180 mm in the zero-degree direction, the location error was 2 % or less for at least 73 % and 99 % respectively of the trials considering all six cases.
- At the lower S/N ratios of 1 to 2 and 1 to 1 under the same conditions, the location and arrival time errors were greater if the combination of source type and source depth resulted in a signal with significant energy in portions of both fundamental modes. This result was in contrast to smaller errors in cases where the signal energy was more highly concentrated in a portion of a single mode.
- The order of ranking from smallest to largest errors in location and arrival times changed with propagation distance due to (i) the higher propagation-distance “attenuation” of the 522 kHz/ S_0 mode relative to the 60 kHz/ A_0 mode, (ii) the higher noise amplitude in the vicinity of 522 kHz, and (iii) the “spreading in time” of the WT magnitude at lower frequencies.
- The order of ranking of errors in arrival times and location also changed with radiation direction changes when the relative WT intensity of the 60 kHz and 522 kHz modes changed with the change of direction.
- Use of the WT technique greatly enhanced the accuracy of arrival times for source location calculations, and also can provide reasonably accurate additional arrival times from AE channels where hits would not even be recorded with threshold based systems. This

- application requires the AE waveform system to record the signals from all the sensors in a local array subset when one sensor channel in that array results in a hit being triggered.
- The errors in location with a fixed threshold are expected to be significantly greater, since the measured arrival times at each hit from a single AE event will correspond to different group velocities due to the factors of geometric attenuation, dispersion, and source amplitude. These factors do not alter the arrival times determined with the WT-based approach.

Alternate Spectrogram Techniques:

The comparison of the WT with the CWD and ADS alternative approaches revealed that the lowest SDs of the arrival times were obtained with the CWD. The improved arrival time results with the CWD were substantial at an S/N ratio of 1 to 2. The poorest results were obtained with the ADS method.

On the Extension of These Techniques to Other Cases

The technique of using the results of joint-time-frequency analysis (such as the WT or CWD) to determine very accurate arrival times (of a certain energetic frequency of a mode corresponding to a specific modal group velocity) in the presence of significant background electronic noise is not expected to be limited to the list of key conditions listed at the beginning of the Conclusion section. The potential main limitation of the approach is possibly for thick plates. In this case, potentially many Lamb modes may be present with significant energy such that either the amplitudes of individual modes making up the time domain are all small and/or the presence of so many energetic modes leads to the extracted mode arrival times not being clearly associated with a particular mode.

References

1. Hamstad, M. A., K. S. Downs and A. O’Gallagher “Practical Aspects of Acoustic Emission Source Location by a Wavelet Transform,” *Journal of Acoustic Emission*, **21**, 2003, 70-94, A1-A7.
2. Hamstad, M. A., A. O’Gallagher and J. Gary, “Examination of the Application of a Wavelet Transform to Acoustic Emission Signals: Part 2. Source Location”, *Journal of Acoustic Emission*, **20**, 2002, 62-81.
3. Gary, John and Marvin Hamstad, "On the Far-field Structure of Waves Generated by a Pencil Break on a Thin Plate," *Journal of Acoustic Emission*, **12** (3-4), 1994, 157-170.
4. Prosser, W. H., M. A. Hamstad, J. Gary and A. O’Gallagher, "Reflections of AE Waves in Finite Plates: Finite Element Modeling and Experimental Measurements," *Journal of Acoustic Emission*, **17**, (1-2), 1999, 37-47.
5. Hamstad, M. A., A. O’Gallagher and J. Gary, "Modeling of Buried Acoustic Emission Monopole and Dipole Sources With a Finite Element Technique," *Journal of Acoustic Emission*, **17** (3-4), 1999, 97-110.

6. Hamstad, M. A., A. O’Gallagher and J. Gary, “Examination of the Application of a Wavelet Transform to Acoustic Emission Signals: Part 1. Source Identification”, *Journal of Acoustic Emission*, **20**, 2002, 39-61.
7. Downs, K. S., Hamstad, M. A., and A. O’Gallagher, “Wavelet Transform Signal Processing to Distinguish Different Acoustic Emission Sources,” *Journal of Acoustic Emission*, **21**, 2003, 52-69.
8. Vallen-Systeme GmbH, Munich, Germany, <http://www.vallen.de/wavelet/index.html>, 2001, software version R2002.0703.9. Hamstad, M. A., and C. M. Fortunko, "Development of Practical Wideband High Fidelity Acoustic Emission Sensors," *Nondestructive Evaluation of Aging Bridges and Highways*, Steve Chase, Editor, Proc. SPIE 2456, Published by SPIE – The International Society for Optical Engineering, Bellingham, WA, 1995, pp. 281-288.
10. Hamstad, M. A., "Improved Signal-to-Noise Wideband Acoustic/Ultrasonic Contact Displacement Sensors for Wood and Polymers," *Wood and Fiber Science*, **29** (3), 1997, 239-248.
11. Huang, Norden E., Zheng Shen, Steven R. Long, Manli C. Wu, Hsing H. Shih, Quanan Zhen, Nai-Chyuan Yen, Chi Chao Tung and Henry H. Liu, “The Empirical Mode Decomposition and the Hilbert Spectrum for Nonlinear and Non-stationary Time Series Analysis.” *Proc. R. Soc. Lond. A*, **454**, 1998, 903-995.
12. LabVIEW™ Signal Processing Toolset, Version 7.0.1, National Instruments Corporation, Austin, TX, 2004.

ACOUSTIC EMISSION TECHNIQUE FOR DETECTING DAMAGE AND MECHANISMS OF FRACTURE IN A KNITTED FABRIC REINFORCED COMPOSITE

CARLOS R. RIOS¹, STEVE L. OGIN², CONSTANTINA LEKAKOU² and K. H. LEONG³

¹) Unidad de Materiales, Centro de Investigación Científica de Yucatán, Mérida Yucatán, Mexico; ²) School of Engineering, University of Surrey, Guildford, Surrey GU2 5XH, UK;

³) Cooperative Research Centre for Advanced Composites Structures Ltd., Fishermans Bend, VIC 3207, Australia. Currently PETRONAS Research, Malaysia.

Abstract

The relationship between fiber architecture and the damage accumulation sequence under tensile loading has been investigated for a Milano weft-knitted reinforced composite oriented at a range of angles to the loading direction (0° to 90°) using acoustic emission (AE) technique among others. In order to observe progressive damage accumulation, model sandwich laminates were fabricated using a single layer of the knitted fabric sandwiched between outer plies of unidirectional glass-reinforced epoxy resin. For comparison, commercial composites manufactured with the same knitted fabric as a reinforcement and Derakane vinyl-ester resin as matrix were analyzed. These materials have been characterized for monotonic and cyclic tensile loading. Results have been compared with those found earlier for a single layer and the sandwich model material with epoxy resin as matrix. AE technique was demonstrated to be an excellent method for materials analysis especially in the second case where the matrix is not transparent. AE count rate was used for damage detection and various failure mechanisms were observed in failed specimens, such as cracking at loop cross-over points, resin matrix cracking, fiber-bundle debonding and tensile fracture of fiber bundles.

Keywords: Composite materials, Textiles, Mechanical properties.

1. Introduction

Experimental results obtained on a model material and a composite manufactured by RTM are presented in this paper. First, the structure of the knitted fabric is described, followed by the results on a single knitted layer/epoxy composite using the 2x68 tex fabric. Second, after outlining the mechanical behavior of this material, and the difficulties encountered in analyzing damage propagation due to the premature failure of the material, results on a model sandwich laminate made up of the knitted fabric between the outer 0° -unidirectional glass fiber plies are discussed. These results include tests where the knitted fabric within the sandwich laminate is oriented at different angles to the loading direction. A detailed microstructural relationship between fabric geometry and cracking behavior is discussed; the acoustic emission technique was used to support the investigation of crack initiation and accumulation, especially to understand the damage development along the sample in order to relate the damage behavior and failure to the textile architecture. These results together with tests on the cyclic behavior of the material enable some conclusions to be drawn about the mechanical behavior of the knitted fabric layer during damage accumulation. At the same time, an RTM composite manufactured with the same knitted fabric as a reinforcement but using Derakane vinyl ester resin as matrix was analyzed in order to

understand the similitude on damage development with the model material. The purpose of this last material was the observation of damage behavior on a structural composite of high fiber volume fraction.

Many authors have commented on the development of damage during the tensile loading of knitted-fiber composites. There has been general agreement that (a) for loading in the wale direction, the initiation of damage occurs due to fiber bundle/resin matrix interface failure at the needle or sinker loops, with subsequent linking of this damage to form long cracks; and (b) for loading in the course direction, that the damage initiates from the sides or legs of the loops [1- 3]. However, in most studies to date, it has only been possible to draw conclusions based on analysis of the final fracture surfaces of the composites. In this work, a knitted fabric reinforced composite layer has been fabricated as part of a sandwich laminate, in which the fabric layer is sandwiched between outer plies of unidirectionally reinforced epoxy resin. The resultant model specimens have enabled the sequence of damage to be investigated directly during tensile loading.

2. Experimental Procedures

Milano weft-knitted fabric produced from E-glass yarns (2x68 tex) was used for manufacturing the sandwich panel using a wet impregnation technique. The knitted cloth was cut to size and fixed inside a steel frame using tape around its edges and the frame was placed in a filament winder to wind unidirectional glass fibers around the cloth. The knitted cloth was fixed in the frame in which the wale direction of the cloth was at different angles to outer 0° plies (0°, 30°, 45°, 60° or 90°). The matrix used for the sandwich panel was an epoxy resin (Astor Stag Epoxide Resin, Astor Stag NMA curing agent and Ancamine K61B accelerator). The panel dimensions were 250 mm x 250 mm and the unidirectional plies on each face of the sandwich panels had a nominal thickness of 1 mm, with an overall panel thickness of about 3.1 mm. The overall fiber volume fraction of the laminates was 0.29 although the fiber volume fraction within the central (knitted fabric) layer was much lower (about 0.13). In addition to the sandwich specimens, panels of knitted-fabric reinforced epoxy resin, without the reinforcing outer 0° plies were also manufactured. RTM materials were produced by placing 5 layers of the Milano weft-knitted fabric in a mold, which was injected with Derakane vinyl ester resin resulting in a high fiber volume fraction of 0.47.

Samples of 230-mm length and 20-mm width were cut from the panels for mechanical testing. Aluminum end tabs (50 mm long by 20 mm wide) were used for the tests and strain gauges were bonded transversally and longitudinally near the center of the coupons. An Instron 1196 testing machine was used for the monotonic tests with a constant crosshead speed of 0.5 mm/min. Load/strain data were collected using a data-logger and acoustic emission (AE) events were recorded using an AECL 2100M system, which employs two guard transducers to reduce external noise. The threshold for the AE equipment was established by performing preliminary analysis in order to enable recording of the AE signals from the tests without spurious noise. The processing unit was set to count the number of acoustic events in 0.1 s intervals. Photographs were taken for two purposes: first to examine partially tested samples at different percentage of strain in order to identify the source of the cracks and to obtain the crack density, and second, to examine the fracture surfaces to obtain an overall idea of the crack propagation and fracture surface contours. Optical microscopy was used to analyze and identify the cracking initiation sites and to related them to the architecture of the knitted textile.

3. Results and Discussion

Figure 1 shows the architecture of the Milano 1x1 knitted fabric, which consists of the interlocking of loops of fiber bundles where two single threads knitted in two separate sets of needles are held together by a row of 1x1 rib course. Note that this fabric consists of two main directions: course, the row of the loops in the width direction; and wale, the row of knit loops in the longitudinal direction.

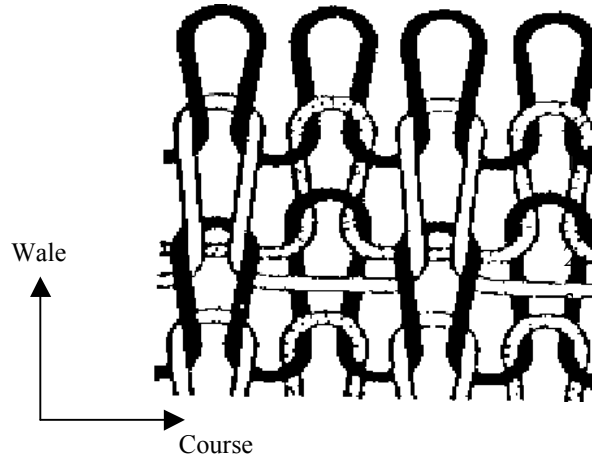


Fig. 1 Architecture of the Milano 1x1 knitted fabric.

Initially laminates containing only one knitted cloth embedded in epoxy resin were manufactured and tested at different angles in order to observe damage progression under tensile loading. However no damage was observed along the samples since samples failed catastrophically when the first signal of damage appeared. No pre-damage was produced. Wale direction presented higher mechanical properties than the others due to a higher portion of fibers oriented at 0° . Fiber volume fraction for single layer laminates was calculated to be 0.13 ± 0.005 .

Due to the sudden fracture of the single layer composite materials, sandwich laminates were made by winding unidirectional glass fibers over the 2x68 tex knitted fabrics as described before. Observation of damage accumulation was facilitated by the transparent nature of the composite, which allowed the plan view damage development to be observed during testing by in situ photography. For all sandwich laminates, the average fiber volume fraction was measured obtaining a value of 0.29 ± 0.002 . Figures 2 and 5 display the strain-stress curve for the samples tested in the 0° (wale), and 90° (course) direction, respectively. For wale direction, the stress-strain curve displays a region of pre-damage, which was registered by AE signal where visual damage is not detected below 1% strain. After this strain value, a first “knee” is observed and a second discontinuity appears at about 1.5%, which is intimately related to the knitted architecture as explains on Fig. 4. AE signals give additional information with respect to the damage development. A small number of AE events are observed between 0.80% and 0.95% strain. This is in advance of the development of the cracks and is related to crack initiation at crossover points in the knitted fabric architecture. Next, in a range of 1.1% to 1.2% strain, the first significant cracks appear producing many more AE events until total fracture of the sample.

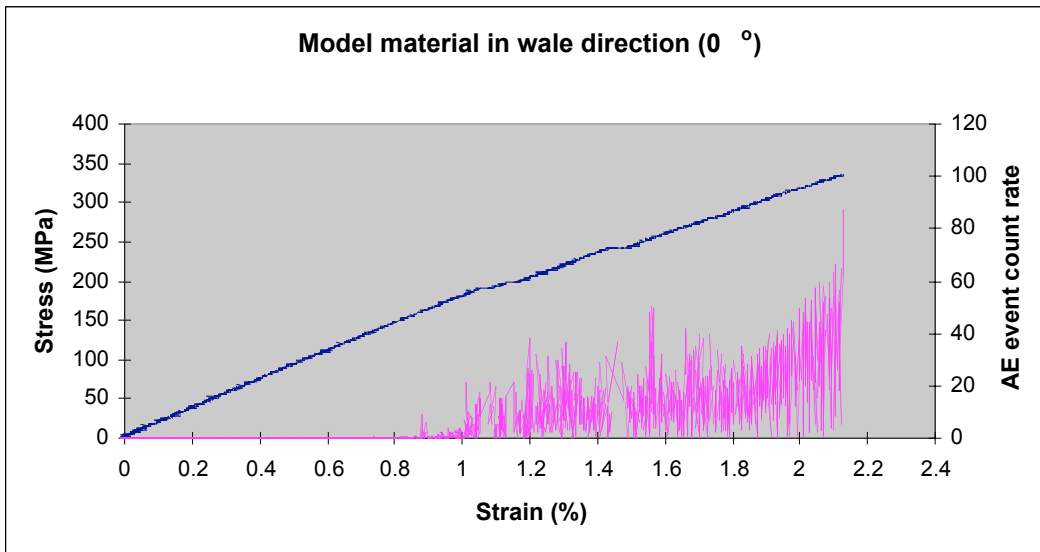


Fig. 2 Stress vs. strain curve for sandwich composite tested in wale (0°) direction.

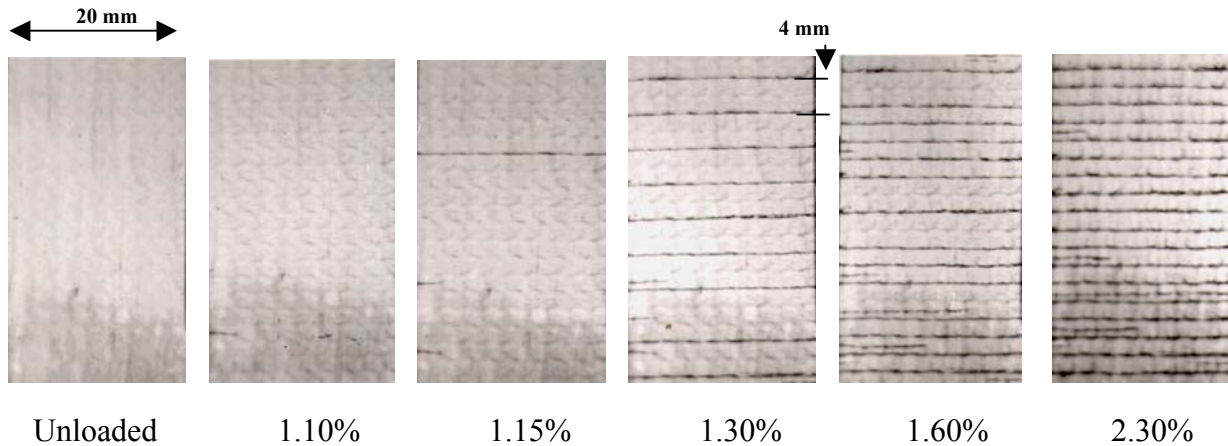


Fig. 3 Crack development for the model sandwich composite tested in wale direction (0°). Applied strains are indicated

The cracking pattern shown in Fig. 3 is intimately connected with the fabric architecture. Figure 4 gives an indication of the sequence of events. The first sign of damage develops at the loop crossover sites, represented by A, which is detected as micro-debonding at low AE signal. Significant cracks (matrix cracking) appeared firstly in the plane where the float stitch of course 2 and 3 are together (represented by the dashed lines) possibly due to the strain magnification caused by adjacent tows. These cracks have a spacing of 4 mm, which is the dimension of the repetitive unit in the knitted fabric. When these sites have been used, then at a higher strain cracks develop where the rib holds threads 2 and 3 (represented by dotted lines), giving a final crack spacing of 2 mm, which is the wale direction dimension of a single loop. This cracking pattern is registered by AE signals in accord to the discontinuities in the stress-strain curve.

For sample tested in 90° (course) direction linearity can be appreciated up to 0.7% strain. In this case visual and audible flaws are observed around 0.9% strain, and the first damage observed by AE is again in the form of micro-cracks at the loop crossover points at lower values. Matrix cracking appeared at a strain of about 0.8% producing a small knee in the stress-strain

curve. During loading in this direction, branched-like cracks were observed to be produced perpendicular to the load direction.

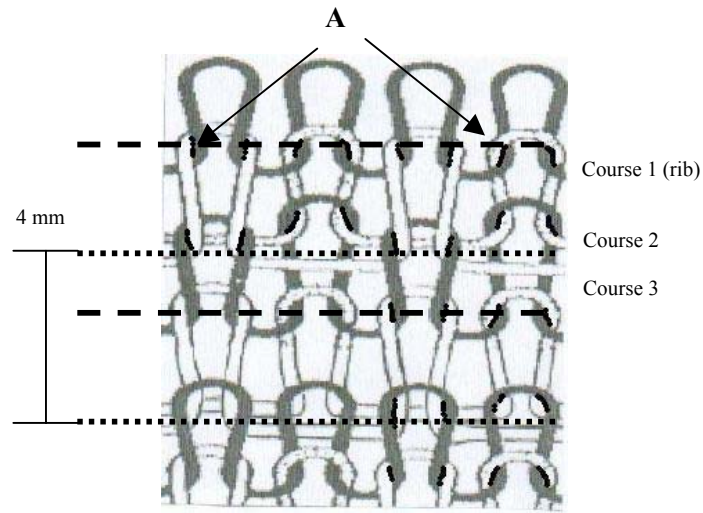


Fig. 4 Schematic diagram showing crack development for the model sandwich laminate with the fabric layer in the 0° direction (Wale).

Therefore, in both cases the AE information suggests that micro-debonding in the initiation sites (cross-over points) occurs due to stress magnification at lower levels below the knee point, registered by AE signal. Later above the knee point, when visual damage is observed in the sample, interfacial debonding and resin matrix cracking take place as demonstrated by some researchers [4, 5]. Finally, fiber fracture arises toward the end of the tensile test.

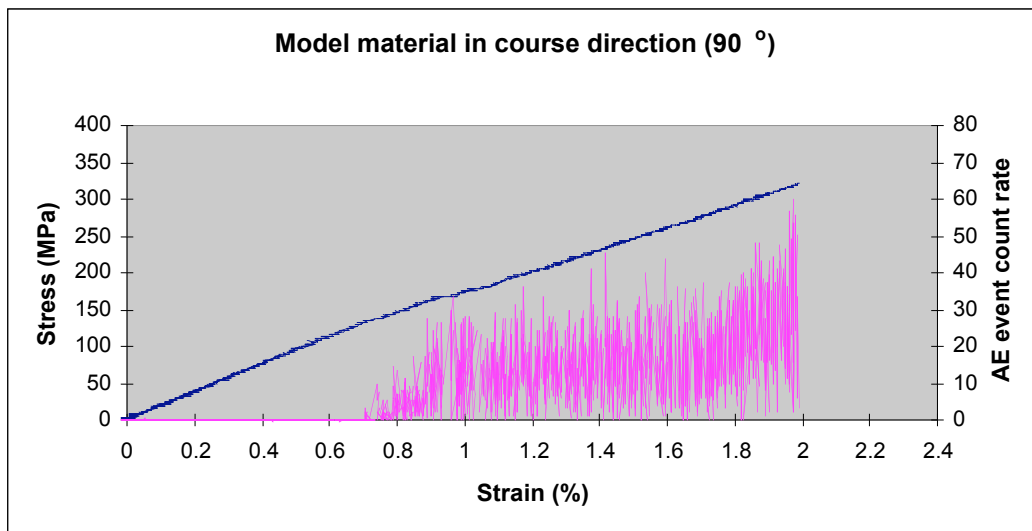


Fig. 5 Stress vs. strain curve for sandwich composite tested in course (90°) direction.

The cracking development sequence can be seen in Fig. 6. At low strains, cracking at the crossover points is visible, again as black spots in the photographs. In this orientation, it is easy for the developing matrix cracks to link up as they grow. Hence, the crack density increases fairly uniformly. Figure 7 shows a schematic of crack formation. The crack initiation points are

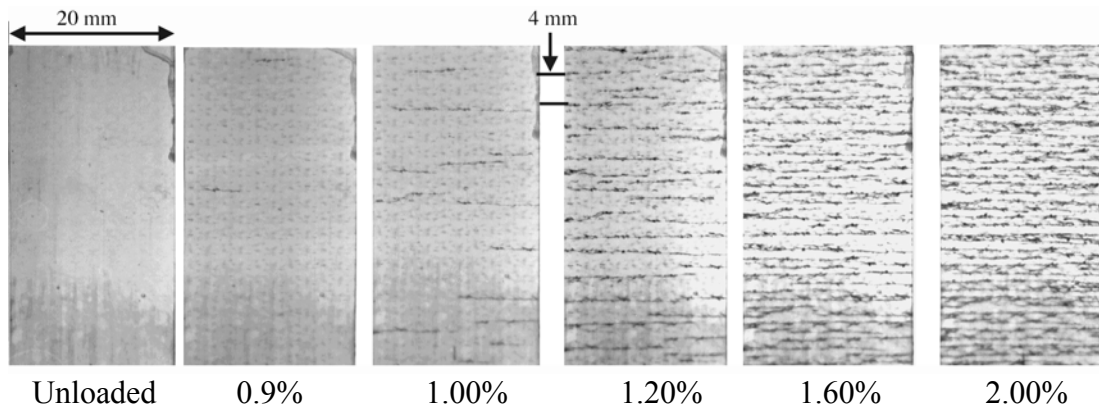


Fig. 6 Crack development for the model sandwich composite tested in course direction (90°). Applied strains are indicated

represented by A, where the yarns are joined together (crossover). All these sites coalesce to propagate the cracks along the sample perpendicularly to load direction by running on the sides or legs of the loops.

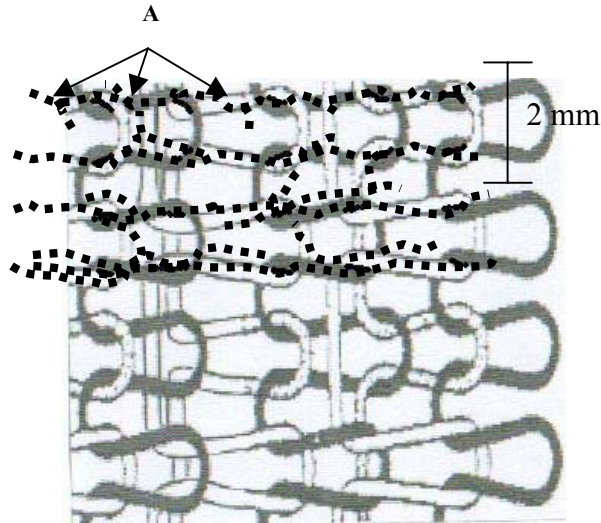


Fig. 7 Schematic diagram showing crack development for the model sandwich laminate with the fabric layer in the 0° direction (Course).

In Fig. 8 the crack density can be seen and compared. In wale direction crack initiation occurs at a strain of 0.85% (pre-damage) although a significant increase in crack density occurs after a strain of 1.1%. The crack initiation strain of 0.9 % is in reasonable agreement with the strain to failure of a single layer of knitted fabric reinforced resin tested alone, which was found to be 0.87%. In Fig. 8 it is noticed that the crack density increases in a course direction sample more rapidly than in samples tested at wale direction. This is due to the transversal branched-like matrix cracks that grow almost randomly along the sample showing no steady section in the curve.

In order to visualize the damage initiation detected by AE signals, data from crack density was plotted against the AE event count rate. Thus, it is possible to observe in Fig. 9, for the sample tested on the wale direction, that the first AE signal appearing before the main cracking damage (just before 1% strain) suggesting that a lower values of strain a kind of micro-damage is

detected (i.e. interfacial debonding). On the other hand, Fig. 10 confirm this statement since AE signal is located before the initiation of significant cracks at 0.85% strain when the sample is loaded to the course direction.

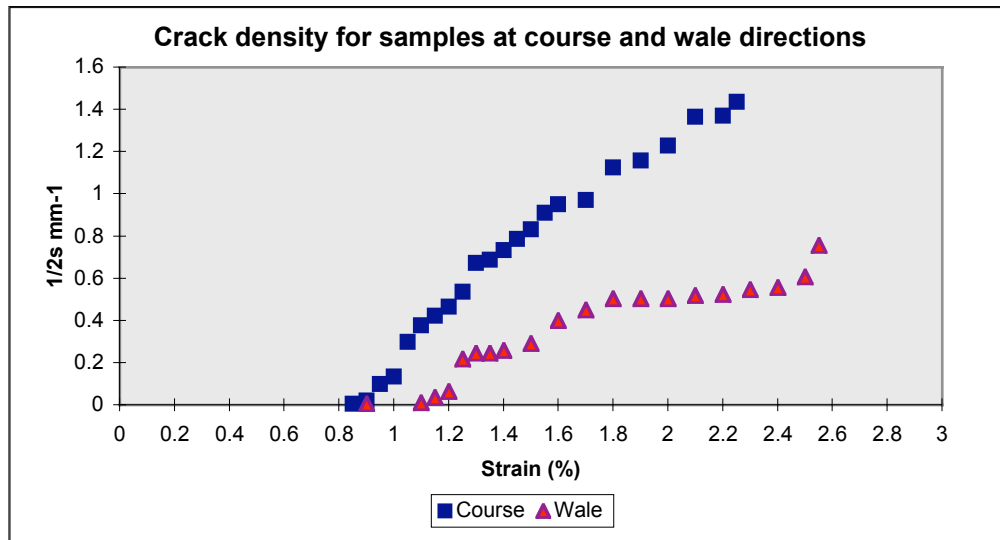


Fig. 8 Crack density vs. strain for sandwich composites.

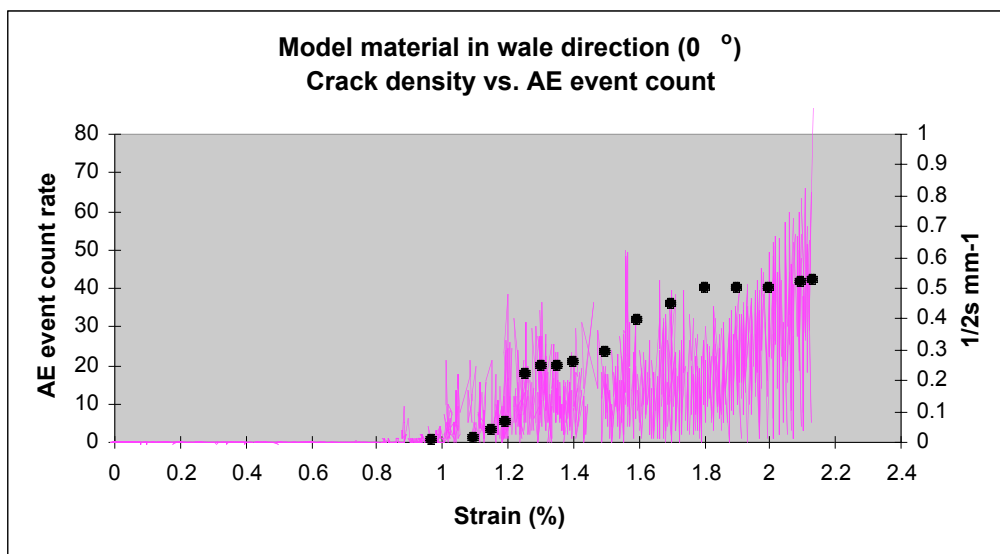


Fig. 9 AE event count rate vs. crack density loaded in wale direction.

Typical stress-strain curves for samples with the wale and course direction of the fabric are shown in Figs. 11 and 12 for a commercial material, made of 5 knitted layers by RTM process, which was tested in order to compare the behavior of a model material with a commercial composite. In this case, Derekan vinyl ester was used as matrix. In general, the stress-strain curves appear non-linear from even very small strains. Overall, the curves show a remarkable similarity to the stress-strain curves of ductile metals. Indeed, they even show a zero “work-hardening rate” region above a strain of 1.7%, with failure at 2%. In these opaque RTM materials, it was impossible to determine the onset of cracking visually and the AE technique was used to monitor damage. AE activity is shown together with the stress-strain curves. AE activity begins at quite low

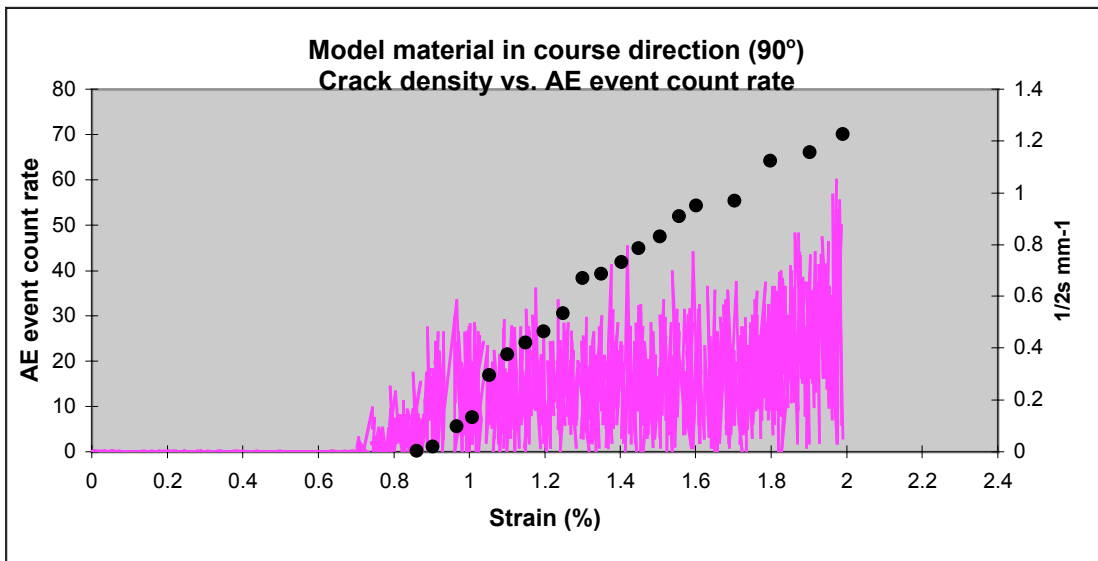


Fig. 10 AE event count rate vs. crack density loaded in course direction.

strains (approximately 0.2% to 0.4%). From strains of about 0.2% to 1%, the AE event count rises slowly, but a dramatic increase is observed from 1.0% strain. For this material, it was difficult to identify the different stages of damage as was demonstrated before. However, further microscopic analysis revealed that micro-debonding were as well presented in the crossover points detected as pre-damage before significant matrix cracking and fiber fracture. Although matrix cracking was difficult to observe, there were indications of such damage on the surface of the sample in the form of light-colored lines crossing the width of the coupon.

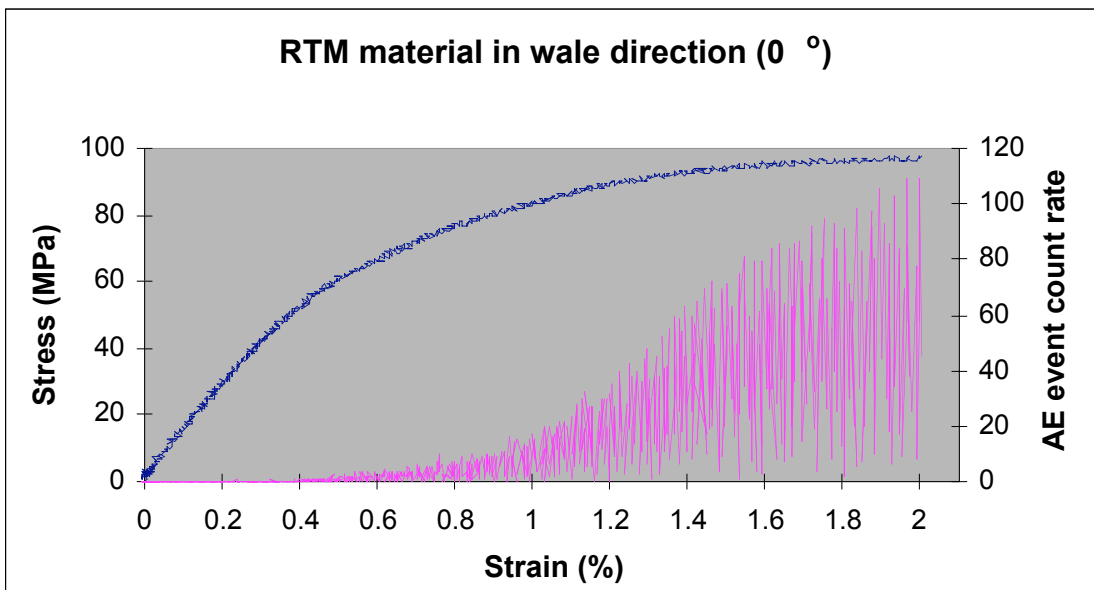


Fig. 11 Stress-strain curve for 5 layers RTM material tested at 0° (Wale) direction.

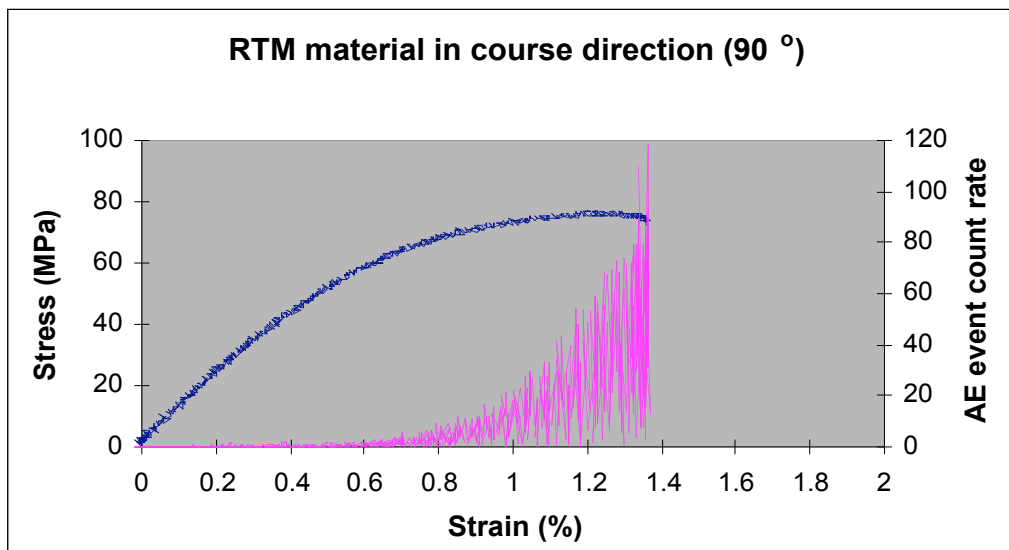


Fig. 12 Stress-strain curve for 5 layers RTM material tested at 90° (Course) direction.

For these materials, identifying the limit of no significant damage was extremely difficult even with the AE signal, since it increases gradually while the sample is loaded. Samples cut at different angles from commercial RTM composite were tested in tensile loading by taking them to a certain strain and, after reaching this point, they were unloaded and reloaded again to a higher strain, and so on until fracture. The samples were tested at the same crosshead speed as in the earlier work (0.5 mm/s) and stress, strain and AE data were recorded. Samples at 0° direction were taken to 0.1% strain, unloaded, reloaded to 0.6%, unloaded, reloaded to 1.0%, unloaded, reloaded to 1.5% strain, unloaded and then reloaded to failure. Figure 13 shows the stress-strain behavior for these cyclic tests, and Fig. 14 shows the stress-cumulative strain results. There are a number of features to be noted, which were common to all the specimens cyclically loaded in this way. Firstly, there is elastic behavior when the material is loaded to 0.1% and then unloaded. It is difficult to see this in Fig. 13 since the two lines superimpose. Although there is elasticity, the curves do not appear to be entirely linear even at this low strain. Secondly, loading to 0.6% strain and unloading produces not only a small hysteresis loop, but also a residual strain (of 0.03%). It should be noted, for comparison, that a strain of 0.6% is above the strain, at which the change in the Poisson's ratio during the monotonic tests suggested as the strain for the onset of matrix cracking. Thirdly, when reloading the sample to 1% strain, the hysteresis loop is 'closed', in the sense that the stress passes through the previous peak stress value at a strain of 0.6% while the specimen is being loaded to a higher strain. Unloading from a strain of 1% produces a much larger residual strain (about 0.15%). Fourthly, when reloading the sample, now to a strain of 1.5%, the hysteresis loop is this time not 'closed'. During this reloading, the stress at 1% strain is lower (by about 3 MPa) than the value on the previous cycle. Fifthly, when unloading and reloading to failure, the hysteresis loop is again not closed, and the stress reduction at 1.5% strain is now larger (about 4.5 MPa). Finally, for each successive reloading to higher strains (above the initial strain of 0.1%) the hysteresis loops have a lower overall slope.

Figure 14 shows two acoustic phenomena, which are important in understanding the mechanism of internal failure. The first one is the Kaiser effect (Ke) in which it is necessary to reach the same former stress value to go on with the AE signal and it is observed at low strain values.

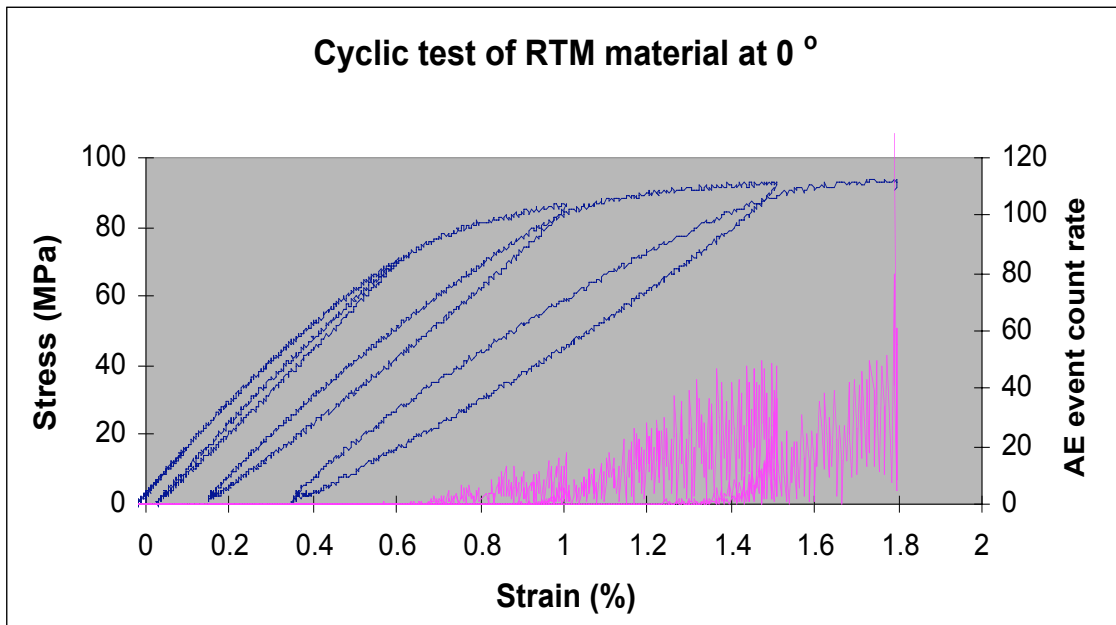


Fig. 13 Cyclic stress-strain curve for 5 layers RTM material at 0° (wale) direction.

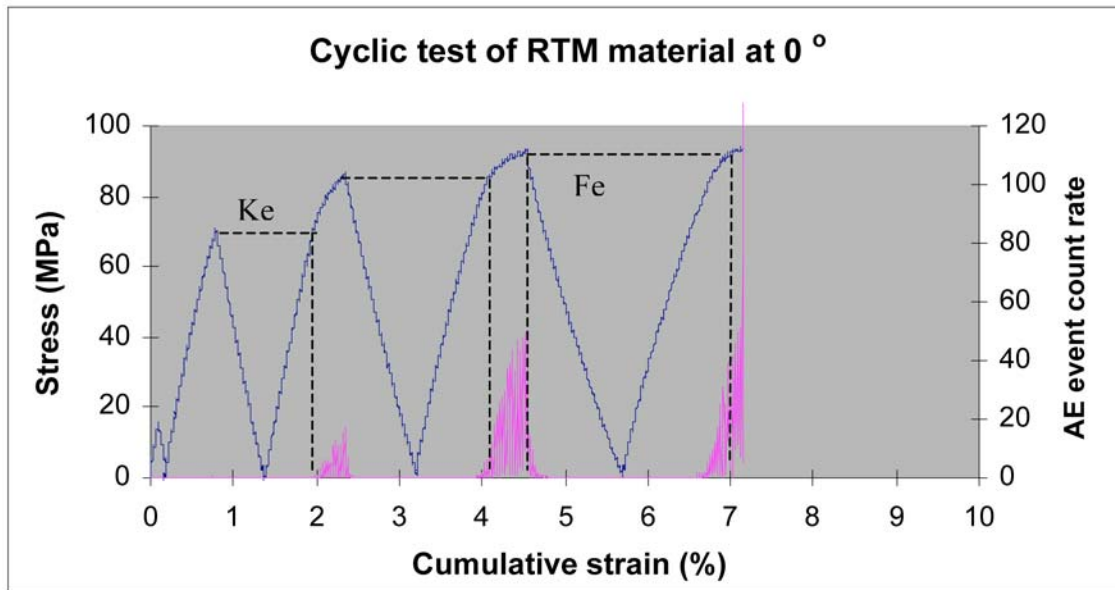


Fig. 14 Cyclic stress-cumulative strain curve for 5 layers RTM material at 0° (wale) direction.

On the other hand, Felicity effect (Fe) is observed at higher strain when reloaded, and AE signal is detected even when the last stress value has not been reached. At the same time, when load is released AE signal is still detected. These effects suggest that at low strain values the knitted fabric reinforcement is receiving the load through the matrix trying to behave elastically; however at higher strains, the fibers are pulled out from the matrix sockets and when the load is released there is friction between the fiber and the matrix when trying to accommodate again in the sockets. Therefore, it is possible to establish that at low strains where Kaiser effect is detected no damage is produced in the materials, and when micro-damage initiates (fiber/matrix debonding), it originates low AE signal, which increases uniformly when matrix cracks are

detected, at higher strain values then Felicity effect is sensed. Finally, load takes the material to fracture and fiber breakage is perceived by AE signal. For these materials, however, it is very difficult to assure when the significant cracks initiate.

Of particular interest in this work is the relationship of the complex fiber architecture of the knitted fabric composite to the damage accumulation under load. For this reason AE technique was used to find out the strain value where micro-damage initiates in the composites materials. Obtaining the data, investigation was done at a macroscopic level by cutting and polishing several pieces in different planes in order to relate the damage initiation and propagation with the geometry of the textile. The two principal material directions, wale and course, were investigated since they represent the two extremes in the orientation of the knitted fabric. Finally, analysis of a course sample loaded to a strain of 0.7%, which is just below the onset of matrix cracking in these specimens (which occurs at 0.8%) provided further evidence of early damage initiation in the form of cracking at the loop crossover points (Fig. 15). This represent fiber/matrix debonding interface detected by AE signal at low strain values (Fig. 5), which some researchers [4, 5] have identified as the first stage in the composite fracture mechanisms: interface debonding, matrix cracking and finally fiber breakage.

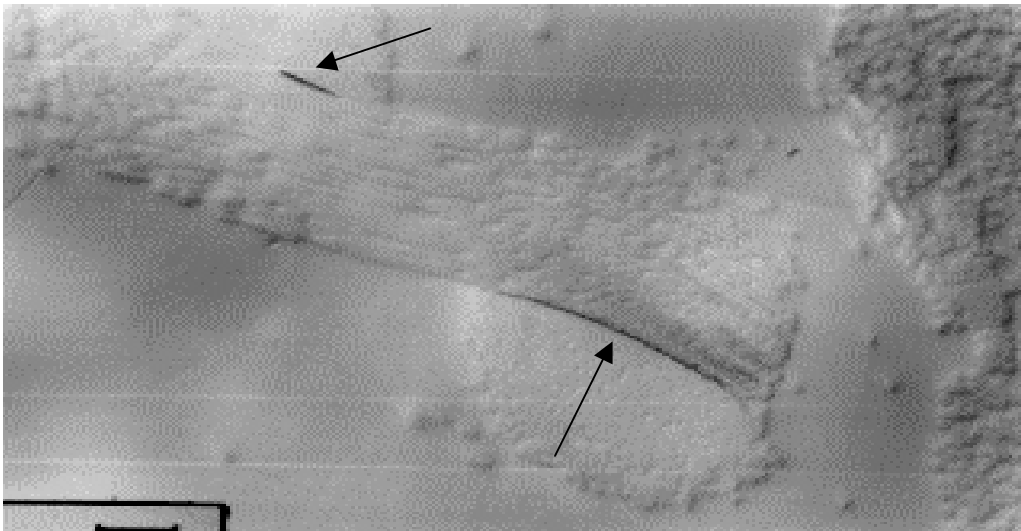


Fig. 15 Evidence of crack initiation sites on crossover points.

4. Conclusions

The advantage of acoustic emission (AE) technique is shown as applied to composite materials in support of the analysis of damage development at lower strain to understand the cracking process by identifying initiation sites, cracking progression and final fracture. By AE, various failure mechanisms such as resin matrix cracking, fiber bundle debonding and tensile fracture of fiber bundles were distinguished. Initial AE signal (event count rate) was attribute to the fiber bundle debonding at the crossover initiation sites, followed by visual matrix cracking on the sample. Micro-cracks originating at the debonded fiber bundles propagated into the resin-rich regions of the laminate and cracks coalesced until catastrophic fracture. Similar mechanism of fracture were observed in both the model and the RTM materials that suggest the intimate effect of the knitted fabric architecture in the final mechanical behavior of the composite. The model sandwich laminates enabled the damage behavior and failure mechanisms to be related to the orientation of the fabric. The observed pre-damage in the knitted fabric layer was identified for

the first time to be damage occurring at the loop cross-over points. The commercial RTM material was difficult to analyze due to the high fiber volume fraction, the tendency for the fabric layers to be crushed out-of-plane during manufacture and the opaque nature of the Durekane vinyl ester used as matrix. However, some features of the knitted fabric architecture were identified and related with the cracking damage. Finally, the influence of the knitted fabric architecture in determining the damage development in the composites was also shown in the results.

Acknowledgements

The author wishes to thank to the Mexican Council for Science and Technology (CONACyT) that financed this research. In the same way, gratitude is expressed to Cooperative Research Centre for Advanced Composite Structures Ltd from Australia for providing the textiles used in this work.

References

1. S. Ramakrishna, N.K. Cuong, H. Hamada. (1997), *J. of Reinforced Plastics and Composites*, **16** (10), 994-965
2. K.H. Leong, S. Ramakrishna, Z.M. Huang, G.A. Bilbo, (2000) *Composites: Part A*, **31**, 197-220
3. X. Ruan, T.W. Chou, (1998) *J. of Composite Materials*.**32** (3), 199-221.
4. S. Ramakrishna, D. Hull (1994), *Composites Science and Technology*, **50**, 237-247.
5. J. Bohse (2004), *European Working Group on Acoustic Emission (EWGAE 2004)*, pp. 339-348.

ACOUSTIC EMISSION DETECTION OF IMPACT DAMAGE ON SPACE SHUTTLE STRUCTURES

WILLIAM PROSSER¹, ERIC MADARAS¹, GEORGE STUDOR²,
and MICHAEL GORMAN³

¹) NASA Langley Research Center, MS 231, 3 E. Taylor St., Hampton, VA 23681, USA.

²) NASA Johnson Space Center, Code ES2, 2101 NASA Road 1, Houston TX 77058, USA.

³) Digital Wave Corporation, 11234A Caley Ave., Englewood, CO 80111, USA.

Abstract

The loss of the Space Shuttle Columbia as a result of impact damage from foam debris during ascent led NASA to develop and implement on-board impact detection technologies. AE sensing, both with accelerometers and ultrasonic sensors, was utilized to monitor a wide variety of impact conditions on Space Shuttle components ranging from insulating foam and ablator materials, and ice at ascent velocities to simulated hypervelocity micrometeoroid and orbital debris impacts. Impact testing was performed on both reinforced carbon composite wing leading edge materials as well as Shuttle tile materials on representative aluminum wing structures. Results of these impact tests are presented with a focus on the acoustic emission sensor responses to these impact conditions. These tests demonstrated the potential for on-board Shuttle impact detection and provided a data base on which to analyze signals from sensors onboard the Shuttle Discovery during the STS-114 Mission. On this flight, arrays of accelerometers mounted on the wing leading edge spar were monitored for potential impact damage. Preliminary results from this Shuttle Wing Leading Edge Impact Detection System (WLEIDS) are discussed.

Keywords: Impact detection, Space Shuttle, Thermal protection system, Reinforced carbon-carbon

1. Introduction

Damage caused by impact of foam insulation shed from the external tank of the Space Shuttle shortly after launch was suspected as a leading candidate for the cause of the loss of the Space Shuttle Columbia during reentry on February 1, 2003. As a result, an experimental test program was initiated during the accident investigation to reproduce this impact event and determine the resulting damage to the thermal protective systems (TPS) on representative Shuttle wing structures. In addition to reproducing the impact and resulting damage that led to the accident, NASA had the foresight to utilize these impact tests to develop and demonstrate acoustic sensor technology to detect impact damage on future Shuttle flights. Previous testing [1, 2] had already demonstrated that such sensors might be used to detect and locate micrometeoroid and orbital debris (MMOD) impact events on spacecraft. Although ascent debris damage was the focus of the Columbia investigation, MMOD had also been identified as a significant potential danger to both the Shuttle and the Space Station [3]. Both low frequency accelerometer and high frequency ultrasonic acoustic emission (AE) sensors were evaluated for this purpose during the accident investigation.

Testing during the investigation successfully validated the capability of these sensors for detecting major impact damage. However, additional testing was necessary to develop this sensing

approach for application to the remaining Shuttle fleet. These tests have included the determination of sensor response to a range of energies of foam impact events including those that are near to and below the threshold of damage. Additionally, impact tests have been performed with a number of other potential impact materials that can damage the Shuttle during ascent including ice, ablator, and metal. Also, since it is desirable to have the impact sensing system not only detect ascent debris impacts, but also those of micrometeoroid and orbital debris (MMOD) during orbit, testing has been performed to measure sensor response to hypervelocity impacts. In addition to impact testing on structural test articles, testing was performed on the Shuttle Endeavor to study wave propagation effects and evaluate differences in structural configuration between Columbia test articles and the remaining Shuttle fleet. An overview of these test results is presented, along with preliminary results from sensors deployed on the Shuttle Discovery during the STS-114 Mission.

2. Columbia Accident Investigation Foam Impact Testing

At the onset of the Columbia accident investigation, it was not known exactly where the foam debris impacted the Shuttle wing. Video images showed that it struck on the lower surface of the left wing. However, the views and resolution available did not indicate whether it struck the leading edge, which consists of reinforced carbon-carbon (RCC), or the lower wing surface, which has thermal protection consisting of tile. Thus, a variety of test specimens were fabricated to investigate the damage caused by foam impacts on these structures. In addition, preliminary testing to calibrate the foam impact gun performance as well as test instrumentation configuration was performed using aluminum plate targets. Accelerometers and acoustic emission sensors were included on all of these tests and successfully detected the impacts in all cases.

As the investigation progressed, sensor data from Columbia and forensics of debris provided indications that the damage had occurred on the leading edge, specifically on RCC panel 8. The focus of the impact testing turned toward foam impacts on leading edge panels mounted on a leading edge support structure (LESS) as shown in Fig. 1. This test article consisted of a section of leading edge spar using the honeycomb structural configuration from Columbia, to which leading edge panels 5-10 were attached. Because of the enormous expense and limited availability of RCC panels, initial testing was performed using fiberglass replicas of the leading edge panels, with final testing performed on flight RCC panels. An array of 8 AE sensors (Digital Wave Corp. model B225-5) was attached on the interior side of the spar. The bandwidth of these transducers was specified by the manufacturer to be 30 kHz to 300 kHz. However, responses well below 10 kHz were measured. Initial testing with the sensors arrayed close to the impact point demonstrated that signals of significant amplitude were produced and that these signals propagated through the attach fittings into the spar. For later testing, the sensors were arrayed along the length of the spar as shown in Fig. 1 to determine how well the signals propagated along the spar, and thus how remote the sensors could be located and detect the impact. As the foam impacts and the attenuation of the complicated structure resulted in very low AE frequency signal content, the AE data was acquired at a sampling frequency of only 500 kHz with a total of 32 K-points acquired for each sensor.

For the defining test of the investigation, a foam block weighing 758 g (1.67 lbs) was launched at a velocity of 237 m/sec, striking panel 8 as indicated in Fig. 1. This impact produced a significant hole in the RCC panel providing conclusive evidence for the Columbia Accident Investigation Board in determining the cause of the accident [4]. The AE signals that were

detected from this foam impact event are shown in Fig. 2. Only 6 dB of gain was applied to the signals from the AE sensors. As would be expected, the largest signal, arriving earliest in time was that from sensor 5, which was nearest the impact site. Quantitatively decreasing arrival times and amplitudes of signals from sensors located further away from the impact point were observed. Although not noticeable in this figure as all signals are plotted on the same scale, signals were detected all the way down to the location of sensor 1, suggesting that impact events can be detected by sensors mounted several RCC panels away, a distance of more than 1 m. Examination of the arrival times for signals from sensors 7 and 8 showed that the impact site could be localized with respect to the upper and lower surface of the leading edge.

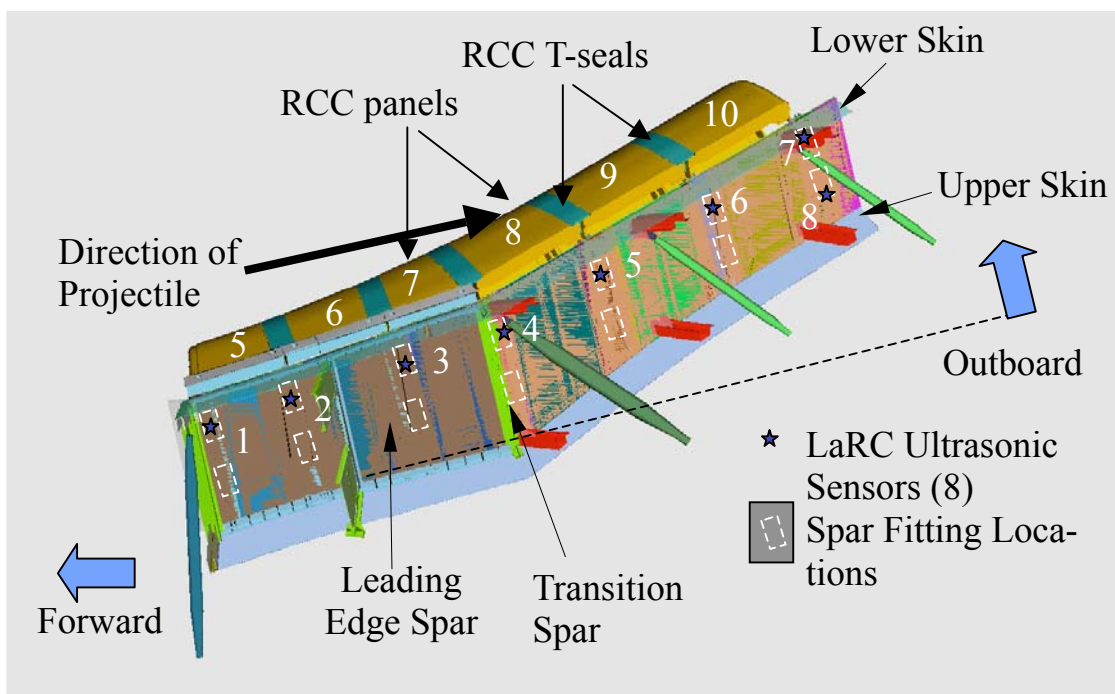


Fig. 1 Leading Edge Support Structure with RCC panels 5-10 and T-seals shown. The locations of the AE sensors 1 through 8 are indicated with black stars.

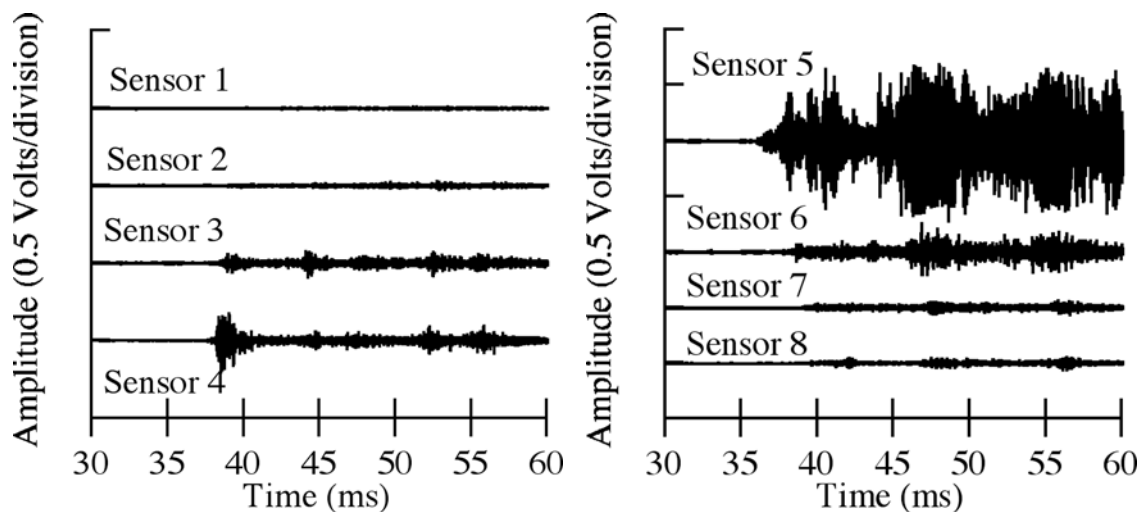


Fig. 2 AE signals from foam impact on Shuttle RCC wing leading edge.

3. Return to Flight Testing

At the completion of the accident investigation, a number of questions remained regarding the capability of acoustic impact sensing on the Shuttle. These included the detectability of much smaller foam impacts including those near or below the threshold of damage, the characteristics of signals caused by other potential impact source materials including ice, ablator, and metal at ascent velocities as well as hypervelocity impacts to simulate orbital impacts. These effects needed to be assessed for impacts on both the leading edge as well as on the tile protected lower wing surface including the main landing gear door. Another issue was that the construction of the wing spar on the remaining Shuttle fleet varied considerably from that of Columbia and the effects of this difference on acoustic wave propagation had to be investigated. Thus, a comprehensive test program was initiated to address these questions. As it is impossible, as well as expensive, to test all possible combinations of impact parameters, a simultaneous modeling effort was initiated to develop capabilities to model impact events on Shuttle wing structures. One key experimental piece of data required for these models was the measurement of the transfer function of the acoustic signals from the RCC leading edge to the spar where sensors are located. Additional experiments were performed to acquire this critical data.

3.1 Launch Debris Impact Testing

Additional foam impact tests were performed on RCC panels over a range of projectile sizes and impact velocities. These impact tests were performed on different panels on the LESS test article, as well as on the T-35 test article, which represented a more outboard section of the wing. This test article allowed impact tests on panels 16 and 17 and further provided the opportunity to evaluate the effect of differing impact locations on measured signals. Signals from small projectiles and/or low impact velocities producing impact energies below the threshold of damage were still readily detected. Variations in the signal amplitude correlated with the impact energy for a given type of impact material. However, different impact materials such as foam and ice exhibited different amplitude- impact energy relationships. In addition to sensors on the spar, sensors were also placed on the RCC panel of the T-35 test article to measure the transfer function response from the RCC panel to the spar. The frequency response plots in Fig. 3 show the significant loss in high frequency signal content that occurs as the signal propagates from the RCC to the wing spar of Columbia construction. Preliminary testing on test articles with the wing spar construction of the remaining Shuttle fleet suggests that this high frequency attenuation might not be as severe.

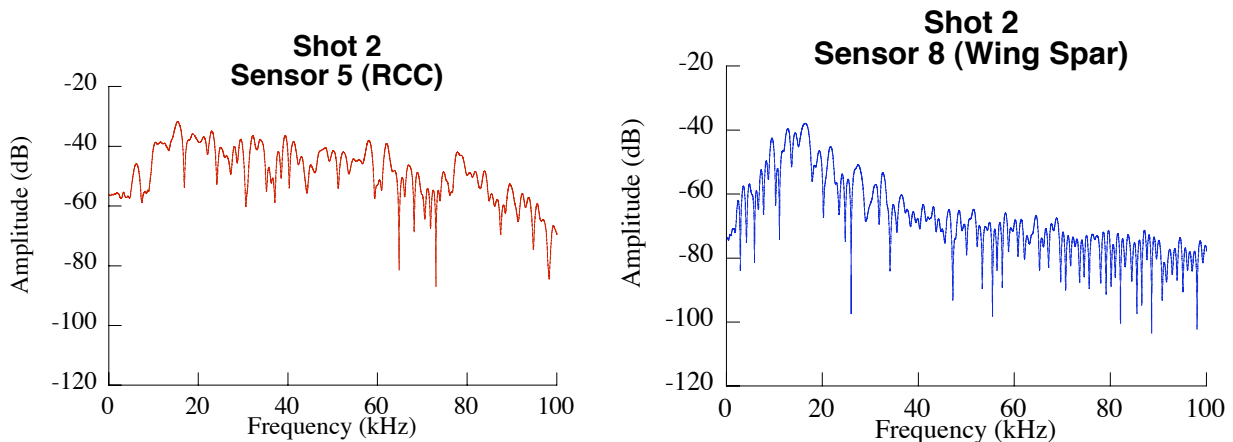


Fig. 3 Frequency content of foam impact signals for sensors on RCC panel and wing spar.

Foam impact tests were also performed on lower wing specimens representative of regions on which the thermal protection material is tile. Specimens from this region of the wing also included a main landing gear door. Representative damage for a wing specimen impacted by foam at approximately 290 m/sec is shown in Fig. 4 in which a hole formed by a tile that was broken away by the impact can be observed. Signals were again readily detected by AE transducers for all impact conditions studied. Although the signals were very complex due to the complicated nature of the source and the complex structural geometry of the tile and wing specimen, source location could be determined using appropriate frequency filtering to selectively analyze the flexural mode of propagation.

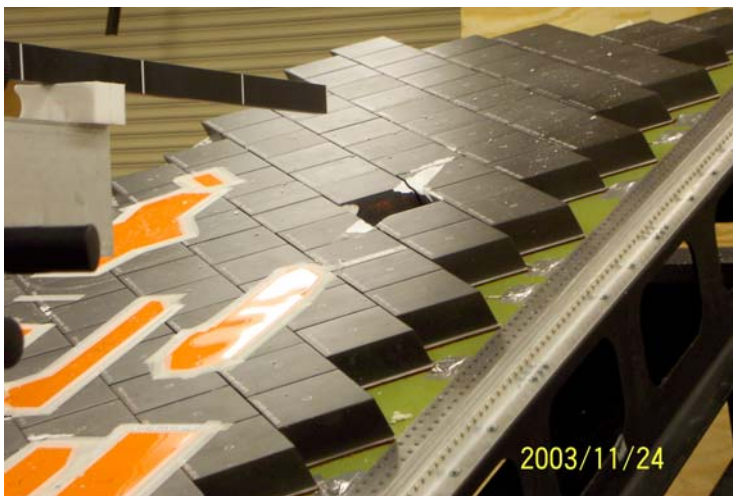


Fig. 4 A wing acreage tile test article showing the resulting tile loss due to a foam impact.

Impact testing on RCC and tile specimens was also performed using other types of potential launch debris. These materials included ice, ablator and metal. Again, the impact velocity and energy was varied over a range from below the damage threshold to that causing substantial damage. AE and accelerometer sensor data were obtained for all tests. Preliminary analysis shows that all impacts were successfully detected with both accelerometers and AE sensors, and that again there was a correlation between signal amplitude and energy of impact for a given impact material.

3.2 Hypervelocity Impact Testing

Hypervelocity impact tests were performed to simulate micrometeoroid and orbital debris (MMOD) damage that can occur once the Shuttle is in orbit. Initial tests were performed on flat metal and fiberglass plates to develop a database to support modeling efforts as well as to determine appropriate instrumentation settings. Figure 5 shows typical damage resulting from two hypervelocity impact events at 6.8 km/s in a fiberglass plate. The smaller impact was created by a 2-mm diameter aluminum projectile while the larger was created by a 6-mm aluminum projectile, which fully penetrated the plate. Figure 6a shows the signals from a hypervelocity impact, while for comparison, a lead break simulated AE signal near the impact site is shown in Fig. 6b. Curiously, the flexural mode amplitude was generally smaller than the extensional mode, especially at the higher energy shots. This is interesting since low velocity impact usually produces a large amplitude flexural mode due to the source motion perpendicular to the plate target. In the present case the attenuators played a role in filtering the low frequencies that generally confirm the presence of a flexural wave. However, the source function for hypervelocity impact is quite a bit different than ball drop at low velocity or a lead break. It is also interesting to note in

comparing these signals that there was 64 dB of attenuation applied to the signals from the hypervelocity impact as compared to 47 dB of gain for the lead break signal. There is a tremendous amount of energy in the hypervelocity impacts. Figure 7 shows the raw signal amplitude, after adjustment for the attenuation, from a series of hypervelocity impacts on a fiberglass plate as a function of impact energy. As shown in this figure, the raw signal amplitude increases with corresponding impact energy until it peaks at nearly 80 volts for an impact energy of nearly 100 J. In the fiberglass plates, for impacts exceeding 100 J, the projectile penetrates the plate and a decrease in AE signal amplitude was observed. However, for actual RCC leading edge specimens, a decrease in AE was not observed after impact penetration.

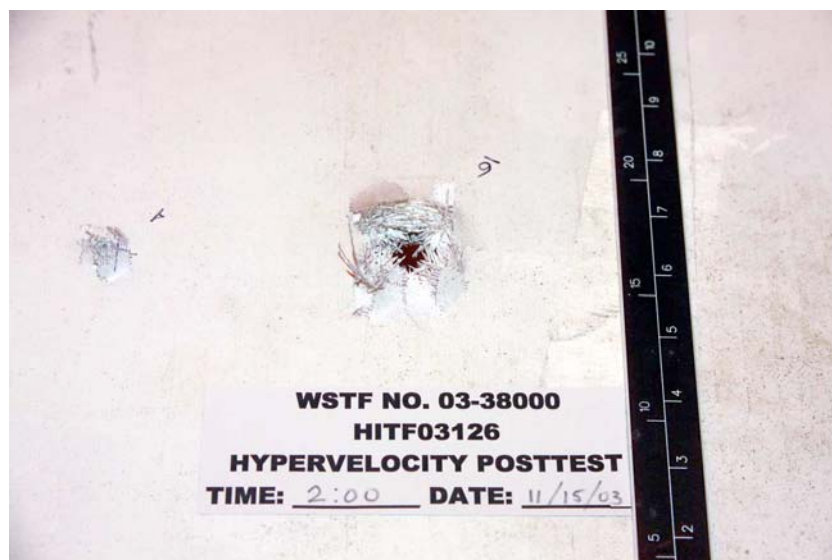


Fig. 5 Fiberglass panel showing damage from two hypervelocity impacts.

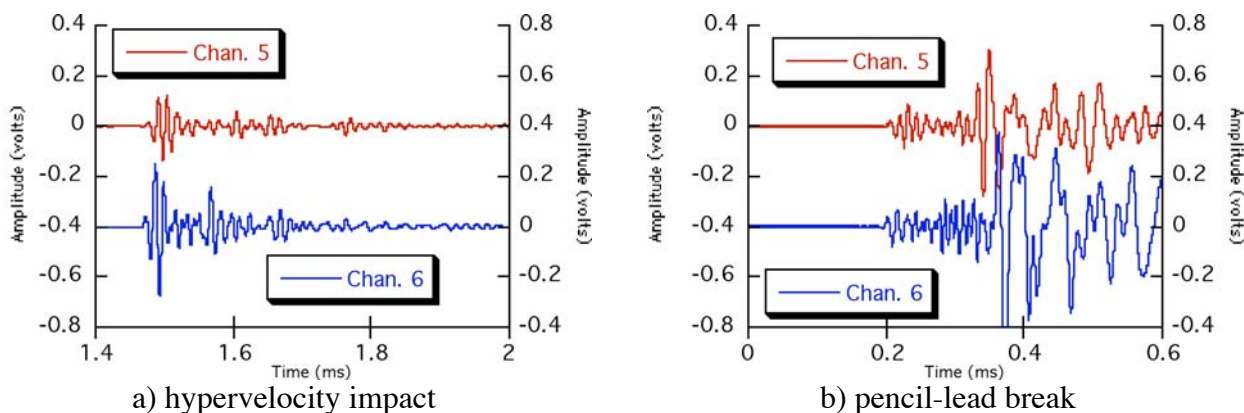


Fig. 6 AE signals produced by a) hypervelocity impact and b) pencil-lead break.

Propagation effects on AE signals from the impacted material through attachment mechanisms to likely sensor locations on the spar were also investigated. Initial testing for this consisted of multiple plates connected by threaded rods, followed by testing on a realistic Shuttle wing spar test article. Again, because of the expense of RCC panels, testing included hypervelocity impacts on a number of fiberglass replicas of a leading edge panel, followed by shots on an actual RCC panel. These tests demonstrated that the much higher frequency hypervelocity impact signals are much more heavily attenuated than was observed for the lower frequency foam impact signals. Further analysis was performed to determine the transfer function from the RCC to the spar where the sensors are located on the flight vehicle.

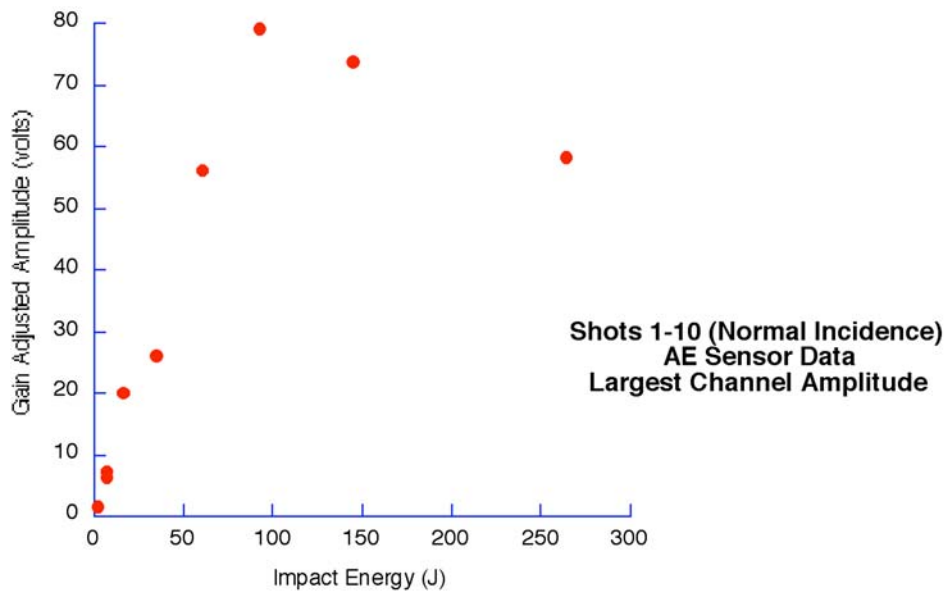


Fig. 7 AE signal amplitude versus impact energy.

3.3 Impact Hammer Testing

Impact hammer and pulsed pitch-catch ultrasonic measurements were made on the wing spar of the Shuttle Endeavor to investigate the effects on wave propagation due to differences in wing spar construction. As noted previously, the LESS and T-35 test articles represented the Columbia wing spar construction which is different from the remainder of the fleet. Transducers were attached to the leading edge of the Shuttle’s wing, as indicated in Fig. 8. At various locations, ultrasonic signals between 10 to 150 kHz were introduced and recorded on the fixed transducers. In addition, a series of low energy, instrumented hammer impacts (9.1, 27.2, 68.1, 113.5 kg) were performed on the wing’s leading edge. Similar experiments were performed on the LESS and T-35 test articles to develop a correlation between the different structures. Figure 9 shows the

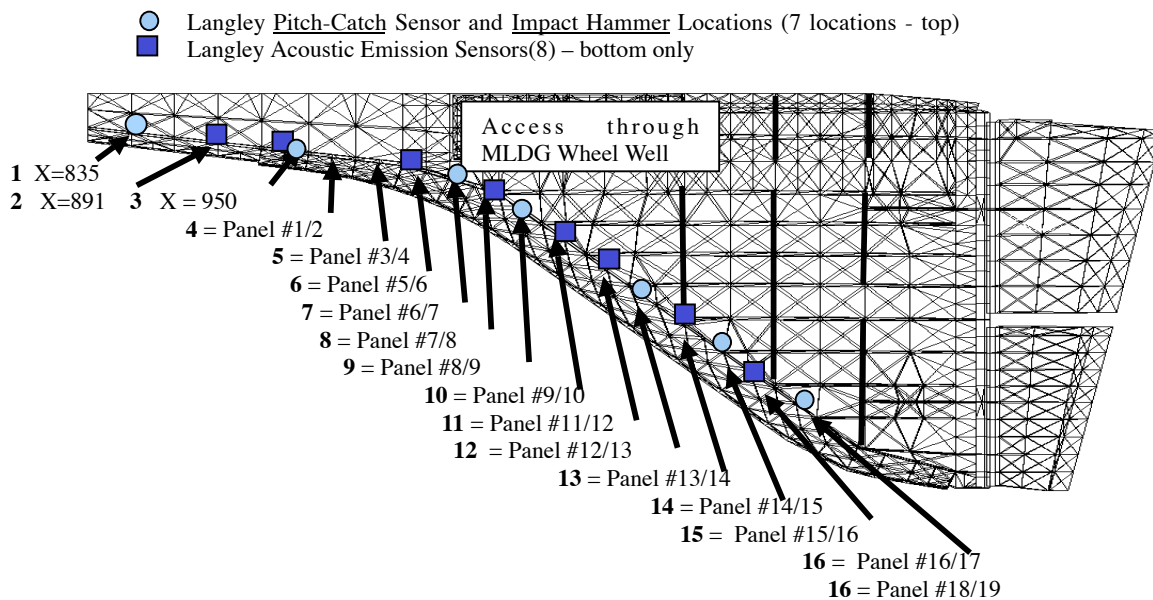


Fig. 8 Layout of transducer locations inside the Shuttle Endeavor’s wing.

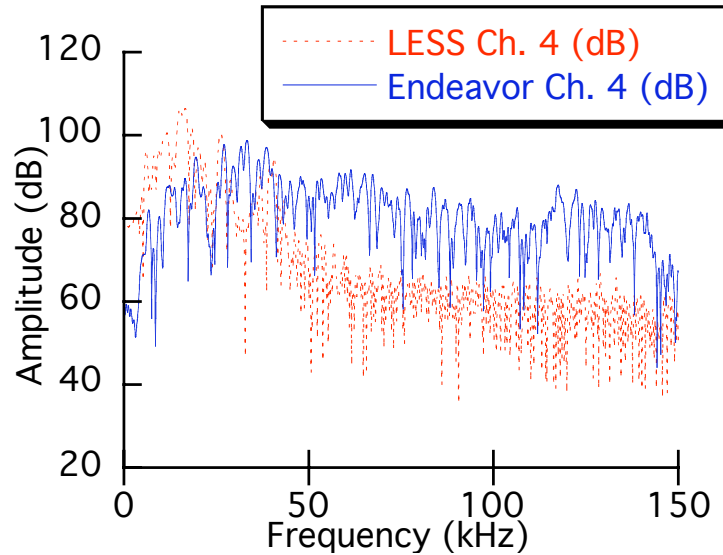


Fig. 9 Frequency response for 68.1-kg hammer impact on Shuttle Endeavor wing spar and Leading Edge Structural System (LESS) test article.

frequency response of AE sensors to a hammer impact on the Shuttle Endeavor wing spar as well as on the LESS test article. Although the overall peak amplitudes of the time domain signal are similar, the frequency response shows that the peak amplitude is at a much lower frequency with much higher frequency attenuation for the LESS as compared to the Shuttle. These differences are significant in that they indicate that higher frequency signal components may propagate from impacts on the Shuttle to and along the spar. Such higher frequencies may enable improved signal to noise for detection as the background noise is expected to decrease with increasing frequencies. However, no database exists for measurements of the background noise for ultrasonic frequencies on the Shuttle. A flight experiment to obtain this information is being planned to enable optimized sensor frequency selection for the next generation to the Shuttle impact sensing system.

4. Shuttle Impact Detection Implementation

Although both accelerometers and ultrasonic AE sensors were demonstrated to be successful at detecting impacts on Space Shuttle structures, accelerometers were chosen for the initial implementation of the WLEIDS because of the availability of existing flight qualified sensors and instrumentation. Arrays of 66 accelerometers were deployed on each wing leading edge spar of the Shuttle Discovery for the STS-114 Mission. The data from these sensors were recorded by arrays of 22 battery-powered data acquisition/wireless transmission units mounted in each wing cavity. Each data acquisition unit recorded the output from three accelerometers as well as one temperature sensor. The system recorded data from all sensors continuously during launch and ascent to orbit, digitizing the signals at a sampling frequency of 20 kHz. Then, to conserve battery life, the system was switched into on-orbit monitoring mode during which smaller sets of sensors were monitored to record the background noise level and any triggering MMOD impacts. During this time, data was also transmitted wirelessly to a laptop computer in the crew compartment and then downlinked to Mission Control at the Johnson Space Center for analysis. Figure 10 shows the key components of the WLEIDS system.

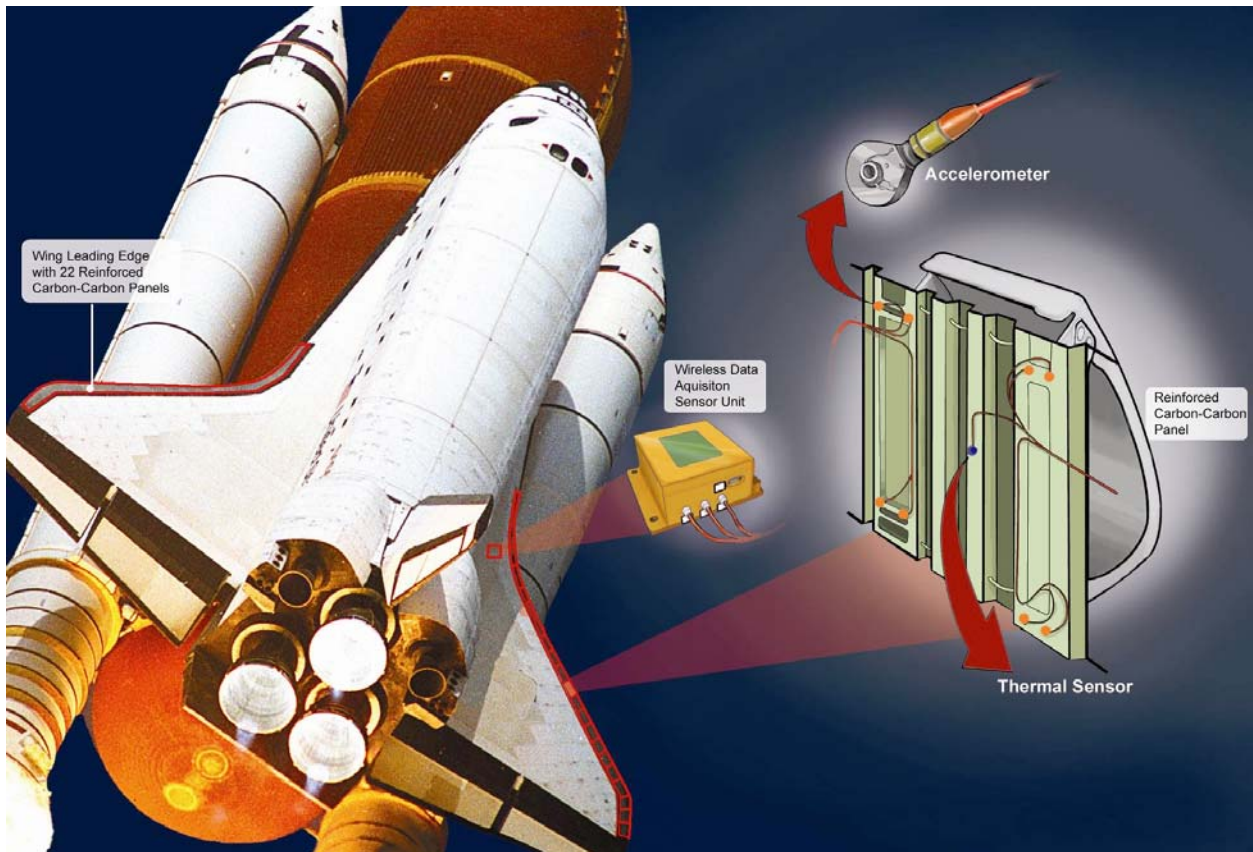


Fig. 10 Key components of the Shuttle Wing Leading Edge Impact Detection System.

Because of limited data acquisition unit battery life and telemetry bandwidth, the complete time history data from all sensors could not be transmitted to Mission Control for analysis during the flight. Preprocessing routines in the data acquisition units calculated Grms (RMS value of the g-forces recorded by the sensors) values for the sensor units and then created summary files of the largest Grms peaks. These summary files were then downlinked for preliminary analysis. Peaks that occurred globally across the wing were discounted as impacts and most often correlated with mission specific events such as main engine ignition, solid rocket booster (SRB) ignition, maximum dynamic pressure, and tank and SRB separation. Local peaks were analyzed as potential impacts by downlinking and evaluating short intervals of the time history response for multiple sensors near a suspected impact location. Additionally, suspected impact events were correlated with other data sources such as video and radar recordings of the vehicle during launch and ascent.

For the STS-114 Mission, the WLEIDS performed exceptionally well. All sensor data acquisition units successfully triggered at launch and data was recorded from all sensors. The summary files were successfully downlinked and led to the identification of only a small number of probable impact events. None of these probable impact events were of amplitude consistent with critical damage to the RCC leading edge and in-flight inspection at the suspected impact locations using the Orbital Boom Sensing System did not reveal damage. The complete time history data from all sensors was retrieved from the vehicle after the flight and is currently being analyzed. The focus of this post-flight analysis is to determine if any potential impacts were missed during the analysis of the summary files during the Mission, and to develop and evaluate improved algorithms for impact signal identification during future flights.

5. Conclusion

AE sensors and accelerometers were used to monitor foam impact tests on Shuttle test articles as part of the Columbia accident investigation. These tests demonstrated that acoustic sensing could be used to detect and locate impact events on the Shuttle wing leading edge. Follow-on testing has demonstrated this capability for a wide range of impact conditions on both the leading edge as well as the lower wing surface. These tests have included much smaller impact energies at and below the threshold of damage, different impact materials, and hypervelocity impact conditions designed to simulate micrometeoroid and orbital debris damage. Additional testing has analyzed the effects of different wing spar constructions on the propagation of impact generated acoustic waves along the spar.

As a result of this testing, an initial impact sensing system was developed and successfully deployed on the Shuttle Discovery on the STS-114 Mission. Accelerometers were used in this Wing Leading Edge Impact Detection System due to the availability of previously flight-qualified sensors and wireless data acquisition units that could be easily integrated into the Shuttle wing spar. The system performed as designed detecting only a small number of probable impact events that were of a magnitude small enough to have not caused damage. Post-flight analysis of the complete data from the Mission is ongoing to develop improved impact detection methodologies for future Shuttle flights.

References

- 1) W.H. Prosser, M.R. Gorman, and D.H. Humes, *Journal of Acoustic Emission*, **17**(1-2), (1999), 29-36.
- 2) J. M. Nelson and B. M. Lempriere, "Space Station Integrated Wall Design and Penetration Damage Control," Final Report for NASA Contract NAS8-36426, (1987).
- 3) GAO, "Space Program: Space Debris is a Potential Threat to Space Station and Shuttle," GAO Report # GAO/IMTEC-90-18. (1990).
- 4) Columbia Accident Investigation Board Report, (August, 2003).

MOMENT TENSORS OF IN-PLANE WAVES ANALYZED BY SIGMA-2D

MASAYASU OHTSU¹, KENTARO OHNO¹ and MARVIN A. HAMSTAD²

¹) Graduate School of Science and Technology, Kumamoto University, Kumamoto, Japan.

²) Department of Engineering, University of Denver, Denver, CO 80208 USA.

Abstract

For quantitative waveform analysis of AE signals, SiGMA (Simplified Green's functions for Moment tensor Analysis) procedure has been developed. Kinematics on AE source, such as crack location, crack type and crack orientation, can be determined from recorded AE waveforms. Since the SiGMA code was originally implemented for three-dimensional (3D) source characterization, the applicability of SiGMA to AE signals detected in a plate-like sample was studied here. Employing a finite-element modeling code, theoretical AE waves of in-plane motion were computed. AE sources were modeled by assuming three types of moment tensors. These tensor elements are recovered by two-dimensional SiGMA code (SiGMA-2D). Comparing results between assumed and recovered sources, the applicability of SiGMA-2D to in-plane AE waves was confirmed.

As a practical application, AE waves due to water leakage from a pipe were analyzed. In laboratory, water leakage from a slit-like defect was generated in a pipe model. It was found that dominant cracking motions at the slit are associated with AE waves due to shear cracks, with orientations approximately parallel to the slit plane. For tensile cracks of AE sources, crack-opening directions are perpendicular to the slit plane. These results show a great promise for clarifying AE generating mechanisms due to water leakage by SiGMA-2D analysis.

1. Introduction

Moment tensor analysis of acoustic emission (AE) waves can identify the kinematics of AE sources, such as location, crack-type classification and crack orientation. Taking into account only the first motions of waveforms, an analytical procedure was implemented as the SiGMA (simplified Green's functions for moment tensor analysis) procedure (Ohtsu, 1991). In three-dimensional (3D) massive body of concrete, the applicability of SiGMA-3D has been confirmed (Ohtsu et al., 1998). In the case of plate-like samples, such as metals and composites, however, the SiGMA-3D procedure is difficult to use. This is because out-of-plane motions of AE waves are basically taken into consideration in the SiGMA-3D analysis. For AE detection in a plate, Lamb waves are predominantly observed as out-of-plane motions, but unfortunately they are not due to the kinematics of AE sources.

Previously, we developed SiGMA-2D for a plate-like sample (Shigeishi and Ohtsu, 1999). Taking into account in-plane motions of AE waves, crack kinematics of AE sources were determined in PMMA and mortar plates with a slit under compressive loading. To confirm the feasibility, results were compared visually with crack traces. One example of SiGMA-2D results in a mortar plate is shown in Fig. 1. An arrow symbol shows a tensile crack with crack-opening orientation, and a cross symbol denotes a shear crack with two orientations of crack-motion and crack-normal vectors. Reasonable agreement was observed between SiGMA results and

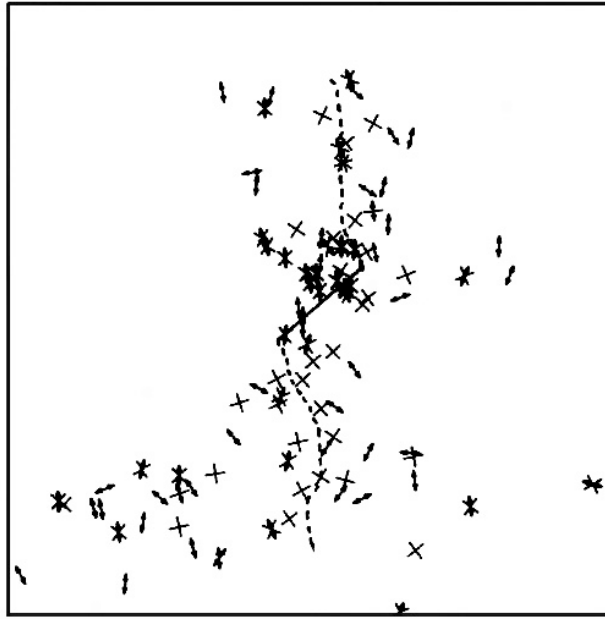


Fig. 1 Results of SiGMA-2D analysis in a mortar sample with a slit.

observed crack traces of the broken lines in Fig. 1. So far, the accuracy and applicability of SiGMA-2D to other types have not yet been fully confirmed.

In order to synthesize AE waves in the plates, a dynamic finite-element modeling code has been developed (Hamstad et al., 2001). Computing theoretical AE waves due to sources of different types, source identification was attempted by applying a wavelet transform (Hamstad et al., 2002).

In the work reported here, the accuracy of the SiGMA-2D code was examined with theoretical in-plane wave motions. By employing the finite-element modeling code with certain moment tensor elements, theoretical AE waves with in-plane motions were synthesized. The moment tensors were recovered by SiGMA-2D analysis of the waves. In addition, as one practical application, AE waves due to water leakage from a slit-like defect in a pipeline model were detected and analyzed by SiGMA-2D.

2. SiGMA Analysis

2.1 Theory of Moment Tensor

As formulated in the generalized theory (Ohtsu and Ono, 1984), AE waves are elastic waves generated by dynamic-crack (dislocation) motions inside a solid. By introducing moment tensor, M_{pq} , the integral representation of the elastic wave $u_k(\mathbf{x},t)$ is represented,

$$u_k(\mathbf{x},t) = G_{kp,q}(\mathbf{x},\mathbf{y},t) M_{pq} * S(t). \quad (1)$$

Here, $G_{kp,q}(\mathbf{x},\mathbf{y},t)$ are spatial derivatives of Green's functions and $S(t)$ represents the source kinetics (often called the source-time function). Inverse solutions of equation 1 are two-fold. Source kinetics are determined from the source-time function $S(t)$ by a deconvolution procedure. Source kinematics are represented by the moment tensor, M_{pq} . In order to perform the deconvolution and to determine the moment tensor, the spatial derivatives of Green's functions or the displacement fields of Green's functions due to the equivalent force models are inherently

required. So far, numerical solutions of the displacement fields have been obtained by finite difference method (Enoki et al., 1986) and by FEM (Finite Element Method) (Hamstad et al., 1999). These solutions, however, need a vector processor for computation and are not readily applicable to processing a large amount of AE waves. Consequently, based on the far-field term of the P-wave, a simplified procedure was developed (Ohtsu, 1991). This is suitable for a PC-based processor and is robust in computation. The procedure was implemented as the SiGMA (Simplified Green's functions for Moment tensor Analysis) code.

Mathematically, the moment tensor in equation 1 is defined by the tensor product of the elastic constants, the normal vector \mathbf{n} to the crack surface and the crack-motion (dislocation or Burgers) vector \mathbf{l} ,

$$M_{pq} = C_{pqkl} l_k n_l \Delta V \quad (2)$$

The elastic constants C_{pqkl} have a physical unit of $[N/m^2]$ and the crack volume ΔV has a unit of $[m^3]$. The moment tensor has the physical unit of a moment, $[Nm]$. This is the reason why the tensor M_{pq} was named the moment tensor. The moment tensor is a symmetric second-rank tensor and is comparable to the elastic stress in elasticity as,

$$[M_{pq}] = \begin{bmatrix} m_{11} & m_{12} & m_{13} \\ m_{12} & m_{22} & m_{23} \\ m_{13} & m_{23} & m_{33} \end{bmatrix} \Delta V \quad (3)$$

All elements of the moment tensor are illustrated in Fig. 2. In a similar manner to stress, diagonal elements represent normal components and off-diagonal elements are shown as tangential or shear components.

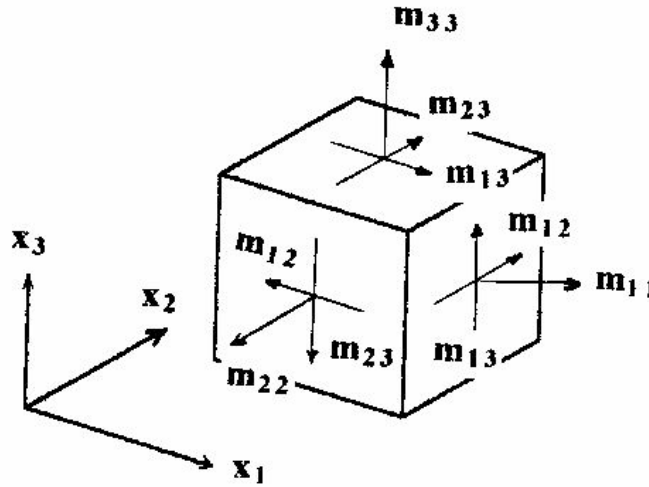


Fig. 2 Elements of the moment tensor.

2.2 Equivalent Force Models

AE sources can be represented by equivalent force models, such as a monopole force, a dipole force and a couple force. Relations among crack (dislocation) models, equivalent force models and moment tensors are straightforward. From equation 2, in an isotropic material we have,

$$M_{pq} = (\lambda_k n_k \delta_{pq} + \mu l_p n_q + \mu l_q n_p). \quad (4)$$

Here, λ and μ are Lamé constants.

In the case that a tensile crack occurs on a crack surface parallel to the x-y plane and opens in the z-direction as shown in Fig. 3, the normal vector $\mathbf{n} = (0, 0, 1)$ and the crack vector $\mathbf{l} = (0, 0, 1)$. Substituting these into equation 4, the moment tensor becomes,

$$[M_{pq}] = \begin{bmatrix} \lambda & 0 & 0 \\ 0 & \lambda & 0 \\ 0 & 0 & \lambda + 2\mu \end{bmatrix} \Delta V \quad (5)$$

Only diagonal elements are obtained, which are shown in Fig. 3. Replacing these diagonal elements as dipole forces, three dipole-forces are illustrated in Fig. 3(c). This implies that combination of three dipoles is necessary and sufficient to model a tensile crack.

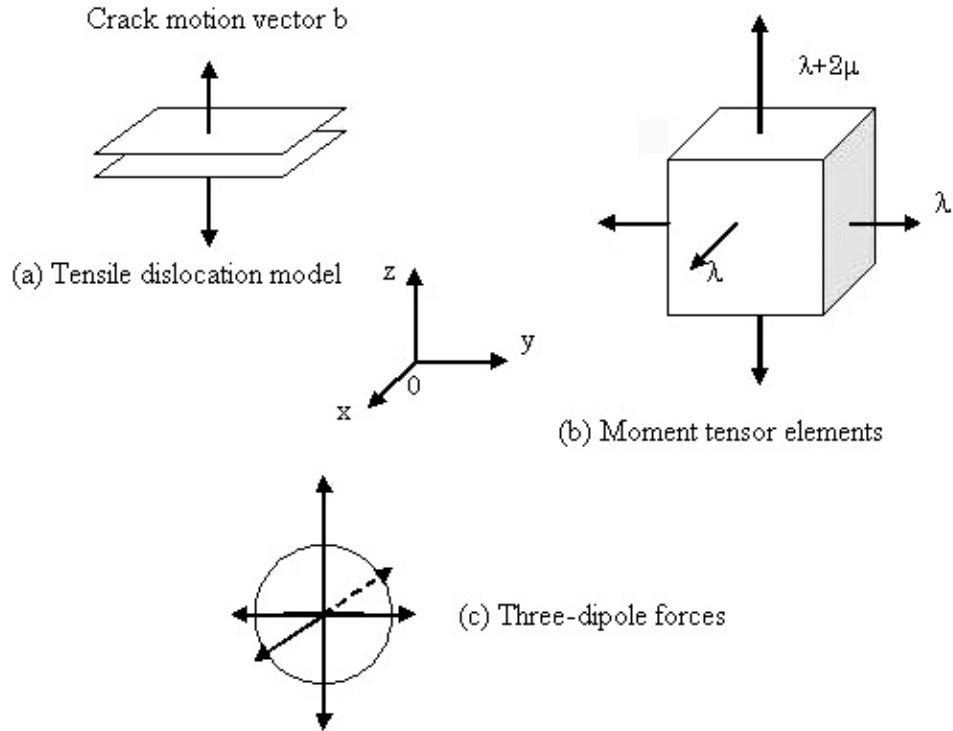


Fig. 3 (a) Tensile dislocation model, (b) related moment tensor elements, and (c) three-dipole forces.

In Fig. 4, the case of a shear crack parallel to the x-y plane is shown with the normal vector $\mathbf{n} = (0, 0, 1)$. Shear motion occurs in the y-direction with the crack vector $\mathbf{l} = (0, 1, 0)$. From equation 4, we have,

$$[M_{pq}] = \begin{bmatrix} 0 & 0 & 0 \\ 0 & 0 & \mu \\ 0 & \mu & 0 \end{bmatrix} \Delta V \quad (6)$$

As seen in Fig. 4(c), the double force couple model is comparable to off-diagonal elements of the moment tensor in equation 6.

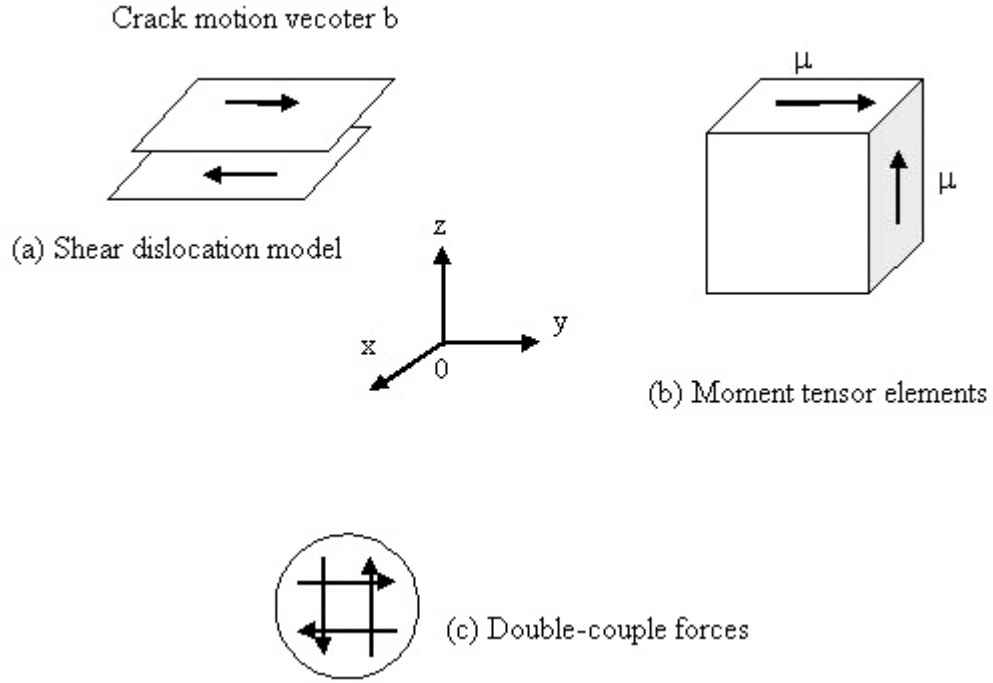


Fig. 4 (a) Shear dislocation model, (b) related moment tensor elements and (c) double-couple forces.

2.3 SiGMA Code

Taking into account only P-wave motion of the far field ($1/R$ term) of Green's function in an infinite space and considering the effect of reflection at the surface, the amplitude of the first motion is derived from equation 1. The reflection coefficient $\text{Ref}(\mathbf{t}, \mathbf{r})$ is obtained as \mathbf{t} is the direction of sensor sensitivity and \mathbf{r} is the direction vector of distance R from the source to the observation point, and $\mathbf{r} = (r_1, r_2, r_3)$. The time function is neglected in equation 1, and the amplitude of the first motion $A(\mathbf{x})$ is represented,

$$A(\mathbf{x}) = C_s \cdot \frac{\text{Ref}(\mathbf{t}, \mathbf{r})}{R} \cdot (r_1, r_2, r_3) \begin{bmatrix} m_{11} & m_{12} & m_{13} \\ m_{12} & m_{22} & m_{23} \\ m_{13} & m_{23} & m_{33} \end{bmatrix} \begin{bmatrix} r_1 \\ r_2 \\ r_3 \end{bmatrix} \quad (7)$$

where C_s is the calibration coefficient of the sensor sensitivity and material constants. Since the moment tensor is a symmetric tensor of 2nd rank, the number of independent elements is six. These are represented in equation 7 as m_{11} , m_{12} , m_{13} , m_{22} , m_{23} , and m_{33} .

These can be determined from the observation of AE waves at more than six sensor locations. In SiGMA procedure, the two parameters, the arrival time (P1) and the amplitude of the first motion (P2), are visually determined from AE waveform as shown in Fig. 5. In the location procedure, the source (crack) location \mathbf{y} in equation 1 is determined from the arrival time differences t_i between the observation \mathbf{x}_i and \mathbf{x}_{i+1} , solving equations,

$$R_i - R_{i+1} = |\mathbf{x}_i - \mathbf{y}| - |\mathbf{x}_{i+1} - \mathbf{y}| = v_p t_i. \quad (8)$$

Here v_p is the velocity of P wave.

After solving equation 8, the reflection coefficient $Ref(t,r)$, the distance R , and direction vector \mathbf{r} are readily obtained to solve equation 7. The amplitudes of the first motions P2 in Fig. 5 at more than 6 channels are substituted into equation 7, and all the elements of the moment tensor are determined. Since the SiGMA code requires only relative values of the moment tensor elements, the relative coefficients C_s are sufficient.

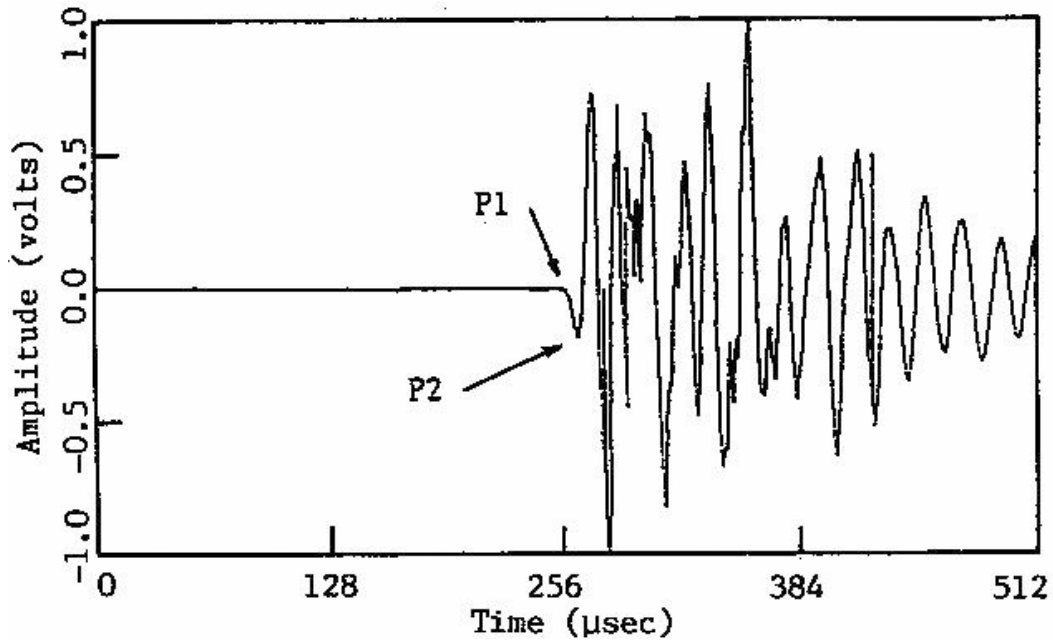


Fig. 5 Detected AE waveform.

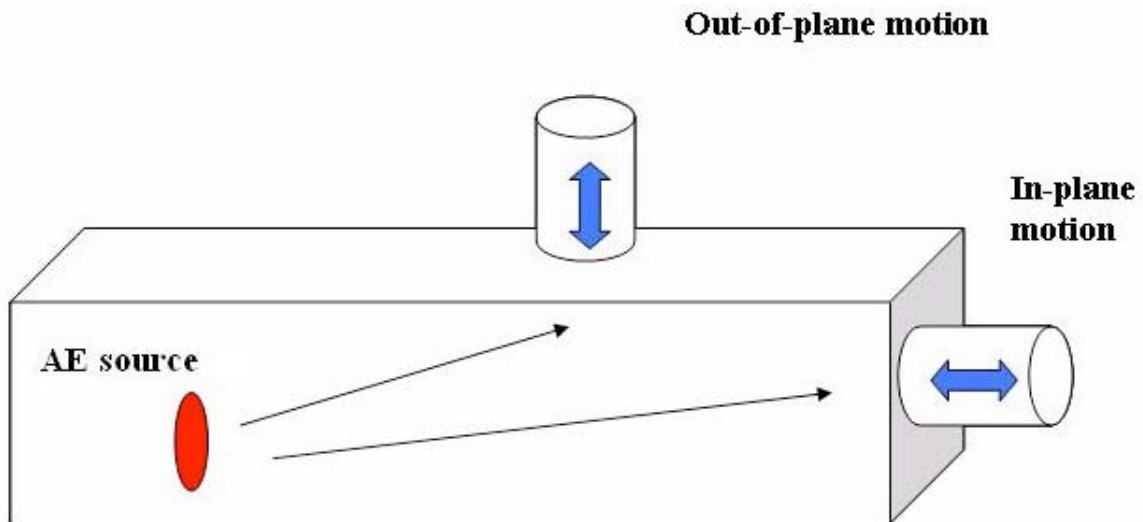


Fig. 6 Detection of AE waves of out-of-plane and in-plane motions.

2.4 Two-Dimensional Treatment

Special care must be taken for the case of a plate-like sample for two-dimensional (2-D) problems. When cracks occur in a plate as shown in Fig. 6, wave motions detected are classified into two types. One is in-plane motion, which can be detected at the edge of the plate. The other is out-of-plane motion. AE waves are often detected as the out-of-plane motions even in the

plate-like sample. In this case, the reflection coefficient in equation 7 is almost equal to zero, and thus the equation is neither well-posed nor solvable.

Consequently, only AE waves of the in-plane motion can be analyzed by SiGMA procedure. Assuming that the z-components of vectors \mathbf{l} and \mathbf{n} are equal to zero, the moment tensor in equation 4 is represented by,

$$[M_{pq}] = \begin{bmatrix} \lambda l_k n_k + 2\mu l_1 n_1 & \mu(l_1 n_2 + l_2 n_1) & 0 \\ \mu(l_1 n_2 + l_2 n_1) & \lambda l_k n_k + 2\mu l_2 n_2 & 0 \\ 0 & 0 & \lambda l_k n_k \end{bmatrix} \Delta V \quad (9)$$

In the case that AE sensors are attached only on the edge of the plate, no motions are detected in the out-of-plane direction. As a result, elements of the tensor in equation 9 could be estimated except for the m_{33} element. Here, $m_{11} + m_{22} = 2(\lambda + \mu) l_k n_k$ and,

$$2(\lambda + \mu) = 2\lambda + \lambda(1 - 2\nu)/\nu = \lambda/\nu.$$

Accordingly, the m_{33} component is readily determined from,

$$m_{33} = \lambda l_k n_k = \nu (m_{11} + m_{22}) \quad (10)$$

where ν is the Poisson's ratio.

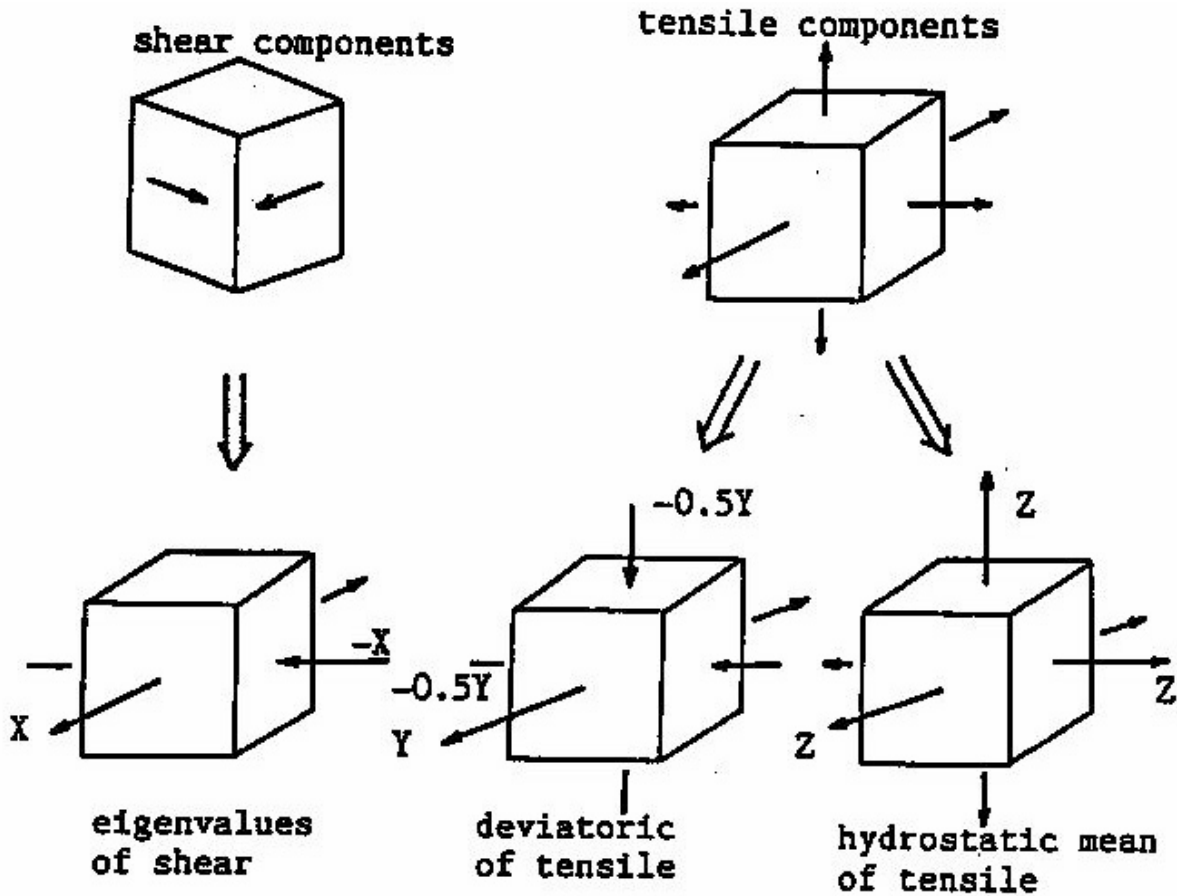


Fig. 7 Unified decomposition of eigenvalues of the moment tensor.

2.5 Unified Decomposition

In order to classify a crack into the tensile or shear type, a unified decomposition of the eigenvalues of the moment tensor was developed (Ohtsu, 1991). In general, crack motion on the crack surface consists of slip motion (shear components) and crack-opening motion (tensile components), as illustrated in Fig. 7. Thus, it is assumed that the eigenvalues of the moment tensor are the combination of those of a shear crack and those of a tensile crack, as the principal axes are identical. Then, the eigenvalues are decomposed uniquely into those of a shear crack, the deviatoric components of a tensile crack and the isotropic (hydrostatic mean) components of a tensile crack. In Fig. 7, the ratio X represents the contribution of a shear crack. In that case, three eigenvalues of a shear crack become $X, 0, -X$. Setting the ratio of the maximum deviatoric tensile component as Y and the isotropic tensile component as Z , three eigenvalues of a tensile crack are denoted as $Y + Z, -Y/2 + Z$, and $-Y/2 + Z$. Eventually the decomposition leads to relations,

$$\begin{aligned} 1.0 &= X + Y + Z, \\ \text{the intermediate eigenvalue/the maximum eigenvalue} &= 0 - Y/2 + Z, \\ \text{the minimum eigenvalue/the maximum eigenvalue} &= -X - Y/2 + Z. \end{aligned} \quad (11)$$

It should be pointed out that the ratio X becomes larger than 1.0 in the case that both the ratios Y and Z are negative (Suaris and van Mier, 1995). The case happens only if the scalar product $l_k n_k$ is negative, because the eigenvalues are determined from relative tensor components. Making the scalar product positive and re-computing equation 11, the three ratios are reasonably determined. Hereinafter, the ratio X is called the shear ratio.

Classification of cracks was proposed elsewhere on the basis of angles between two vectors \mathbf{l} and \mathbf{n} (Ouyang et al., 1992). But, the crack classification based on the angle is not reasonable, because the relationship between the angle and the shear ratio X is nonlinear (Ohtsu, 1995).

In the present SiGMA code, AE sources with shear ratios less than 40%, are classified as tensile cracks. The sources with $X > 60\%$ are classified as shear cracks. In between 40% and 60%, the cracks are referred to as mixed-mode.

From the eigenvalue analysis, three eigenvectors $\mathbf{e1}, \mathbf{e2}, \mathbf{e3}$ are also obtained. Theoretically, these are derived as,

$$\begin{aligned} \mathbf{e1} &= \mathbf{l} + \mathbf{n} \\ \mathbf{e2} &= \mathbf{l} \times \mathbf{n} \\ \mathbf{e3} &= \mathbf{l} - \mathbf{n}. \end{aligned} \quad (12)$$

Here \times denotes the vector product, and the vectors \mathbf{l} and \mathbf{n} are interchangeable. In the case of a tensile crack, the vector \mathbf{l} is parallel to the vector \mathbf{n} . Thus, the vector $\mathbf{e1}$ could give the direction of crack-opening, while the sum $\mathbf{e1} + \mathbf{e3}$ and the difference $\mathbf{e1} - \mathbf{e3}$ give the two vectors \mathbf{l} and \mathbf{n} for a shear crack.

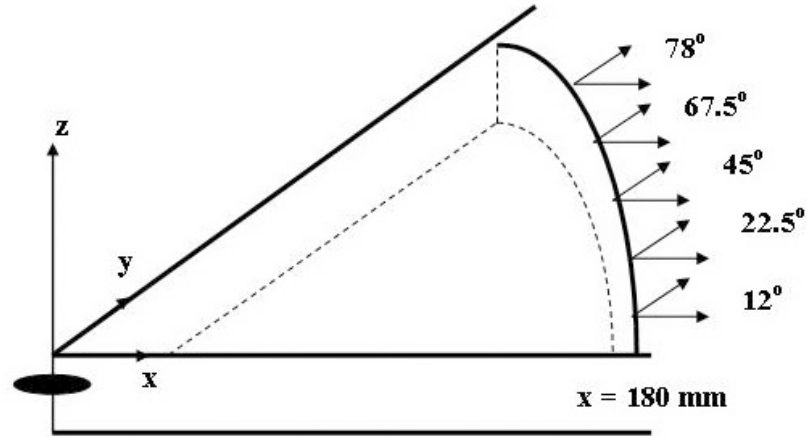
To locate AE sources, at least 5-channel system is necessary for 3-D analysis. Since 6-channel system is the minimum requirement for the moment tensor, 6-channel system is required for SiGMA-3D analysis. In the 2-D problem, a 3-channel system is applicable to determine the moment tensor elements, but generally a 4-channel system is necessary for 2-D location analysis. Consequently, a 4-channel system is the minimum recommended for SiGMA-2D analysis.

3. IN-PLANE THEORETICAL WAVEFORMS

3.1 Source Models

In order to study the accuracy of SiGMA-2D, in-plane theoretical waves are analyzed. These were computed by employing the FEM-based AE signal database (Downs et al., 2003). The configuration of the detection is illustrated in Fig. 8. As a propagating medium, we selected aluminum with P-wave velocity of 6320 m/s and Poisson's ratio of 0.34. The sources were located at the coordinate origin at 1.41 mm depth. In-plane waves were calculated at five locations 180 mm from the source. The radiation angles were set to 12°, 22.5°, 45°, 67.5° and 78°. In-plane displacements (waves) in both the x-direction and the y-direction were computed with 0.1-μs increment of 2000 words at each observation point

At the origin, three moment tensors were considered as source models. One model consists of three dipole forces, corresponding to the nucleation of a tensile crack. The crack surface is perpendicular to the x-axis and parallel to the y-axis. The second model was one dipole force applied in the x-direction, and the third model was a shear crack with out-of-plane orientation.



**Source depth
= 1.41 mm**

Fig. 8 Five observation points for in-plane theoretical waveforms.

(1) Tensile crack

Configuration of the source is illustrated in Fig. 9. An associated dipole-force model is also given. The moment tensor is represented by,

$$[M_{pq}] = \begin{bmatrix} 1 & 0 & 0 \\ 0 & 0.52 & 0 \\ 0 & 0 & 0.52 \end{bmatrix}. \quad (13)$$

(2) One dipole-force model

The model is given in Fig. 10. The moment tensor is obtained as:

$$[M_{pq}] = \begin{bmatrix} 1 & 0 & 0 \\ 0 & 0 & 0 \\ 0 & 0 & 0 \end{bmatrix}. \quad (14)$$

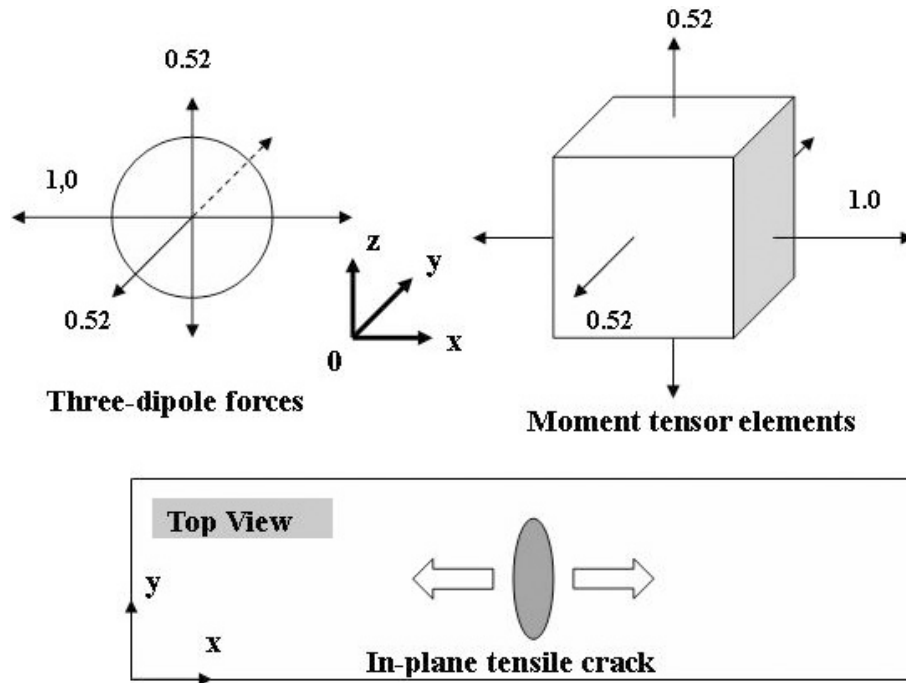


Fig. 9 Source model of in-plane tensile crack and corresponding moment tensor elements.

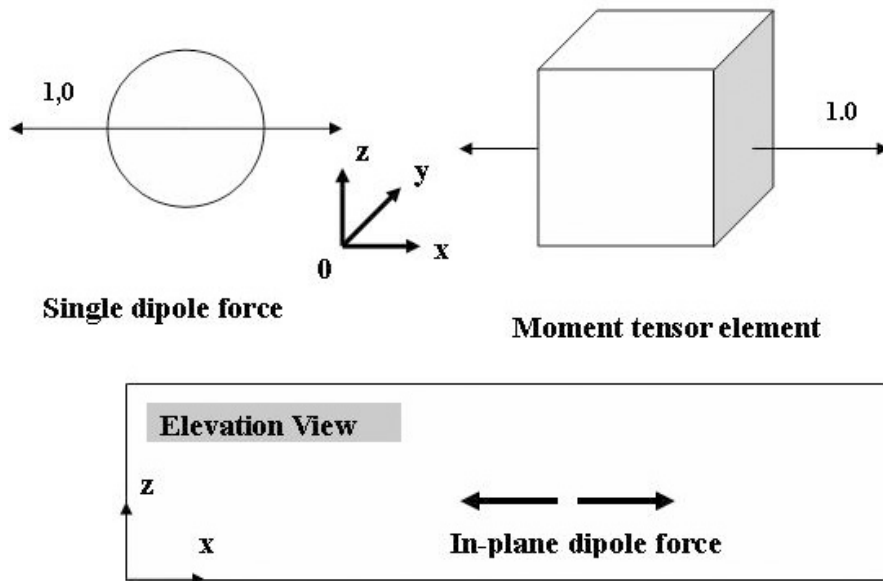


Fig. 10 Dipole-force model and corresponding moment tensor elements.

It is noted that no crack is equivalent to this model, because three dipole-forces are associated with a tensile crack and a shear crack is modeled by double couple-forces.

(3) Shear crack inclined 45° to x-axis.

A source model and the double-couple force model are illustrated in Fig. 11. The eigenvalues of the corresponding moment tensor are represented by,

$$[M_{pq}] = \begin{bmatrix} -1 & 0 & 0 \\ 0 & 0 & 0 \\ 0 & 0 & 1 \end{bmatrix}. \quad (15)$$

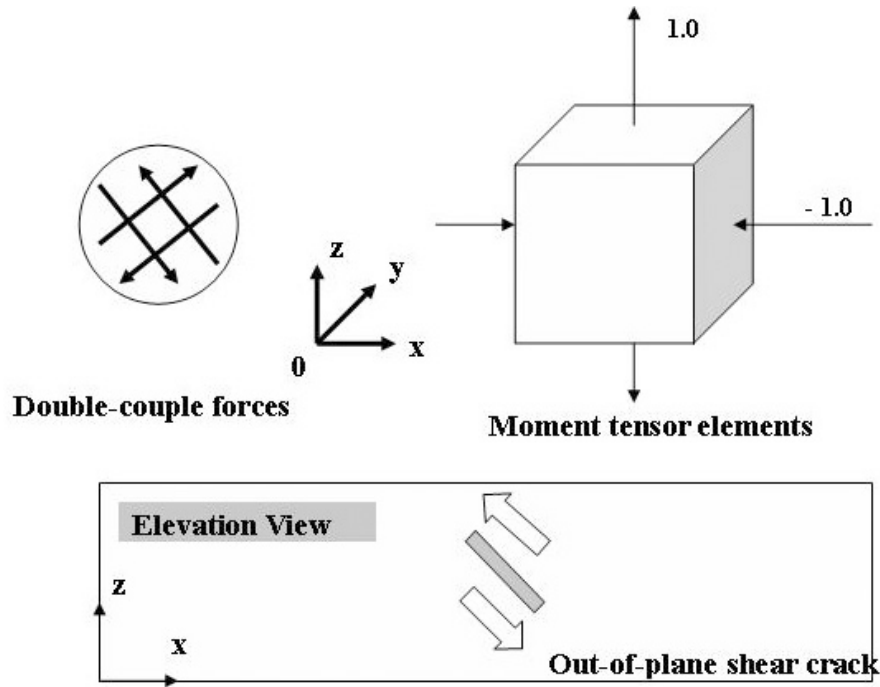


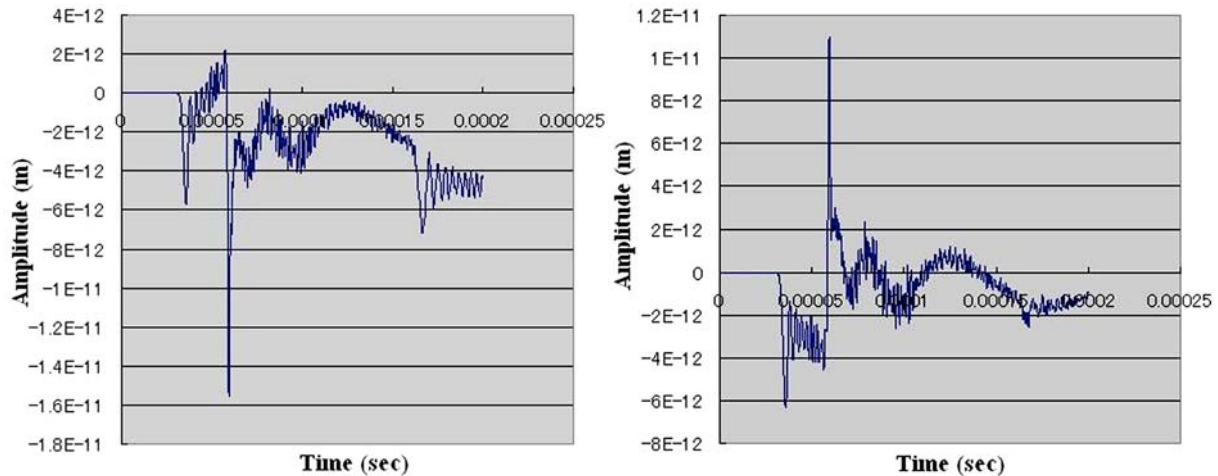
Fig. 11 Source model of out-of-plane shear crack and corresponding moment tensor elements.

3.2 Results of SiGMA-2D Analysis

Examples of waveforms computed are shown in Fig. 12. Applying SiGMA-2D to the first arrivals of these waves, moment tensor elements are recovered by equation 7. For the tensile crack, tensor elements in equation 13 are recovered,

$$[M_{pq}] = \begin{bmatrix} 1 & -0.01 & 0 \\ -0.01 & 0.25 & 0 \\ 0 & 0 & 0.43 \end{bmatrix}$$

Here, the tensor elements are normalized by the maximum value, and the element m_{33} is calculated by equation 10. It is noted that the elements m_{22} and m_{33} are recovered as smaller values than those in equation 13.



(a) X-displacement at 45°; shear crack.

(b) Y-displacement at 45°; shear crack.

Fig. 12 Examples of theoretical waves by FEM analysis.

For the case of one dipole-force model in equation 14, results are obtained as,

$$[M_{pq}] = \begin{bmatrix} 1 & -0.02 & 0 \\ -0.02 & -0.06 & 0 \\ 0 & 0 & 0 \end{bmatrix}.$$

Since the model does not correspond to a crack, the element m_{33} is not computed. Comparing with equation 14, a good agreement is found.

In the case of the shear crack in equation 15, tensor elements are recovered as,

$$[M_{pq}] = \begin{bmatrix} -1 & 0.01 & 0 \\ 0.01 & 0.26 & 0 \\ 0 & 0 & 0 \end{bmatrix}.$$

Because this source corresponds to a shear crack, the scalar product $l_k n_k$ in equation 10 is equal to zero. Accordingly, the element m_{33} is again not computed. As a result, agreement with equation 15 is not so clear that element m_{33} is not comparable to that in equation 15 and fairly large error is observed in the element m_{22} . This is because dominant motions are generated in the out-of-plane direction due to shear motion of out-of-plane orientation, and no information from out-of-plane motions was obtained.

These results imply that the elements of the moment tensors are recovered reasonably well by SiGMA-2D in the case that such dominant source motions are generated in the in-plane direction as one dipole-force model. For the general cases of cracking, crack types are classified correctly, but the loss of information on out-of-plane motions can result in large errors.

4. LEAK DETECTION

4.1 Experiment

As one practical application, SiGMA-2D was applied to AE events due to water leakage. A slit-like defect is modeled, through which water leakage occurs. A defect model of PMMA and AE sensor locations are shown in Fig. 13. The defect is a slit of 1 mm width and 5 mm length located at the center of the 10-mm thick plate. AE events were detected by a 4-channel system, which consists of AE sensors of 150 kHz resonance (R15, PAC) and the sampling frequency for recording waveforms is 1 MHz.

The slit model was attached at the edge of a water chamber in a pipe model as shown in Fig. 14. By employing a large water chamber, 0.3 MPa pressure was constantly applied to the model in laboratory. AE events due to leakage were detected. Detected AE waves for one event are shown in Fig. 15. Although mostly continuous-type AE events were observed, in some cases the first arrivals could be determined as illustrated in the figure.

4.2 Analysis

During the leakage test, 109 AE events with detectable first arrivals were analyzed. The results are classified by the shear ratio X as plotted in Fig. 16. It is found that almost 40 % of the events have the shear ratio of over 80 %. This implies that dominant source motions at the slit-like defect due to leakage are shear-type motions. This result might be associated with the fact

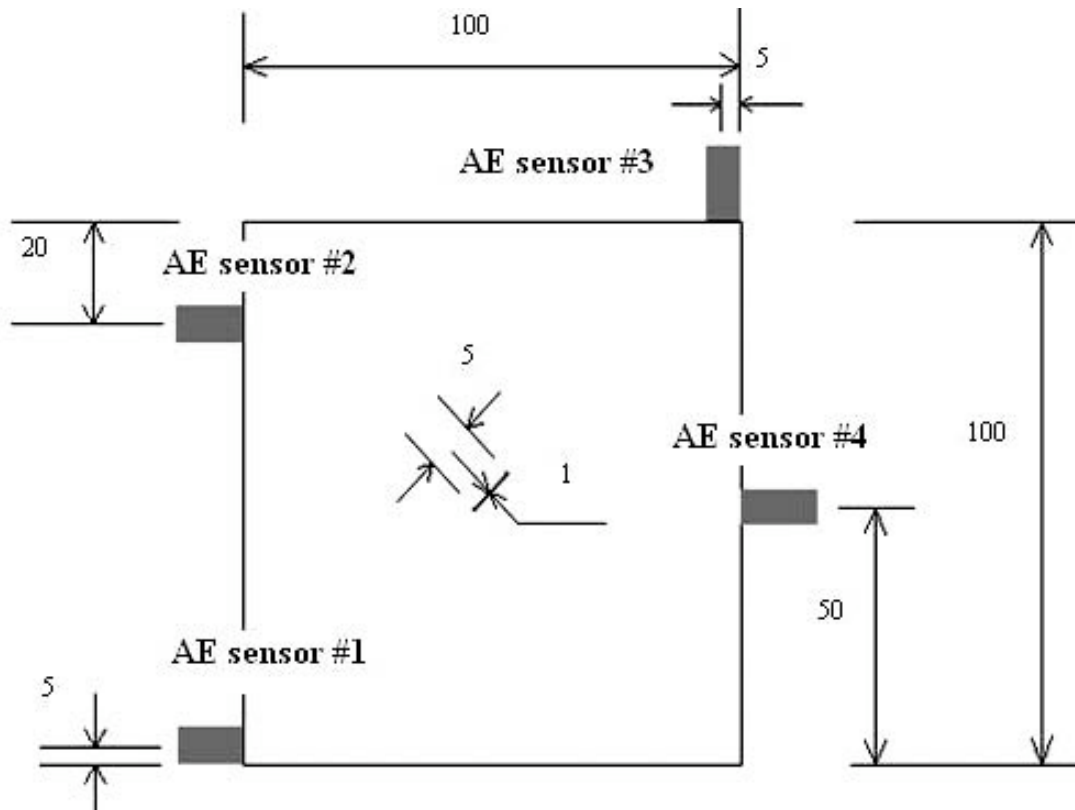


Fig. 13 Slit model for a defect (dimensions in mm).

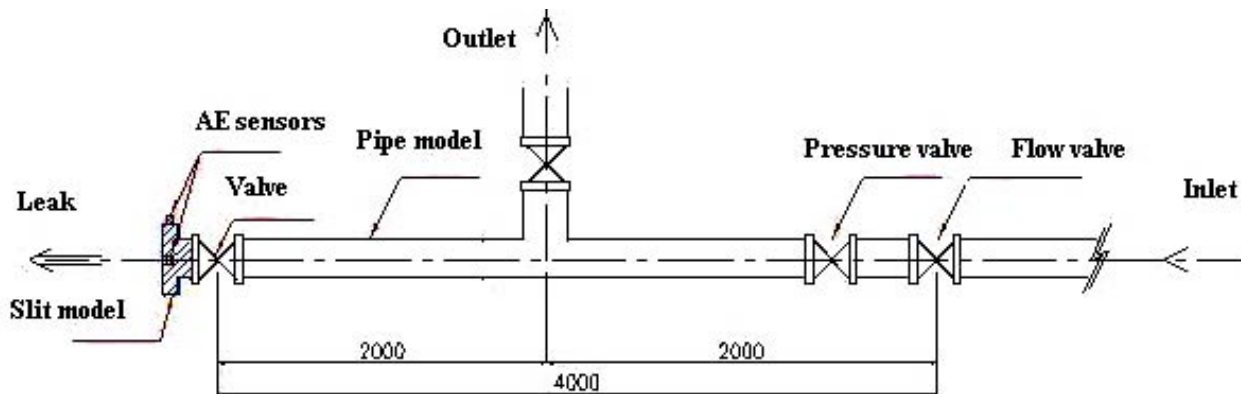


Fig. 14 Pipe model for water leakage (dimensions in mm).

that only large AE events were identified as the burst-type and readable for the analysis. That is, slip motions on the slit surface were mostly detected as AE events due to leakage.

Next, crack orientations were estimated. Typical events having the shear ratios smaller than 10% are plotted in Fig. 17. Because these are classified as the tensile cracks, crack-opening directions obtained are indicated. It is found the source opening directions are almost vertical to the slit surface, suggesting that water flows due to leakage open the slit. Some events of the shear ratios larger than 80 % are plotted in Fig. 18. It is clearly observed that orientations of the shear events are parallel to the slit surface. This implies that the dominant source motions detected as AE events are in-plane shear motions at the slit-like defect. This may result from dynamic water outflow through the slit.

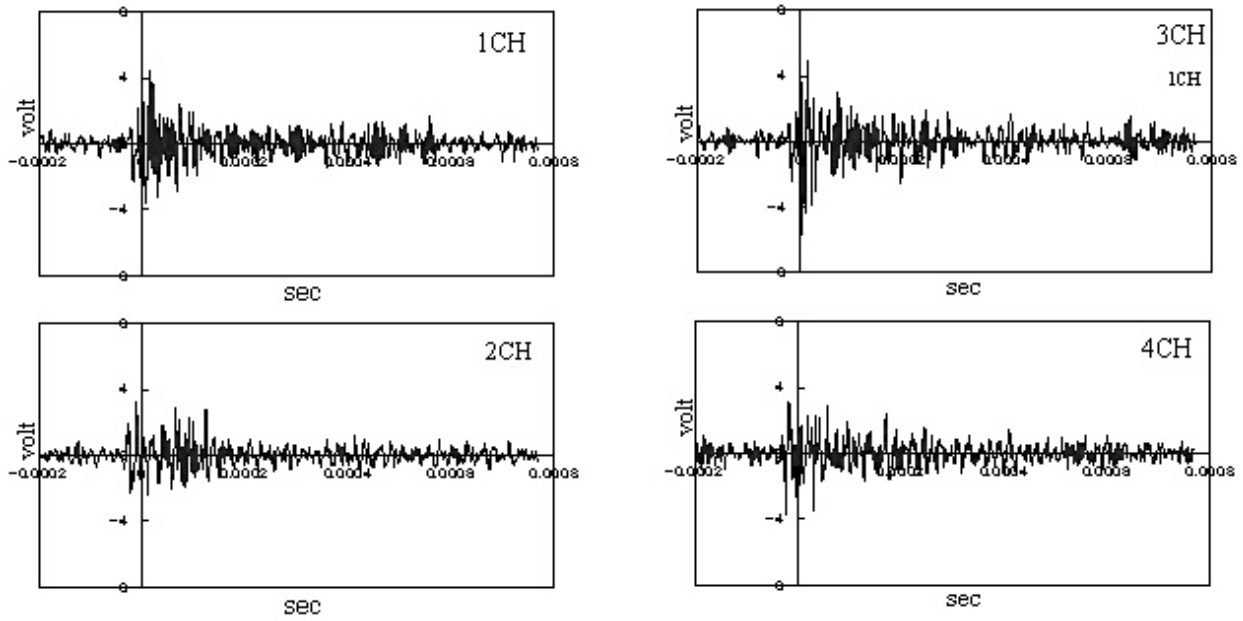


Fig. 15 Examples of detected AE waves.

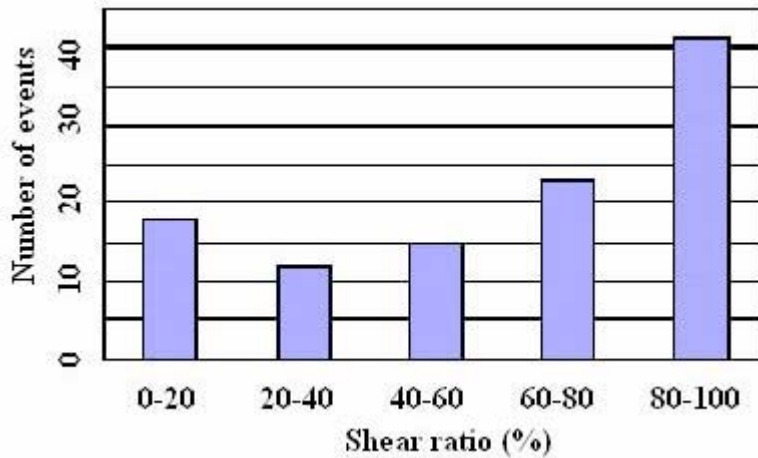


Fig. 16 Results of SiGMA-2D analysis for water leakage from a slit-like defect.

5. CONCLUSION

The applicability of SiGAM-2D analysis to in-plane motions of AE waves was studied. Employing an FEM code, theoretical waves were computed by assuming moment tensor elements, and the in-plane displacements were analyzed by SiGMA-2D. The accuracy of SiGMA-2D was numerically examined.

The elements of the source moment tensors are recovered reasonably well by SiGMA-2D in such case that dominant source motions are generated in the in-plane direction as one dipole-force model. For the general cases of cracking, loss of information on out-of-plane motions can result in large errors, while crack types are classified correctly.

As a practical application, AE waves due to water leakage from a slit were detected and analyzed. Dominant motions at the slit-like defect are found to be AE waves of shear type for

the large events, of which first arrival motions can be read. For the tensile events, crack-opening directions were vertical to the slit surface, suggesting that water flows due to leakage open the slit. Orientations of the shear events are parallel to the slit surface. This implies that dominant motions detected as AE events are in-plane shear motions at the slit-like defect, which may result from dynamic water outflow through the slit. These results show promise for clarifying AE generating mechanisms due to leakage by the moment tensor analysis.

References

Downs, K. S., Hamstad, M. A. and O’Gallagher, A., (2003), "Wavelet Transform Signal Processing to Distinguish Different Acoustic Emission Sources," *Journal of AE*, **21**, 52-69.

Enoki, M., Kishi, T. and Kohara, S., (1986), "Determination of Micro-cracking Moment Tensor of Quasi-cleavage Facet by AE Source Characterization," *Progress in Acoustic Emission III*, JSNDI, Tokyo, pp. 763-770.

Hamstad, M. A., O’Gallagher, A. and Gary, J., (1999), "Modeling of Buried Monopole and Dipole Source of Acoustic Emission with a Finite Element Technique, *Journal of AE*, **17**(3-4), 97-110.

Hamstad, A. M., O’Gallagher, A. and Gary, J., (2001), "Effects of Lateral Plate Dimensions on Acoustic Emission Signals from Dipole Sources," *Journal of AE*, **19**, 258-274.

Hamstad, A. M., O’Gallagher, A. and Gary, J., (2002), "A Wavelet Transform Applied to Acoustic Emission Signals: Part 1: Source Identification," *Journal of AE*, **20**, 39-61.

Ohtsu, M. and Ono, K., (1984), "A Generalized Theory of Acoustic Emission and Green's Functions in a Half Space," *Journal of AE*, **3**(1), 124-133.

Ohtsu, M., (1991), "Simplified Moment Tensor Analysis and Unified Decomposition of AE Source: Application to in Situ Hydrofracturing Test," *J. Geophys. Res.*, **96**(B4), 6211-6221.

Ohtsu, M., (1995), "Acoustic Emission Theory for Moment Tensor Analysis," *Research in Non-destructive Evaluation*, **6**, 169-184.

Ohtsu, M., Okamoto, T. and Yuyama, S., (1998), "Moment Tensor Analysis of Acoustic Emission for Cracking Mechanisms in Concrete," *ACI Structural Journal*, **95**(2), 87-95.

Ouyang, C., Landis, E. and Shah, S. P., (1992), "Damage Assessment in Concrete using Acoustic Emission," *Nondestructive Testing of Concrete Elements and Structures*, ASCE, pp. 13-24.

Shigeishi, M. and Ohtsu, M., (1999), "Identification of AE Sources by using SiGMA-2D Moment Tensor Analysis," *Acoustic Emission: Standard and Technology Updated*, ASTM STP 1353, pp. 175-188.

Suaris, W. and van Mier, J. G. M., (1995), "Acoustic Emission Source Characterization in Concrete under Biaxial Loading," *Materials and Structures*, No. 28, 1995, pp. 444-449.

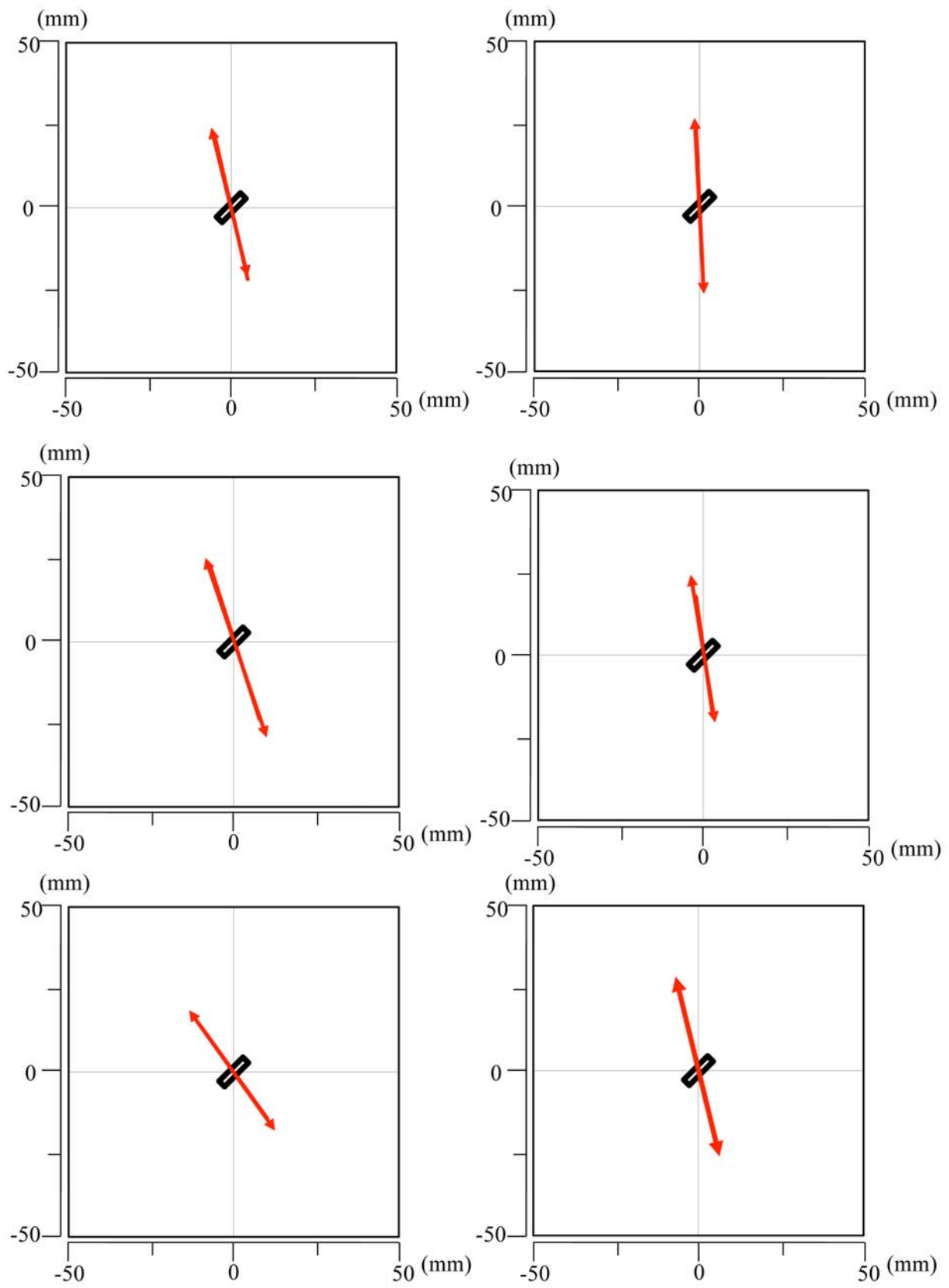


Fig. 17 Crack orientations for tensile events.

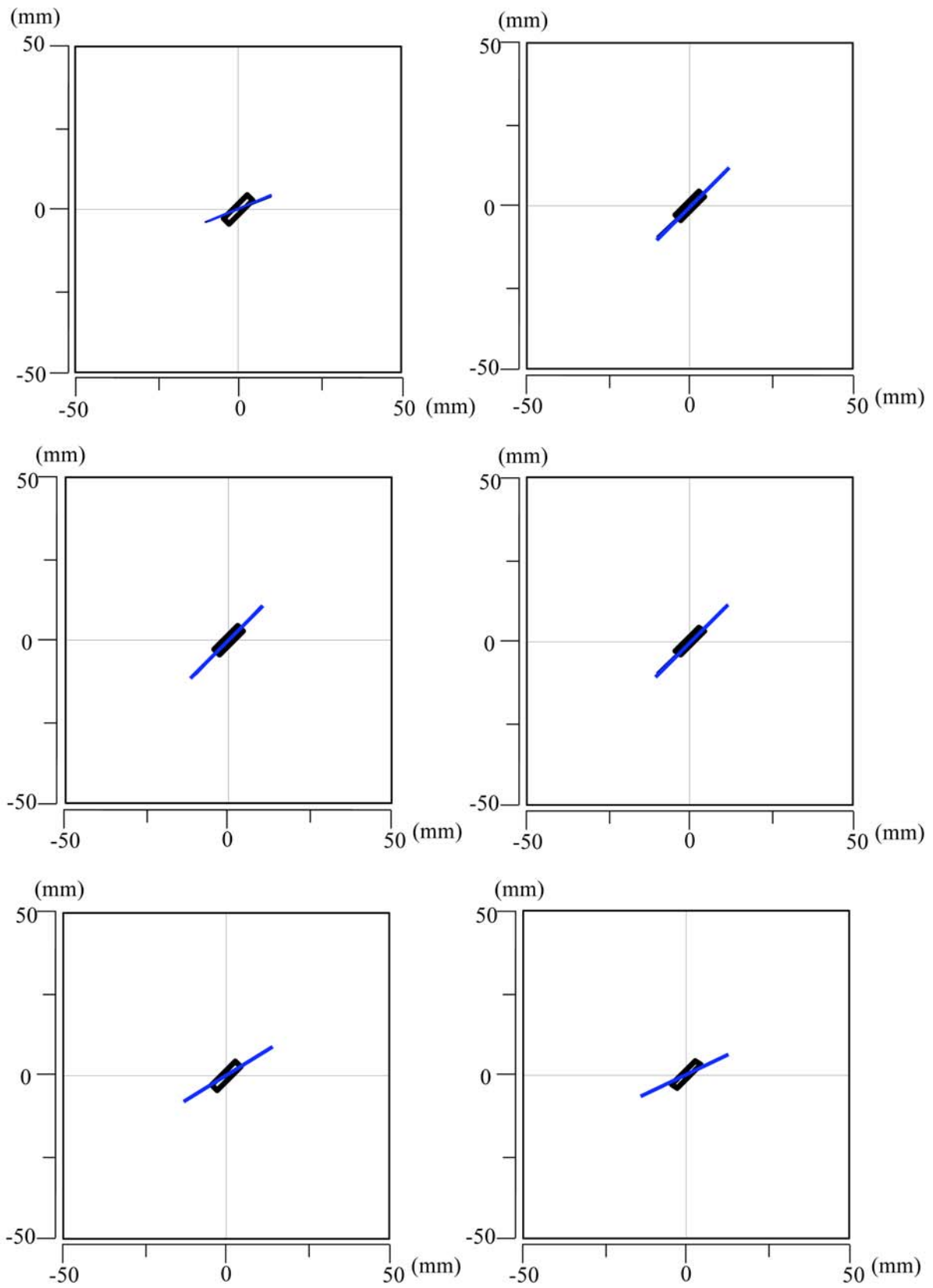


Fig. 18 Crack orientations for shear events.

DEVELOPMENT OF AN OPTICAL MICRO AE SENSOR WITH AN AUTOMATIC TUNING SYSTEM

HIROSHI ASANUMA, HIRONOBU OHISHI, and HIROAKI NIITSUMA
Graduate of Environmental Studies, Tohoku University, Sendai 980-8579, Japan

Abstract

A prototype optical micro AE sensor, which has a mechanism for automatic tuning of the operating point, was fabricated using micro electromechanical systems (MEMS) technologies, and its performance was evaluated. The AE signal is detected by an interferometric pattern of returning lightwave from a Fabry-Perot interferometer (FPI) which consists of a half mirror at the edge of an optical fiber and a full mirror on a moving mass. The mechanical part of the micro optical AE sensor was designed to have a resonant frequency at 50 kHz. The linearity and sensitivity of this sensor is highly dependent on the initial gap length between the fiber and the moving mass because of non-linearity in the interferometric pattern of the FPI. To control gap length, we fabricated electrodes on the cover glass plate. This allows the initial gap to be automatically tuned by electrostatic force. Laboratory tests to evaluate performance of the AE sensor have demonstrated that the linearity, sensitivity and signal to noise ratio were improved by the automatic tuning.

Keywords: AE sensor, MEMS, Optical sensor, Fabry-Perot interferometer, Automatic tuning

1. Introduction

Technologies related to micro-electromechanical systems (MEMS) have progressed remarkably over the last decade and commercial products, which use the MEMS technology, are now widely available. Micro-sensors fabricated by the MEMS technology are one of the major and promising application areas of this technology. Micro-mechanical sensors, micro-acoustic and micro-seismic sensors, micro-medical sensors, and micro-optical sensors have been developed and their advantages over existing sensors have been demonstrated.

The authors have been developing microsensors mainly for geophysical/near-surface environmental measurement under the "Subsurface Microsensing Project" since 1993 [1]. Capacitive accelerometer, fiber sensors, optical hydrophone and ultrasonic sensors are studied in the project, and some of the sensors have now become commercially available [2, 3].

One of the major research areas currently under investigation in the project is the field of optical acoustic/seismic/ultrasonic microsensors using the principles of the Fabry-Perot interferometer (FPI) [4, 5], because of the simplicity in the principle and the availability of MEMS technologies for fabrication. The FPI is a variation of interferometers, where a multiply reflected lightwave at a gap of full and a half mirrors is outputted. The interferometric pattern (spectra) of the output changes associated with gap length. We have employed this property by fabricating a FPI which consists of a half-mirror at the fiber end and a full mirror on the moving mass/diaphragm and have detected displacement of the moving mass/diaphragm. Although the prototypes of the optical microsensors with FPI worked successfully [4, 5], we have found that

the precise control of the gap length presents a fabrication difficulty. In many cases, the authors inserted an optical fiber with a half mirror to the silicon/glass structure at the final stage of the fabrication, and the gap length is defined manually at this stage. The typical gap length of the FPI in the microsensors in our group is 20-40 μm , and the variation in the gap length is not negligibly small for the commercial use of the sensors where a laser with a single wavelength should be used to reduce the system cost.

Considering above mentioned problems, the authors had started to develop an ultrasonic/AE sensor which can automatically control its operating point to have the best performance. The concept, principles, fabrication process and results from laboratory tests are described in this paper.

2. Outline of the Autotuning Mechanism

The concept of the automatic tuning of the FPI sensor, which was employed in this study is shown in Fig. 1. The FPI consists of a half mirror at the end of the optical fiber and a full mirror on a moving mass, which is suspended by thin silicon beams. The interferometric pattern of the FPI changes with the reflectivity of the mirrors that is uniquely defined for each sensor, and the length of the gap which changes by externally applied acceleration. The typical initial gap length is around 20-40 μm , and it is determined by the manual process of inserting the fiber into the glass/silicon/glass structure. In the micro-accelerometer with an automatic tuning mechanism, an electrode is fabricated on a bottom glass plate, and an electrostatic force is generated by applying a voltage to it to change the length of the initial gap. The sensitivity and linearity of the sensor depends on the interferometric pattern of the FPI for a wavelength λ and this system automatically finds the optimum operating point by changing the gap length (see Fig. 2).

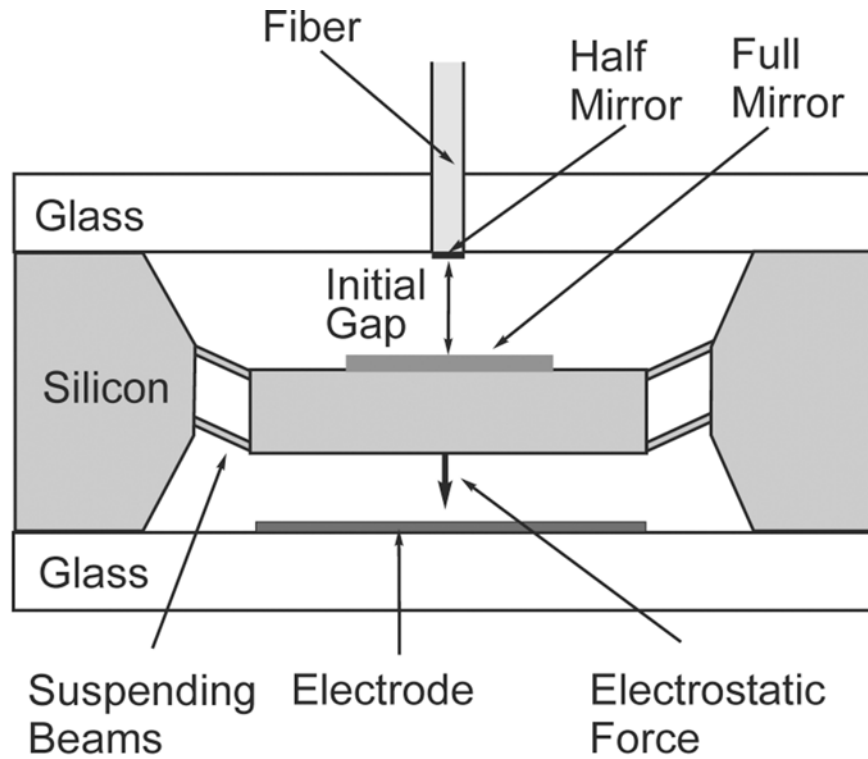


Fig. 1: A schematic view of the optical micro-accelerometer with an electrode to control the initial gap.

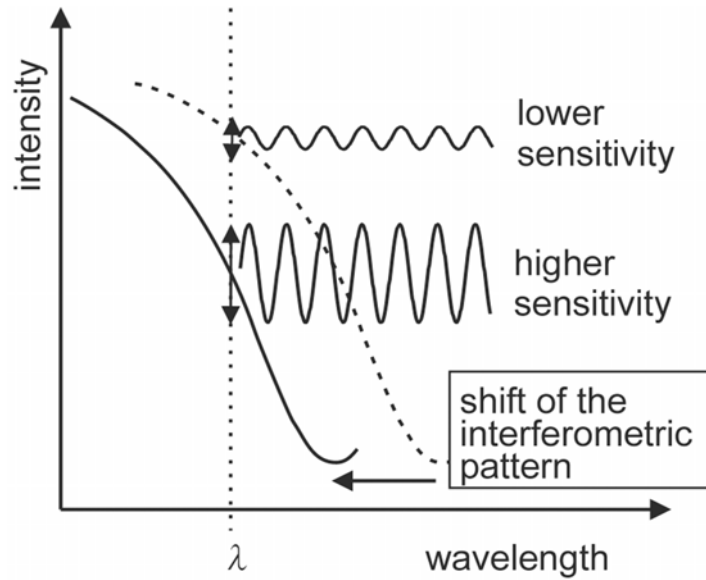


Fig. 2: Concept of changing the operating point of the FPI sensor.

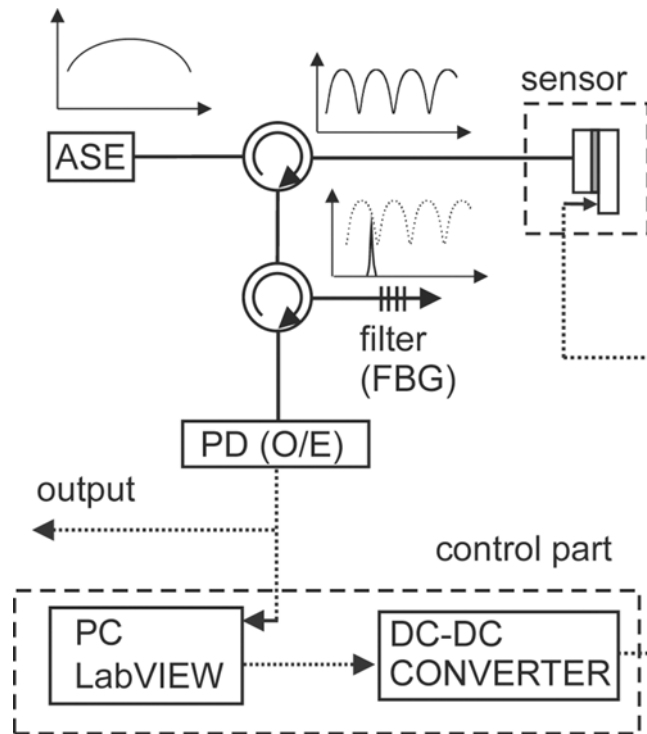


Fig. 3: Block diagram of the sensing system.

A block diagram of the prototype system incorporating automatic tuning is shown in Fig. 3. A wideband lightwave source (ASE: Amplified Spontaneous Emission) is used as an input of the lightwave to the sensor. The interfered lightwave at the sensor is then transmitted to an optical narrow-band filter using the FBG (Fiber Bragg Grating) [6]. The intensity of the filtered lightwave is converted to voltage at a photodiode (PD) and sent to both data display/acquisition as an output and to a PC with system control software. To start the system, the PC sends a control signal to the DC-DC converter and the optical response is collected for different gap lengths. The software finds the optimum operating point where the maximum sensitivity/linearity is obtained and then continuously applies a static voltage to hold this operating point.

3. Design and Fabrication of the Sensor

The mechanical part of this sensor is a resonant system in the first order. We have designed the prototype to have a resonant frequency at 50 kHz. Considering the damping effect in the sensor, which is mainly influenced by air damping in the gap of glass/silicon, we can design a system in the state of critical damping or over-damping for wideband performance. However, we decided to design the system to have strong resonance, suppressing the damping factor, because there are some unknown points in the behavior of the air damping at higher frequency and we preferred higher sensitivity rather than a flat frequency characteristic in this study.

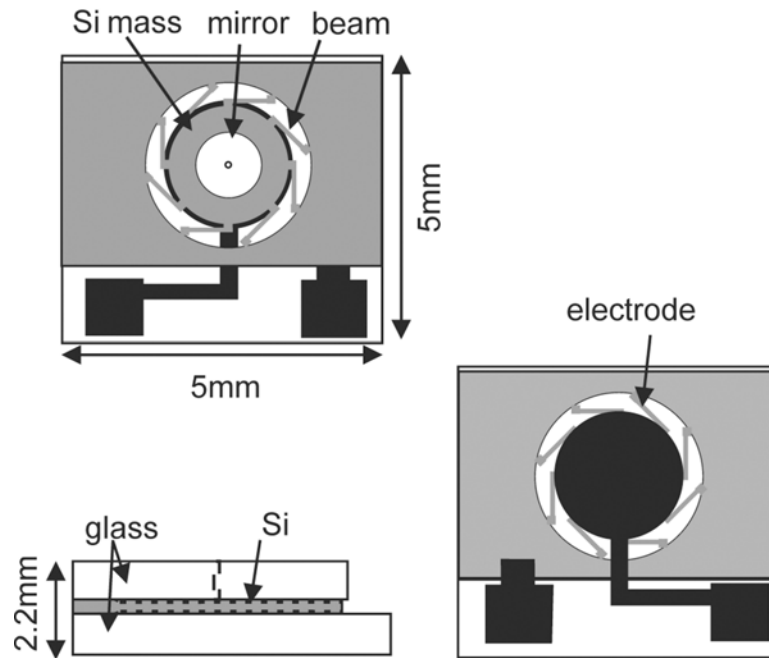


Fig. 4: An external view of the sensor.

The external form of the sensor is shown in Fig. 4, where top, bottom and side views of the sensor are shown. The sensor has a “sandwich” structure of glass/silicon/glass and has a dimension of 5 mm x 5 mm x 2.2 mm. A moving mass with an aperture of $1.96 \times 10^{-7} \text{ m}^2$, is suspended by 16 beams with a width of 20 μm .

The MEMS process mainly consists of a combination of standard techniques including photolithography, etching, and sputtering. A part of the process of the silicon structure is shown in Fig. 5. A technique of anodic bonding was used for the bonding of the silicon and glass parts. Almost all the process, except for the sputtering of a half mirror on the end of the optical fiber, can be realized by conventional MEMS facilities. Because a number of microsensors can be fabricated on a single silicon wafer, which has a typical size of 4”/8” in the industry, cost reduction and uniform performance of the sensors can be expected. A photo of the assembled sensor is shown in Fig. 6. The software for automatic tuning was developed using a commercial software package (LabView).

4. Evaluation of System Performance

The interferometric pattern of the fabricated sensor at different applied voltages to the electrode for the control of the gap length is shown in Fig. 7. It is seen that the interferometric

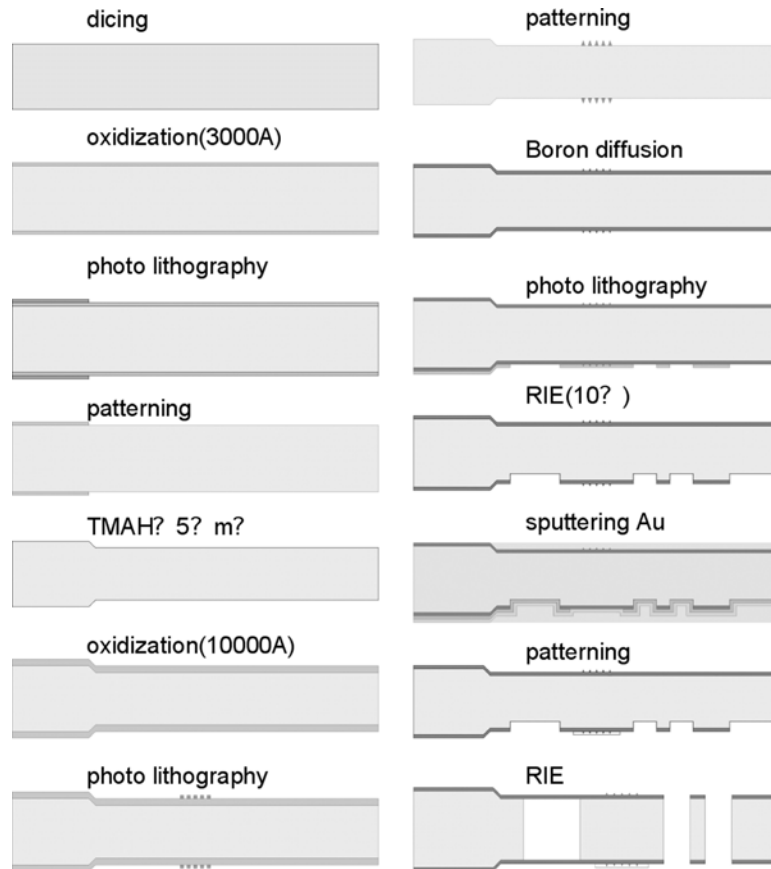


Fig. 5: A process chart of the silicon part.

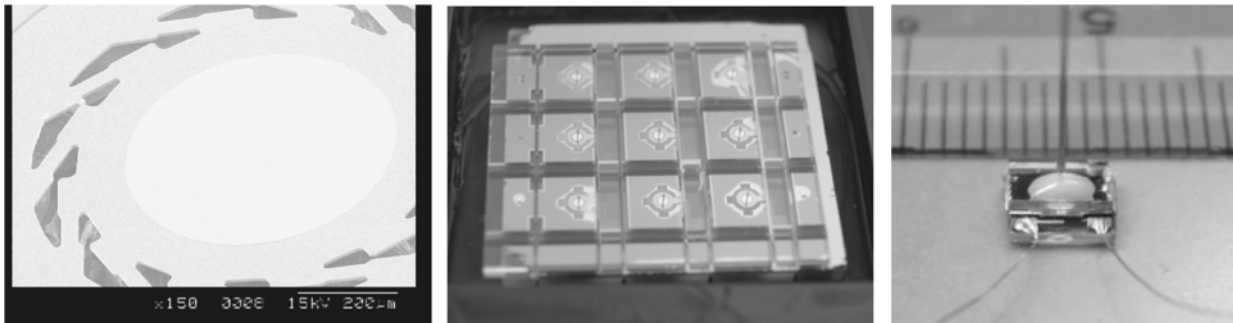


Fig. 6: Fabricated sensor. Moving mass on silicon (left), sensors before dicing (center), and finished product (right).

pattern has moved approximately 6 nm after applying 200V to the electrode. This shift corresponds to a change in the gap length approximately $0.18 \mu\text{m}$. It is also seen that the interferometric pattern is distorted after applying 200V, suggesting that the silicon mass did not displace uniformly relative to the electrode.

Because of difficulties in precisely evaluating the absolute sensitivity in the frequency range of several tens of kHz, we inputted a sinusoidal wave from a PZT transmitter to a thin ($t = \sim 20$ mm) rock specimen and observed the output. Figure 8 shows the output from the optical sensor and that from PZT receiver for an input of 50-kHz sinusoidal wave. In this experiment, the automatic tuning was disabled as the objective was to prove that the optical sensor itself was working. It is seen from Fig. 8 that the transmitted signal is detected by both optical and

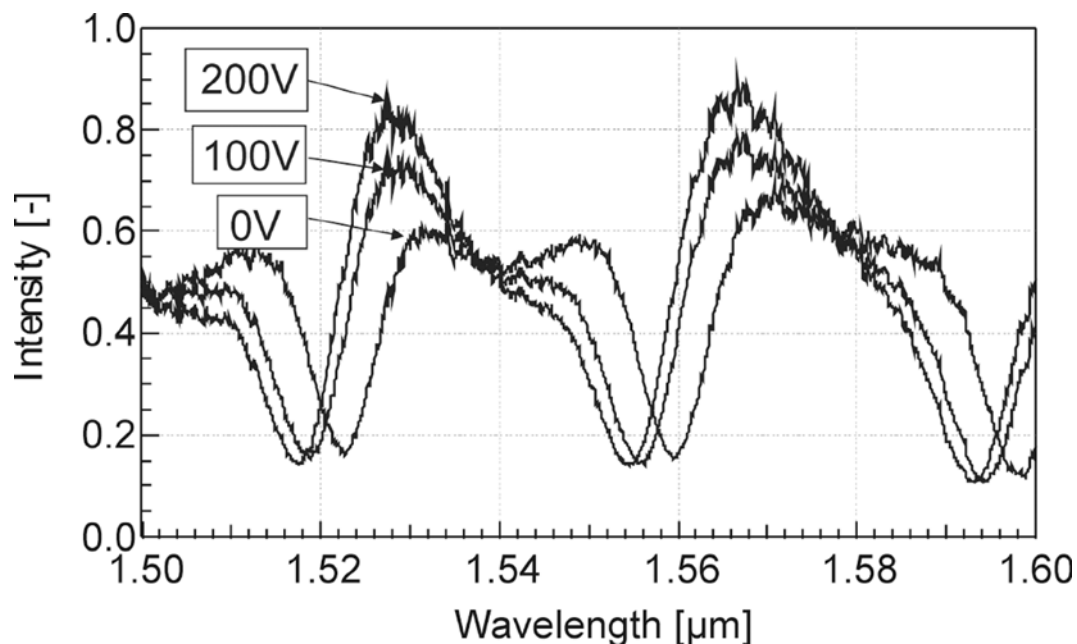


Fig. 7: Interferometric pattern for different voltage to the electrode.

reference detectors. We interpret the distortion that appeared in the trace to have resulted from the effects of transmission of the acoustic signal in the heterogeneous rock specimen and from power instability of the optical source (ASE). Because our measurements recorded the sensitivity of the overall system, which is the sum of the sensor sensitivity and the sensitivity/gain of the processing circuit, it was not possible to determine the sensitivity of the sensor in isolation.

The waveform and power spectral density from the optical microsensor with and without the automatic tuning for an input of 40 kHz sinusoidal wave propagated through rock specimen is shown in Fig. 9. It is seen that the detected signal is more stable after the automatic tuning. The intensity of the spectra at 40 kHz is increased approximately 6 dB after the shift of the operating point by the automatic tuning. The signal to noise ratio around 40 kHz is approximately 50 dB, although higher contamination by noise, mainly from the optical source and photodiode, is seen in lower frequency.

5. Conclusions

This paper describes the principles, design, fabrication and evaluation of a micro-optical AE/ultrasonic sensor with a mechanism for automatic tuning. It has been demonstrated that the prototype of the sensing system successfully worked at the optimum operating point where the FPI had the best sensitivity and linearity.

The automatic tuning system brings additional merits to the improvement of sensitivity/linearity. The shift of operating point of the FPI allows the use of a laser working at a single wavelength, bringing a further cost reduction of the system since a tunable laser is now not required. If a wideband optical source is used such as the ASE in this study, an array of sensors could be realized because the interfered light wave could be multiplexed on one fiber.

There some points still to be investigated/improved in this system before commercialization. One is the improvement of the dynamic range. A system to compensate for the noise in

roduced by instability of the ASE will effectively work to suppress noise under 10 kHz. The use of an optical amplifier in the input line or a low-noise OE will further improve SNR around the operating frequency of the sensor. In the prototype we applied a maximum voltage of 200V, but this was insufficient to move the mass in a wide range. Further optimization of the design of the mechanical parts consisting of the moving mass, suspending beams and electrodes could improve the performance of the automatic tuning system.

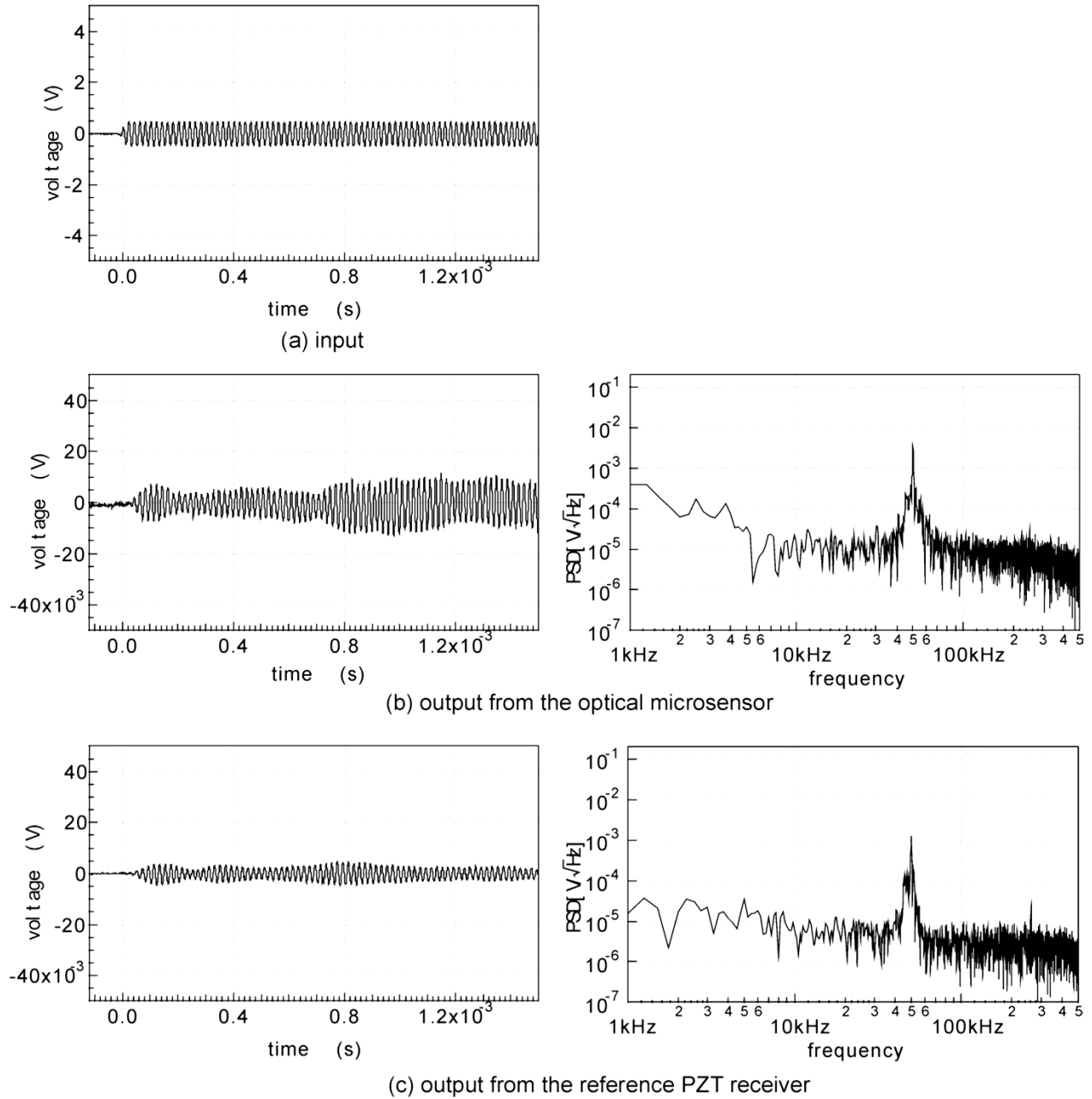
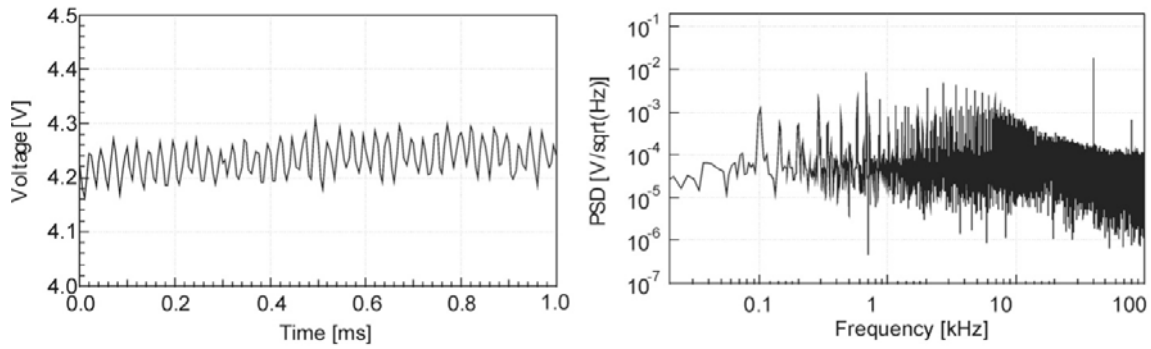


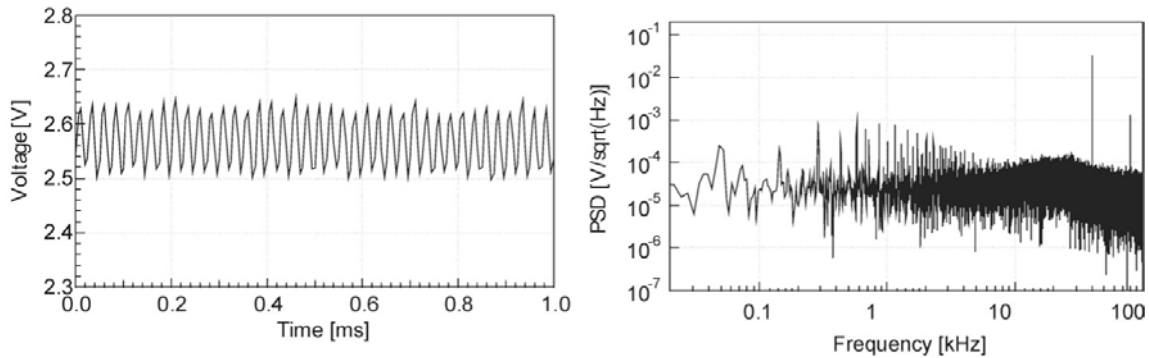
Fig. 8: Outputs from optical and reference sensors for input of 50 kHz sinusoidal waves.

Acknowledgments

Most of the fabrication process in this study was done using facilities in the Venture Business Laboratory, Tohoku University. The authors also wish to acknowledge Prof. M. Esashi,



(a) without automatic tuning



(b) with automatic tuning

Fig. 9: Trace and power spectral density from the optical micro-sensor without/with the automatic tuning for an input of 40-kHz sinusoidal waves.

NiCHE, Tohoku University, Dr. M. Nishizawa, MEMS CORE, S. Takashima, formerly of Graduate School of Environmental Studies (currently working in OKI Electronics), and Dr. P. Chopra, ANU, Australia for their comments, suggestions and encouragements for this study.

References

- [1] H. Niitsuma: *Ultrasonic Technology*, **8** (2000), 4.
- [2] H. Asanuma, M. Nishizawa, G. Suzuki, Y. Yoshida, H. Niitsuma and M. Esashi: *Proc. ASME InterPACK01, (2001)(CDROM)*
- [3] S. Takashima, H. Asanuma and H. Niitsuma: "A water flowmeter using dual fiber Bragg grating sensors and cross-correlation technique", *Sensors and Actuators A: Physical*, **116**, 66-74 (2004).
- [4] M. Shiga, C. Suzuki, M. Yamada, M., Kitahara, M., and H. Niitsuma: *Progress in Acoustic Emission XI, (2002)*, JSNDI, Tokyo, pp. 152-159.
- [5] H. Asanuma, S. Hashimoto, G. Suzuki, H. Niitsuma, and M. Esashi: *SEG 2001 Expanded Abstracts, (2001)*, 45-47.
- [6] K. O. Hill, Y., Fujii, D. C. Johnson, and B. S. Kawasaki: *Appl. Phys. Lett.*, **32**, (1978), 647-649.

DEVELOPMENT OF STABILIZED AND HIGH SENSITIVE OPTICAL FIBER ACOUSTIC EMISSION SYSTEM AND ITS APPLICATION

HIDEO CHO, RYOUHEI ARAI and MIKIO TAKEMOTO
Faculty of Mechanical Engineering, Aoyama Gakuin University,
5-10-1 Fuchinobe, Sagamihara, Kanagawa, 228-8558 JAPAN

Abstract

We developed a novel fiber-optic acoustic emission (AE) monitoring system and applied this to gas-leak detection. The system is a Mach-Zehnder, homodyne-type optical fiber laser interferometer with a phase compensation feedback circuit. The phase compensation was given by a piezo-actuator, which can maintain the system at being quadrature condition. The system was demonstrated to measure the in-plane motion of elastic waves. The system can also detect Ao-mode Lamb waves generated by pulse YAG laser and cylindrical waves produced by lead breaking on a 2-inch steel pipe. We also detected continuous cylindrical waves from gas leakage through a hole of 0.3-mm diameter in a 4-inch steel pipe. RMS voltage of the AE signals, monitored by the sensor fiber wound around the pipe, was found to increase with gas pressure

Keywords: Optical AE sensor, Gas leak detection, Feedback control, Mach-Zehnder type interferometer

1. Introduction

Optical-fiber AE sensor is an attractive alternate AE sensor and can offer a number of advantages such as the long-range monitoring of large structures as pipelines, tanks and bridges. This is possible due to the low optical loss. Fiber sensor can be set on the structure surface in arbitrary shapes due to its flexibility. AE system with fiber sensor is expected to be free from electro-magnetic noise, and can be used for high temperature structure under corrosive environment. Utilization of optical fiber sensors in ignitable environment is most attractive. Low cost and lightweight are another advantage.

A number of optical sensors have been developed. Most of these were designed to detect the low frequency vibration as a dynamic strain meter. Some optical sensors designed to detect ultrasonic waves have been reported. For instance, Pierce et al. [1] reported that the ultrasonic waves generated by PZT transmitter in FRP could be detected by the optical interferometer using a single-mode optical fiber. Tsuda et al. [2] developed a novel optical AE system utilizing a FBG (Fiber Bragg Grating) fiber. They measured large amplitude steady ultrasonic waves repeatedly generated by a PZT transmitter, but could not detect transient elastic waves. Kageyama [3] developed an optical fiber system utilizing the Doppler effect, and reported that the sensitivity of sensor is the same level as the resonant-type AE sensor. One of the authors [4] developed a homodyne Mach-Zehnder-type optical sensor and detected Lamb wave AE signals. Stability of the developed system is, however, poor due to large drift by temperature changes.

Objective of this study is to develop a highly stable optical fiber AE sensor. We developed a system with feedback control circuit with a PZT actuator and applied the system to detect the cylindrical wave AE signals from gas leak in pipe.

2. Optical Fiber AE Sensor System

A new optical AE system developed in house is schematically shown in Fig. 1. The system is composed of the sensing and feedback control section. The sensing section is a homodyne Mach-Zehnder type interferometer. We used a laser-diode (LD) (Mitsubishi Electronic, FU-427SLD) with 1310 nm wavelength as a light source. Transmitted laser beam from the LD was split into two optical fibers with a 3-dB 1x2 coupler. One is the fiber as the sensor (object) and the other is the fiber for reference beam. We used a communication-grade single-mode fiber covered with PVC. The part of the sensor fiber was attached on the sample surface by an appropriate method. Output of the sensor fiber modulated by AE signals was interfered with the laser of the reference beam by coupling at another 2x2 coupler. Interfered laser beam was split into two beams again and then detected separately by two photodiodes (Thorlabs, PDA400). Here the two lasers were at 180° out of phase. Then, two signals were combined with a difference amplifier to improve the signal-to-noise ratio. The output of the difference amplifier was digitized by a digital oscilloscope via a band-pass filter and fed to a personal computer.

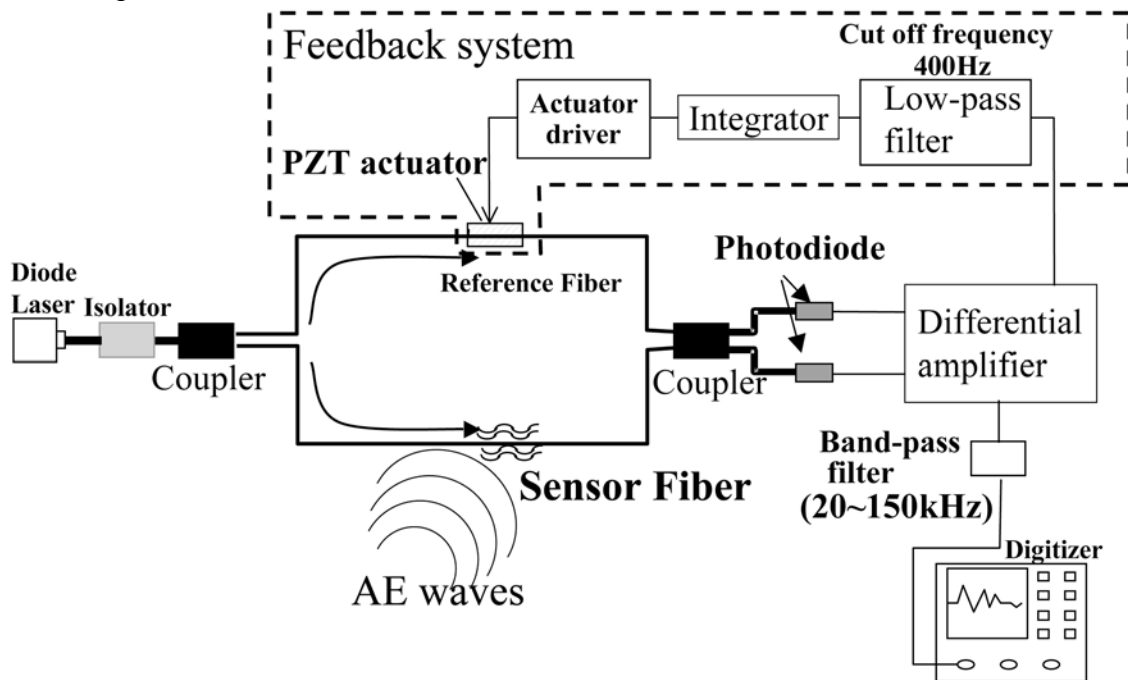


Fig. 1 Improved optical fiber AE monitoring system with a feedback control system using PZT actuator.

The system does not need any vibration control stage and optical components alignment system, which are inevitable for an in-air laser interferometer, since the laser is transmitted in the optical fiber from the LD to the photodiode detector. The system, however, tends to be sensitive to low-frequency drifts by temperature change and environmental noise. We improved the system by adding an automatic low-frequency feedback control circuit. A phase difference between the sensor and reference lasers was also needed to keep the system at quadrature condition. This means that the phase difference between two lasers must be $\pi/2$. For this part, we developed a feedback system, which uses a PZT actuator as a phase shifter. The reference fiber was glued firmly on the rectangular PZT actuator of 20 mm length x 3 mm width x 2 mm thickness (NEC-TOKEN, AE0203D08) so that the fiber is in the actuation direction. Feedback control was achieved utilizing small changes of the reference fiber length by stretching and shortening the

PZT actuator by an error signal. Error signals must correspond to the low frequency drifting. Thus this signal was produced by integrating the output with an operational amplifier, to which the low-frequency component, extracted by a low-pass filter with cut-off frequency of 400 Hz, was fed. Figure 2 compares outputs of the system with and without a feedback control circuit. Large oscillation of the system without feedback control was eliminated by adapting the feedback control circuit. The system with the feedback control can keep the system at quadrature condition.

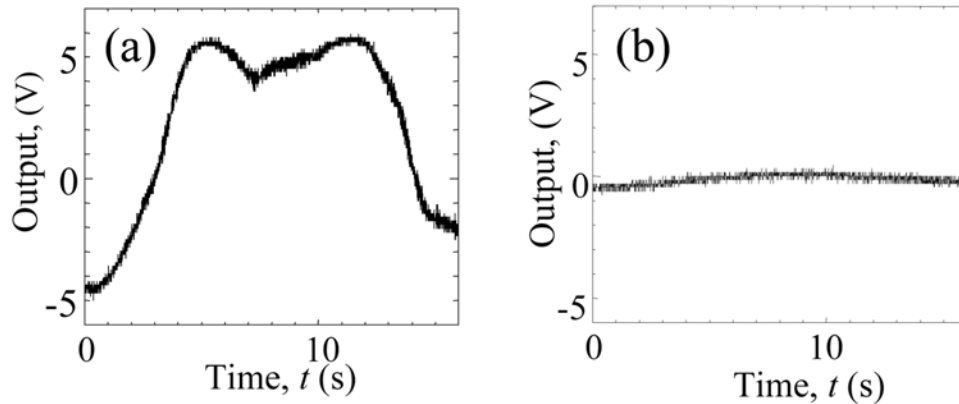


Fig. 2 Comparison of system outputs with (b) and without (a) a feedback control.

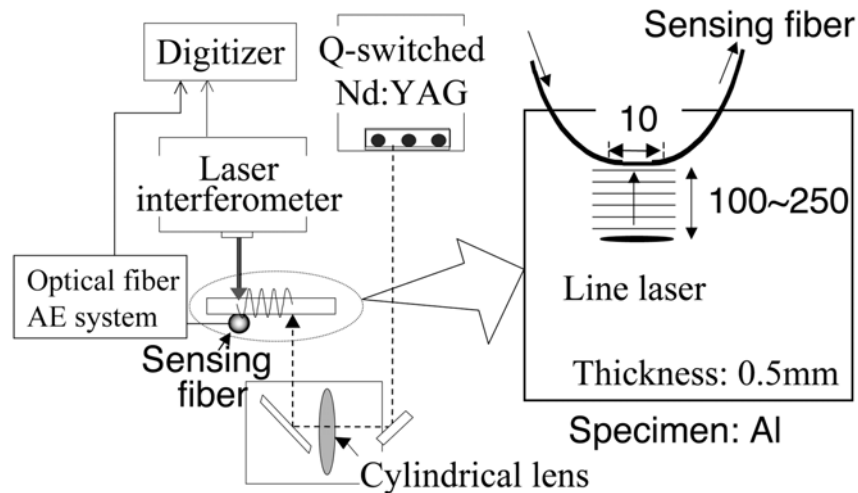


Fig. 3 Experimental setup for evaluating performance of the optical AE system.

3. Characteristic of Developed System

In order to study which vibration mode can be detected at what frequency by the improved system, we detected laser-induced Lamb waves using the experimental setup of Fig. 3. We generated the Lamb waves on a thin Al plate of 0.5-mm thickness by a line focused Q-switched YAG laser beam of 8-mm length. The Lamb waves were detected by the sensing fiber set on the plate 100 to 250 mm from the source. The sensing part of the fiber was glued by epoxy resin so that it is parallel to the line laser. We also detected the out-of-plane displacement of Lamb waves at the opposite side of sensing fiber by a commercial heterodyne-type laser interferometer.

Figure 4 compares the waveforms detected by the optical fiber system (a) and by the commercial interferometer (b). These waves were different in their frequency range. The optical

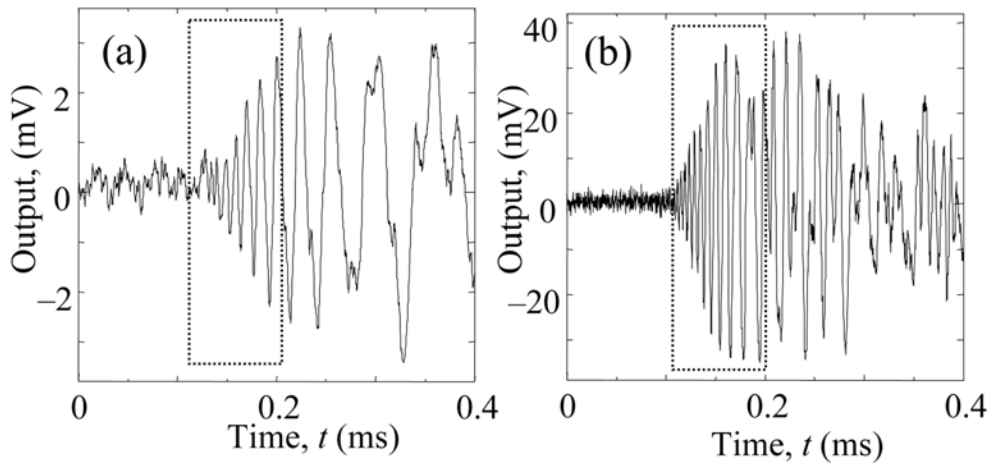


Fig. 4 Detected waves by the developed system (a) and commercial laser interferometer (b).

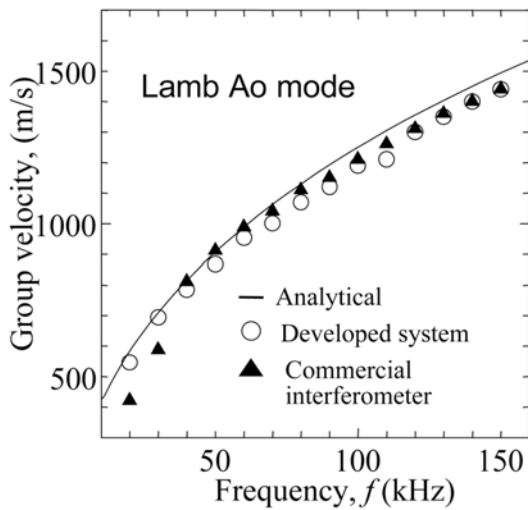


Fig. 5 Group velocities of Ao mode Lamb waves measured by the developed system and commercial laser interferometer.

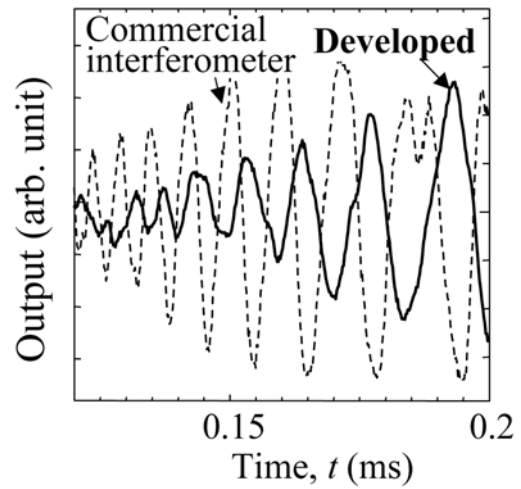


Fig. 6 Overlapping of the first portion of Lamb waves in Fig. 4.

fiber system detected Lamb waves with low-frequency components since a 20 – 150 kHz band-pass filter was used. Both waves, however, clearly show the characteristics of Ao-mode (fundamental mode of anti-symmetric) Lamb waves. Shown in Fig. 5 are the overlaps of experimental group velocity dispersion curves on the theoretical one. Group velocities by the optical fiber system (open circles) agree well with that by the commercial interferometer and also theoretical one. First portion of the waves in Fig. 4 was superposed in Fig. 6. It is noted that phase of the waves detected by the developed system was in $\pi/2$ out of that by the commercial interferometer. This can be explained by the in-plane and out-of-plane displacement of the Ao-mode waves.

Figure 7 shows theoretical distribution of in-plane and out-of-plane displacement of the Ao-mode at 100 kHz across the plate. The out-of-plane displacement is positive or the same in phase and constants over the thickness. In contrast, the phase of in-plane displacement at upper and lower surfaces was opposite or at $\pi/2$ difference. This strongly implies that the developed fiber system detects the in-plane motion of elastic waves.

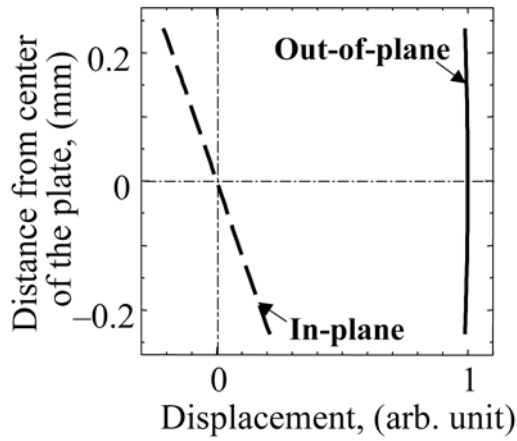


Fig. 7 Comparison of in-plane and out-of-plane displacement of Lamb Ao mode through plate wall at $f=100$ kHz.

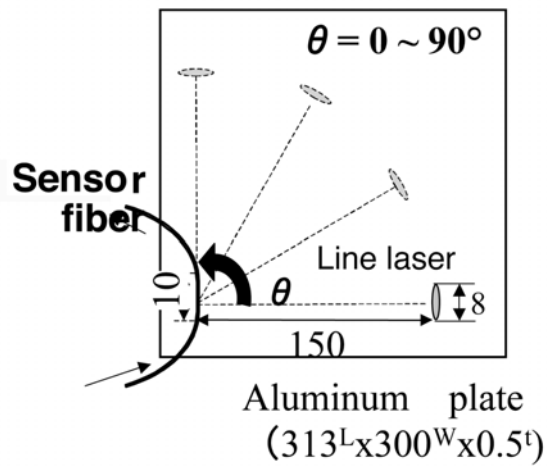


Fig. 8 A method for studying the directivity of line optical fiber sensor's sensitivity.

We next measured the directivity of sensor's sensitivity using the setup of Fig. 8. Sensing fiber was glued on the Al plate so as its axis (longitudinal direction) be parallel to the line laser. The line laser moved along a circle of 150 mm radius. We measured the Lamb waves as a function of angle θ . Here the angle $\theta=0$ implies that the fiber be parallel to the line laser. It is also noted that the line laser produces a plane Lamb wave, which propagates in the normal direction of the line laser. Figure 9 compares the waveforms at $\theta=0$ (a) and $\theta=90^\circ$ (b). The waves (a) agree well with the predicted waveform of Ao-mode Lamb waves. Contrary to this, the waves (b) are deformed and show low frequency components. Distribution of the maximum amplitude at 30, 50 and 80 kHz, obtained by wavelet transform, was shown in Fig. 10. The amplitude was normalized by the maximum amplitude at each frequency. There observed no clear directivity of the sensor sensitivity. However, the waveform significantly changes depending on the angle. This is supposed to be due to the integration of the waves along the axis of the sensor fiber.

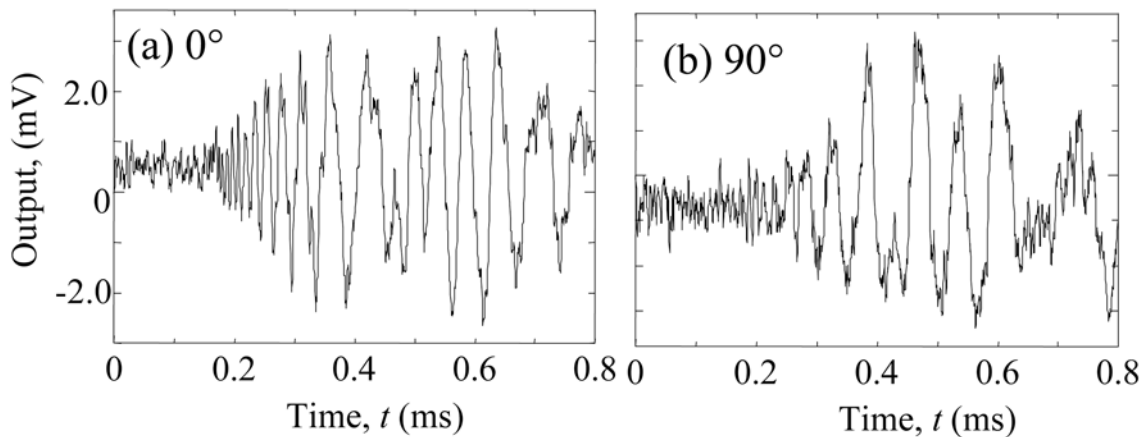


Fig. 9 Comparison of Lamb waves detected by optical sensor fiber parallel (a) and perpendicular (b) to the source laser line.

4. Application to Detection of the Gas Leakage of Pipe

Detection of gas leak was attempted. Various sensing methods have been proposed [5] so far, but these cannot be applied to buried pipes. Fiber sensor can be a useful sensor to detect the gas

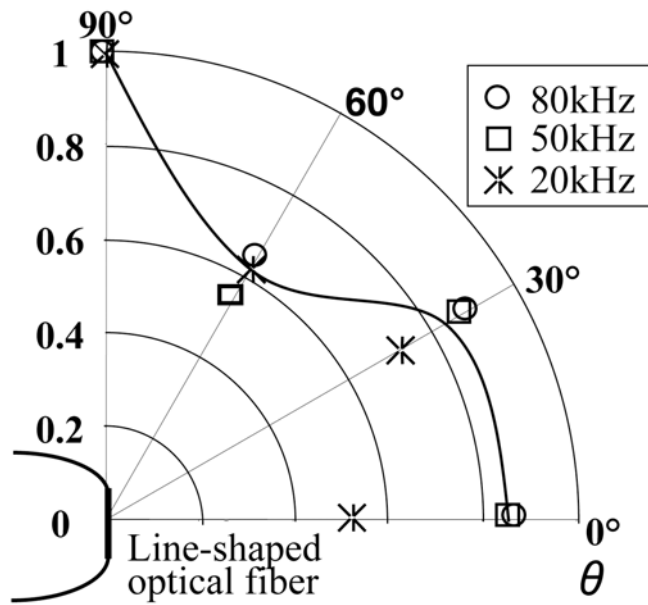


Fig. 10 Sensitivity distribution of line-shaped optical fiber sensor.

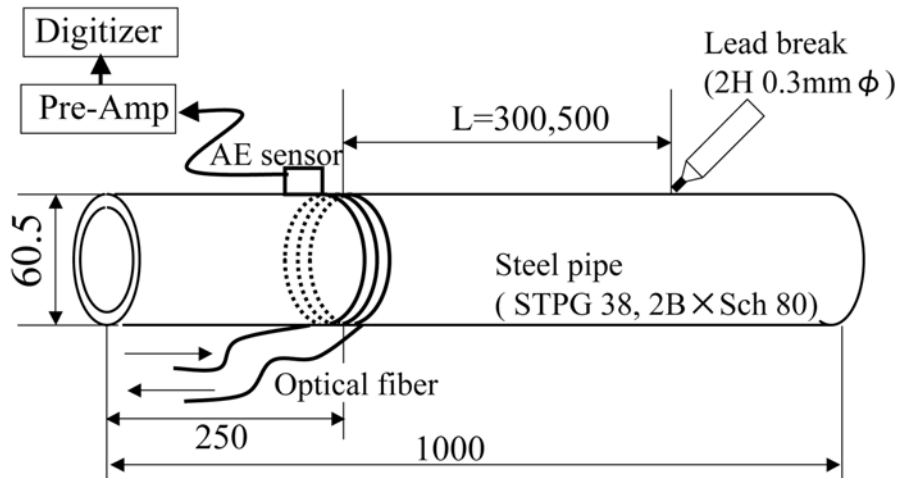


Fig. 11 Experimental setup for detecting transient cylindrical waves due to lead breakage on a 2-inch pipe.

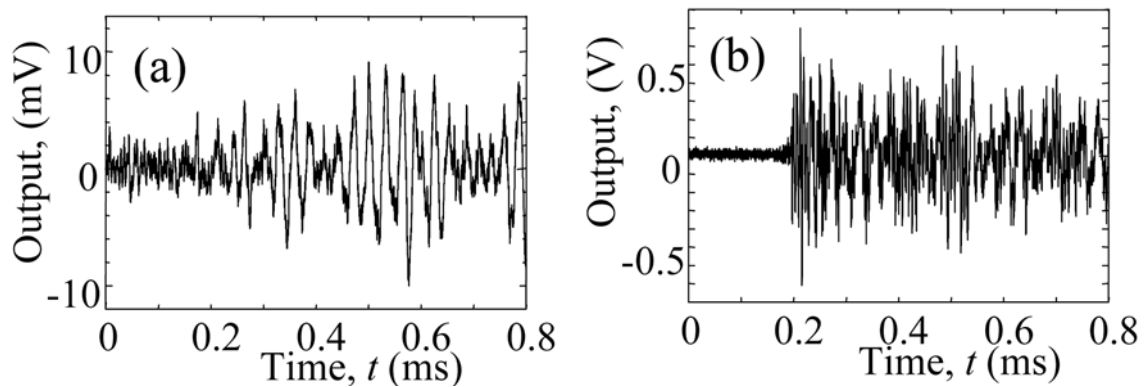


Fig. 12 Comparison of waves detected by the optical fiber system developed here (a) and the commercial system using a piezoelectric AE sensor (b).

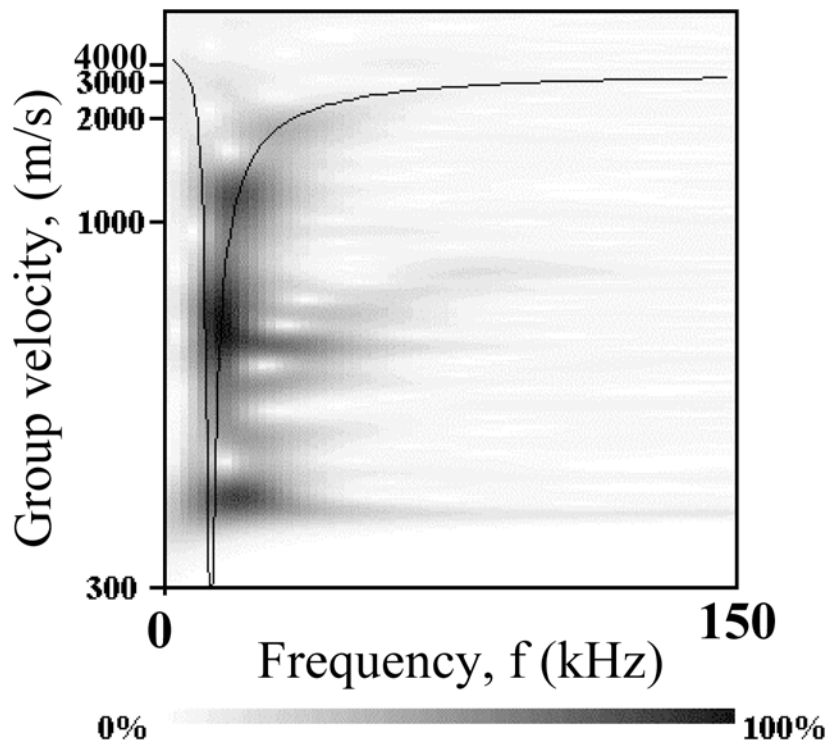


Fig. 13 Contour map of wavelet coefficients for the waves shown in Fig. 12(a).

leakage of long distance pipelines and buried pipes. We first detected the cylindrical waves of a 1000 mm long 2-inch steel pipe (STPG 38, 2B x Sch. 80). As shown in Fig. 11, the cylindrical waves were generated by breaking a pencil-lead and detected by the sensor fiber wound around the pipe. The fiber was wound three turns at 300 or 500 mm from the source and fastened by rubber sheet and steel band. For comparison, a small PZT type AE sensor (PAC, PICO) was mounted near the fiber. Figure 12 compares the waveforms detected by the developed system and PZT sensor. The waveform by the developed system was much different from that by PZT sensor due to their different frequency characteristic. The fiber system, however, detected the lower frequency component of the cylindrical waves. Figure 13 shows the wavelet contour map of the waves of Fig. 12(a) and theoretical group-velocity dispersion of L(0,1) mode. Strong wave components (dark part) coincide with the dispersion of L(0,1) mode in lower frequencies. It was found that the breathing-type cylindrical waves can be effectively detected by the wound fibers due to the high sensitivity of the fiber to in-plane motion.

We next monitored the cylindrical wave AE signals from gas leak through the pipe wall using the system shown in Fig. 14. Here argon gas from 0 to 0.6 MPa was leaked through a small hole of 0.3-mm diameter. Sensing fiber was wound one turn around the pipe at 1200 mm from the hole. Figures 15 shows the AE signals from the gas leak. Gas pressure above 0.2 MPa produced continuous AE waves. Frequency of the AE increases with gas pressure. Root mean square voltages (RMS) of the waves are shown in Fig. 16 as a function of gas pressure. The RMS at 0.2 MPa was 2.7 mV and 4 times larger than that at 0 MPa. Here the RMS at zero pressure (pressure 0) means the noise level. This demonstrates that the developed optical AE sensor can clearly detect AE signals from gas leakage. The RMS also increased with gas pressure. Decrease of the RMS at 0.6 MPa appears to be due to the limited frequency band of the system (20-150 kHz).

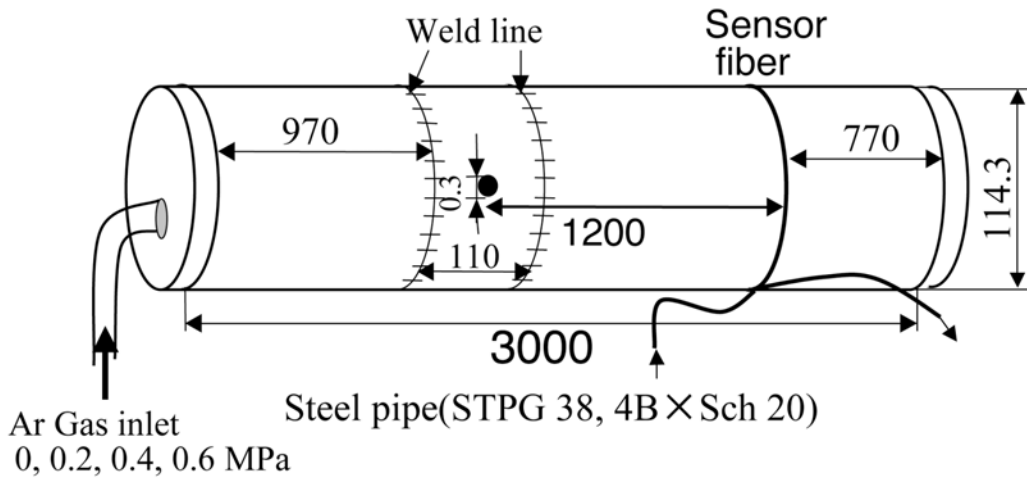


Fig. 14 Experimental setup for detecting gas leakage through 0.3-mm diameter hole in a 4-inch steel pipe.

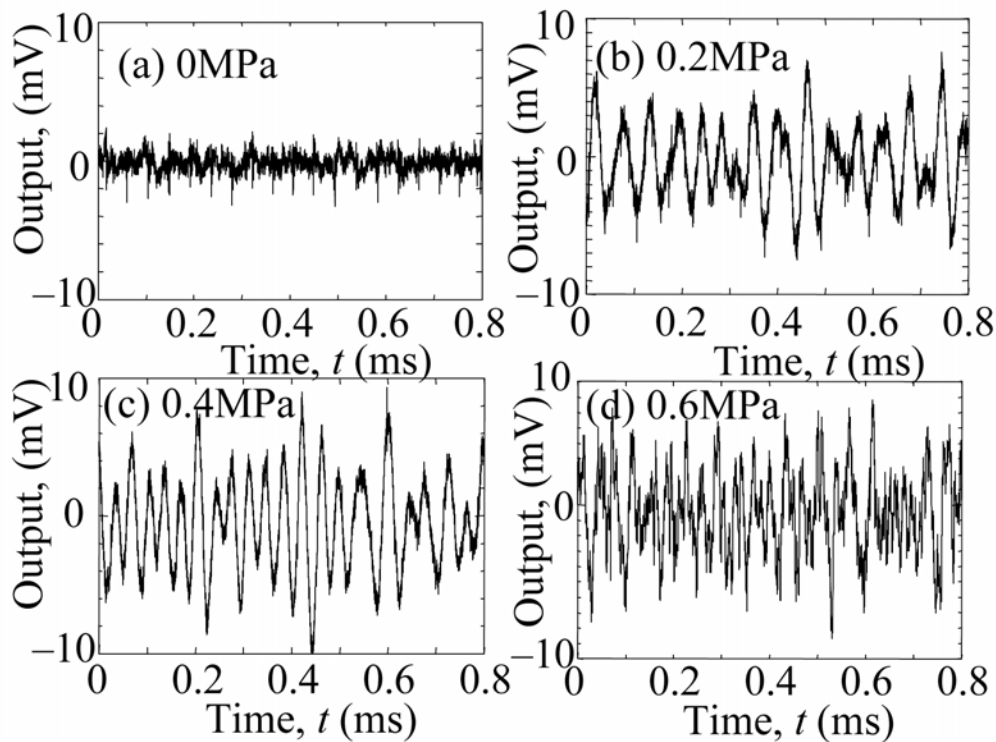


Fig. 15 Detected AE waves due to gas leakage through 0.3-mm diameter hole on the 4-inch pipe wall.

6. Conclusion

We developed an optical fiber AE system with a phase-compensation feedback control circuit and applied the system to AE monitoring from gas leakage. Results are summarized below:

- (1) The feedback control circuit developed in house makes the system at quadrature condition and provide with a high stability and robustness for low frequency drifting.
- (2) We detected the laser-induced Lamb was by the developed system and found that the developed system sensitive to the in-plane motion of the elastic waves. The system can detect

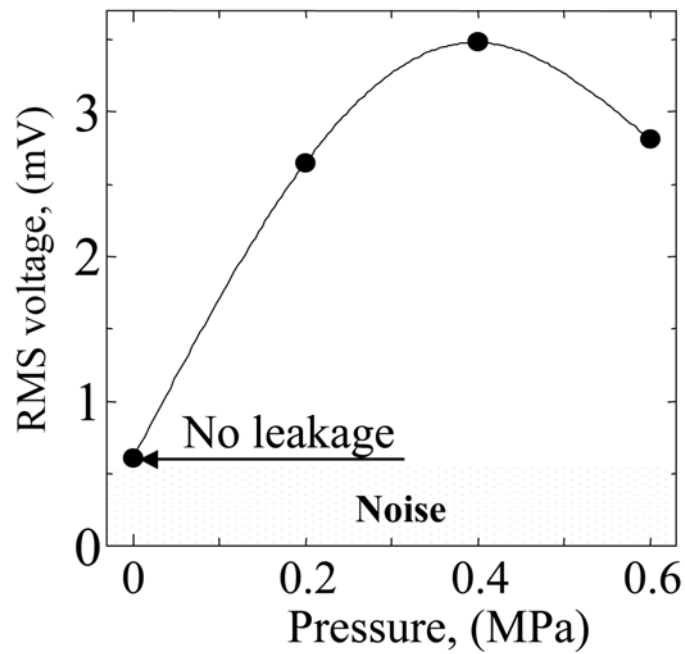


Fig. 16 Root mean square voltage of AE waves as a function of internal gas pressure.

the weak and transient AE produced by pencil-lead break

- (3) The system can detect weak and continuous type L-mode cylindrical wave AE signals from the 0.2 MPa gas leakage through the pipe wall. Both the RMS and frequency of cylindrical waves increased with gas pressure.

Acknowledgment

This research was conducted as part of the High-Technology Research Center Program and the Center of Excellence (COE) Program, funded by the Ministry of Education, Culture, Sports, Science and Technology of Japan.

References

- [1] S. G. Pierce, W. R. Philp, A. Gachagan, A. McNab, G. Hayward and B. Culshaw: *Applied Optics*, **35**(25), 5191-5197, (1996).
- [2] H. Tsuda: *J. Japan. Soc. NDI*, **52**(10), 539-542, (2003). (in Japanese)
- [3] K. Kageyama, I. Ohsawa, M. Kanai, Y. Tanma, T. Nakanishi, M. Shinomura, K. Nagata and F. Matsumura: *Structural Health Monitoring and Intelligent Infrastructure*, Z. S. Wu and M. Abe (eds) pp. 285-290, (2003).
- [4] T. Matsuo and M. Takemoto: *Prog. Acoustic Emission XI*, Tokushima, JSNDI, pp. 169-175 (2002).
- [5] For instance, Y. Morishita, H. Mochizuki, K. Watanabe, T. Nakamura, T. Nakajima and T. Yamauchi: *Journal of Nuclear Science and Technology*, **32**(3), 237-244, (1995).

HIGH PRECISION GEOPHONE CALIBRATION

MASAHIRO KAMATA

Schlumberger K.K., 2-2-1 Fuchinobe, Sagamihara, Kanagawa 229-0006 Japan

Abstract

Geophones are commonly used in seismic signal detection and are widely sold with response parameters with specified tolerances. High precision seismic analysis can extract subtle information from seismic records, but requires knowledge of the *in-situ* response parameters of the sensors. The geophone response is specified at room temperature; however, geophone response changes with the orientation with respect to gravity, temperature and aging. The changes due to temperature and tilt may exceed the tolerance limits, so there is a need to perform *in-situ* calibration to know the exact response. In the impedance calibration method, the impedance of a geophone can be measured by injecting current. From the impedance, it is possible to describe all of the response parameters except for the moving mass. The dynamic method is also known for calibration of a vibration sensor relative to a reference sensor. The reference sensor can be fabricated with a pre-measured moving-coil mass so that all the geophone parameters can be determined. Alternatively the reference sensor can be calibrated by using a reciprocity method making use of three vibration sensors. We have developed unique geophones that output signals proportional to acceleration. Complete calibration schemes have been established, and all the geophones are fully calibrated during the manufacturing process. A method has been described to re-evaluate the geophone's moving mass to make *in-situ* calibration in the working environment with the impedance method.

Keywords: Geophone, Seismic sensors, Moving-coil accelerometer, Calibration, Impedance method

1. Introduction

A geophone consists of a pair of moving coils suspended in a magnetic field by means of a pair of springs as shown in Fig. 1. The spring is usually pre-stressed to compensate the natural displacement of the coil due to gravitational force so that the coil is centered in the magnetic field.

The output of a geophone is usually terminated by a shunt resistance R as shown in Fig. 2 to provide external damping. The current flowing in the moving coil reduces coil motion. The amount of shunt resistance is chosen so that the total damping factor is 70%.

The equation of motion for the moving coil relative to the magnetic flux for given external displacement u may be written as;

$$m \frac{d^2 \xi}{dt^2} + c \frac{d\xi}{dt} + k\xi = m \frac{d^2 u}{dt^2} - Bli \quad (1)$$

where ξ : coil displacement; k : spring constant; m : moving mass of coil; c : friction coefficient; g : gravitational acceleration; B : magnetic flux density; l : length of coil wire; i : current; u : external displacement.

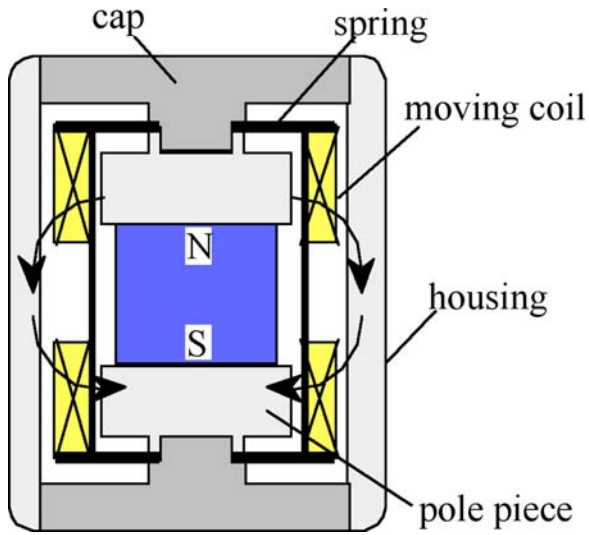


Fig. 1 Structure of a geophone.

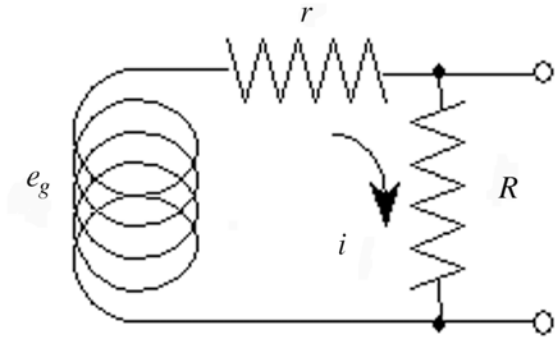


Fig. 2 Damping control.

ξ is the relative position of the moving coil inside the geophone. The first term in the left hand side of equation (1) is the inertial force, the second term is the friction force proportional to the velocity, and the last term is the spring force. The summation of the three forces balances with the force due to external displacement and the damping force caused by the electric current.

The electric signal generated by the moving coil is expressed in terms of magnetic flux density, length of coil wire and velocity of the coil as;

$$e_g = Bl \frac{d\xi}{dt} \quad (2)$$

For a given external displacement, $u = a \sin(\omega t)$, the response may be expressed as;

$$e_g = A \sin(\omega t - \theta) \quad (3)$$

The amplitude response and phase may be found from equations (1), (2) and (3) as;

$$A = a \frac{S_0 \omega \left(\frac{\omega}{\omega_0} \right)^2}{\sqrt{\left\{ 1 - \left(\frac{\omega}{\omega_0} \right)^2 \right\}^2 + \left(2\zeta \frac{\omega}{\omega_0} \right)^2}} \quad \text{and} \quad \tan(\theta) = \frac{2\zeta \frac{\omega}{\omega_0}}{1 - \left(\frac{\omega}{\omega_0} \right)^2} \quad (4, 5)$$

where

$$\omega_0 = \sqrt{\frac{k}{m}}, \quad \zeta = \zeta_0 + \frac{S_0^2}{2(r+R)m\omega_0}, \quad \zeta_0 = \frac{c}{2m\omega_0}, \quad \text{and} \quad S_0 = Bl.$$

The geophone parameters are the natural frequency f_0 , the open circuit sensitivity S_0 , the open circuit damping, the coil resistance r , and the moving mass m . The response of a geophone is determined with four geophone parameters and the shunt resistance R .

For $\omega > \omega_0$, equation (3) may be approximated as $e_g = S_0(a\omega) \cos(\omega t)$. The sensitivity is proportional to the velocity ($a\omega$) of the vibration at above the natural frequency. Figure 3 shows

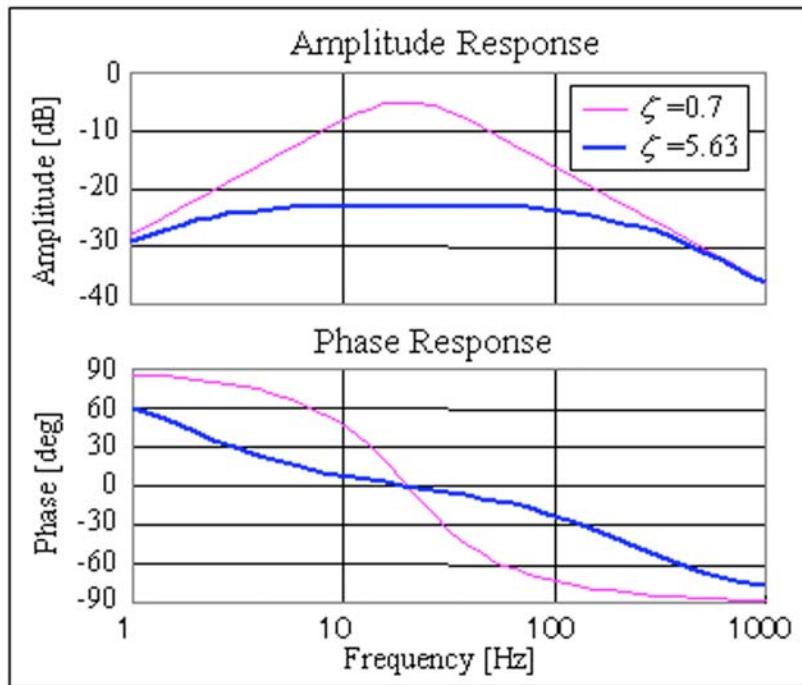


Fig. 3 Geophone response.

the amplitude response $e_g/S_0(a\omega)$ and phase response of a geophone with 10 Hz natural frequency and 0.7 damping.

2. Geophone Response in Measurement Environment

Coil resistance is almost double at 200°C and open circuit damping is reduced by 20% as shown in Figs. 4 and 5. Natural frequency f_0 , and the open circuit sensitivity S_0 change by a few percent each. (Figs. 6 and 7)

The geophone parameters are measured when the geophone is positioned vertically. In practice, geophones are planted by stamping into the ground by foot, and so are not necessarily vertical. In borehole seismic acquisition, a downhole tool with geophones is deployed in a borehole that may not be vertical. Figures 8, 9 and 10 show measured results of a geophone under tilt. There is a few percentage points change observed at $\pm 30^\circ$ tilt.

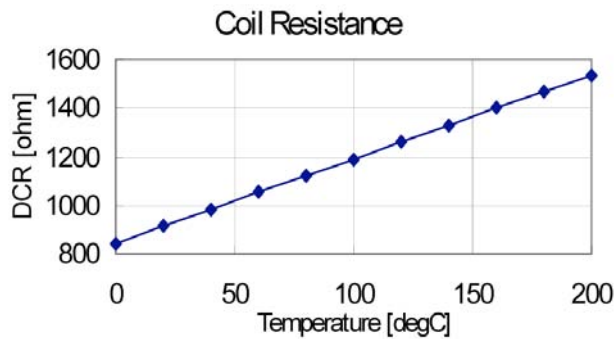


Fig. 4 Coil resistance change.

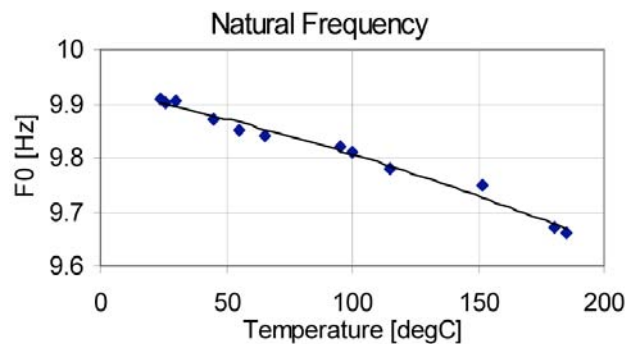


Fig. 5 Natural frequency change.

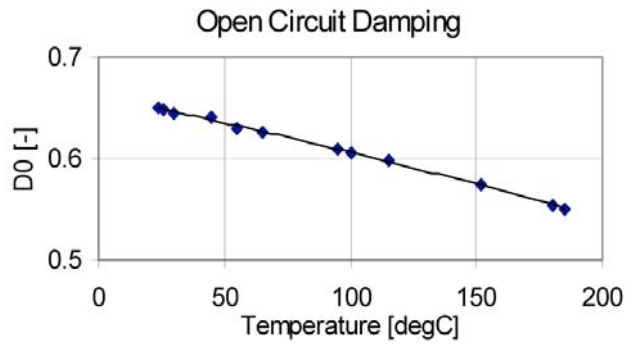


Fig. 6 Open circuit damping change.

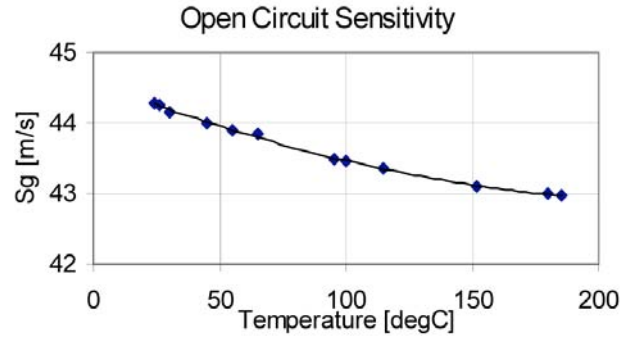


Fig. 7 Sensitivity change.

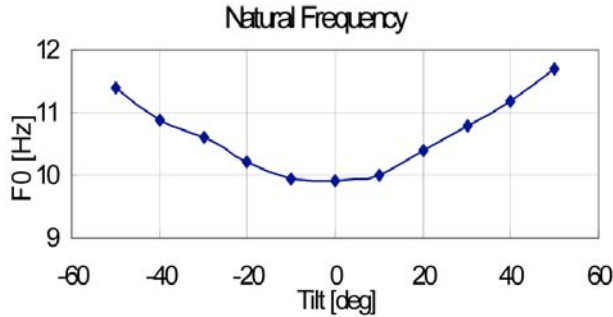


Fig. 8 Natural frequency shift by tilt.



Fig. 9 Open circuit damping shift by tilt.

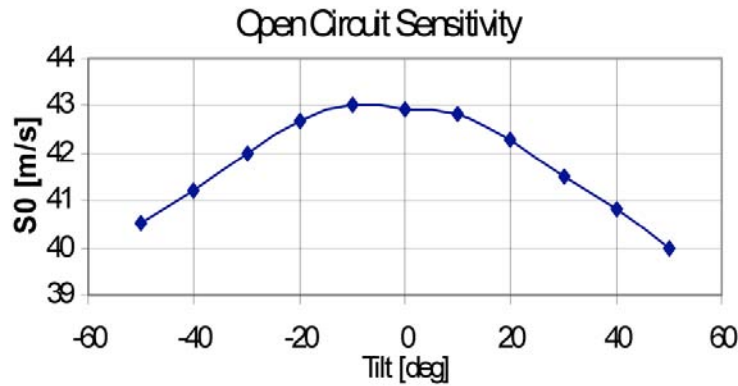


Fig. 10 Open circuit sensitivity shift by tilt.

3. Geophone Accelerometer

We have developed a unique geophone that responds to acceleration between $1/10 \times f_0$ and $10 \times f_0$. A light moving coil is suspended in a strong magnetic flux density.

The imaginary short circuit of an operational amplifier applies a large damping current so that the geophone responds to acceleration at near its natural frequency. See the schematic diagram in Fig. 11. For $\omega = \omega_0$, equation (3) may be approximated as

$$e_g = (a\omega^2) \frac{S_0}{2\zeta\omega_0} \sin(\omega t). \quad (6)$$

Equation (6) shows that a response is in proportion to acceleration. In general, equation (3) is rewritten as acceleration form (7);

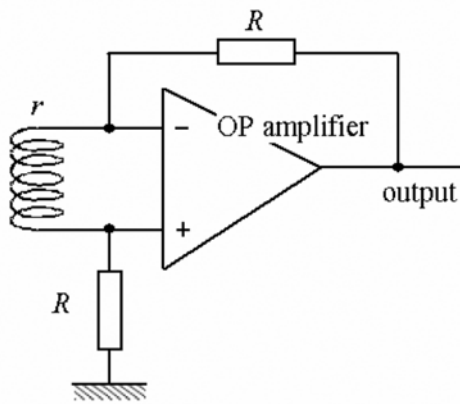


Fig. 11 Imaginary short circuit.

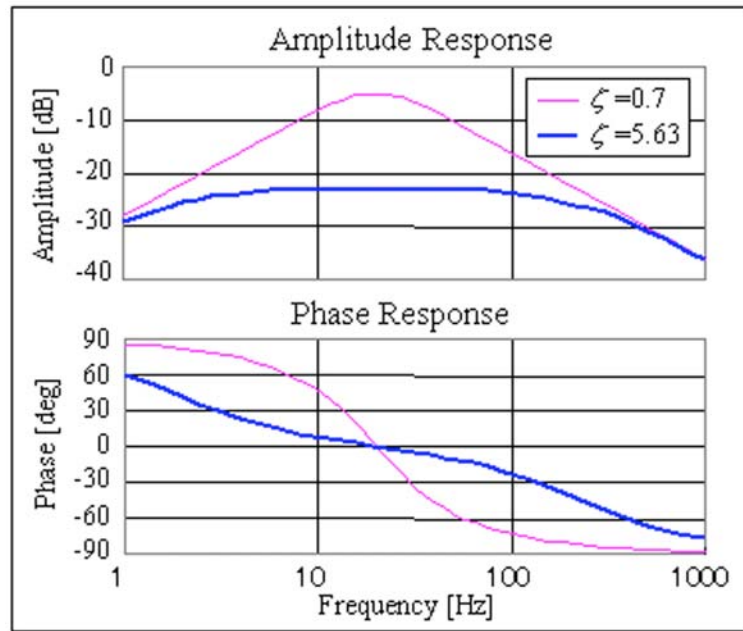


Fig. 12 GAC response.

$$e_g = (a\omega^2) \frac{\frac{S_0}{\omega_0} \left(\frac{\omega}{\omega_0} \right)}{\sqrt{\left\{ 1 - \left(\frac{\omega}{\omega_0} \right)^2 \right\}^2 + \left(2\zeta \frac{\omega}{\omega_0} \right)^2}} \sin(\omega t - \theta). \quad (7)$$

When the damping factor is large, the damping term in equation (7) becomes dominant and the frequency range becomes wider. The natural frequency is chosen to be in the middle of the seismic band at about 20 Hz. For this natural frequency, the natural displacement of the coil due to gravity is not large and the GAC design is omni-tiltable. (See Fig. 12.)

The GAC was originally introduced for borehole seismic acquisition to obsolete the need for a gimbal-mount mechanism. A second generation GAC sensor is now being used in seabed and land seismic recording.

4. Geophone Calibration Method

4.1 Impedance Method

A current runs into the moving coil that is suspended in a magnetic flux B . The force acting to the moving coil is Bli , where B is the magnetic flux density, l is the effective wire length of the moving coil and i is the current. The equation of motion for the moving coil may be written as;

$$m \frac{d^2\xi}{dt^2} + c \frac{d\xi}{dt} + k\xi = Bli \quad (8)$$

Since the output signal is (see Fig. 13);

$$e_0 = e_g + ri \quad (9)$$

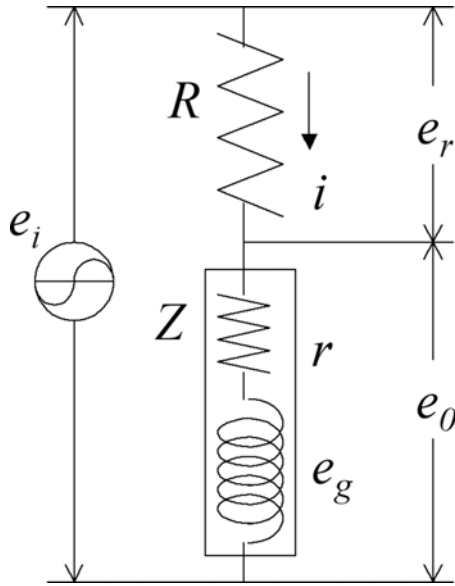


Fig. 13 Impedance method.

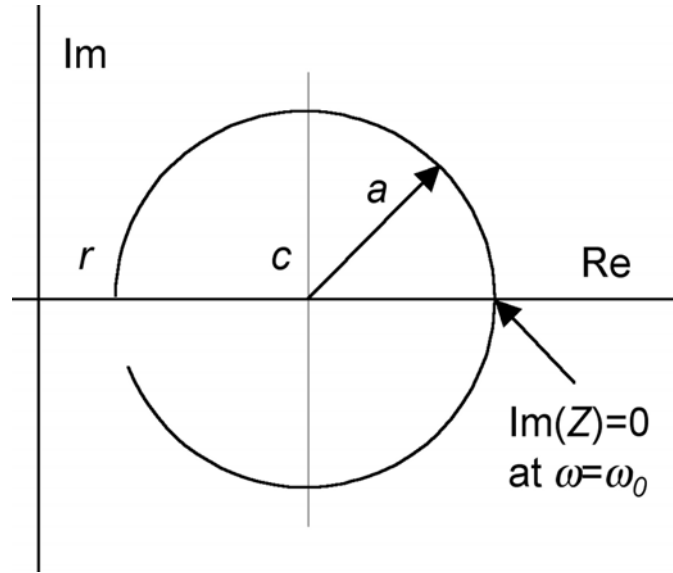


Fig. 14. Geophone impedance circle.

Equation (8) may be rewritten in terms of output signal as;

$$\frac{d^2 e_0}{dt^2} + 2\zeta_0 \omega_0 \frac{de_0}{dt} + \omega_0^2 e_0 = -r \left(\frac{d^2 i}{dt^2} + 2\zeta_0 \omega_0 \frac{di}{dt} + \omega_0^2 i \right) - \frac{S_0^2}{m} \frac{di}{dt} \quad (10)$$

The impedance may be found from the Laplace transformation of equation (10) as

$$Z(j\omega) = r + \frac{S_0}{m\omega_0} \frac{j \left(\frac{\omega}{\omega_0} \right)}{\left\{ 1 - \left(\frac{\omega}{\omega_0} \right)^2 \right\} + 2j\zeta_0 \left(\frac{\omega}{\omega_0} \right)} \quad (11)$$

The real and imaginary parts of the impedance equation show a circle on a complex plane as shown in Fig. 14. At $\omega = \omega_0$ and $\omega = 0$, the imaginary part is zero. At $\omega = 0$, the real part is the DC resistance of the coil.

The absolute value of equation (11) yields an expression for the impedance circle as;

$$a^2 = \{ \text{Re}(Z) - c \}^2 + \{ \text{Im}(Z) \}^2 \quad (12)$$

The impedance is calculated by the output signal e_0 and the current injected in a geophone as;

$$Z = -\frac{e_0}{i} \quad (13)$$

Measurement of impedance at two frequencies, ω_1 and ω_2 gives four equations by considering the real and imaginary parts of the impedance.

$$\text{Re}(Z_1) = r + \frac{2 \frac{S_0^2}{m\omega_0} \zeta_0 \left(\frac{\omega_1}{\omega_0}\right)^2}{\left\{1 - \left(\frac{\omega_1}{\omega_0}\right)^2\right\}^2 + \left(2\zeta_0 \frac{\omega_1}{\omega_0}\right)^2} \quad (14)$$

$$\text{Im}(Z_1) = \frac{\frac{S_0^2}{m\omega_0} \left\{1 - \left(\frac{\omega_1}{\omega_0}\right)^2\right\} \left(\frac{\omega_1}{\omega_0}\right)}{\left\{1 - \left(\frac{\omega_1}{\omega_0}\right)^2\right\}^2 + \left(2\zeta_0 \frac{\omega_1}{\omega_0}\right)^2} \quad (15)$$

$$\text{Re}(Z_2) = r + \frac{2 \frac{S_0^2}{m\omega_0} \zeta_0 \left(\frac{\omega_2}{\omega_0}\right)^2}{\left\{1 - \left(\frac{\omega_2}{\omega_0}\right)^2\right\}^2 + \left(2\zeta_0 \frac{\omega_2}{\omega_0}\right)^2} \quad (16)$$

$$\text{Im}(Z_2) = \frac{\frac{S_0^2}{m\omega_0} \left\{1 - \left(\frac{\omega_2}{\omega_0}\right)^2\right\} \left(\frac{\omega_2}{\omega_0}\right)}{\left\{1 - \left(\frac{\omega_2}{\omega_0}\right)^2\right\}^2 + \left(2\zeta_0 \frac{\omega_2}{\omega_0}\right)^2} \quad (17)$$

From equations (14-17), it is possible to find the four geophone parameters, r , ζ_0 , ω_0 , and S_0 . Inserting Z_1 and Z_2 into Equation (12) gives the center and radius of the impedance circle.

$$c = \frac{\text{Im}(Z_1)^2 - \text{Im}(Z_2)^2 + \text{Re}(Z_1)^2 - \text{Re}(Z_2)^2}{2\{\text{Re}(Z_1) - \text{Re}(Z_2)\}} \quad (18)$$

$$a = \sqrt{\text{Im}(Z_1)^2 + \{c - \text{Re}(Z_1)\}^2} \quad (19)$$

The DC resistance r is found to be;

$$r = c - a \quad (20)$$

From impedance equations (14-17), ζ_0 , ω_0 , and S_0 may be found as,

$$\omega_0 = \sqrt{\frac{(A\omega_1 - \omega_2)\omega_1\omega_2}{(A\omega_2 - \omega_1)}} \quad \text{where } A = \frac{\text{Re}(Z_1) - r}{\text{Re}(Z_2) - r} \bullet \frac{\text{Im}(Z_1)}{\text{Im}(Z_2)} \quad (21)$$

$$\zeta_0 = \frac{(\omega_0^2 - \omega_1^2)\{\text{Re}(Z_1) - r\}}{2\omega_0\omega_1\{\text{Im}(Z_1) - r\}} \quad (22)$$

$$S_0 = \sqrt{\frac{m \operatorname{Im}(Z_1) \{(\omega_0^2 - \omega_1^2)\}^2 + 4\zeta_0^2 \omega_0^2 \omega_1^2}{(\omega_0^2 - \omega_1^2) \omega_1}} \quad (23)$$

4.2 Dynamic Method

In the dynamic calibration method, a geophone is mounted on a shaker with a reference sensor with a known response. The sensitivity may be evaluated as

$$S_g = \frac{e_0}{e_r} S_r \quad (24)$$

where

S_g : sensitivity of a geophone to be calibrated

S_r : sensitivity of the reference geophone

e_0 : output signal from the geophone to be calibrated

e_r : output signal from the reference geophone.

Calibrated accelerometers are commonly sold in the market; however, their calibration is usually to 1% accuracy. It is known that the temperature coefficient of a piezoelectric accelerometer is about 0.1%/°C; however, the coefficient is not calibrated nor warranted by manufacturers. We do not know if this temperature coefficient can be applied to any calibrated accelerometers we can purchase. A five-degree temperature change can cause 0.5% error, and it is difficult to measure the temperature of the accelerometer, since the temperature of the housing may not be the same as the temperature of the piezoelectric element.

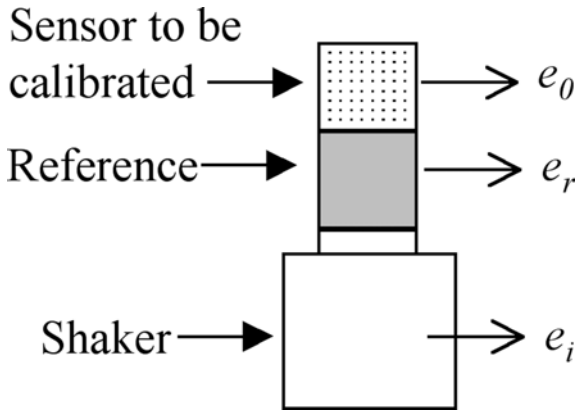


Fig. 15 Dynamic method.

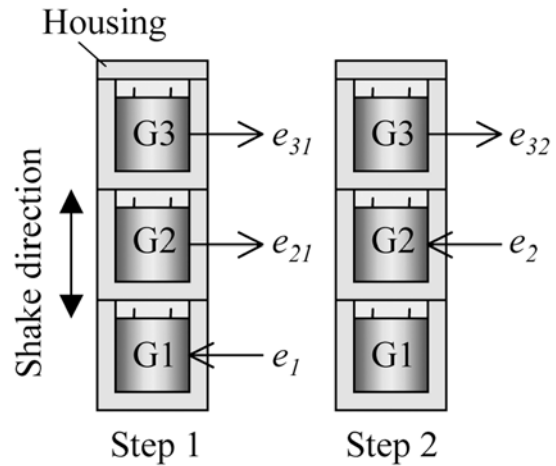


Fig. 16 Reciprocity calibration.

4.3 Reciprocity Calibration

An alternative to the dynamic method is the reciprocity method of calibration to determine geophone sensitivities. In the reciprocity method, three geophones are mounted together as shown in Fig. 16. A current may be injected into a geophone to shake the entire assembly and the output from the other geophones may be measured. Let e_{ij} denote a signal from geophone i responding to signal input to shaker geophone j . Geophones G2 and G3 output signals are then e_{21} and e_{31} when shaking G1. Then by injecting signal into Geophone G2 we get e_{32} as the output

from G3. A geophone shakes the entire mass M along with three geophones. For the driving signal $e_0 \sin \omega t$, the force may be approximated as;

$$F = \frac{S_j e}{Z_j(\omega)} \sin \omega t \quad (25)$$

Outputs, e_{21} , e_{31} , and e_{32} can be expressed in terms of the driving signal. The sensitivity S_i of each geophone may be solved as

$$S_1 = \sqrt{\frac{e_{12} e_{13}}{e_{21}} \frac{M}{e_0} \frac{\{Z_1(\omega_i)\}^2}{Z_2(\omega_i) X_i(\omega_i)}} \quad (26)$$

$$S_2 = \sqrt{\frac{e_{12} e_{23}}{e_{13}} \frac{M}{e_0} \frac{Z_2(\omega_i)}{X_i(\omega_i)}} \quad (27)$$

$$S_3 = \sqrt{\frac{e_{13} e_{23}}{e_{12}} \frac{M}{e_0} \frac{Z_2(\omega_i)}{X_i(\omega_i)}} \quad (28)$$

where

$$X_i(\omega) = \frac{\omega^3}{(\omega_i^2 - \omega^2)^2 + (2\zeta_i \omega_i \omega)^2} \quad (29)$$

It is then possible to calibrate the sensitivities of three geophones by knowing their impedances.

4.4 Moving Mass Determination and *in-situ* Calibration

The dynamic method requires a reference geophone for high precision calibration. The moving coil mass of the reference geophone is measured during assembly. By knowing the amount of moving mass, the absolute sensitivity can be calibrated by the impedance method. The reciprocity method can also be used to provide absolute sensitivity calibration. With the reference geophone, the absolute sensitivity of a geophone may be obtained by the dynamic method.

In the impedance method, the amount of the moving mass, m was assumed, and the sensitivity was derived based on the assumed moving mass. If the absolute sensitivity is obtained by the dynamic or reciprocity method, it is then possible to re-evaluate the moving mass. The absolute moving mass, m_0 may be found by using equations (23) and (24) as

$$m_0 = m \left(\frac{S_g}{S_0} \right)^2 \quad (30)$$

The moving mass is a constant that does not change with temperature or tilt of the geophone. Once the moving mass is known, a geophone can be tested *in-situ* any time by the impedance method by injecting current.

5. Conclusion

A high precision geophone calibration method has been established. The method integrates the impedance and dynamic methods and determines the amount of moving mass. All the Geophone Accelerometers, GACs are fully calibrated during the manufacturing process to determine DC resistance, natural frequency, open circuit damping, open circuit sensitivity, and moving mass by impedance and dynamic methods. Since the moving mass does not change with

temperature or tilt, it is also possible to make *in-situ* calibration in the working environment by just injecting calibration signals. The moving mass does not change in temperature or in tilt. It is also possible to make *in-situ* calibration at working environment by just injecting calibration signals.

References

- 1) A. Obuchi, M. Kamata: "Moving Coil Accelerometer", Japanese patent P3098045, H12, Oct.10
- 2) A. Obuchi and T. Fujinawa: "Moving Coil Dynamic Accelerometer", 53rd EAEG Meeting, May, 1991 (B021)
- 3) M. Kamata: "An Accelerometer for Seismic Signal Detection", Proc. 6th Conference of Underground and Civil Engineering Acoustic Emission, May 1999, Tohoku University, Sendai, Japan, pp. 25-26.
- 4) Peter W. Rodgers, Aaron J. Martin, Michelle C. Robertson, Mark M. Hsu, and David B. Harris: "Signal Coil Calibration of E-M seismometers", Bulletin of the Seismological Society of America, **85**, (3), 845-850, June 1995.
- 5) Mark Harrison, A.O. Sykers, and Paul G. Marcotte: "The Reciprocity Calibration of Piezoelectric Accelerometers", Journal of Acoustical Society of America, **24**, (4), July 1952.
- 6) Thomas B. Gabrielson: "Apparatus and Method for Calibration of Sensing Transducers", U.S. patent No. 5,644,067, July 16, 1996.

DEVELOPMENT OF HEAT-RESISTANT OPTICAL FIBER AE SENSOR

PORNTHAP CHIVAVIBUL¹, HIROYUKI FUKUTOMI¹, SHIN TAKAHASHI² and YUICHI MACHIJIMA²

¹) Central Research Institute of Electric Power Industry (CRIEPI),
2-11-1 Iwado Kita, Komae, Tokyo 201-8511, Japan.

²) LAZOC Inc., 7-3-1 Hongo, Bunkyo, Tokyo 113-8656, Japan.

Abstract

A heat-resistant optical fiber AE sensor with sustainable sensitivity and with no temperature compensation has been developed. This sensor has utilized the Fiber Doppler (FD) sensing principle that detects frequency shifts of laser light transmitted through an optical fiber in proportion to strain velocity, which was discovered recently. Gold coating was applied to the optical fiber to improve the temperature-limit of the conventional optical fiber. The sensitivity was measured from room temperature to 600°C with the quasi-AE wave generated by PZT sensor. A long-term heat exposure test at 600°C was also conducted for over 1000 hr. Both experiments showed that the sensor retained its sensitivity. The durable, low-cost and heat-resistant sensor can invite a new scope to structural health monitoring in a variety of high-temperature conditions.

Keywords: Acoustic Emission sensor, Optical fiber, Heat resistance

1. Introduction

Acoustic emission (AE) has been extensively used in the petrochemical, nuclear, and aerospace industries. This technique provides a distinct advantage over other conventional nondestructive testing techniques because it allows for the real time monitoring of in-service structures. Generally, the PZT transducer is used as an AE sensor. There are a number of commercially available PZT sensors suitable for detecting AE in various applications. However, it is difficult to directly apply these sensors at elevated temperatures because the Curie point of the PZT is approximately 300°C. Although this problem can be solved by using waveguides, the quantitative AE analysis becomes difficult because of the change of waveforms at the waveguide/structure connection.

Recently, AE sensors using optical fiber have been developed [1-5]. Optical fibers, in general, have the following features: (1) small diameter and light weight, (2) flexibility, (3) immunity to electromagnetic interference, and (4) durability and corrosion resistance. The optical fiber sensor developed by Kageyama et al. [3, 4], which is based on a new finding called Fiber Doppler (FD) that the frequency of lightwave transmitted through a bent optical fiber is shifted by vibration or elastic wave at the bent region, has the following good characteristics: (1) wide bandwidth from 0.1 Hz to 3 MHz, (2) expandable dynamic range, and (3) high-sensitivity. The main element of optical fiber is quartz that has heat resistance up to about 800°C. Kageyama et al. succeeded in detecting elastic wave at 500°C with carbonized polyimide-coated optical fiber sensor, but the life time was only about 2 hr [5]. This fiber broke when the temperature increased to 600°C. In the present study, we have developed an optical fiber AE sensor based on

gold-coated optical fiber for high temperature application. The characteristics of this sensor at the elevated temperatures were examined.

2. Principle of the Optical Fiber Sensor

Laser light reflected from the surface of a moving object is shifted in frequency by an amount $2v/\lambda_0$, where v is the velocity of the surface and λ_0 is the wavelength of the laser radiation in air. It is well known as the Laser-Doppler effect. A similar effect is observed in a lightwave transmitted through a bent optical fiber. Frequency of a lightwave transmitted through a curved optical fiber is shifted in response to vibration/motion of the curved region [5]. The phenomenon can be explained as follows. Lightwave is transmitted in the optical fiber by repeated reflection on the interface between core and cladding as schematically shown in Fig. 1. In the case of straight optical fiber as shown in Fig. 1(a), reflection angles at point A and B are the same, and Doppler shifts at point A and B cancel each other ($f_{D,A} + f_{D,B} = 0$). In the case of a curved optical fiber (Fig. 1(b)), the reflection angle, α_A , at point A is larger than the angle, α_B , at point B, and different Doppler shifts are obtained ($f_{D,A} + f_{D,B} \neq 0$). As a result, the frequency is shifted along the curved region, which vibrates or moves.

A lightwave in a curved optical fiber can be considered as a light beam as shown in Fig. 2. The frequency shift, df_D , that occurs in an infinitesimal element, ds , is expressed by equation (1) according to the Doppler effect. The total frequency shift, f_D , along the curved light beam can be obtained as equation (2) by integrating equation (1), where V , n and k are velocity vector, normal vector, and curvature, respectively (See Fig. 2), and λ is wavelength of the laser light in an optical fiber.

$$df_D = -\frac{V \cdot n}{\lambda} d\theta \quad (1)$$

$$f_D = -\frac{1}{\lambda} \oint kV \cdot n ds \quad (2)$$

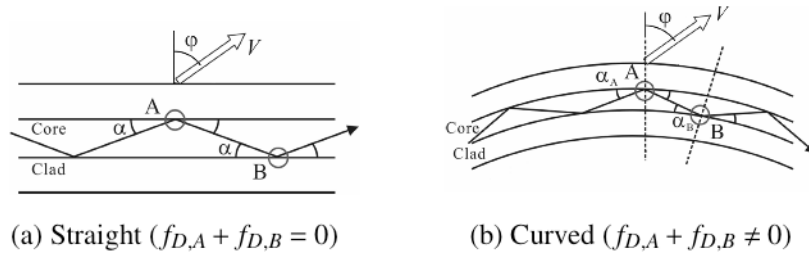


Fig. 1 Doppler effect in an optical fiber.

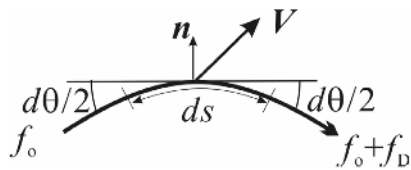


Fig. 2 Light beam in a curved optical fiber.

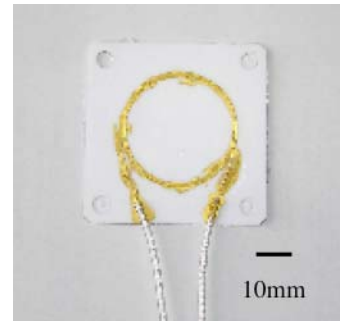


Fig. 3 Optical fiber sensor.

2. Experiments

2.1 Optical Fiber Sensor System

Figure 3 shows the optical fiber sensor used in the present study. It consists of 5.5 loops of fiber entirely bonded to a ceramic plate by using a gold paste. The dimensions of the ceramic plate is 50 x 50 x 0.6 mm and optical fiber sensor has 30-mm diameter. The fiber (TOTOKU Electric) used in this study had no polyimide layer and was coated with gold with a thickness of about 20 μm . Figure 4 shows an optical sensing system. Laser doppler velocimeter (Melectro, V1002) based on the heterodyne interference technique is used. The He:Ne laser with a power of 1 mW is used as a light source. It is separated into two beams by a half mirror. One of the beams is sent to the sensor, in which the frequency is changed from f_0 to $f_0 \pm f_d$ by vibration or elastic wave. The other beam is guided to the acousto-optic modulator and the frequency is shifted from f_0 to $f_0 + f_M$ ($f_M = 80$ MHz). These beams are then combined again after passing a half mirror in order to produce beating signals with a frequency of $f_M \pm f_d$. The combined beam is sent to a photodetector to transform light into electric current and then demodulated by a demodulator.

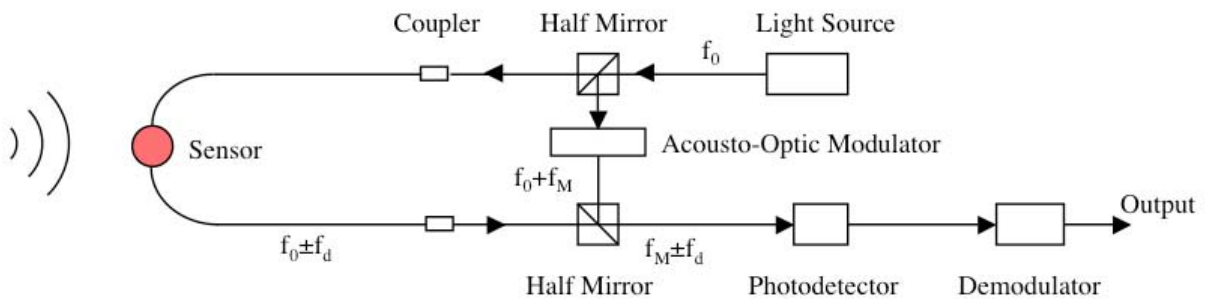


Fig. 4 System of the optical fiber sensor.

2.2 Experimental Procedures

In order to examine the potential of the developed optical fiber AE sensor, the quasi-AE measurement was carried out at elevated temperatures. Figures 5 and 6 show the test piece and schematic diagram of the measurement system, respectively. The test piece was machined from a SUS304 plate with two long legs for applying PZT sensors to generate and detect AE signals. This test piece was cleaned and the optical fiber sensor was bonded with a ceramic cement (Three Bond, 3713B). An electric oven (Chino, MF-2000) was used to heat the test piece and the temperature was measured by the thermocouple attached to the test piece. PZT sensors (PAC R-15; frequency = 150 kHz) were attached to the end of the legs with silicone grease (Shin-Etsu Chemical, HIVAC-G). One of the PZT sensors was driven by an electric pulse generator (PAC, C-101-HV) to generate quasi-AE waves. The optical fiber sensor and the other PZT sensor detected the generated quasi-AE signals. The signals detected by the optical fiber sensor were filtered with an HPF of 10 Hz and an LPF of 250 kHz. The signals detected by PZT sensor were amplified by 40 dB with a pre-amplifier (PAC, 1220A). Both signals were then recorded on a digital oscilloscope (Yokogawa Electric, DL-750) with 10 MHz sampling and 10 k length setting. At least 20 signals were recorded in each test condition. Various maximum temperatures of 200, 300, 400, 500 and 600°C were selected for measurement. The test piece was heated to the maximum temperature and kept for 1 hr before measuring. A long-term heat exposure was also made at 600°C up to 1000 hr.

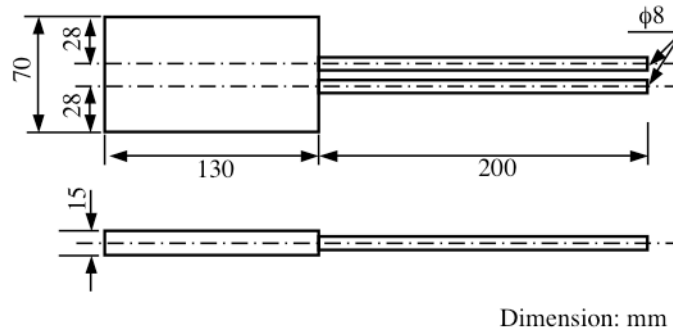


Fig. 5 Test piece.

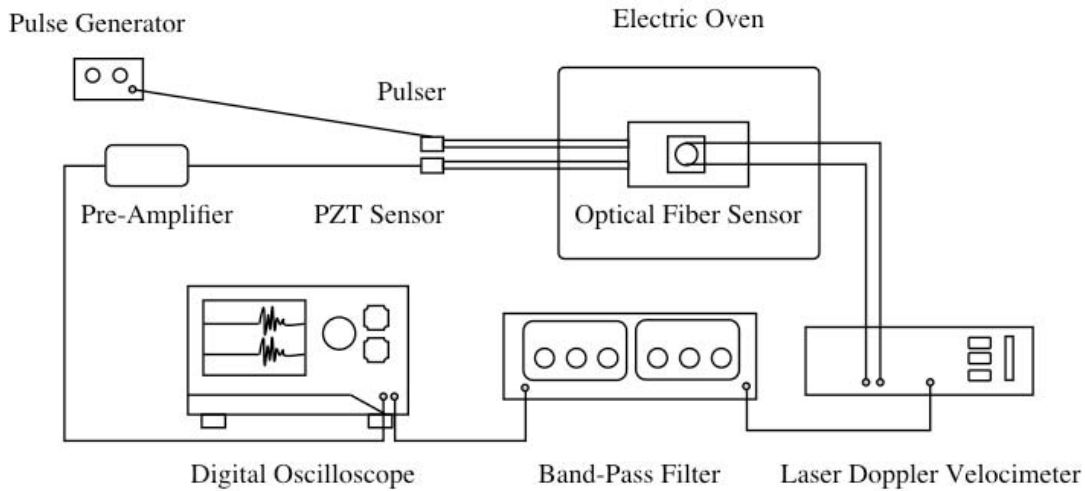


Fig. 6 Measurement system.

3. Results and Discussion

Figure 7 shows signals detected by the optical fiber sensor and the PZT sensor at each test temperature. The signals detected from the optical fiber sensor are similar for all test temperatures while decrease in amplitude of signals detected by the PZT sensor with increasing test temperature is clearly observed. The lower amplitudes of signals detected by the optical fiber sensor compared to those detected by the PZT sensor is due to a small number of fiber loops. Figure 8 shows the maximum amplitudes of signals detected by the optical fiber sensor as a function of test temperature. Twenty signals from each test temperature are used for this plot. The maximum amplitude increases from RT to 300°C and remains constant up to 400°C and then slightly decreases up to 600°C. This behavior may arise from a change in structure of ceramic bonding or gold paste between sensor/test piece and sensor/ceramic plate due to the heat effect. However, it has not been identified yet. It clearly shows that the optical fiber sensor has high heat-resistance. The previous investigation on the gold-coated conventional fiber (fiber with polyimide layer) shows that the fiber broke at about 500°C and the AE signals generated from the fiber itself were detected between 300 and 400°C. This behavior is due to the sublimation of polyimide. Therefore, using non-polyimide optical fiber improves the heat resistance of the sensor. However, pure quartz optical fiber shows loss in flexibility. Figure 9 shows a result obtained from long-term heat exposure at 600°C. Average amplitudes of waveforms are plotted as a function of exposure time. A scattering in amplitude is observed. This behavior may arise from the uncertainty due to attaching and detaching the pulser in each measurement. However, we can say that the new optical fiber sensor maintains its sensitivity up to 1000 hr at 600°C.

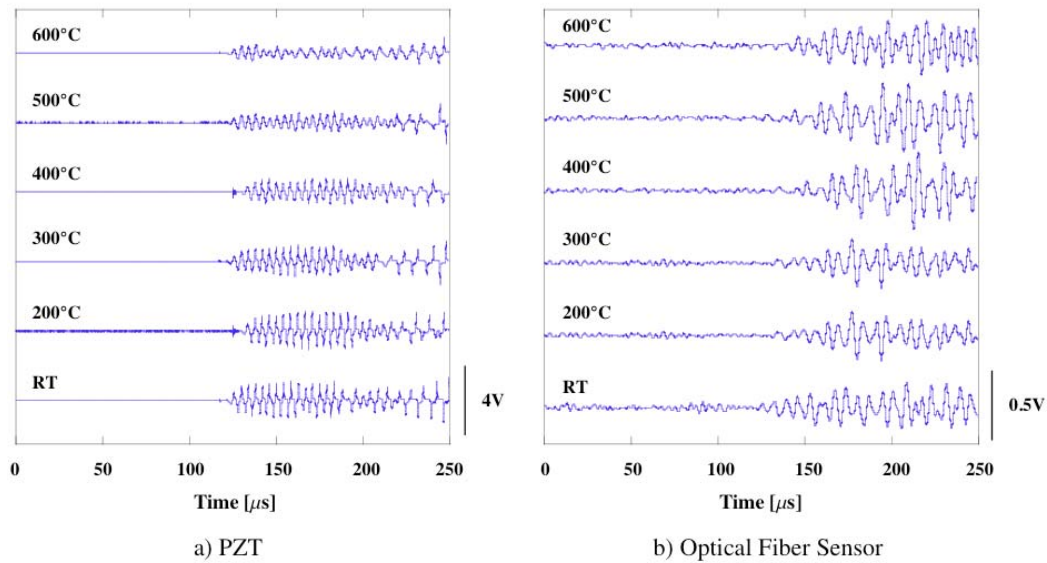


Fig. 7 Detected quasi-AE waves.

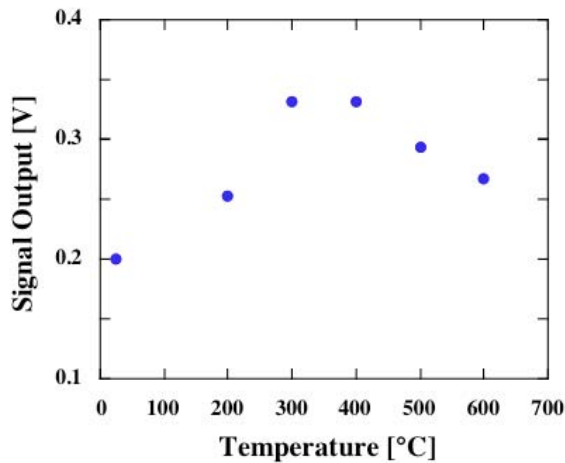


Fig. 8 Maximum amplitude at each temperature.

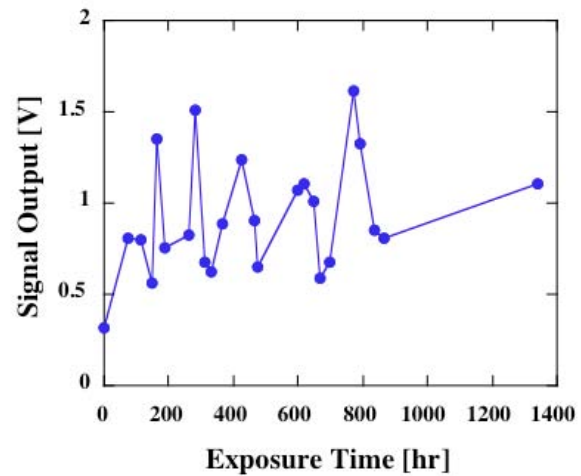


Fig. 9 Maximum amplitude in the long-term exposure.

4. Conclusion

We have developed a new optical fiber sensor based on gold-coated optical fiber. Although this new sensor shows lower sensitivity than that of a conventional PZT sensor, it can be used up to 600°C . Its sensitivity does not change even in the long-term heat exposure up to 1000 hr at 600°C . The good heat-resistance of this sensor enlarges an application field of AE technique in structural health monitoring and research. However, an improvement of sensitivity is required.

References

- [1] I. Read, P. Foote and S. Murray: Meas. Sci. Technol. **13** (2002), N5.
- [2] S. G. Pierce, W. R. Philip, A. Gachagan, A. McNab, G. Hayward and B. Culshaw: Appl. Opt. **35** (1996), 5191.
- [3] K. Kageyama *et al.*: Japan patents 2001-193840 (2001).
- [4] K. Kageyama *et al.*: Japan patents 2002-023091 (2002).
- [5] K. Kageyama, H. Murayama, I. Ohsawa, M. Kanai, T. Motegi, K. Nagata, Y. Machijima and F. Matsumura: *Int. Workshop on Structural Health Monitoring 2003*, (2003) Stanford, CA.

DAMAGE DETECTION SYSTEM FOR STRUCTURES WITH SMART AE SENSORS

TAKAHITO YANASE and SEI IKEGAYA

JUST Co. Ltd., 2-4-1 Azamino-minami, Aoba, Yokohama 225-0012, Japan.

Abstract

We conducted experiments on reinforced concrete structures using a damage detection system using Smart AE sensor. This system consists of a Smart AE sensor and a computer and is simpler than conventional AE systems. The Smart AE sensor contains an AE transducer, CPU, memory and USB terminal on the substrate and its size is about 20 mm x 80 mm. The main feature of Smart AE sensors is to convert AE waves received by the AE transducer into digital data, transmitting them to the personal computer. The personal computer receives the digital data for damage index of the structure, and displays it for monitoring.

Keywords: Damage detection system, Smart AE sensor, Reinforced concrete structures

1. Introduction

In Japan, many concrete structures have been used for more than 30 years. The maintenance and repair techniques for these existing structures are becoming significant. The maintenance is performed at regular intervals by visual inspection and nondestructive inspection. In order to improve the efficiency of the inspection, some damage detection systems for the structures were developed and applied to real structures. Although the sensors currently used by such damage detection systems are mainly optical fiber sensors, some sensors as listed below can also be used for damage detection system. 1) Acceleration transducer, 2) Displacement transducer, 3) AE sensor.

We choose AE sensor as the sensor of a damage detection system, because it has been often applied to experiments in laboratory. In laboratory experiments, it was useful to evaluate correctly the position of the damage using multiple AE sensors. However, such measurement systems are complex and expensive, so we needed improvement to apply it to the damage detection system. On real structures, it is often possible to estimate the area where damage by external force occurs. Only one AE sensor is necessary to detect the damage around it, and the damage detection system becomes simple.

We have developed a damage detection system, which consists of a personal computer and a Smart AE sensor. A Smart AE sensor is attached to the area of expected damage. It is connected to a PC by a USB cable. The Smart AE sensor can process the AE waves from an AE transducer, convert them to digital data and transmit the data to the personal computer. The AE waveforms are changed into the AE (or threshold-crossing) counts per unit time and this is used as the damage index for the structure by the Smart AE sensor. Multiple AE sensors can be connected to a PC simultaneously. In this paper, we describe the damage detection system applied to structural experiments of the concrete.

2. Outline of Damage Detection System

The single-channel damage detection system is shown in Fig. 1, and the detail of Smart AE Sensor is shown in Fig. 2. A Smart AE sensor includes an AE transducer, CPU, memory and a USB terminal on the substrate. Its size is approximately 20 mm x 80 mm.

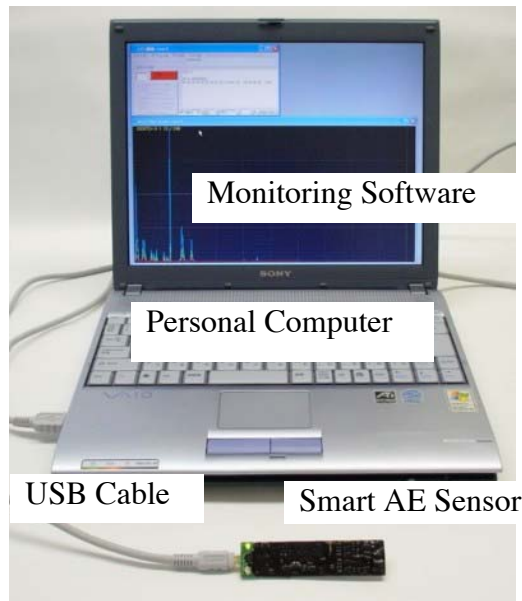


Fig. 1 Damage detection system.

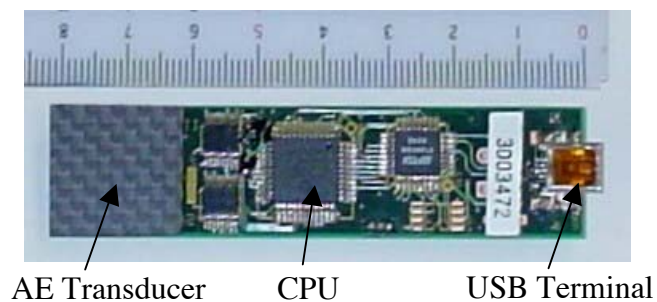


Fig. 2 Detail of Smart AE sensor.

Functions of the Smart AE sensor are:

- 1) The AE transducer receives AE wave generated from the damage.
- 2) The AE waves are changed into digital data as damage index or AE count rates.
- 3) The digital data is transferred to the personal computer (PC) by the USB cable.

Here, the damage index is the AE counts per second and PC always displays it. Since it is not necessary to process AE waveform data, this damage detection system can display the damage in real time. The amount of data obtained by this system is much smaller as compared with the waveform data obtained by the conventional AE method and it is possible to connect four sets of Smart AE sensors to one PC simultaneously.

In the second-generation damage detection system, shown in Fig. 3, it has larger memories and operates for one month or more by a battery. We are going to use the next type of Smart AE sensor. In the following experiment, we use this new type of Smart AE sensor.

3. Experiments

3.1 Specimens and Testing Method

We carried out two experiments with the Smart AE sensor on the specimen. One is on a pre-stressed concrete beam specimen (PS1) and the other on a reinforced concrete column specimen (RN47). The monitoring of damage occurrence was performed throughout experiment by the new damage detection system.

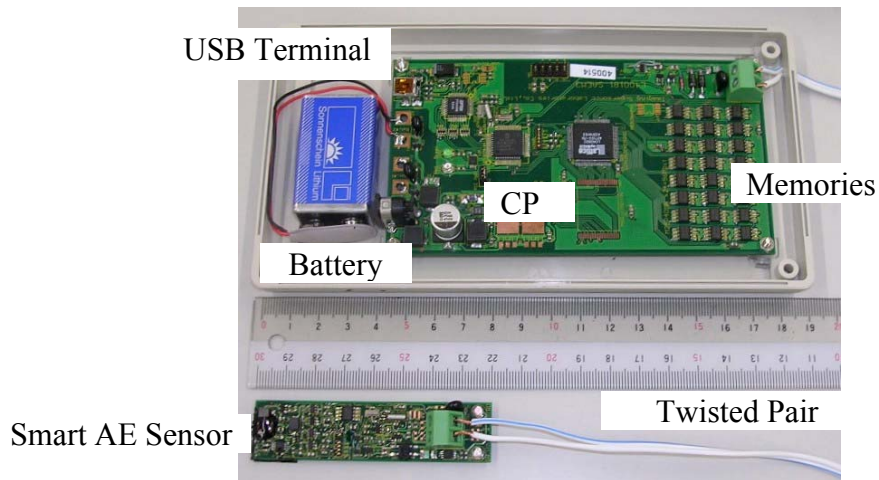


Fig. 3 Next generation of Smart AE sensor.

The form and the arrangement of bars of the specimens are shown in Figs. 4 and 5. For the pre-stressed concrete beam specimen (PS1), the size of rectangular section was 200 mm x 300 mm, and the length of the span was 3,000 mm. The PC strand was arranged in the position of 75 mm from the section bottom at the center of the span, in order that the edge tensile stress of the concrete stays below 0.5 N/mm^2 . The specimen was supported by pin devices at both ends. The load applied to two points, which were distant from a center every 250 mm. The Smart AE sensor was attached to the specimen surface of the span at the central part with the adhesive.

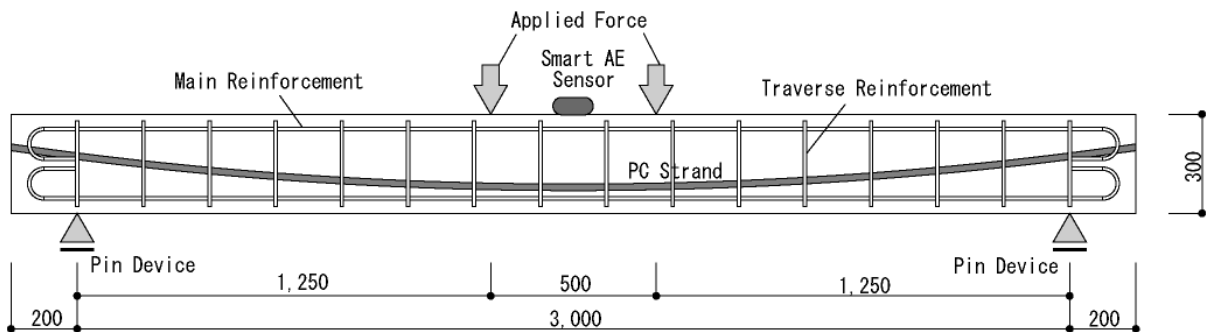


Fig. 4 Outline of specimen (PS1).

For the reinforced concrete column specimen (RN47), the size of rectangular section was 275 mm x 350 mm, and the height of the column was 700 mm. See Fig. 5. There was less quantity of the transverse reinforcements than usual structure so that shear failure was expected. Gradual increase in horizontal load was applied repeatedly to the specimen. Axial load was not applied. The Smart AE sensor was attached on the specimen surface at the mid-height part with the adhesive.

3.2 Results for Pre-stressed Concrete Beam

The relationship between applied force (P) and displacement for PS1 specimen is shown in Fig. 6. When applied force is 34 kN, the bending crack occurred in the center of span. The yielding of main reinforcement and PC strand occurred at P=52 kN and 86 kN, respectively.

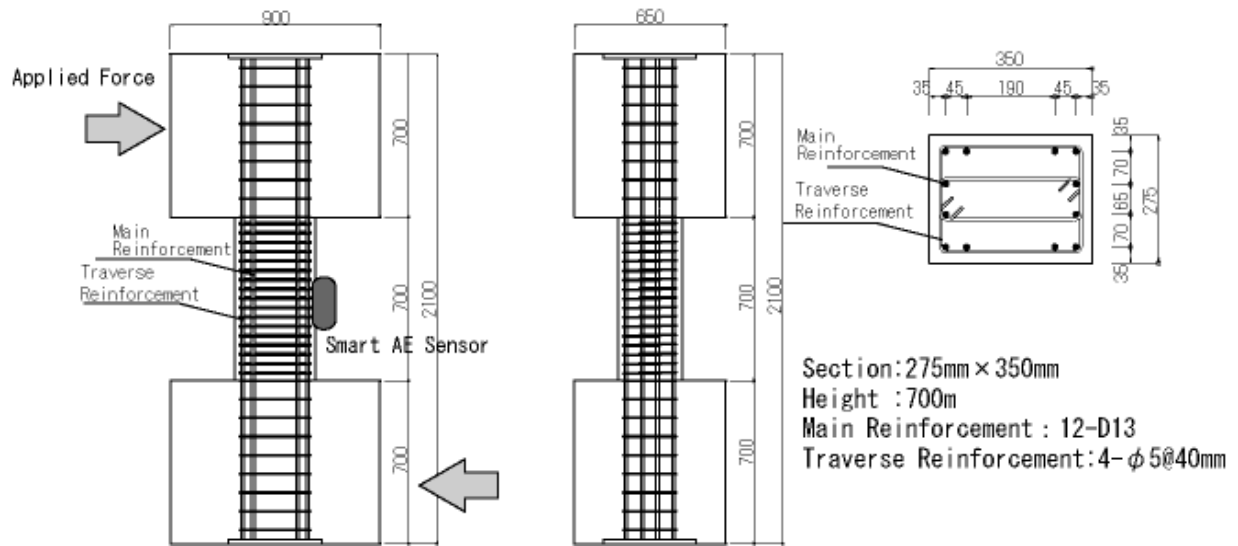


Fig. 5 Outline of specimen (RN47) and loading direction.

When compressive failure of concrete occurred at the upper surface, applied maximum force was 91 kN.

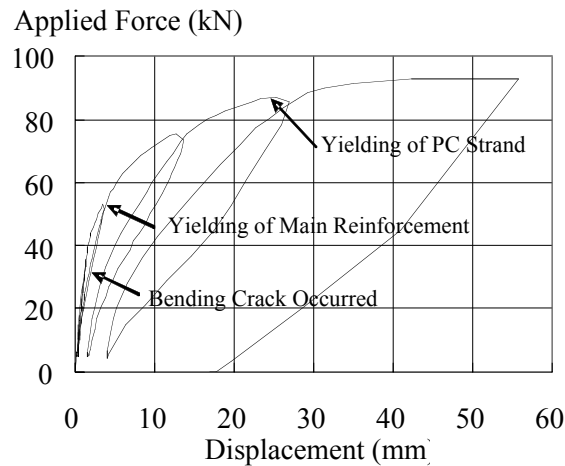


Fig. 6 Relationship between applied force and displacement. PS1

The relationship between displacement and AE counts as damage index is shown in Fig. 7. The horizontal axis shows the loading step (time). The displacement increased gradually with the loading. AE counts were first observed to rise, when bending crack occurred. AE counts were observed actively at the peak displacements. Fewer number of AE counts were observed below the prior displacement, which is called Kaiser effect. Note very high AE counts during the unloading toward the end of experiment. This shows extensive concrete damage.

3.3 Results for Reinforced Concrete Column

The relationship between shear force (Q) and deflection angle (R) for RN47 specimen is shown in Fig. 8. The crack pattern after experiment is shown in Fig. 9. When shear force was near $Q = 80$ kN of first loading cycle, bending crack occurred at both ends of the specimen. When shear force was near $Q = 140$ kN on the second loading cycle, shear cracks occurred. When deflection angle was $R = 15 \times 10^{-3}$ rad., the shear force was 380 kN. The width of shear

cracks, which occurred along the diagonal, became large after the maximum shear force, and shear failure occurred.

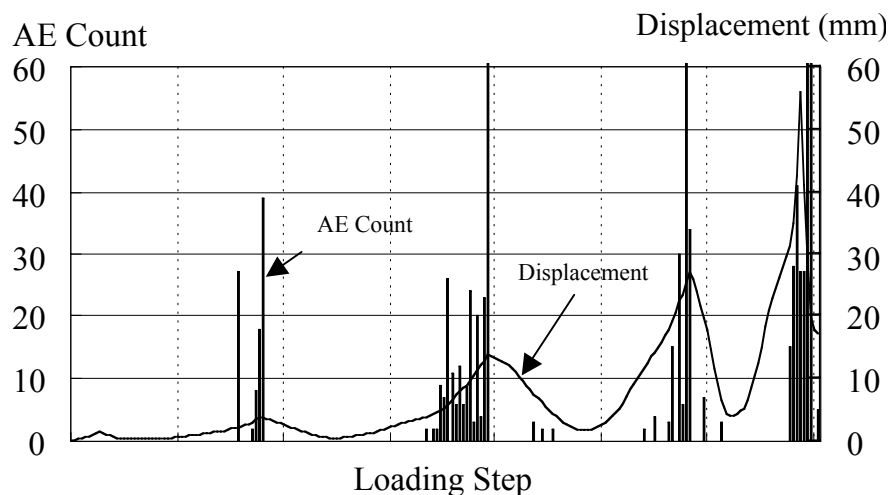


Fig. 7 The relationship between displacement and AE count.

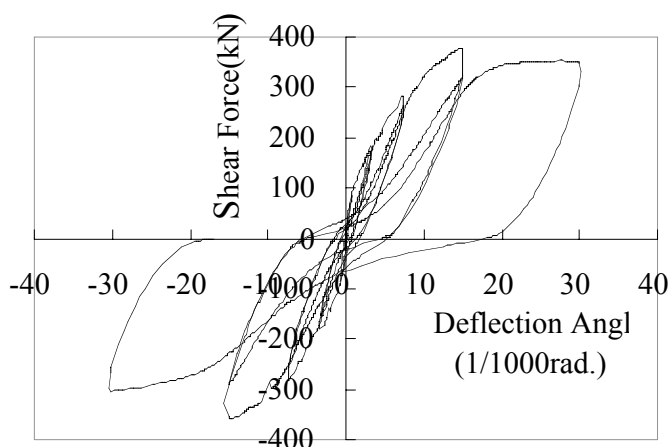


Fig. 8 Relationship between shear force and deflection.

RN47

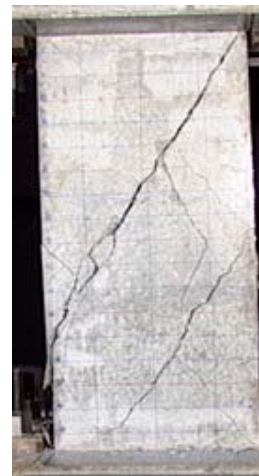


Figure 9 Shear failure.

The deflection angle and AE counts vs. time of loading are shown in Fig. 10. The horizontal axis represents the loading step. The deflection angle changed gradually upon loading and unloading. AE counts were first observed, when a shear crack appeared on the second loading cycle. High AE counts were observed at the end of the second cycle, then increased intensively near peak deflection angle during the fourth cycle. Few AE count was observed during fifth loading cycle, indicative of Kaiser effect. AE counts were observed even during the unloading after the fourth loading cycle. This shows permanent damage of the concrete. Beyond the sixth loading, AE counts were almost always present.

4. Conclusion

We carried out experiments using a simple and low-cost damage detection system using the Smart AE sensor.

- 1) Occurrence of damage of the structure can be detected with the damage detection system.

- 2) The damage index transmitted from Smart AE sensor is observed as the concrete damage progressed.
- 3) Kaiser effect was clearly observed, just as in the conventional AE methods.

Reference

- (1) S. Ikegaya and T. Yanase : Experimental Study on Health Monitoring for Structure Used by Smart AE Sensor, *Proceeding of National Conference on Acoustic Emission*, 2003, JSNDI, Tokyo, pp. 55-58.

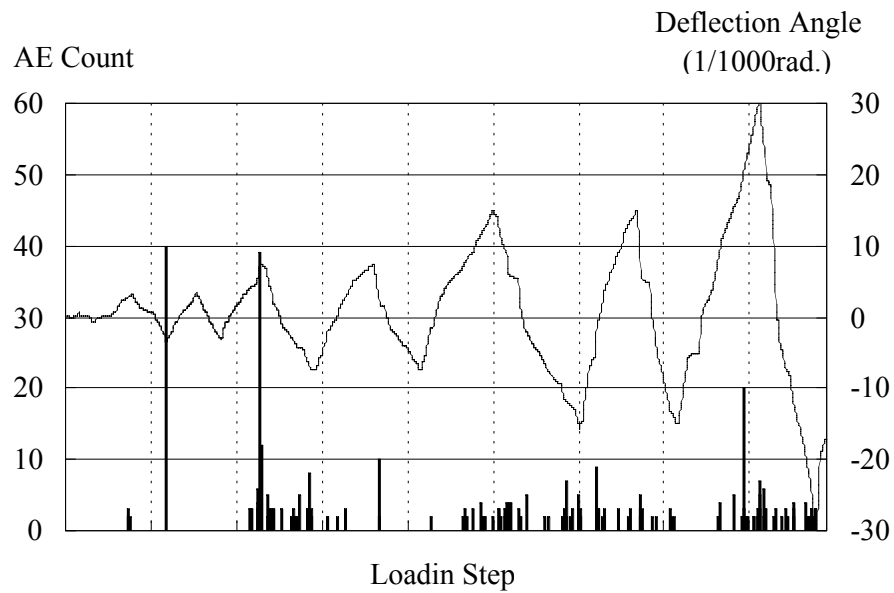


Fig. 10 Relationship between displacement and AE counts (RN47 Specimen).

HIERARCHICAL FRACTURE PROCESS IN BRITTLE ROCKS BY MEANS OF HIGH-SPEED MONITORING OF AE HYPOCENTER

XINGLIN LEI*, OSAMU NISHIZAWA, ANDRE MOURA and TAKASHI SATOH

Geological Survey of Japan (GSJ), National Institute of Advanced Industrial Science and Technology (AIST), Higashi 1-1-1, Tsukuba, Ibaraki, 305-8567, Japan; *Also at Institute of Geology & Laboratory of Tectonophysics, China Seismological Administration, Beijing, China.

Abstract

Damage evolution and fault formation processes in brittle rocks under stress were studied based on data collected with a high-speed recording system of acoustic emission (AE) waveforms. Experimental results show that the faulting process is hierarchical. Quasi-static nucleation of faults represents dynamic fractures of the asperities on the fault plane; likewise, a quasi-static nucleation process characterized by dynamic microcracking precedes the fracture of an asperity. The progressive fracturing of multiple and coupled asperities results in short-term precursory fluctuations in both the b -value and event rate of AE. For proposing more general models, three granites of different grain size distributions were used for fracture tests under triaxial compression with two different loading rates of 27.5 and 2.5 MPa/min. The damage creation in these intact brittle rocks shows a typical process characterized by three phases of microcracking activity: named as primary, secondary, and nucleation phases. For applying the experimental results to real problems, the damage evolution was quantitatively modeled from two approaches: 1) the corrosion-aided sub-critical crack growth theory for crack population with fractal size distribution; 2) renormalization-group theory applied to second-order phase transition with the time of the global failure assimilated to a critical time. The event rates and b -values in the secondary and nucleation phases can be modeled well by the first model. Energy release calculated from the event rates and magnitude can be modeled well by the second model with two domains corresponding to the secondary and nucleation phases. These results confirm that 1) the larger the grain size, the stronger the crack-crack interaction; 2) the faster the loading rate (stress-rate), the stronger the interaction; 3) the secondary domain, i.e., the nucleation phase, shows normally longer interaction than the first domain, indicating the increase of interaction distance.

Keywords: Damage evolution, Rock fracture, Microcrack, Renormalization-group

1. Introduction

The study of damage evolution in rock and other industrial materials like cement under stress is a subject of widespread interest, with relevance to both artificial applications such as optimization of geothermal recovery, oil recovery, safe design of nuclear waste repositories, rock bursts, and natural processes such as volcano eruptions and earthquakes. It is important to predict the time of catastrophic failure that corresponds to the lifetime of industrial material or the occurrence of rock burst and earthquake. For this goal, challenges on modeling the damage evolution have been made through both experimental and theoretical approaches.

In laboratory, damage evolution in stressed materials has been studied extensively by a number of methods including 1) the direct observation of sample surface by scanning electron

microscopy [e.g., 1] or optical microscopy [e.g., 2] operated during or after a fracture test; and 2) monitoring the hypocenter distribution of acoustic emission (AE) events caused by microcracking activity [e.g., 3, 4]), which is the so-called AE technique. AE technique is advanced in the analysis of the microcracking activity inside the sample volume and can be performed under confining pressure, which is very important in the simulation of underground conditions.

The recently developed high-speed multi-channel waveform recording technology has made it possible to monitor the hypocenters of AEs associated with spontaneously/unstably fracturing processes in stressed samples with high precision. The system is capable of recording AE waveforms in 32 channels at sampling rates up to 5000 events per second, and has been successfully used to study the final stage (quasi-static) of fracturing nucleation in intact brittle rocks. It has been applied to the analysis of the fracture process of hornblende schist [5], granitic rocks [6], and mudstone containing quartz veins, which play a role as strong asperities [7]. Lei et al. [5] observed that once a shear fault is initiated or nucleated in fine-grained homogeneous rock, the shear fault grows quasi-statically with a process zone at the fault front. It is found that the process zone is governed by progressive triggering of tensile microcracking, in agreement with the microscopic examination on a torque test revealed by Cox and Scholz [2].

More recently, it has been observed that the microcracking activity associated with the fracture of inhomogeneous fault consists of 3 stages or phases with a spatial hierarchical structure [8]. These long-term microcracking phases referred to as primary, secondary and nucleation can be identified from the changes in event rates, b -values, and AE hypocenter distribution. It was suggested that the predictability of catastrophic fracture is strongly dependent on the heterogeneity on the potential fault plane. A homogeneously healed fault is notably unpredictable, whereas a fault of non-homogeneous healing strength or asperity distribution undergoes a predictable fracturing process with a remarkably clear nucleation phase that can be observed as a precursory anomaly of the b -values or other statistical parameters of AE activity. The appearance of a nucleation phase with rapidly decreasing b -values, a non-linearly increasing event rates and spatio-temporal clustering can be considered to be a signal of the initiation of catastrophic fracture.

The above described experiments agree with the general knowledge that global failure comes from spatially distributed micro-separations including microcracking, fiber rupture, interfacial debonding, etc., which is in contrast to the case of perfect crystal where global failure occurs from a few or even from only one unstable crack. The multi-step character of arising damages, reflecting the discrete nature of the fracturing process, makes it possible to compare the diffusion of damages in brittle materials with the diffusion on random lattices [9, 10]. This analogy has been the starting idea for extensive numerical simulations applied to the lattice models of fracture, which predicted the existence of scaling laws in the vicinity of fracture in brittle materials [11]. The fracturing of stressed materials is considered then as analogous to a critical phenomenon happening at a second-order phase transition in analogy to percolation phenomenon [12, 13]. The moment of rupture is similar to a critical point, so that the fracturing process can be described by a renormalization-group scheme [14]. In the vicinity of the critical point of rupture, there exists a critical region [15, 16], where the variations of the free energy, which is the energy release in the case of rock fracture, can be characterized by a power law of time normalized by the critical time decorated by log-periodic oscillations [17]. Such oscillations, which are useful for prediction purpose, are related to complex exponents that appear in renormalization-group solutions for critical phenomena [18].

However, above model based on critical phenomena is somewhat mathematical. The physical bases behind the model parameters are still unclear. Hence, further studies are required for linking mathematical models with physical mechanisms in order to elaborate reasonable prediction schemes. Another approach for modeling the damage evolution with some physical bases has been proposed by considering the sub-critical crack growth under stress as the result of stress-aided corrosion at the crack tip. Some models based on the experimental results of a single macroscopic extensional crack have been proposed [e.g., 19, 20] and later extended to crack population with fractal size distribution [21]. The models can fit not only energy release (here events rate) as the model from the renormalization-group solutions but also the b -value in the magnitude-frequency relation. Hence these models could explain some precursory anomalies such as quiescence [22] and b -value decrease [23] associated with large earthquakes, although they are unable to take account for interaction phenomena.

In this paper, we will at first introduce the most recent experimental results associated with the hierarchical fracturing process. Then we will model the damage evolution based on detailed AE measurement by two different models come from firstly, the stress corrosion constitutive laws and secondly, the renormalization-group scheme. We will discuss next on some possible physics behind the model parameters and the relation between these models.

2. Experiment and Data Processing

It is normally observed that the AE rates may reach several thousands per second prior to the catastrophic failure [e.g., 8]. For clarifying the damage evolution through the monitoring of the spatio-temporal distribution of AE events, a high-speed waveform recording system has been developed. The system has the following advantages.

- i) It has a rapid waveform recording facility on 32 channels with a sampling rate up to 25 MHz and dynamic range of 12 bits.
- ii) The mask time of the system is less than 200 μ s, thus it is possible to record AE waveforms without any important loss, particularly when the AE activity is very high - on the order of several thousands per second.
- iii) The system has a 2-channel detector to capture the values of peak amplitudes with an effective dynamic range of 55 dB, which corresponds to a magnitude range of about 2.75. Further, since the peak detector shares a common base-clock with the waveform recording system, it is possible to obtain a complete set of temporal and spatial distribution of AE events.
- iv) The piezoelectric transducers (PZT) function not only as receivers of acoustic signals, but also as acoustic sources for measuring the P- and S- velocity during experiment. Being a receiver or transmitter is controlled by an automatic switching system.
- v) It can record stress and strain data on 16 channels with 16-bit resolution and 100 kHz sampling rate.
- vi) AE hypocenters can be determined automatically by using the first arrival time data of P-waves and measured P velocities. The location error of an AE hypocenter is generally less than 1~2 mm and 2~3 mm for fine-grained and coarse-grained rocks, respectively.

Test samples were normally shaped as cylinders of 125 mm (100 mm for some earlier tests) in length and 50 mm in diameter. All samples were dried under normal room conditions for more than one month and then compressed with constant stress rate including creep (sample was loaded with constant stress rate to a stress level of ~95% fracture strength and then held constant) at room temperature. During the deformation confining pressure was kept constant at 40-60

MPa. Under these conditions, a rock sample normally fractures with a shear fault of $\sim 30^\circ$ with the maximum stress axis. Table 1 is a list of rocks and their dominant grain sizes referred to in this paper. These granitic rocks contain mainly quartz, K-feldspar, and biotite. Granitic Porphyry has a very low density of pre-existing microcracks due to recrystallization. Other rocks contain relatively higher density of pre-existing microcracks. The size and spatial distribution of the pre-existing microcracks are controlled by the grain size distribution. Hence, from the microscopic (from μm to mm) point of view, the larger the grain size is, the more heterogeneous the rock.

Table 1 Dominant grain size in test samples.

Rock	Westerly Granite, WG	Oshima Granite, OG	Inada Granite, IG	Granitic Porphyry
Major grain size (mm)	<1-2	1-5	1-10	1-10

A total of 32 PZT sensors (5 mm in diameter, resonant frequency of 2 MHz) were mounted on the surface of each test sample to detect AE signals from microcracking events. A series of 6-8 cross-type strain gauges (12-16 channels) were mounted on the surface of the sample to measure local axial and circumferential strains. The local volumetric strain (ε_v) was calculated from the axial (ε_a) and circumferential (ε_c) strains according to the equation $\varepsilon_v = \varepsilon_a + 2\varepsilon_c$.

The mechanics of rock deformation and crack growth can be inferred from AE statistics, because the number of AE events is proportional to the number of growing cracks and AE amplitudes are proportional to the length of crack growth increments [23, 21, 25, 26]. The well-known Gutenberg and Richter [27] relationship,

$$\log_{10} N = a - bM \quad (1)$$

where N is the number of events of magnitude M or greater, holds for not only earthquakes but also AE events in laboratory [e.g., 28, 29]. In equation (1), a is a constant and b is the seismic b -value. An estimate of the b -value in the Gutenberg-Richter relation can be obtained by using either the least-squares method or the maximum likelihood method [30].

3. Hierarchical Fracturing Process

The final stage of the damage evolution prior to the catastrophic fracture is the most important subject because it is associated with the predictability based on either precursory phenomena or damage constitutive law. Some recent experimental results have improved our understanding on the fracture behavior leading to the catastrophic failure. For instance, the fracture of a shear fault containing several unbroken asperities in a granitic porphyry is examined in detail by Lei et al. [24, 32]. A detailed description of the test sample, identification of asperities, and experimental setup can be found from the cited references. Since this result has provided us some physical bases for understanding the mathematical models presented in the following sections, it is convenient to briefly summarize the results here. As shown in Fig. 1(a), AEs caused by the fracture of individual asperities exhibit similar characteristics to the sequence for natural earthquakes, including foreshock, mainshock, and aftershock events. Foreshocks, initiated at the edge of the asperity, occur with an event rate that increases according to a power law of the temporal distance to the mainshock, and with a decreasing b -value (from ~ 1.1 to ~ 0.5). One or a few mainshocks then initiate at the edge of the asperity or the front of the foreshocks. The aftershock period is characterized by a remarkable increase and subsequent gradual decrease in

the b -value and decreasing event rates obeying the modified Omori law, which has been well established for earthquakes. The fracture of neighboring asperities is then initiated after the mainshock of a particular asperity, presumably due to redistribution of the strain energy accumulated within an asperity, which is released by the mainshock, resulting in enhancement of the stress concentration around the nearest neighboring intact asperities. The progressive fracturing of multiple, coupled asperities results in short-term precursory fluctuations in both the b -value and event rate (Fig. 1(b)), which may prove useful in the prediction of catastrophic failure. For applying the experimental results to real problems, a constitutive model must be established firstly based on experimental data and then examined again and again based on measurable data from real applications.

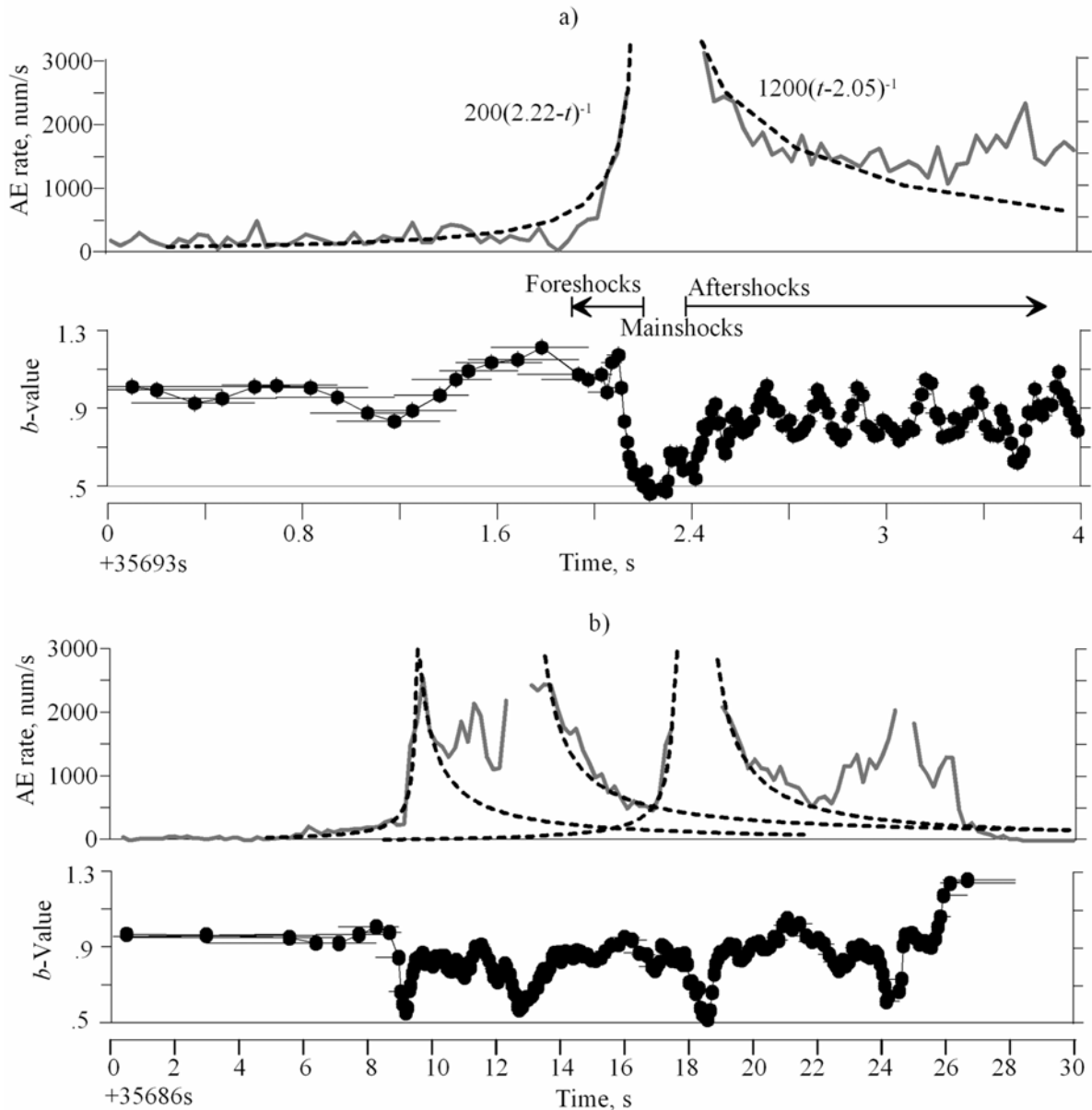


Fig. 1 AE data associated with the fracture of an individual asperity (a) and coupled asperities (b) on the fracture plane. The b -values are calculated for sets of 100 (in a) or 500 (in b) events with a running step of 25/125 events by the maximum likelihood method. The standard error for the estimated b -value is $\sim 0.1b$ or $0.05b$. Dashed line denotes the power law of temporal distance from the main shock.

3. Damage Model Based on Sub-Critical Crack Growth Theory

Under stress, sub-critical crack growth can occur as a result of stress-aided corrosion at the crack tip though the details are still unclear. The quasi-static rupture velocity V is found experimentally to be related to the stress intensity factor K by Charles' law [33]:

$$V = \frac{dc}{dt} = V_0 (K / K_0)^n \quad (2)$$

where c is the half-crack length and n is referred to as the stress corrosion index that has a typical value in the range 20-60 for polycrystalline rocks [19]. In the classic Griffith crack loading conditions, $K = Y\sigma c^q$ with $q = 1/2$, $Y = \sqrt{\pi}$. The solution of the differential equation (2) depends on the loading history $\sigma(t)$. Under static loading, the crack length predicted from the above equation of V and definition of stress intensity K has the form,

$$c = c_0 (1 - t / t_f)^{2/(2-n)} \quad (3)$$

where c_0 is the initial crack length at an arbitrary initial time $t = 0$, and t_f is the failure time [19]. For a time-varying stress, a similar equation is a good approximation if the stress-drop is small compared to the ambient remote stress [34]. For stress-aided corrosion crack, Meredith and Atkinson [20] showed that the event rate N has also a non-linear relationship to the stress intensity in the same manner as the above Charles' power law as:

$$N = N_0 (K / K_0)^{n'} \quad (4)$$

where n' is referred to as an 'effective' stress corrosion index and found to be equal to n within a few percent in brittle rocks [22].

The above model is somewhat based on the experimental results of microcracking during a single extensional macroscopic crack growth. However, it can be modified for a crack population of fractal size distribution by introducing only an effective mean value for each parameter [21]. Put the definition of K with $q = 1/2$ into equation (2) then the event rate can be expressed as

$$\log N = \frac{2n'}{2-n} \log \left(1 - \frac{t}{t_f} \right) + n' \log \left(\frac{\sigma}{\sigma_0} \right) + \log N_0 \quad (5)$$

For examining the fracture model, three granites WG, OG and IG are selected for systematic fracture tests. As listed in Table 1, the major difference of these granites is their grain size distribution. Two runs have been operated with constant stress rate at 27.5 MPa/m and 2.5 MPa/m, respectively. The confining pressure was kept constant at 50 MPa for all tests. Consistent with the previous study [8], the experimental data demonstrate that the damage creation, or in other words the microcracking activity, in these brittle rocks is characterized explicitly by three typical long-term phases referred to as primary, secondary and nucleation, respectively (Fig. 2). The above theoretical model is applicable to the secondary and nucleation phases but not to the behavior of the primary phase. Main features and fitting results are summarized as follows:

Primary phase: The event rate is low and increases slightly with stress or time. The b -value increases with increasing stress or time slightly from an initial value of 0.5~1.0 to 1.0~1.4. This initial value and increment depends strongly on grain size and density of pre-existing microcracks. In the fine-grained WG, the primary phase has a small number of events, the b -value is initially high and shows only a small increase (from ~1.3 to ~1.4). On the other hand, in the

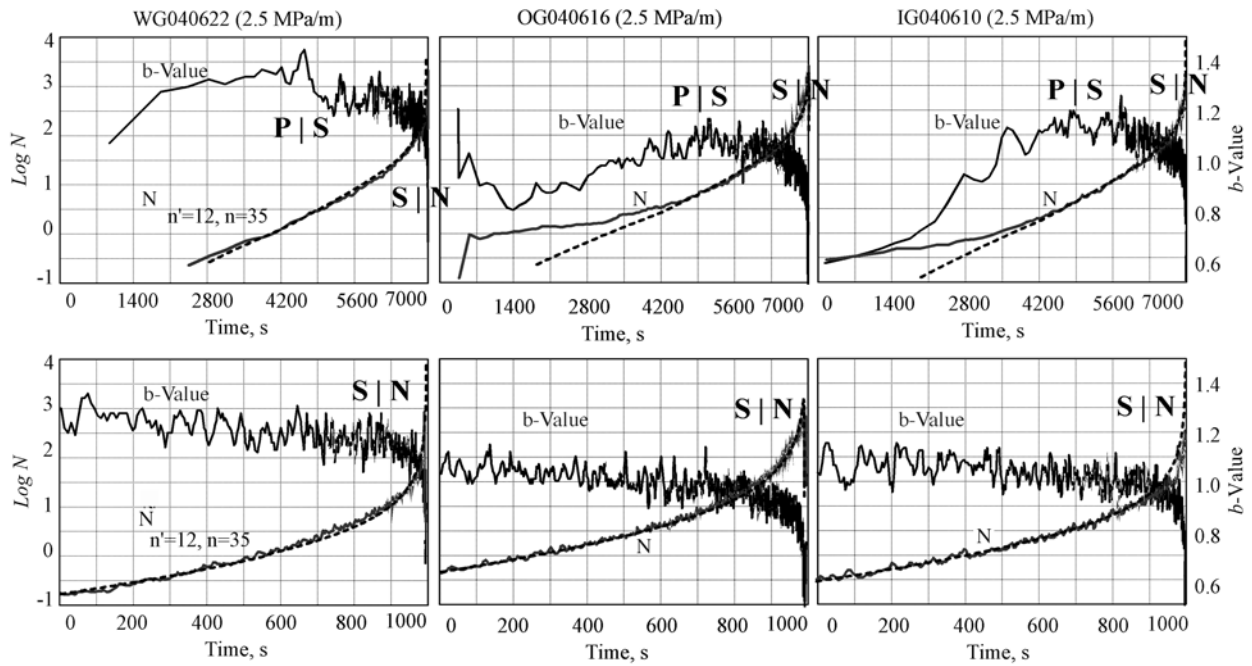


Fig. 2 The b -values and event rates of Westerly, Oshima, and Inada granite samples under constant stress-rate loading at 2.5 MPa/s. Dashed lines show the fitting results of equation (5). Lower plots are zoom up views of the last 1000 seconds, corresponding to the secondary and nucleation phases. “P | S” and “S | N” mark the transitions from the primary to secondary and secondary to nucleation, respectively.

coarse-grained IG, the primary phase has a larger number of events, the b -value is initially low and shows a large increase (from 0.5 to 1.2). The medium-grained OG shows a primary phase similar to IG, but with a smaller event number, higher initial b -value, and smaller b -value increase. In an earlier work, it has been found that the coarse-grained granitic porphyry (GP) sample of a very low pre-existing microcrack density demonstrates a primary phase of a small number of events [8]. Therefore, we conclude that the primary phase reflects the density and size distribution of pre-existing microcracks, which are somehow controlled by grain size distribution. Since the major mechanism of microcracking in the primary phase is an initial opening (tensile) or rupturing (shear) of pre-existing microcracks rather than crack-growth, the theoretical model based on sub-critical crack-growth is presumably inapplicable.

Secondary phase: The secondary phase corresponds to the microcracking activity following the primary phase. This phase shows increasing event rates and slightly decreasing b -values with increasing stress or time. The event rate data can be fitted very well with the theoretical model given that this phase is associated with the growth of pre-existing microcracks. For WG, OG, and IG samples, event rate N can be represented well by equation (5) with parameters $n' = 12$ and $n = 35$. Interaction between cracks and linkage of neighbor cracks become higher and higher as both the density and mean length increase together. That probably justifies that $n' \sim 0.3n$.

Nucleation phase: The nucleation corresponds to the period where event rate rapidly increases and the b -value decreases to the global minimum of 0.5-0.8.

Experimental data show also short-term fluctuations on both the event rate and b -value on the three long-term backgrounds. The amplitude of the fluctuations is function of the grain size

in a positive relation. The larger the grain size, the larger the amplitude. The fluctuations change both in amplitude and period following the fracture evolution, and therefore they may be useful for failure prediction. However, this kind of fluctuation cannot be modeled from the above fracture constitutive laws but fortunately recent models based on renormalization-group theory are able to describe this phenomenon.

4. Damage Model Based on Renormalization-Group Theory

In this section, we describe a scheme for modeling the damage evolution based on the renormalization-group theory. The key to this approach is to consider the stressed materials or rocks as a thermodynamic system with the supplied energy coming from the applied external load and, its transformation up to rupture, as a second-order phase transition. This transformation is highly irreversible and the system state is never in equilibrium. Micro-separations are the dominant irreversible processes, and the energy release, which has not been consumed by irreversible transformations such as crack advances and plastic deformation around the crack tip, is converted into the decrease of the free energy of the system.

Concerning the catastrophic regime, we are currently far from establishing a behavior law from the statistical approach on a purely thermodynamic point of view. This is because fracturing is both a non-linear and unstable process where the long-distance interactions play a major role and the material properties are every time modified. However, based on the fact that the moment of rupture is similar to a critical point, the fracturing process can be described by a renormalization-group scheme [14]. In the vicinity of the critical point of rupture, there exists a critical region, where the variations of free energy, here referred to as the energy release rate, can be characterized by a power law of the normalized time $x = (t_c - t)/t_c$, where t_c is the critical time, i.e., time of rupture, decorated by log-periodic oscillations [18]. For monophasic medium, the self-similar extrapolated form of the energy release far from the neighborhood of the critical point is written as [35]

$$\frac{E(x = (t_c - t)/t_c)}{E(x = 0)} = \cos(cx^\alpha \sin g(x) \exp h(x)) \exp(cx^\alpha \cos g(x) \exp h(x)), x \in [0,1] \quad (6)$$

where $g(x) = \rho \sin(\omega \ln x - \varphi)$, $h(x) = \rho \cos(\omega \ln x + \varphi)$, $E(0) = E_c$, ρ , φ , c , parameters, α and ω the real and imaginary part of the complex critical exponent $z = \alpha + i \omega$. There is no theoretical limit for ω whereas α belongs to the interval $[0, 1]$, as we are concerned with second-order phase transitions. The value of α is correlated to both the heterogeneity and the disorder of the structure of materials. For pure crystals, the damage is not diffuse and the rupture is unpredictable, so one has $\alpha \rightarrow 0^+$. The value of ω is somehow related with the interaction of events. Longer interaction distance (both spatial and temporal) results in larger ω .

The scheme from single domain can be extended to multi-domain in order to take account for successive dominant damage mechanisms in different stages or phases as presented in the previous section. Since the primary phase has a very low energy release rate, it is not considered here.

The cumulative energy release for above-mentioned experiments is shown in Fig. 3 together with the corresponding 2-domain fits based on the least-squares method. We focus on the first domains where damage randomly occurs over the whole sample, which confirm that 1) the higher the grain size, the longer the interaction, and the higher the ω ; 2) the faster the loading

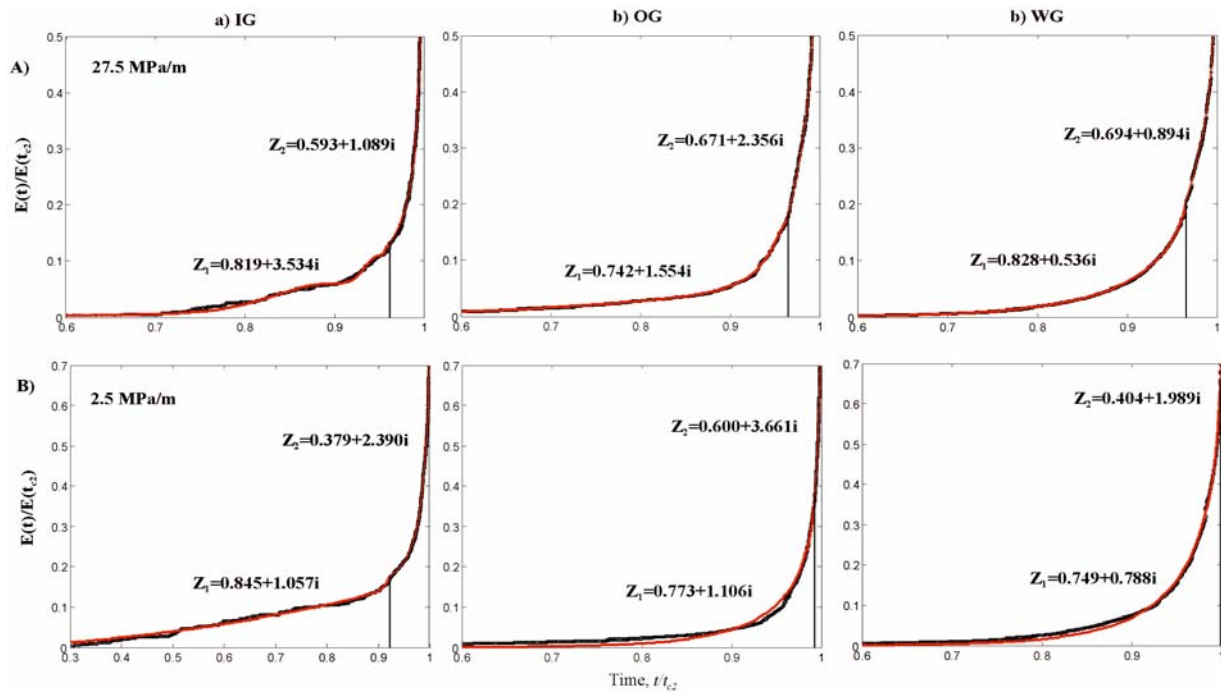


Fig. 3 Dimensionless cumulative energy release versus dimensionless time. a), b) and c) correspond to Inada, Oshima, Westerly granites, respectively. Upper and lower rows correspond to the results of fast and slow loading conditions, respectively. The black circles and the red lines represent the measurement data and the fits, respectively. Vertical dotted line indicates the boundary between the domains 1 and 2, respectively.

rate (stress-rate), the higher the ω , and therefore the stronger the interaction; 3) the secondary domain, i.e., the nucleation phase, shows normally a higher ω than the first domain indicating the increase of interaction distance.

5. Conclusion

In our experiment, the nucleation of shear fault was found to correspond to the fracture of coupled asperities on the fault plane. The fracture of individual asperities has similar characteristics to the sequence of natural earthquakes, consisting of foreshocks, mainshock, and aftershocks. The progressive fracturing of multiple, coupled asperities during the nucleation of shear faulting results in short-term precursory fluctuations in both the b -value and event rate. For proposing more common models, three granites of different grain size distribution were used for fracture test under triaxial compression at two different loading rates of 27.5 and 2.5 MPa/min, respectively. The damage creation in these intact brittle rocks showed a typical damage creation process characterized by three phases of microcracking activity named as: primary, secondary, and nucleation phases, respectively. The primary phase reflects the initial opening or rupture of pre-existing microcracks, showing increases of event rate and b -value with increasing stress. The secondary phase corresponds to the sub-critical growth of the microcrack population, showing an increase of event rate and a decrease of b -value with increasing stress. The nucleation phase corresponds to the initiation and accelerated growth of the final fracturing along one or a few major fracture planes. In the nucleation phase, the b -value decreased rapidly to the minimum value. Both the event rate and b -value in the secondary and nucleation phases can be modeled very well by the model based on the sub-critical crack growth theory. Energy release data calculated from the event rate and magnitude can be modeled quite

well by the theoretical model considering materials failure as a second-order phase transition. These results confirm that the higher the grain size, the longer the interaction, and the higher the ω . Experimental results also indicate that the faster the loading rate (stress-rate), the higher the ω , and therefore the stronger the interaction.

Our results indicate that the precursor-based predictability of the catastrophic failure strongly depends on the pre-existing heterogeneity and loading condition. The three-phase model is meaningful for transforming the experimental results to real problems associated with rock bursts, volcanic eruptions as well as tectonic earthquakes.

Acknowledgments

This work was partially supported by the National Basic Research Program of China 2004CB418405 and the Joint Earthquake Science Foundation under Contract No.104146.

References

- 1) Y. Zhao: Int. J. Rock Mech. Min. Sci. **35** (1998), 349.
- 2) S.J.D Cox and C.H. Scholz: J. Geophys. Res. **93** (1988), 3307.
- 3) D.A. Lockner, J.D. Byerlee, V. Kuksenko, A. Ponomarev and A. Sidorin: Nature **350** (1991), 39.
- 4) X.L. Lei, O. Nishizawa, K. Kusunose, T. Satoh: J. Phys. Earth, **40** (1992), 617.
- 5) X.L. Lei, K. Kusunose, M.V.M.S. Rao, O. Nishizawa and T., Satoh: J. Geophys. Res., **105** (2000), 6127.
- 6) X.L. Lei, K. Kusunose, O. Nishizawa, A., Cho. A. and T. Satoh: Geophys. Res. Lett., **27** (2000), 1997.
- 7) X.L. Lei, O. Nishizawa, K. Kusunose, A. Cho and T. Satoh: Tectonophysics, **328** (2000) 329.
- 8) X.L. Lei, K. Masuda, O. Nishizawa, L. Jouniaux, L. Liu, W. Ma, T. Satoh, K. Kusunose: J. Struct. Geol., **26** (2004), 247.
- 9) J. Bernasconi and W.R. Schneider: J. Phys. A: Math. Gen., **15** (1983), 729.
- 10) S. Dietrich and D. Sornette: Physica, **A252** (1998), 271.
- 11) M. Sahimi and S. Arbabi: Phys. Rev. Lett., **77** (1996), 3689.
- 12) H.J. Herrmann and S. Roux: *Statistical Models for the Fracture of Disordered Media*. North-Holland, Amsterdam (1990).
- 13) D. Sornette: *Critical phenomena in natural sciences: chaos, fractals, self-organization and disorder: concepts and tools*, Springer Series in Synergetics, Berlin (2000), 257.
- 14) J.C. Anifrani, C. Le Floch, D. Sornette and B. Souillard: J. Phys. I France, **5** (1995), 631.
- 15) L. Lamagnère, F. Carmona and D. Sornette: Phys. Rev. Lett., **77** (1996), 2738.
- 16) D. Sornette and J.V. Andersen: Eur. Phys. J., **B1** (1998), 353.
- 17) D. Sornette: Phys. Rep., **29** (1998), 239.
- 18) M. Nauenberg: J. Phys., **A8** (1975), 925.
- 19) S. Das and C.H. Scholz: J. Geophys. Res., **86** (1981), 6039.
- 20) P.G. Meredith and B.K Atkinson: Geophys. J. R. astr. Soc., **75** (1983), 1.
- 21) I.G. Main, P.R. Sammonds and P.G. Meredith: Geophys. J. Int., **115** (1993) 367.
- 22) I.G. Main and P.G. Meredith: Geophys. J. Int., **107** (1991), 363.
- 23) I.G. Main, P.G. Meredith and C. Jones: Geophys. J., **96** (1989), 131.
- 24) X.L. Lei, K. Kusunose, T. Satoh and O. Nishizawa: Phys. Earth Planet. Inter., **137** (2003), 213.

- 25) X. Sun, H.R. Hardy and M.V.M.S. Rao: *Acoustic Emission: Current Practice and Future Directions* ASTM-STP-1077 (1991), p. 365.
- 26) S.J.D. Cox and P.G. Meredith: *Int. J. Rock Mech. Min. & Geomech. Abstr.*, **30** (1993), 11.
- 27) B. Gutenberg and C.F. Richter: *Seismicity of the Earth and Associated Phenomena* (1954), Princeton Univ. Press, Princeton, NJ.
- 28) C.H. Scholz: *Bull. Seism. Soc. Am.*, **58** (1968) 399.
- 29) F. Liakopoulou-Morris, I.G. Main and B.R. Crawford: *Geophys. J. Int.* **119** (1994), 219.
- 30) T. Utsu: *Geophys. Bull.* **13** (1965), 99.
- 31) K. Aki: *Bull. Earthquake Res. Inst. Univ. Tokyo* **43** (1965), 237.
- 32) X.L. Lei: *Earth Planet Sci. Lett.* **213** (2003), 345.
- 33) R.J. Charles: *J. Appl. Phys.* **29** (1958), 1549.
- 34) I.G. Main: *Geophys. J.* **92** (1988), 455.
- 35) V.I. Yukalov, A. Moura and H. Nechad: *J. Mech. Phys. Solids*, **52** (2004), 453.

MEASUREMENT OF HYDRAULICALLY ACTIVATED SUBSURFACE FRACTURE SYSTEM IN GEOTHERMAL RESERVOIR BY USING ACOUSTIC EMISSION MULTIPLET-CLUSTERING ANALYSIS

HIROKAZU MORIYA¹, HIROAKI NIITSUMA¹ and ROY BARIA²

¹) Graduate School of Environmental Studies, Tohoku University, Sendai, 980-8579, Japan.

²) GEIE, Soultz-sous-Forêts, Alsace, France.

Abstract

AE/Micro-seismic events can be induced by pressurizing a subsurface formation and then used to identify hydraulically activated fracture and fluid flow direction in subsurface reservoir. Recently, with the development of advanced mapping techniques using similar AE events, faulting dynamics in the Earth's crust have been studied based on such events, and internal structures in the fault zone have been estimated from the precise source locations of those events. In this paper, the pore-pressure of seismically activated fractures during hydraulic stimulation of geothermal reservoir at Soultz HDR field, France is estimated based on the high-resolution mapping method of induced AE events. The AE events with similar waveforms are analyzed, and the seismically activated fracture planes are estimated using the precise source locations determined by the multiplet-clustering analysis. The tectonic stress measured by hydraulic fracturing method in borehole is introduced into the calculation of critical pore-pressure for frictional shear slip of fractures according to Coulomb's law. The estimated critical pore-pressure suggests that the fluid pressure in pre-existing fractures are higher near the permeable fracture zones in the well, and declines as the fractures are away from the intersecting portions.

Keywords: AE multiplet, Fracture, Pore-pressure, Geothermal

1. Introduction

The measurement of permeable fracture is important in engineering fields, such as the extraction of geothermal energy through subsurface fractures. The Acoustic Emission (AE) method is useful in estimating the location of subsurface fractures and their orientations. Advanced mapping techniques for induced AE events are progressing in order to estimate the fracture system in the reservoir, where the clustering analysis, collapsing method, multiplet-clustering analysis, etc. had been developed [1-4]. The multiplet-clustering analysis is a method to determine the relative locations of AE clusters consisted of multiplets and within the AE events with similar waveforms [5]. A multiplet, which is a group of similar AE events, is considered to be the expression of stress release on the same subsurface fracture, and their source locations of induced AE multiplet reflect the fracture plane behaving as a shear slip plane due to an increase of pore-pressure in the fracture. The multiplet-clustering analysis makes it possible to estimate the fracture planes, which would cause shear slip, and the method has been applied to induced AE events in geothermal reservoirs.

On the other hand, the measurement of pore-pressure distribution is important to understand the fluid flow and the effect of hydraulic fracturing for enhancing the permeability in subsurface fracture system. However, the direct measurement of pore-pressure is impossible for fractures

away from wells, although the spatial distribution and the gradient of pore-pressure are an indispensable indication of fluid flow around the well.

The orientation of subsurface fracture derived from the source locations of multiplet provides us an estimate of stress condition on the fracture plane, if the principal stress directions and the magnitudes are known. According to Coulomb's law, the shear slip associated with fluid injection is caused by the decrease of normal stress on fracture surface due to an increase of pore-pressure during fluid injection. If the shear slip is controlled by the Coulomb's law, we can calculate the critical pore-pressure for shear slip by using the orientations of fractures, the directions and magnitudes of principal stresses, which controls the dynamics of the fractures.

In this paper, we describe the method for estimating the critical pore-pressure distribution by using the orientations of subsurface fractures derived from AE multiplets and the regional stress field. The result of application to Soultz geothermal field is shown and the feasibility of the present method is discussed.

2. Induced AE Events at Soultz Field

The European HDR project at Soultz-sous-Forêts was founded by France, Germany and the European Commission (EC) in 1987. Well GPK-1 is located at the Soultz HDR field site. The well was drilled to 3,590 m depth (open hole below 2,850 m depth), and since 1987 it has been used for a number of detailed experiments. A major hydraulic fracturing experiment was undertaken at GPK-1 in September 1993. For twenty days, about 45,000 m³ of fresh water was injected into granite 'reservoir rock' with 10 MPa maximum wellhead pressure, whilst the flow rate was increased to 50 l/s. Through the test, it was demonstrated that the fracture network in the basement rock was well developed, with enhanced permeability and a substantial increase in transmissivity [6]. An inspection was undertaken of the borehole wall by BHTV (Borehole Televiewer) and FMI (Formation Micro Imager) after completion of the hydraulic fracturing experiment, and stress measurements related to hydraulic fracturing were also performed [7].

Induced AE events were detected using three downhole 4-component detectors and one hydrophone, installed in wells #4550, #4616, #4601 and EPS1. The 4-component detector consists of accelerometers mounted in a housing and set in sand at the bottom of the borehole. The three 4-component seismic detectors and hydrophone were set at depths of 1,500 m, 1,420 m, 1,600 m and 2,850 m, respectively. The downhole seismic detectors were installed in the same basement rock, and high quality signals were readily detected, since the influence of surface waves could be ignored and the transfer function from source to detectors is simple. The frequency band of the acquisition system was from 10 Hz to 1 kHz, and the signals were digitized by 5 kHz sampling frequency [6].

Using these detectors, source locations for more than 10,000 events have been determined [6]. Figure 1 shows source locations for all of the analyzed events, with the location of 10,182 events having been plotted. As shown in this figure, the seismic cloud has approximate dimensions of 0.5 by 1.2 by 1.5 km, striking N30°W and dipping nearly vertically [2].

Multiplet-clustering analysis is a method for precise determination of AE event locations and is used to identify subsurface fractures and fracture networks. A multiplet is a group of micro-seismic events with very similar waveforms, despite different origin times, and is likely the expression of stress release on the same structure. The relative source locations of similar events

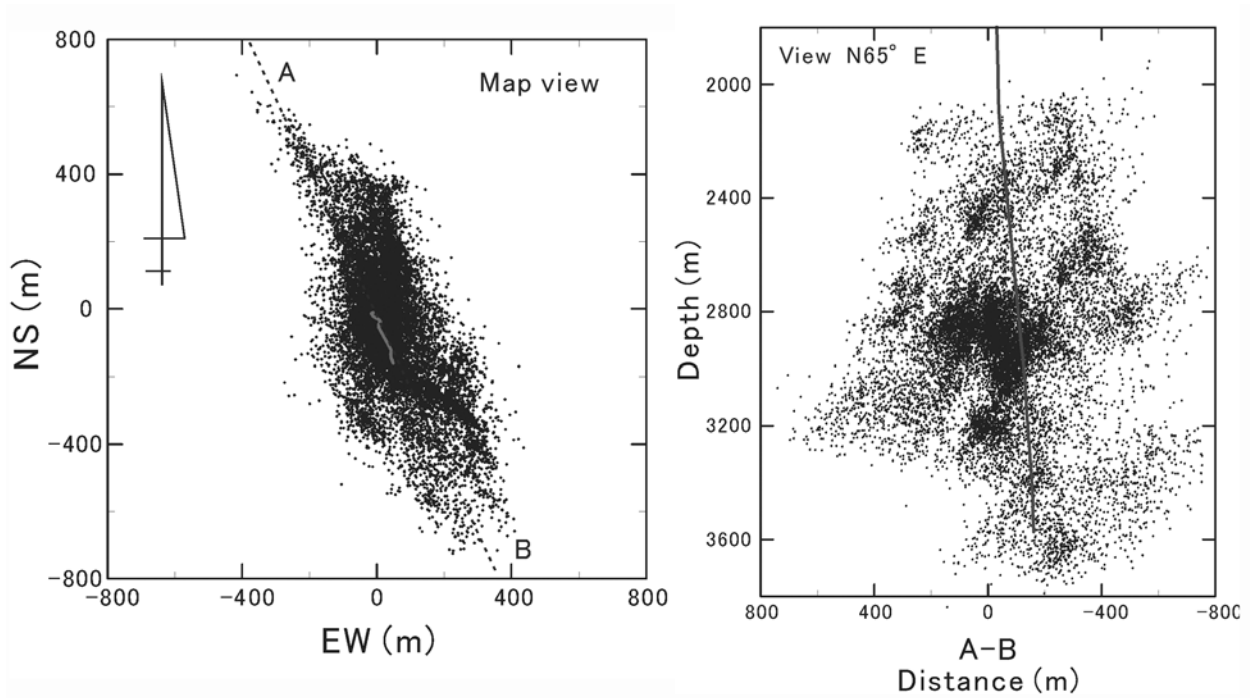


Fig. 1 Source locations of induced AE events, where the events determined by JHD method. The cross section is the view toward N65°E. Thick line denotes fracturing well GPK1.

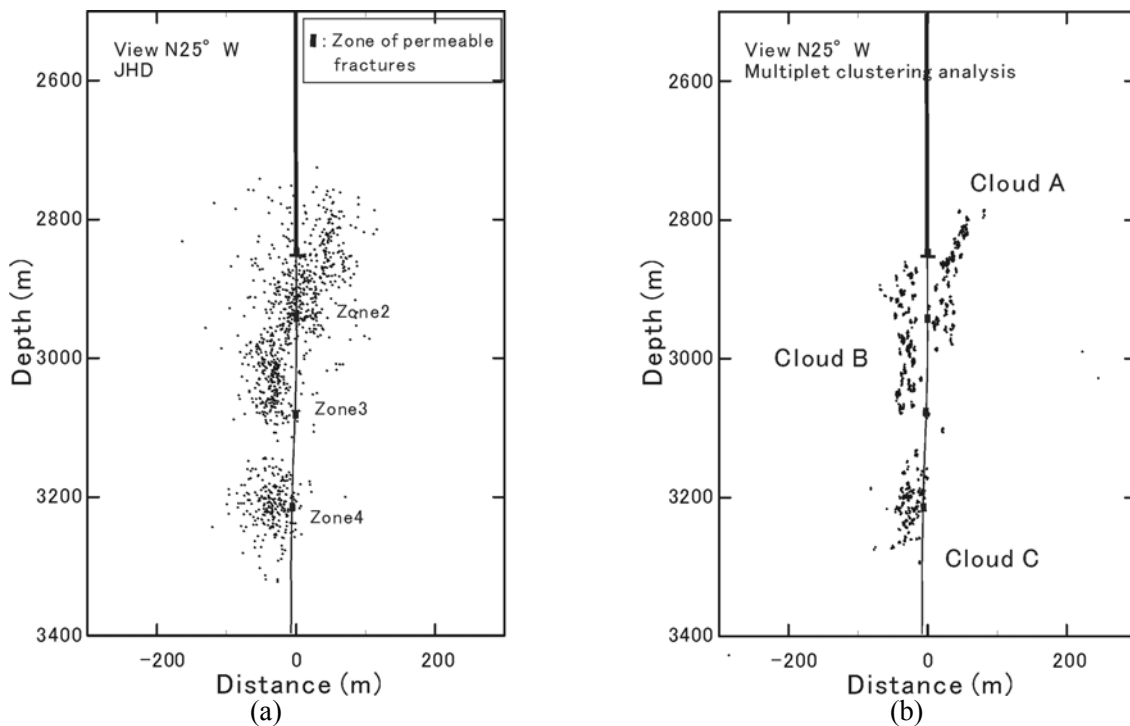


Fig. 2 Source locations of multiplets determined by (a) JHD and (b) multiplet-clustering analysis. Closed boxes along well describe the permeable fracture zones detected by well loggings. Thick line denotes fracturing well GPK1. The casing shoe is at the depth of 2,850 m.

can be determined with high resolution and accuracy by using the moving-window cross-spectrum analysis technique. Deduced seismic clusters, called multiplet clusters, are indicative of seismically activated structures, and the orientations of these structures can be estimated using the seismic clusters even though the absolute locations of the multiplet clusters cannot

themselves be determined. We have determined the relative locations of multiplet clusters as well as the relative locations of similar events by using the multiplet-clustering analysis. Figure 2 shows the source locations of AE events before and after the multiplet-clustering analysis, where about 1000 events identified as multiplets are analyzed.

3. Method for Calculation of Critical Pore-Pressure for Shear Slip

In principle, the pore-pressure for shear slip of a plane can be calculated if the orientation of the plane and the stress field are known. In our case, the estimates of fracture orientations are obtained from AE multiplets detected during fluid injection into subsurface reservoir. Then, we calculate the critical pore-pressure of fractures by using the orientations of fractures and the regional stress field in the corresponding field. The procedures for the calculation of the critical pore-pressure are described as follows.

In the Soultz field, the stress directions and magnitudes had been measured by hydraulic fracturing method in borehole [8]. According to Coulomb's law of friction, the relationship among shear stress, τ , normal stress, σ_N , the coefficient of friction, f_S , and pore-pressure, P_P , within a fracture surfaces at the moment of shear slip (critical condition) due to an increase in pore-pressure are described as follow,

$$\tau - f_S(\sigma_N - P_P) = 0. \quad (1)$$

The cohesion is ignored in the above formulation. The critical pore-pressure for shear slip P_C can be found as follow,

$$\begin{aligned} P_C &= P_P - P_h \\ &= \sigma_N - \frac{\tau}{\mu_S} - P_h. \end{aligned} \quad (2)$$

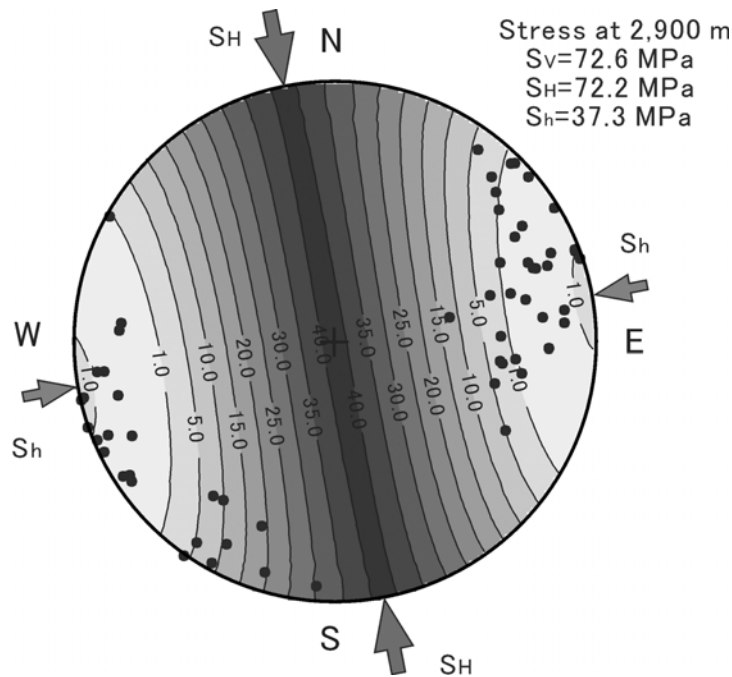


Fig. 3 Stereographic projection (Schmidt net, lower hemisphere) of fracture planes estimated using multiplet and the calculated critical pore-pressure.

P_C means the increase of fluid pressure to induced shear slip. When the orientation of a plane is given, the normal and shear stresses acting on the plane can be calculated. In our case, we have estimates of fracture orientations and their depths from the source distribution of individual multiplets, and the depth of fracture plane can be estimated from the center of gravity of source locations of each multiplet. Figure 3 shows the stereographic projection of calculated P_C and the poles of fracture planes derived from the multiplets, where the coefficient of friction is 0.8. We can see that the fracture planes are favorably oriented to principal stresses as the shear slip can be easily caused. Figure 4 shows the calculated critical pore-pressure for each fracture plane and the relationship to the depth, where the size of circle represents the value of critical pore-pressure. Zones in Fig. 4 describe the depth intervals of permeable fracture zones in fracturing well GPK1, where the permeable fractures are confirmed using FMI and temperature loggings [9].

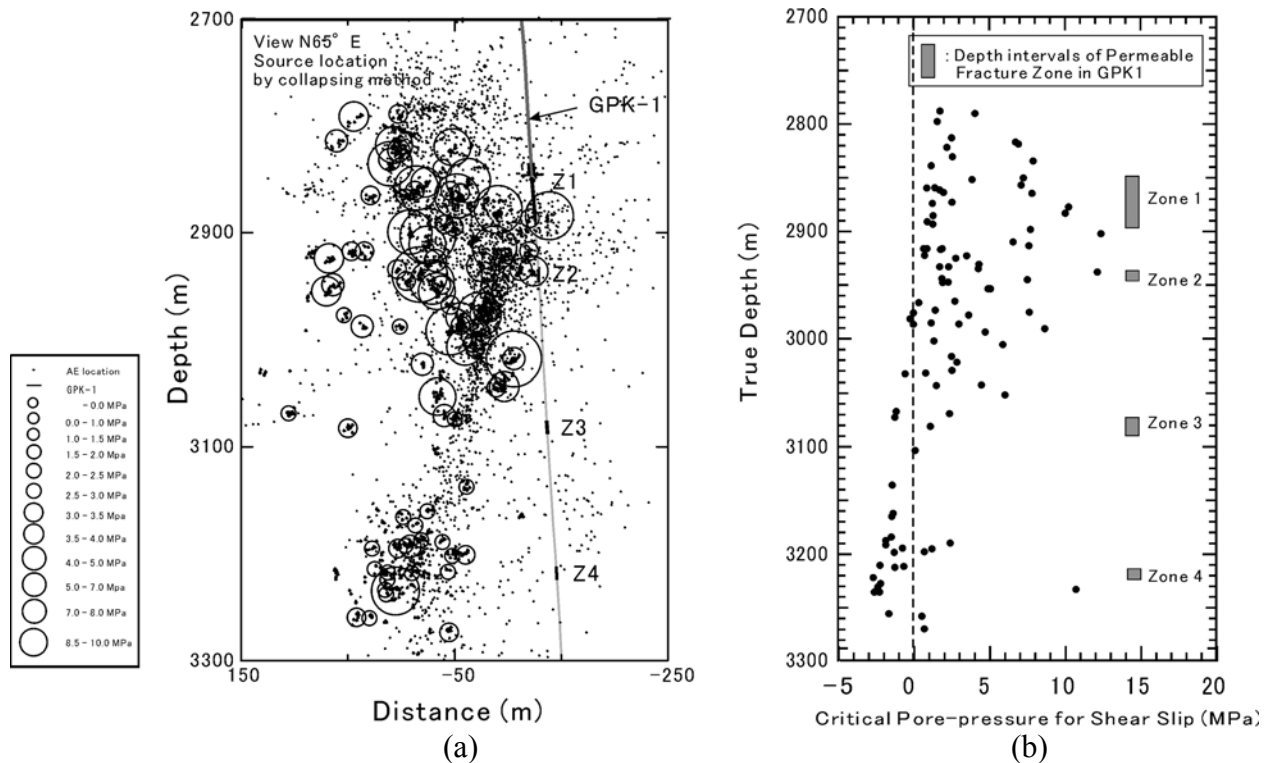


Fig. 4 The calculated critical pore-pressure for each fracture plane and the relationship to the depth, where the size of circle represents the value of critical pore-pressure.

The estimated critical pore-pressure for shear slip suggests that the fluid pressure in fractures is higher near the fractured zones 1 and 2 around 2,900 m, and declines as the fractures are away from the zones. The result in Fig. 4 implies that the fluid pressure was transmitted into fractures, and that the pore-pressure around zones 1 and 2 increased up to near maximum fluid pressure in fracturing well. It is reported that the fractures in zone 1 and 2 are permeable under low flow rate [9]. Then, the fluid pressure easily penetrated to the fractures near the zone 1 and 2, and the fractures with variable orientations caused shear slips. This explanation would support the pore-pressure distribution in Fig. 4. On the other hand, the P_C becomes below zero around 3,200 m. The same result can be also obtained when the critical pore-pressure is calculated using the orientation of fractures detected by well logging. Then, the reason for lower value of P_C would be that the stress magnitudes are estimated lower than the actual values.

4. Conclusion

We have introduced AE multiplet to estimate the critical pore-pressure for shear slip of fractures during hydraulic stimulation of geothermal reservoir. Because the precise source locations of multiplets can be determined using the similarity of the waveforms, the orientation of subsurface fracture planes can be also estimated from the source distribution. The stress field measured by the hydraulic fracturing method in borehole has been introduced to calculate the stress condition on the estimated fracture planes. The critical pore-pressures for shear slip of fractures have been calculated by using the orientation of fractures and the stress field. The distribution of estimated pore-pressure has suggested that fluid pressure in fractures is larger around hydraulically alternated fracture zones, and declines as the fractures are distant from the permeable zones. The estimation method based on induced micro-seismic multiplets is effective in evaluating the fluid pressure of subsurface fractures away from wells.

References

- 1) H. Niitsuma, M. Fehler, R. Jones, S. Wilson, J. Albright, A. Green, R. Baria, K. Hayashi, H. Kaieda, K. Tezuka, A. Jupe, T. Wallroth, F. Cornet, H. Asanuma, H. Moriya, K. Nagano, W. Phillips, J. Rutledge, L. House, A. Beauce, D. Alde, and R. Aster, Current status of seismic and borehole measurements for HDR/HWR development, *Geothermics*, **28** (1999), 475-490.
- 2) W. S. Phillips, Precise microearthquake locations and fluid flow in the geothermal reservoir at Soultz-sous-Forêts, France. *Bull. Seism. Soc. Am.*, **90** (2000), 212-228.
- 3) R. H. Jones and R. Stewart, A method for determining significant structures in a cloud of earthquakes, *J. Geophys. Res.*, **102** (1997), 8245-8254.
- 4) H. Moriya, K. Nagano, and H. Niitsuma, Precise source location of AE doublets by spectral matrix analysis of triaxial hodogram, *Geophysics*, **59** (1994), 36-45.
- 5) H. Moriya, H. Niitsuma and R. Baria, Multiplet-clustering Analysis Reveals Structural Details within Seismic Cloud at the Soultz Geothermal Field, France. *Bull. Seismol. Soc. Am.*, **93** (2003), 1606-1620.
- 6) R. Baria, J. Baumgärtner and A. Gérard, European HDR research programme at Soultz-sous-Forêts (France) 1987-1996. *Geothermics*, **28** (1999), 655-669.
- 7) A. Getter and C. Dezayes, Fracture evaluation in GPK1 borehole by using FMI data, Field Report, BRGM Orléans (1993).
- 8) G. Klee and F. Rummel, Hydraulic fracturing stress measurements in the geothermal borehole GPK1, Soultz-sous-Forêts. Report no. 04-93, MeSy, Bochum (1993).
- 9) K. F. Evans, The effect of the 1993 stimulations of well GPK1 at Soultz on the surrounding rock mass: Evidence for the existence of a connected network of permeable fractures. *Proc. World Geothermal Congress 2000*, **6** (2000), pp. 3695-3670.

A MODELING METHOD ON FRACTAL DISTRIBUTION OF CRACKS IN ROCKS USING AE MONITORING

YOSHINORI WATANABE¹, KEN-ICHI ITAKURA¹, KAZUHIKO SATO¹,
YOSHIAKI FUJII², RAO BALUSU³, HUA GUO³ and XUN LUO³

¹Department of Computer Science and Systems Engineering, Muroran Institute of Technology, 27-1 Mizumoto, Muroran, Hokkaido, 050-8585, Japan;

²Division of Structural and Geotechnical Engineering, Hokkaido University Sapporo, Hokkaido, 060-8628, Japan; ³Exploration and Mining, CSIRO, Brisbane Technology Court, Pullenvale, QLD 4069, Australia.

Abstract

For underground mining and construction, it is important to obtain a discontinuities' model of rocks for simulations to evaluate rock stability around the working space and fluid flow in these rocks. We have developed a method using the fractal property of acoustic emission (AE) source distribution to construct a feasible crack distribution model. We confirmed the usefulness of the model through laboratory experiments for granite specimens. The experiments demonstrated that the AE source distribution was fractal and that the relationship between amplitude and frequency of AE was fractal. Crack distributions in the specimen and on the surface were both fractal. Based on the results, 3-D crack distribution models were constructed using AE monitoring data obtained. This model describes the crack as a disk. The disk orientation was determined by a moment tensor analysis of AE waveforms. In this study, we applied the modeling method to uniaxial and triaxial compression tests on specimens of coal measures rocks (sandstone, siltstone and coal). Results showed that micro-cracking activity, which occurred prior to failure, differed depending on the rock type. We obtained characteristic models for each rock type. This technique was also applied to a micro-seismic data set obtained during mining at an underground Australian coal mine. The crack distribution model of roof rock on a longwall mining panel showed that most cracks were located in roof rock in front of the working face.

Keywords: Crack, Crack distribution model, Moment tensor, Fractal, Micro-seismicity, Coal mine

1. Introduction

Existing crack distribution models for rock mass have been developed based on crack systems' stochastic and fractal characteristics [1–5]. These crack distribution models are useful for simulation of structural stability and fluid flow, etc. To establish a much more feasible model that represents the actual rock crack system, we developed a method using source location and moment tensor analysis for acoustic emission (AE) data [6,7]. This method describes the crack as a disk without thickness. The fractal dimension of sectional lines that appeared on the specimen surface was adjusted to coincide with the dimension of lineaments that were extracted from an actual crack image of the same surface of the specimen by correcting the AE parameters. That is, the relative AE energies for respective events were altered iteratively until both fractal dimensions were matched. Through

application of this technique to laboratory experiments (uniaxial compression tests) for granite specimens, we confirmed that the AE source distribution was fractal and that the relationship between amplitude and frequency of AE was also fractal. Crack distributions in the specimen and on the surface were both fractal. Consequently, it became possible to construct a reasonable 3-D crack distribution model according to fractal properties of AE source and amplitude-frequency distributions [6, 7].

As a next step, this modeling method was applied for the evaluation of an underground rock mass during stress change by coal excavation in an Australian coal mine. The rock mass comprised siltstone, sandstone and coal. A series of laboratory experiments was carried out for these coal measures rock samples before constructing a large-scale 3-D crack distribution model of an underground coal mine.

2. Experimental Procedures

2.1 Rock Specimens and Experimental Conditions

For 17 pieces of coal measures rock specimens (11 sandstone, 2 silt stone and 4 coal specimens), uniaxial and triaxial compression tests were conducted while changing the confining pressure and the strain rate. These core sample rocks were extracted from approximately 301 m to 334 m below the surface of an underground coal mine of Australia. Specimens were cut from the core samples and ground into a cylinder of 30-mm diameter and 60-mm height. The confining pressure of triaxial compression test were set at 1, 4, 9 and 14 MPa for sandstone, 1 and 9 MPa for siltstone, 1, 4 and 9 MPa for coal specimens in addition to the uniaxial compression tests. For the sandstone specimens, the strain rate was set at $2.5 \times 10^{-6}/s$, $5 \times 10^{-6}/s$ and $25 \times 10^{-6}/s$. For other specimens, the strain rate was fixed at $5 \times 10^{-6}/s$. However, the influence of the strain rate was not evident through the tests.

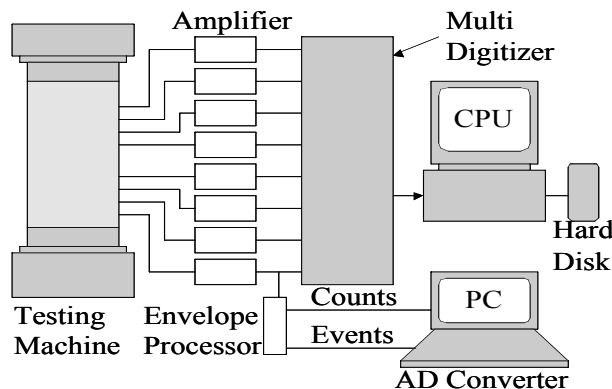


Fig. 1 AE monitoring system.

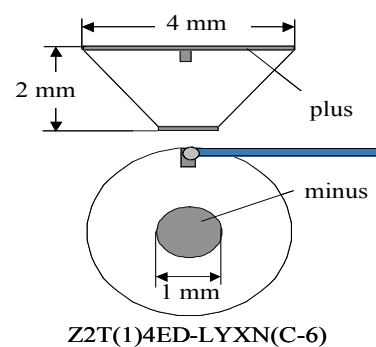


Fig. 2 PZT element as an AE sensor.

2.2 Apparatus

Figure 1 shows an AE monitoring system for laboratory experiments. As an AE sensor, 10 pieces of PZT elements (shown in Fig. 2) were attached to the surface of the specimen. After attaching sensors to the surface of the specimen, the specimen was covered by end-pieces and oil shield plastics, and set into a pressure vessel. Setting the confining pressure

as constant, Eight sensors were selected from the 10 elements while checking individual sensitivity. AE waveforms from the 8 sensors were digitized with a sampling time of 100 ns using a Multi-Digitizer (APC-5108; Autonics Corp.), and recorded on a hard disk of PC. All signals were amplified 35 dB using preamplifiers (AE2A; Physical Acoustics Corp.). The frequency band of the system was restricted using a 100–400 kHz bandpass filter of the pre-amplifier. The numbers of AE events and AE counts that were detected by the one of the sensors were also digitized and recorded on a hard disk of another PC. These events and counts were regarded to represent the total amount of AE activity during the experiment.

3. Modeling Procedure

3.1 Disk Crack Model

This crack distribution model was constructed under the assumption that micro-cracking in rock coincides with an occurrence of AE event in most brittle rocks under stress. According to that assumption, the micro-crack inside the rock with AE generation was described as a disk in this crack distribution model. To arrange the disk-type crack into a 3-D rock space, the following must be known:

- 1) crack location (coordinate of the disk center),
- 2) crack size (disk diameter),
- 3) crack orientation (normal vector of the disk), and
- 4) crack type (tensile strength, shear and other characteristics).

The crack location, i.e. the coordinate of the center of disk, was determined by AE source location. In this model, the crack size is represented by the relative energy of an AE event. The relative energy was calculated from the amplitude of the AE waveform considering the correction of propagation loss and directional sensitivity of the AE sensor. The crack orientation was determined from the result of moment tensor analysis of AE waveforms [8]. However, in the case of a shear crack, it is difficult to choose a shear plane from conjugate directions. Therefore, in this modeling method, the orientation of the shear crack plane was determined randomly. The crack type was determined by the tensile crack ratio obtained from the principal value of the moment tensor and Poisson's ratio. AE events that were classified as tensile cracks were those with a ratio of more than 60%. A ratio or less than 40% was regarded as a shear crack; others were inferred to be a combination type.

3.2 Compensation by Fractal Property of AE Amplitude-Frequency Distribution

If the amplitude-frequency distribution of AE are regarded as fractal, the number of AE events with smaller size amplitude could occur during loading of laboratory experiments. Figure 3 shows a typical amplitude-frequency distribution of AE. Assuming a fractal property based on the linearity of a higher amplitude region, many AE events are expected to have occurred according to the difference between the observed number and the estimated line. These events with small amplitude seemed not to be detected by the AE monitoring system used for the experiments. In this modeling method, small AE events were added into the model that was constructed using AE data analysis. The crack number and size were estimated from the amplitude-frequency distribution. Locations, orientations and types of compensation cracks were arranged randomly in the rock space with regard to the statistics of crack distributions obtained by AE data analysis.

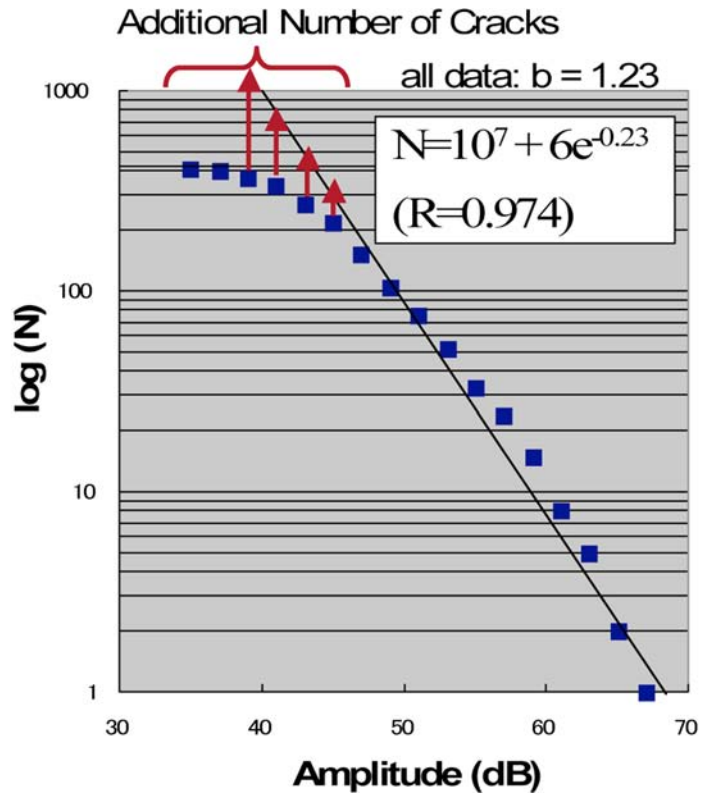


Fig. 3 Amplitude-frequency distribution.

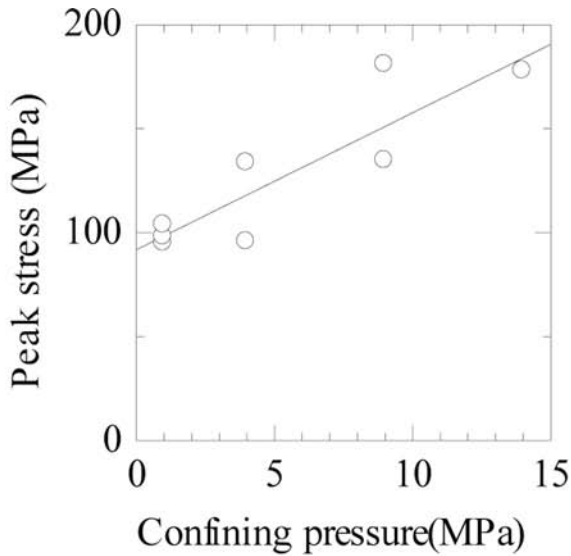


Fig. 4 Confining pressure effect for peak stress.

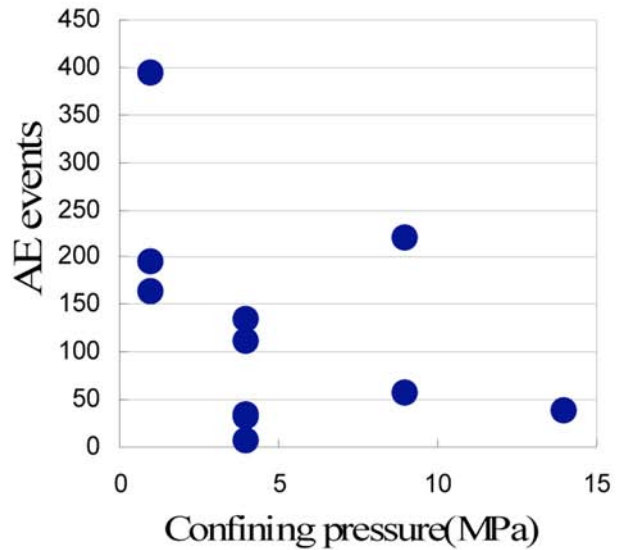


Fig. 5 Confining pressure effect for number of AE events.

4. Experimental Results

4.1 Effect of Confining Pressure

Figure 4 shows the relationship between confining pressure and peak stress of triaxial compression tests for sandstone. This figure shows the confining pressure effect: the peak stress increases with increasing confining pressure. Figure 5 shows the relationship between confining pressure and the number of AE events that were detected during load increase.

The number of AE events tends to decrease with increased confining pressure. The relative energy of AE events also decreased concomitant with the increasing confining pressure. Siltstone and coal also showed these tendencies.

4.2 AE Source Locations

Figures 6, 7 and 8 show typical results of AE source location for siltstone, sandstone and coal. The confining pressure was 1 MPa for these specimens. These results were displayed three-dimensionally from different perspectives by means of virtual reality modeling language (VRML). Pictures in the figures show specimens after loading tests. In Figs. 6 and 7, most AE sources were located along the fracture planes. However, in the case of coal specimen shown in Fig. 8, almost all AE events were characterized as concentrated into the center region of the specimen. Identical results were obtained from two other coal specimens in the low confining pressure of 1 MPa. Observation of the specimen showed that these concentrations of AE events reflected the coal specimens' crush zone.

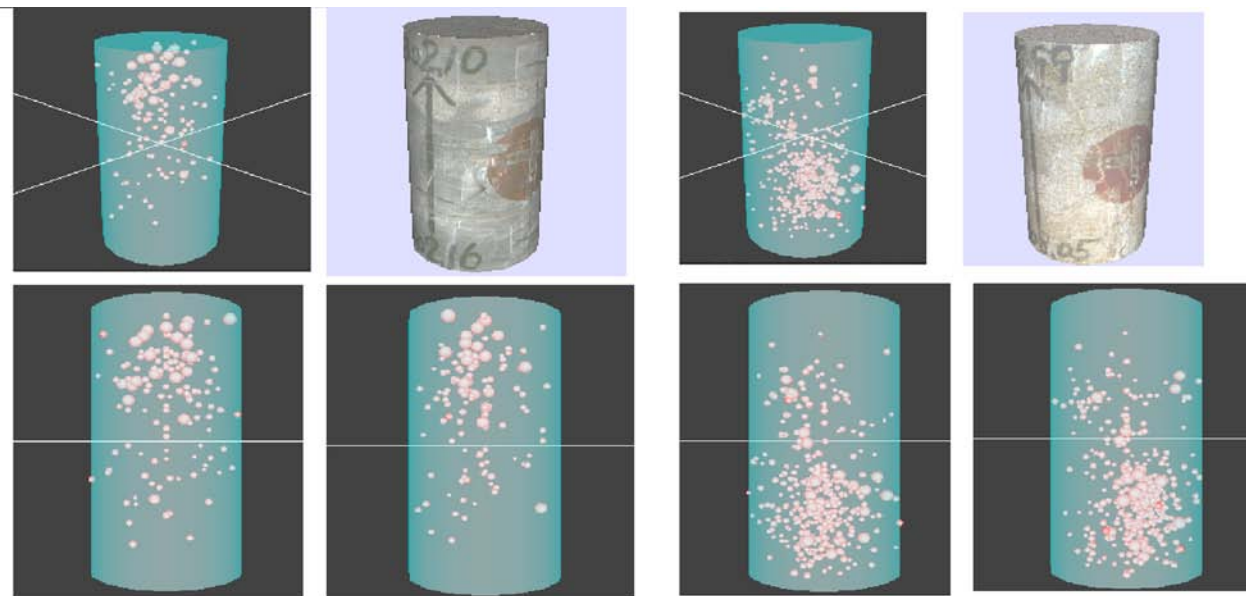


Fig. 6 AE source locations (siltstone).

Fig. 7 AE source locations (sandstone).

4.3 Crack Distribution Models of Specimens

Figure 9 shows typical results of crack distribution models for siltstone, sandstone and coal specimens. In addition to the cracks determined by AE data analysis, small cracks were included. The darkest disk indicates the shear crack. The brighter color disk shows the tensile crack; the brightest disk is for the combination type crack. Regarding siltstone and sandstone specimens, orientations of the tensile crack planes were almost parallel to the loading axis; the shear crack planes were perpendicular (vertical) to it. The percentages of tensile cracks and shear cracks for sandstone specimens were about 30–40% and 40–50% respectively. A tendency for shear cracks to be slightly dominant for the sandstone specimens was shown by the coal specimens as well. However, no relationships were found between the percentage of tensile and shear cracks and the confining pressure.

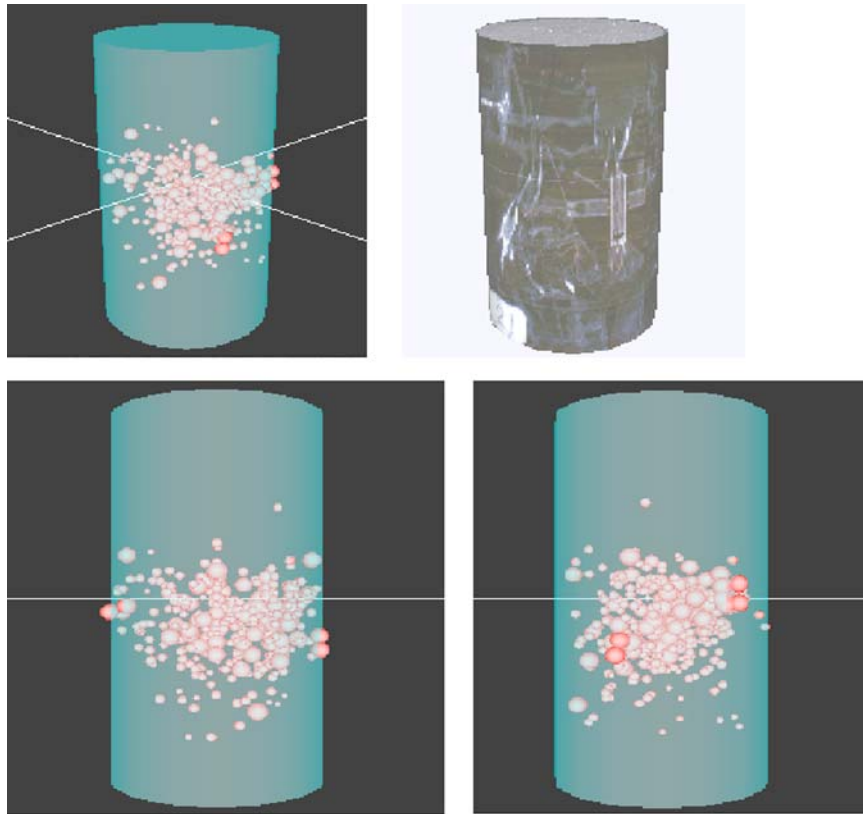


Fig. 8 AE source locations (coal).

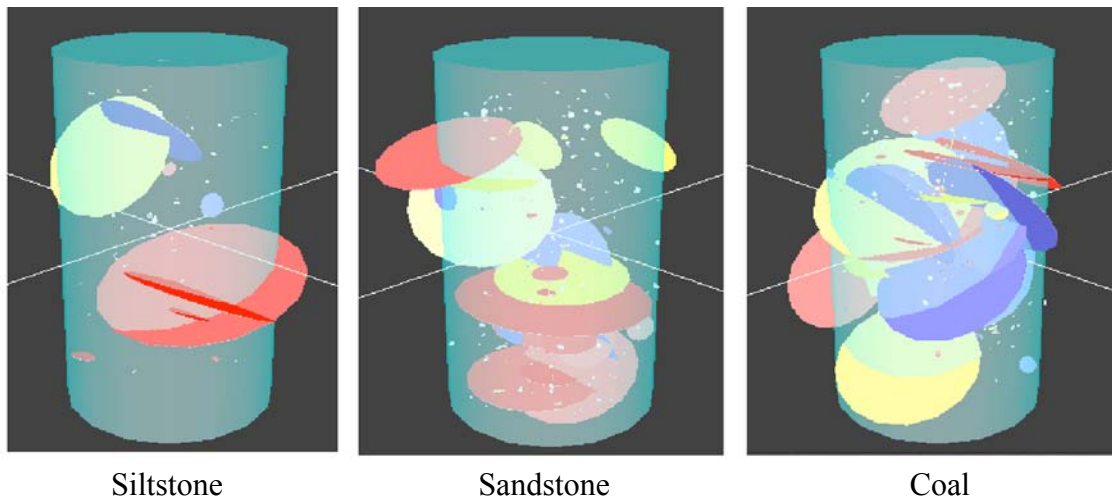


Fig. 9 Crack distribution models.

5. Crack Distribution Model During Mining of Underground Coal Mine

5.1 Micro-seismic Monitoring of Coal Mine

Micro-seismic monitoring was conducted in an underground coal mine of Australia using 20 triaxial velocity meters (geophone). Figure 10 shows the plan view of underground mining panel in the depth of about 285–335 m from the surface. Micro-seismicity was recorded during mining of longwall No. 4, which is 400 m wide and 600 m long. Geophones (GS-20DX; Oyo Geospace Corp.) were installed from the surface inside the four drill holes.

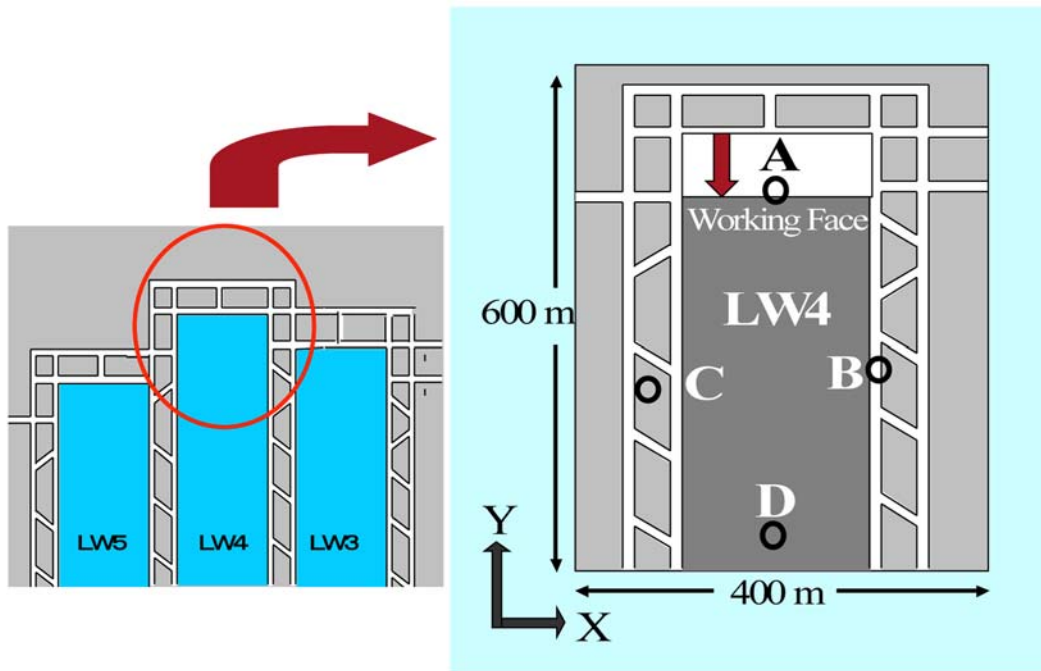


Fig. 10 Plan view of longwall mining panel.

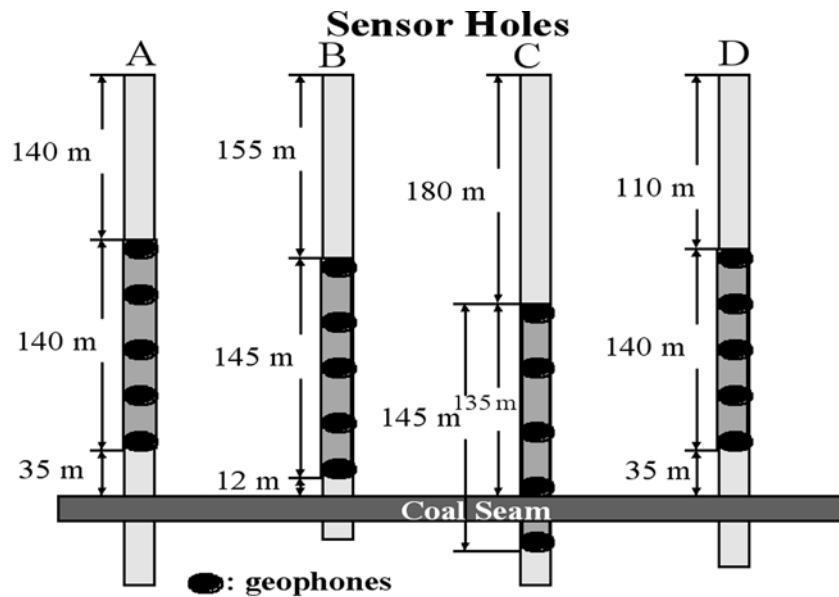


Fig. 11 Vertical projection of geophone locations.

Figure 11 shows the vertical projection of the drill holes and the locations of triaxial geophones. During mining of longwall No. 4, 170,000 micro-seismic events were triggered.

5.2 Crack Distribution Model of Coal Mine

This report relates the results of three periods: the first period of 5–8, October 1999; the second period of 18–20, October 1999; and the third period of 26–28, October 1999. Figures 12, 13 and 14 show results of final crack distribution model that were constructed using micro-seismic data analysis. Figure 12 shows the crack distribution model during mining of the first period. It was found that most cracks were generated in the sandstone roof rock; the crack locations were in front of the longwall working face. Figures 13 and 14

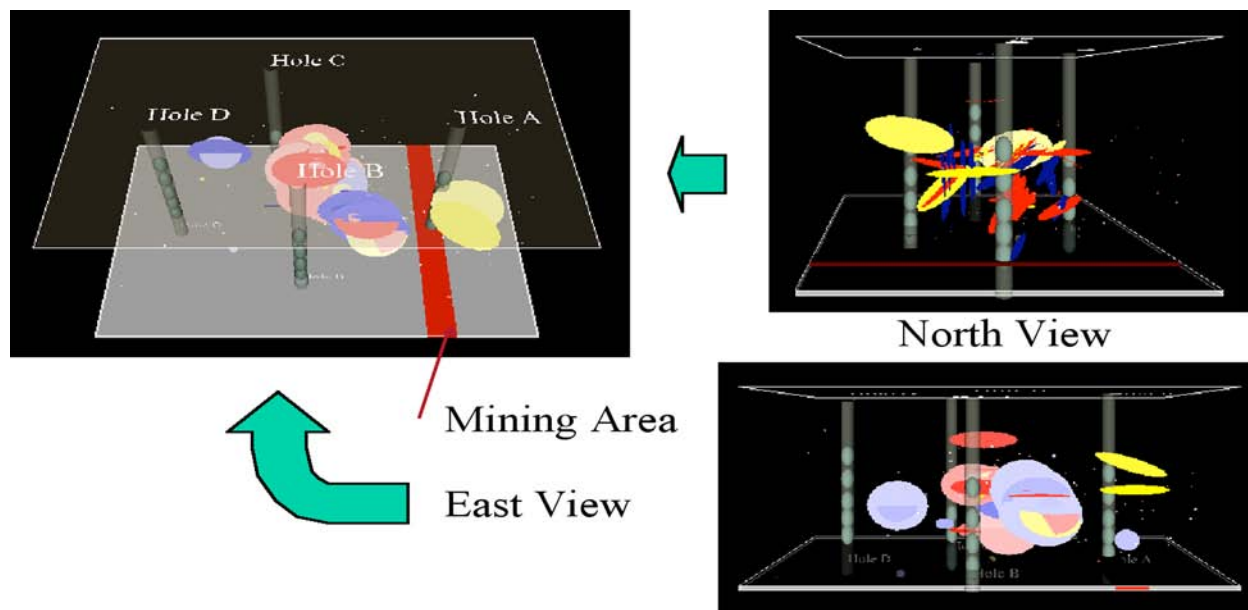


Fig. 12 Crack distribution model of first mining period.

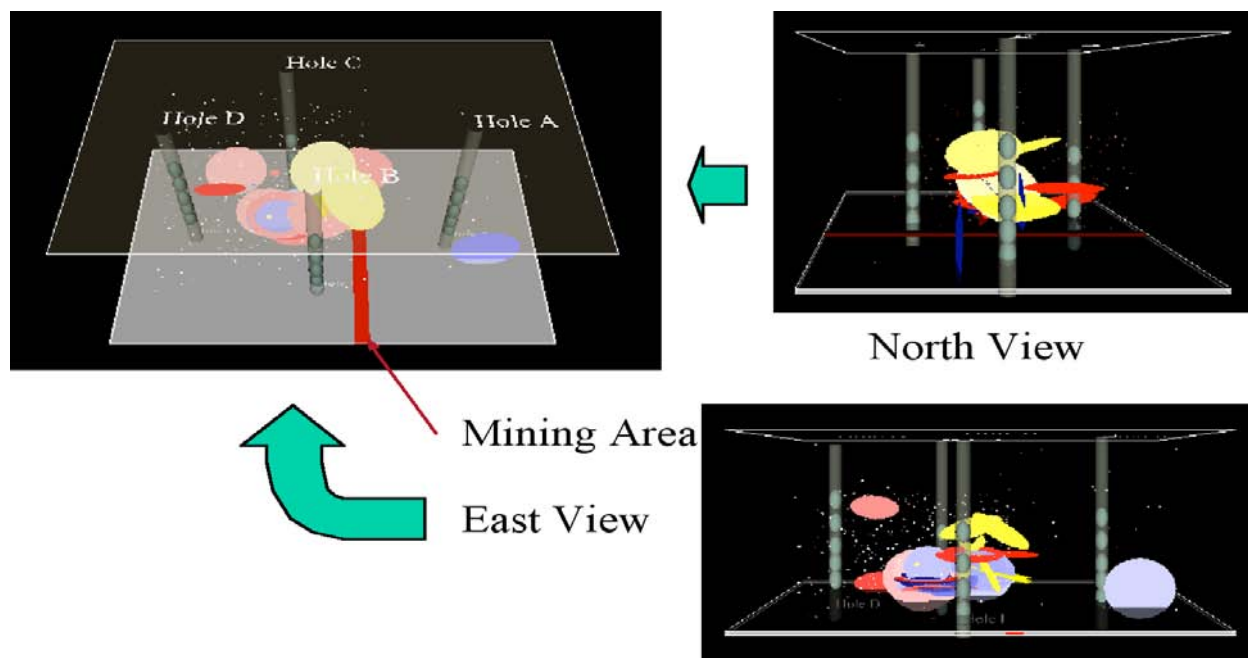


Fig. 13 Crack distribution model of the second mining period.

illustrate that the locations of cracks became closer to the mining area with advance of working face. In the third period, many shear type cracks were concentrated around drill hole C. Subsequently, the geophones of this drill hole were broken. Through the mining periods, it was clear that the shear-type cracks were dominant in the roof rock. This result accorded with results of laboratory experiments using sandstone specimens.

6. Conclusions

This paper introduced a method to construct 3-D crack distribution model using AE monitoring data. We described its application to coal measures rock specimens and to an underground coal mine.

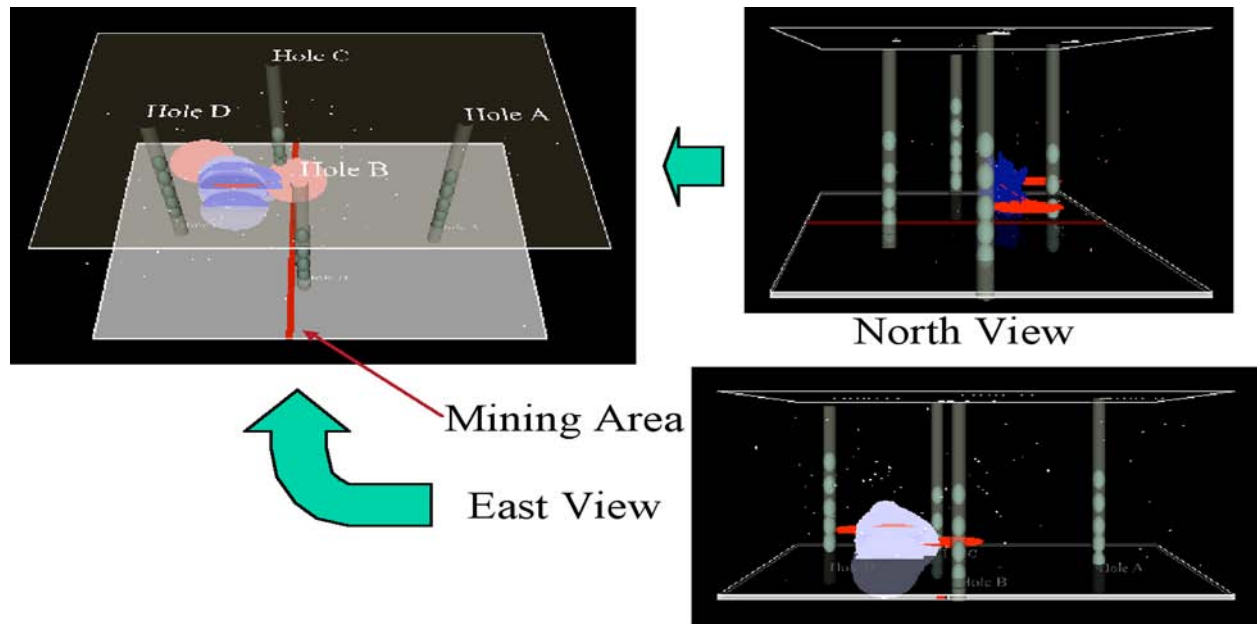


Fig. 14 Crack distribution model of the third mining period.

Uniaxial and triaxial compression tests were carried out for 17 pieces of siltstone, sandstone, and coal rock samples. The number of AE events decreased with the increase of confining pressure. Crack distribution models showed that shear type cracks were dominant for coal and sandstone specimens.

For 170,000 AE waveforms recorded in the mine, AE source location and moment tensor were analyzed to construct a crack distribution model of the longwall panel. The AE activity and 3-D crack distribution model showed that the most cracks were generated in the roof rock of the longwall panel; furthermore, they were located in front of the working face. The dominant crack type developed inside the roof rock was shear type, as in the sandstone specimen, under the triaxial stress state.

The effectiveness of this modeling method, which considers the fractal properties of AE, was demonstrated through a series of laboratory experiments and subsequent application to micro-seismic data of field monitoring. As the next step, we plan to conduct a simulation that uses this crack distribution model to evaluate gas flow in an underground coal mine.

References

- 1) Ivanova, V. et al.: Development of stochastic models for fracture systems, *Rock Mechanics*, Daemen & Schults (eds.), Balkema, Rotterdam (1995), pp. 725–730.
- 2) Chiles, J.P.: Fractal and Geostatistical Methods for Modeling of a Fracture Network, *Mathematical Geology*, **20**, 6 (1988), 631–654
- 3) Kaneko, K. et al.: Evaluation of Rock Discontinuities – In-situ Measurement and Modeling –, *Proc. Workshop on Characterization of Subsurface Cracks* (1990), pp. 25–29. (in Japanese)

- 4) Watanabe, M., Y. Nakayama and H. Takahashi: Fractal Characterization of Subsurface Fracture Network, *Proc. 2nd Workshop on Characterization of Subsurface Cracks* (1992), pp. 80–85. (in Japanese)
- 5) Yamamoto, H. and K. Kojima: Modeling of Rock Fracture Systems Using the Concept of Fractal, *Proc. 2nd Workshop on Characterization of Subsurface Cracks* (1992), pp. 75–79. (in Japanese)
- 6) Itakura, K. et al.: Modeling Method for Cracks in Rocks based on the Fractal Structure of the AE Source Distribution, *J. of MMIJ*, **114**, 12 (1998), 918–924. (in Japanese)
- 7) Watanabe, Y., K. Itakura and K. Sato: 3-D Crack Distribution Model Based on Crack Image Analysis and Fractal of AE Sources from Stressed Rock Specimen, *Proc. 6th Domestic Conf. on Subsurface and Civil Engineering AE* (1999), pp.100–105. (in Japanese)
- 8) Sato, K. and Fujii, Y.: Source Mechanism of a Large Scale Gas Outburst at the Sunagawa Coal Mine in Japan, *PAGEOPH*, **129** (1989), 325–343.

INTERPRETATION OF RESERVOIR CREATION PROCESS AT COOPER BASIN, AUSTRALIA BY ACOUSTIC EMISSION

YUSUKE KUMANO¹, HIROKAZU MORIYA¹, HIROSHI ASANUMA¹, NOBUKAZU
SOMA², HIDESHI KAIEDA³, KAZUHIKO TEZUKA⁴,
DOONE WYBORN⁵ and HIROAKI NIITSUMA¹

¹) Graduate School of Environmental Studies, Tohoku University, Sendai 980-8579, Japan;
²) AIST, Tsukuba 305-8569, Japan; ³) CRIEPI, Abiko 270-1194, Japan; ⁴) JAPEX Research
Center, Chiba 261-0025, Japan; ⁵) Geodynamics Limited, Brisbane, Australia.

Abstract

Hydraulic stimulation of an engineered geothermal reservoir has been carried out at Cooper Basin hot-dry-rock (HDR) field, Australia in 2003. AE monitoring network, which consists of four near surface and one downhole stations, detected approximately 32,000 triggers during the stimulation and approximately 12,000 of them have been located on-site by the single-event determination method (SED). The location of AE showed a sub-horizontal structure that is consistent with the state of tectonic stress and the orientation of existing fractures in the corresponding field. We have estimated the composite focal mechanism, and it showed a reverse fault with a low inclination to West. The plane of the nodal plane agrees well with the structure by the locations of AE. We found that the plane from the focal mechanism is nearly under the critical stress state for shear slip at Cooper Basin. The AE activity was higher than that at Soultz field, where EU and other organizations are carrying out an HDR project, suggesting that the stress state in Cooper Basin site is closer to critical.

Keywords: HDR, Hydraulic fracturing, Tectonic stress, Focal mechanism, Cooper Basin

1. Introduction

The analysis of AE from the hydraulic fracturing/stimulation of hot-dry-rock (HDR) geothermal reservoir is an important method, which enables us to estimate the detailed structure inside the reservoir and the process of reservoir creation. Researchers who worked in worldwide HDR projects in the area of AE/seismic monitoring collaborated to develop advanced AE mapping methods, which has much higher resolution and reliability (super-resolution mapping). The super-resolution mapping techniques have made the integrated interpretation of AE mapping, logging, hydraulic record in fracturing operation and geological information to understand reservoir physics [1]. The post-analysis of AE location and source mechanism analysis using the super-resolution mapping techniques has been done in worldwide HDR projects [2], and mechanism of the reservoir extension has been successfully interpreted in many case.

An HDR project to develop a commercial geothermal power plant is underway at Cooper Basin, Australia, managed by a public company, Geodynamics Limited. In this site, the temperature exceeding 250°C is expected inside the granitic basement at depths below approximately 4,000 m [3]. It has been reported that the maximum tectonic stress is sub-horizontal (East to West) in the central part of Australia (Fig. 1). Because the reservoir extends normal to

the minimum principal stress direction in theory, it was expected that hydraulic fracturing creates the reservoir extending horizontally.

The first hydraulic stimulation to create an HDR reservoir was carried out in November and December 2004 to demonstrate and evaluate the potential of geothermal energy in this site. The Japanese team, consisting of the authors and people from Geodynamics Ltd., deployed an AE monitoring network, and monitored AE during the stimulation. We detected 32,000 triggers during injection of 20,000 m³ of liquid into the granitic basement over 3 weeks, and 11,724 AE events were located on-site [4].

In this paper, we report the analysis of the induced AE events, where we located the AE sources by the super-resolution mapping techniques as a post-analysis and investigated relationship among tectonic stress, focal mechanism, and AE source location. We also discuss the reservoir structures based on the analysis of AE events.

2. AE Monitoring during Hydraulic Fracturing

Figure 1 shows the tectonic stress state and the reservoir pressure as a function of depth, and the maximum stress direction. The hydraulic fracturing was carried at the site, where the horizontal compressional stress is dominant. Therefore, it was expected that the nearly horizontal reservoir was created, because the minimum principal stress direction is vertical. Figure 2 show the history of pump operation during the fracturing.

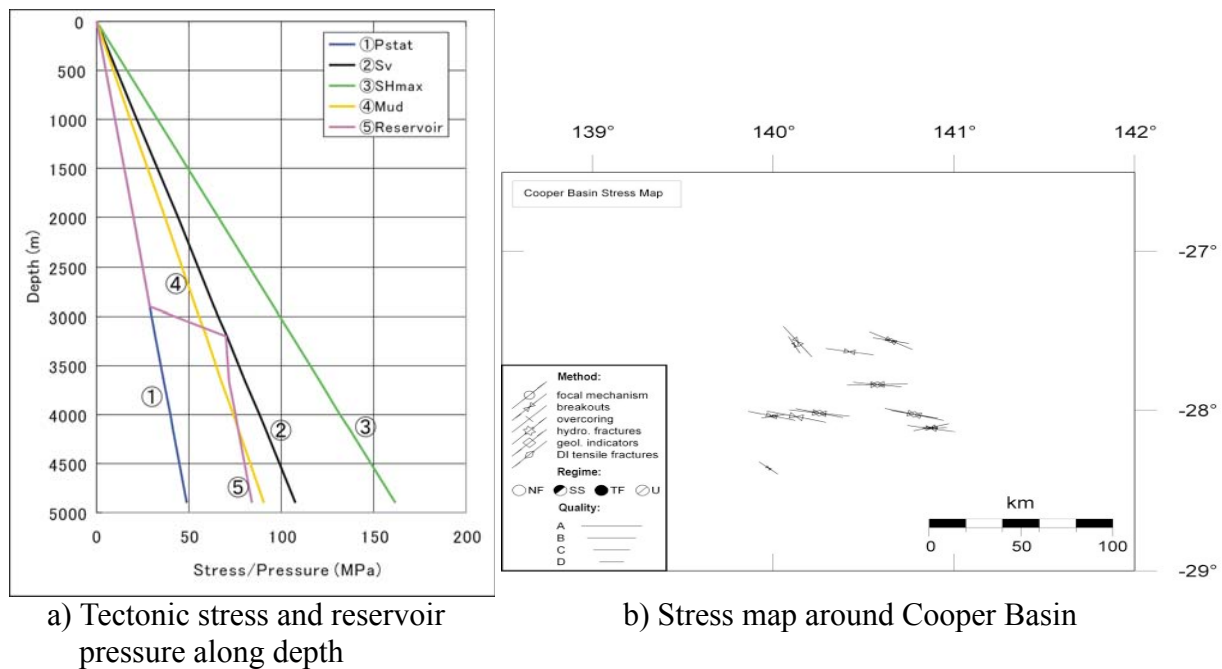


Fig. 1: Tectonic stress at Cooper Basin [3].

Figure 3 shows a plan view around the injection well “Habanero1” and AE monitoring stations deployed at Cooper Basin site. The injection well was drilled to a depth of 4,421 m (754 m into granite). Several sub-horizontal over-pressured fractures were found in the granitic section in the well, and most of the existing fractures were plugged to stop lost circulation and inject the water into a targeted fracture at a depth of 4,254 m. This single fracture remained as an initial dominant feed point into the formation. The monitoring network consists of one deep

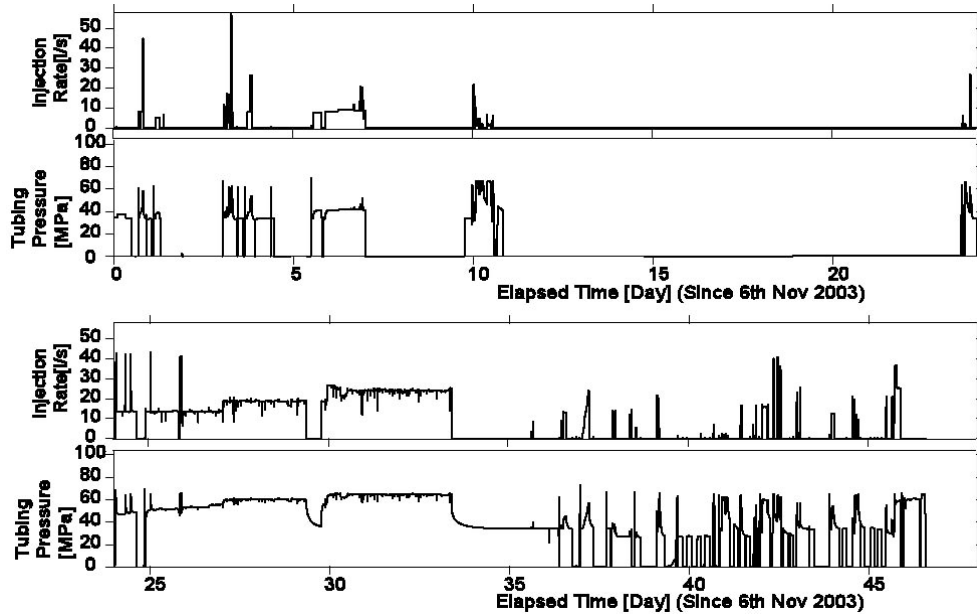


Fig. 2: Pumping data during the first hydraulic fracturing.

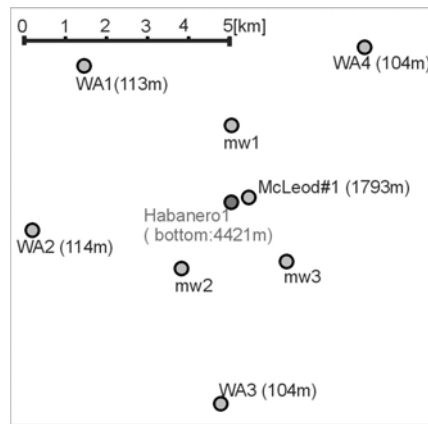


Fig. 3: Plan view of AE monitoring network.

downhole and four near surface stations. All the monitoring stations are deployed in sedimentary rock over granitic basement.

3. AE Source Location

Three-dimensional distribution of AE sources estimated by the single-event determination (SED) [5, 6] is shown in Fig. 4. We can see that the hydraulic stimulation brought a sub-horizontal AE cloud that has lower inclination to West. The AE cloud has a thickness of approximately 300 m and horizontal extension of approximately 3 km North to South. Figure 5(a) shows the three-dimensional distribution of AE sources located by the collapsing method [7] as well as a vertical cross section near the injection well. The collapsing method is one of the statistical optimization techniques of the AE to estimate structure of AE sources in large scale. The plan view in Fig. 5(a) is similar to that of Fig. 4, although the thickness of the AE cloud after collapsing is thinner than that by SED. The thickness of the AE cloud in Fig. 5(b) is 30 or 50 m, and the all-inclusive structure has low inclination to West. We can also see that the AE cloud is composed of several large sub-parallel structures.

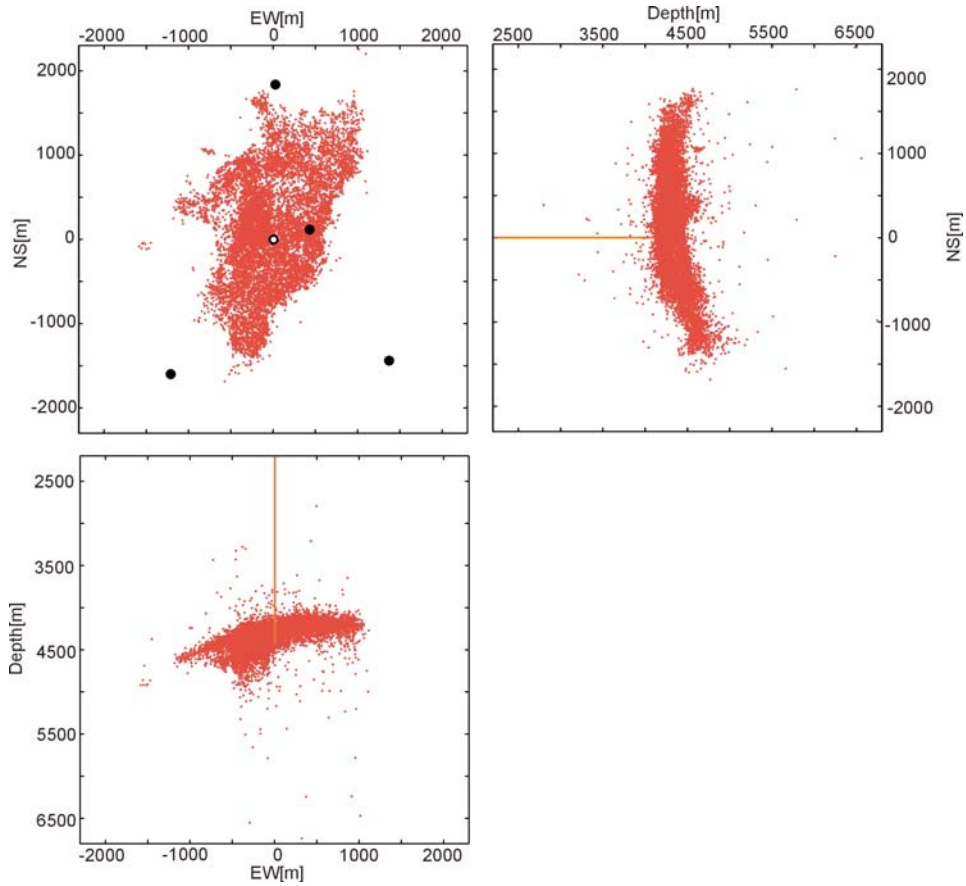
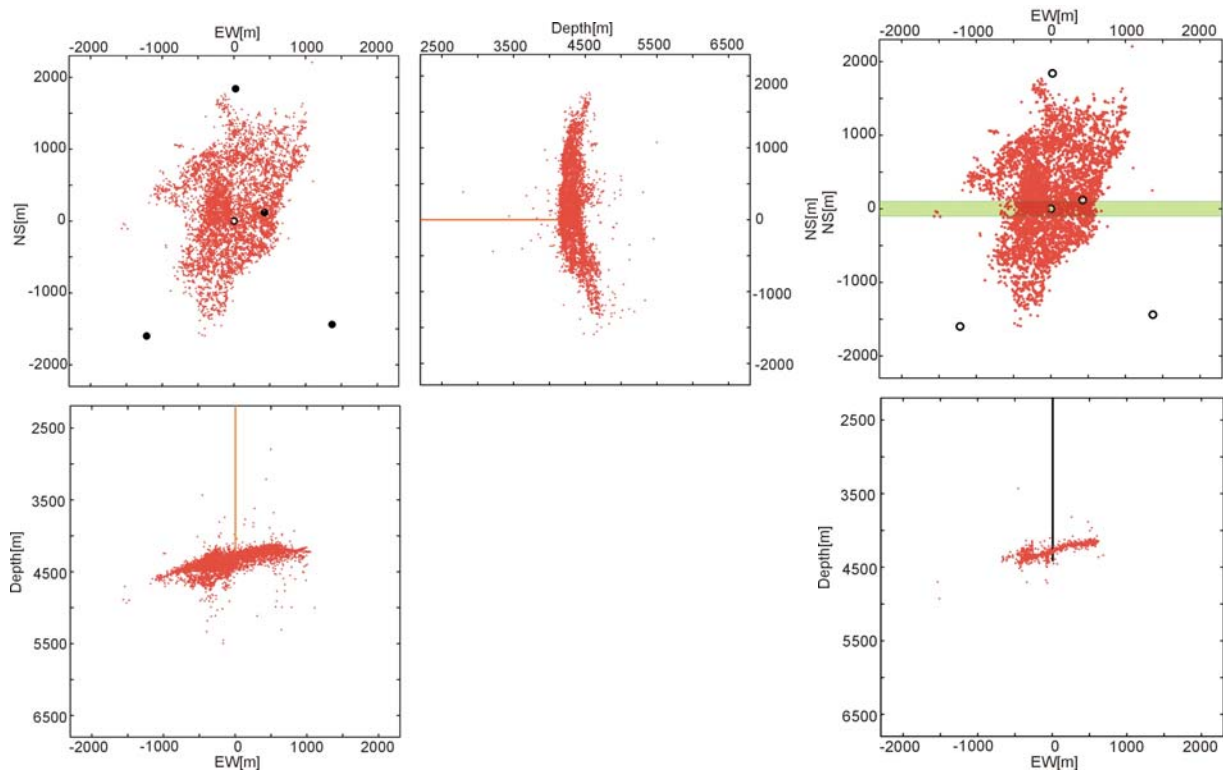


Fig. 4: 3-D AE source distribution by single event determination (SED).



a) 3-D distribution
b) Cross sectional view
Fig. 5: 3-D AE source distribution located by collapsing method.

4. Focal Mechanism

We observed the polarity at the onset of the P-wave of over 1,000 events with a magnitude larger than M0.3. We have found that almost all the events showed similar polarity, implying that the focal mechanism of AE events was similar. Thus, we decided to estimate focal mechanism by the composite focal mechanism method [5]. Figure 6 shows distribution of polarity at the onset of P-wave in the lower hemisphere of the stereographic projection. AE signals detected by stations at WA-1 and 2 showed dilatational motion, and those for WA-3, 4 and McLeod-1 showed compressional motion. Figure 6 shows the estimated fault plane solution. Since the observation network was sparse, the unique solution cannot be determined. Therefore, only one reliable nodal plane is drawn in Fig. 6. Another plane can be expected to have low inclination, dipping to West. Referring the orientation of the entire AE cloud, the plane shown in Fig. 6 is considered an auxiliary fracture plane and the actual plane is considered a thrust fault with a lower inclination to West. The low inclination of the plane consists with all-inclusive structure of the AE cloud.

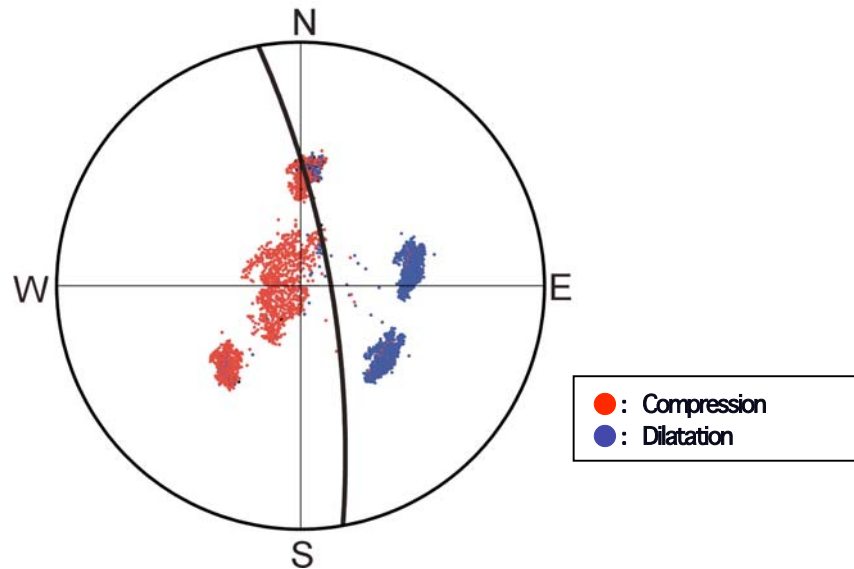


Fig. 6: Distribution of first motion of P-wave on lower hemisphere stereographic projection.

5. Discussion

We have obtained a thin AE cloud with the thickness of 30-50 m by the collapsing method. This result suggests that the AE cloud is a single-planer structure at many portions but in some part the layered AE clouds are separated 200-300 m and they are connected with sub-vertical cloud. According to the source locations by the collapsing method, we can interpret that single fracture and the group of sub-parallel fractures were stimulated, although we cannot yet eliminate the possibility of “over-collapsing” because this method is based on statistical theory and not directly related to the physical phenomena. On the other hand, the global orientation of the AE cloud is consistent with the fault-plane solution estimated by the composite focal mechanism model.

We have drawn a Mohr’s stress circle of tectonic stress at the depth of 4,400 m (Fig. 7), assuming that the maximum horizontal stress is the first principal stress and the minimum is

vertical. This assumption is supported by the result of focal mechanism from AE. We also plotted a direction of a plane from the focal mechanism analysis (Fig. 7). From this figure, we can find from the focal mechanism that the pre-existing subsurface fractures were under nearly critical stress state for shear slip before the hydraulic fracturing.

We compared the characteristics of AE from hydraulic fracturing with the data collected at Soutz HDR field in 2003. The hydraulic fracturing at Cooper Basin induced AE events and events appeared at a distant point from the injection well from the initial stage of the stimulation. These characteristics of AE are consistent with the assumption that AE was induced at fractures, which were favourably oriented to the principal stress and were under critical stress state before the fluid injection.

The structure of AE source by the collapsing method is simple and we can find several large sub-parallel structures. Results of focal mechanism analysis, discussion with Mohr's circle and comparison with Soutz data were consistent with the phenomena that limited fracture was dominantly stimulated. AE multiplet analysis or clustering analysis must be done to confirm it, because it has been proved that these methods are effectively used to estimate phenomenon of AE sources [8].

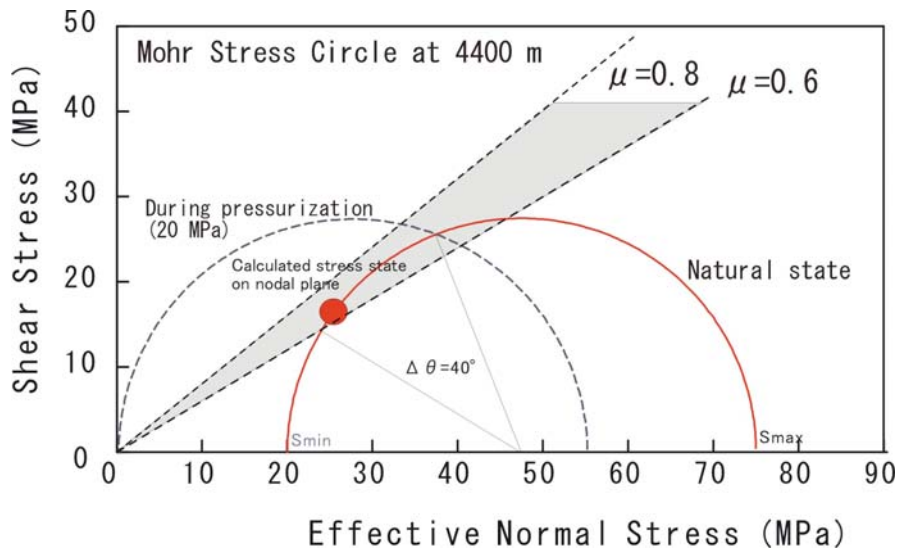


Fig. 7: Mohr Stress Circle at the depth of 4400 m.

6. Conclusions

We analyzed AE during a hydraulic fracturing at Cooper Basin HDR site, Australia. The AE cloud extended sub-horizontally with small inclination to west. The orientation of the AE cloud is consistent with the focal mechanism estimated by composite model as well as tectonic stress at the field. The stress analysis showed that the AE was induced at existing fracture that is under nearly critical stress state. These results can be interpreted by a reservoir creation process where single or limited number of sub-parallel fracture with horizontal extension was mainly stimulated in this field. The authors will try to obtain further interpretation of the reservoir creation process through multiplet analysis.

Acknowledgements

The seismic monitoring/mapping at the Habanero-1 site by the Japanese team would not have been realized without much help from Geodynamics especially from Dr. B. de Graaf. We also highly appreciate all the contributors to the project from Japanese side. We would like to express our thanks to Dr. P. Chopra, ANU/Geodynamics, for his scientific discussion with some comments and recommendations.

References

- 1) M. Fehler, A. Jupe and H. Asanuma, More Than Could: New techniques for characterizing reservoir structure using induced seismicity, *The Leading Edge*, **3** (2001), 324-328.
- 2) K. F. Evans, H. Moriya, H. Niitsuma, R. H. Jones, W. S. Phillips, A. Genter, J. Sausse, R. Baria, Microseismicity and permeability enhancement of hydro-geologic structures during massive fluid injections into granite at 3km depth at the Soultz HDR site, *Geophys. J. Int.* (2004), (submitted).
- 3) Swenson, D, P. N. Chopra and D. Wyborn, Initial calculations of performance an Australian Hot Dry Rock reservoir, *Proc. WGC 2000*, (2000), 3907-3912.
- 4) H. Asanuma, Y. Kumano, T. Izumi, N. Soma, H. Kaieda, K. Tezuka, D. Wyborn and H. Niitsuma, 2004. SEG 2004 Expanded Abstracts (in-press).
- 5) T. Lay and T. C. Wallace, *Modern global seismology*, Academic Press Inc. (1995).
- 6) K. Aki and P. G. Richard, *Quantitative seismology, Theory and methods*, W. H. Freeman, New York (1980).
- 7) R. H. Jones and R. A. Stewart, A method for determining significant structures in a cloud of earthquake, *J. Geophys. Res.*, **102** (1997), 8245-8254.
- 8) H. Moriya and H. Niitsuma, Subsurface stress field determination using multiplets in down-hole three-component microseismic measurement, *Proc. 2nd North American Rock Mechanics Symposium*, **2** (1996), pp. 853-858.

MICROMECHANICS OF CORROSION CRACKING IN CONCRETE BY AE-SIGMA

FARID A. K. M. UDDIN and MASAYASU OHTSU

Graduate School of Science and Technology, Kumamoto University, Kurokami,
Kumamoto 860-8555, Japan.

Abstract

Nucleation of micro-cracking due to corrosion is identified by AE-SiGMA, by which crack kinematics of locations, types and orientations are quantitatively determined. These kinematical outcomes are obtained as three-dimensional (3-D) locations and vectors, and 3-D visualization is developed by using VRML (Virtual Reality Modeling Language). Thus, the cracking modes are investigated for different crack patterns and the cracking mechanisms of 594 events were identified. It is confirmed that the mechanisms of micro-cracking due to corrosion of reinforcement are nearly equally of the mode-I, mixed-mode and mode-II failure. This is because cracks in concrete propagate in zigzag path, dynamic motions on micro-crack planes consist of the crack-opening mode and the shear mode.

Keywords: AE-SiGMA, Corrosion cracking, Moment tensor, Virtual reality modeling language (VRML)

1. Introduction

Corrosion of reinforcing-steel bar (rebar) in concrete is a major cause of the deterioration in reinforced concrete structures. For making decision on maintenance and repair works, the identification of cracking mechanisms due to corrosion is important. Expansion caused by corrosion products generates micro-cracks. The mechanisms of micro-cracking can be investigated experimentally by acoustic emission (AE). AE-SiGMA (Simplified Green's functions for Moment tensor Analysis) was developed as a powerful technique for the moment tensor analysis [1]. Crack kinematics of locations, types and orientations are quantitatively determined. Because these kinematical outcomes are obtained as three-dimensional (3-D) locations and vectors, VRML (Virtual Reality Modeling Language) was implemented [2]. In this paper, mechanisms of corrosion cracking in concrete are studied by using 3-D visualization of AE-SiGMA results.

2. Experimental Procedures and SiGMA

To simulate crack patterns due to rebar corrosion in concrete, an expansion test was carried out. Concrete was made up of mixture proportion as water (W):cement (C):sand (S):gravel (G) = 0.5:1.0:2.41:2.95 by weight. The maximum size of aggregate was 20 mm. At the fresh state, slump value and air content were 7.0 cm and 5.0 %, respectively. Concrete specimens of dimensions 25 x 25 x 10 cm were tested. A circular hole of 3 cm diameter was created at the location of reinforcement.

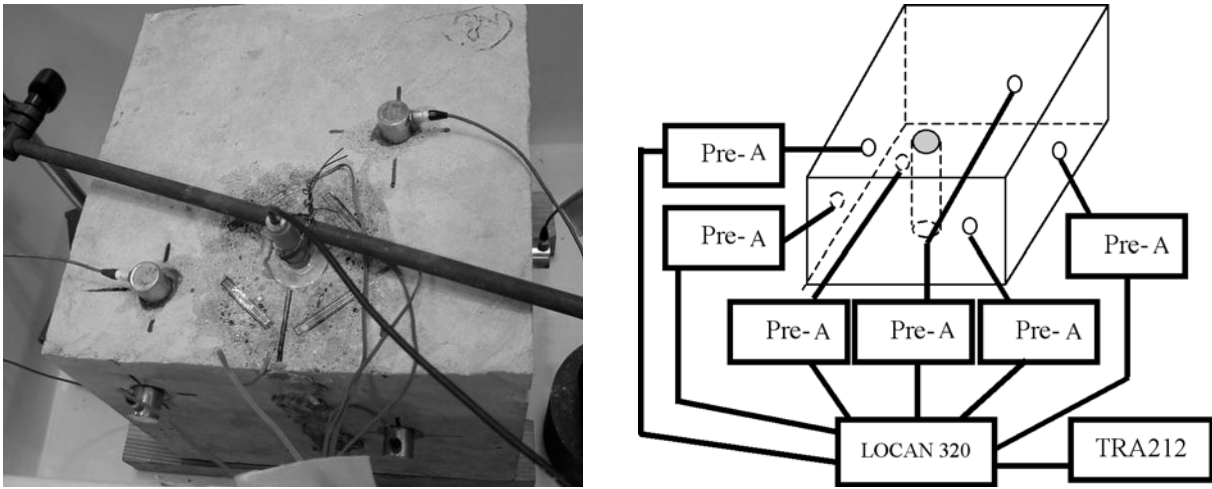


Fig. 1 Arrangement of AE sensors and measuring system.

In the test, dolomite paste (water:dolomite = 1:2) was employed as an expansive agent and cast into a circular cavity of the specimen as shown in Fig. 1. Expansion pressure was measured by using an embedded pressure gauge. AE events were detected by a six-channel system of AE sensors (PAC, UT1000). Arrangement of AE sensors and the measuring system are also illustrated in Fig. 1. AE waves were amplified 50 dB with a preamplifier, and waveforms and events exceeding the threshold level of 50 dB were recorded and analyzed by AE-TRA212 system (PAC), at 1- μ s sampling interval.

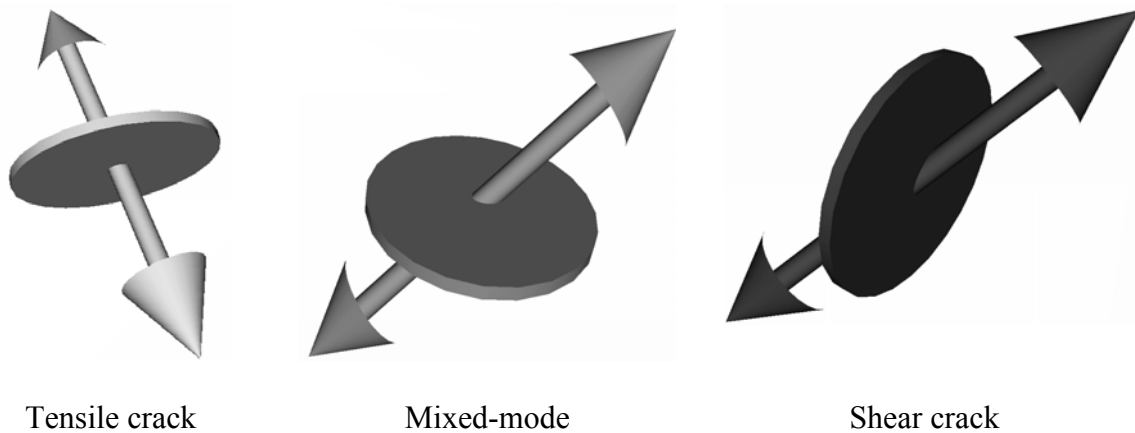


Fig. 2 VRML models for tensile crack, mixed-mode, and shear crack.

In a previous paper [3], classification of cracks is denoted only by symbols. Crack orientations, however, are not so easily represented in a two-dimensional (2-D) projection. To improve this aspect, VRML was introduced. Crack models of tensile, mixed-mode and shear cracks are shown in Fig. 2. Cracks are classified into tensile, mixed-mode and shear cracks from the shear ratios. AE sources, of which the shear ratios are smaller than 40%, are classified as tensile cracks. These greater than 60% are referred to as shear cracks. In between 40% and 60% of the shear ratios, AE sources are classified as mixed mode.

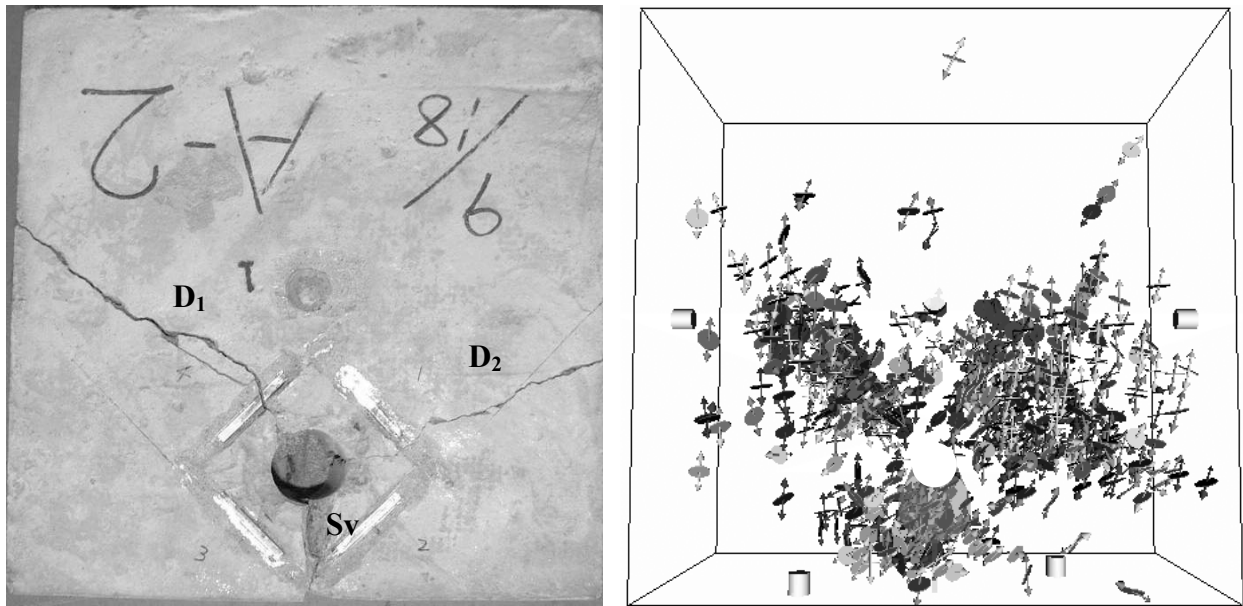


Fig. 3 Observed cracks (left) and visualized results (right) of AE-SiGMA in the specimen.

In the expansion test, peak pressure was measured as 17.1 MPa after about 18 hours elapsed. Observed cracks on the specimen, and results of AE-SiGMA are shown in Fig. 3. Surface crack ‘Sv’, diagonal cracks ‘D₁’ and ‘D₂’ are observed. According to the results of AE-SiGMA, tensile, mixed-mode and shear cracks are intensely observed near these three crack traces. During the test, it was observed that surface cracks ‘Sv’ was first nucleated and propagated vertically to the surface in the region of concrete cover. This is followed by the diagonal cracks ‘D₁’ and ‘D₂’, running diagonally towards the inside.

Table 1 Results of AE-SiGMA.

Type of crack	Total Number of AE events	Number of AE events classified		
		Tensile	Mixed-mode	Shear
Surface crack ‘Sv’	102	40 (6.7%)	33 (5.6%)	29 (4.9%)
Diagonal crack ‘D ₁ ’	197	69 (11.6%)	66 (11.1%)	62 (10.4%)
Diagonal crack ‘D ₂ ’	295	103 (17.4%)	100 (16.8%)	92 (15.5%)
Total	594	212 (35.7%)	199 (33.5%)	183 (30.8%)

3. Identified Mechanisms Of Corrosion Cracking

By AE-SiGMA, the cracking mechanisms of 594 events were identified. Of these, 35.7 % of the events are classified into tensile, 33.5% events into mixed-mode and 30.8% events into shear cracks, as summarized in Table 1 and shown in Fig. 4. These AE events are classified as associated with crack patterns ‘Sv’, ‘D₁’ and ‘D₂’ in Table 1.

3.1 Surface Crack

Out of 594 events analyzed, 102 events were associated with the surface crack and 40 (6.7%) events are classified into tensile mode, 33 (5.6%) events into mixed-mode and 29 (4.9%) events into shear cracks. As seen in Fig. 3, the crack mechanisms of all 3 modes are mixed around the

surface crack. Relations between AE sources and expansion pressure are shown in Fig. 5. Nucleation of the surface crack is observed around the peak pressure as high AE activities. At this stage, the tensile cracks are most numerous. Mixed-mode and shear cracks are slightly less active in the whole stage. This implies that cracking mechanisms of the surface crack are crack-opening type, consisting of both tensile and shear motion due to zigzag crack extension.

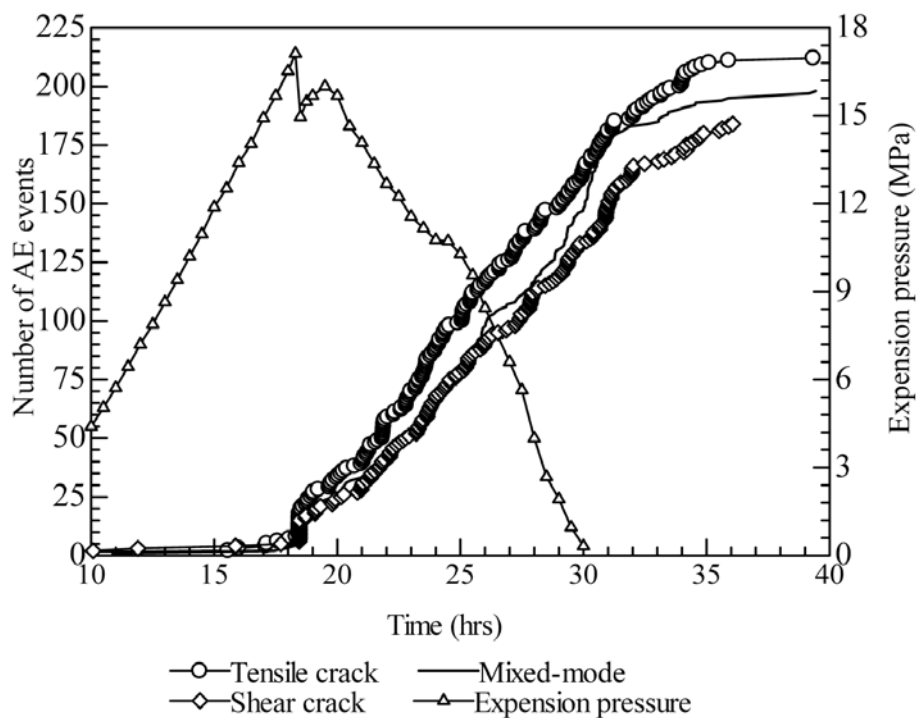


Fig. 4 Expansion pressure and activities of classified cracks.

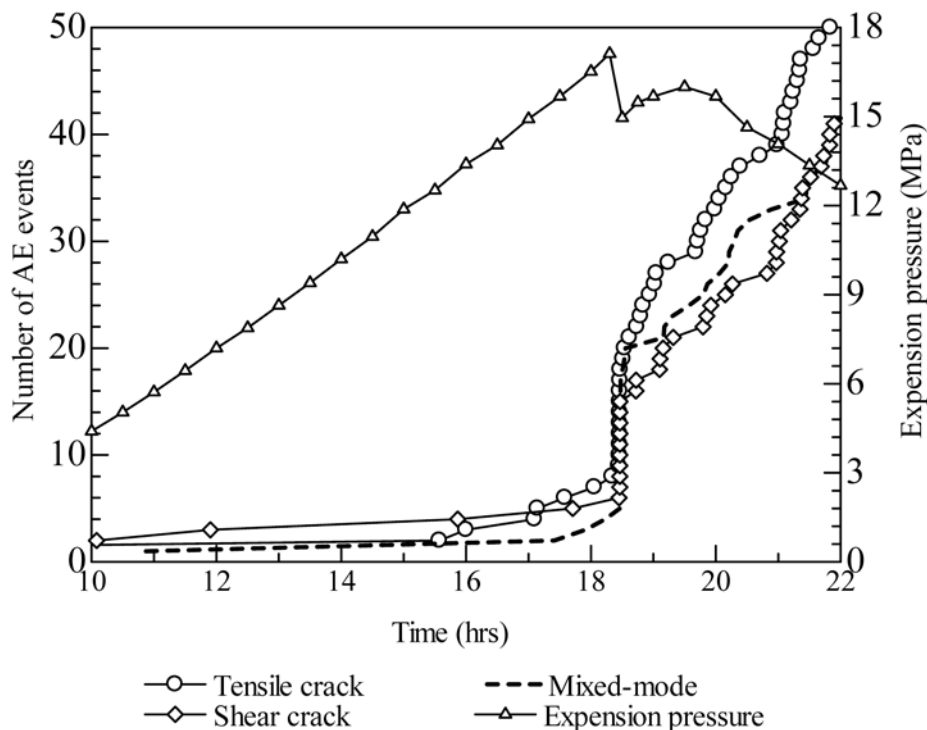


Fig. 5 Expansion pressure and activities of classified cracks for the surface crack 'Sv'.

3.2 Diagonal Cracks

For the diagonal crack ‘D₁’ and ‘D₂’, 197 and 295 events in total were analyzed, respectively, as shown in Table 1. 69 (11.6%) events are classified into tensile mode, 66 (11.1%) events into mixed-mode and 62 (10.4%) events into shear cracks for the diagonal crack ‘D₁’. For the diagonal crack ‘D₂’, 103 (17.4%), 100 (16.8%) and 92 (15.5%), respectively, for the three modes. As confirmed by VRML visualization of AE-SiGMA results in Fig. 3, these three modes were concentrated along the diagonal cracks. Results of AE activities and expansion pressure for the diagonal cracks ‘D₁’ and ‘D₂’ are shown in Figs. 6 and 7. All three modes of cracks became equally active over the whole stages, but the tensile cracks were always the most numerous.

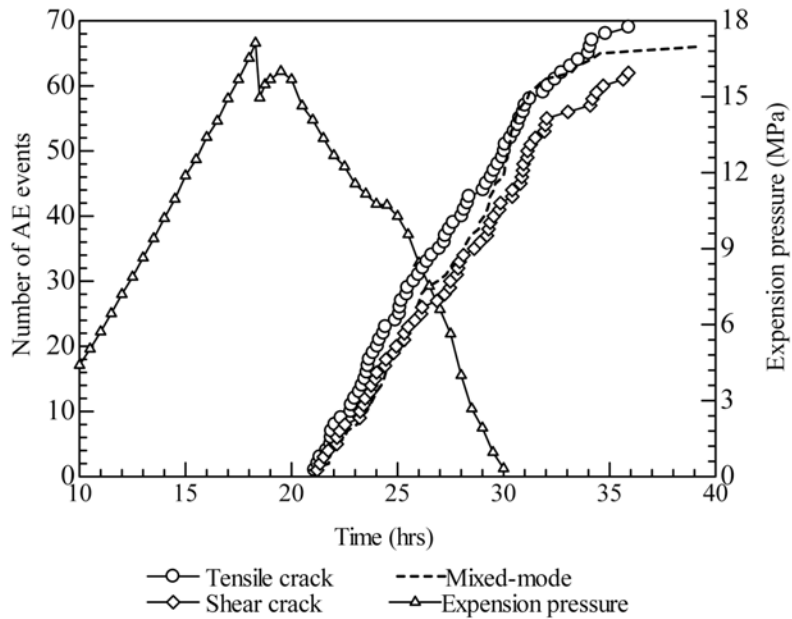


Fig. 6 Expansion pressure and activities of classified cracks for the diagonal crack ‘D₁’.

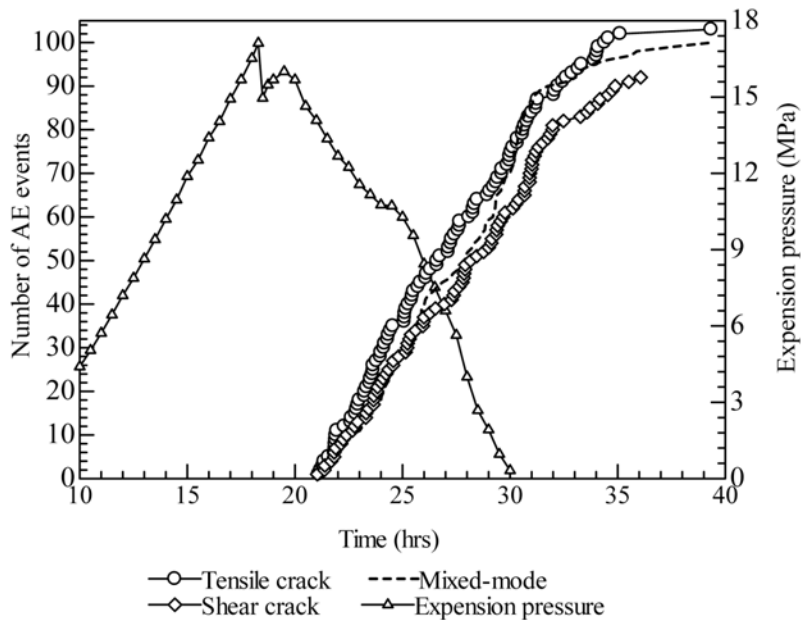


Fig. 7 Expansion pressure and activities of classified cracks for the diagonal crack ‘D₂’.

4. Conclusion

The traces of the surface crack and the diagonal cracks are identified by AE-SiGMA results with VRML. It is confirmed that AE sources are clustered close to the final failure surfaces. According to the results of AE-SiGMA, the number of AE events increases just before crack extension. Depending on the crack types, the contributions of mode I and mode II are varied during crack extension. These results are summarized, as follows:

1. Mechanisms for nucleating the surface crack and the diagonal cracks due to expansion of corrosive products are identified by AE-SiGMA results.
2. The surface crack starts to be initiated when the expansion pressure reaches the peak. According to AE-SiGMA results, all three modes were nearly equally observed. However, mixed-mode and shear cracks were less active and tensile cracks mostly active. Mixed-mode cracks were a little more active than shear cracks at the post-peak region. Following the surface crack, the diagonal crack is prone to extension.
3. For the diagonal cracks, both tensile and mixed-mode cracks became equally active, while shear-mode cracks were slightly less over the whole stage.
4. Mechanisms of corrosion cracking in concrete are of crack-opening failure, but the cracks follow zigzag paths, thus explaining nearly equal contributions of mixed-mode and mode-II cracks. The results show a great promise to apply AE-SiGMA procedure for inspection, identifying the mechanisms of corrosion cracking in concrete.

Acknowledgment

The authors wish to thank to Assoc. Prof. M. Shigeishi and Mr. Y. Tomoda, Mr. J. Shimasaki of Kumamoto University, and Mr. T. Itoh of Kawada Industries Co., for their valuable assistance in carrying out experiments and analyses. A part of this research is financially supported by the foreign-researcher fellowship from the Japan Society for the Promotion of Science (JSPS).

References

- 1) M. Ohtsu, T. Okamoto, and S. Yuyama: Moment Tensor Analysis of Acoustic Emission for cracking Mechanics in Concrete, *ACI Structural Journal*, **95** 2 (1998), 87.
- 2) M. Ohtsu and M. Shigeishi: Three-Dimensional Visualization of Moment Tensor Analysis by SiGMA-AE, *e-Journal of Nondestructive Testing*, ISSN: 1435-4934, **7** 9 (2002).
- 3) M. Ohtsu and S. Yoshimura: Analysis of Crack Propagation and Crack Initiation due to Corrosion of Reinforcement, *Journal of Construction and Building Materials*, **11** 7-8 (1997) 437.

EVALUATION OF PARAMETER DEPENDENCIES OF AE ACCOMPANYING SLIDING ALONG A ROUGH SIMULATED FRACTURE

KATSUMI NEMOTO, HIROKAZU MORIYA and HIROAKI NIITSUMA

Graduate School of Environmental Studies, Tohoku University, 6-6-20 Aramaki-aza-aoba, Aoba, Sendai, Miyagi 980-8579, Japan.

Abstract

Understanding shear slip behavior on fractures is indispensable for understanding earthquake mechanisms. In this study, we have investigated the characteristics of AE accompanying sliding along simulated fracture surfaces in an attempt to evaluate the dependencies of AE on sliding velocity and stress applied on the fracture. Our sliding experiments using pre-fractured granite specimens were conducted at room temperature and under a confining stress between 5 MPa and 20 MPa. Sliding velocity was kept constant during the experiments in the range of 1.15 $\mu\text{m/s}$ to 1155 $\mu\text{m/s}$. We evaluated the characteristics of AE by determining the m -value, which shows the statistical characteristics of AE [1]. Evaluation of parameter dependencies of the m -values reveals that the m -values have little dependence on stress state on the fracture and that they have negative dependence on sliding velocity. The small m -value indicates that AE events with larger maximum amplitude occur. Therefore, our results imply that high sliding velocity has a tendency to generate higher energy AE events during the sliding. This suggests that the characteristics of braking or slip of asperities on the fracture during the sliding were affected by sliding velocity rather than stress on the fracture.

Keywords: Earthquake mechanisms, Laboratory sliding experiments, Asperity, Contact state

1. Introduction

Earthquakes, when it happens, will bring out enormous damage. Thus, it is important to understand the physical mechanisms and to feed back the understanding for prediction. Considering that earthquakes would be caused by dynamic failure or slip at the crustal faults, it is significant to clarify the physical mechanisms of the dynamic behavior on faults for understanding of the mechanisms of earthquakes. On the crustal faults, fault surfaces have contacted each other under compressive stress due to a tectonic stress. When shear displacement occurs on the fault, micro-earthquakes would be caused by dynamic failure or slip of contact spots, which contact actually on the faults associated with the shear displacement. Therefore, investigation of source distributions and source parameters such as failure area, elastic energy released with micro-earthquakes by observing micro-earthquakes would provide the significant information of physical state on the faults, for example, contact state of the faults. On the other hands, AE events can be observed during shear slip on an artificially prepared fracture in sliding experiments simulating a fault movement. We might understand the characteristics of micro-earthquakes by evaluating the characteristics of the AE observed during a sliding of the fracture in laboratory experiments as an analogue of micro-earthquakes on the crustal faults.

In this study, sliding experiments simulating fault movement using a granite specimen under confining stress are conducted in order to evaluate the dependencies of AE characteristics on stress acting on a simulated fracture and sliding velocity.

2. Sliding Experiments Using a Rock Specimen under Confining Pressure

2.1 Preparation of a Rock Specimen Containing a Simulated Fracture

Figure 1 shows the photograph of a rock specimen used in experiment. Rock type is Iidate granite, of which grain size is approximately 1 mm. The size of the cylindrical specimen is 30 mm in diameter and 92 mm in axial length. The specimen has a precut surface split in half with an angle of 30° from the axial direction. This precut surface was roughened by hands with 16-grit silicone-carbide abrasives, of which the mean particle size is 1 mm. A borehole of 3 mm in diameter was drilled along the axis in the lower half of the specimen to reach to the simulated fracture. The specimen was saturated with water using a vacuum pump prior to the experiment and was used under the condition for the fracture being filled in water during the experiment.

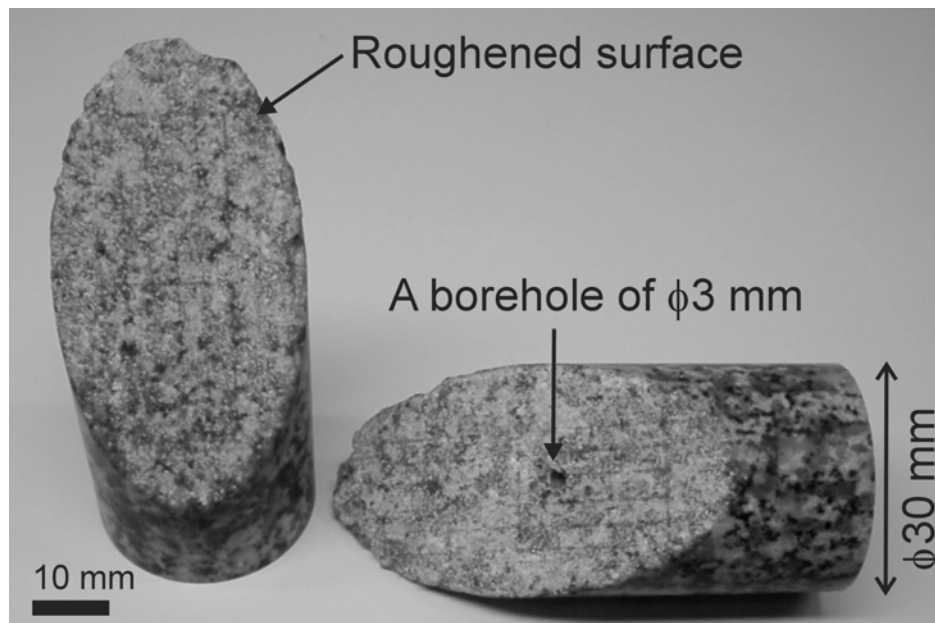


Fig. 1 Rock specimen containing a simulated fracture and a borehole. The left figure is the upper part, and the right is the lower part. A borehole in the lower part is indicated.

2.2 Experimental Procedure and Condition

All experiments were conducted under a constant confining pressure at room temperature. Figure 2(a) shows a schematic illustration of our experimental system. Figure 2(b) shows an overview of the apparatus during sliding experiments. The apparatus consists of a pressure vessel, a loading machine, and confining pressure generation system. The pressure vessel has a capability of maximum confining pressure of 25 MPa. The loading machine (Instron 8803) is a hydraulic servo-controlled uni-axial loading machine. The servo-control system of the loading machine allows accurate control of a ram position. Maximum loading capacity of the machine is 500 kN and a stiffness is 1.07 MN/mm. The confining pressure system consists of an accumulator, of which capacity is 10 l and a double-plunger pump. The accumulator was adopted in order to keep a confining pressure constant.

The specimen was jacketed with two rubber tubes and attached with upper and lower steel end caps. It was placed on the bottom of the pressure vessel. After the fracture was filled with distilled water, confining pressure was applied to the vessel by injecting water using a hand

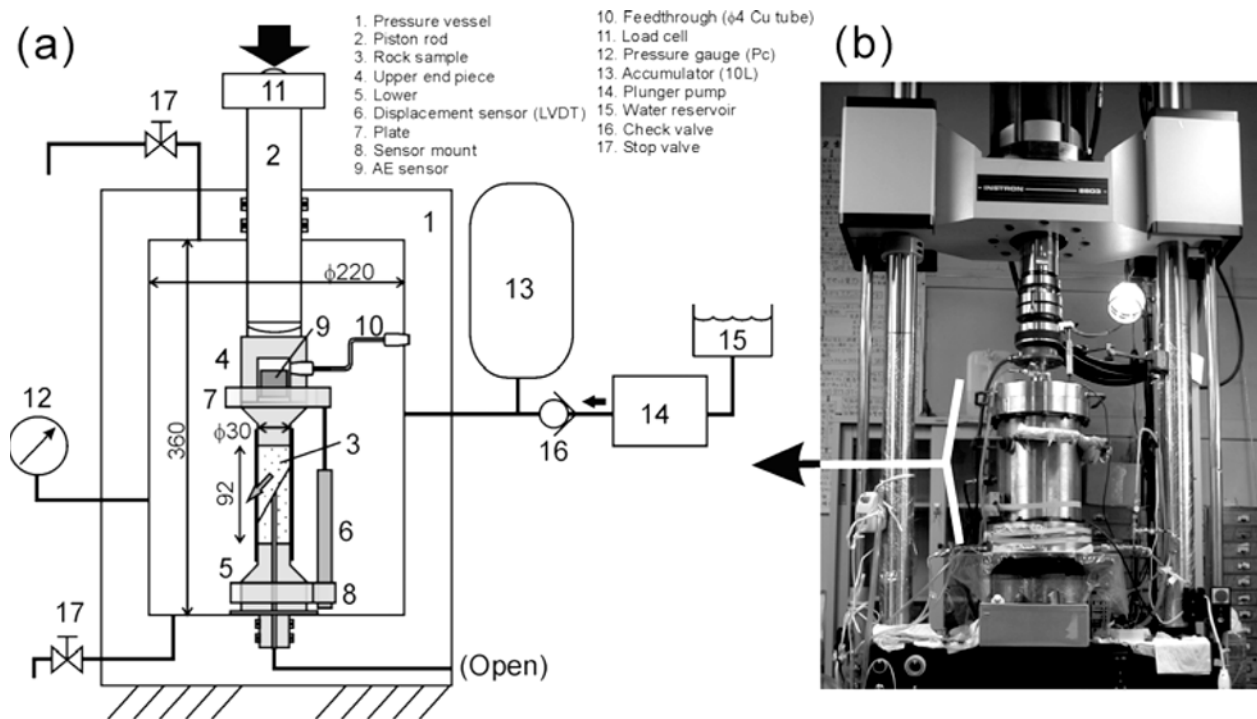


Fig. 2 Experimental apparatus in this study; (a) Schematic illustration of experimental system (b) Overview of the apparatus during sliding experiments.

pump. The specimen was held for 30 min to stabilize the confining pressure. After that, we made an initial sliding by 0.5 mm on the fracture and held this condition for an hour in order to stabilize the surface contact state. After the holding, we made sliding via 10 to 11 mm in axial displacement until the jackets were broken by shear displacement on the fracture.

Two series of sliding experiments were conducted in order to investigate effects of normal stress and that of slip velocity on AE activity during the sliding of fracture. To investigate effects of normal stress, confining pressure was kept constant at 5, 10, 15 and 20 MPa, respectively, and sliding velocity was kept constant at 11.5 $\mu\text{m/s}$. The normal stresses acting on a fracture during sliding in each experiment were calculated as 7.5, 14.5, 21 and 28 MPa from the axial load and confining pressure during experiments, respectively. In the experiments to investigate effects of slip velocity, constant slip velocity was varied as 1.15, 11.5, 115 and 1155 $\mu\text{m/s}$ under constant confining pressure of 10 MPa, or normal stress of 14.5 MPa. Pore pressure, which indicates a pressure of water in the fracture aperture, was 0.1 MPa (atmospheric pressure) in all experiments.

We measured the axial load, confining pressure, and axial displacement as mechanical parameters indicating sliding behavior on the fracture. The axial load was measured with a load cell placed on the top end of a loading piston of the vessel. The axial displacement was measured with a pressure-proof displacement transducer (LVDT) attached to the lower end cap. These signals from transducers were digitized and recorded with a data recorder continuously with a sampling frequency of 200 Hz after applying a low-pass filter, with a cutoff frequency of 80 Hz. Normal stress and shear stress acting on the fracture were calculated from the axial load and confining pressure recorded with the data recorder after the experiments. Sliding displacement along the fracture was calculated as a component along the slip fracture of the axial displacement measured by the LVDT.

AE events accompanying sliding were detected with a broadband-type piezoelectric AE sensor (Fuji-Ceramics Co., Type 1045S, frequency band of 100 kHz to 1 MHz) embedded in a cavity of the upper end cap. A 40-dB preamplifier and a main amplifier of 30 dB gain amplified the signals from the AE sensor. The AE signals were digitized and recorded with a sampling frequency of 5 MHz after applying band-pass filter of 200 kHz to 1 MHz. The characteristic parameters of AE events such as triggering time and peak amplitude were recorded by AE data acquisition system (NF, 7600 module). We counted AE event rates per unit slip displacement by regarding the number of triggers as the number of AE events. The mechanical parameters such as axial load, axial displacement and confining pressure, and the AE event rates were recorded with two different data acquisition systems, respectively. To synchronize the data from the two systems, a common signal generated by a function generator was recorded by both systems during the experiments.

3. Results of Sliding Experiments

3.1 General Observation in Sliding Behavior and AE Characteristics on a Simulated Fracture

Figure 3 shows a representative result of our sliding experiment where the confining pressure and the sliding velocity were kept constant as 15 MPa and 11.5 $\mu\text{m/s}$, respectively. As shown in Fig. 3(a), the normal stress and shear stress increased with an increase in slip displacement during the initial stage of sliding over approximately 0.5 mm. On the other hand, the normal stress and shear stress took almost stable value of 20 MPa and 10 MPa, respectively, after the initial stage. In Fig. 3(b), the friction coefficient μ during sliding shows the value of 0.45 ~ 0.5. Here, $\mu = \tau/\sigma_n$, where τ is shear stress and σ_n is normal stress applied to the fracture calculated from the axial load and the confining pressure observed during experiment. Friction coefficient μ ranged from 0.5 to 0.6 in all experiments, indicating that our experiments were appropriate.

AE event rates in unit slip shown in Fig. 3(c) decreased as the cumulative slip displacement increased over several mm and stabilized finally. This phenomenon is known as the evolution process on fracture surfaces [2]. The m-values were evaluated by using every 500 AE events. An m-value represents the amplitude distribution of the AE events detected, indicating statistical characteristics of AE accompanying the sliding of fracture. Figure 3(d) shows the m-values estimated. The m-values ranged from 1.5 to 2.5 and gradually increased with an increase in the cumulative slip displacement. The gradual increase may reflect the evolution process as mentioned above, implying the fracture surfaces were varying with the increase in cumulative slip displacement.

3.2 Effects of Confining Pressure on m-value

Figure 4(a) shows a relationship between the m-values estimated with every 500 AE events and confining pressure. Figure 4(b) shows the frequency distributions of the m-value. These results imply that the confining pressure, and in turn, stresses acting on the fracture surfaces have little effect on the m-value. This independency of m-values on the stress condition on the fracture suggests that the AE characteristics are little affected by the normal stress acting on the fracture surfaces in the stress range used in this study.

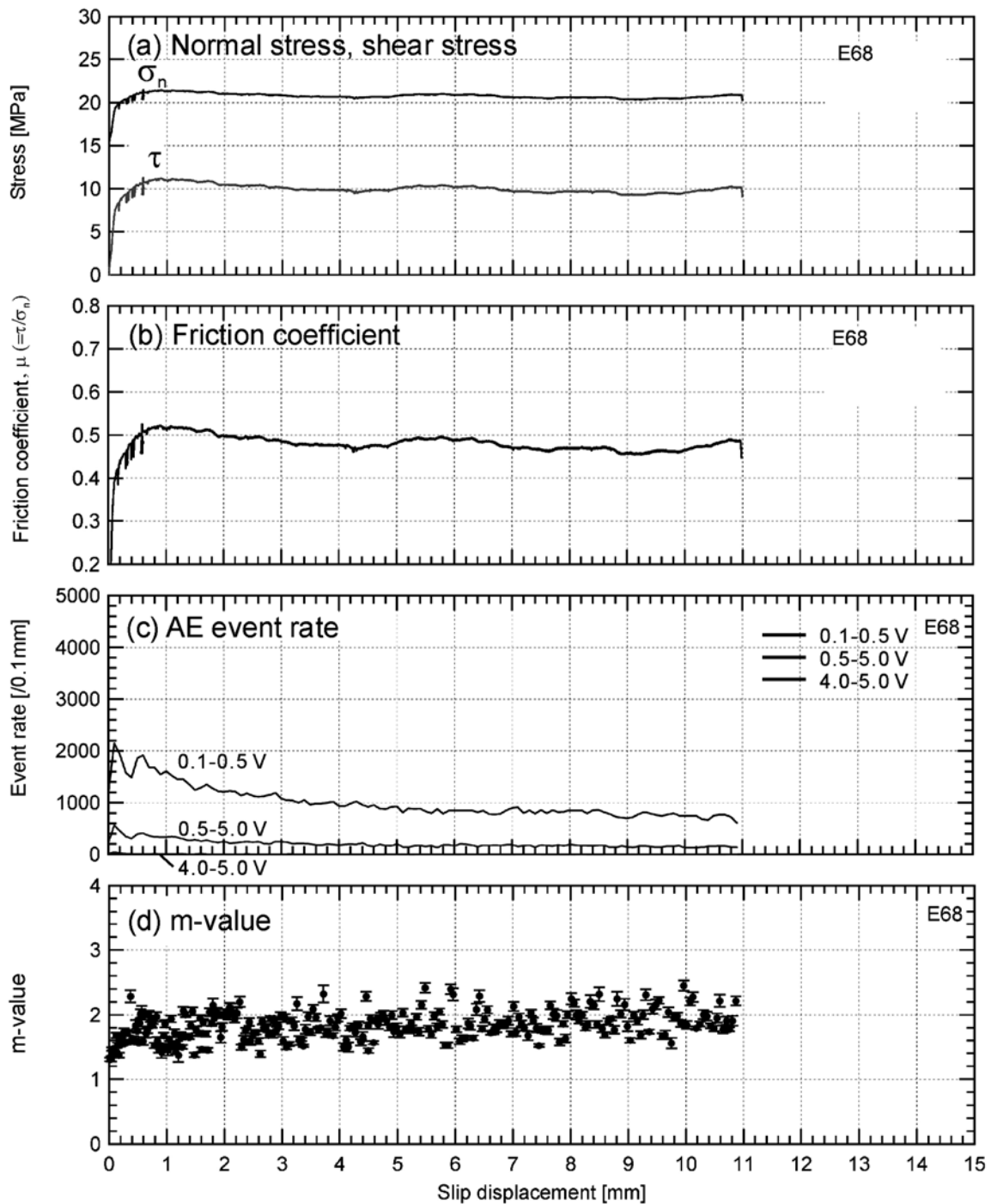


Fig. 3 Representative results of sliding experiment shown as a function of slip displacement; (a) Normal stress and shear stress on a fracture calculated from axial load and confining pressure, (b) Friction coefficient, (c) AE event rates, (d) m-values estimated with every 500 AE events.

3.3 Effects of Sliding Velocity on m-value

Figure 5(a) shows the m-values shown as a function of sliding velocity. The m-values have distributions on sliding velocity because the sliding velocities were calculated as an instantaneous velocity from sliding displacement. Figure 5(b) shows the frequency distributions of the m-value. These figures suggest that the m-value decreases as the sliding velocity increases even

though a limited number of m -values could be estimated in the experiments indicated "D" and "E", in which the sliding velocity was $1155 \mu\text{m/s}$. This negative dependency of m -value on sliding velocity implies that the contact state of fracture surfaces inferred from AE characteristics changes with the sliding velocity.

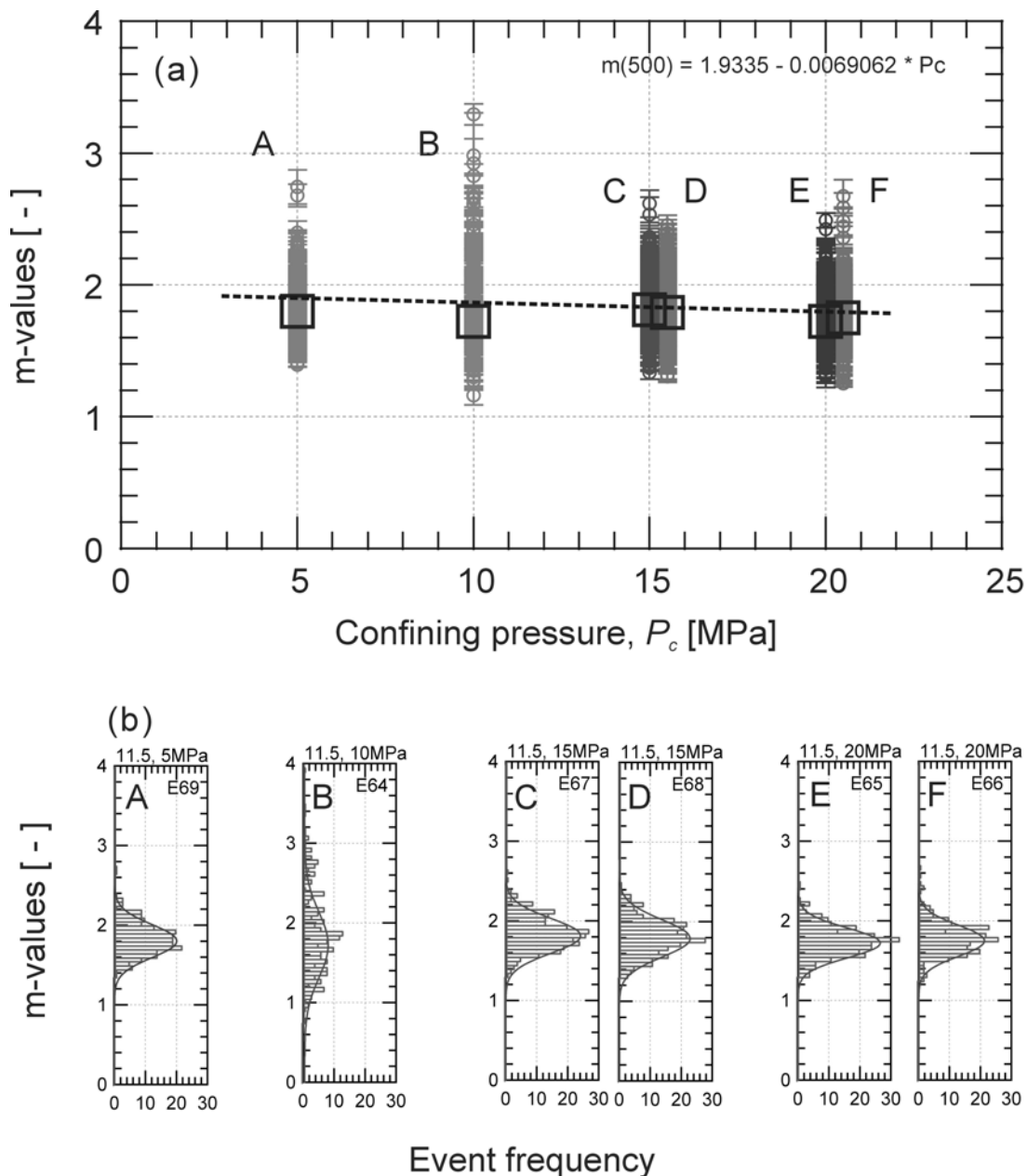


Fig. 4 Confining pressure dependency of m -value; (a) Relationship between the m -values and confining pressure, (b) Frequency distributions of m -values in each experiments. Alphabets from A to F indicate frequency distributions of each experiment indicated with alphabets in (a).

4. Discussion

Our experiments showed that stresses on the fracture had almost no effect on the m -value in a series of experiments where the normal stress were changed from 7.5 MPa to 28 MPa. It is reasonable that characteristics of AE accompanying sliding would reflect the contact state of the

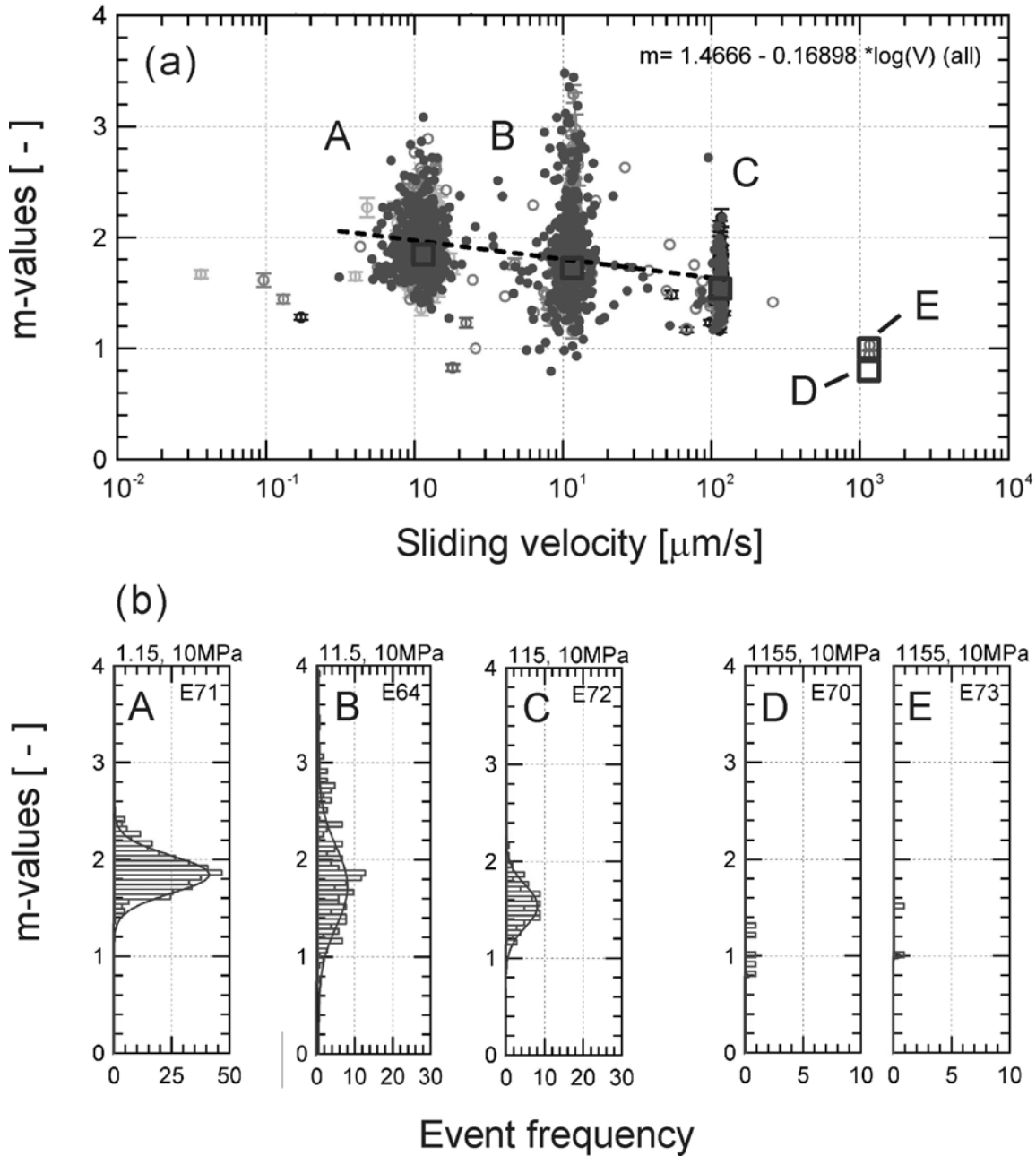


Fig. 5 Sliding velocity dependency of m-value; (a) relationship between the m-values and sliding velocity. (b) Frequency distributions of m-values in each experiment. Alphabets from A to F indicate frequency distributions of each experiment indicated with alphabets in (a).

fracture surfaces because AE would be generated with slip or break of asperities on the surfaces, on which two rough surfaces contact and coalesce each other [3]. Dieterich and Kilgore [4] conducted direct observation of contact state on roughened surface, revealing that the distribution of the real contact area did not significantly change with an increase in a static normal stress applied on a fracture, although the real contact area itself increased with an increase in normal stress, through the detailed experiments using quartz plates roughened with abrasive. The m-value indicates the amplitude distribution of AE events. The amplitude of AE events may depend on contact state on the fracture surface during a sliding because AE would be generated by slip or break of asperities contacting each other. Therefore, we could interpret the m-value as an

indicator for the contact state of fracture. Based to this interpretation of the relationship between the m-value and the fracture contact state, the insensitivity of the m-values to stresses acting on the fracture observed in our experiments suggests that no significant changes in the distribution of contact area occurred in the range of 7.5 MPa to 28 MPa in normal stress and fracture surfaces, which we have prepared.

On the other hands, the negative dependency of m-value on sliding velocity indicates that the number of AE events with large amplitude increased with the increase in sliding velocity, implying sliding velocity has large effect on AE characteristics. Considering that AE events would occur as consequence of slips or breaks of small asperities, we could interpret the increase in amplitude of AE with the increase in sliding velocity as an increase in elastic energy released by slip or break of asperities.

In the experimental seismology, the investigation for the effect of sliding velocity on AE activity was carried out using a dry granite specimen under bi-axial compression condition at room temperature in order to reveal mechanisms of earthquakes occurring on the plate boundary in a subduction zone [5]. The results have also suggested the negative effect of sliding velocity on the m-value, and the possibility of micromechanics on the asperity contacts. However, mechanisms of the negative effect on the m-value still remain as an open question.

5. Conclusion

The results of sliding experiments using a rock specimen containing an artificially prepared fracture under confining pressure condition ranging from 5 MPa to 20 MPa showed the insensitivity of m-value, which represents the characteristics of AE accompanying the sliding of a fracture, on normal stress acting on the fracture and also showed the negative dependency on sliding velocity in the range of 1.15 $\mu\text{m/s}$ to 1155 $\mu\text{m/s}$.

The mechanism of the insensitivity of normal stress on the m-value was interpreted as an insensitivity of the distribution of surface contact area on the normal stress shown by Dieterich and Kilgore (1996). The mechanism of the negative dependency of sliding velocity was interpreted as a consequence of an increase in elastic energy released by slip or break of asperities associated with the increase in sliding velocity. Therefore, it has been revealed that sliding velocity affects the AE characteristics that may reflect contact state of fracture surfaces.

References

- 1) M. Ishimoto and K. Iida: Bulletin of the Earthquake Research Institute, Tokyo Imperial University (in Japanese), **17** (1939), 443-478.
- 2) P. Sammonds and M. Ohnaka: *Geophys. Res. Lett.* **5** 5 (1998), 699-702.
- 3) F. B. Bowden and D. Tabor: *The Friction and Lubrication of Solids*, vol. 2, Clarendon Press, Oxford (1964).
- 4) J. H. Dieterich and B. D. Kilgore: *Tectonophysics*, **256** (1-4) (1996), 219-239.
- 5) Y. Yabe: *Geophys. Res. Lett.* 10.1029/2001GL014369, 21 May 2002. (2002).

AE CHARACTERIZATION OF THERMAL SHOCK CRACK GROWTH BEHAVIOR IN ALUMINA CERAMICS BY DISC-ON-ROD TEST

SHUICHI WAKAYAMA, SATOSHI KOBAYASHI and TOSHIYA WADA

Department of Mechanical Engineering, Tokyo Metropolitan University
1-1, Minami-Ohsawa, Hachioji, Tokyo 192-0397, Japan.

Abstract

Crack growth behavior from a pre-crack in alumina under thermal shock was evaluated by acoustic emission (AE) technique. In the Disc-on-Rod test used in the present study, the central region of heated specimen was quenched by means of contacting with a cool copper rod. AE signals during crack growth were detected by an AE sensor attached on the opposite end of the copper rod. The temperature distribution on the specimen was measured by an infrared camera and the crack growth behavior was observed by a digital video camera. In this study, microscopic crack growth behavior from the pre-crack was characterized by the Disc-on-Rod test system, and the onset of crack growth was detected by the AE measurement. Then, the critical stress intensity factors for different pre-crack length were calculated and angles of crack deflection were investigated by FEM. Consequently, the crack growth behavior under thermal shock was well understood by the AE technique.

Keywords: Alumina, Thermal shock fracture, Crack growth, Fracture mechanics, Stress intensity factor

1. Introduction

The application of ceramics at elevated temperature often involves rapid heating and cooling conditions leading to thermal stress that causes thermal shock fracture. Thermal stress field is resulted from the temperature distribution due to transient heat flux under temperature difference. Under the transient thermal stress, the thermal shock fracture process consists of the microcrack initiation and accumulation, the main-crack formation and the main-crack growth to final fracture. Furthermore, in the fracture process, it is considered that there is an interaction among temperature distribution, stress field and main crack. Therefore, it is important to characterize both the thermal stress field and the fracture process dynamically and simultaneously. However, in conventional studies, those requirements have not been satisfied. For example, the macroscopic crack growth process was investigated based on fracture mechanics, whereas the precise evaluation of the micro-fracture process and thermal stress was still insufficient [1,2]. Thus, new experimental technique for the investigation of thermal shock fracture behavior, Disc-on-Rod test, has been developed by the authors [3-5]. In the Disc-on-Rod test, transient thermal stress field can be calculated by FEM from the directly measured temperature distribution. In addition, the micro-fracture process can be characterized by the AE analysis.

The objectives of this study are to develop this technique and to characterize crack growth behavior of ceramics during thermal shock. The micro-fracture process was investigated by AE analysis. Furthermore, the result of AE analysis was verified by the observation of crack growth behavior by a digital video camera. Consequently, the crack growth behavior was characterized based on fracture mechanical approach.

2. Experimental Procedures

2.1 Preparation of Specimens

The material used were alumina ceramics (ADS-11) offered by Toshiba Ceramics Co., Ltd. Table 1 shows the material properties of ADS-11. Disc specimens with 20-mm diameter and 0.6-mm thickness were cut from sintered rods and both surfaces were polished with 1- μm diamond slurry. Specimens were dehydrated at 150 °C for 2h in vacuum to avoid the influence of the stress corrosion by the water.

Table 1 Material Properties of Alumina.

	Grain Size [μm]	Density [kg/m^3]	Elastic Modulus [GPa]	4 Points Bending Strength σ_B [MPa]	Thermal Conductivity [W/mK]	Coefficient of Thermal Expansion $\times 10^{-6}$ [°C]	Fracture Toughness [$\text{MPa}\cdot\text{m}^{1/2}$]
ADS-11	6	3900	360	350	30.0	7.8	4.5

2.2 Introduction of Pre-crack

Figure 1 shows a pre-crack introduced into the specimen. An indentation was generated at the center of the specimen using a Vickers indenter. Figure 2 shows schematic illustration of procedure to grow the pre-crack from the indentation. Only the edge of the specimen was supported, and the specimen was subjected to flexural loading by a metal rod of 4-mm diameter. The pre-crack was propagated from the indentation. The pre-crack length was controlled by monitoring AE signals detected by an AE sensor attached on the outer part of the specimen. Thus, specimens with a long pre-crack (Type A), a short pre-crack (Type B) and without pre-crack (Type C) were prepared.

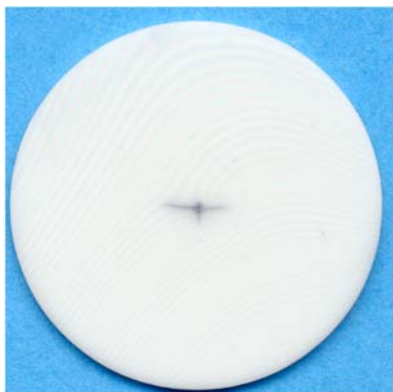


Fig. 1 A pre-crack introduced into the specimen (Type A).

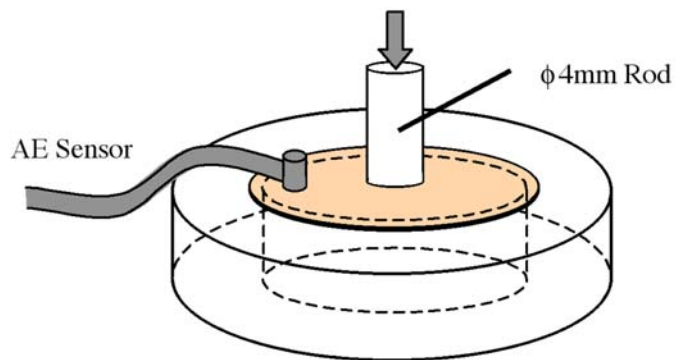


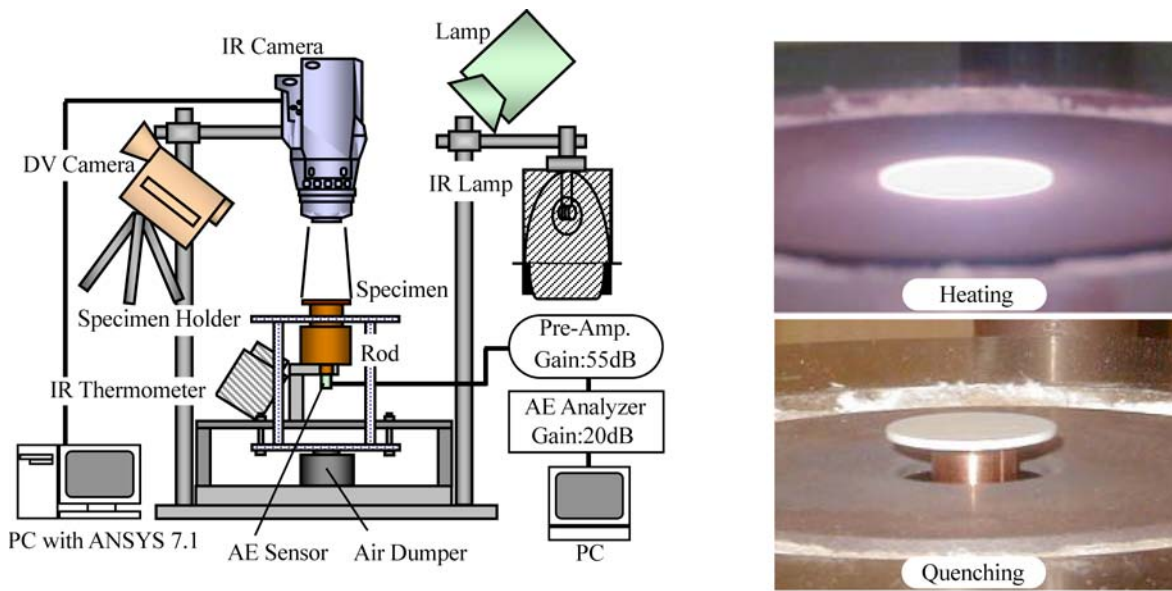
Fig. 2 Schematic illustration of procedure to grow the pre-crack from the indentation.

2.3 Thermal Shock Test and Acoustic Emission Measurement

The apparatus of thermal shock test and AE measuring system are schematically shown in Fig. 3. A thin disc specimen was heated uniformly to the required temperature by an infrared lamp. Only the central part of disc was quenched by contacting with a copper rod. Initial

temperature was 480-530°C and the contact area of the rod was 8-mm diameter. Contact speed was controlled by an air damper to restrain the generation of noise due to contacting. During a thermal shock test, the temperature distribution on the disc surface was measured by a high-speed (30 frame/s) infrared camera (IRC). At the same time, the macroscopic crack growth behavior was observed by a digital video camera (DVC). Then, the transient thermal stress was calculated from the measured temperature distribution using a commercial FEM code (ANSYS).

AE signals during thermal shock test were detected by an AE sensor attached on the bottom end of the copper rod to prevent the heat damage to the sensor. The rod was used both as a coolant and a waveguide. The AE sensor with an integral pre-amplifier and the resonant frequency of 180 kHz was used, and the initiation of microcrack can be detected with excellent sensitivity. The total gain of the AE system was 75 dB (main amplifier, 20 dB; pre-amplifier with sensor; 55 dB) and the threshold level was 40 dB, or 18 μ V at the input of the pre-amplifier. AE signals were fed to an AE analyzer, and sent to a personal computer and analyzed further.



(a) Thermal shock test apparatus.

(b) Photograph during thermal shock test.

Fig. 3 Apparatus of thermal shock test and AE measuring system.

3. Results and Discussion

3.1 AE Generation Behavior

Figures 4(a) and (b) show typical AE generation behavior in Type A (pre-crack half length of 2.3 mm) and Type B (pre-crack half length of 0.2 mm), respectively. In the AE generation behavior in Type A (Fig. 4(a)), it can be seen that both cumulative AE events and energy increased remarkably at 0 s and high amplitude AE signals were detected during 0~0.28 s. Furthermore, the onset of crack growth was observed at 0 s by DVC and the crack growth was also observed during 0~0.28 s by DVC. Therefore, it was ascertained that remarkable increase in both cumulative AE events and energy corresponded to the onset of crack growth and high amplitude AE signals corresponded to the crack growth. The former was similar to the result of previous study [3-5]. The fracture process in type A was initiated when the crack began to propagate at 0 s upon contacting with the copper rod, followed by its gradual propagation at low speed for 0~0.28 s and finally reaching the edge of the disc along radial direction at 0.28 s.

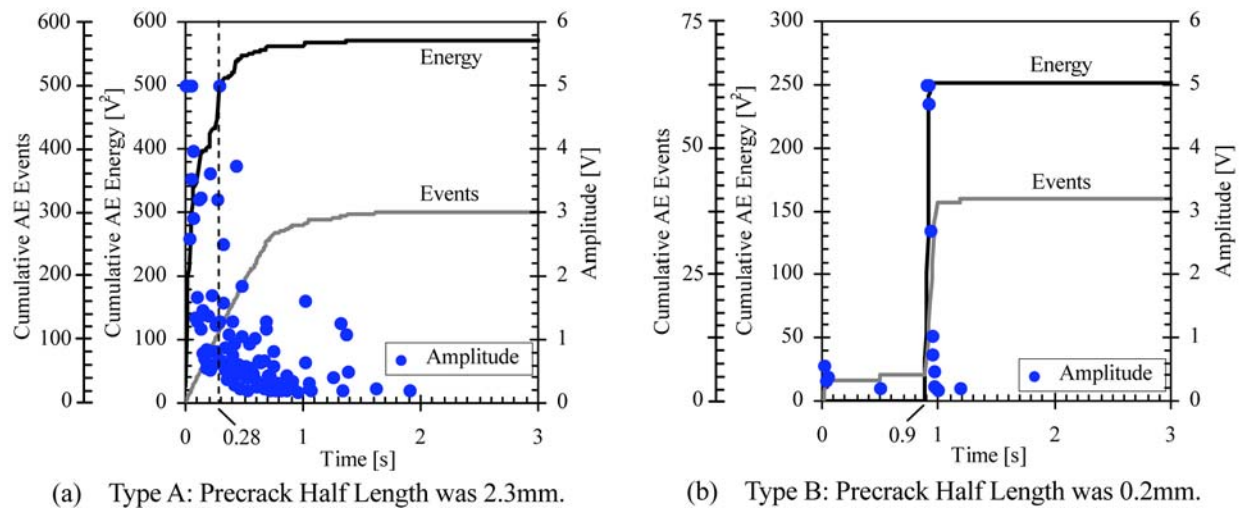


Fig. 4 AE generation behavior and crack growth process.

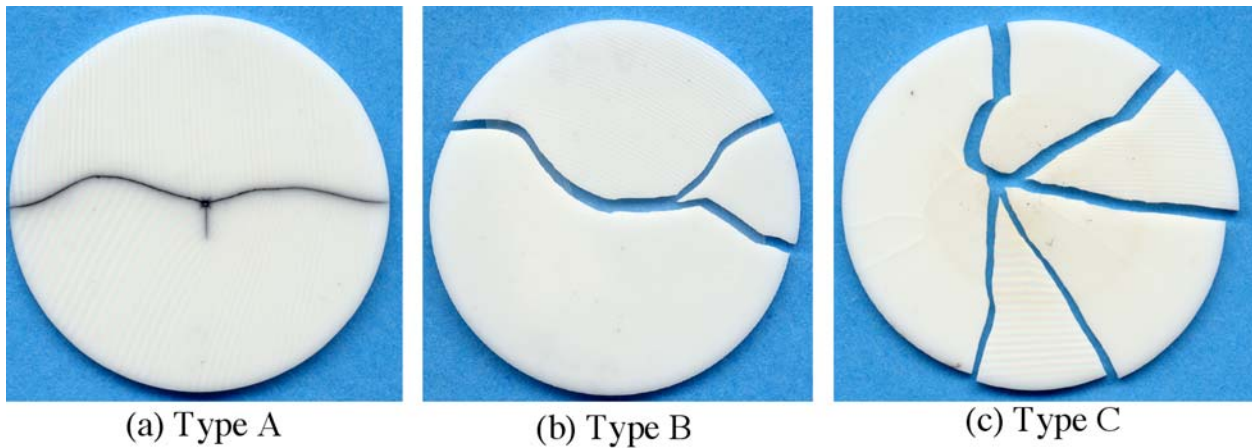


Fig. 5 Crack paths due to thermal shock fracture.

On the other hand, the AE generation behavior in Type B (Fig. 4(b)) shows that both cumulative AE events and energy increased suddenly at 0.9 s. Simultaneously, the fast crack growth was observed by DVC. Therefore, the fracture process in type B began when the crack started to propagate at 0.9 s and reached the edge of the disc along radial direction within 0.03 s. Consequently, it was understood from the AE behavior that in type A the crack propagated in a stable manner for a relatively long period (0.28 s), while in type B the crack propagated in an unstable manner for a short period (0.03 s). The dependence of fracture behavior on the pre-crack length showed good agreement with analytical prediction by Hasselman [6]. Thus, the AE technique shows that it can achieve the characterization of crack growth behavior and determination of the onset and stability of crack growth.

3.2 Macroscopic Fracture Behavior due to Thermal Shock

Figure 5(a), (b) and (c) show the photographs of fractured specimen of Type A, Type B and Type C, respectively. The specimens of Type A were not completely separated, while the specimens of Type B were separated into 2~3 pieces and the Type C specimens were separated into 2~6 pieces. This implies that the number of crack branching decreased with an increase in the pre-crack length. In addition, as mentioned above, it was recognized from the AE generation behavior that the crack growth rate decreased with an increase in the pre-crack length. Hence, it

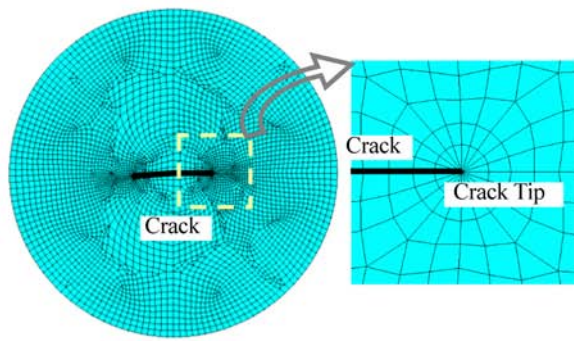


Fig. 6 FEM model of specimen with pre-crack.

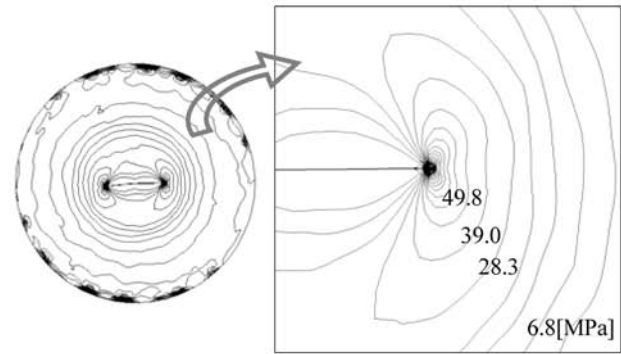


Fig. 7 Tangential stress distribution.

was suggested that the longer pre-crack length was, the smaller the number of crack branching and the crack growth rate were. It appears that this result was caused by the difference in strain energy at the onset of crack growth.

3.3 Thermal Stress Field and Stress Intensity Factor

Since the ratio of the thickness to diameter was very small ($= 0.03$) and the pre-crack in Type B penetrated along the thickness, FEM analysis was carried out assuming the 2-dimensional problem. Figure 6 shows FEM model with the pre-crack bent at the indentation. The thermal stress field at the onset of crack growth was computed from the corresponding temperature distribution, which was determined by the infrared camera measurement. Figure 7 shows the obtained tangential stress field in the polar coordinate, where the origin is the center of the specimen. In Fig. 7, the stress concentration is observed at both pre-crack tips. Strain energy release rates were also calculated using virtual crack closure method and stress intensity factors were determined.

Based on the maximum hoop stress criterion [7] and the minimum strain energy density criterion [8], the angles of crack deflection were examined. K_I and K_{II} obtained from this study were substituted for equations proposed in both of these theories and the deflection angles were cal-

Table 2 Stress intensity factors and angles of crack deflection.

	Stress Intensity Factors [$\text{MPa}\cdot\text{m}^{1/2}$]		Angles of Crack Deflection [$^\circ$]		
	K_I	K_{II}	Experiment	Minimum Strain Energy Density Criterion	Maximum Hoop Stress Criterion
Type A	2.38	0.06	6.0	2.9	2.9

culated. Table 2 shows K_I , K_{II} and the calculated deflection angles. In this study, there was no difference between the deflection angles determined from the two criteria, but those values showed fairly good agreement with the experimental result.

4. Conclusions

Fracture behavior in alumina ceramic discs during thermal shock subjected to the Disc-on-Rod test was investigated by the AE technique. From the AE generation behavior and the observation of the crack growth behavior, the following conclusions were obtained.

- 1) The crack growth behavior under thermal shock was understood from the AE generation behavior.
- 2) It was ascertained by DVC observation that remarkable increase in both cumulative AE events and energy corresponded to the onset of crack growth.
- 3) The angles of crack deflection determined by FEM from two types of the criteria showed fairly good agreement with the experimental result.

Acknowledgment

The authors would like to thank Toshiba Ceramics Co., Ltd. for their offer of ceramic samples. The present study was partly supported by the Grant-in-Aid for Scientific Research (No.15260349) from the Ministry of Education, Culture, Sports, Science and Technology of Japan.

References

- 1) G. A. Schneider and G. Petzow: *J. Am. Ceram. Soc.*, **74** (1991), 98.
- 2) Y. Mizutani et al.: *J. Ceram. Soc. Japan*, **103** (1995), 494.
- 3) S. Wakayama: *Progress in Acoustic Emission IX* (1998), p. III-73, AE Group, Los Angeles.
- 4) K. Nishino et al.: *Progress in Acoustic Emission X* (2000), p. 319, JSNDI, Tokyo.
- 5) S. Wakayama et al.: *Proc. of 7th Japan International SAMPE*, (2001), p. 585, Tokyo.
- 6) D. P. H. Hasselman: *J. Am. Ceram. Soc.*, **52** (1969), 600.
- 7) F. Erdogan, G.C. Sih: *J. Basic Eng.*, **85** (1963), 519.
- 8) G.C. Sih: *Int. J. Frac.*, **10** (1974), 305.

FATIGUE DAMAGE PROGRESSION IN PLASTICS DURING CYCLIC BALL INDENTATION

AKIO YONEZU, TAKAYASU HIRAKAWA, TAKESHI OGAWA
and MIKIO TAKEMOTO

Department of Mechanical Engineering, College of Science and Engineering,
Aoyama Gakuin University, Fuchinobe, Sagamihara, Kanagawa 229-8558, Japan.

Abstract

AE (acoustic emission) is utilized to monitor the progression of sub-surface damage in a transparent PVC (poly-vinyl-chloride) plate subjected to contact fatigue by cyclic ball indentation. We monitored AEs from sub-surface damage by four small AE sensors mounted on the four edges of a square plate, and estimated both the source location and fracture mode. The AE analysis revealed that Mode-II lateral cracks initiated at cycle number, $N = 8.9 \times 10^4$. AE sources of corresponding events were located in front of progressing sub-surface lateral cracks at the depth of 516 μm . We could not, however, monitor AE from Mode-I radial crack possibly due to small crack opening. Finite element method (FEM) predicted lateral crack initiation at approximately 500 μm below the surface with the maximum shear stress.

Keywords: Cyclic ball indentation, Poly-Vinyl-Chloride plastics, Fatigue damage progression.

1. Introduction

Engineer Polymers or Plastics are widely used for contact components such as bearings and gears in industrial fields due to their excellent performance at low cost. Understanding the mechanism of cyclic contact damage is important for practical applications [1, 2]. No study on cyclic contact for plastics has been performed so far and fatigue fracture process has remained to be understood [3, 4].

In the present study, cyclic ball indentation tests were performed on PVC (poly-vinyl-chloride) to study the mechanism of cyclic contact fatigue. The initiation and progression of fatigue damage were monitored by AE (acoustic emission) technique. We studied the cyclic fatigue mechanism by AE analysis, observed the indentation damage and analyzed using finite element method (FEM).

2. Materials and Experimental Procedures

We used transparent PVC as samples of 20-mm square with 5-mm thickness. Cyclic ball indentation tests were performed using an electro-hydraulic testing machine equipped with a ball indenter and two eddy current sensors (displacement resolution: 0.4 μm). We prepared four types of indenter balls with diameters $d = 5, 10, 15$ and 20 mm. A software for controlling cyclic indentation test was developed in house. The system measures the relationship between indentation force (F) and indentation depth (h) at high resolution under various testing conditions, controlling the maximum indentation force (F_{max}) and the stress ratio ($F_{\text{min}}/F_{\text{max}}$), $R = 0.05, 0.1$ and 0.5.

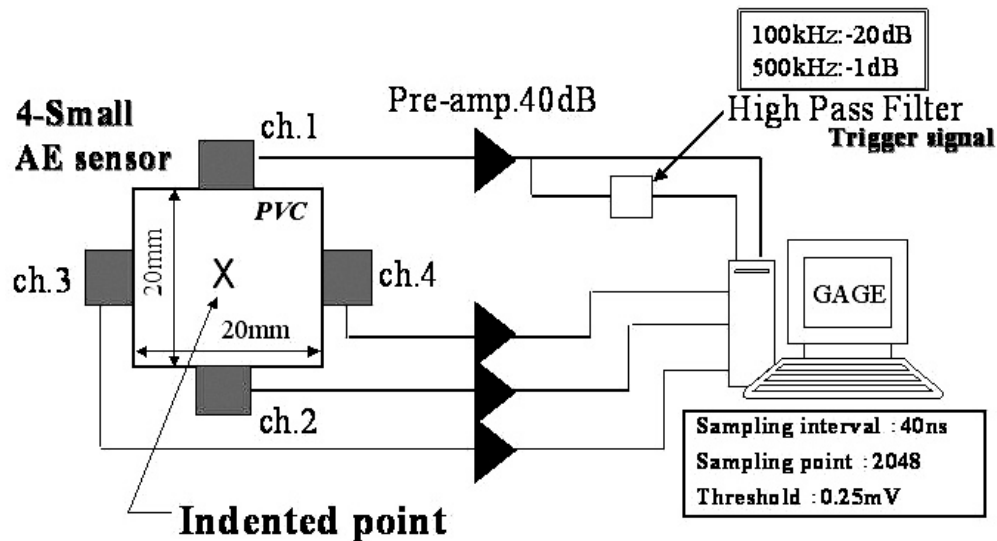


Fig. 1 AE monitoring system for cyclic ball indentation.

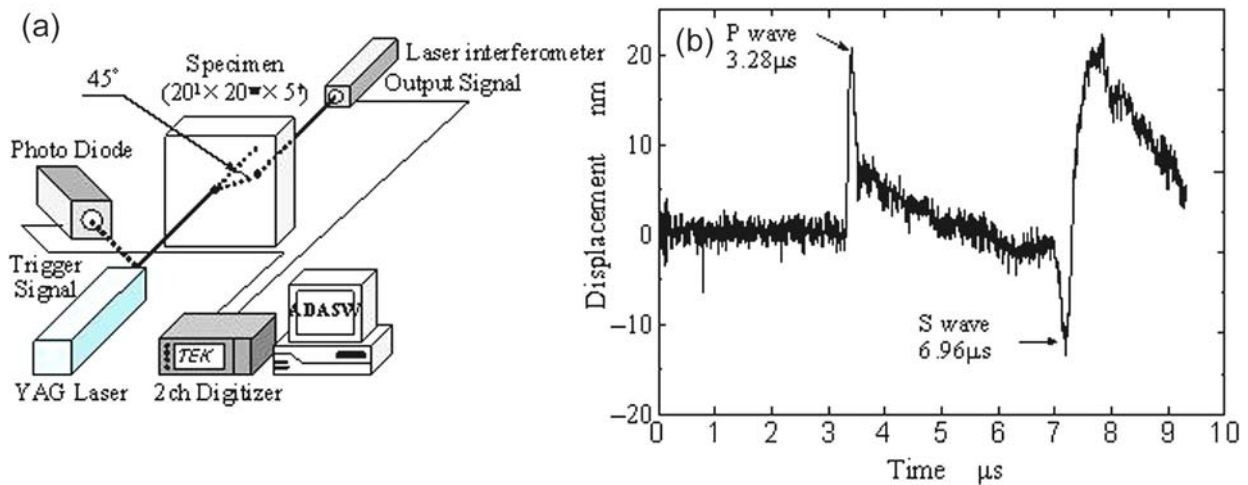


Fig. 2 (a) Experimental setup to measure the P wave velocity, (b) detected P wave and S wave.

In these tests, the maximum number of cycle was set as 10^6 cycles and cyclic frequency (f) as 5 Hz. All tests were performed at room temperature.

We monitored AE signals using four small AE sensors mounted on the side surfaces of a specimen. As shown in Fig. 1, the AE system consists of resonant-type sensors (Type PICO, PAC), 40-dB preamplifiers (9913, NF Circuit Block), A/D converter (Gage Applied Inc.) and a personal computer. Output of channel-1 sensor was branched into another circuit for triggering via a high-path filter. This eliminated low-frequency noise due to cyclic contact.

3. Results and Discussion

3.1 Determination of the Elastic Wave Velocity in Plate Specimen

We first studied the characteristics of AE waves using a laser system (Fig. 2). YAG laser pulses were point-focused at the center of specimen surface as shown in (a). Out-of-plane displacement was measured by a laser interferometer on the back-plane. In order to detect the shear

(S-) wave as well the longitudinal (P-) wave, the measurement point was changed from the epicenter to $1t$ -off ($t =$ the specimen thickness) epicenter. The timing of pulse laser irradiation was monitored by a photodiode and used as trigger signal. Outputs of the interferometer were digitized by a two-channel digitizer (sampling interval 4 ns and sampling point 4096 points) and fed to a personal computer. Figure 2(b) shows a detected waveform at $1t$ -off epicenter. First pulse at $3.28 \mu\text{s}$ was the P-wave traveled at velocity (V_p) of 2156 m/s. S-wave arrived at $6.96 \mu\text{s}$ traveled at velocity (V_s) of 1016 m/s. Young's modulus (E) of PVC was calculated as 3.78 GPa, and Poisson's ratio (ν) as 0.36. These values were found to be similar to those determined by indentation and compressive loading test. The static tests gave, $E = 3.55 \text{ GPa}$ and $\nu = 0.42$.

We next detected the elastic waves by a small AE sensor mounted on the side surface of the specimen. Velocity of the first arrival wave was measured as 2194 m/s and coincided with the velocity determined by laser system. Since the sheet velocity (C_E) of symmetric (S_0)-Lamb mode of PVC was slower and measured as 1794 m/s, we need to estimate the source location using the P-wave velocity.

3.2 Fatigue Damage Progression during Cyclic Ball Indentation Testing

We performed the cyclic ball indentation testing with the maximum indentation force, $F_{\text{max}} = 981 \text{ N}$, stress ratio, $R = 0.1$, and indenter diameter, $d = 10 \text{ mm}$. Figure 3 shows the variation of the maximum and minimum indentation depth (h_{max} and h_{min}) with the number of cycles, N . This figure also shows cumulative AE counts. We detected first AE at $N = 8.9 \times 10^4$ cycles and AE counts increased rapidly with cycle numbers. This test was terminated at $N = 1.01 \times 10^5$ cycles when total AE event counts reached 4097. Figure 4(a) shows the post-test micrograph of the indentation damage. White semi-elliptical cracks near the contact area (not clear due to transparency of PVC) in the photograph is sub-surface cracks induced by cyclic contact. A large crack near the top and a smaller one at the bottom can be seen. Figure 4(b) shows a magnified view of (b) on the periphery of contact area. It shows a fine radial crack in the radial direction. Cross section along the line A-A' in Fig. 4(a) is shown in Fig. 5. We observed sub-surface cracks at the depth of $516 \mu\text{m}$. This is the white semi-elliptical lateral crack observed in Fig. 4(a).

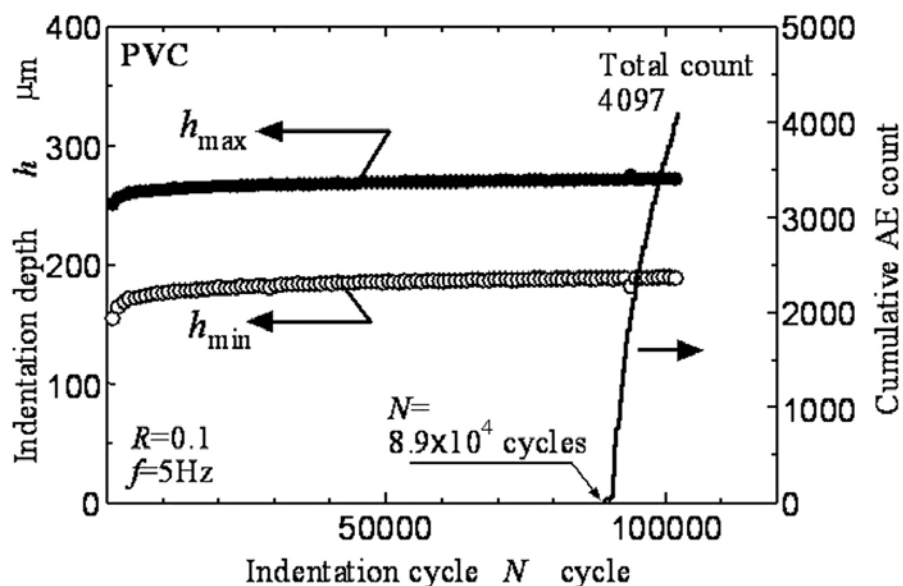


Fig. 3 Indentation depth and cumulative AE counts as a function of indentation cycles.

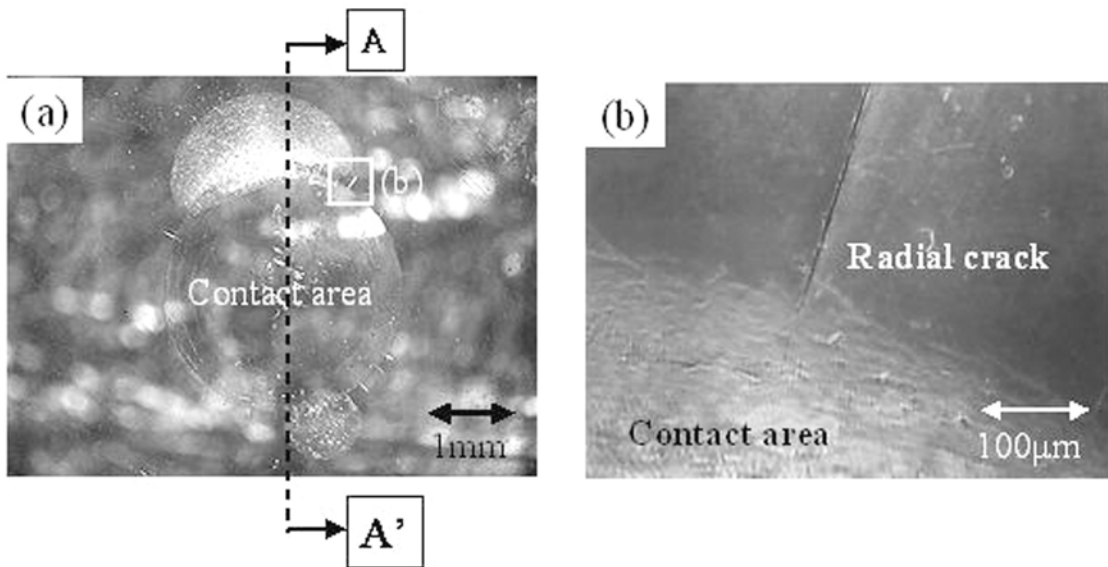


Fig. 4 (a) Surface photograph of indentation damage, (b) magnified view of area marked (b).

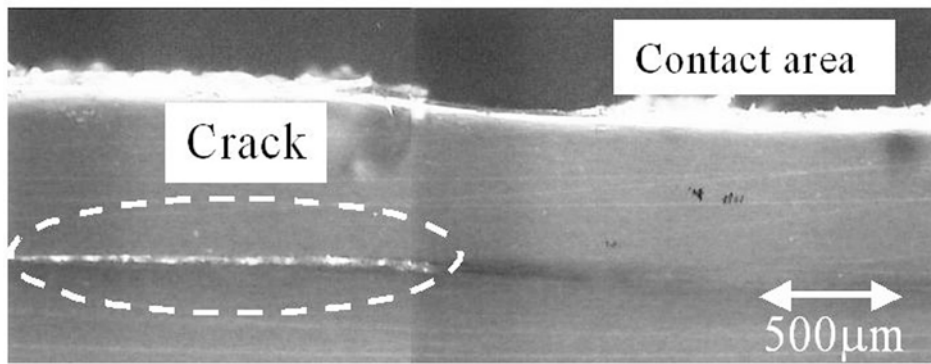


Fig. 5 Cross sectional view of indentation damage (A-A' line of Fig. 4(a)).

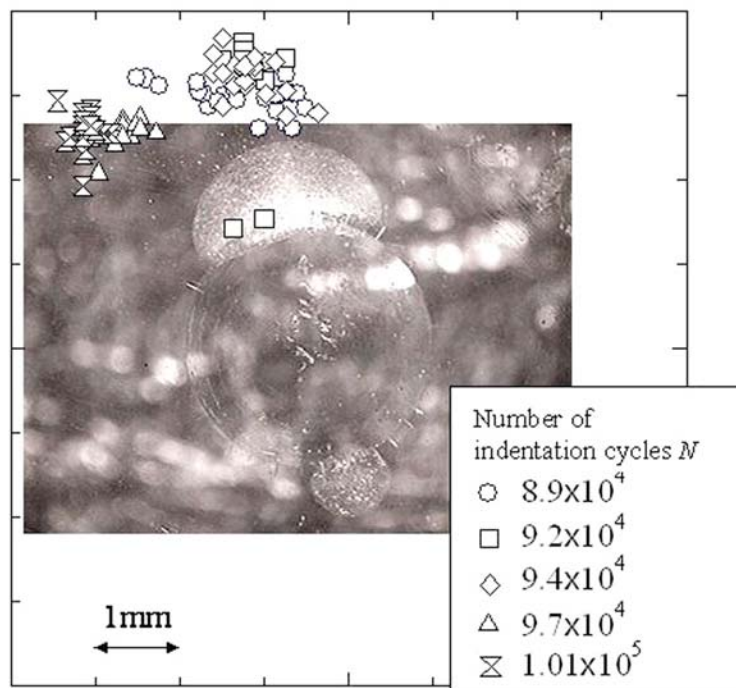


Fig. 6 AE source locations during cyclic ball indentation.

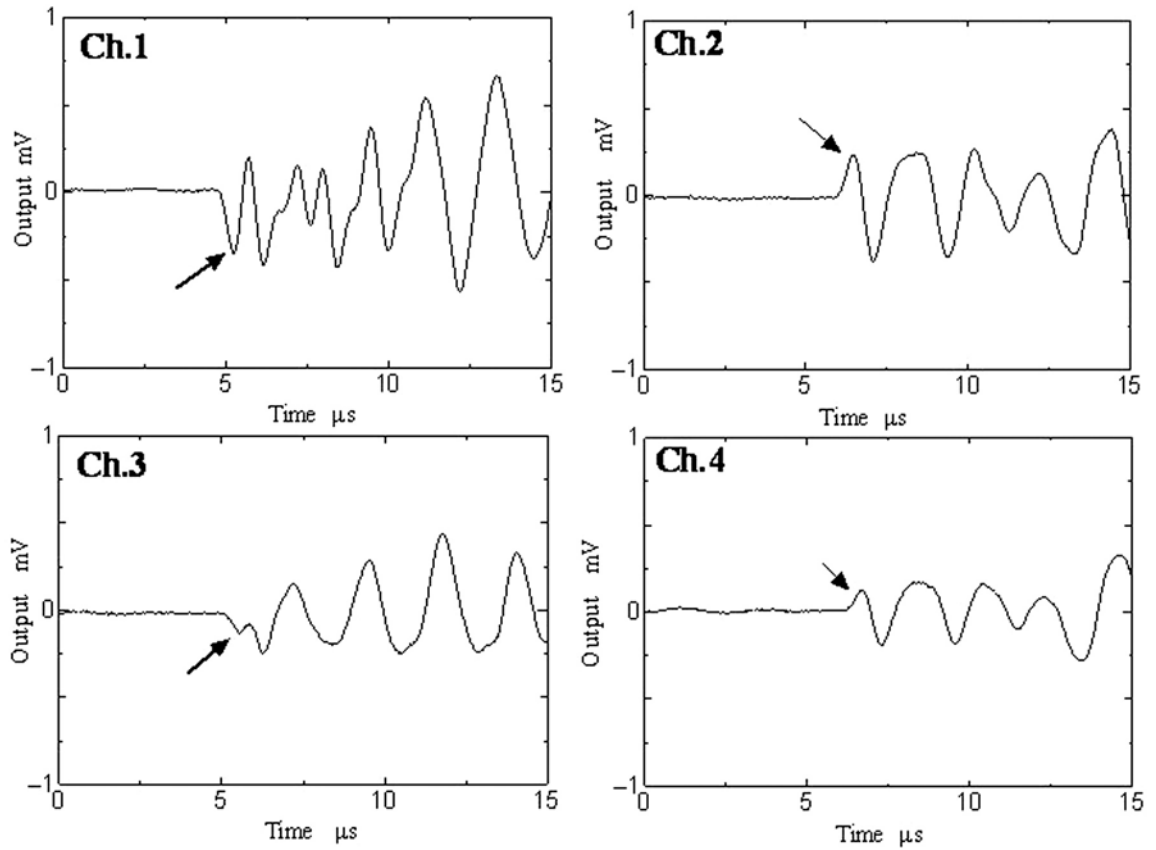


Fig. 7 Detected AE waveforms during cyclic ball indentation test (EC.3005, $N=9.7 \times 10^4$ cycles).

We analyzed AE waveforms to study the progression of fatigue damage. Figure 6 shows change of AE source locations estimated for AE events detected between $N = 8.9 \times 10^4$ and 10.1×10^4 cycles. It is noted that AE sources are located slightly ahead of the periphery of the white crack. Location of source moves away from the contact area with increasing N .

Next, we examined the fracture types based on the radiation pattern of longitudinal waves [5]. Figure 7 shows a set of AE waveforms. The polarity of the first arrival waves (marked by an arrow) from channel 1 and 3, mounted on the adjoining side surfaces, were negative while those from channel 2 and 4 are positive. This polarity distribution indicates shear or Mode-II type fracture [5]. The first-peak amplitudes of channel 1 and channel 2 were much larger than those of channel 3 and channel 4. This implies that the sliding vector of the lateral crack is in the direction connecting channels 1 and 2 (vertical in Fig. 1). This polarity distribution was observed for all AE events during the test. It is concluded that the AEs were produced by Mode-II lateral cracks. In contrast, we could not detect any AEs from Mode-I radial cracks, even though some of them were clearly visible. This is possibly due to small crack volumes of the radial cracks.

3.3 Mechanism of Lateral Cracks

We examine next lateral crack mechanisms, based on the experimental data and FEM for different size balls. Figure 8 shows the depth of the lateral crack initiation site, h_{lateral} as a function of ΔF . The h_{lateral} were determined by cross sectional observation. Symbols with downward arrows indicate no lateral crack initiation. All lateral cracks developed at $550 \mu\text{m}$ below the surface. This depth is independent of ΔF .

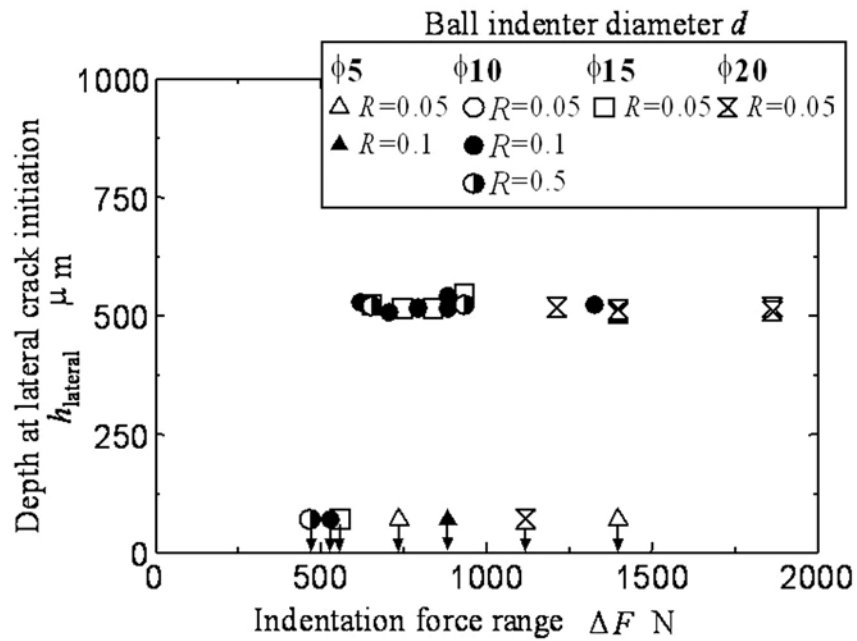


Fig. 8 Depth at lateral crack initiation $h_{lateral}$ as a function of indentation force range ΔF .

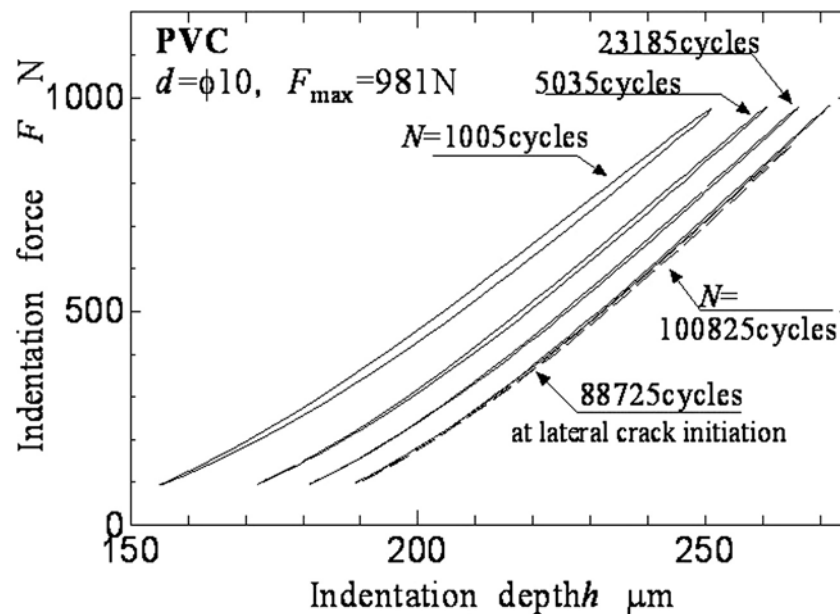


Fig. 9 F - h curve during the cyclic ball indentation test.

Figure 9 shows typical F vs. h curves of the specimen at pre-determined N values. Test condition is the same with that of Fig. 3. This revealed that the F vs. h curve differences between loading (upper curve) and unloading (lower curve) decreased with increasing N . The area surrounded by two curves represents the stored deformation energy (E_d) in a single loading cycle [6]. The E_d decreased with increasing N , as shown in Fig. 10, and decreased to a low, constant value beyond $N = 4.5 \times 10^4$ cycles. PVC produced permanent dent and deformed elastically after a large number of cyclic contacts.

Two-dimensional stress distribution under the contact area in the transverse section was calculated to study the driving force and depth of lateral cracks using finite element method (FEM)

with MARC (K7-2) and MENTAT II (V3.2.0). Two-dimensional FEM model with 1588 elements and 1645 nodes for a permanent dent is shown in Fig. 11. Diameter d of the permanent dent was given by the measured value after the test, and the permanent depth h was determined from $F-h$ curve in Fig. 11. Young's modulus $E = 3.78$ GPa and Poisson's ratio, $\nu = 0.36$ were used. We calculated the stress distribution using elastic contact analysis with $F_{\max} = 981$ N and $d = 10$ mm.

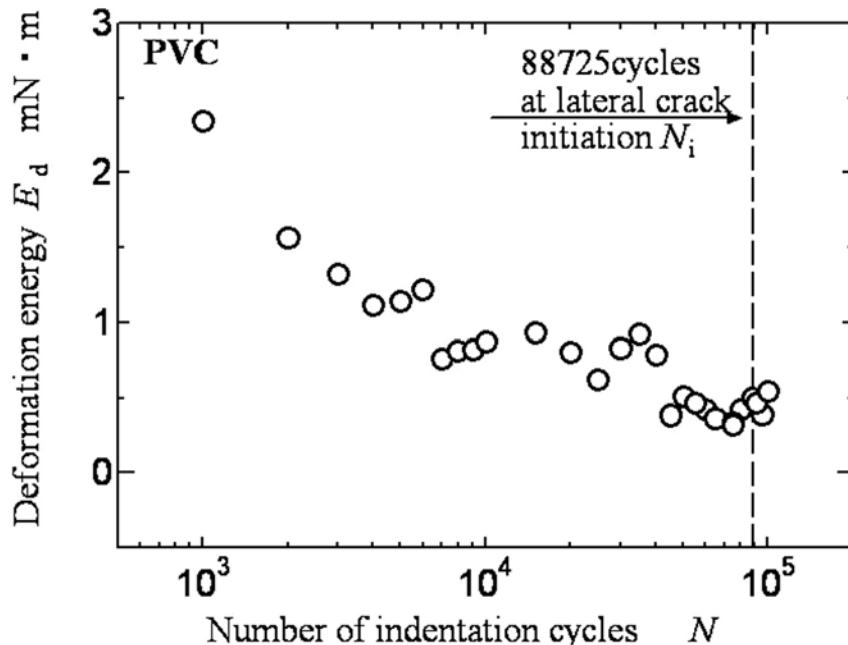


Fig. 10 $F-h$ curve during the cyclic ball indentation test.

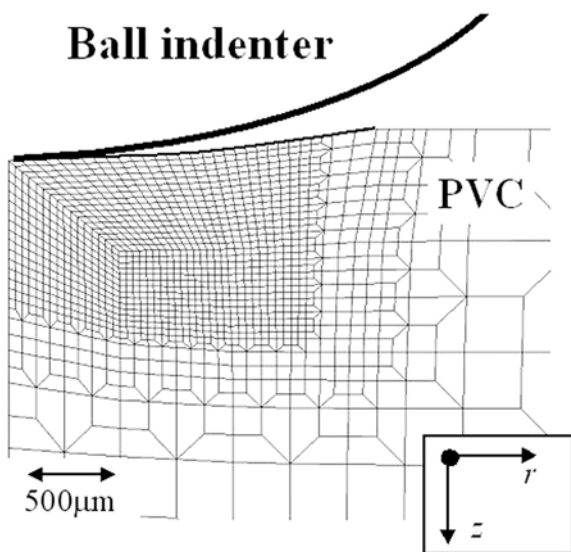


Fig. 11 FEM model for ball indentation test with $d = 10$ mm diameter.

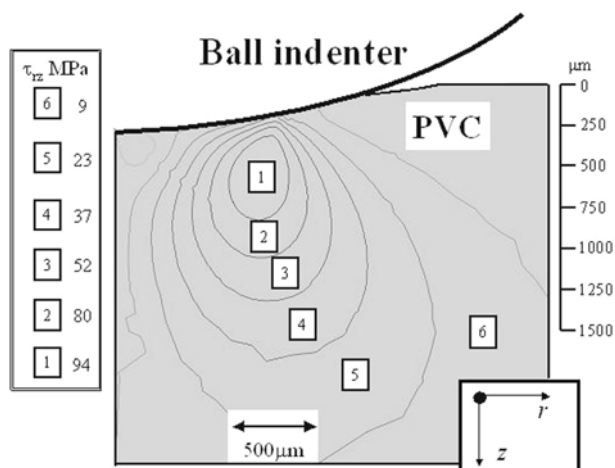


Fig. 12 Shear stress τ_{rz} with contours at $F_{\max} = 981$ N with $d = 10$ mm diameter.

Figure 12 represents the contour map of shear stress τ_{rz} at F_{\max} of 981 N during ball indentation test with $d = 10$ mm diameter. Maximum $\tau_{rz,\max}$ of 94.3 MPa is generated at the depth of 512

μm from the surface. This depth agrees quite well with the experimental depth of 516 μm in Fig. 8. It indicates that the lateral crack is produced at the depth of maximum shear stress.

6. Conclusions

Utilizing AE technique, we studied damage progressing in PVC (poly-vinyl-chloride) plastics subjected to cyclic ball indentation test. Results are summarized below.

1. In the test with maximum indentation force of 981 N and indenter diameter of 10 mm, sub-surface lateral crack initiated and grew with cyclic ball indentations. This crack was Mode II fracture and produced AE signals. Sources of these events were located ahead of growing lateral cracks. The lateral crack developed at 516 μm from the surface where the maximum shear stress is generated.
2. The depth of lateral crack initiation was observed to be about 500 μm and independent of indentation force, stress ratio and indenter diameter.

Acknowledgment

This work was performed as a part of the Center of Excellence (COE) Program, funded by the Ministry of Education, Culture, Sports, Science and Technology.

References

- 1) e.g. A. Otsuka, K. Togo, H. Ishida, S-K Yoo, M. Shibata: J. Soc. Mat. Sci. Japan **41**, 466, (1992) 1136 (in Japanese).
- 2) J. Uchida, T. Ogawa, M. Takemoto, Y. Kobayashi and Y. Harada: J. Material testing research, **49-3** (2004) 140 (in Japanese).
- 3) T. Bushimata, H. Sakuta, K. Shinohara and T. Endo: J. Eng. Design. **36-11** (2001) 485 (in Japanese).
- 4) A. Makabe, K. Yahuso, T. Suzuki and H. Yaryo: J. Soc. Mat. Sci. Japan, **50-12** (2001) 1311 (in Japanese).
- 5) M. Ohtsu: J. Soc. Mat. Sci. Japan, **32-356** (1982) 52 (in Japanese).
- 6) J.L. Loubet, J.M. Georges and G. Meille: Am. Soc. Test. Mater, **889** (1985), 72.

EVALUATION OF FATIGUE DAMAGE FOR FRM WITH AE METHOD

MASANORI TAKUMA and NOBORU SHINKE

Faculty of Engineering, Kansai University, Yamate, Suita, Osaka 564-8680, Japan.

Abstract

Composite materials have the merit that its structure can be designed in accordance with the functional requirement and are widely used as structural members. However, fatigue phenomenon cannot be avoided and mechanisms on the growth of fatigue damage are complicated. The fatigue damage becomes a serious problem in evaluating the reliability of structures. In this report, the parameters for evaluating the fatigue damage of fiber-reinforced metals (FRM) with AE method are proposed. Detected AE signals during fatigue testing were analyzed with weighted-mean-frequency distribution and wavelet transform methods. As the results, the possibility of evaluating the damage by the features of the frequency distribution graphs and the fractal dimension that represented the complexity of the time fluctuation of wavelet coefficient is shown.

Keywords: FRM, Fatigue damage, Weighted-mean-frequency distribution, Wavelet transform, Fractal theory

1. Introduction

The technology of the composite materials progressed from the development of fiber-reinforced plastics (FRP) to fiber-reinforced metals (FRM), by which the heat-resistance and the fatigue resistance, etc. were improved. The FRM materials are used as structural members under difficult environment and the excellent results are reported. However, it is necessary to establish the monitoring techniques, which can evaluate the fatigue damage. This is essential in order to avoid fatigue breakdown, which causes many of the accidents of the structures. In this study, the information processing techniques (i.e. the weighted-mean-frequency distribution, the wavelet transform and the fractal theory) were applied for analyzing the AE signals (cf. Fig. 1). The features of the frequency components for each fracture mode (i.e., the crack propagation of matrix and the breaking of reinforcement material, etc.) were extracted. After that, the database for evaluating the fatigue damage was constructed by using the features. The damage and the fracture mechanism of FRM are evaluated by comparing the features in the database with the features of the detected signals during the fatigue testing.

2. Analysis Methods of AE Signal

2.1 Weighted-Mean-Frequency Distribution (WMFD)

In the fatigue process of composite materials, extremely numerous AE events are detected and the complicated multiple fracture modes are included in an event. Therefore, it is difficult to judge which type the detected signal belongs to. For this reason, it is necessary to extract the features of the frequency distribution on the basis of the FFT analysis result. In this study, the weighted-mean-frequency distribution (WMFD) method [1] was employed for extracting the features of the distribution. The distribution graph by this method is obtained from the

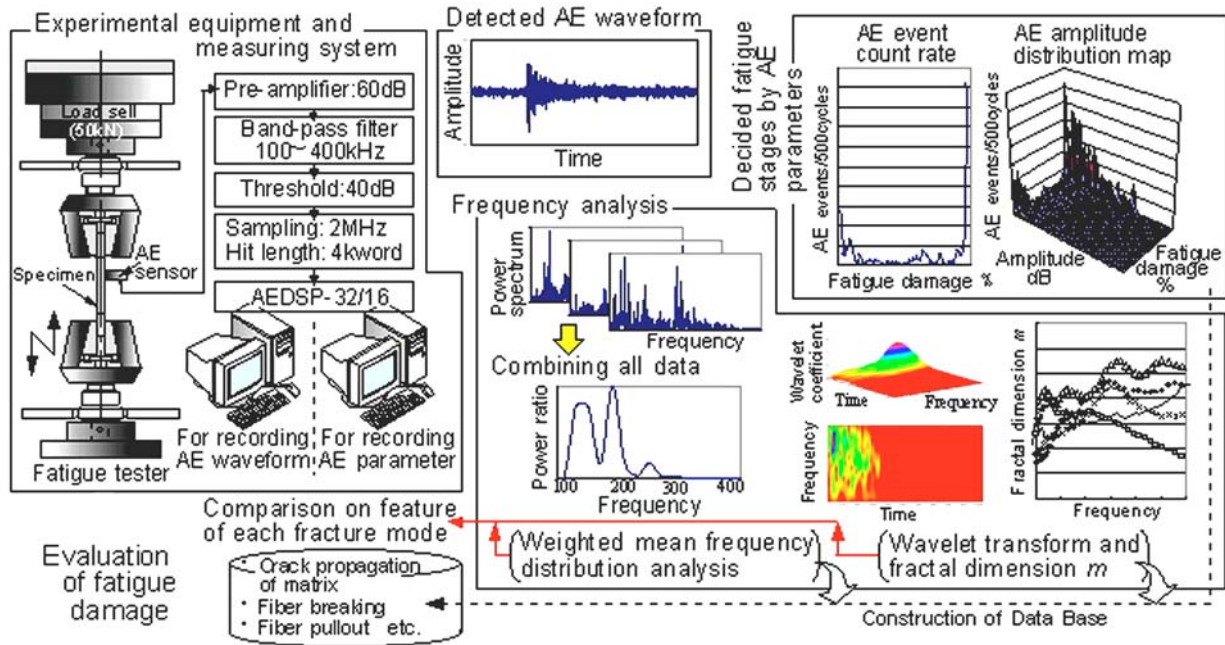


Fig. 1 Concept of this study.

following process: (1) FFT analysis result is divided by the mesh and each mesh is weighted. (2) A frequency distribution graph, in which many analysis results were combined, is shown by adding the weight at every mesh. By applying this method, it becomes possible that the growth of the damage is grasped from the change in the features of the graph in each fatigue stage.

2.2 Wavelet Transform (WT)

The frequency analysis results with FFT are effective for the identification and discrimination of the microscopic destruction factor, and FFT contributes to the solution of the fracture mechanism [2]. However, it is not suitable for the analysis of the signals, whose the statistical properties change with time [3]. Therefore, another method that transforms a signal into a time-frequency domain is needed for analyzing the non-stationary or transient signals such as AE.

Wavelet transform (WT) is one of the methods for supplementing the shortcoming of FFT. The WT of the signal $f(x)$ is defined by:

$$[WT f](a, b) = \int_{-\infty}^{\infty} \psi^*(x) f(x) dx \quad (1)$$

where ψ^* is the complex conjugate of the wavelet function $\psi_{a,b}(x)$. The function $\psi_{a,b}(x)$ is defined by $|a|^{-1/2} \psi((x - b)/a)$. The function $\psi_{a,b}(x)$ is the mother wavelet (e.g., Gabor wavelet) with the scale parameter a and the shift parameter b , and provides a set of localized functions in both frequency and time. The scale parameter a gives the width of window and consequently frequency as the mother wavelet is expanded or compressed in time. The shift parameter b determines the position of the window in the time, and thus defines that which part of the signal $f(x)$ is being analyzed. Therefore, it is possible to make the optional wavelet of the angular frequency w_0/a in time b by changing the both parameters, and the optional function is represented by putting the various optional wavelets together (cf. Fig. 2). The wavelet

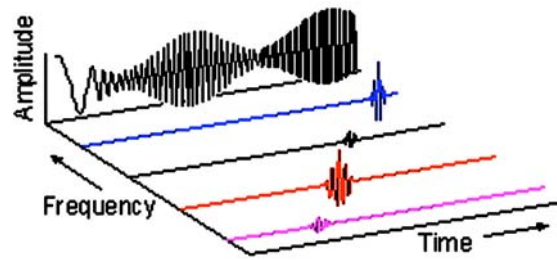


Fig. 2 Wavelets in time-frequency plane.

coefficient increases, if $\psi((x - b)/a)$ resembles $f(x)$, and the intensity is correspondent to the amplitude of $f(x)$ [4]. Therefore, the coefficient shows the activity of the component with the frequency ω_0/a in time b . This becomes effective for the analysis of the AE signals, in which sudden fluctuations and many phenomena are mixed, when the transform result is represented on the plane of b and $1/a$. However, the evaluation method of the result is not established yet. Therefore, it is possible to contribute to the grasp of the fracture phenomena and the evaluation of fatigue damage if the features (i.e., the complexity of the time fluctuation waveform of the wavelet coefficient in each frequency component) of the WT result can be evaluated quantitatively. This is very important for grasping each fracture mode by the features of the analysis result. Thus, the fractal dimension that is employed when the various shapes and the phenomena in the nature are quantitatively classified was applied for extracting the features of WT result. This time, the dimension of time fluctuation waveform of wavelet coefficient in each frequency component was found with Box-counting method [5] (cf. Fig. 3).

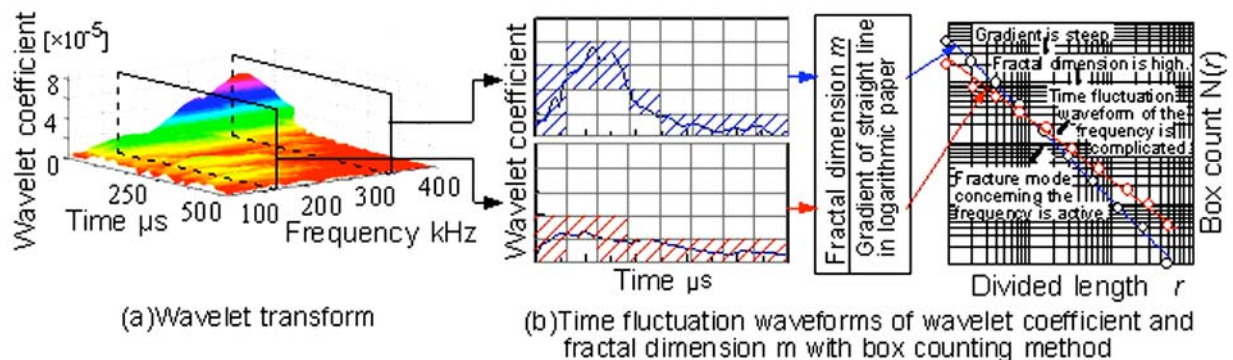


Fig. 3 Fractal analysis in this study.

3. Specimens and Experimental Methods

Figure 4 shows the dimensions of the specimens and material details. The fatigue test was carried out under the load control (i.e. the stress amplitude (σ_a) 52 MPa, the loading frequency = 2 Hz and the stress ratio $R \approx 0$). The emitted signals from the specimen were detected by a wideband AE sensor (NF 900S-WB) and they were recorded on two computers using Mistras system (cf. Fig. 1). The following experiments and data analyses were carried out in order to elucidate the fracture mechanism and to evaluate the fatigue damage from the detected signals.

(a) Features of AE signals on the damage (i.e. the crack propagation of matrix and the fiber breaking, etc.) were extracted from the two testing that were the fatigue test of aluminum alloy and the tensile test of carbon fiber. The database for evaluating the damage was structured by using the features.

(b) By comparing the features in the database with the detected AE signals during the fatigue testing of FRM, the elucidation of fracture mechanism and the evaluation of fatigue damage are carried out.

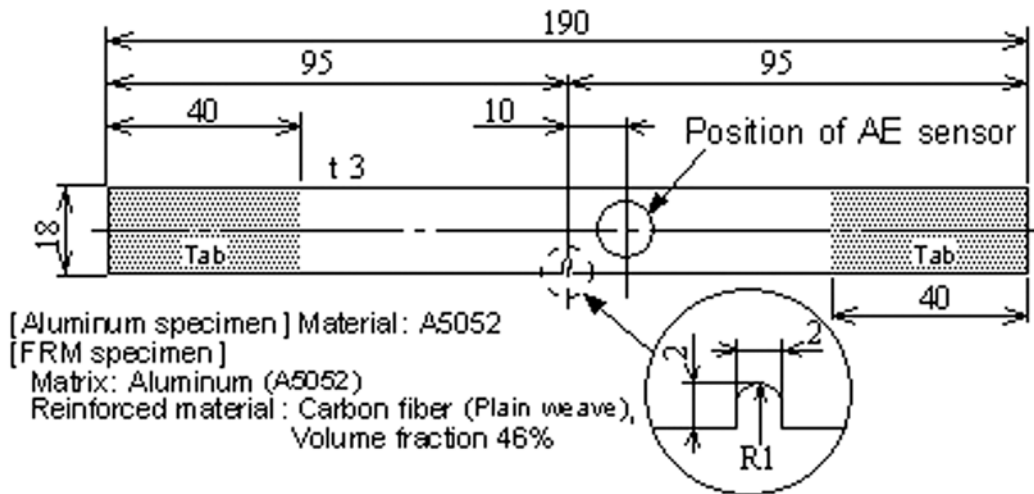


Fig. 4 Dimensions of specimen and material details.

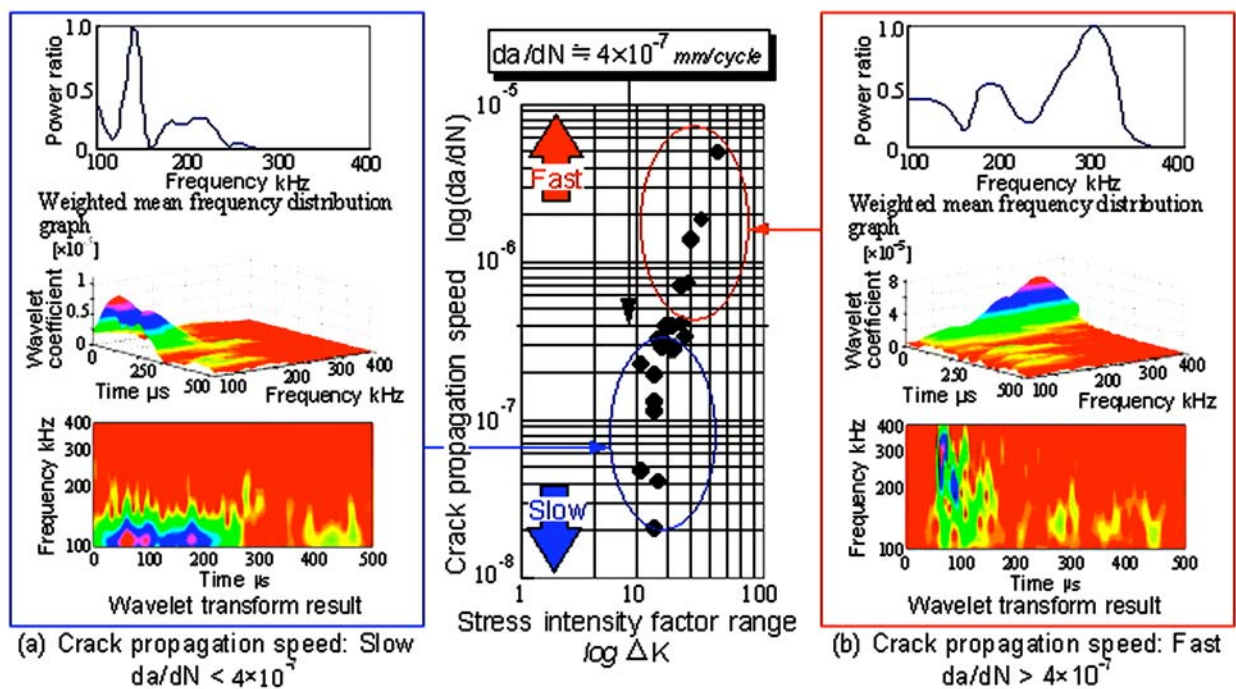


Fig. 5 Frequency distributions in relationship between stress intensity factor range (ΔK) and crack propagation rate (da/dN) in fatigue process of matrix (i.e., aluminum).

4. Experimental Results and Discussion

4.1 Features of AE signals of matrix and fiber

Figure 5 shows the result of the fatigue test for the matrix (i.e., the aluminum alloy: A5052). In this figure, the analysis results (i.e., the WMFD and WT) of the AE signals are superimposed on the relationship between the crack propagation rate da/dN and the stress intensity factor

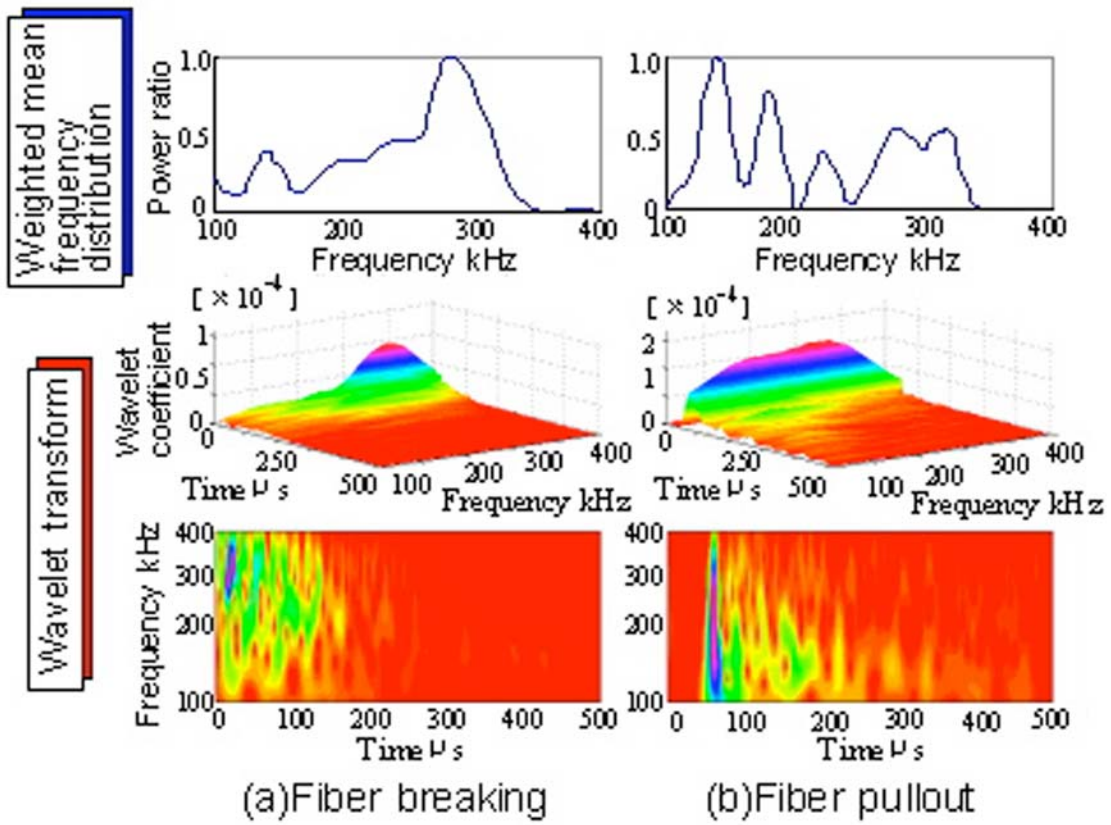


Fig. 6 Typical frequency distribution of fiber breaking and fiber pullout.

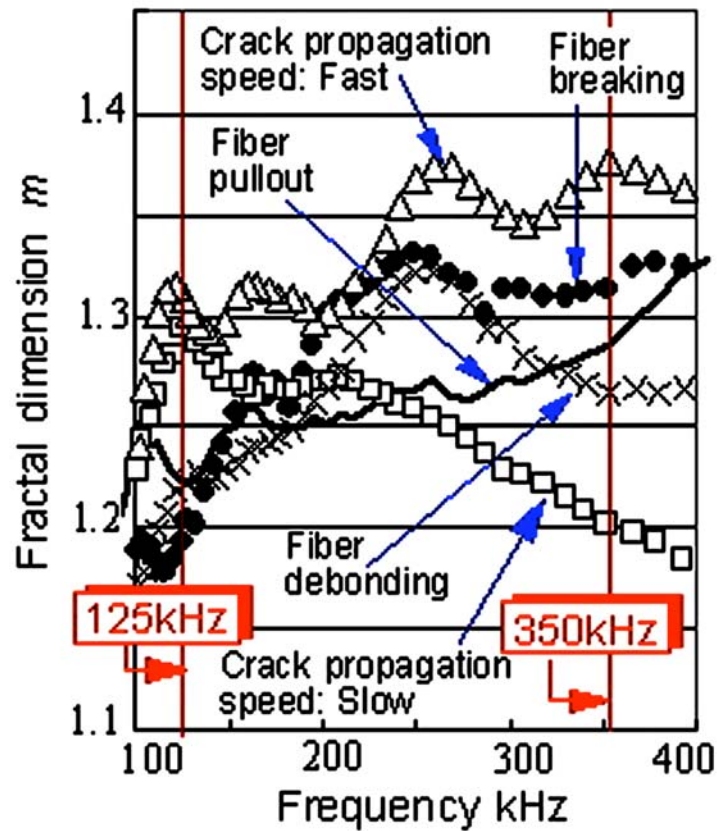


Fig. 7 Typical fractal dimension m for each fracture mode.

range ΔK . From this result, it is understood that the features of the frequency distribution of the signals depend on the rate da/dN . In short, though the frequency components 100 to 150 kHz are active when da/dN is slower than 4×10^{-7} mm/cycle, the components over 300 kHz are active when da/dN is faster than 4×10^{-7} mm/cycle. Therefore, it is possible to discriminate the difference of the rate da/dN . However, it is difficult that each fracture mode is discriminated with the WMFD when we considered Fig. 6 that shows the analysis results on the fiber pullout and the fiber breaking because the frequency component of the fiber pullout is 100 to 150 kHz and the component of the fiber breaking is near 300 kHz. Thus, the application of the fractal dimension m of time fluctuation waveform of wavelet coefficient in each frequency was tried for extracting the features of each fracture mode. The results are shown in Fig. 7 and the following can be considered from the figure.

Table 1 Frequency components on each fracture mode of specimen.

Fracture mode \ Feature	Peak of weight mean frequency distribution graph	Fractal dimension m of time fluctuation of wavelet coefficient	
		350kHz	125kHz
Crack propagation speed of aluminum: Fast	250~300kHz	1.34~1.40	Nearly 1.30
Crack propagation speed of aluminum: Slow	100~150kHz	1.20~1.25	
Fiber breaking	270~390kHz	1.29~1.33	Nearly 1.20
Fiber pullout	120~150kHz	1.27~1.29	
Fiber debonding	180~240kHz	1.23~1.27	

(1) The fluctuations of the dimension m of each frequency for the fiber pullout and the fiber breaking are comparatively smaller than the fluctuations of the crack propagation of the matrix.

(2) The dimension m around 100 kHz is high when the propagation rate da/dN of the matrix is slow, and the dimension m of 250 to 300 kHz rapidly increases when the rate da/dN is fast.

(3) By using WT, it became possible to discriminate the differences of each fracture mode, in which it is difficult to discriminate the mode with the WMFD. One is the discrimination between the fiber breaking and the fast crack propagation, and the other is the discrimination between the fiber pullout and the slow crack propagation. The dimension m of 125 and 350 kHz were noticed because the difference between two dimensions is large.

The obtained dimension m for discriminating each mode by the consideration of the above is shown in Table 1.

4.2 Relationship between Fracture Modes and Fatigue Damage

From the results (i.e. the AE event rates, the AE amplitude distribution and the crack initiation point) of the fatigue test of FRM specimen, the fatigue phenomena were divided in 4 stages as shown in Fig. 8. These stages are the early stage (i.e. the range of many AE events right after the test starts), the middle stage (i.e., the stable range of the event rates until crack initiation point), the late stage (i.e., the crack propagation range) and the stage before fracture

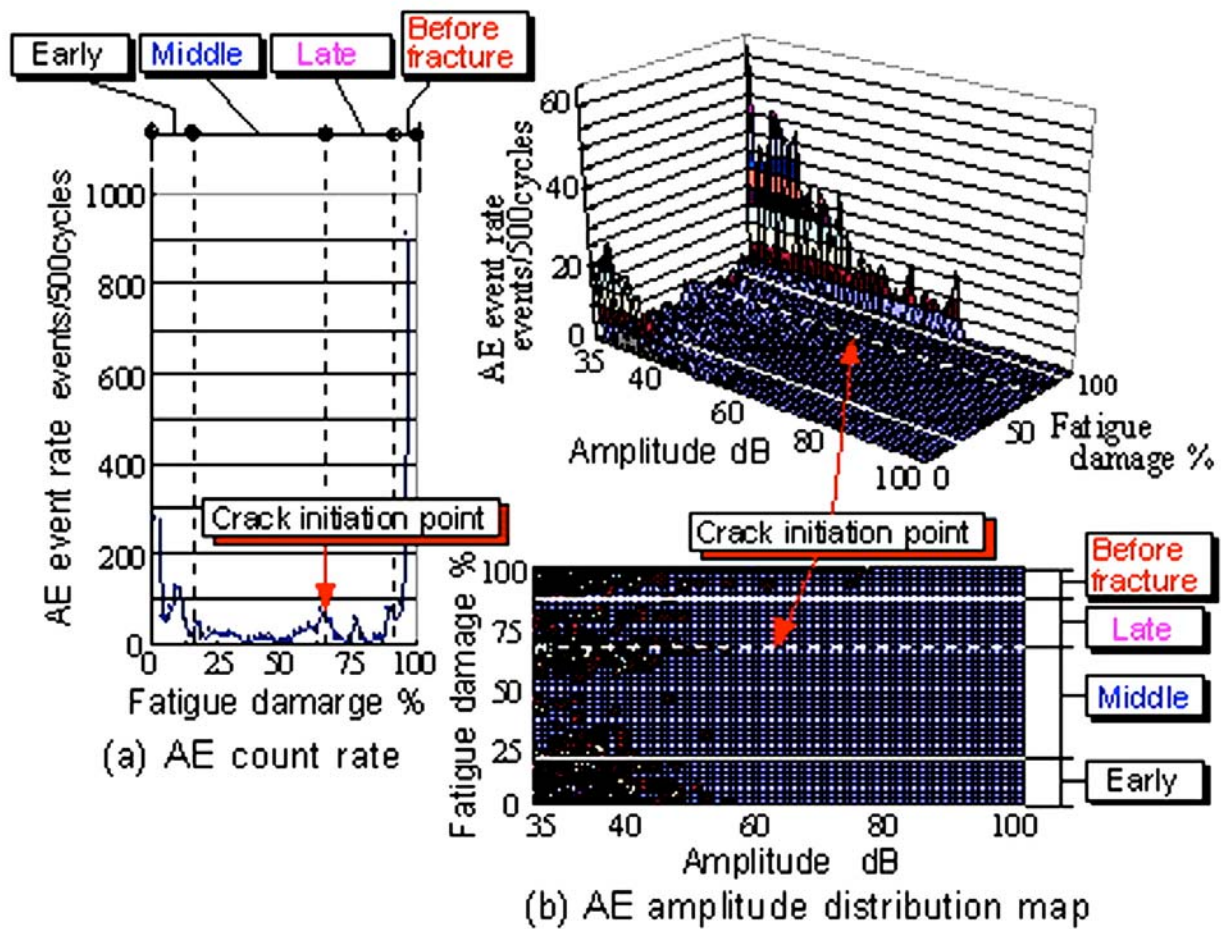


Fig. 8 Fatigue phenomena divided into 4 stages by AE counts and amplitude distribution.

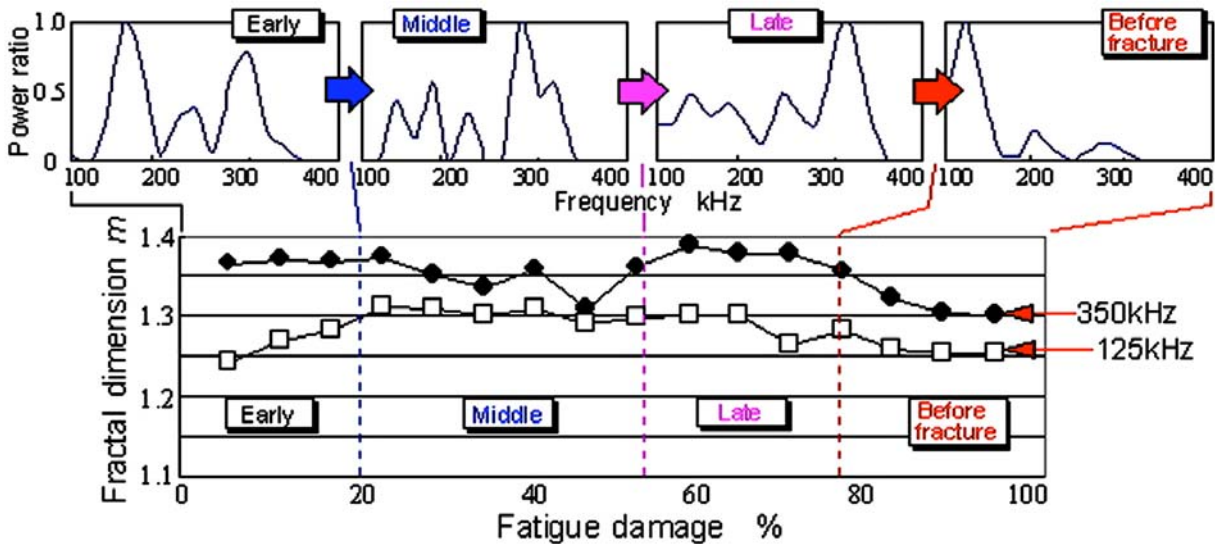


Fig. 9 WMFD graphs and fractal dimension m on the time fluctuation of wavelet coefficient at 125 and 350 kHz in each fatigue stage.

(i.e., the range of many AE events again), respectively. The feature extraction in each stage was tried by considering the results of the WMFD graphs, the behavior of the fractal dimension m on the time fluctuation of wavelet coefficient and Table 1.

Figure 9 shows the relationship between the analysis results (i.e. the WMFD graphs and the behavior of the fractal dimension m) and the fatigue damage %. As the results, the following became clear.

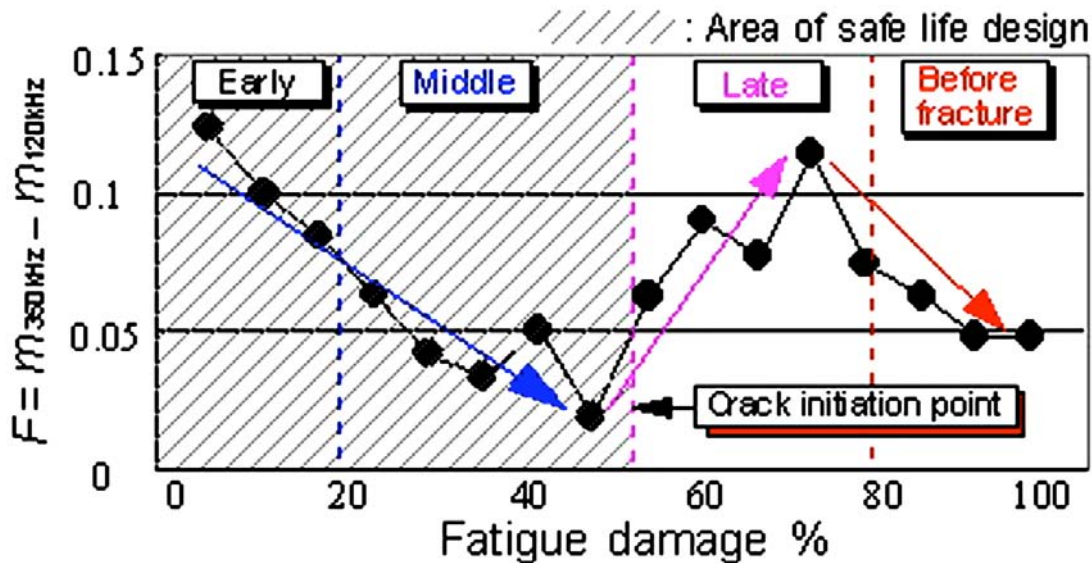


Fig. 10 An example on evaluation of fatigue damage.

Early stage: From the result of the WMFD graph, it is clear that the activities of the frequency components 150, 250 and 300 kHz are high. Since the dimension m at 125 and 350 kHz shows 1.25 and 1.35, respectively, it appears that the fiber pullout and the fiber breaks are taking place. It is also likely that many causes of the fatigue fracture intermingle in an AE signal and many signals are emitted from the stress concentration zones of the defects inside the specimen.

Middle stage: In addition to the activity of 300 kHz, the activities of 120 to 200 kHz are strong. The fractal dimension m of 350 kHz is higher than that of 125 kHz. However, the dimension m of 125 kHz shows the increasing tendency, while the dimension m of 350 kHz gradually decreased from 1.35. From these, it seems that the activity of the fiber breaks gradually decreases, and the activity of the matrix damage increases. Therefore, even if the crack is not found on the surface of the specimen, it is likely that the main fracture mode inside is changed from the fiber breaks to the matrix damage.

Late stage: The dimension m comes to show the high value beyond 1.35 and the occurrence ratio of 300 kHz increase. From this, it can be judged that the main factor in this stage is the rapid crack propagation.

Before fracture: The main frequency component of the detected signals is near 100 kHz, and the dimension m of 125 and 350 kHz is converged to 1.25 and 1.30, respectively. In this stage, it is the high possibility that the main factor of the fatigue phenomenon is not the crack propagation of matrix but the fiber pullout if the rate of crack propagation was high in the last stage. From the above, it can be predicted that the fatigue process approaches the end when the dimension m rapidly decreases.

4.3 Application to Evaluation of Fatigue Damage

In order to find a parameter that describes the relationship between the behavior of the dimension m and the fatigue damage, we defined the parameter F as follows;

$$F = m_{350\text{kHz}} - m_{125\text{kHz}} \quad (2)$$

Here $m_{350\text{kHz}}$ and $m_{125\text{kHz}}$ is the fractal dimension of 350 and 125 kHz, respectively. Figure 10 shows an example of the evaluation on fatigue damage by the parameter F . From this result, it can be seen that the parameter F appears to show different stages of the fatigue damage.

5. Conclusion

Composite materials have the merit in fulfilling its structural design requirement with comparative ease. However, the fracture mechanism and the fatigue damage of the materials are complicated. Therefore, the establishment of the technique, which evaluates the reliability and the safety of the structure materials, is desired. The following became clear from the experiments for establishing the evaluation technique of the fatigue damage of FRM with AE method.

(1) The WMFD is possible to grasp the features on the frequency distributions of the detected AE signals from the fracture phenomena.

(2) Fractal property was recognized in the time fluctuation waveform of wavelet coefficient in each frequency component after the WT of the signals. The possibility of evaluating the fracture mode and the fatigue damage by the dimension m is shown.

(3) By the frequency analysis of AE signals, it is possible to relate matrix damage by the fracture of the reinforced fiber with the final fatigue fracture.

Acknowledgment

The authors are grateful for valuable assistance of Yoichiro Koyama of Kansai University. This research was supported by a grant from Life Cycle Engineering Working Group in ORDIST (Organization for Research and Development of Innovative Science and Technology) of Kansai University.

References

- 1) T. Asano and S. Somiya: Prepr. of Jpn. Soc. Mech. Eng., (1994), 74.
- 2) Y. Ichida, K. Kishi and Y. Hasuda: J. Jpn. Soc. Prec. Eng., **58**(5) (1992), 841.
- 3) Q.Q. Ni, Y. Misada, K. Kurashiki and M. Iwamoto: *Proc. National Conference of AE*, (1997), p. 173.
- 4) H. Inoue: J. Soc. Mat. Sci., **45** 2(1996), 1353.
- 5) M. Kurose, M. Tsuda, T. Sasaki, Y. Hirose, Y. Yoshioka: J. Soc. Mat. Sci., **43**(1) (1994), 1489.

ACOUSTIC EMISSION BEHAVIOR OF FAILURE PROCESSES OF GLASS-FIBER LAMINATES UNDER COMPLEX STATE OF LOADING

JERZY SCHMIDT¹, IRENEUSZ BARAN¹ and KANJI ONO²

¹) Foundry Research Institute, Laboratory of Applied Research
30-418 Kraków, ul. Zakopianska 73, Poland.

²) MSE Department, University of California, Los Angeles, CA 90095 USA.

Abstract

The strength of laminates made from glass fiber fabric with epoxy resin matrix was determined. The studies were carried out on two laminates with different resin types. The measurements were taken on pipe samples subjected to uniaxial and biaxial loading at three different temperatures. The process of crack formation was examined by acoustic emission (AE). For this purpose, a multi-parameter analysis of AE signals was applied. It was observed that the type of resin used for the laminate matrix had a significant effect on crack development, while it had no effect on the laminate strength. The laminates were noted to have similar strength under both uniaxial and biaxial state of stress. The application of AE enabled determination of the onset of laminate failure. The analysis of the failure process used the pattern recognition classification with Visual Class program. A classification tool was designed and constructed; it bore the features common to all the tests. Using this tool, the mechanisms of failure prevailing in the loading process were determined along with their intensity and range within which they may have some impact on the laminate failure process.

Keywords: Glass fiber fabric, Laminate composites, Failure processes

1. Introduction

The aim of this study is to determine the laminate strength under the conditions of uniaxial and biaxial loading and to evaluate the effects of laminate matrix on the failure processes with acoustic emission (AE). It is well recognized that AE is valuable in evaluating failure of composite pipes [1], but AE experiments during biaxial loading of composites have been limited [2,3] requiring further research.

Since we need an analysis on the failure processes occurring during the loading of a sample, we employed the AE technique. As the examined materials are used in civil aviation, we tested the strength of the composite laminates at temperatures of 20°C, 54°C and 72°C, as commonly applied in this technology. Analyzing the work of Owen and Griffith [4], confirming a significant and negative impact of the edge effect on laminate strength, pipe-shaped samples were proposed for use here. Laminates were composed of nine layers of Interglass fabric wetted with two types of epoxy resin, viz. Ep53 and L285. The internal diameter of pipes was 50 mm, the wall thickness 2.5 mm, while their length was 300 mm, cut from longer pipes. The samples wetted with

resin were wound on mandrill and hardened at 20°C for 12 h and at 60°C for 8 h. Additionally, the samples for tests at 72°C were hardened at 80°C for 8h.

For the measurement of acoustic emission a special device is required to eliminate the generation of acoustic signals from a sample holder. It is also indispensable to ensure a constant rate of the load increment because of its possible effect on the composite strength. In view of these requirements, a special measuring system was designed utilizing a numerical control system operating in the Schenck PSB100 testing machine. A pressure generator installed on this machine enabled loading of samples with internal pressure at a constant rate of pressurization using a synthetic oil medium. The sample was placed in a thermostat filled with synthetic oil, providing temperature control at an accuracy of $\pm 1^\circ\text{C}$. Pressure was controlled by two pressure gauges made by Hottinger. Two types of clamps were used on the samples, thus producing two states of stress. In the first case, the clamp was put on the sample ends and it produced in the walls of a sample a biaxial state of stress with the hoop (circumferential)-to-axial stress ratio equal to $\sigma_1/\sigma_2=2$ (Mode II loading). In the second case the sample was free to move on its axis, thus producing zero axial stress $\sigma_2=0$ (Mode III loading)[3].

The values of acoustic emission parameters measured during loading were recorded by PAC MISTRAS-2001 and Vallen AMSY-5 systems. The AE signals were detected by two wideband (WD) sensors made by PAC. The frequency range was 100-1000 kHz. The recorded AE signals were next subjected to numerical analysis with Mistras software and exported to Visual Class analysis. In the case of AMSY-5 system, the Visual AE and Visual Class programs were used.

2. Testing of Laminate Strength

Comparing the results of tests conducted under uniaxial (Mode III) and biaxial (Mode II) loading, one can observe little effect of the second component of the state of stress on the laminate strength (Fig. 1). These results confirm the difficulties in the choice of relevant criteria, which could be used in evaluation of the laminate failure [5]. The difficulties in finding proper criteria of the laminate failure behavior were also noted by Owen and Griffith [3]. Only subjective evaluation of the experimental results could enable their comparison with the computed results based on selected criteria of failure. For laminates examined in this study and positive components of the state of stress, the most sensitive seems to be the criterion of maximal stresses.

Results indicate insignificant effects of hardening temperature on the strength of both laminates, although laminates hardened at 80°C have slightly higher strength. The test temperature generally decreases the strength of samples. The drop was highest for 80°C-cured Ep53 matrix. An exception is at 54°C, L285 epoxy matrix retained the same strength. The effect of resin type on the laminate strength is negligible under some conditions, and both resins give composites of strength within 20% at all temperatures.

The examined laminates are characterized AE event counts recorded during the loading. As shown in the lower graphs of Fig. 1, L285 epoxy matrix produced 5 to 20 times higher counts than the corresponding Ep53 matrix laminates. The differences are evident regardless of curing or test temperature used and suggest that failure of these two laminates proceeds by different

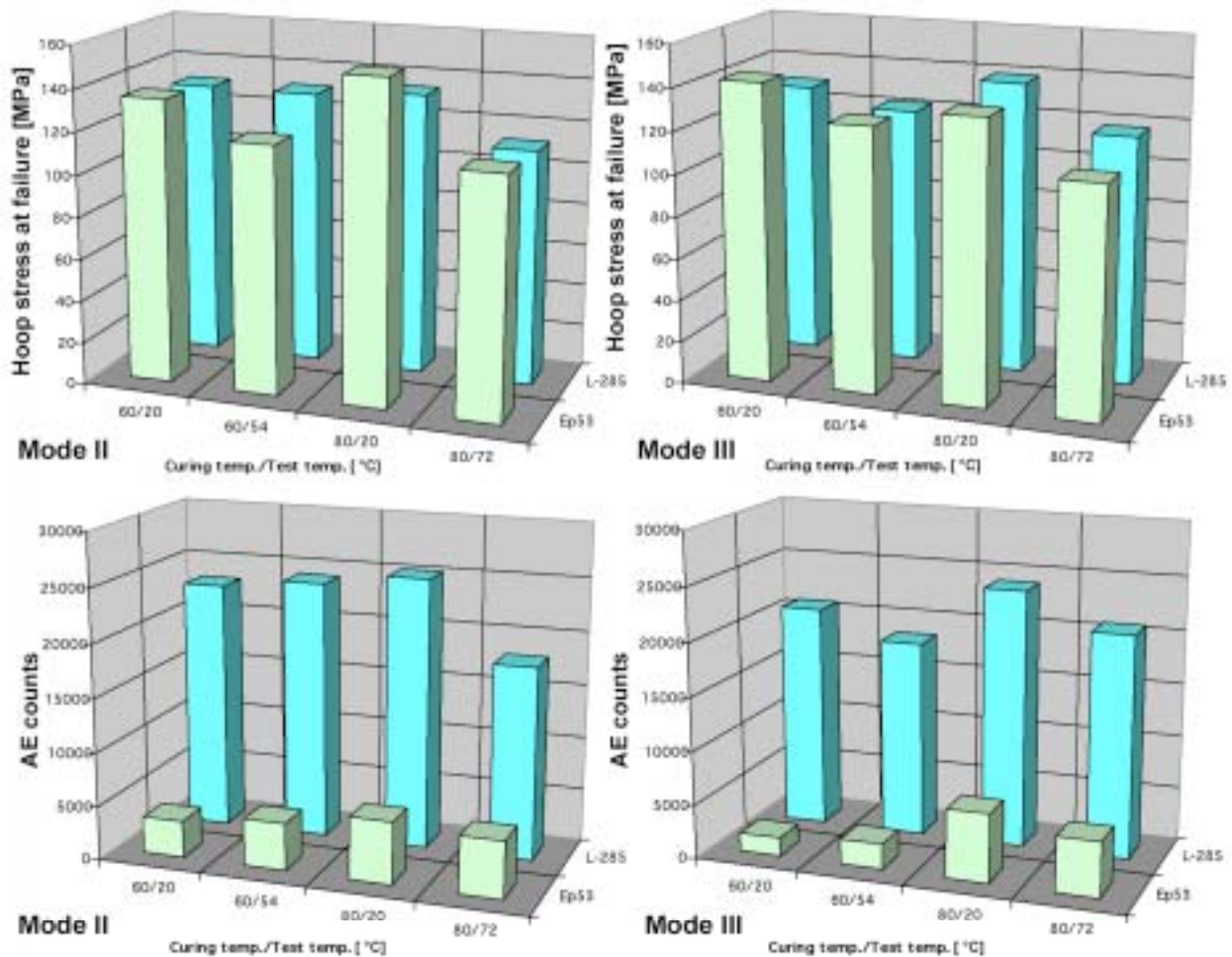


Fig. 1. Statistical result of strength and AE events of pipe specimens for resins EP53 and L285. Loading mode II (left figures) and mode III (right) are shown. Two cure temperatures (60 and 80°C) were used. Test temperatures were 20, 54 and 72°C as indicated.

mechanisms. Mode II of loading renders more AE events than Mode III, although the difference is not drastic as one may expect from the change from uniaxial to biaxial loading. Figure 2 shows this difference clearly; in L285 matrix laminates, AE event rates are nearly constant throughout the loading and the cumulative plot shows a linear increase. In Ep53 matrix laminate, AE activities show distinct peak just before failure and the summed curve illustrates increased slope toward the end of loading.

The test temperature had some effects on the strength of the examined laminates. Cumulative AE events similarly had relatively minor changes with both matrix resins in Mode II tests. For the Ep53 resin under Mode III, however, AE events varied several times between two cure temperatures (60 and 80°C) as indicated in Fig. 1. With increased test temperatures, differences in AE event rates are also observed (see Fig. 3). AE event rates increased just before failure in Ep53 resin laminates regardless of test temperature (Fig. 2). This suggests in L285 a greater number of microcracks form preceding the failure of sample and the greater activity due to debonding process of the matrix and glass fiber fabric, while Ep53 has most damage just prior to failure.

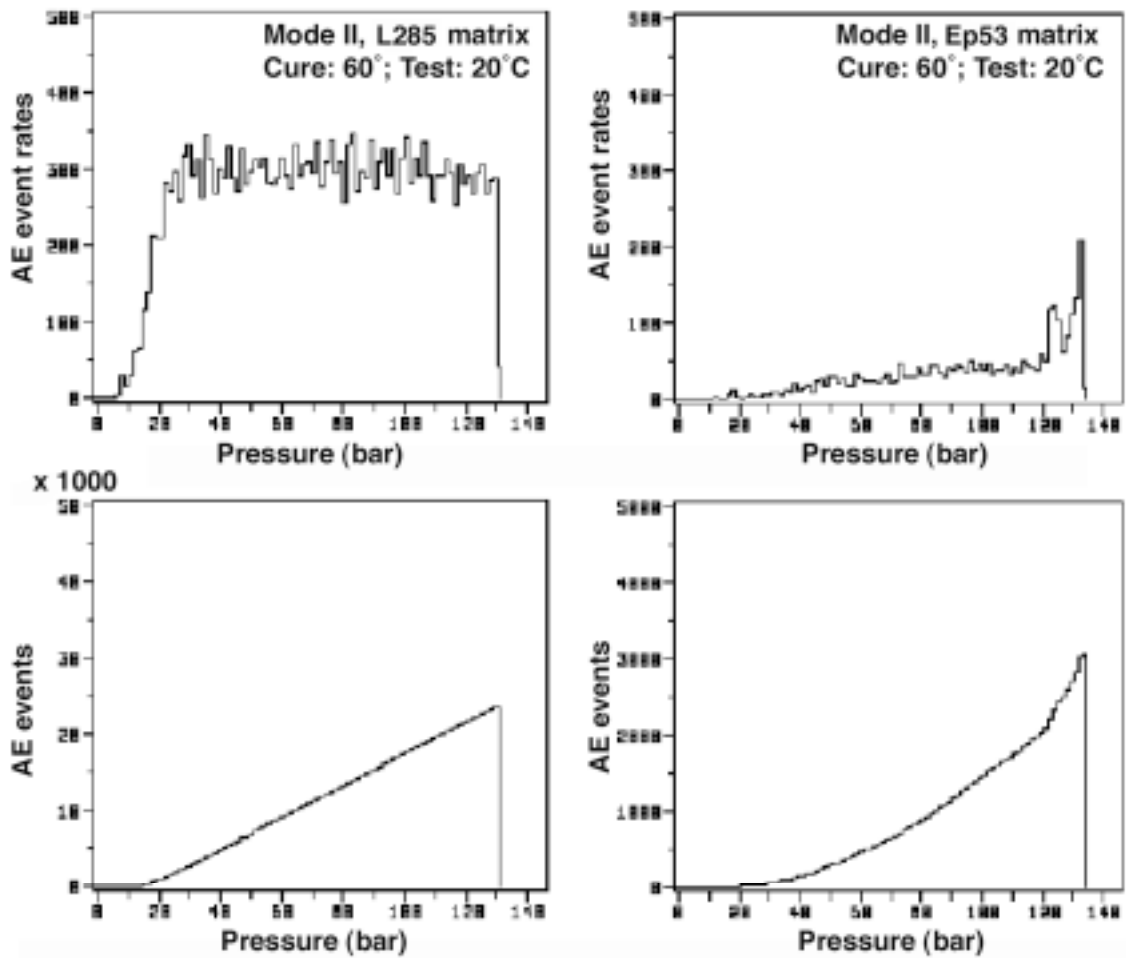


Fig. 2. AE activity and AE summation during loading (Mode II) for L285 and Ep53.

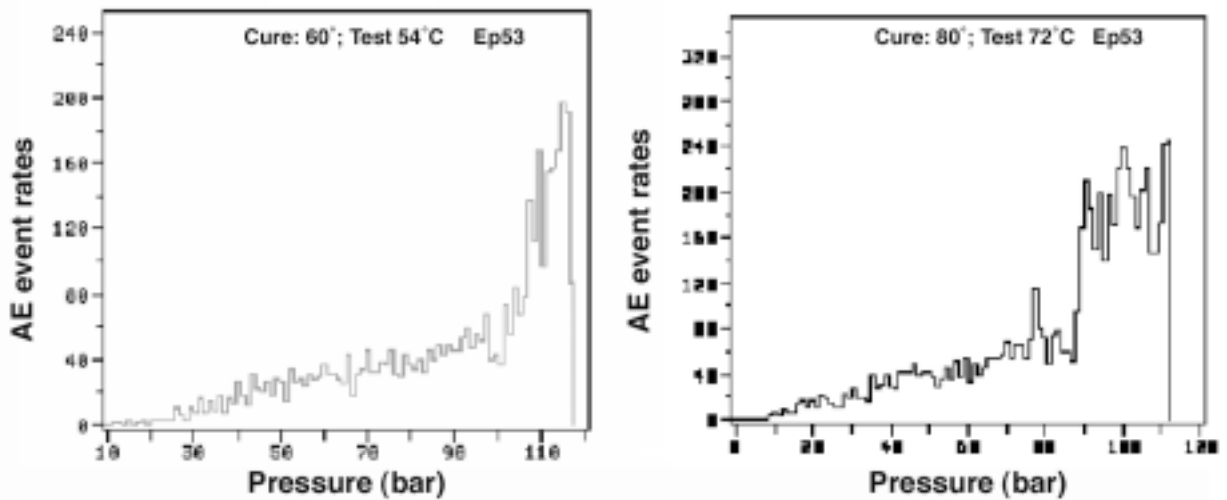


Fig. 3. AE event rates during loading (Mode II) for EP53 at different cure and test temperatures.

The AE signals recorded during the test were subjected to a multi-parameter analysis, computing the total of AE signals count, the total of AE events, mean time of AE signals duration, energy of AE events, and mean effective voltage.

The AE signals indicating the onset of failure appears at a low loading stage. In the case of Ep53 resin laminate, cracks start appearing at ~20% of the failure pressure for mode Mode II loading and at 30% failure pressure for Mode III loading. For laminate containing L285 resin, the onset of failure was recorded at still lower pressure, viz. ~15% failure pressure for mode Mode II and ~20% failure pressure for mode Mode III.

3. ANALYSIS of the LAMINATE FAILURE PROCESS

The results obtained here indicate the possibility of using AE in practical evaluation of the resin and laminate failure process. In order to provide robust and efficient evaluation technique, we developed a method of pattern recognition classification by using the Vallen Visual Class program. Because of the signal recording technique adopted by PAC Mistras system, which was different from AMSY-5 and used in the beginning to obtain AE data, some additional steps were needed to use the Visual Class program in a most effective way. At later stages, AE signals in the process of laminate failure were recorded via an AMSY-5 system.

Having noted certain similarities in the failure behavior of samples of each type of the laminate, it was considered to be both sufficient and representative to analyze using the reference pattern for classification with samples tested at 20°C. Since it was necessary to provide high clarity of the recorded signals, we selected for analysis the measuring data covering the load range from 10% to 95%. The classification proceeded according to the previously adopted work organization schedule as follow:

1. The analysis was conducted separately at the beginning, making classification for each resin type and mode of loading,
2. Within the obtained group of classes, the classes with similar features were combined into one whole set, thus obtaining one single class,
3. After accumulation of the source classes (groups of signals) a classifying tool with features common to the entire conducted studies was obtained.

Four classes (designated by the numbers from 1 to 4) prevailing in the process of laminate samples loading were thus obtained.

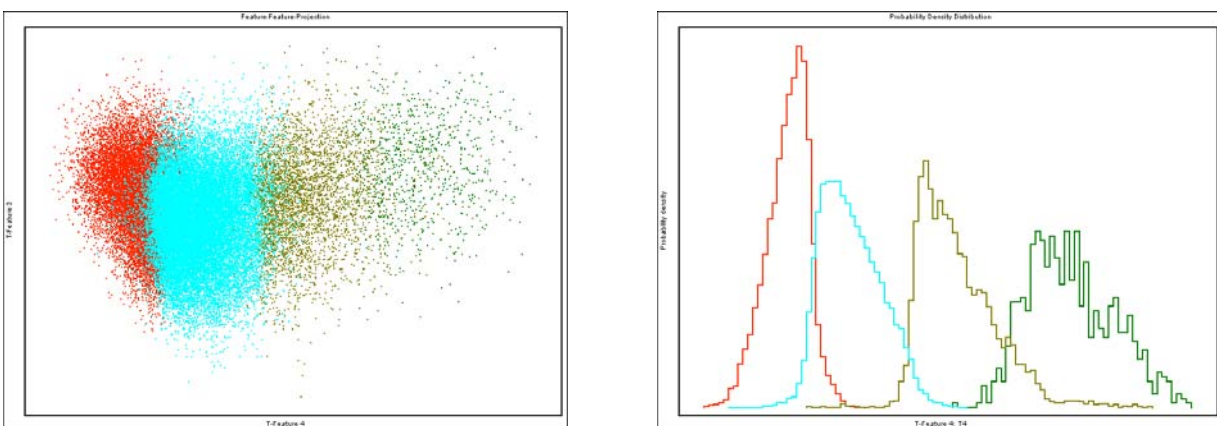


Fig. 4. Statistical results of separation of prototype classes.

The correct nature of the applied procedure has been proved in a graphic form as an image of the classification features division (Fig. 4). Classification thus developed was used in the analysis of crack propagation during loading of the tested pipe-shaped laminate samples. The results of analysis expressed as a share of each class in the loading process of samples prepared from both laminates and tested by two modes of loading were plotted in the form of bar diagrams (Fig. 5). The height of bars stands for a percent share of each class in the full process of sample loading.

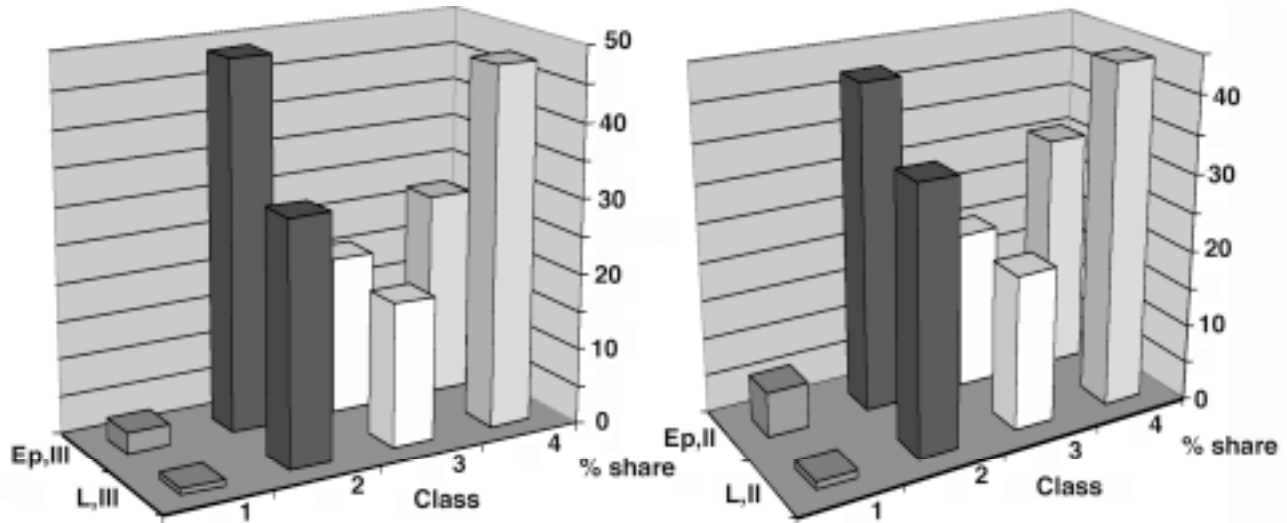


Fig. 5. Percent share of separated class for Mode II and Mode III with two types of resin.

In recording of AE signals, the threshold level of 46 dB (re. 1 $\mu\text{V}/0$ dB) for discrimination was applied. The reason was accumulation of too many signals generated below this level and caused by the laminate structure as well as a large volume of the laminate subjected to deformation. An output has been restricted in the loading process analysis for the amount of class 2 events, which occurs below the threshold of 46 dB.

Knowing the typical features of AE signals corresponding to each class enabled ascribing to each class the prevailing mechanisms of failure active during sample loading. To this purpose some published results of the experiments and simulation works made for the glass fabric reinforced resin-based composites were used [6,7]. In this case, the most important features of AE signals are expressed by the values of signals amplitude, frequency, and intensity. Using the available information on a relationship between AE parameters and failure mechanism as well as the data obtained in experimental analysis and in analysis of the classification effectiveness, the prevailing mechanisms corresponding to each class were determined.

- Class 1 fiber breakage
- Class 2 matrix microcracking + propagation
- Class 3 fiber/matrix friction + fiber/matrix debonding
- Class 4 matrix friction + fiber/matrix debonding

Using the developed classification tool in practice, the zones of occurrence of all the classes described by different selected AE parameters were determined in the tested samples during the laminate stress increase (Fig. 6). The determination of such zones enables us to separate the

occurrence of individual mechanisms of failure in the process of sample destruction. The zones determined for Mode II and III of an effect of the individual classes prove that the stress direction σ_2 can exert a small effect only on both the static strength of the laminate and the individual mechanisms of its destruction. The differences in AE activity in the laminates based on Ep53 resin and L285 resin, observed for the whole population of the tests, were further supported by different share of the classes, and hence by different share of the mechanisms in failure of the samples.

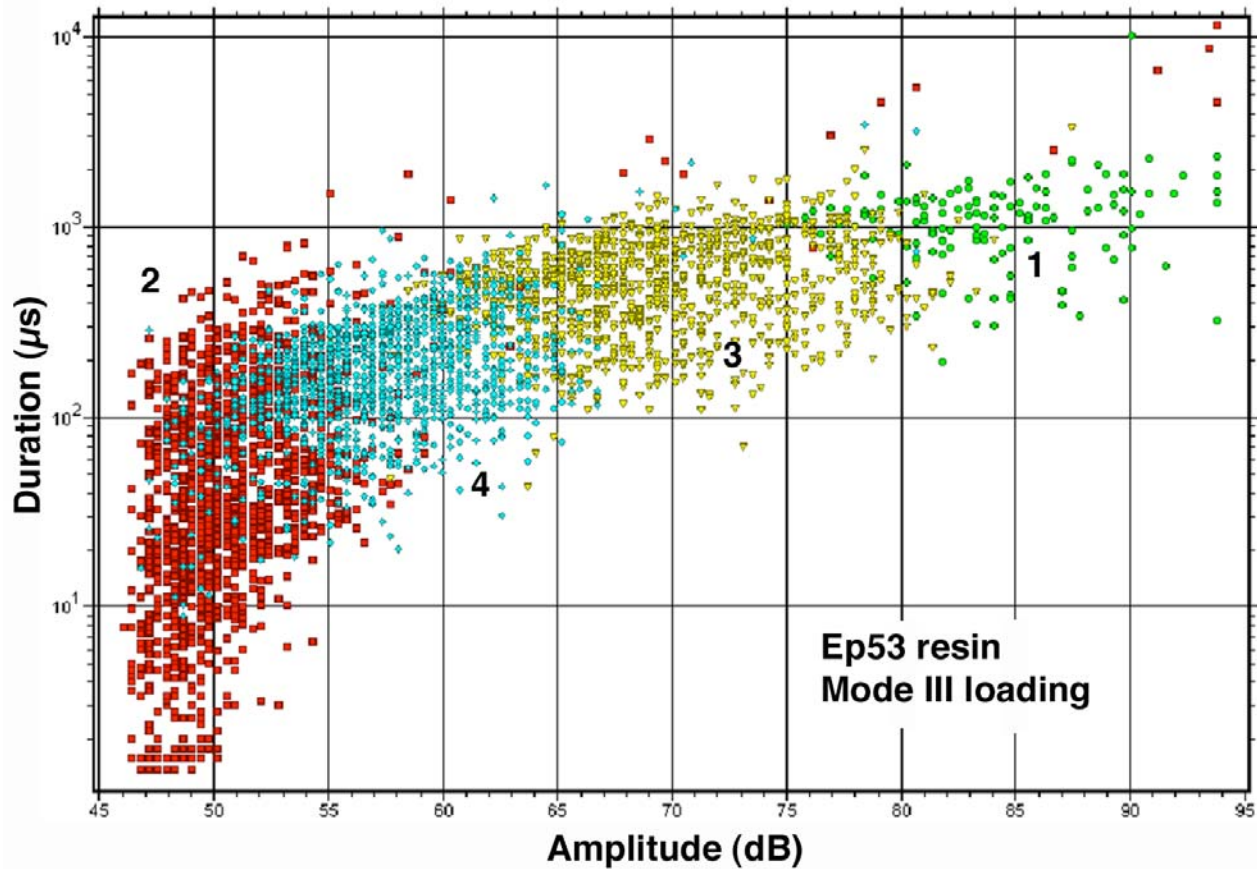


Fig. 6. AE results for separated class: Duration vs. Amplitude. Class 1 to 4 are indicated.

The basic differences between the two types of laminates noted at the same level of stress during loading result from different intensities of the internal friction behavior of the matrix and from the initiation and propagation of microcracks. In both laminates the process of failure starts with microcracks in the matrix. For L285 resin this process is much more intensive. In parallel, from the very beginning of AE activity, the process of the resin debonding from the glass fiber fabric is also developing at a high rate. In both resin laminates, the different AE activity is caused by different physical properties, and hence by different wettability and adhesion of each of the resins to the glass fibers. These effects cause some important differences in AE data set from the loading process of both laminates. Within the whole examined range of the laminate loading, individual damages and cracks in the fibers can be observed. For both laminates this process occurs at a similar level.

4. Conclusions

1. The type of resin used as a matrix for the laminate made from the glass fiber fabric has no effect on the static strength of the laminate.
2. The biaxial state of stress with principal stresses ratio $\sigma_1/\sigma_2=2$ has no effect on the strength of the laminate made from the glass fiber fabric wetted with epoxy resin.
3. The process of laminate failure starts at a loading corresponding to roughly 15% of the failure stress.
4. Under the condition of static loading at 20°C, the rate of crack propagation is uniform for the L285 resin matrix, while it increases quite significantly for the Ep53 resin matrix at higher stress levels just before failure. Ep53 composites showed the same characteristic at higher test temperatures as well.
5. Laminates with the matrix made of L285 resin are characterized by a greater number of AE events suggesting a greater number of microcracks preceding the failure of sample and the greater activity due to debonding process of the matrix and glass fiber fabric.
6. Hardening at high temperatures raises the laminate strength only by a very small degree.
7. Applying in the analysis of laminate failure, AE method of the pattern recognition classification enables us to determine the ranges of occurrence of the individual mechanisms of failure during loading of sample.
8. Existence of various mechanisms of crack formation may, depending on the resin type used for the laminate matrix, have some effect on the long-term strength of laminate.

References

1. T.J. Fowler and R.S. Scarpellini, "Acoustic emission testing of FRP pipes", Emerging High Performance Structural Plastics Technology, A. Green, ed., ASCE, New York, 1982, pp. 50-63.
2. L. Golaski and K. Ono, "Acoustic Emission Analysis of Laminate Failure Mechanisms with Reference to Failure Criteria", AECM 5, Proc. Fifth International Symposium on Acoustic Emission From Composite Material, ASNT, Columbus, OH, 1995, pp. 170-178.
3. J. Schmidt, I. Baran, L. Golaski: "Failure Behaviour of Glass Fabric Laminates: Independence on Resin Matrix and Temperature", Integrity Reliability Failure, 19-22 July 1999, Porto, pp.56-57.
4. M.J. Owen, J.R. Griffith, "Evaluation of biaxial stress failure surfaces for a glass fabric reinforced polyester under static and fatigue loading", J. of Mat. Sci. **13**. 1978. 1521-1537.
5. A. Neimitz: "The Review of the Failure Criteria for Composites", in Proc. Joint French-Polish Seminar: Failure of Heterogeneous Materials. Paris 1994, Polytech. Swietokrzyskiej 1996, pp. 5-26.
6. S. Benmedakhene, M. Kenane, M.L. Benzeggagh: "Initiation and growth of delamination in glass/ epoxy composites subjected to static and dynamic loading by acoustic emission monitoring", Comp. Sci. and Tech., **59**. 1999. 201-208.
7. F. Meraghni, F. Desrumaux, M.L. Benzeggagh: "Implementation of a constitutive micro-mechanical model for damage analysis in glass matrix reinforced composite structures", Comp. Sci. and Tech., **62**. 2002. 2087-2097.

ROLLING CONTACT FATIGUE DAMAGE OF WC-Co CERMET SPRAYED COATING AND ITS AE ANALYSIS

JUNICHI UCHIDA¹, TAKESHI OGAWA¹, MIKIO TAKEMOTO¹,
YOSHIFUMI KOBAYASHI¹ and YOSHIO HARADA²

¹) Department of Mechanical Engineering, Aoyama Gakuin University, Fuchinobe, Sagamihara 229-8558, Japan. ²) Tocalo Co., Ltd., 4-13-4, Fukaekita, Higashinada, Kobe 658-0013, Japan.

Abstract

Rolling contact fatigue tests were performed for three kinds of WC-Co cermet-sprayed steels in order to study the influence of spraying conditions on the rolling contact fatigue damage. Testing machine for rolling contact fatigue with AE monitoring system was developed using a thrust bearing. Displacements of the pulley were measured for real-time observation of the peeling, while acoustic emission (AE) method was utilized to detect both the peeling and flaking. Two modes of damage were found in the WC-Co cermet-sprayed coatings, i.e. peeling and flaking. The former was initiated by micro-fracture around the WC particles near the surface due to the contact force, and the latter by macro-crack initiation attributed to repeated shear stress by the plane-sphere contact. The peeling damage initiated in the early stage of rolling contact fatigue test, and increased contact areas and thus reduced damage rate. Subsequently, flaking damage took place by Mode-II crack initiation developed by cyclic shear stress under contact stress distribution.

Keywords: Rolling contact fatigue, Sprayed coating, WC-Co cermet, Peeling, Flaking

1. Introduction

WC-Co cermet coatings sprayed by high-velocity oxygen fuel (HVOF) method have been widely used for wear-resistant applications since high-performance coatings are available [1]. It was observed that cracks initiated in the coating progressed to the substrate boundary and led to the final fracture of specimens, when the coating was harder than the substrate and the boundary was well bonded [2]. This behavior is important for fatigue strength evaluation of sprayed components, because the coating cracks determine the fatigue strength of sprayed components [3]. Therefore, it is important to evaluate fatigue resistance of the sprayed coatings. We constructed a contact fatigue testing machine to evaluate the fatigue resistance of sprayed coating itself so that the maximum amplitude of cyclic shear stress is within the sprayed coating.

In the present study, rolling contact fatigue tests were performed for three kinds of WC-Co cermet-sprayed steels in order to study the influence of spraying conditions on the rolling contact fatigue damage. Detailed observation of fatigue damage and acoustic emission (AE) monitoring were simultaneously conducted in order to analyze the influence of spraying conditions on the strength and fracture mechanism of rolling contact fatigue.

2. Experimental Procedures

The substrate material is 12-mm-thick alloy steel, JIS-SCM440, oil-quenched from 870°C after 1h heating and tempered at 560°C for 2h. The specimens were spray-coated WC-12%Co

Table 1 Parameter for spraying conditions, elastic properties and residual stress of WC-12%Co sprayed materials.

Spraying condition	Oxygen flow rate Nm ³ /h	Fuel flow rate l/h	Gas pressure MPa	Young's Modulus E_c GPa	Poisson's ratio ν_c	Residual stress σ_r MPa
A	30	8	0.48	157	0.15	-70 -35
B	40	12	0.83	197	0.14	-347 -391
C	50	16	1.71	217	0.24	-668 -465

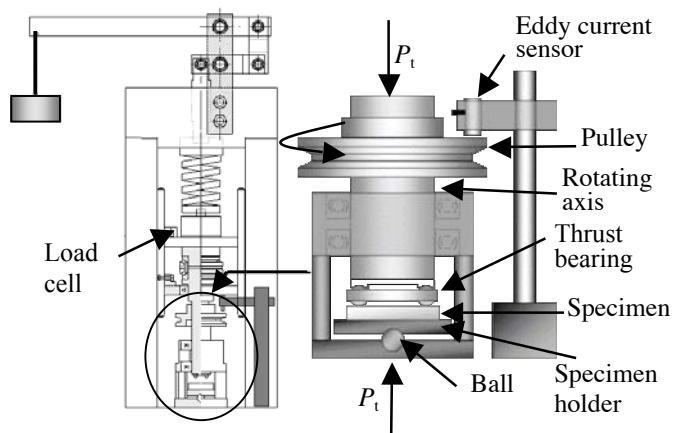


Fig. 1 Rolling contact fatigue testing machine.

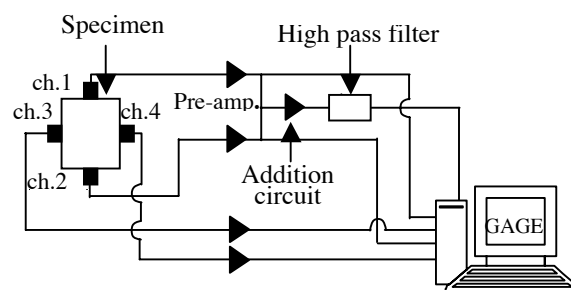


Fig. 2 AE monitoring system.

by HVOF method using CJS system of OSU Co. with constant conditions of hydrogen gas supply: 4 Nm³/h, spraying distance: 350 mm, gun velocity: 500 mm/s, pitch: 5 mm and 8 passes. Other spraying conditions are listed in Table 1, where the spraying conditions A, B and C are used for sprayed specimens A, B and C, respectively. Table 1 also presents the mechanical properties estimated by the inverse analysis of surface acoustic waves (SAW) and residual stress by cutting method [4]. The sprayed thicknesses A, B and C were 390, 500 and 500 μm , respectively. The sprayed surfaces were polished by diamond paste and the finished thicknesses were between 100 and 200 μm .

The rolling contact component is a steel ball made of high-carbon chromium steel, JIS-SUJ2, with the diameter of 5.56 mm. It is a part of thrust bearing, No.51200, with the inner and outer diameters of 10 and 26 mm, respectively, having 9 steel balls. Figure 1 shows the rolling contact fatigue machine developed in house. The sprayed specimen was mounted on a holder supported by a steel ball at the center. Thrust force, P_t , was applied to the bearing rotating on the specimen at 400 rpm. Cyclic frequency of rolling contact by the 9 balls was then controlled as 30 Hz. Maximum shear stress by the ball contact was confirmed to be 25 to 30 μm below the surface by finite element analysis using a commercial code, MARC. The cyclic rolling contact made a groove on the coating surface due to fatigue damage. The depth of the groove was monitored indirectly in terms of the pulley displacement measured by eddy current sensor using our special averaging software. The resolution of the measurement was about 1 μm .

Figure 2 shows a schematic illustration of AE monitoring system. Four small AE sensors (PAC, PICO) were mounted on the side surfaces of the specimen. AE signals were amplified by 40 dB, and acquired by a PC-based wave analyzer (Gage Applied Science). In order to detect damage signals properly, AE signals of channels 1 and 2 were added and filtered out the lower frequency component. The high-pass filter reduced the signal amplitude by 8.7 dB at 100 kHz

and by 1.8 dB at 1 MHz. Without the high-pass filter, no AE signal from fatigue damage was obtained because of continuous acquisition of low frequency noise from cyclic contacts.

3. Results and Discussion

3.1 Observation of Rolling Contact Fatigue Damage

Variations of displacement of pulley, D , with the number of cycles, N , are presented in Figs. 3 and 4, which demonstrate influences of spraying conditions and contact force, respectively. For all the cases, D increased rapidly just after starting the tests, followed by moderate increase in D . Subsequently, D increased again except for specimen C at $P_t = 180$ N for the cases in Figs. 3 and 4. The changes in D tend to occur at larger values of N , when the P_t value is lower or the spraying pressure is higher, namely it is the largest for the specimen C. As will be discussed later, the three stages of the changes in D resulted from damage mechanisms developed by rolling contact fatigue.

After the tests shown in Fig. 3, the grooves were observed on the specimen surfaces by a surface roughness measuring instrument (Taylor Hobson, FORM TAYSURF). Figure 5 shows three dimensional configurations together with the sections indicated by A-A', B-B' and C-C' in the upper figures. The depth of the grooves can be determined by drawing inscribed circle in the section profiles, and these agreed fairly well with the final displacement, D , in Fig. 3.

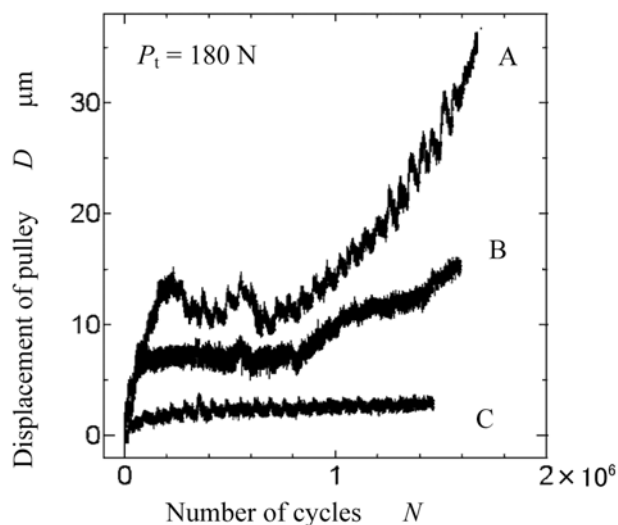


Fig. 3 Displacement change for different sprayed conditions at $P_t = 180$ N.

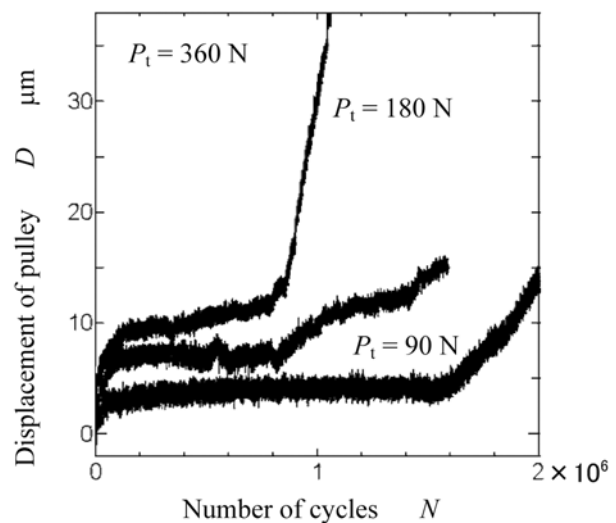


Fig. 4 Displacement change at different P_t values for specimen B.

The groove surfaces were observed by scanning electron microscope (SEM) and presented in Fig. 6. The surface exhibits fine granular appearance observed as dark area, while the bright area is flat and damaged much less than the dark area by rolling contact fatigue. The dark area is dominant in the specimen A, but it is reduced in specimens B and much reduced in specimen C. The lower micrographs of Fig. 6 are magnified appearances of the upper micrographs. Figure 6(d) shows a small hole, which might be a trace of removal of a small particle with several tens of μm . Figures 6 (e) and (f) demonstrated crack initiation on the groove surface in specimens B and C.

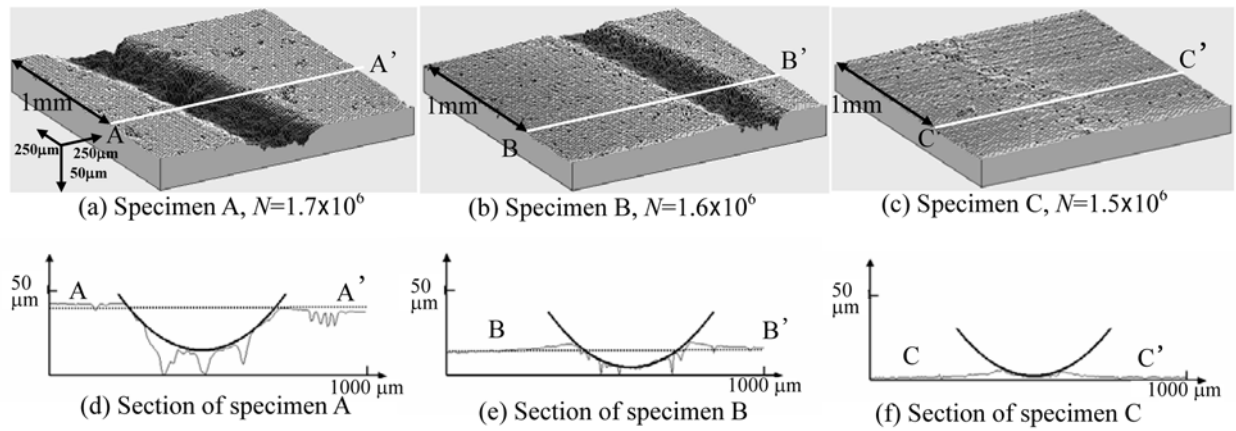


Fig. 5 Three dimensional configurations and sections of grooves at $P_t = 180$ N.

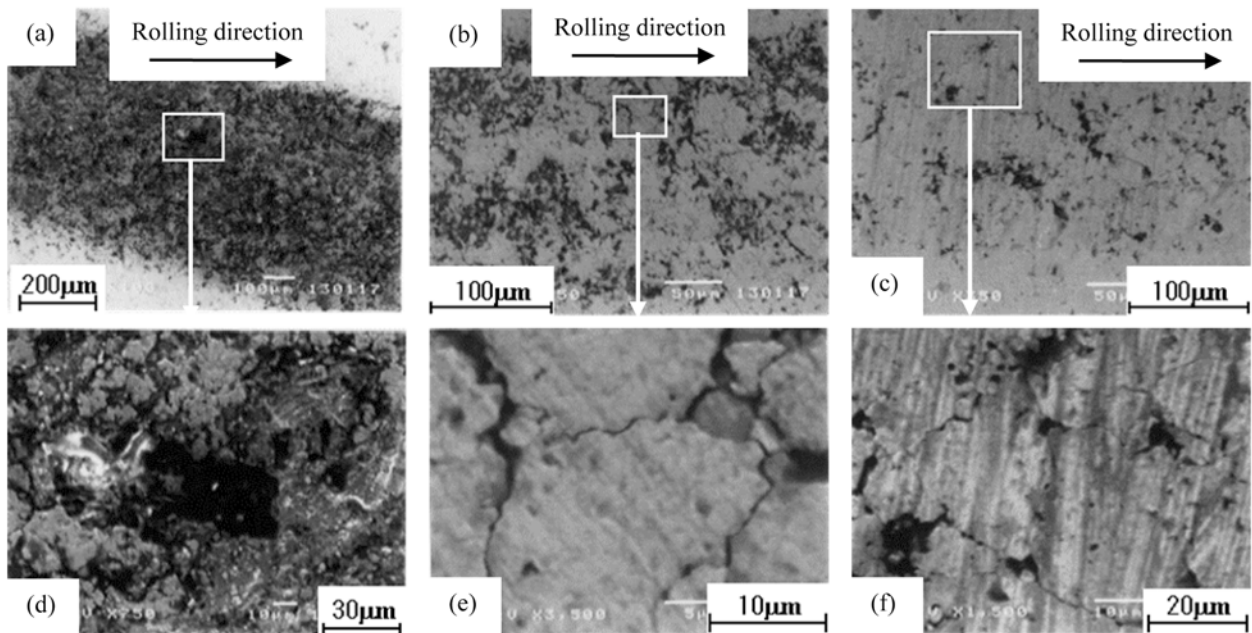


Fig. 6 SEM micrographs of damaged surfaces at $P_t = 180$ N. (a) specimen A: $N = 1.7 \times 10^6$, (b) specimen B: $N = 1.6 \times 10^6$ (c) specimen C: $N = 1.5 \times 10^6$. The magnified micrographs of specimens A, B and C, are shown in (d), (e) and (f), respectively.

After the surface observations, the specimens were cut and observed on the section of the grooves. The SEM micrographs are presented in Fig. 7. Subsurface lateral cracks were observed in specimens B and C at the depth of about $30 \mu\text{m}$ from the surface. This depth coincides with the location of maximum shear stress predicted by FEM analysis. On the other hand, cracking around the particles and the particle removals can be found in specimen A.

3.2 AE analysis

Other specimens were prepared for AE analysis during the rolling contact fatigue tests at $P_t = 180$ N. Figure 8 represents the simultaneously monitored displacement D and cumulative AE event counts, N_{AE} , with the number of rolling contact cycles, N . The variations of D are slightly different from those in Fig. 3. However, general trends are the same, which support the repro-

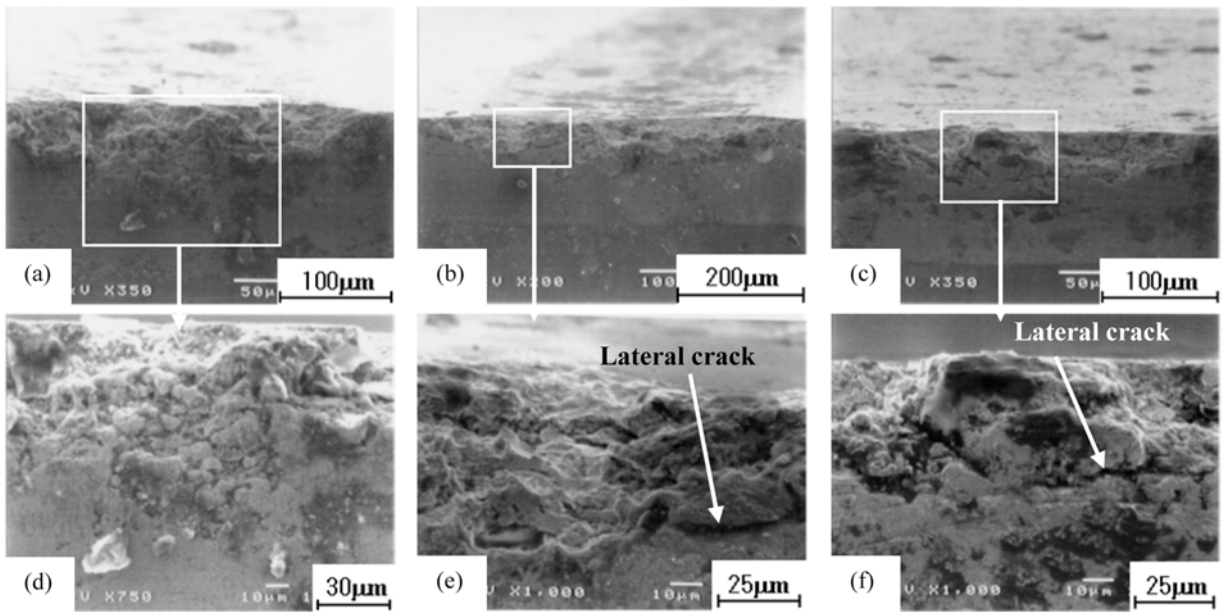


Fig. 7 Sectional view of grooves at $P_t=180\text{N}$. (a) specimen A, (b) specimen B, (c) specimen C. The magnified micrographs of specimens A, B and C, are shown in (d), (e) and (f), respectively.

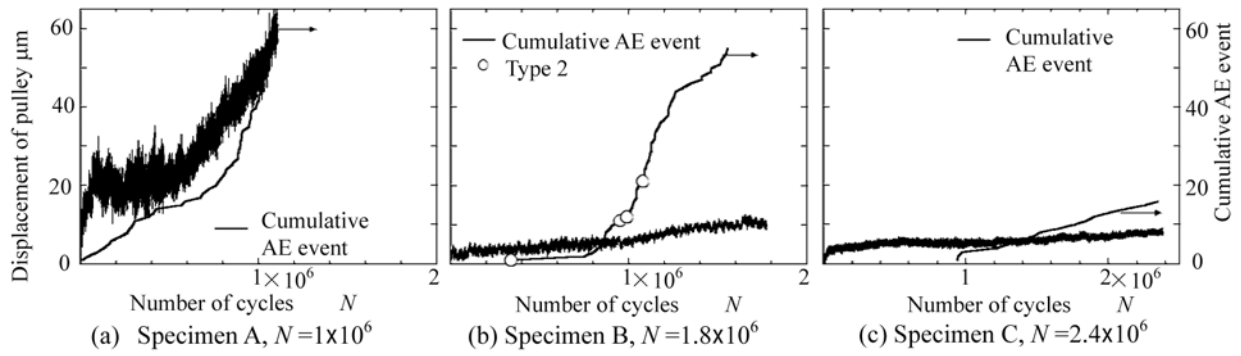


Fig. 8 Displacement of pulley and cumulative AE event on $P_t=180\text{N}$.

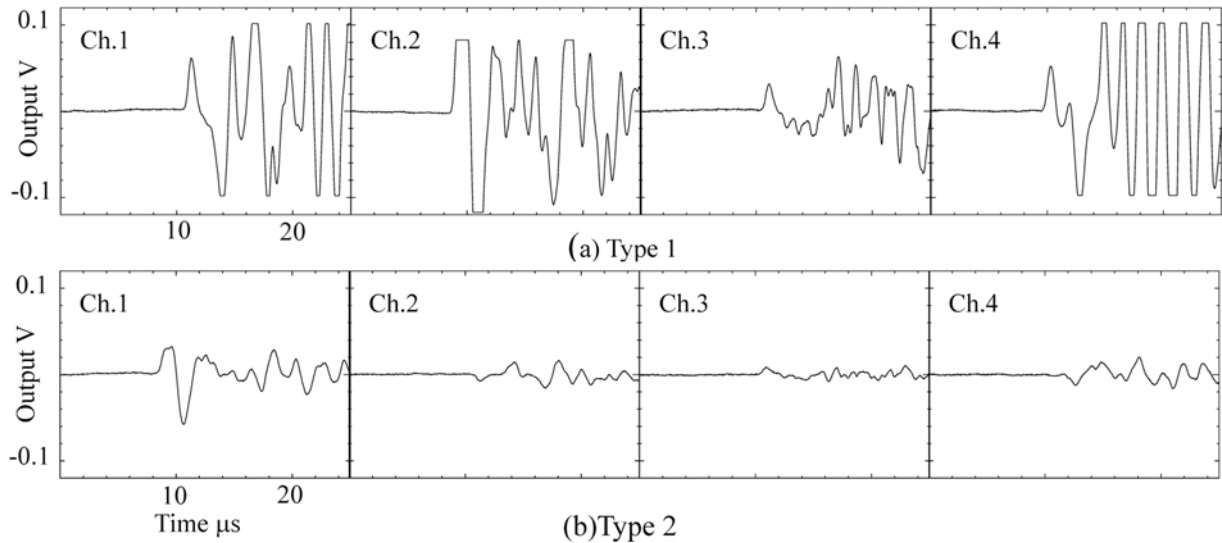


Fig. 9 Detected AE signals.

ducibility of these experiments. For the specimen A, AE signals were detected just after the beginning of the test, and then showed higher rates of increase in N_{AE} after $N = 5 \times 10^5$ cycles together with the second increase of D . For the specimen B, the first increase of D was obscure in this experiment. The first AE signal was detected at $N = 3.5 \times 10^5$ cycles, and the rate of increase in N_{AE} became higher after $N = 8 \times 10^5$ cycles. Subsequently, the second increase of D was found after $N = 1 \times 10^6$ cycles. For the specimen C, the first AE signal was detected at $N = 9.5 \times 10^5$ cycles, then N_{AE} slowly increased, but the rate of increase was constant and the second increase of D was not observed.

Examples of the AE signals are shown in Fig. 9. For the AE waves in Fig. 9(a), or type 1, polarities of the first peaks were all positive, while in type 2 they were reversed between diagonal locations, i.e., ch. 1 vs. ch. 2 or ch. 3 vs. ch. 4, as shown in Fig. 9(b). These AE signals were denoted as type 1 and 2, respectively. Most of the detected AE signals represented the characteristics of type 1. However, four signals of type 2 were found in the test for specimen B, and distinguished by open circles in Fig. 8(b).

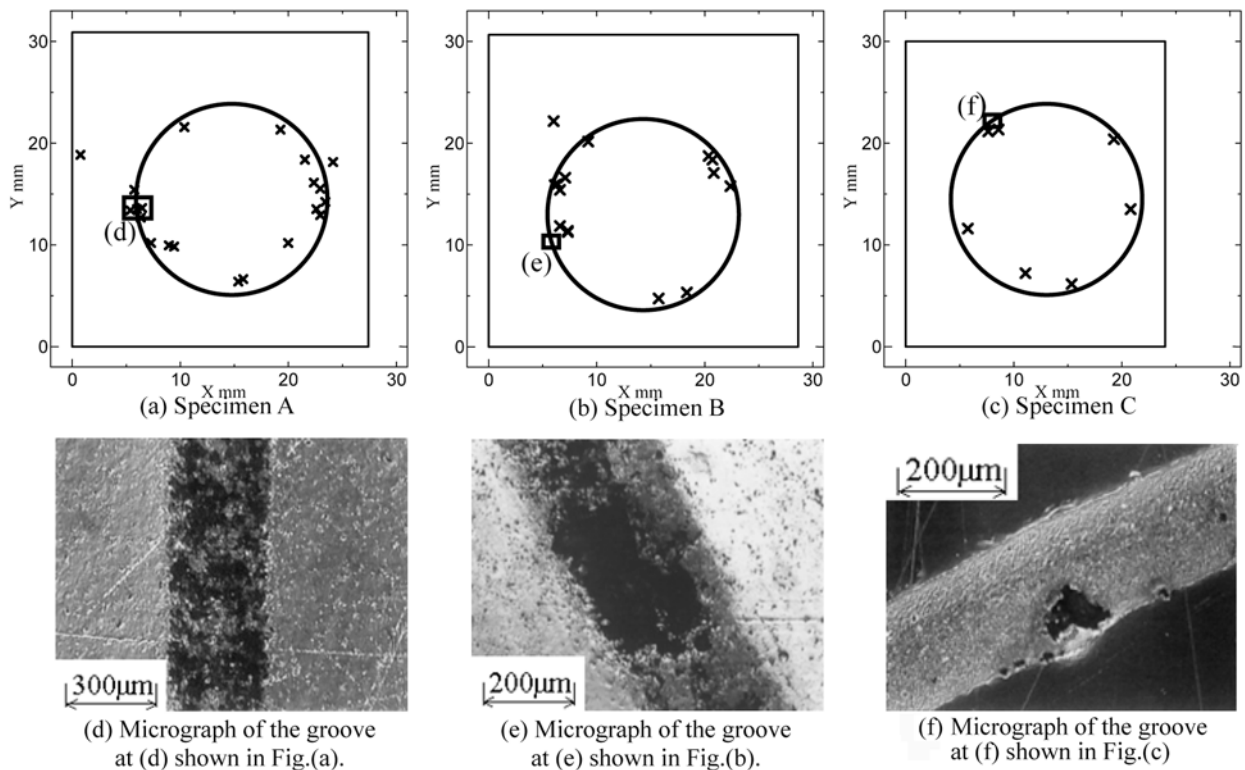


Fig. 10 AE source locations at $P_t = 180$ N and the micrographs of the grooves.

In order to analyze the AE signals, traveling velocity of the longitudinal (P-) wave was determined for specimen B. Here, YAG laser pulses were radiated on the specimen surface and the first arrival waves were detected on the back surface using a laser interferometer. The P-wave velocity, V_P , was measured as 5929 m/s. Next, the AE sensor was mounted on the side surface of the specimen, and the YAG laser pulse was radiated at the distance of 20 mm from the sensor. The traveling time was 3.35 μ s, and resulted in the wave velocity of 5970 m/s, which agreed with the V_P . Therefore, the first peaks of the detected AE signals are the P-wave, and used for the analysis of AE source location. The results are demonstrated in the upper illustrations of Fig. 10, where the numbers of analyzed AEs were limited because of small amplitudes of the first peaks. The circles in the figures indicate the rolling contact location, where the grooves are observed.

The analyzed locations are distributed near the grooves. The lower micrographs of Fig. 10 show contact damages at the rectangular marks shown in the upper illustrations. Specimen A exhibits uniform damage on the specimen surface, while the specimens B and C present removals of larger particle. Those damage mechanisms are denoted as peeling and flaking, respectively.

AE source analysis was conducted by the simulation of AE wave pattern, using artificial AE source. Figure 11 represents schematic illustrations of the artificial AE source excited by line focused pulse YAG laser and shear type PZT element for Mode I and II cracking, respectively. Figure 11 presents corresponding AE waveforms with the AE sources. The polarities of the first peaks are the same between the diagonal AE sensors for Mode I cracking, while they are reversed for Mode II cracking. Therefore, type-2 AE signals shown in Fig. 9 reflect the subsurface Mode-II crack initiation, which leads flaking damage on the specimen surface.

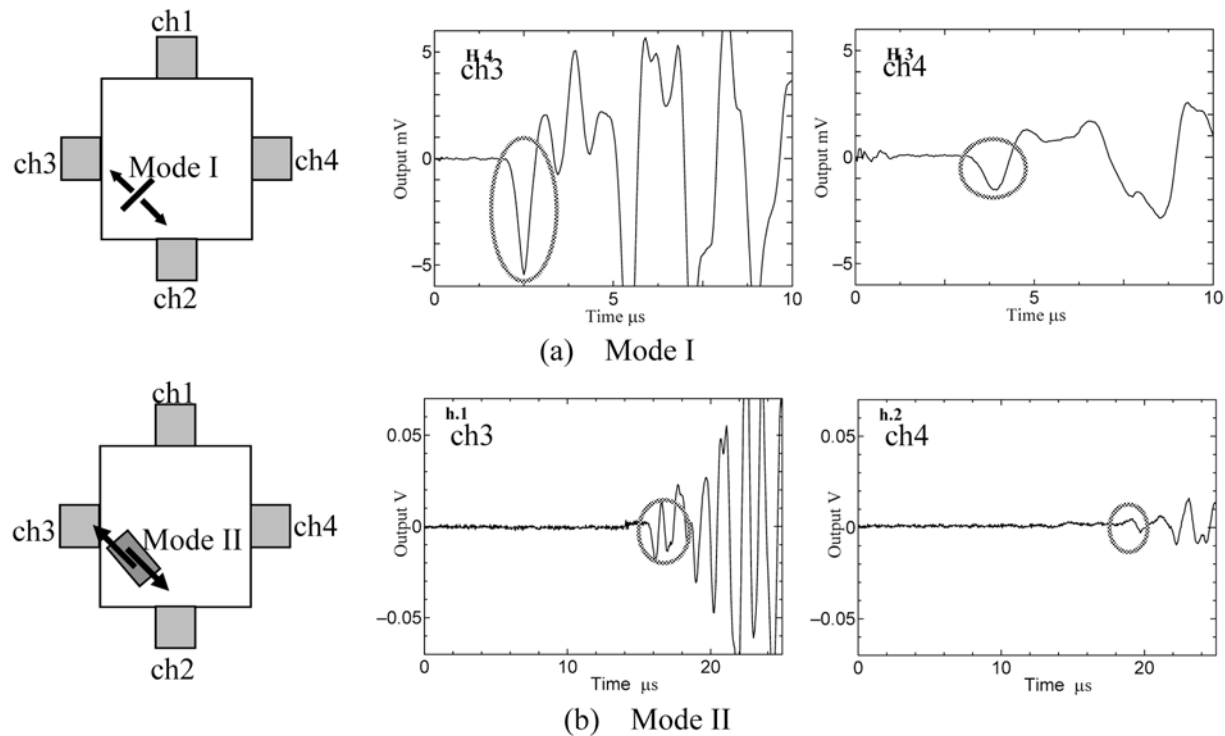


Fig. 11 Detected AE waves from simulated AE sources of mode I and mode II cracking.

3.3 Fracture Mechanism of Rolling Contact Fatigue

The above observation and AE analysis reveal the fracture mechanism of rolling contact fatigue of WC-Co cermet-sprayed materials as schematically illustrated in Fig. 12. When the rolling contact stress is applied, small cracks initiate around WC particles, which are peeled off from the specimen surface. This behavior corresponds to the initial increase in displacement D in Figs. 3 and 4 and produces the groove resulting in the increase in contact area and decrease in contact stress. Therefore, the peeling damage becomes less significant with increasing D . In the subsequent rolling contacts, cyclic shear stress initiates the subsurface lateral crack as shown in Fig. 12(b) and leads to the flaking mechanism caused by Mode-I cracks. The AE analysis monitored these cracking mechanisms and agrees with this sequence of events.

The spraying condition affected the strength of rolling contact fatigue. As shown in Figs. 3 and 8, D and N_{AE} increased most rapidly for the specimen A, whose spraying pressure is the

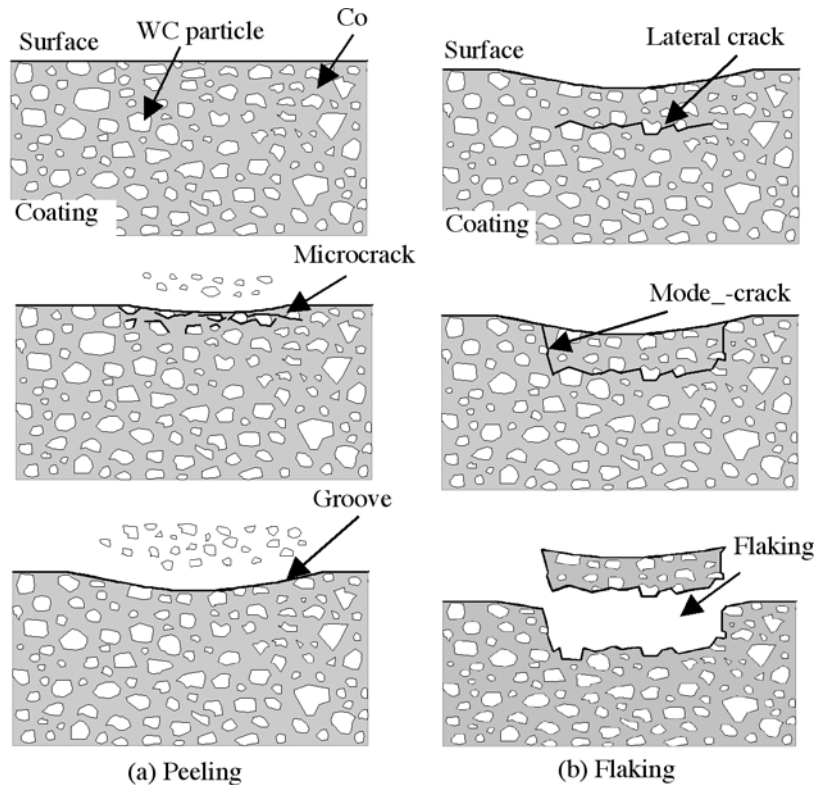


Fig. 12 Damage mechanisms of rolling contact fatigue.

lowest. For specimen A at $P_v = 180$ N, the peeling damage developed so quickly that the lateral crack did not grow large enough to develop flaking damage. In contrast, specimen C exhibits the highest fatigue strength. For specimen C at $P_v = 180$ N, peeling damage was hardly seen, but the subsurface lateral cracks developed and lead the flaking damage. The strength characteristics of specimen B was in between those of specimens A and C.

4. Conclusion

Rolling contact fatigue tests were performed for three kinds of WC-Co cermet-sprayed steels in order to study the influence of spraying conditions on the rolling contact fatigue damage. Results are summarized as follows.

- (1) Two modes of rolling contact fatigue damage were found in the WC-Co cermet-spray coatings. They are peeling and flaking.
- (2) The strength of rolling contact fatigue is enhanced with increasing spraying pressure.
- (3) The rolling contact damage developed more quickly with increasing contact stress.

References

- 1) K. Tani, H. Nakahira, J. Thermal Spray Technology, ASM International, **1** (1992), 333.
- 2) D.S. Platt, Master Thesis, Thayer School of Engineering Dartmouth College, Hanover, USA (1981).
- 3) T. Ogawa, K. Tokaji, T. Ejima, Y. Kobayashi and Y. Harada, Materials Science Research International, **4-1** (1998), 12.
- 4) A. Ishida, T. Ogawa, M. Takemoto, Y. Kobayashi and Y. Harada, J. Material Testing Research Association of Japan, **45-1** (2000), 289.

BORON EFFECTS ON AE EVENT RATE PEAKS DURING TENSILE DEFORMATION OF Ni₃Al INTERMETALLIC COMPOUND

K. YOSHIDA, Y. MASUI, T. NAGAMACHI and H. NISHINO

Faculty of Engineering, The University of Tokushima
2-1 Minami-josanji, Tokushima 770, JAPAN.

Abstract

Tensile testing of Ni₃Al intermetallic-compound single crystals with no additive, 0.25 and 0.50 at. % boron has been performed using acoustic emission (AE) method in order to examine the interaction between boron atoms and mobile dislocations. Boron additives increase the yield strength of Ni₃Al by 276 MPa/at. %. AE event rates have two peaks at yield point and in work-hardening region. The peak event rates and the distance between these peaks increase with an increase in boron contents. The latter results from the difficulty of the homogeneous deformation due to active cross-slip because the stacking fault energy decreases with boron. The total AE event counts near yield point increase with boron, implying that boron atoms act as interstitials in Ni₃Al and their frictional drag acts as AE sources. Furthermore, the inhomogeneous dislocation motion not from the cross-slip may generate AE during the second peak.

Keywords: Intermetallic compound; Ni₃Al; Tensile test; Boron additive; Yield strength

1. Introduction

We can make use of acoustic emission (AE) generated during deformation in materials to study the dislocation motion, the interaction of dislocations with inclusions and precipitates, and the dynamic behavior of micro-cracking. For example, the AE behavior during the yielding of age-hardened copper and aluminum alloys has been investigated [1-5]. When dislocations bypass precipitates, the diameter and distribution of precipitates affect the AE behavior. When dislocations shear and pass through precipitates, the anti-phase boundary energy and the frictional resistance to dislocation motion in precipitates mainly affect the AE behavior [5]. However, no information is available on the AE behavior during deformation of precipitates themselves that are often intermetallic compounds [6].

Intermetallic compounds have been considered as heat resisting alloys of the future. That is partly because the yield strength of some intermetallic compounds increases with increasing temperature in a certain high temperature range. Ni₃Al is one of such intermetallic compounds, but polycrystalline Ni₃Al fails due to intergranular fracture because of the brittleness of grain boundary [7]. Additions of a small amount of boron [8] or some third elements [9], and unidirectional solidification [10] have been found to reduce the grain boundary brittleness. In the case of boron doping, several studies from basic point of view have been conducted to understand the solubility of boron atoms in Ni₃Al, effect of boron additive on yield strength, lattice parameter change and interaction between boron atoms and dislocations and deformation mechanism of Ni₃Al including boron additives [11-14]. In addition, several *in situ* straining experiments in a transmission electron microscope have been performed to determine dynamical dislocation mechanism in stoichiometric Ni₃Al [15-17]. However, there is no data on the AE behavior of Ni₃Al single crystal during tensile deformation.

In this paper, the effect of boron additives on two peaks of AE event rates during tensile deformation has been investigated using Ni₃Al intermetallic-compound single crystals. The interaction of mobile dislocations with boron atoms has been discussed analyzing the AE behaviors obtained.

2. Experimental Procedures

Ni-24 at. % Al (~Ni₃Al) with no additive, 0.25 and 0.50 at. % boron was prepared from pure nickel (99.97 wt. %), pure aluminum (99.9 wt. %) and pure boron (99.9 wt. %) by a high-frequency induction-melting method under argon atmosphere at 1823 K. Melting and casting were carried out twice to make ingots homogeneous. Single crystals were grown from such ingots by a modified-Bridgman technique. Tensile specimens with a gage size of 1 mm x 3 mm x 12 mm were spark-machined. All the specimens were annealed under argon atmosphere at 1473 K for 20 h and cooled in furnace. The surface layer was removed by mechanical polishing and electro-polishing in a 10% sulfuric-acid and 90% ethyl-alcohol solution. Tensile test was performed using an Instron-type machine at a strain rate of $2.8 \times 10^{-4} \text{ s}^{-1}$. After the tensile test, the dislocation structures in the specimens were observed using a transmission electron microscope (TEM). Only Ni₃Al X-ray diffraction peaks were observed for all the single crystals. All the tensile tests were performed to a strain of 0.25. After tensile tests, we could not find any macro-cracks, and thus all specimens used were considered to be ductile.

Two-channel system (PAC: MISTRAS-2001) was used to obtain AE data that consists of rms (root-mean-square) voltage, cumulative event counts, event rates and peak amplitude. Two AE transducers with 200-kHz resonance frequency were used, and the signals were amplified 60 dB with a band-pass filter with the range of 0.1 to 1.2 MHz. Threshold level was 31.6 μV at the input of preamplifier. AE data were recorded on a pen recorder and a microcomputer. Only AE events generated between two transducers within time interval of 2 μs were sent into the AE data memory to detect the AE in the deformed part.

3. Results and Discussion

Figure 1 shows the stress-strain curves and AE activities (AE event rates and rms voltages) of Ni₃Al single crystals with no additive, 0.25 and 0.50 at.% boron during tensile deformation. The yield strength increases linearly with increasing boron contents as shown in Fig. 2. The flow stress at the strain of 0.25 also increases with the increase of boron. The behavior of AE event rates is similar to that of rms voltages. The AE event rates have two peaks during tensile deformation of Ni₃Al single crystals regardless of boron contents. The first peak is located near the yield point and becomes more active with an increase of boron contents. The second peak exists in the work-hardening region and its height decreases gradually with an increase of boron contents.

The deformation in all Ni₃Al single crystal regardless of boron content is macroscopically uniform over the specimen gage section. The primary slip system is mainly active in Ni₃Al intermetallic compound as in other fcc materials. Some cross slip systems are also found. That is so different from the results obtained by the directionally solidified specimens [18].

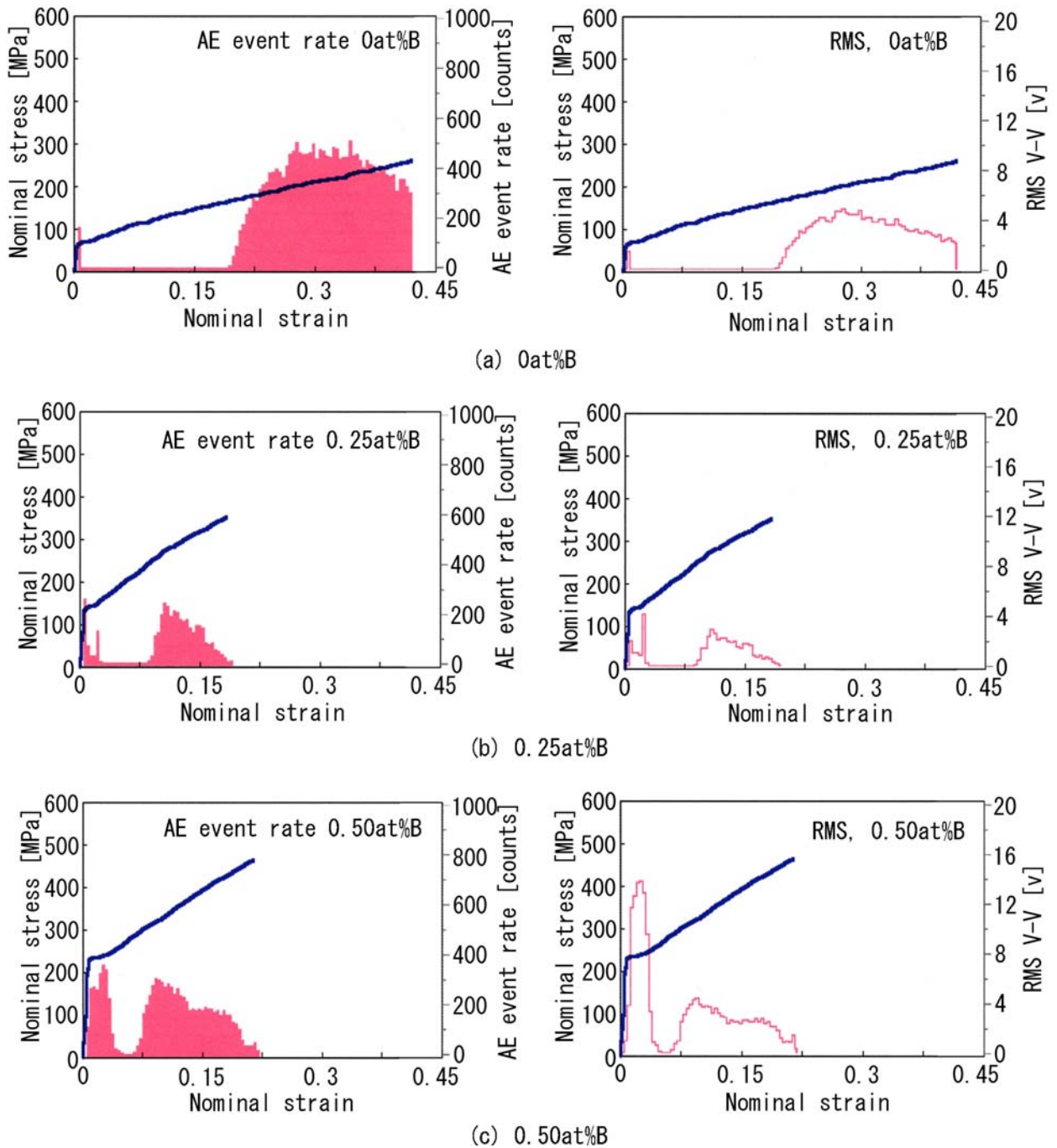


Fig. 1 Stress-strain curves, AE event rates (left) and rms voltages (right) of Ni_3Al single crystals during tensile deformation with (a) no additive, (b) 0.25 at. % B and (c) 0.50 at. % B.

The slope $\Delta\sigma/\Delta C$, where $\Delta\sigma$ is the change in yield strength and ΔC is the change in concentration, indicates a very large strengthening effect of 276 MPa/at. % boron. This value is smaller than that estimated by Baker et al. [14] who used coarse-grained ($d = 0.5\text{-}2$ mm) stoichiometric Ni_3Al , where grain boundary segregation of boron is expected. Therefore, this value is reasonable in Ni_3Al single crystal. The same value in $\sigma_{0.25}$ was 497 MPa/at.% boron in the previous paper [19]. The work-hardening rate appears to become larger with increasing boron contents.

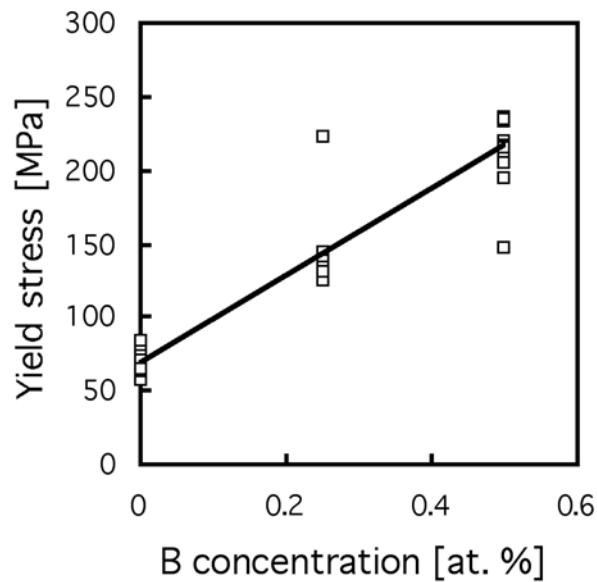


Fig. 2 Yield strength as a function of boron contents

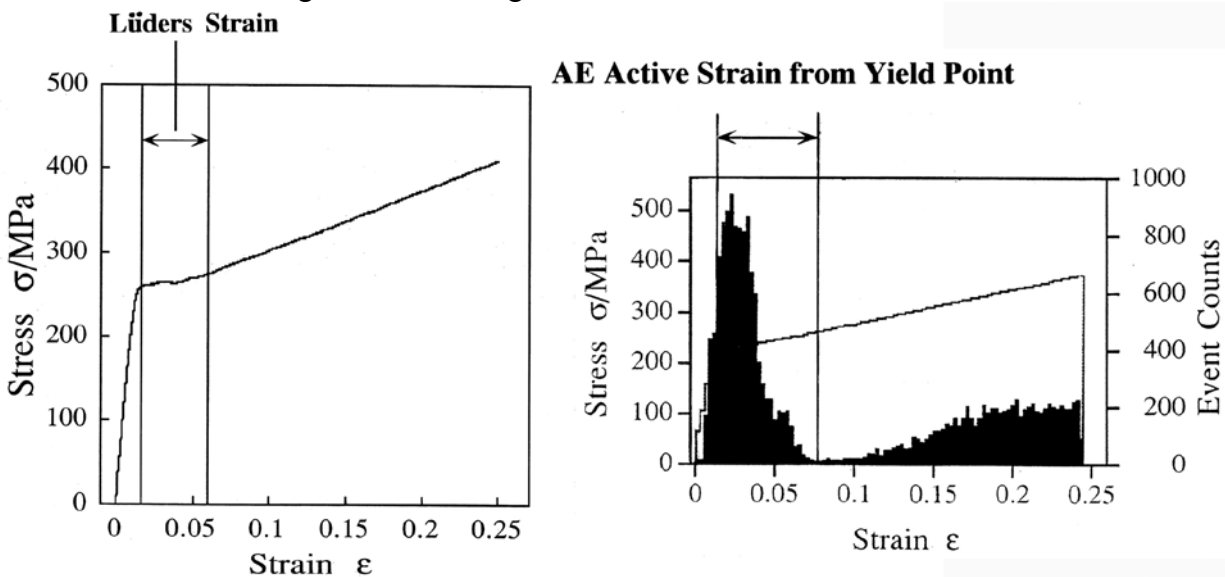


Fig. 3 Definition of Lüders strain and AE active strain from yield point.

The AE activity in the yielding region is mainly related to the yield point strains that are known as Lüders strain and AE active strain from the yield point defined in Fig. 3. Figure 4 shows the relation between AE active strain from the yield point and Lüders strain. The AE activity increases with increasing the Lüders strain. This may imply that the source of the AE means the more breakaway of pinned boron atoms from mobile dislocations.

We next consider the AE activity in the work-hardening region. Figure 5 shows the relation between the boron concentration and the nominal strain at the second peak of the detected AE. The nominal strain at the second peak of the AE decreases with an increase of boron content. If the secondary AE activity depends on another inhomogeneous plastic deformation, the boron contents clearly give the effect to hasten the inhomogeneous plastic deformation. Generally speaking, the AE activity during plastic deformation decreases gradually after yielding or in the work-hardening region, unless there occurs micro-cracking in matrix, secondary phase precipitates, inclusions and on the interfaces. However, the AE here is re-activated to show the second peak in the work-hardening region. It is interesting to find what the source of the AE is.

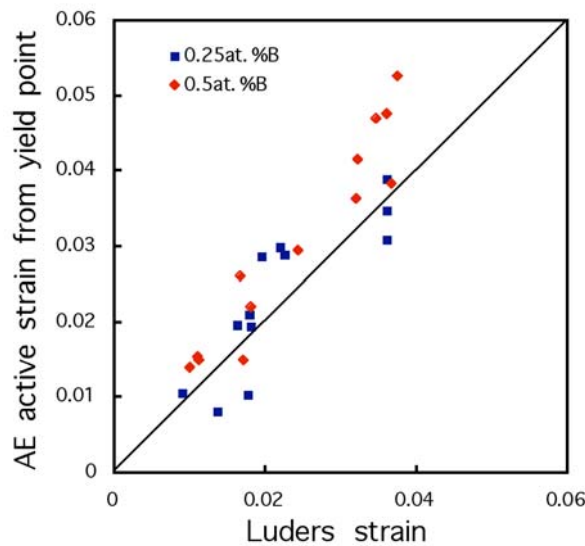


Fig. 4 Relation between AE active strain from yield point and Lüders strain.

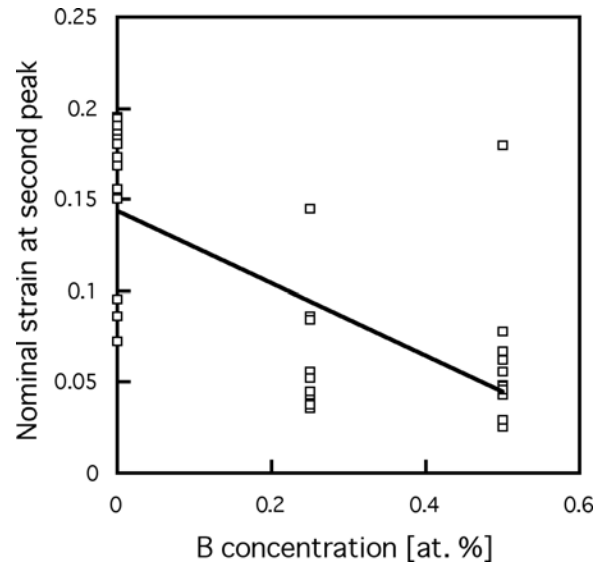


Fig. 5 Relation between the boron concentration and the strain at the second peak.

Amplitude distribution during tensile deformation has been examined to determine the source of AE. Figure 6 shows an example of amplitude distributions of AE in the specimen with 0.50 at. % boron in stage 1 and stage 2. The stages mean the region of $\epsilon = 0$ to 0.05 and $\epsilon = 0.05$ to 0.25, respectively. The amplitude in both stages has a peak between 50 dB and 60 dB. The amplitude in this region may be related to the plastic deformation or the inhomogeneous dislocation motions. Therefore, these AE activities that consisted of the first and second peaks of the AE event rate are considered to contain the same source of AE during plastic deformation.

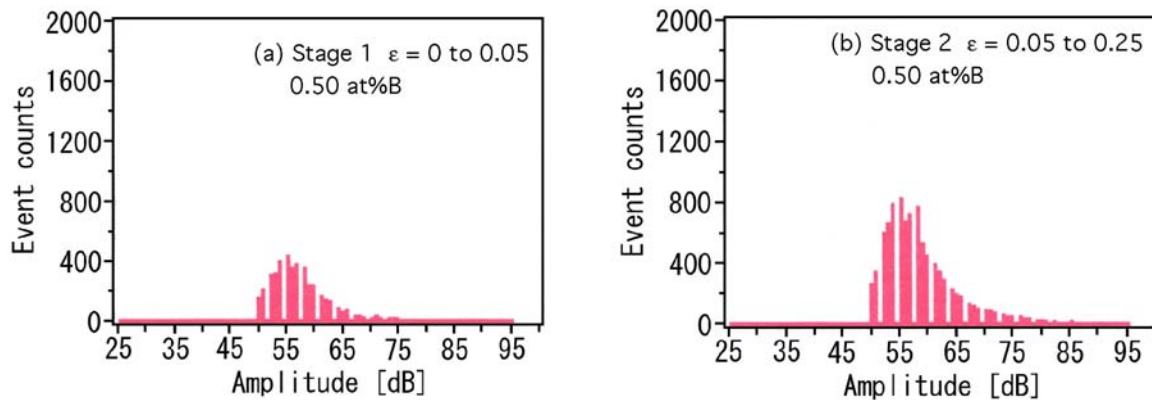


Fig. 6 Typical amplitude distributions of AE in the specimen with 0.50 at. % B in (a) stage 1 and (b) stage 2.

We next discuss the AE sources. Boron acts as interstitial in Ni_3Al because a boron atom is much smaller than either Ni or Al atom. It is considered that plastic deformation is mainly performed due to anti-phase-boundary (APB)-coupled dislocations, called super-lattice dislocations, within the range of boron contents used here. TEM photograph of super-lattice dislocations are shown in Fig. 7. [14] It is known that the APB energy is lowered due to the boron addition and that the yield strength is enhanced as shown in Fig. 2 because of the increase in lattice parameter due to the boron addition. It is possible that the increase in the yield strength promotes microscopically inhomogeneous plastic deformation. If so, the increase in the yield strength arises

from the frictional drag of boron atoms on mobile dislocations. This is one of the AE sources. In this case, the amplitude may be comparatively small. It appears that the AE activities at the yield point and in work-hardening region corresponds to the same dislocation source. The generation of cross slip appears to be consistent with that of the AE during work-hardening where the AE event rates have shown the second peak. The cross slip is easy to operate and induce the homogeneous deformation in the specimen with no boron additive because of the large APB energy or the narrow super-lattice dislocation spacing, as shown in Fig. 8. As a result, the uniform plastic deformation continues and delays the secondary AE activity as shown earlier in Fig. 5. With increase of the boron additives, the inhomogeneous plastic deformation is hastened in the work-hardening region because the super-lattice dislocation spacing is extended as shown in Fig. 8. After the cross slip, the secondary AE activity occurs. Molenat et al. [16] considered this to be due to the APB jumps so as to gain more strain in this region. The APB jumps occur when the leading super-partial is dissociated in a parallel (111) plane and may cause the AE second peak in the work-hardening region. Unlocking is enhanced by the resolved shear stress acting on (100) plane.

The binding energy of a boron atom to an edge dislocation is considered to be large (~ 0.7 eV) and is comparable to that calculated for carbon in iron (~ 1.0 eV) [14]. This magnitude indicates a strong interaction between a boron atom and an edge dislocation. In the case of this study, one suggestion is that larger amplitude AE events can be detected when more Lüders strain occurs. The more scattering of AE event counts at the yield point with increasing boron contents suggests that the boron produces an asymmetrical strain field, possibly by some of the boron atoms occupying interstitial sites on the Ni_3Al unit cell edge as mentioned by Baker et al. [14].

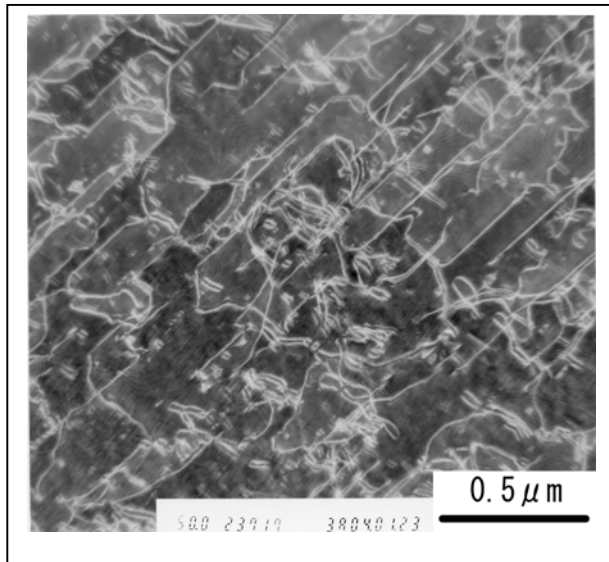


Fig. 7 Typical dislocation distribution of the specimen with 0.50 at. % B after the strain of 0.225.

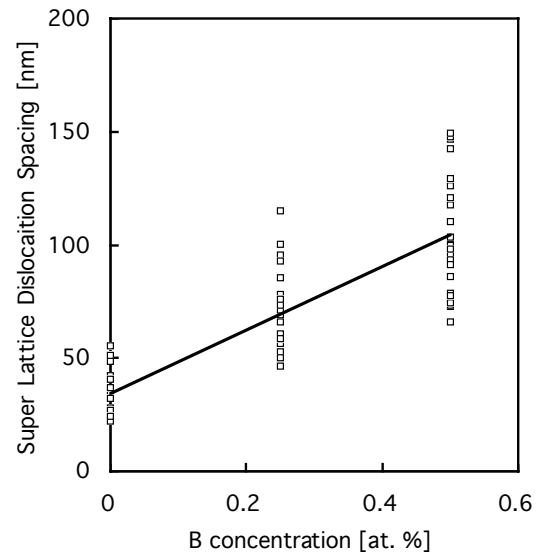


Fig. 8 Effect of boron content on super-lattice dislocation spacing.

6. Conclusion

Acoustic emission measurement and tensile testing in boron-doped Ni_3Al single crystals have shown that:

- (1) Boron activates the AE activity.

- (2) Boron has a large strengthening effect at yield point of 276 MPa/at.% boron.
(3) AE activities have two peaks that are at the yield point and in the work-hardening region.
(4) The first peak is due to a frictional drag of boron atoms on mobile dislocations, including the interaction between boron atoms and mobile edge dislocations as shown in a solute atmosphere model.

References

- [1] Masuda, J., J. Japan Inst. Met., **46** (1982) 620.
- [2] Kishi, T. and Sakakibara, Y., J. Japan Inst. Light Met., **34** (1984) 472.
- [3] Heiple, C. R., Carpenter, S. H. and Christiansen, S. S. Acta Met., **38** (1990) 611.
- [4] Sakamaki, K., Yoshida, K., Takagi, H. and Yoshida, M. JSME Int. J., **33** (1990) 362.
- [5] Yoshida, K., Pang, B., Zhu, A., Sakamaki, K. and Takagi, H., J. Japan Inst. Met., **60** (1996) 809.
- [6] Zhu, A., Yoshida, K., Takagi, H. and Sakamaki, K., Intermetallics, **4** (1996) 483.
- [7] Aoki, K. and Izumi, O., J. Japan Inst. Met., **41** (1977) 170.
- [8] Aoki, K. and Izumi, O., J. Japan Inst. Met., **43** (1979) 190.
- [9] Takasugi, T., Izumi, O. and Masahashi, N., Acta Met., **33** (1985) 1259.
- [10] Mawari, T. and Hirano, T., Intermetallics, **3** (1995) 23.
- [11] Liu, C. T., White, C. L., and Horton, J. A., Acta Met., **33** (1985) 213.
- [12] Weihs, T. P., Zinoviev, V., Vien, D. V. and Schulson, E. M., Acta Met., **35** (1987) 1109.
- [13] Baker, I., Schulson, E. M. & Horton, J. A., Acta Met., **35** (1987) 1533.
- [14] Baker, I., Huang, B. and Schulson, E. M., Acta Met., **36** (1988) 493.
- [15] Horton, J. A., Baker, I. and Yoo, M. H., Phil. Mag. **A63** (1991) 319.
- [16] Molenat, G. and Caillard, D., Phil. Mag. **A64** (1991) 1291.
- [17] Molenat, G. and Caillard, D., Phil. Mag. **A69** (1994) 939.
- [18] Yoshida, K., Saito, T., Zhu, A., Takagi, H., and Sakamaki, K., Intermetallics, **6** (1998) 1.
- [19] Yoshida, K., Horikawa, K. and Sakamaki, K., *Progress in Acoustic Emission XI*, **16** (2002), JSNDI, p. 15.

AE AND ELECTROCHEMICAL NOISE ANALYSIS FOR FRACTURE STUDY OF HARD SURFACE FILM

AKIO YONEZU, HIDEO CHO, TAKESHI OGAWA and MIKIO TAKEMOTO

Department of Mechanical Engineering, College of Science and Engineering,
Aoyama Gakuin University, 5-10-1, Fuchinobe, Sagamihara, Kanagawa, 229-8558, Japan.

Abstract

We propose a new hybrid technique of AE, corrosion potential and FEM for studying the fracture mechanism of hard surface films during micro-Vickers indentation. This method makes it possible to determine the fracture strength of the film when hard film is deposited on soft substrate. Both the AE and corrosion potential fluctuation of PVD-TiN film deposited on AISI-304 steel in hydrochloric acid (1 mol/l HCl + 0.01 mol KSCN) were simultaneously monitored during Vickers indentation test. We observed characteristic potential change in mV scale due to non-faradic reaction during loading to 20 N. Timing of the potential fluctuations coincided well with strong AE events. Both the AE and potential fluctuation were found to be produced by the Mode-I fracture of the film bending during loading. The number of equidistance step-wise terrace or rippled cracks observed in pyramidal indentation agreed well with the number of potential fluctuation. It was found that potential fluctuation analysis, jointly utilized with AE analysis, can reveal the fracture process of the film.

Keywords: Hard surface film, Indentation test, Electrochemical noise analysis, Finite element method, Fracture strength

1. Introduction

Hard surface coatings are widely used to improve the functionality of the metals. Hard films such as ceramic are brittle and often suffer damages as cracking and exfoliation. Evaluation of fracture strength of the hard thin films is important for a practical application. Though various test methods such as scratch and external loading have been utilized so far, property of the film tends to change depending on the test method and mechanical characteristics of the substrate. It is generally difficult to determine the intrinsic fracture strength of the film.

One of the authors once attempted tensile and compressive loading of the specimens with CVD-TiN film deposited on steel substrate [1, 2]. They studied the crack dynamics of the film using quantitative source inversion technique. They also used finite-element method (FEM) to determine the fracture strength of the film and residual stress [1], and revealed extremely large compressive residual stresses. External tensile loading hardly generates crack in the film due to large compressive residual stresses. Ikeda et al. [3-5] reported that external loading of WC-Co plate with CVD-diamond resulted in the unstable fracture of the substrate. This implies that the external loading method cannot be used for evaluating the intrinsic fracture strength of films.

We previously performed micro-indentation tests to TiN film deposited onto soft and ductile stainless steel substrate AISI-304 [6, 7], and monitored AE to study the fracture mechanism of the films. Fracture mode analysis [8, 9] revealed that a number of AEs by Mode-I fracture were

produced during loading. Indentation test of the hard film on the soft substrate makes the evaluation of the fracture strength of the film possible, since the film tends to suffer surface Mode-I cracks due to tensile stresses induced by film bending. It was made unclear whether the AEs were produced by Mode-I tensile crack or friction or cracking by compressive loading. In order to determine the fracture strength of the film, we must clarify the film fracture process and mechanism during indentation testing.

Monitoring of corrosion potential fluctuation or electrochemical noise (EN) analysis has been successfully utilized to study the initiation of localized corrosion and stress corrosion cracking (SCC) [10-12]. The potential fluctuation is caused by non-faradic anodic or cathodic local current [12]. If we use EN analysis, we can monitor the process of film cracking. Thus, we simultaneously monitored EN and AE during indentation testing and analyzed the details of the crack progression.

In this study, we first monitored AEs during indentation testing in air of TiN film deposited onto WC-Co cermet and AISI-304 steel. Effect of hardness of the substrate on the damage characteristics of the film was studied. Next we utilized AE and EN analysis during indentation test in specially designed solution. We investigate the fracture behavior of the film. Finally, we estimated the fracture strength of TiN film using FEM [6, 7].

2. Materials and Experimental Procedures

The hard films tested are TiN films of a few μm thick. The TiN films were deposited by PVD method onto metastable austenitic stainless steel (AISI 304) and WC-Co cermet. Here, sample with AISI-304 substrate has a middle layer of 0.5- μm thick titanium deposited with ion bombardment in order to improve the interfacial strength. These samples are designated as TiN/Ti/AISI304 and TiN/WC-Co, and coated by hollow cathode discharge (HCD) and arc ion discharge (AID), respectively. Film thickness and specimen size are shown in Table 1.

Table 1 Materials and specimen size.

Film/Substrate	TiN/Ti/AISI304	TiN/WC-Co
Film thickness μm	4	2
Material shape mm	20 x 20 x 2	20 x 20 x 5

We performed micro-indentation test by an electromagnetic type servo-testing machine equipped with a Vickers indenter and two eddy current sensors. This machine can measure the indentation force (F) and indentation depth (h) or F - h curve with high resolution. Maximum indentation force (F_{max}), were optionally changed depending on the purpose. All tests in air were performed with loading rate (dF/ds) of 5 mN/s and holding time (t_v) of 10 s at room temperature.

We monitored AEs using four resonant-type small sensors (PICO: PAC). They are mounted on the film surface to monitor the Lamb wave AEs. We also used a wideband frequency sensor (WD: PAC), which was mounted on the bottom surface of the specimen, as shown in Fig. 1. The WD sensor signal was set on the trigger channel. Sensor outputs were amplified to 60 dB by pre-amplifiers (PAC), and digitized by an A/D converter (Gage Applied Inc.) and fed to a personal computer. AEs are digitized at an interval of 40 ns with 2048 points. The threshold value for channel 1 (trigger channel) was set at 25 μV .

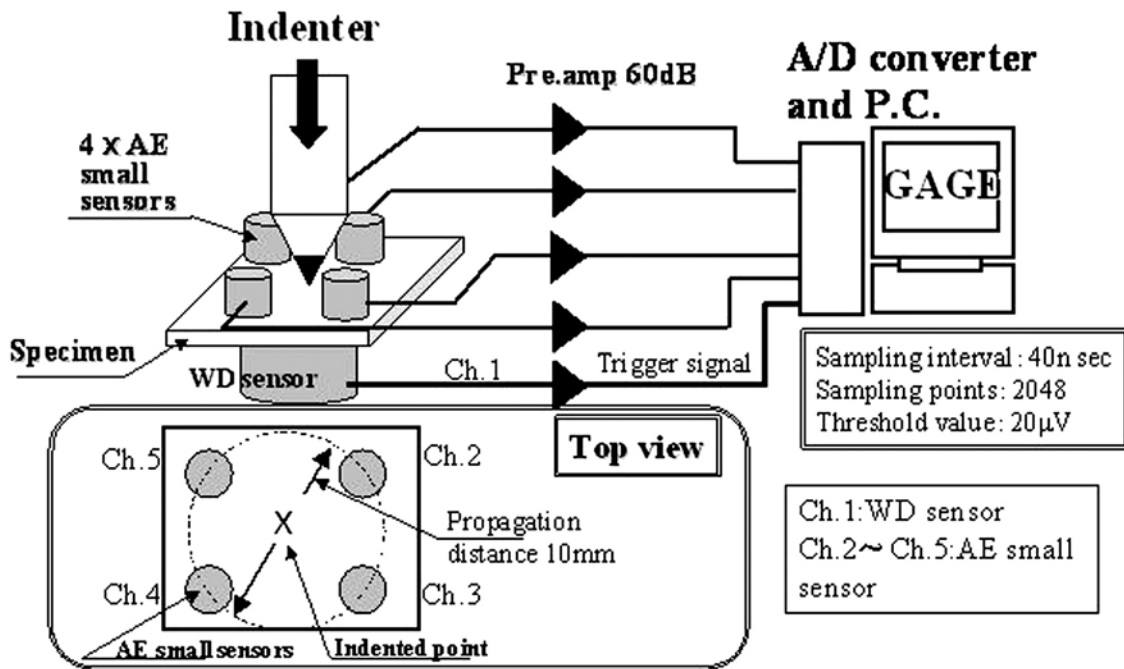


Fig. 1 Experimental setup for AE system for indentation testing.

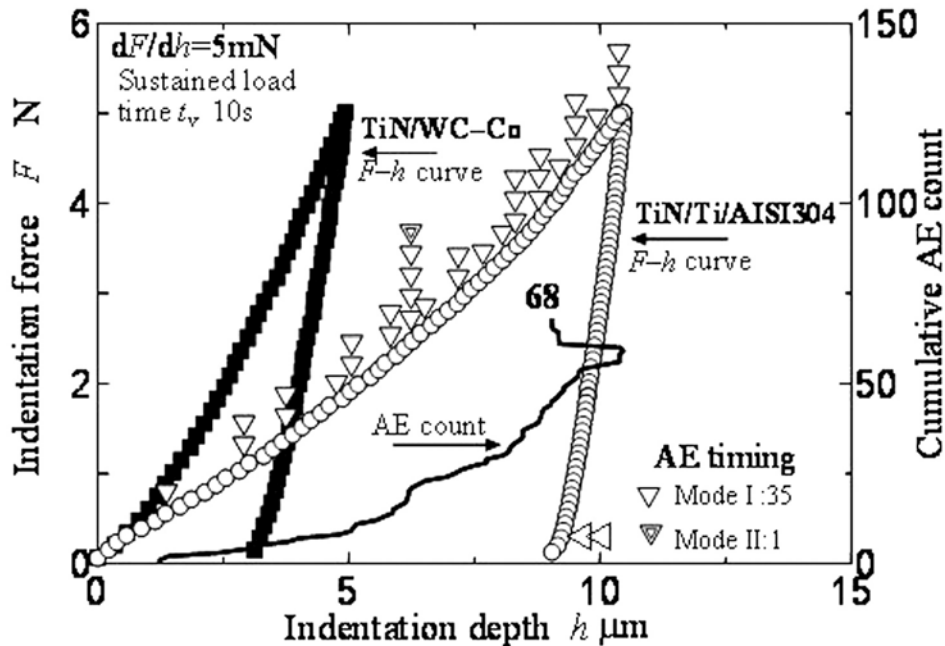


Fig. 2 F - h curve with cumulative AE count for TiN/Ti/AISI304 and TiN/WC-Co.

We also monitored the corrosion potential fluctuation induced by film fracture in a solution. A 20-mm diameter plastic cell was glued on the specimen surface. This cell is connected to another cell with Ag/AgCl reference electrode (GS-5015C: TOA-DKK). The solution was hydrochloric acid (1 mol/l HCl + 0.01 mol KSCN) [14], which can monitor the damage occurrence sensitively. Output of the electrode was digitized by a digital voltmeter (RE6871E: ADVAN-TEST) at resolution of 1 μ V and time interval of 76 ms. This indentation test in solution was performed with $F_{\max} = 20$ N, $dF/ds = 1$ mN/s and $t_v = 60$ s at room temperature.

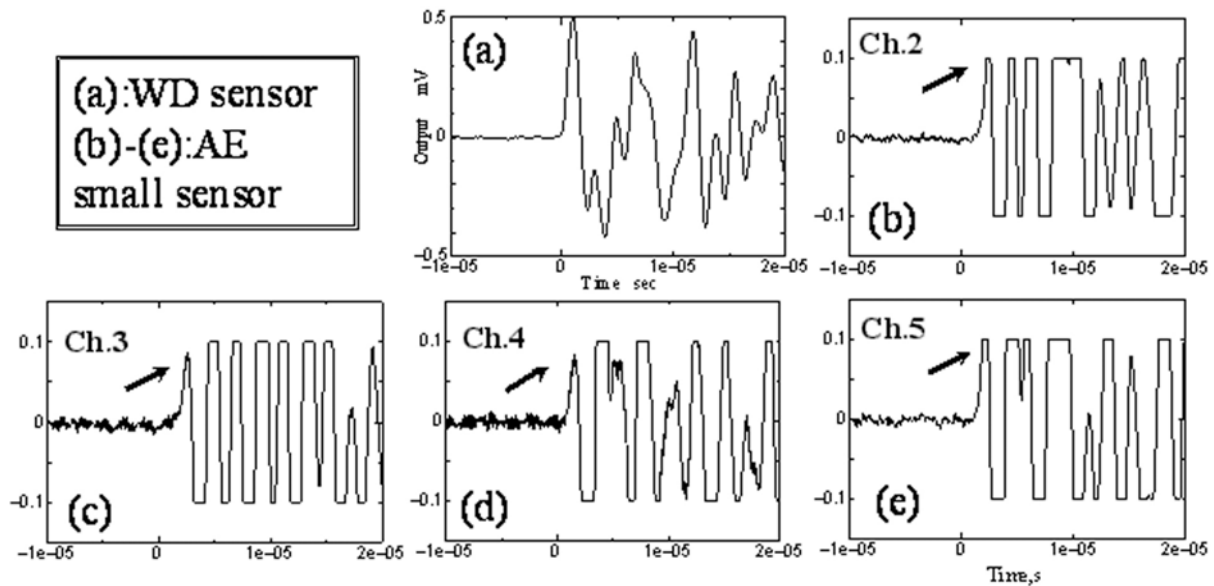


Fig. 3 Typical AE waveforms detected by AE small sensor during the indentation testing.

3. Results and Discussion

3.1 Analysis of micro-crack behavior during Vickers indentation test

Figure 2 shows the $F-h$ curves and cumulative AE counts. The specimen TiN/Ti/AISI304 produced a number of AEs from small force, while TiN/WC-Co produced no AEs. Figure 3 shows the typical AE waveforms detected during loading of TiN/Ti/AISI304 specimen. It is noted that polarities of first S_0 mode Lamb waves are all positive as indicated by arrows, indicating Mode-I opening fracture type. Open triangles in Fig. 2 indicate the AEs from Mode-I opening fracture types estimated by the fracture-type classification method [8, 9]. Most AEs detected are produced by Mode-I crack with opening vector in the direction parallel to the film surface. We detected only one AE from Mode-II crack at around 2.5 N.

Figure 4 shows the micrographs of indenter contact region. There observed a number of steps in the pyramidal indentation of the specimen TiN/Ti/AISI304. These steps are film cracks, known as the ripple cracks. In contrast, two small median cracks from the corners of indentation were observed for TiN/WC-Co.

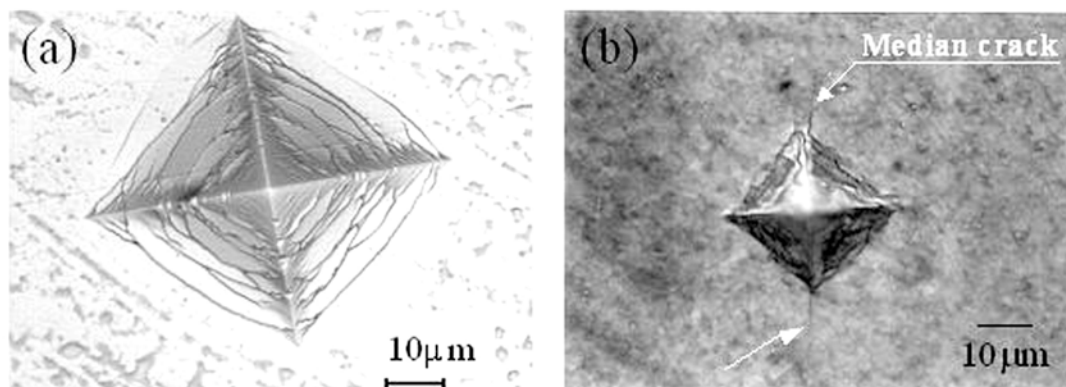


Fig. 4 Micrographs of contact region for TiN/Ti/AISI304 (a) and TiN/WC-Co (b), tested with $F_{\max} = 5$ N using Vickers indenter.

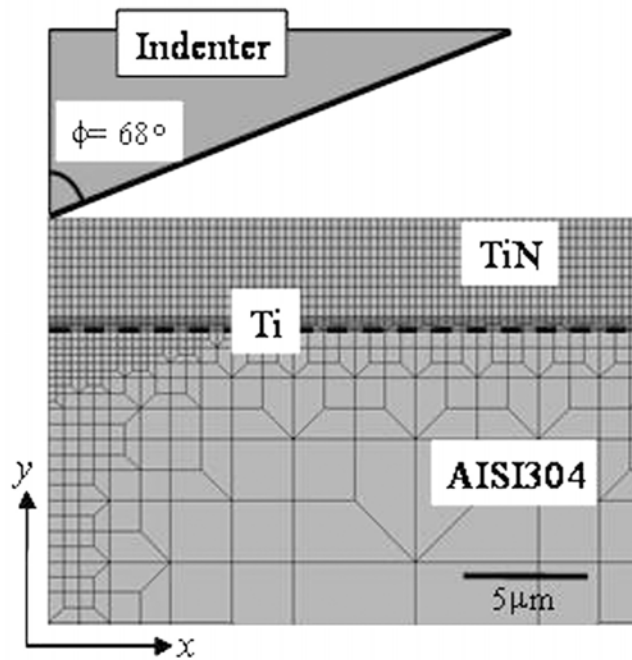


Fig. 5 FEM analysis model for TiN/Ti/AISI304 and TiN/WC-Co.

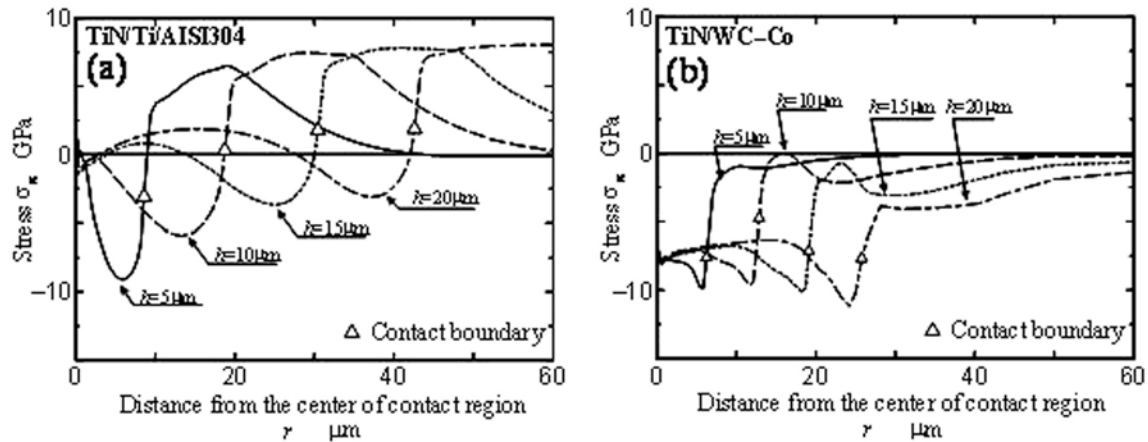


Fig. 6 σ_x distribution for TiN/Ti/AISI304 (a) and TiN/WC-Co (b).

3.2 Stress analysis of thin films subjected to Vickers indentation test

In order to study the influence of the substrate on the film damage, we analyzed stress distribution by FEM as shown in Fig. 5. Here the film thickness was set as $4 \mu\text{m}$. The yield strength (σ_{ys}) of the film is assumed to be 7 GPa. This value was estimated by three times the Vickers hardness value [13]. Figure 6 shows stress σ_x distribution in the direction parallel to the specimen surface for indentation depth h from 2 to $10 \mu\text{m}$. Horizontal axis (r) designates the distance from the center of indentation. Open triangles on the curves indicate the contact boundary. Figure 6(a) indicates that the σ_x is compressive in the contact region, while it changes to tensile stress outside the contact region. This stress distribution, with large tensile stress higher than the tensile strength of the film, strongly indicates that crack is produced by the tensile stress induced by bending of the film. A number of Mode-I cracks, appeared as ripple crack, are produced outside the contact point with progression of indentation. In contrast to this, only the compressive σ_x is induced for TiN/WC-Co, as shown in Fig. 6(b). The cermet substrate does not suffer plastic de

formation. Thus, the crack morphology for TiN/WC-Co specimen is similar to that observed for monolithic ceramics.

3.3 Monitoring of micro-cracks using electrochemical noise analysis

Figure 7 shows the $F-h$ curves and cumulative AE counts. 254 events were detected during the loading and 17 events during the unloading. We analyzed the fracture mode of 60 events with large amplitude of So-Lamb wave. Timing of Mode-I type AEs, with all positive polarities, were shown by open triangles near the $F-h$ curve. The Mode-I AEs were detected from small loads and produced at an almost constant rate with increasing load. This behavior is quite similar to that found in Fig. 2 for TiN/Ti/AISI304.

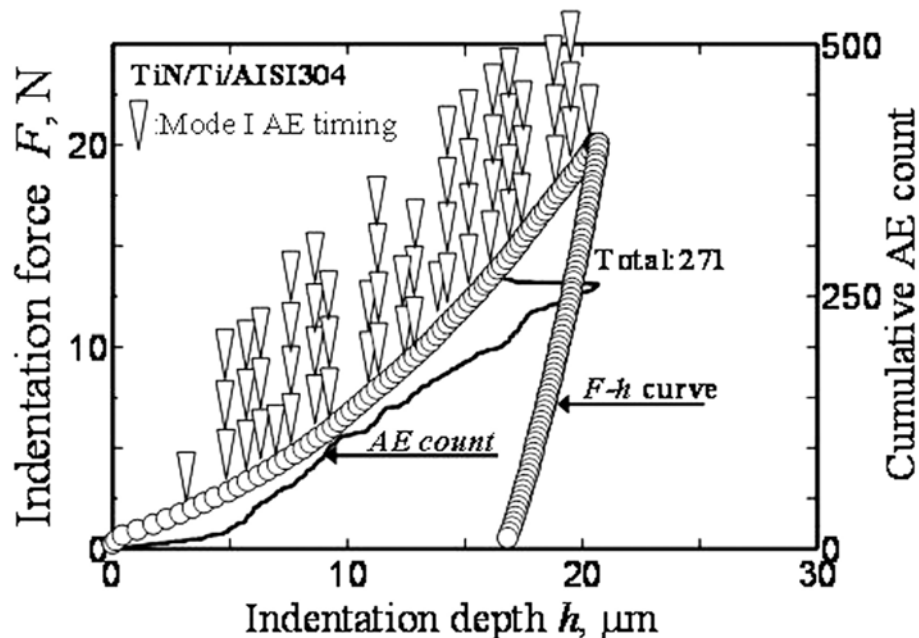


Fig. 7 $F-h$ curve with cumulative AE count for TiN/Ti/AISI304 in HCl solution.

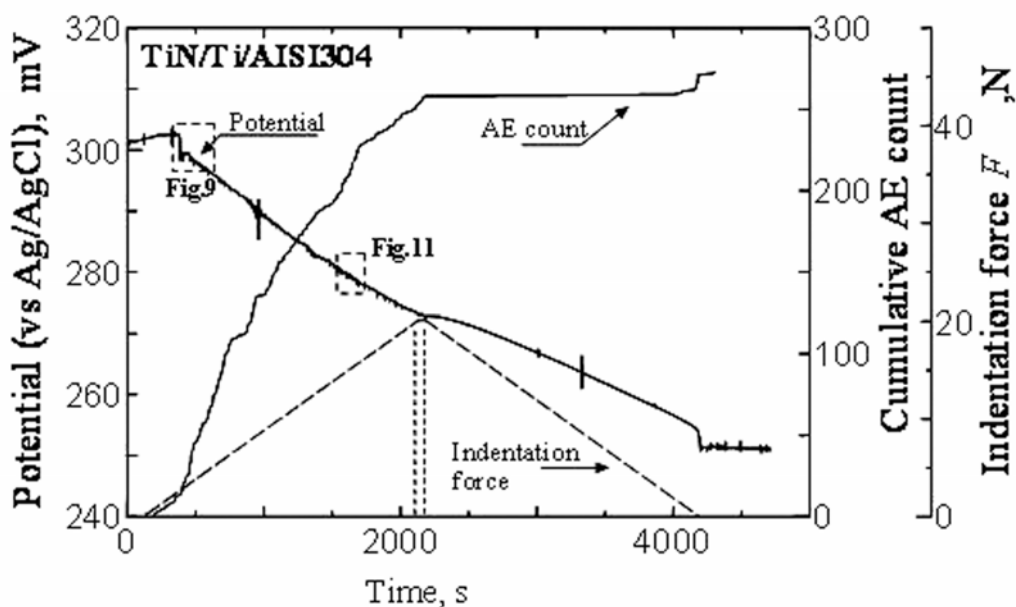


Fig. 8 Variation of potential noise with cumulative AE count during indentation test.

Figure 8 shows overall changes of corrosion potential or electrochemical noise (EN) and cumulative AE count as a function of loading time. Loading history is also shown by the dashed line. The corrosion potential shifts from 300 mV vs. Ag/AgCl of TiN to active direction, with a number of RD-type potential fluctuations (rapid drop to active potential and gradual recovery). First drop was observed at a low load of $F = 2.5$ N, corresponding to the loading time of 380 s.

Shown in Fig. 9 is the potential fluctuation in the range from 303 to 296 mV. Note the position in the loading history in Fig. 8. RD type fluctuations with large and small amplitudes were frequent. Figure 10(a) shows typical RD type fluctuation, which is caused by local anode current flows due to the film fracture [12]. Figure 10(b) shows changes of cumulative counts of RD-type fluctuations with the drop velocity of above 2 mV/s, AE event counts and indentation force with time. Most ENs and AEs were detected during loading. We observed a good coincidence between the two, AE and EN. This strongly suggests that the ENs were produced by film cracks occurring outside the contact region. FEM results (Fig. 5) suggested that ripple cracks were generated by the film bending, since large bending stress occurred outside the contact region.

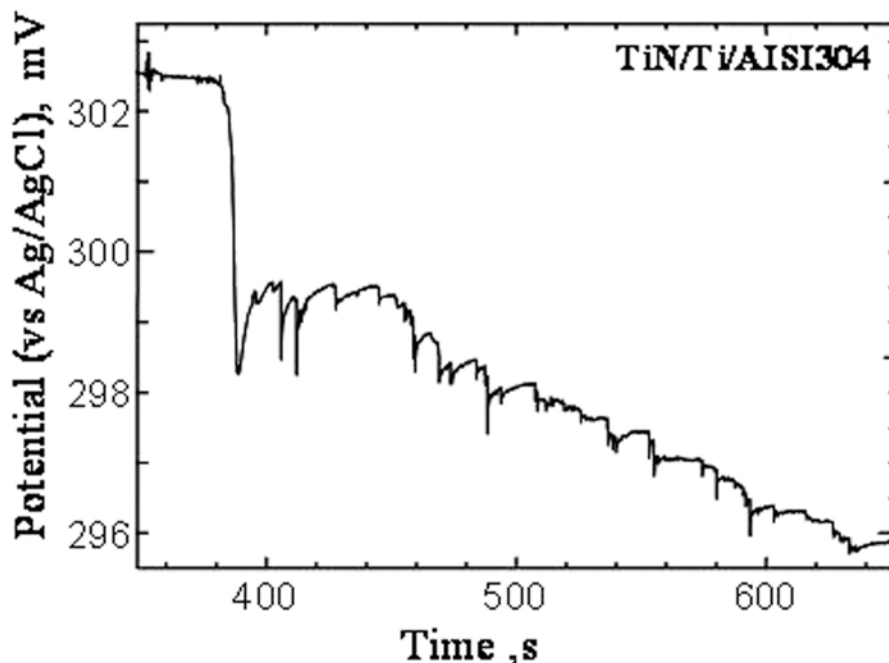


Fig. 9 Potential fluctuation during the indentation testing.

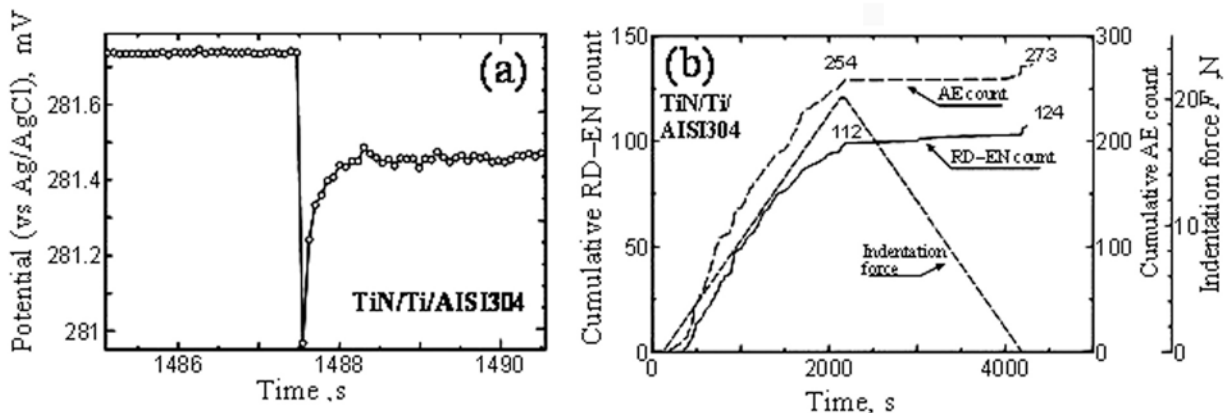


Fig. 10 Typical RD-type EN detected (a) and cumulative RD-type EN and AE counts (b) during the indentation testing.

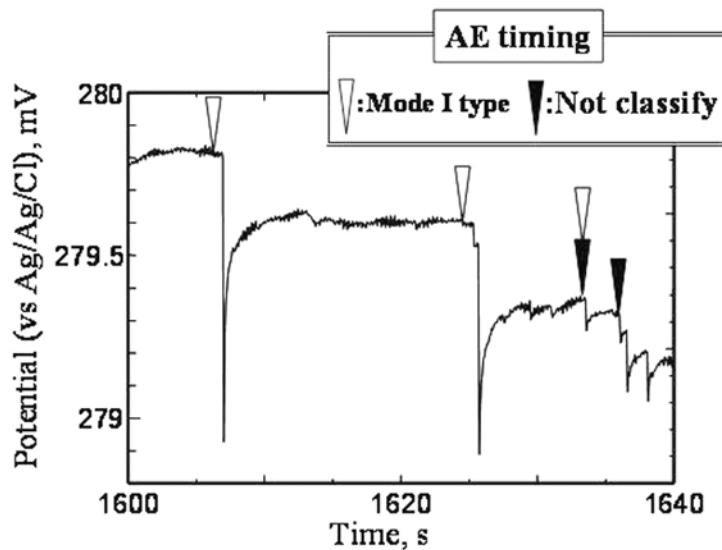


Fig. 11 Examples of RD-type ENs with AE timing.

Figure 11 shows an example of RD-type ENs and the timing of AEs. It is noted that an RD-type EN was detected just or slightly after an AE timing. Similar behavior was observed over the entire potential range.

Figure 12 compares SEM photographs of the indentation induced in air (b) and in solution (a). A partial film delamination was observed near the edge of pyramidal indentation in solution, suggesting the film damage by solution diffused into the film cracks. We counted the number of cracks on each pyramidal plane in Fig. 12(a). Figure 13 shows the number of cracks found in the contact region as a function of distance from the center of indentation, r . Total number of cracks counted was as 28 to 35 on one pyramidal plane. The total number of cracks reaches 128 and coincides well with the cumulative RD-type ENs number of 112 shown in Fig. 10. Thus, we conclude that both AEs and RD-type ENs were produced by the film fracture of TiN.

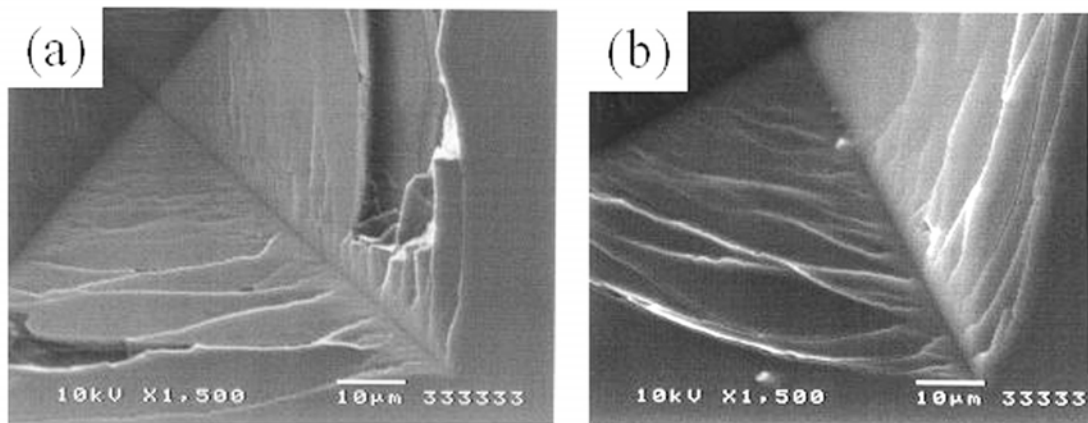


Fig. 12 Micrographs of the contact region for TiN/Ti/AISI304 tested with $F_{\max} = 20$ N in HCl solution (a) and in air (b).

4. Conclusion

In order to study the fracture mechanisms and strengths of PVD-TiN film, both acoustic emission (AE) and electrochemical noise (EN) were monitored simultaneously during indenta-

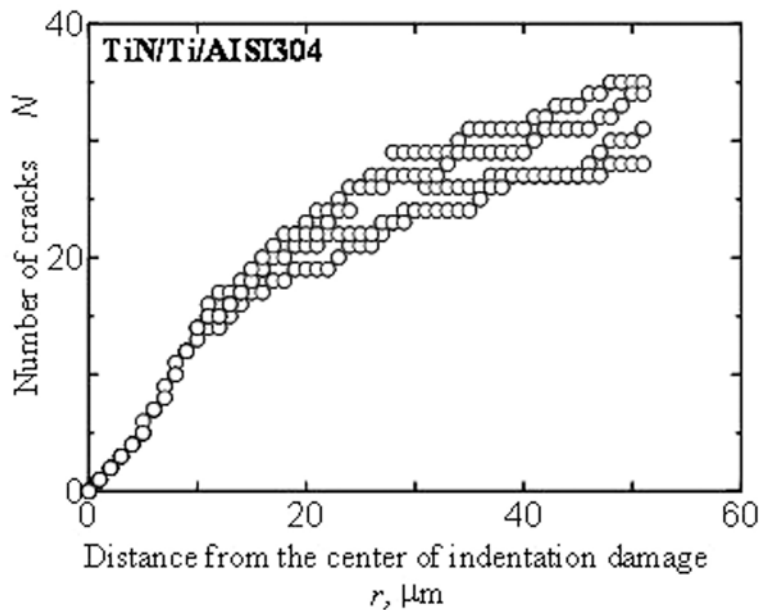


Fig.13 Number of cracks as a function of the distance from the center of contact region.

tion tests. Effects of substrate hardness on the film fracture and the fracture process of TiN film deposited on AISI-304 steel in 1 mol/l hydrochloric acid solution were analyzed in detail. Results are summarized below.

1. TiN film deposited on WC-Co cermet developed small median cracks at the corners of pyramidal indentation. TiN film on AISI-304 steel, however, sustained a number of film cracks (ripple cracks) but no median cracks. In the latter material, AEs from Mode-I film cracks were detected from low indentation loading and increased with the load. FEM analysis predicted that Mode-I film cracks was produced by large tensile stresses due to the film bending.
2. Simultaneous monitoring of AEs and ENs for the TiN film on AISI-304 steel in the solution of hydrochloric acid revealed that the number of EN coincides with that of AEs. Rapid shift of the potential to active direction (RD-type EN) is induced by the Mode-I film fracture near the indentation. EN analysis, jointly utilized with AE analysis, can reveal the fracture process of the film.

Acknowledgement

This work was performed as a part of the Center of Excellence (COE) Program, funded by the Ministry of Education, Culture, Sports, Science and Technology.

References

- (1) S. Ogawa, T. Fukai, T. Futatugi and M. Takemoto: Surf. Tech., **46** (1995), 456 (in Japanese).
- (2) S. Ogawa, H. Cho, K. Yamanaka and M. Takemoto: J. Soc. Mech. Eng. **63** (609) (1997), 1057 (in Japanese).
- (3) R. Ikeda, M. Nakanishi, T. Ogawa, M. Takemoto: Journal of Material Testing Research, **47**, 4 (2002), 231 (in Japanese).

- (4) R. Ikeda, Y. Hayashi, M. Takemoto: *Prog. Acoustic Emission XI*, (2002), JSNDI, Tokyo, p. 53.
- (5) R. Ikeda, Y. Hayashi, M. Takemoto: *J. Acoustic Emission*, **21** (2003), 131.
- (6) A. Yonezu, T. Ogawa and M. Takemoto: *Proc. ICF11* (2005) 4209.pdf.
- (7) A. Yonezu, T. Ogawa and M. Takemoto: *J. Soc. Mat. Sci. Japan.*, **54**, 11 (2005) 1030-1035. (in Japanese).
- (8) A. Yonezu, T. Ogawa and M. Takemoto: *Prog. Acoustic Emission XI*, (2002), JSNDI, Tokyo, p. 86.
- (9) R. Ikeda, M. Hayashi, A. Yonezu, T. Ogawa: *Journal of Material Testing Research*, **49**, 3 (2004), 157 (in Japanese).
- (10) H. Inoue, K. Yamakawa, and N. Fukuda: *J. Soc. Mat. Sci. Japan.* **43** (1994), 1400 (in Japanese).
- (11) H. Inoue, K. Yamakawa, T. Kikuchi and Y. Yoneda: *Zairyo-to-Kankyo*, **45**, (1996) 717 (in Japanese).
- (12) H. Inoue: *Zairyo-to-Kankyo*, **52**, (2003) 544 (in Japanese).
- (13) D. Tabor: *The Hardness of Metals*, Oxford University Press, (1951) 154.
- (14) T. Fukai: Doctoral thesis, Osaka University (1995).
- (15) S. Fujimoto and M. Takemoto: *Zairyo-to-Kankyo*, **53**, (2004) 309 (in Japanese).

THE ORIGIN OF CONTINUOUS EMISSIONS

KANJI ONO¹, HIDEO CHO² and M. TAKUMA³

¹) Dept. of Materials Science and Engr., University of California, Los Angeles, CA 90095, USA.

²) Department of Mechanical Engr., Aoyama Gakuin University, Sagamihara, Kanagawa, Japan.

³) Department of Mechanical Engr., Kansai University, Yamate, Suita, Osaka, Japan.

Abstract

We have studied the random nature of continuous acoustic emission, typically observed during the plastic deformation of metallic materials. In particular, the yielding of variously treated A533B HSLA steel samples was used as the emission source. Signal amplitude distribution was found to be Gaussian. Some minor deviation can be also seen when burst emissions are superimposed. Time-series analysis techniques were applied to obtain chaos parameters. Signals proved to be stochastic. When a laser excitation source is applied on tensile samples of common geometries, resultant simulated AE signals exhibit Gaussian distribution. The synthesis of these two sets of observation points to the resolution of the origin of the continuous emissions, which has been the subject of long running speculation.

Keywords: Continuous emissions, Gaussian distribution, Laser excitation, Time-series analysis, Chaos

1. Introduction

We observe continuous-type acoustic emission (AE) signals during the plastic deformation of metals and alloys, especially in the beginning stages [1,2]. Such continuous signals were found to exhibit Gaussian random distribution [3], but little progress has occurred since that time. In contrast, pulse-like AE signals, commonly known as burst emissions, are generated from distinct elastic energy release processes, such as cracking and martensitic phase transformation [4]. These burst-type AE signals correspond to specific physical events and can be characterized with Green's functions using methods such as deconvolution analysis, moment tensor analysis and simulation analysis when conditions are favorable. Strong research efforts have resulted in good understanding of the origin of burst emissions from various materials (For recent review, see refs. 5-7).

A large body of mathematical work exists dealing with stochastic and chaotic processes. Of special interest here is the time-series analysis. Applying this methodology, Bukkapatnam et al. [8] examined AE signals associated with flank wear and found them to emerge from a low-dimensional attractor of a chaotic process. They produced a compact set of signal features that enabled them to generate neural network for wear estimation. Recently, Nishiura et al. [9] showed that continuous emissions during shear-type machining processes can be characterized using methods of time-series analysis. They were able to differentiate continuous-type AE signals from several distinct stages of tool wear in machining by determining maximum Lyapunov exponents and correlation dimension. Signals from tensile, shear or mixed fracture processes generated distinct shifts in these parameters. Their findings implied that the observed AE signals also have their origin in chaotic non-linear dynamical systems. At present, the only information we utilize in defining continuous emission signals is the root-mean-square (rms) voltage,

averaged over a certain duration. Our interest is to examine continuous-type AE signals and to deduce other characteristic parameters if they exist.

Another objective of this work is to simulate continuous emission signals in order to identify the origin of such emission. It is generally believed that continuous emissions are the consequence of many individual AE bursts occurring in random sequence. However, no definitive evidence has been obtained. Ono (unpublished work, 1978) attempted to generate random emission signals via the superposition of random-amplitude pulses with randomly varied intervals. Two sets of random noise generator and AE equipment were used in the experiment. Each pulse was narrow-band filtered to represent typical burst emission (often referred to as a damped sinusoid). Resultant signals contained regular features and randomizing effort was unsuccessful. The present work utilizes laser excitation of typical mechanical test samples and a non-contact, broadband detection method. Digitalized signals are conducive to the superposition procedures and we attempt to artificially generate continuous emission signals.

2. Analysis of Continuous Emission Signals

We generated continuous emission signals by the plastic deformation of steel samples. These are of round half-size ASTM E-8 tensile sample geometry. The gage diameter is 6.4 mm and the parallel section length is 32 mm. The grip section was threaded with 1/2"-20 thread and the total length was 85 mm. Material was A533B steel, oil-quenched from 930°C and tempered at 550°C for 2 hr. An AE sensor (either AET MAC375 or PAC WD) was placed on one end with resin couplant. AE signals were recorded using a PAC Mistras board running under MI-TRA software with external triggering of 100-ms interval. Digitization rate was 2 MHz and the record length was 20 kw. Typical stress-time and rms-voltage-time curves are shown in Fig. 1. Here, the rms-voltage data was manually obtained from digitized data using the statistical function of Excel.

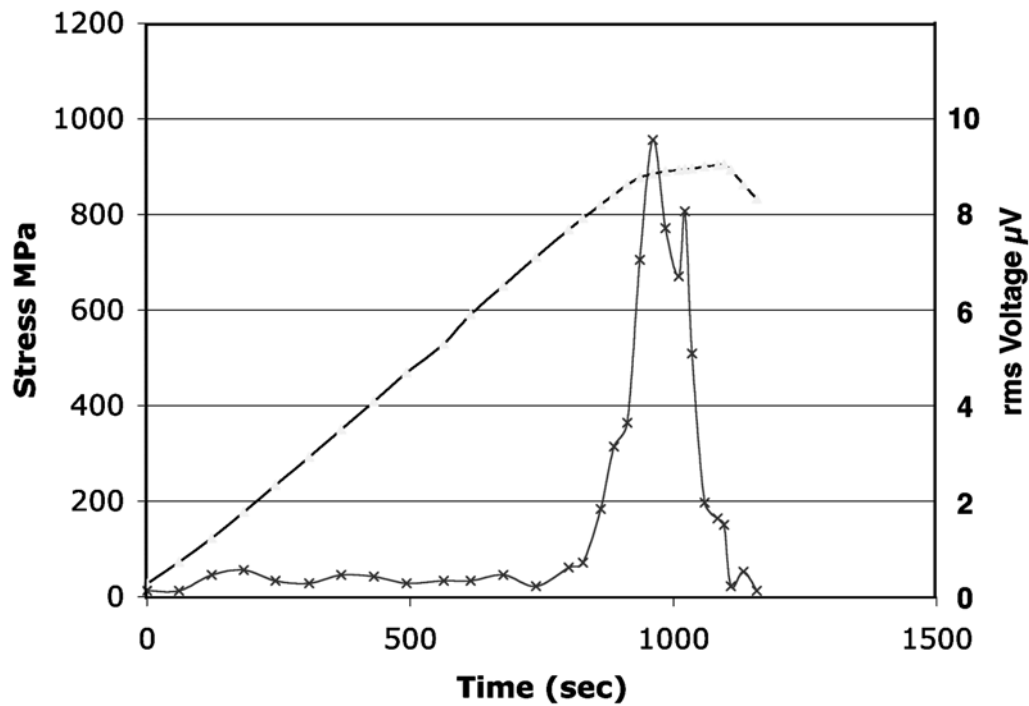


Fig. 1 The stress-time and rms-voltage-time curves for an A533B tensile sample.

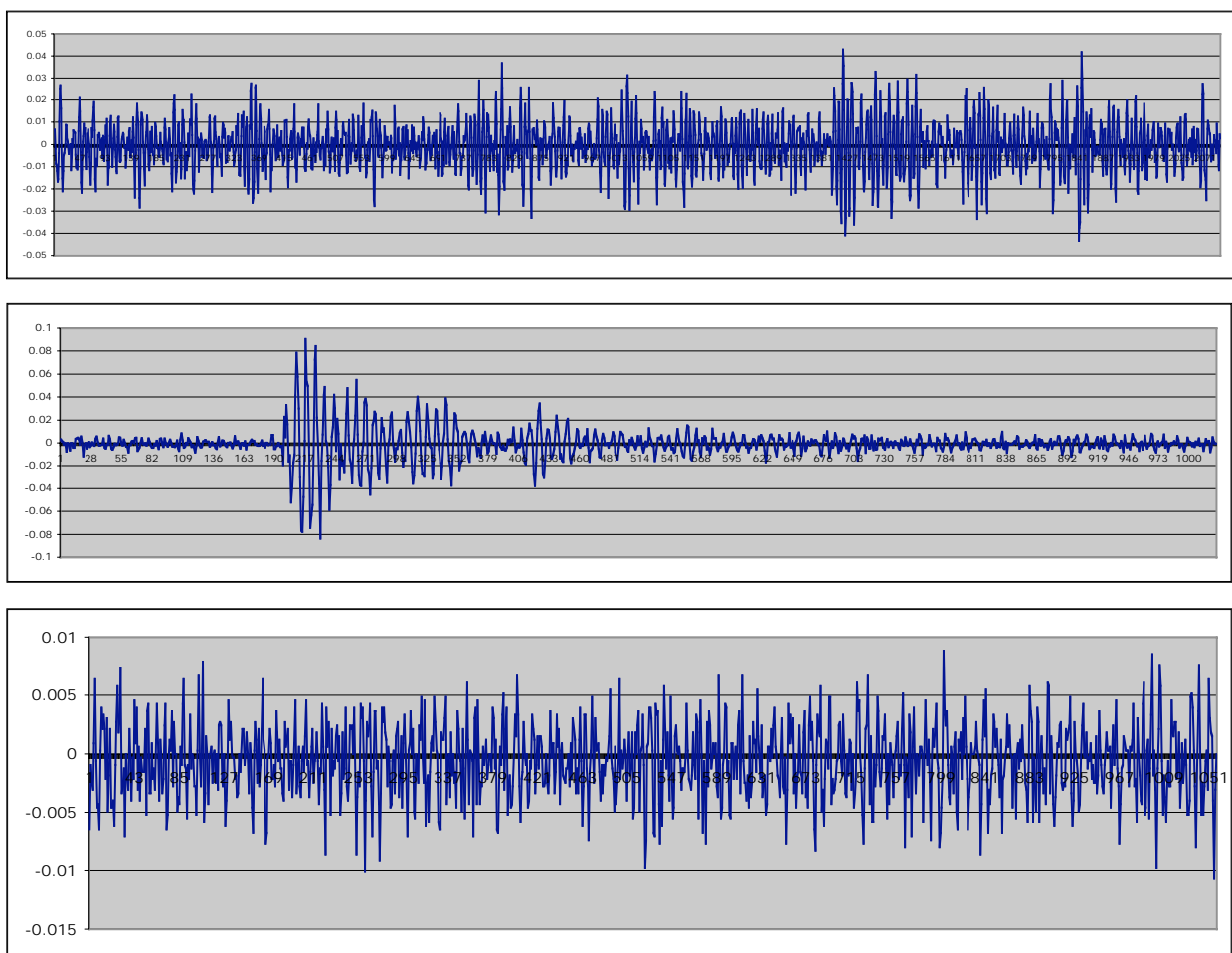


Fig. 2 Representative signals. Top: E, Middle: G, Bottom: H

Figure 2 shows representative signals. Here, E is a continuous signal near the maximum signal level at yielding and H is the preamplifier noise, while G is a burst emission signal for comparison. Details of these and other signals examined are tabulated in Table 1. In the case of E, one can see wave trains appearing repeatedly, although each high activity zone differs from all others. Signal H shows more uniformity in peak distribution and no definitive wave train is discernible. As usual, the burst signal G indicates a rapid rise followed by slower decay in amplitude. Figure 3 gives wavelet transform result for a part of continuous emission E. While several of the high coefficient value regions are separated by the round-trip time, these are

Table 1 Summary of signal characteristics. (Type: B=burst, C=continuous, MC = MAC375)

Signal	Type	rms V	Data length	Sensor	Fractal dimension	Lyapunov exp.	Correlation dimension
A	C	2.83 μ V	1 kw	MC		0.491	0.0889
B	B	10.01	1	MC		0.549	-0.825
C	C	4.46	20	WD	1.42	0.529	-2.01
D	C	5.76	20	WD	1.62	0.441	-1.265
E	C	10.11	20	WD	1.65	0.440	-1.856
G	B	13.33	1	WD	1.24		
H	C	3.27	2	WD	1.4		

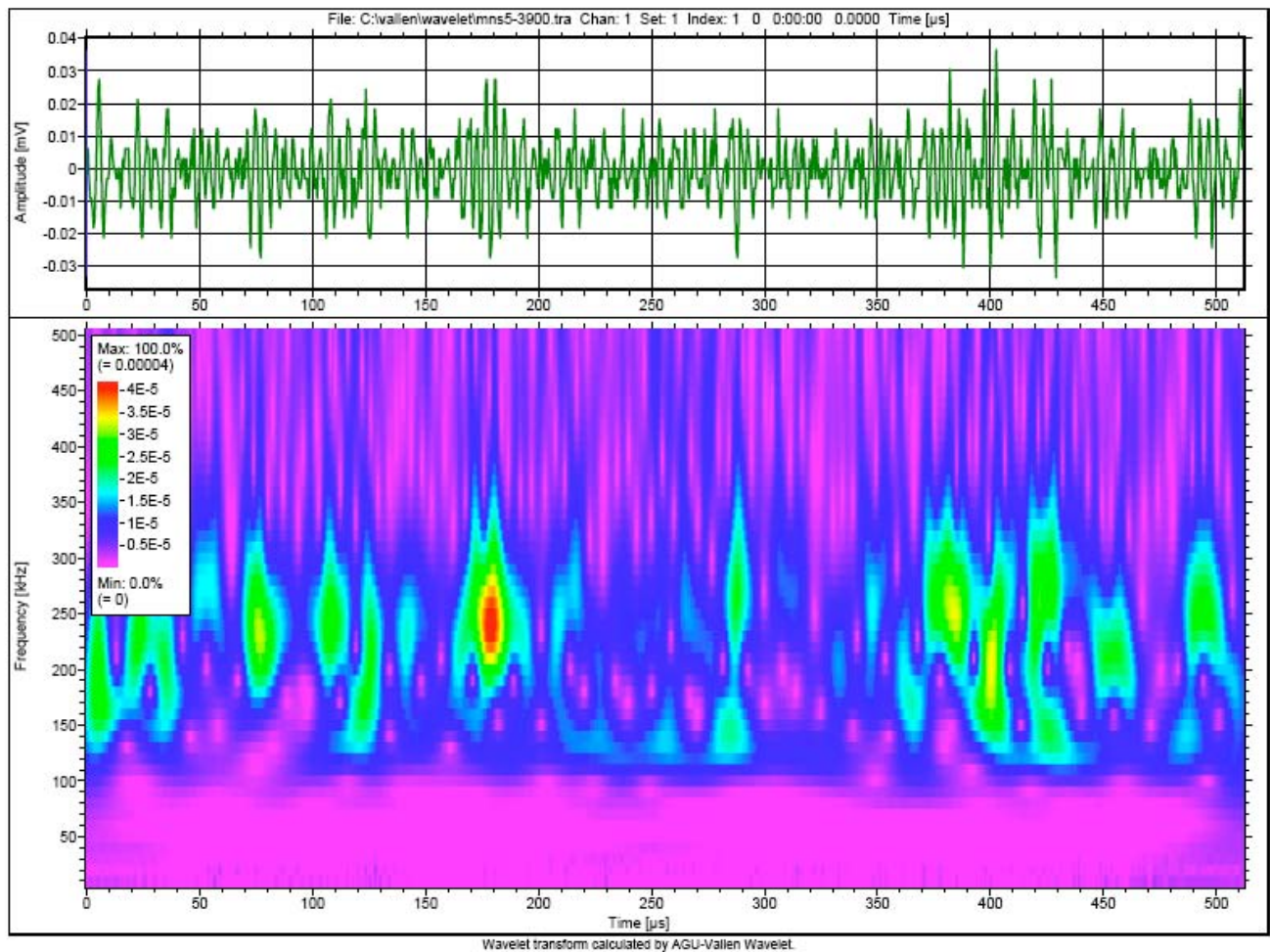


Fig. 3 Wavelet transform of continuous emission, E.

generally unrelated. When the cumulative amplitude distribution of signal H is plotted against amplitude, it coincides with that of normal distribution, as shown in Fig. 4. Although signals E and H look different, both signals follow the normal distribution. All other continuous emission signals also have the same normal distribution characteristics.

Using sets of data of 1024-points, the fractal dimension of all the signals was calculated as a function of frequency. Five curves for signals C to H are shown in Fig. 5. For the signals except G, fractal dimensions were similar above 350 kHz and varied from 1.5 to 1.65. These signals were obtained using a WD sensor that has sensitivity peaks in 100-300 kHz. This is reflected in the changes observed for signals D and E, both of which have increased rms voltage levels over the background noise. Here, the fractal dimensions increased from ~ 1.5 to almost 1.7. Signal C is only slightly above the background and show the essentially same curve as that of signal H. Burst signal G shows consistently lower fractal dimension (1.07 – 1.35) than the rest.

In the frequency range of 200-300 kHz, the average fractal dimension appears to increase with the rms voltage of continuous emission signals. As listed in Table 1, it varies from 1.4, 1.45, 1.62 and 1.65. For the burst signal, it is markedly lower at 1.24. Since fractal dimension of 1.999 corresponds to Brownian motion and that of 2.0 to random white noise, the present result implies that stronger continuous emission signals become less predictable.

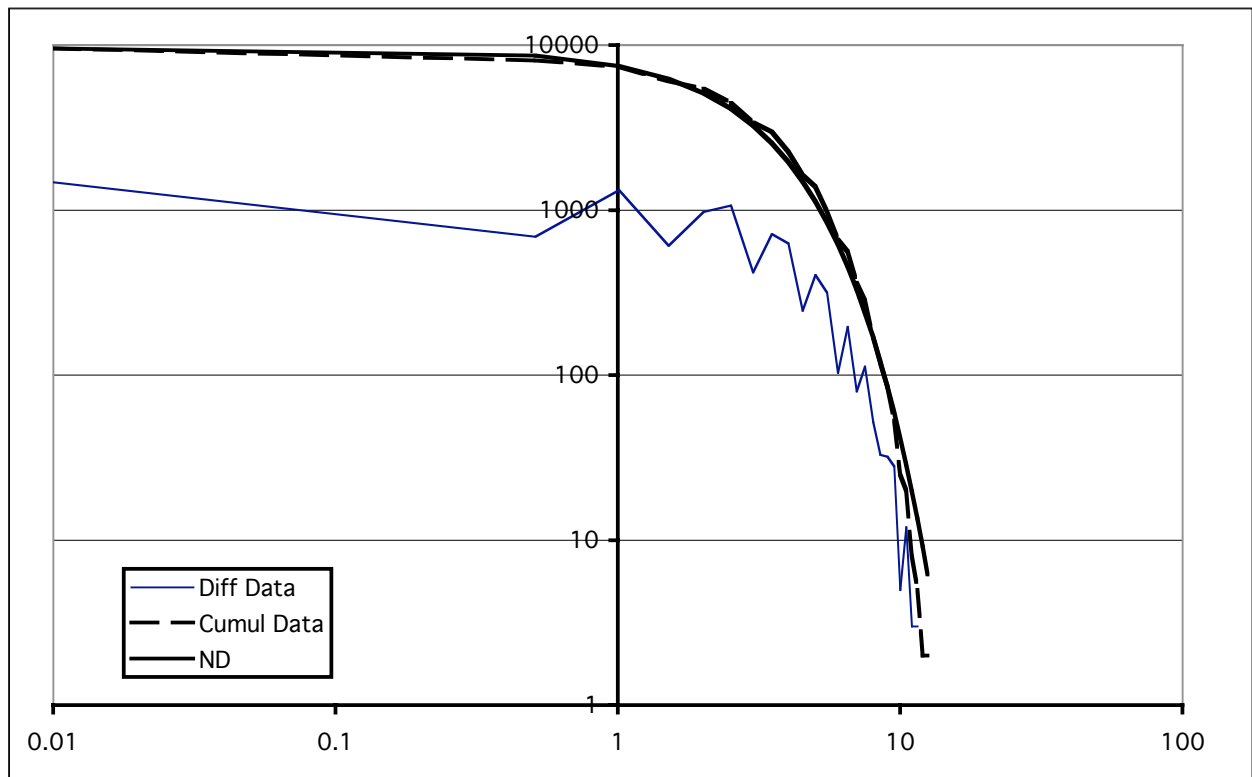


Fig. 4 Differential and cumulative distribution vs. amplitude (in μV) of signal H. ND = normal distribution.

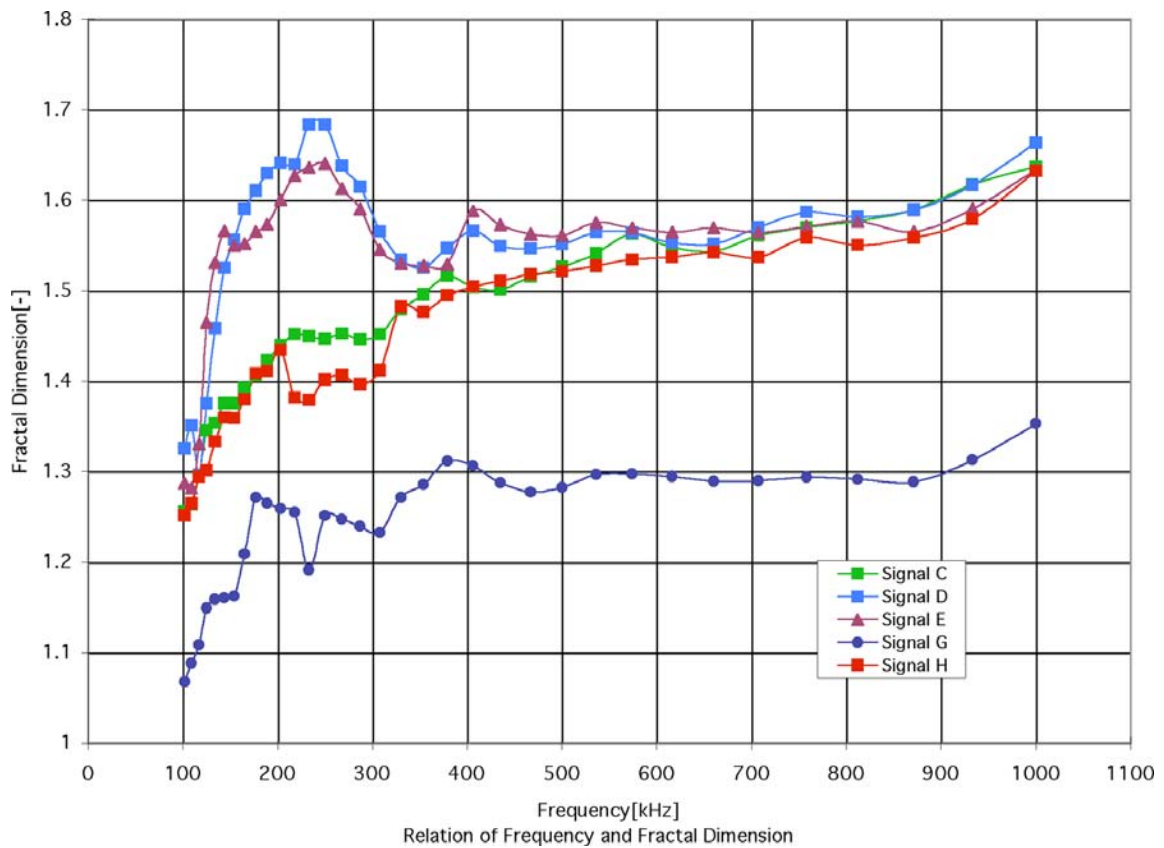


Fig. 5 Fractal dimension of the signals, C to H, as a function of frequency.

Parameters used in time-series analysis include correlation dimension and Lyapunov exponent. Figure 6 shows a plot of correlation index $J(m)$ against embedding dimension m for signal C. This plot indicates convergence above $m=12$ at $J(m) = 10$, or the correlation dimension to be 10. For signal D, correlation dimension was found to be 10.1. For signal E, no convergence resulted. When the value of correlation dimension is at this level, signals are best described as stochastic or random, rather than being chaotic. The maximum Lyapunov exponent and correlation integral values were obtained for signals A – E and listed also in Table 1. While these vary depending on signals examined, allowing the signals to be differentiated, no consistent changes can be recognized in the data.

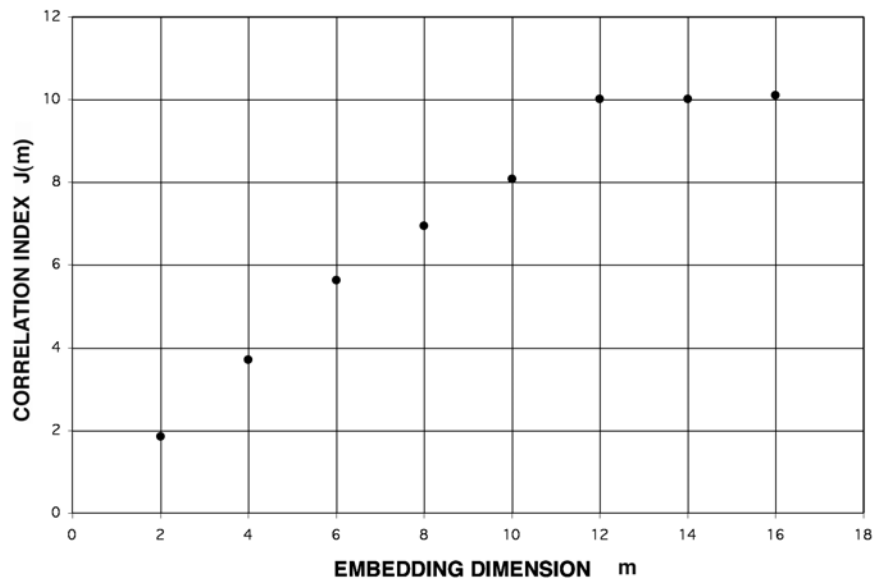


Fig. 6 Correlation index $J(m)$ vs. embedding dimension m for signal C.

It is concluded from these findings that the continuous emission signals examined exhibit stochastic or random behavior. No new parameter that can characterize continuous emission signals in terms of chaotic behavior is identified. The average fractal dimension appears to correlate with the rms voltage and further evaluation is warranted.

3. The Origin of Continuous Emission Signals

It is generally believed that continuous emission signals result from the superposition of numerous distinct AE events [1,2]. In the case of a high-strength aluminum alloy, the use of a broadband sensor resolved individual AE pulses in the post-yield region, where the fracture of particles is the source of the observed AE activities [10]. During the yielding of many metals and alloys, it is natural to attribute a slip step as the source of an AE event. When the slip step is large and strain rate is high as in the case of dynamic strain aging, we have observed a spike of AE activity. Accompanying a load drop of dynamic strain aging, Armentrout and Carpenter [11] reported a sudden increase in the amplitude of continuous emission, which was a single burst AE. In usual yielding, no confirmation of individual slip step linking to a single AE event has been reported.

Our attempt to simulate continuous emission signals starts from the excitation of representative tensile samples using energetic laser pulses. Laser pulses were from a YAG laser (Continuum; 1-3 mJ output), focused on the end of a tensile sample. Acoustic signal detection utilized

a laser interferometer (Thalen Laser; SH-140) with bandwidth of 20 kHz to 2 MHz. Two round-bar steel samples (parallel gage section and hour-glass type) and one flat steel sample were used. Signals were averaged 1000 times to improve the signal-to-noise ratio.

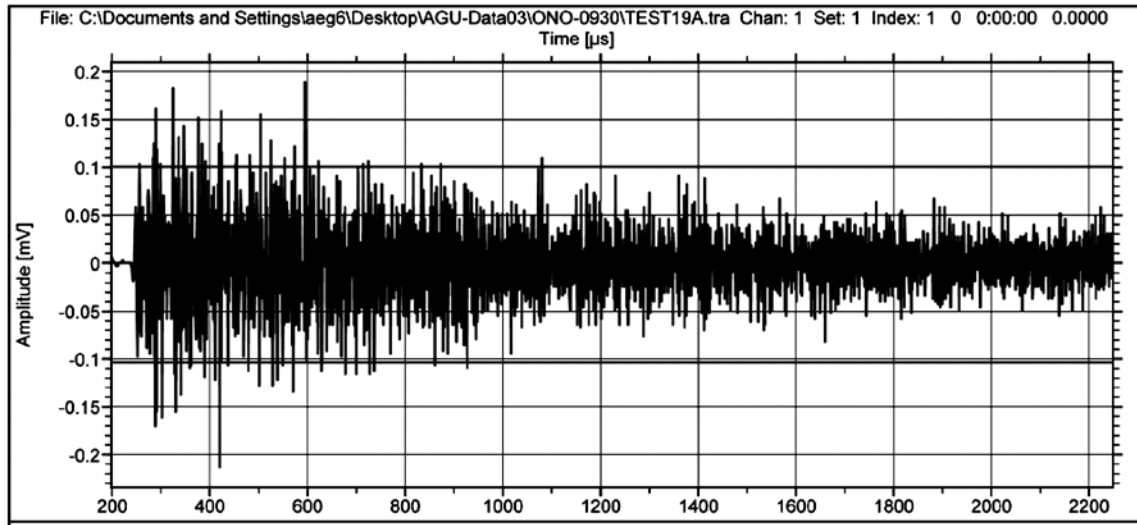


Fig. 7 Laser-excited signal on a round-bar tensile sample. Detected by non-contact method.

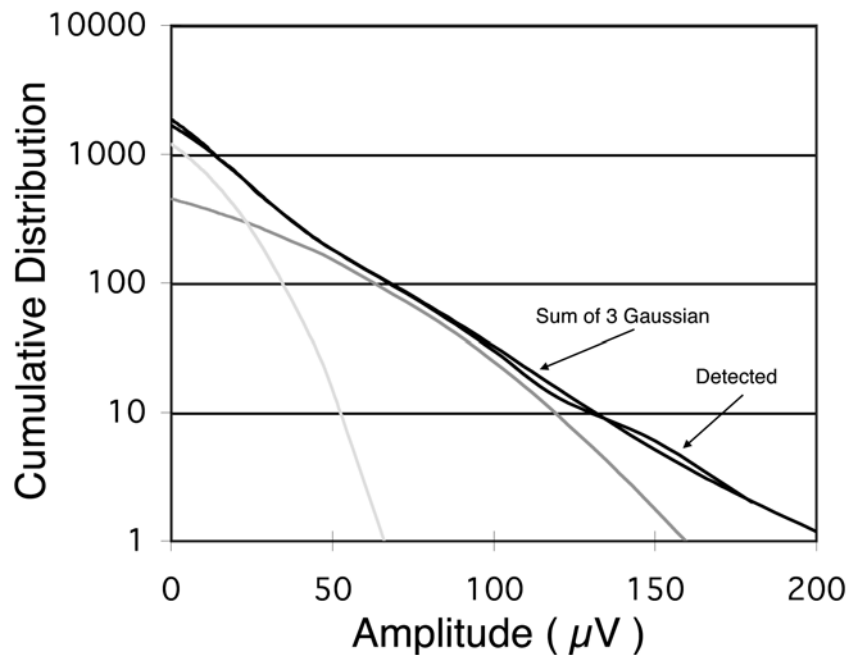


Fig. 8 Cumulative amplitude distribution of detected laser-induced signal and sum of 3 Gaussian distribution (Two of the Gaussian distributions are shown).

Figure 7 shows one such detected signal on a round-bar sample. This exhibits typical characteristics of an AE burst; namely, a sharp rise, followed by a slow decay extending over 2 ms. With a non-contact detection, this decay lasts beyond 10 ms. The wavelet coefficients show broadband response as expected, but give sharp peaks at 80-150 kHz range and at 350-500 kHz range. Some periodicity exists, but distinct reverberation peaks are absent. The cumulative amplitude distribution of this signal is shown in Fig. 8. The data is nearly log-linear and can be represented by the superposition of three sets of Gaussian distribution. The third one makes only

a minor contribution, but keeps the distribution curve matched well below 10 counts. This is surprising to find as the sample had well machined ends and most length was round bar. Apparently, the shoulder sections make wave reflections complex, randomizing the waves reaching the detection end. The other contributor is the point source nature of the laser excitation, unlike the commonly used AE or ultrasonic sensor source.

A result of random summation of ten signals is shown in Fig. 9. Starting times were picked arbitrarily and the amplitude was varied for each wave, which is identical to Fig. 7. Thus, the origin of continuous AE signals with Gaussian distribution can be traced to the small source size and the irregular reflections and refractions of sample geometry. This produces spreading waves that are randomized through bouncing at the shoulders and enlarged grip regions.

4. Conclusion

Continuous AE signals were examined using the method of time-series analysis and found to be stochastic. No useful parameter based of chaotic behavior was found. Using laser-excited source for AE bursts, the random superposition of such excited waves can produce randomized signals that simulate continuous AE signals from plastic deformation. This confirms the long-held belief regarding the origin of continuous emissions.

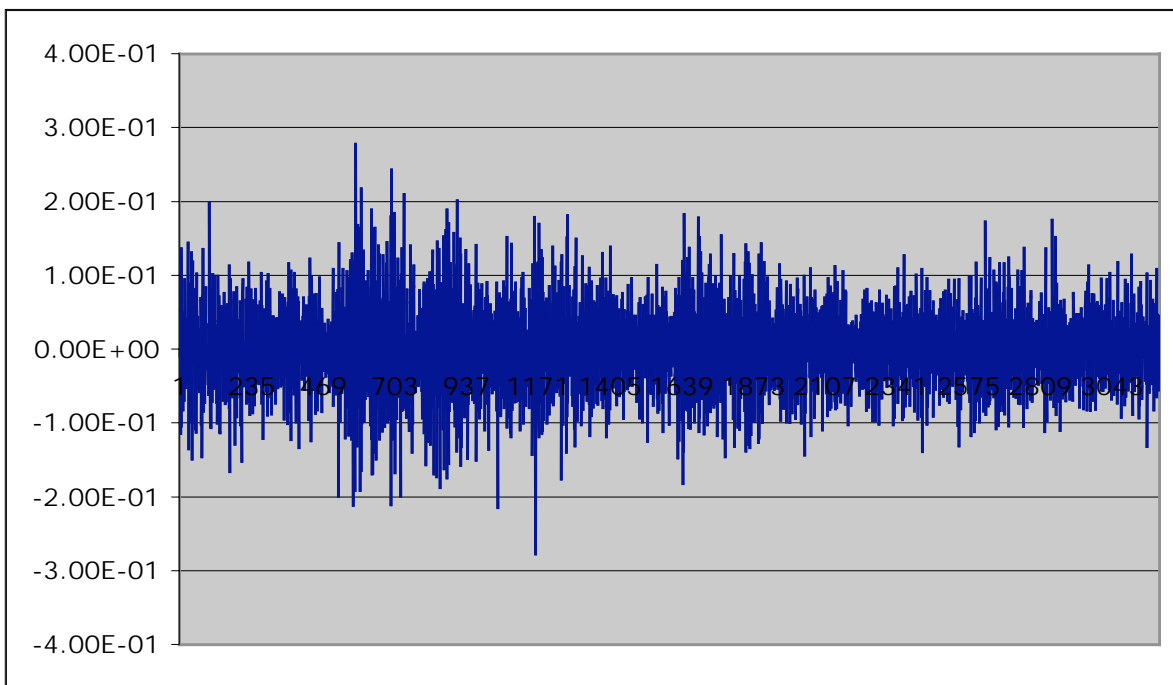


Fig. 9 Simulated continuous emission signal. Total signal duration = 1.6 ms. Ten signals of Fig. 7 were summed after selecting arbitrary starting time and scaling amplitude.

References

1. C. R. Heiple and S.H. Carpenter, "Acoustic Emission Produced by Deformation of Metals and Alloys - A Review: Part I", *J. Acoustic Emission*, **6**, 1987, 177-204.
2. C. R. Heiple and S.H. Carpenter, "Acoustic Emission Produced by Deformation of Metals and Alloys - A Review: Part II", *J. Acoustic Emission*, **6**, 1987, 215-238.
3. K. Ono, "Amplitude Distribution Analysis of Acoustic Emission Signals", *Materials Evaluation*, **34**, 1976, 177-184.
4. Kanji Ono, "New Goals for Acoustic Emission in Materials Research", a chapter in "*Acoustic Emission – Beyond the Millennium*," eds. T. Kishi, M. Ohtsu and S. Yuyama, (2000), Elsevier, pp. 57-76.
5. M. Enoki, T. Kishi, "Acoustic Emission Source Characterization," a chapter in "*Acoustic Emission – Beyond the Millennium*," eds. T. Kishi, M. Ohtsu and S. Yuyama, (2000), Elsevier, pp. 1-18.
6. M. Takemoto, H. Nishino and K. Ono, "Wavelet Transform-Application to AE Signal Analysis," a chapter in "*Acoustic Emission – Beyond the Millennium*," eds. T. Kishi, M. Ohtsu and S. Yuyama, (2000), Elsevier, pp. 35-56.
7. M. Ohtsu, "Moment Tensor Analysis of AE and SiGMA Code," a chapter in "*Acoustic Emission – Beyond the Millennium*," eds. T. Kishi, M. Ohtsu and S. Yuyama, (2000), Elsevier, pp. 19-34.
8. K. Bukkapatnam, S.R.T. Kumara and A. Lakhtakia, "Analysis of Acoustic Emission Signals in Machining," *Trans. ASME, J. Manuf. Sci. and Engr.*, **121**, 2000, 568-576.
9. T. Nishiura, N. Shinke, M. Takuma, and K. Akamatsu, "Evaluation of Tool Life in Shearing Process – Application of AE Method," *Proc. 14th Acoustic Emission Conf.*, 2003, JSNDI, pp. 131-134.
10. C.M. Scala and S. McK. Cousland, *Materials Science and Engr.*, **76**, 1985, 83-88.
11. D. L. Armentrout and S. H. Carpenter, "An Investigation of Lüders Band Deformation and the Associated Acoustic Emission in Al - 4.5% Mg Alloys", *J. Acoustic Emission*, **15**, 1997, 43-52.

PRECURSOR OF HYDROGEN INDUCED GLASS LINING CHIPPING BY AE MONITORING

KOHEI MURAKAMI and MIKIO TAKEMOTO

Faculty of Science and Engineering, Aoyama Gakuin University, Fuchinobe, Sagamihara,
Kanagawa, 229-8558 Japan.

Abstract

Glass lining serves as corrosion-resistant barrier and is composed of two layers, i.e., a porous ground coat and a dense top coat. Pores in the ground-coat serves for moderating the mismatches of mechanical and thermal properties of steel substrate and brittle glass layer, and also for trapping the hydrogen gas induced via the substrate. Chipping is a sudden fly-off of the lining layer and cannot be repaired on site. We monitored precursor of the chipping by AE and laser surface-acoustic wave (LSAW) technique. We monitored AE signals before half of the time to cause final large scale chipping. The time of first AE coincides the time when hydrogen ion reaches the ground coat. AE are supposed to be produced by the cracks connecting the pores in the ground coat. LSAW technique was demonstrated to be useful in monitoring the precursor of the chipping.

Keywords: Glass lining, Chipping, Hydrogen, Laser ultrasonic, Source dynamics, Waveform matching

1. Introduction

Glass linings (GLs) are widely used for corrosion-resistant equipment in food and chemical industries, but tend to suffer various damages due to their brittleness. Among the damage of GLs, hydrogen-induced damage, generally known as chipping, is a serious problem since no effective countermeasure exists [1]. Utilization of steels with a trace of titanium is recognized to be effective for trapping the hydrogen gas in the steels, but is not the essential countermeasures.

Chipping sometimes occurs after a couple of days or after a few years of service. The worst case is the chipping in the manufacturing locations. Previous research suggested that the chipping was induced by diffusible hydrogen, which was induced into the substrate steel from water in the clay, milling water, and cleaning by acid solutions. No method to evaluate the susceptibility to chipping has been established [1-3]. Glass linings are generally composed of two layers; porous ground coat near the steel substrate and dense cover coat. Pores in the ground coat are designed to moderate the stress mismatch between the steel substrate and GL, and to trap the hydrogen gas and hence contribute to reduce the chipping.

We attempted to study the precursor of chipping by AE and LSAW (Laser Surface-Acoustic Wave) monitoring. AE was demonstrated to detect the micro-cracking of the porous ground coat (GC hereafter) from early times, and the LSAW the change of acoustic properties associated with the micro-cracking of the GC.

2. Specimen and Acoustic Properties of Glass Lining

Specimen is a corrosion-resistant GL. It is composed of 0.2-mm thick ground coat (GC) and 0.8-mm thick cover coat (CC). This GL was deposited on carbon steel (JIS SS400) of 3-mm thickness, 61-mm width and 100-mm length. Figure 1 shows a typical cross-sectional structure of the GL. The GC contains a number of large spherical pores of 50 to 200 μm diameter while the CC isolated fine pores of 10 to 50 μm . Porosity by a laser microscope was measured as 3.5 % in the CC and 48 % in the GC. Chemical composition and baking conditions are not reported.

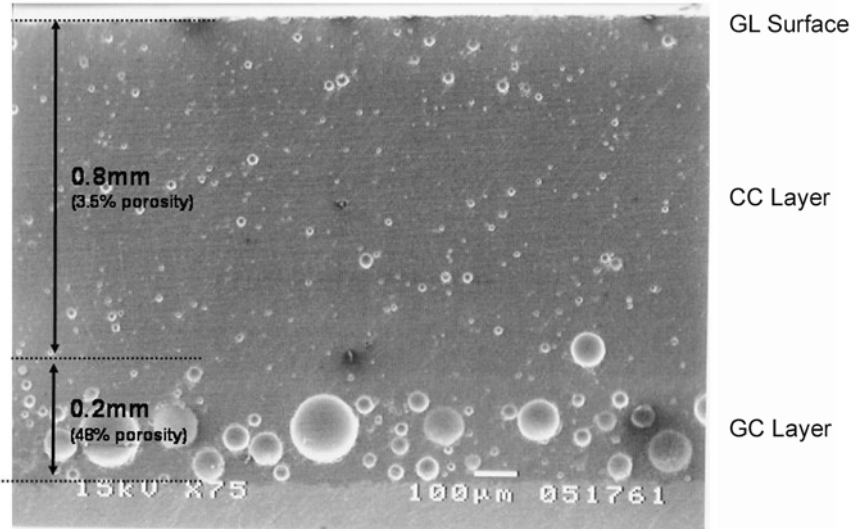


Fig. 1 Transverse structure of glass lining. CC: cover coat, GC: ground coat.

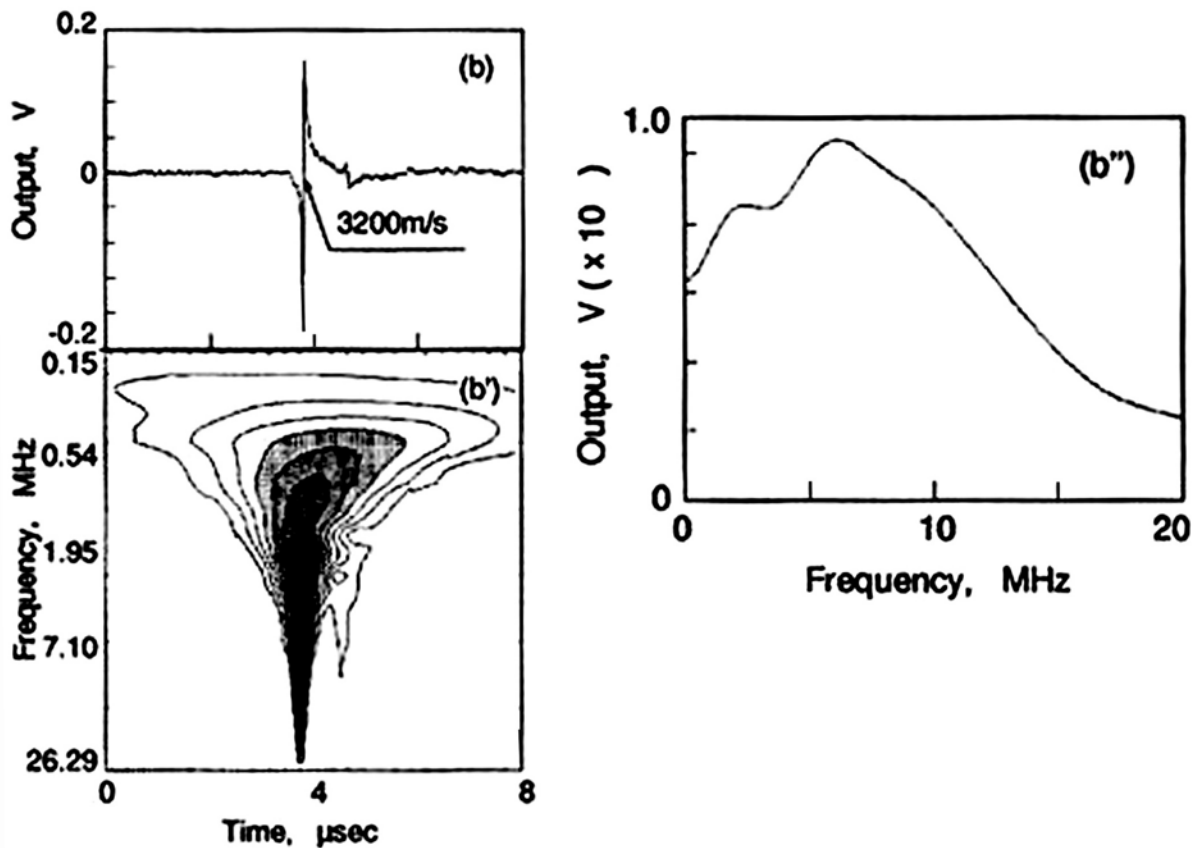


Fig. 2 Waveform of LSAW measured on the glass lining.

Table 1 Acoustic and elastic properties.

	ρ kg/m ³	C_p m/s	C_s m/s	C_r m/s	E GPa
GL	2460	6539	3447	3201	76.4
SS400	7870	5920	3255	3010	214

First we measured the SAW velocities of the GL using a laser ultrasonic system [4, 5]. Figure 2(a) shows the waveforms of dispersive Rayleigh waves at a propagation distance of 12.12 mm in the axial direction of the specimen. The Rayleigh velocity, determined by the zero-crossing time method, was from 3191 m/s to 3214 m/s. The velocities of SSCW (Surface skimming compressive wave) were measured as 6530 ± 40 m/s. Estimated acoustic and Young's modulus are shown in Table 1. Figure 2(b) shows the wavelet contour map of LSA waves. It indicates that the velocity at higher frequencies above 4 MHz or in the surface layer less than 0.8 mm is non-dispersive, suggesting a homogenous structure of the GL. Late-arrival lower frequency components (surface depth over 0.8 mm) indicate that the GC layer has a lower velocity than the steel substrate, possibly due to the large voids in the GC.

3. AE Monitoring of Chipping

Figure 3 shows AE monitoring method from the GL chipping during hydrogen charging. Hydrogen was supplied to the steel substrate in an area of 20 mm square by cathodically charging at current density of 0.05 A/cm² in a 0.5 kmol/m³ sulfuric acid solution with 4 kg/m³ CH₄N₂. Eight small AE sensors (PAC, Type PICO with center frequency of 0.45 MHz) were mounted on both surfaces of the specimen. Sensor outputs were amplified 40 dB and digitized by an A/D converter. The AE system with 40 dB amplification did not detect any noise from hydrogen gas bubbles. A plot of cumulative AE counts with charging time is shown in Fig. 4.

AE events increased from 38 ks (10.5 hr). A large-scale chipping, shown in Fig. 5, of about 30 mm x 50 mm (1200 mm²) suddenly occurred at 48.6 ks (13.5 hr). A number of fragmented glass pieces from 0.5 mm² to 200 mm² were launched from the substrate with large sounds. We observed at the right edge of the exfoliated GL a porous GC of 2 mm x 4 mm square. First arrival time of diffusible hydrogen at GL/substrate is calculated as 11.3 ks by using the hydrogen diffusivity coefficient of 5.22×10^{-7} cm²/s in the steel. Thus the time lag of 11 ks between 11.3 ks and 22 ks, at which the first AE was detected is supposed to be the time during which the hydrogen gas pressure increases in the voids of the GC. In another word, this is the time during which the voids serve as the gas container.

Figure 6 shows typical AE waveforms detected at 43407 and 48646 s. As AE signals were detected as Lamb waves with weak So-component, the source locations were estimated using the first arrival sheet velocity of the So-wave. The sheet velocity of the substrate and GL is approximately the same since both the Young's modulus and density of the substrate are approximately 3 times that of the GL. In spite of this fact, we observed some strange waveforms for channel 1 and 2. For the event at 48646 s just before the final large chipping, the arrival of the

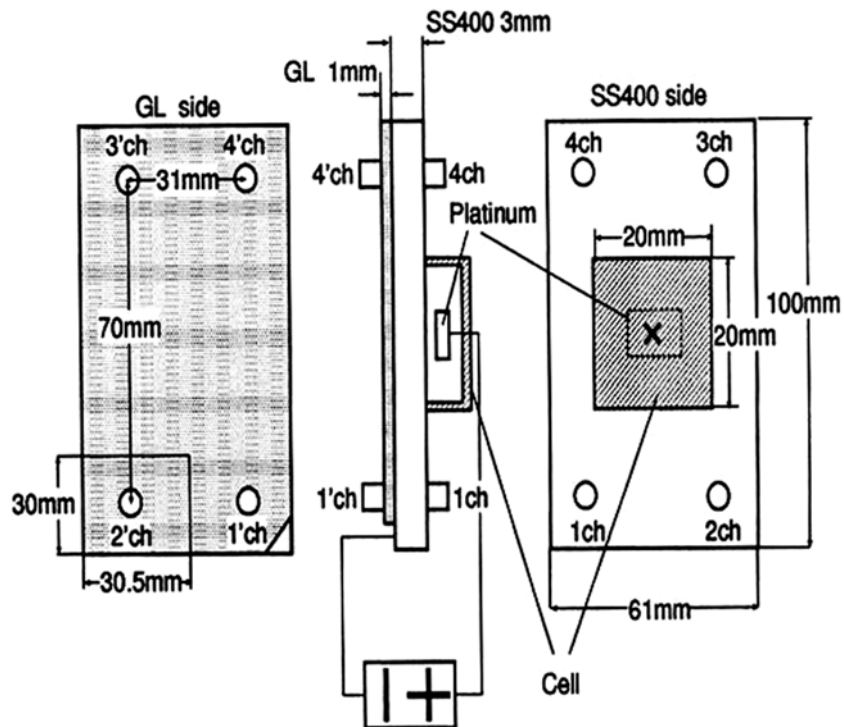


Fig. 3 AE monitoring system for glass lining on the steel plate absorbing hydrogen.

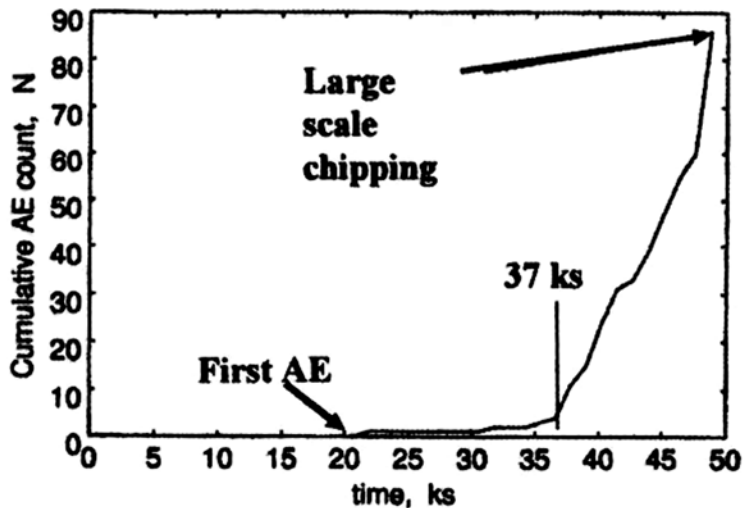


Fig. 4 Cumulative AE count with hydrogen charging time for glass lining on the steel plate.

So-packet to the Ch.-1 and -2 sensors on the steel substrate were very weak, while the amplitudes of So-component from Ch.-1' and -2' sensors on the GL were much stronger.

Strange characteristics observed here may be due to the damage location in the GC. Strong Lamb waves propagated along GL layer, of which GC was partially exfoliated from the substrate. Source location was performed for 40 events with sufficient amplitude on all channels and results are shown in Fig. 5. Most sources were located in a small "fish-scale"-type chipping area. Surface and transverse photos in this area show cracks connecting the voids. Crack openings are measured as 0.01 to 0.04 mm. These values are surprisingly large compared to those of delayed fracture of the high strength steels.

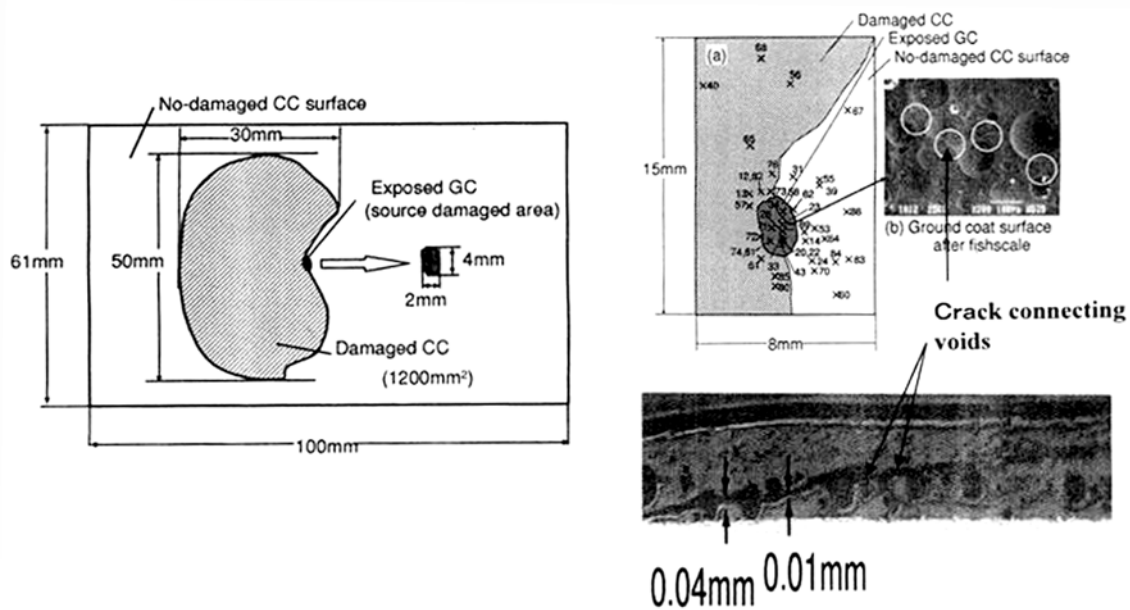


Fig. 5 Surface and transverse sketch and photographs of the glass lining suffered hydrogen induced large chipping

From these data, it is concluded that 1) voids in GC can hold the hydrogen gas pressure, 2) fish-scale chipping is a typical delayed fracture and occurs when the hydrogen gas pressure reaches a critical pressure, 3) AE signals are produced by the generation of micro-cracks connecting the voids in the GC. Thus, AE can be used to monitor the precursor of the large sudden chipping of the GL.

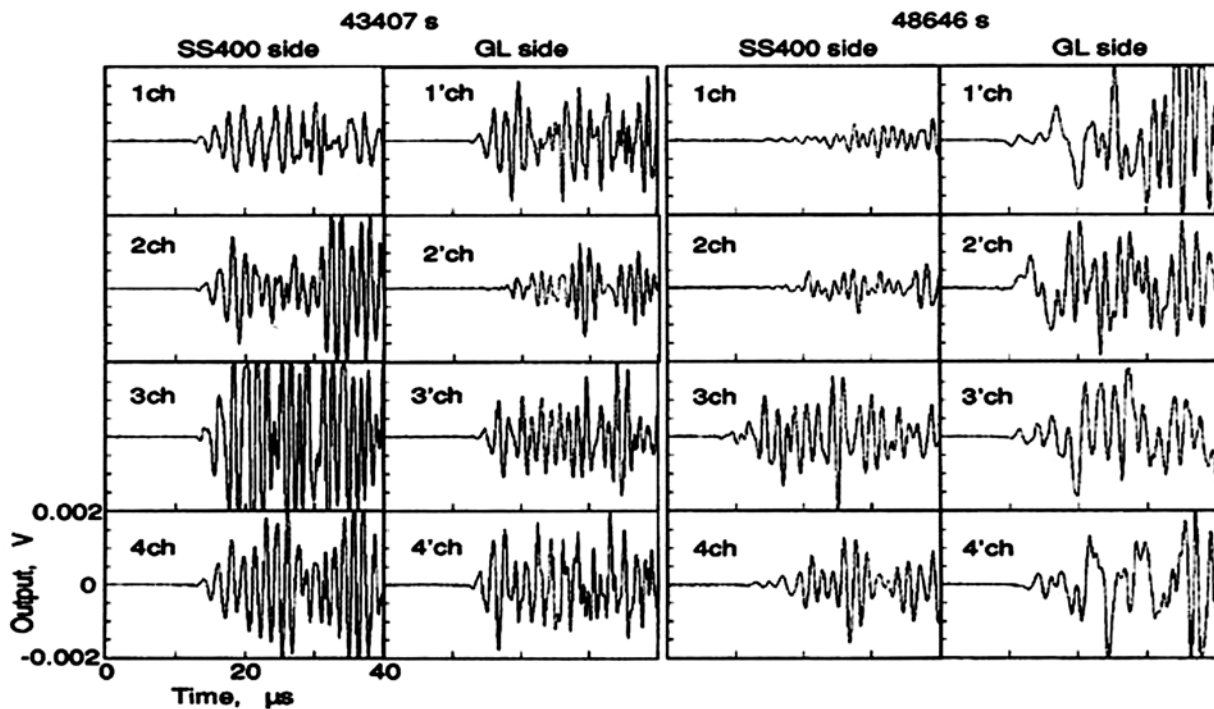


Fig. 6 Lamb-wave AE signals detected on glass lining and substrate before a large-scale chipping.

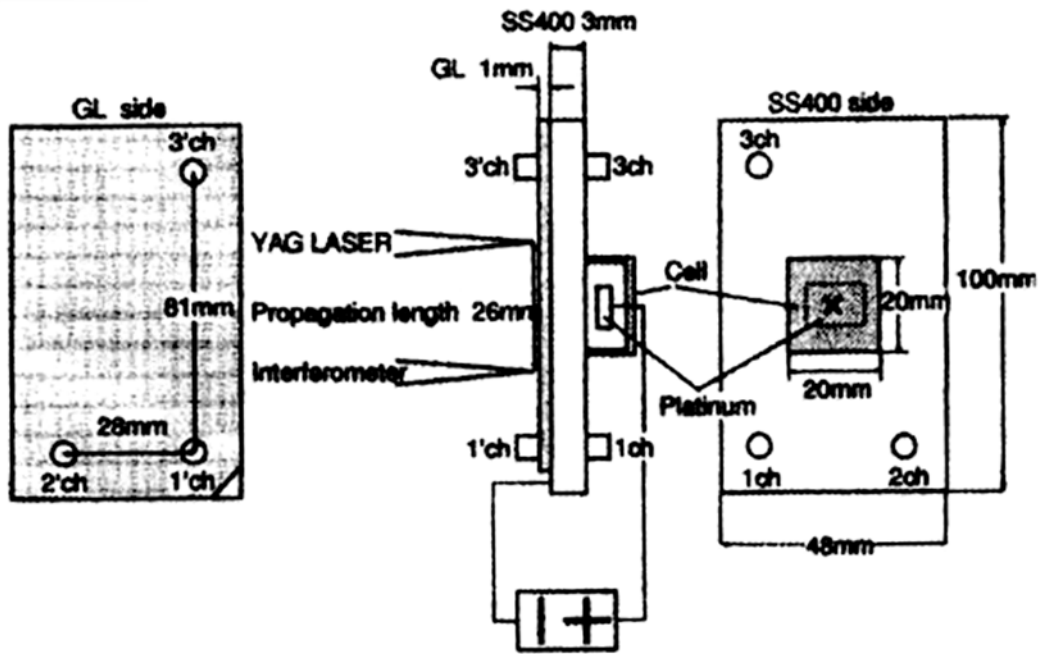


Fig. 7 Monitoring of laser-excited surface waves and AE during hydrogen charging.

4. AE Source Analysis

Another experiment, approximately the same as that in the previous section, was attempted. In this test, damages monitoring by the LSAW system was simultaneously performed. As shown in Fig. 7, LSAW waves were monitored on the surface of the GL. Figure 8 shows the cumulative AE counts with the charging time. A large-scale final chipping of 2000 mm² occurred at 60842 s (17 hr). AE counts rapidly increased at 20 ks just before the final chipping. Timing of both the first AE and final chipping agreed with those in Fig. 4. Twenty-seven events are located at the origin of the chipping, as shown in Fig. 9.

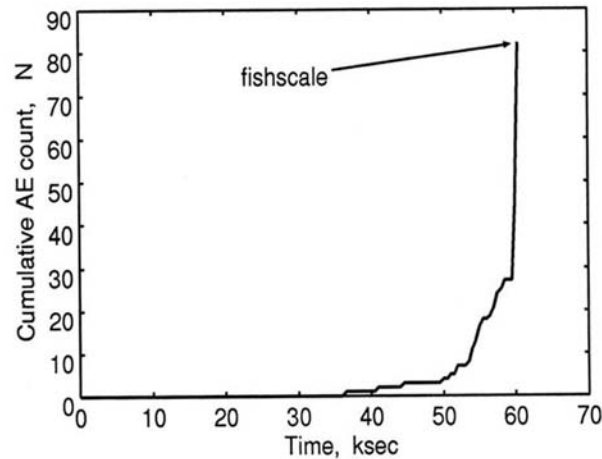


Fig. 8 Cumulative AE counts with hydrogen charging to the steel with GL.

Fracture dynamics were estimated by the waveform matching of the first-arrival So-component. Detail of the waveform simulation can be found elsewhere [6]. The overall transfer function was determined utilizing the pulse-laser breakdown of silicone grease in a slit as the source. Source parameters of the break-down was first determined by the deconvolution of the

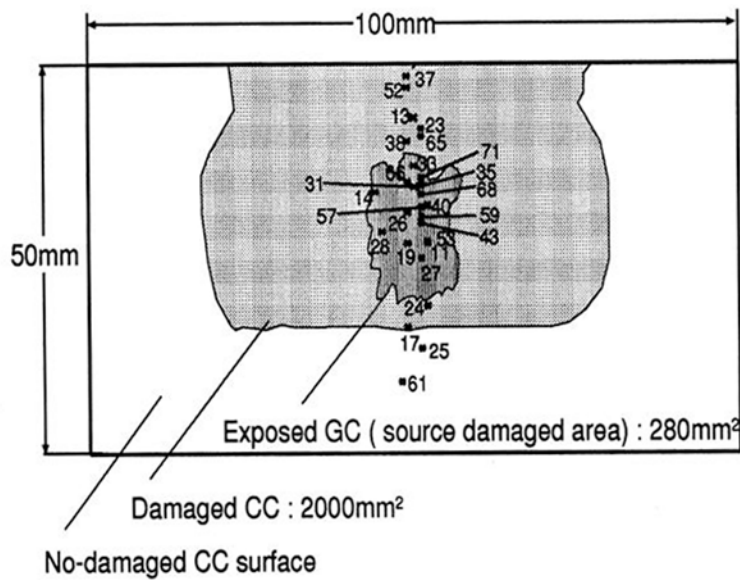


Fig. 9 Chipped glass lining and source location of AE signals.

out-of-plane displacement of a large block measured by a laser interferometer with the theoretical Green's function of the second kind [7]. Source parameters of chipping AE signals were estimated by matching the first So-mode waveform computed using the overall transfer function to the detected waveform. Figure 10 compares experimental and computed waveforms of the So-packets. Source parameters are shown in Fig. 11. The average crack volume $3.5 \times 10^{-16} \text{ m}^3$ appears to correspond to the volumes of the cracks connecting the voids in the GC.

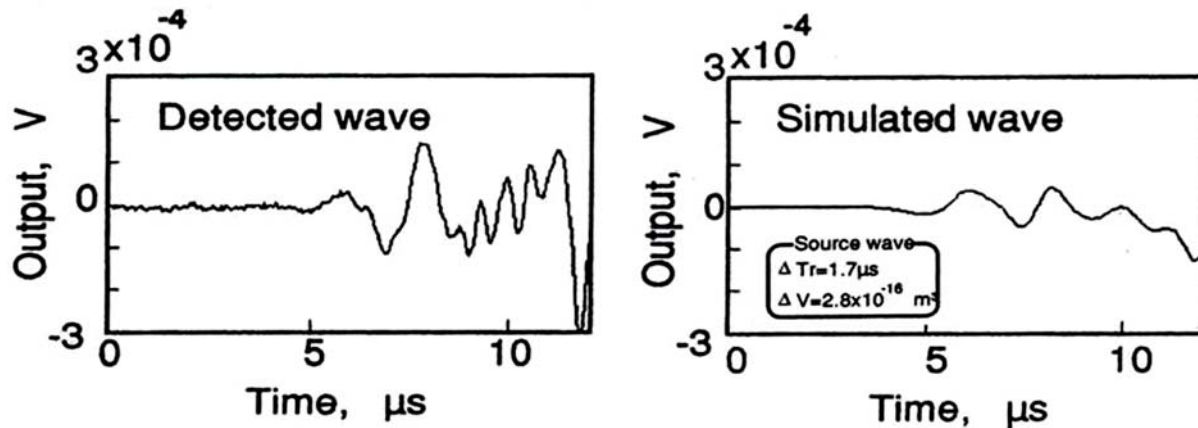


Fig. 10 Lamb wave AE detected and simulated for a step-wise crack generation.

5. Monitoring of Lining Degradation by LSAW

As mentioned in the previous section, the low-frequency components of the dispersive Rayleigh wave represent the characteristics of GC. Thus, we monitored periodically the SAWs of the GL using the laser ultrasonic system. Figure 12 shows the change of the SAWs with time. Slight waveform difference can be seen in the later times. Cross-correlation was determined and is shown in Fig. 13. It decreases with the charging time, but shows three discontinuous changes at around 11 ks, 45 and 55 ks. Here, the 10 ks is the time when the hydrogen reaches the GC. At around 50 ks as shown in Fig. 8, AE events increased rapidly. Cross-correlation of SAWs can predict the minute changes in the GC when the SAW is measured at the same position.

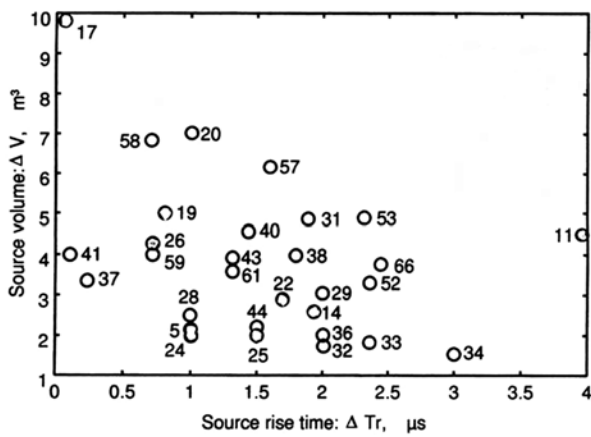


Fig. 11 Source parameters of Mode-I micro-cracking.

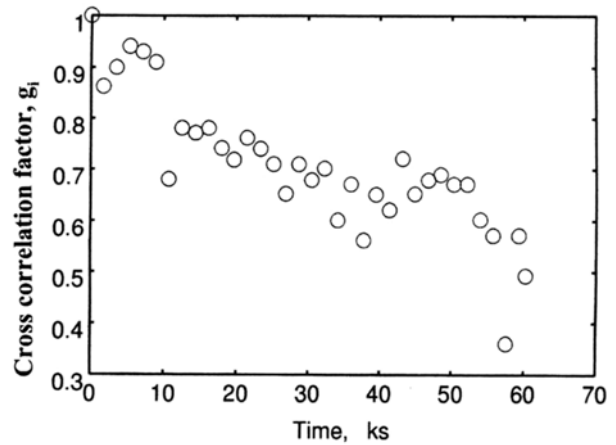


Fig. 13 Change of cross-correlation factor of LSAW with hydrogen charging time.

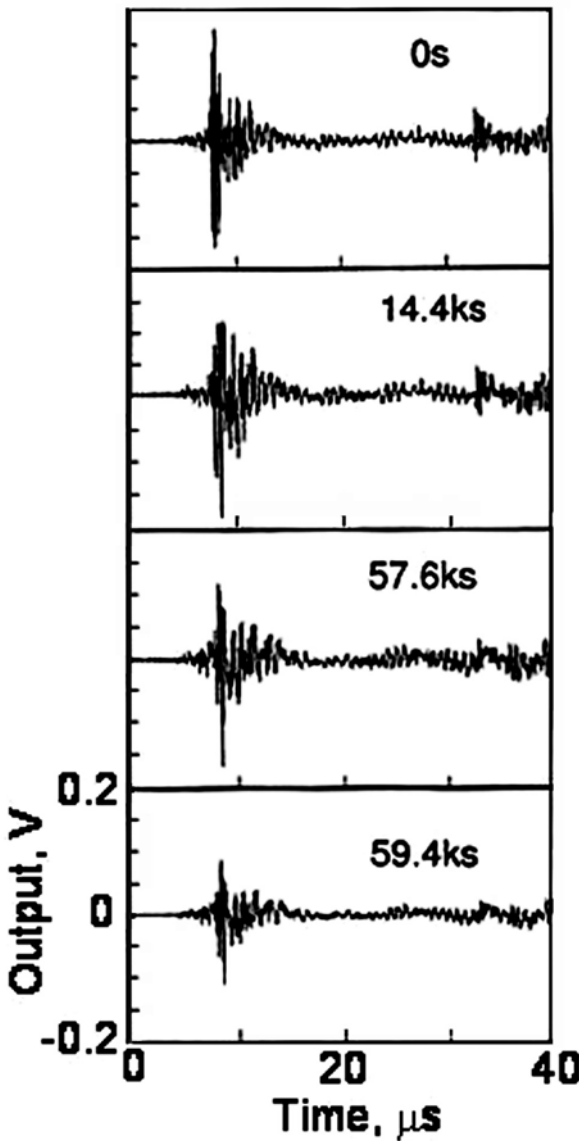


Fig. 12 Change of laser SAWs with hydrogen charging time.

5. Conclusion

AE and LSAW were monitored to study the precursor of hydrogen-induced chipping of the glass lining. Results obtained are summarized below:

- 1) Acoustic properties of Glass lining were studied using an LSAW system. Both the Young's modulus and density of the cover coat are approximately 3 times smaller than those of the steel substrate, but the sheet velocity was found to be the same for the dense cover coat and the substrate. Group velocity dispersion of the Rayleigh waves represents the structural change in the porous ground coat.
- 2) Large scale chipping of the cover coat, deposited on 3-mm thick carbon steel, occurred at 49 ks to 60 ks after the hydrogen charging to the substrate. AE signals are produced by micro-cracking, connecting the voids in the ground coat. These are detected from less than half the time of the final chipping. Hydrogen gas pressure in the ground coat produces micro-cracking when its pressure reaches the critical value.
- 3) Source parameters of micro-cracks were estimated by the waveform matching of the first arrive So-mode, using the overall transfer function experimentally determined. Breakdown of silicone grease in a narrow slit is useful in simulating the Mode-I crack normal to surface in the thin

ground coat. Crack volume and rise time were estimated as $3.5 \times 10^{-16} \text{ m}^3$ and less than $1 \mu\text{s}$, respectively.

- 4) LSAW measured on the lining showed slight changes reflecting the structural changes in the ground coat. Cross-correlation factor of the SAWs showed discontinuous changes corresponding to those observed for AE count change.

References

- 1) C.G. Bergeron, J. Amer. Ceramic Soc. **36** (1953), 373.
- 2) Y. Nakazato, H. Kubiminato, N. Fukuda, T. Sonobe and H. Nagaishi, *Kawasaki Seitetsu Giho in Japanese*, **7** (1977), 70.
- 3) I. Takahashi, A. Yasuda, K. Ito and N. Ohashi, *Kawasaki Seitetsu Giho in Japanese*, **5** (1975), 53.
- 4) H. Cho, S. Ogawa, K. Yamanaka and M. Takemoto, *JSME Int. Jr. Series A*, **41** (1998) 439.
- 5) Y. Mizutani, M. Takemoto and K. Ono, *J. Acoustic Emission*, **16** (1998) S115.
- 6) H. Suzuki, M. Takemoto and K. Ono, *J. Acoustic Emission*, **14** (1995) 442.
- 7) H. Suzuki, M. Takemoto and K. Ono, *Progress in AE, VII* (1994), JSNDI, Tokyo, p. 457.

REAL-TIME EXECUTING SOURCE LOCATION SYSTEM APPLICABLE TO ANISOTROPIC THIN STRUCTURES

YU KUROKAWA, YOSHIHIRO MIZUTANI and MASAMI MAYUZUMI

Department of Mechanical Sciences and Engineering, Tokyo Institute of Technology,
Ookayama, Meguro, Tokyo 152-8552, Japan.

Abstract

In this study, we developed a real-time executing source location system for anisotropic thin structures such as CFRP (Carbon Fiber Reinforced Plastics) tanks. The system consists of AE sensors, an A/D converter on a PC and a computer with proprietary software. We suggest two algorithms to realize the real-time executing source location. The first algorithm is a frequency filtering algorithm utilizing a fast continuous wavelet transform. The second algorithm is a fast source location calculation algorithm for unidirectional anisotropic structures. In the second algorithm, the affine coordinate transform is used. The calculation time for each source location is reduced to less than 15 ms with reasonable accuracy.

1. Introduction

The fracture monitoring of CFRP (Carbon Fiber Reinforced Plastics) is important for assuring structural reliability. AE testing is one of the most effective methods for monitoring fracture. The AE source location can be estimated by considering the arrival times and the velocity of the AE signals. However, special techniques are required for conducting the source location on anisotropic thin structures. The AE in thin plates, such as CFRP structures, propagates as Lamb waves and its velocity depends on the frequency [1]. Due to its dispersive nature, it is difficult to determine the arrival time from the AE waveform. Furthermore, in anisotropic structures, the velocity of the AE has an orientation dependence due to the structural anisotropy. The orientation dependence needs to be taken into account for precise source location to be achieved.

Several papers [2-7] dealing with the source location on anisotropic materials or thin plate-like CFPR structures have been reported so far. For example, Promboon [2] and Blahacek [3] used neural networks for the source location. This method could be adopted without understanding the elastic wave propagation characteristics in the material, but the network needs learning before the utilization. Kwon et al. [6] utilized wavelet and inverse wavelet transform for locating pencil-lead breaks on aluminum and cross-ply CFRP plates. This method improves the source location accuracy, but the anisotropy issue remains unresolved. In order to overcome these problems, Yamada et al. [7] have used the wavelet transform as a frequency filter for determining the arrival time of AE signals. However, the wavelet transformation calculation required for this method is time consuming. Another problem is that the source location is estimated by scanning the virtual source. The method required an iterative calculation at a significant computational cost. For these reasons, the source location algorithm for anisotropic thin structures had been found to be less than suitable for real-time execution. Therefore, we introduced two new algorithms for speeding up both the frequency filtering and the source location calculation.

Figure 1 shows a schematic image of our final goal. The AE sensors are mounted on a CFRP tank during a field test and staff monitors AE during the test. The source location is displayed on a computer screen simultaneously with the generation of AE. The two new algorithms proposed in this study are used in the analysis software and enable real-time source location.

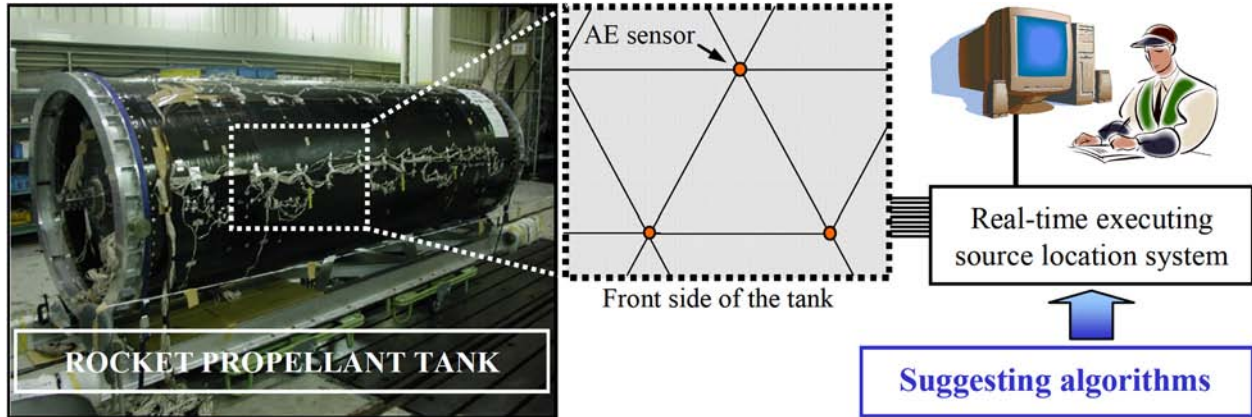


Fig. 1 Schematic image of our final goal

2. Acceleration of the Source Location Calculation

In this study, we suggest two new algorithms for accelerating the source location calculation. One is a new frequency filtering algorithm using the fast continuous wavelet transform. This algorithm enables the immediate extraction of the specific frequency component from the Lamb wave AE. The other algorithm is a new source location algorithm utilizing an affine coordinate transform. This algorithm also shortened the calculation time for source location.

2.1 Fast Frequency Filtering Algorithm

In the source location calculation, the continuous wavelet transform is used as a frequency filter. The general wavelet transform of real function $f(t)$ is defined as

$$W(a, b) = \frac{1}{\sqrt{a}} \int_{-\infty}^{\infty} f(t) \psi^* \left(\frac{t-b}{a} \right) dt \quad (1)$$

where $a > 0$ and the superscript * denotes a complex conjugation. The analysis function for the wavelet transform can be defined as in equation (2).

$$\psi_{a,b}(t) = \frac{1}{\sqrt{a}} \psi \left(\frac{t-b}{a} \right) \quad (2)$$

Its elements are generated by shifting and scaling a mother wavelet $\psi(t)$. The parameters a and b stand for the scale and shift of the mother wavelet. The calculation of equation (1) is time consuming because the iterative calculation needs to be performed many times with different values of the parameter b . On the other hand, equation (1) can be transformed into equation (3) utilizing Parseval's theorem [8].

$$W(a, b) = \frac{1}{2\pi} \int_{-\infty}^{\infty} \hat{f}(t) \left\{ \sqrt{a} \hat{\psi}(a\omega) \right\} e^{i\omega b} d\omega \quad (3)$$

where $\hat{\psi}(\omega)$ donates the Fourier transform of $\psi(\omega)$. Equation (3) can be calculated using the

following steps;

- 1) Calculate the Fourier transform of $f(t)$ utilizing an FFT.
- 2) Calculate $\widehat{\psi}(a\omega)$ using an FFT or other suitable technique.
- 3) Multiply $\widehat{f}(t)$ by $\widehat{\psi}(a\omega)$. Calculate equation (3) using an Inverse FFT.

A schematic image of the methods stated above is shown in Fig. 2. The general wavelet transform is represented by the convolution of an analytic signal with a mother wavelet function in the time domain (see the left side of Fig. 2). This convolution is time consuming because an iterative calculation is required. On the other hand, the fast wavelet transform used in this study is shown in the right side of Fig. 2. As shown in this figure, the convolution of the two signals is calculated in the frequency domain and the calculation cost is much lower than the general wavelet transform. In this research, the computation time for filtering has been shortened 55 times, from 72 ms to 1.3 ms by this modification.

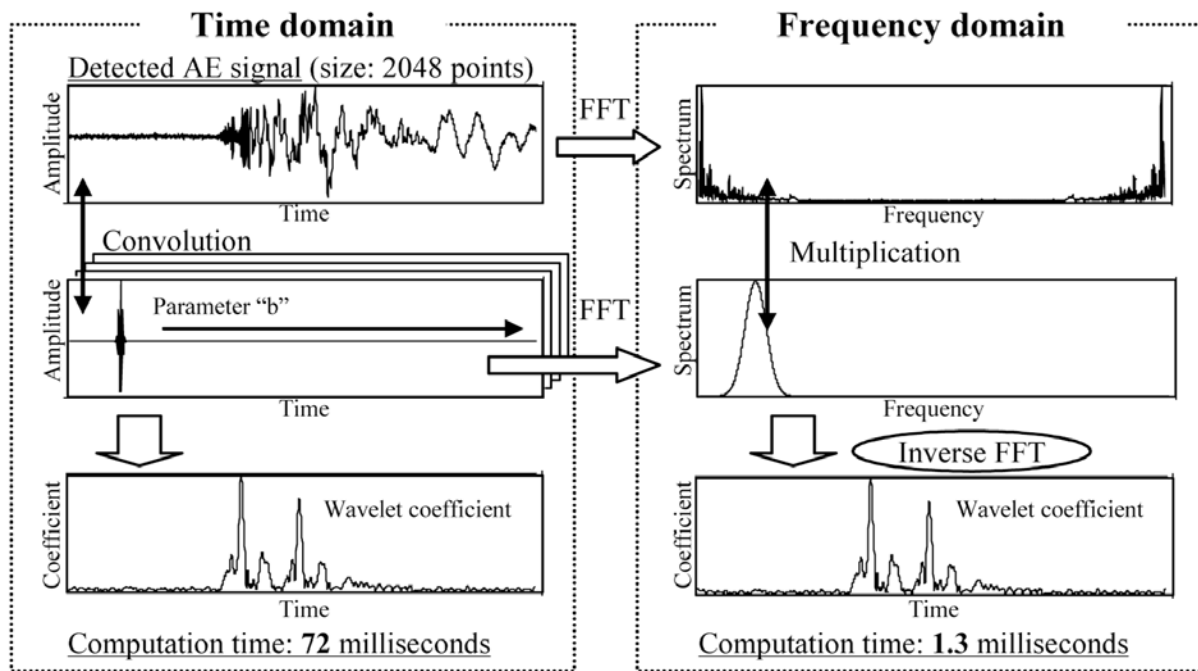


Fig. 2 Comparison of wavelet transform between the time domain and the frequency domain.

2.2 Source Location Algorithm using an Affine Coordinate Transform

The source location on anisotropic thin structures is complicated due to the velocity anisotropy of AE signals. For example, Yamada et al. [7] used the scanning of the virtual source method, as shown in the left side of Fig. 3. The method is computationally intensive and is not suitable for use with real-time source location systems. If velocity anisotropy does not exist, the source location can be calculated immediately using simple simultaneous equations. In our new procedure, the coordinate system is transformed by an affine transform in order to negate the effect of the velocity anisotropy. The right side of Fig. 3 is a schematic representation of this method. The primary requirement is that velocity anisotropy can be approximated by an elliptical function. The new source location algorithm consists of the following steps;

- 1) Perform an affine coordinate transform using equations (4) and (5) to compensate for the velocity anisotropy effect. The V_0 is the velocity of AE at $\theta = 0^\circ$, V_{90} is at $\theta = 90^\circ$.

According to this process, the location of the sensors: (X_1, Y_1) , (X_2, Y_2) , (X_3, Y_3) are transformed to (X_1', Y_1') , (X_2', Y_2') , (X_3', Y_3') , respectively.

2) Calculate the source location on the transformed coordinate system using one of the standard AE source location methods. The estimated source location is shown as (x', y') in Fig. 3.

3) Perform an inverse affine transform using equations (6) and (7) for the estimated source by Step 2 as (x', y') and the source location on the original coordinate system is determined as (x, y) .

The calculation cost is drastically reduced using this algorithm compared to the scanning virtual source method. In this research, the computation time for source location using this modification has been shortened by three orders of magnitude, from 3.3 s to 3.2 ms.

$$(X', Y')^T = C(X, Y)^T \quad (4)$$

$$C = \begin{pmatrix} 1 & 0 \\ 0 & V_0/V_{90} \end{pmatrix} \quad (5)$$

$$(x, y)^T = C^{-1}(x', y')^T \quad (6)$$

$$C^{-1} = \begin{pmatrix} 1 & 0 \\ 0 & V_{90}/V_0 \end{pmatrix} \quad (7)$$

3. Specimen and Velocity Anisotropy

For this study, we prepared a $820 \text{ mm}^L \times 300 \text{ mm}^W$ CFRP plate ($[90^\circ]_7$) with a 1-mm-thickness aluminum liner. A schematic drawing of the specimen and the source location system are shown in Fig. 4. The total thickness of the composite plate is 2 mm. The Y-axis in Fig. 4 corresponds to the fiber direction of the front CFRP layer. This specimen simulates the propellant tank wall of a future rocket being developed in Japan. We first investigated the orientation dependence of the AE velocity using pulses produced by pencil-lead break on the front surface. We measured the velocity anisotropy every 10° angle (θ) at a particular frequency (f), and approximated it by an elliptical function, $V(f, \theta)$; see Fig. 5. The measured and approximated orientation dependence of the 300-kHz components are shown in Fig. 5 as an example. We subsequently investigated the frequency dependence of the AE signals by utilizing a wavelet transformation by changing the filtering frequency. The frequency dependence of the AE velocity, which we used for source location, is shown in Fig. 6.

4. Source Location System and Experimental Results

The source location experiment used three AE sensors (PAC, type PICO; 4.0 mm diameter). The sensors were mounted on the front surface (CFRP side) at the corners of an equilateral triangle, 200 mm on a side. The AE signals were artificially produced using pencil-lead breaks and steel-ball drops. Outputs of the AE sensors were digitized using an A/D converter on a PC (National Instruments, NI-5122; 14-bit resolution). The sampling frequency and points are 2.5 MHz and 2048 points, respectively. The digitized data is automatically analyzed in the computer and the results are displayed on a computer screen.

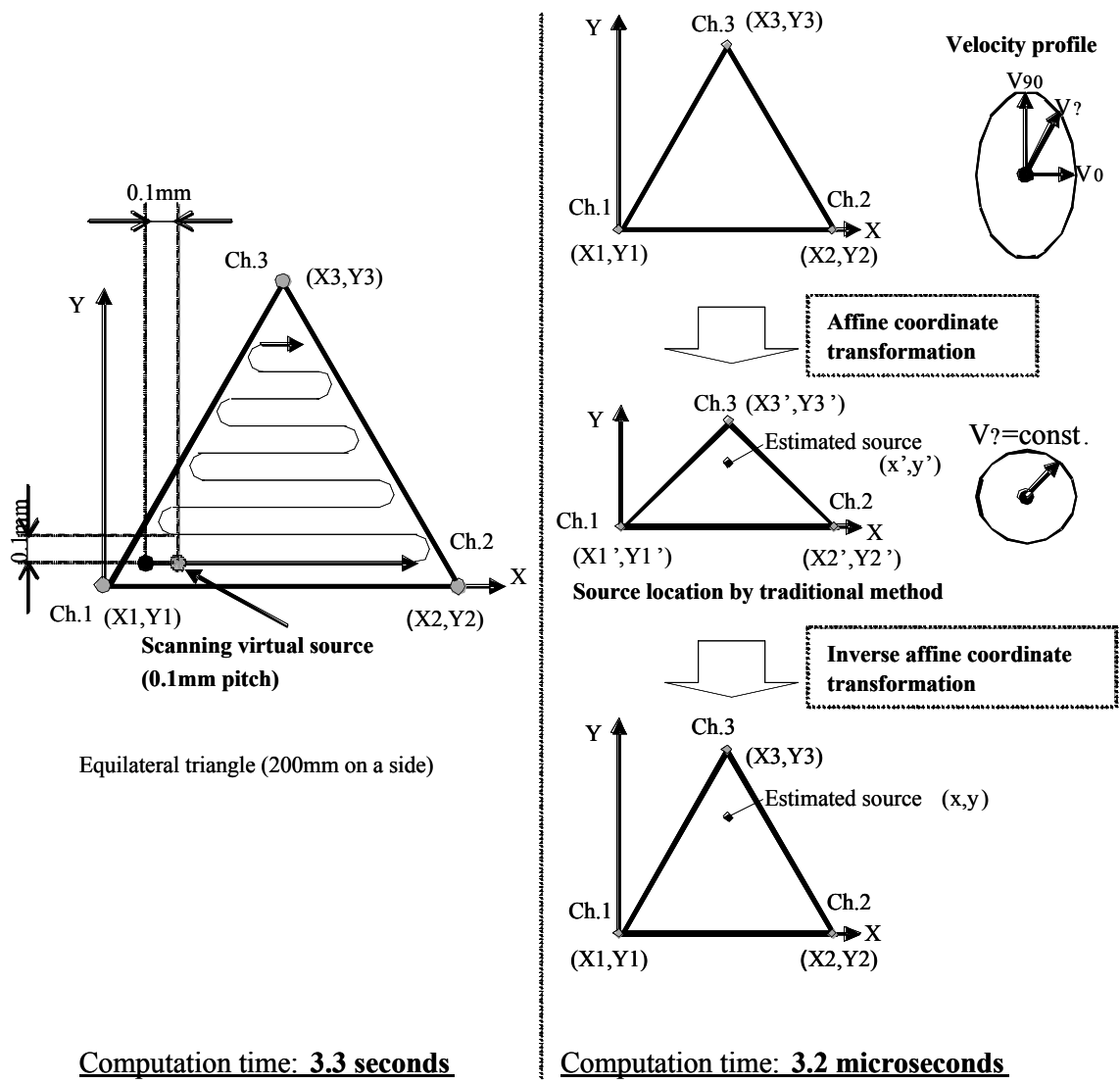


Fig. 3 Comparison of source location methods.

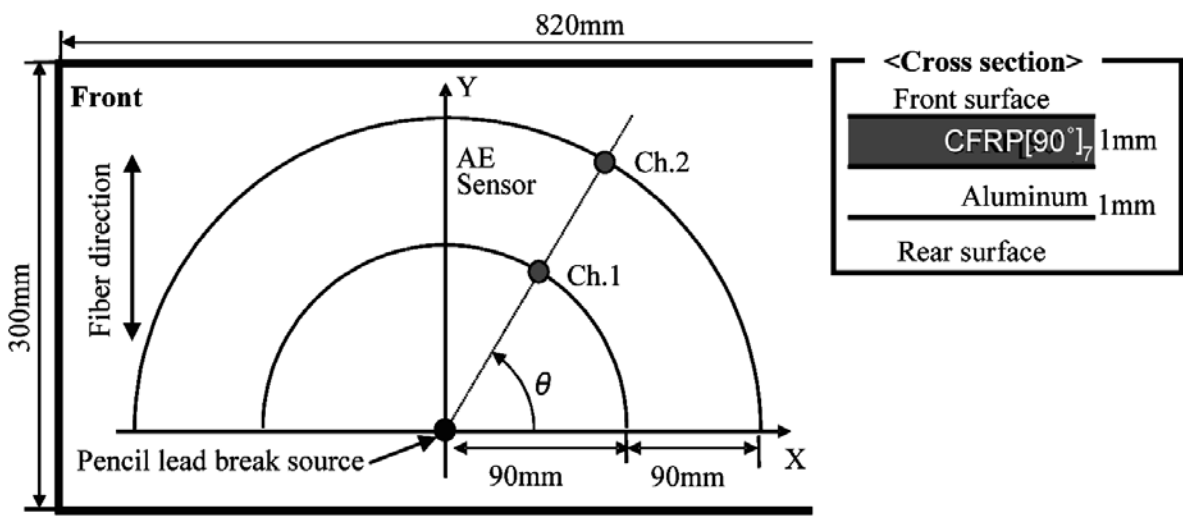
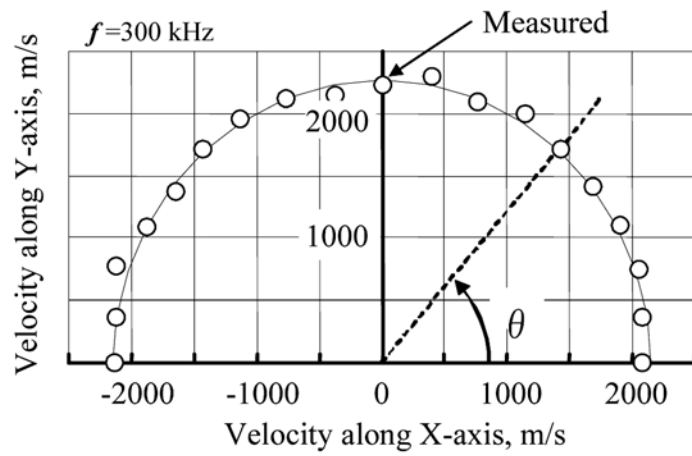


Fig. 4 Schematic illustration of the specimen and the measurement of the orientation and frequency dependence of the AE velocity.



Ellipse Fitting:
$$V(f, \theta) = \frac{V_0 \cdot V_{90}}{\sqrt{V_0^2 \sin^2 \theta + V_{90}^2 \cos^2 \theta}}$$

Fig. 5 Orientation dependence of the AE velocities in the specimen.

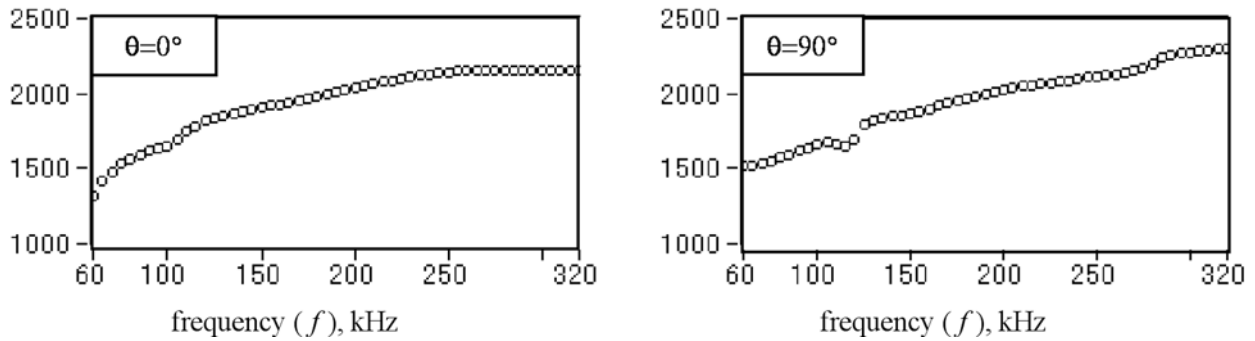


Fig. 6 Frequency dependence of the AE velocity in the specimen.

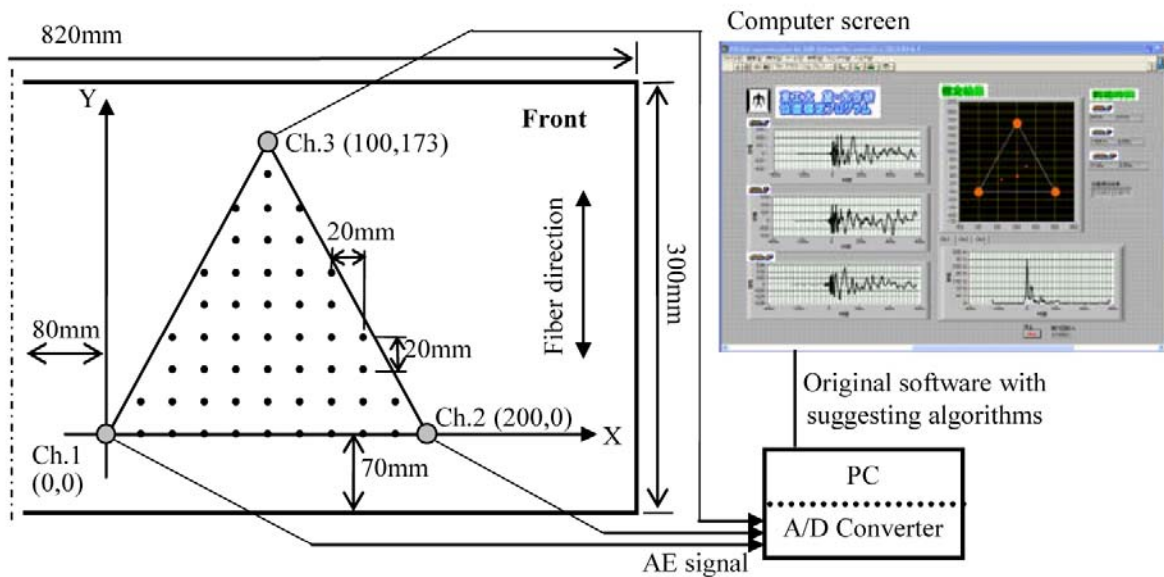


Fig. 7 Schematic illustration of the source location system.

In this study, we conducted the source location using the following steps:

- 1) Detect the AE signals using three AE sensors.
- 2) Compare the maximum amplitude of three AE signals and find the weakest signal.
- 3) Calculate FFT and detect the maximum spectrum.
- 4) Search the spectrum from 320 kHz to 60 kHz and find frequency f that exceeds 4% of the maximum spectrum first. The frequency " f " was used for the source location (Step 2 to Step 5 are shown in Fig. 8).
- 5) Using the frequency " f ", conduct the wavelet transform for each signal and determine the AE arrival time from the first peak timing of wavelet coefficient.
- 6) Calculate the source location by the affine transformation algorithm using the arrival time differences.

An example of detected AE signals produced by the pencil-lead break source and the steel-ball drop source at $(x,y) = (100,120)$ [mm] in Fig. 7 are shown in the left side of Fig. 9 and Fig. 10, respectively. Dispersive AE signals propagating as Lamb waves (primary A-mode) were observed. It is difficult to determine the arrival times from the waveform. On the other hand, its wavelet coefficients are shown in the right side of the same figures. The peaks were obtained clearly, and the source location results were $(x,y) = (100.6,119.2)$ and $(100.5,121.0)$ [mm], respectively. The required time for source location is less than 15 ms for any AE sources.

Figure 11 indicates the source location results with pencil-lead break and steel-ball drop sources. The source positions are indicated by squares and the estimated source positions by gray circles in the figure. The maximum error of 6.1 mm and average error of 1.8 mm were obtained for the pencil-lead break source. For the steel-ball drop source, the average error was 3.9 mm and the maximum error was 12 mm. The large error is attributed to the problem of estimating the arrival time from the wavelet results, arising from the lower frequency contents of steel-ball sources.

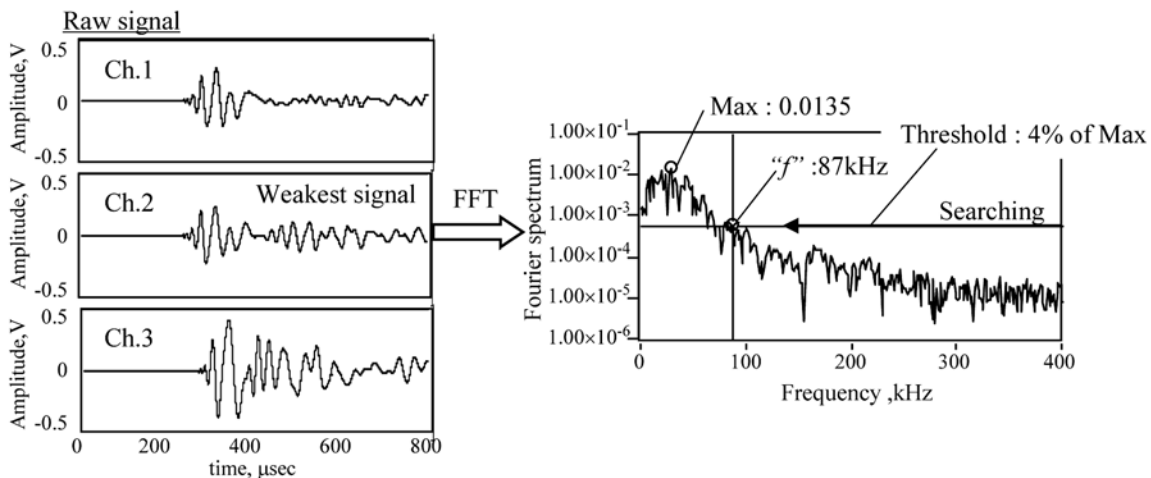


Fig. 8 The method for determining the suitable frequency for source location.

5. Conclusion

We developed a real-time execution source location system applicable to anisotropic thin structures. Two new algorithms for speeding up the source location are proposed. The first algorithm is a frequency-filtering algorithm, which uses a fast continuous wavelet transform. The second algorithm is a fast source location calculation algorithm for unidirectional anisotropic

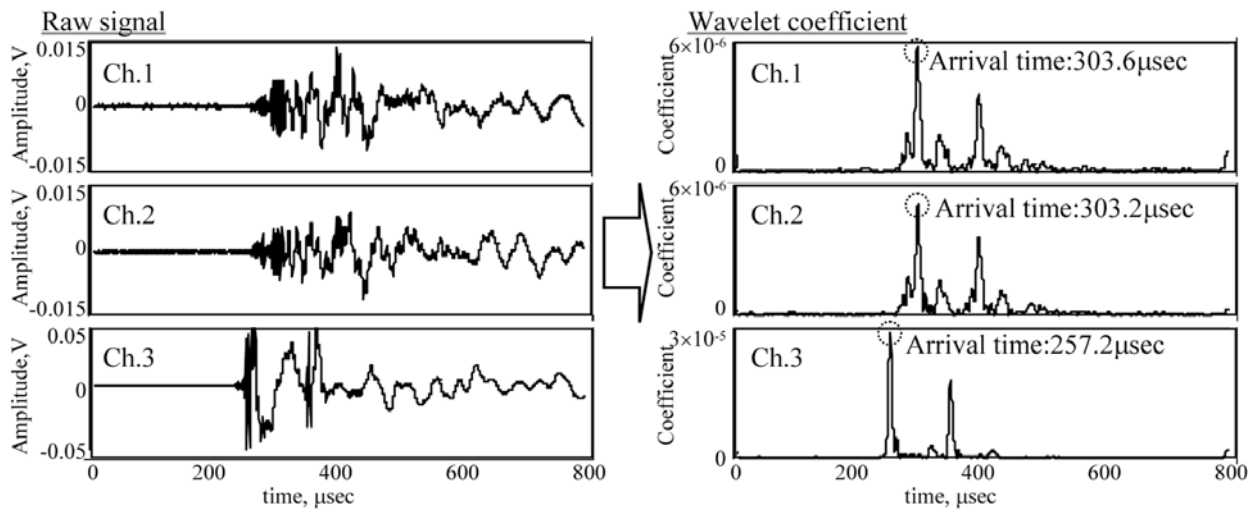


Fig. 9 Example of detected AE signals and the wavelet coefficients produced by pencil-lead break source.

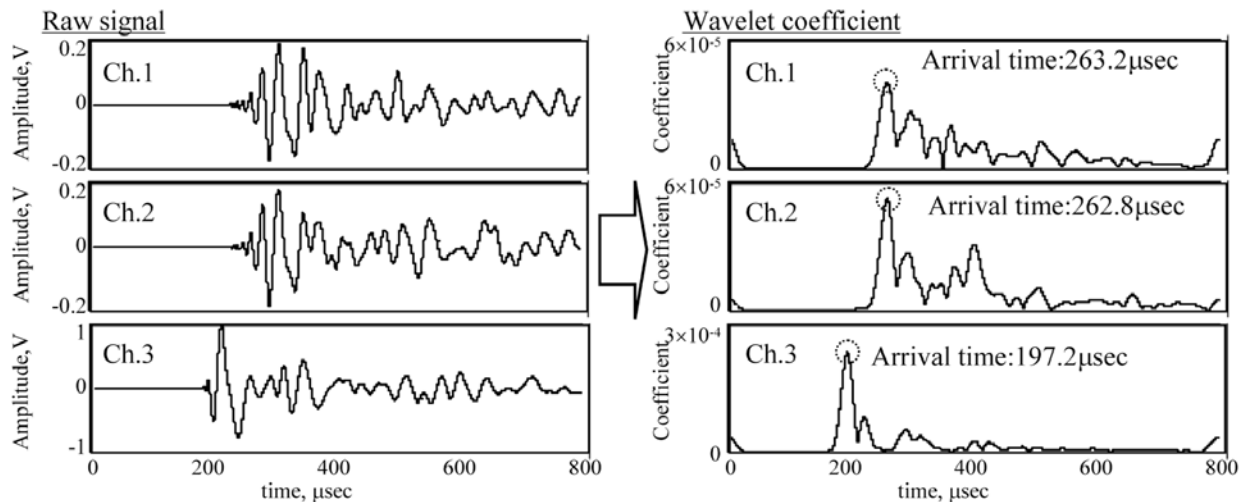


Fig. 10 Example of detected AE signals and the wavelet coefficients produced by steel-ball drop source.

structures. With both improvements, the online monitoring of anisotropic thin structures is now possible. The validity of the developed system is examined using lined CFRP plates. The calculation time for each source location is less than 15 ms with a good location accuracy.

References

1. M.R. Gorman and W.H. Prosser, "AE Source Orientation by Plate Wave Analysis", *J. Acoustic Emission*, **9**, (1991) 283-288.
2. Y. Promboon and T.J. Fowler, "Source location on fiber reinforced composites", paper presented at 6-th Int. Symp. on AE from Composite Materials, San Antonio, Texas, 1998.
3. M. Blahacek and Z. Prevorovsky, "Probabilistic definition of AE events", *European Conference on Acoustic Emission Testing*, Prague, 2002, pp. I/63-I/68.

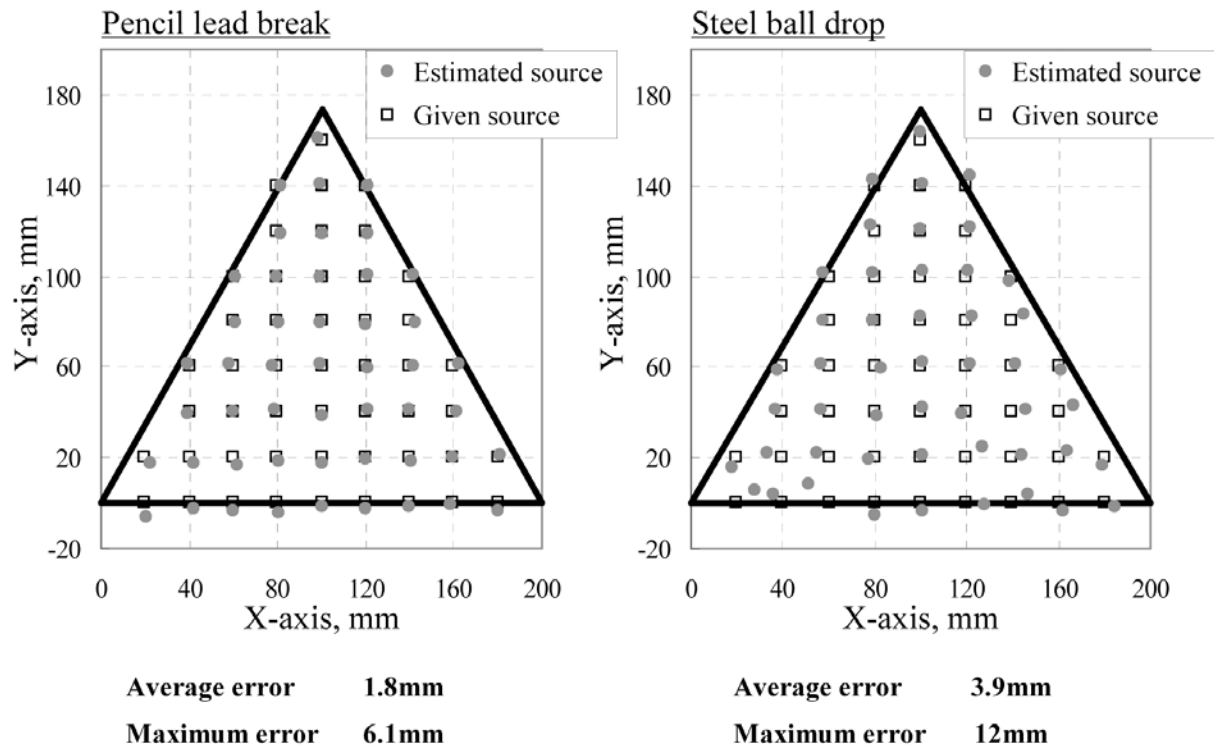


Fig. 11 Source location results for pencil-lead break and steel-ball drop sources.

4. V. Venkatesh and J.R Houghton, "Neural Network Approach to Acoustic Emission Source Location", *J. Acoustic Emission*, **14** (2), (1996), 61-68.
5. S.M. Ziola and M.R. Gorman, "Source Location in Thin Plates Using Cross-Correlation", *J. Acoustic Soc. Am.*, **90** (5), (1991) 2551-2556.
6. O.Y. Kwon and Y.C. Joo, *Progress in Acoustic Emission VIII*, (1998), JSNDI, Tokyo, pp. 9-17.
7. H. Yamada, Y. Mizutani, H. Nishino, M. Takemoto and K. Ono, *J. Acoustic Emission*, **18** (2000), 51-60.
8. C.K. Chui, *An Introduction to Wavelets*, Academic Press, (1992), pp. 60-61.

INVESTIGATION ON AE SIGNAL/NOISE PROCESSING IN CORROSION DAMAGE EVALUATION OF TANK BOTTOM

ZHENGWANG LI¹, SHIGENORI YUYAMA¹, MINORU YAMADA², KAZUYOSHI SEKINE³, SHIGEO KITSUKAWA⁴, HIROAKI MARUYAMA⁵ and SHIGEO KONNO⁶

¹) Nippon Physical Acoustics Ltd., 8F Okamoto LK Bldg., 2-17-10, Higashi, Shibuya-ku, Tokyo 150-0011, Japan; ²) National Research Institute of Fire and Disaster, Mitaka, Tokyo 181-8633, Japan; ³) Yokohama National University, Yokohama, 240-8501, Japan; ⁴) High Pressure Institute of Japan, Chiyoda, Tokyo 101-0025, Japan; ⁵) Japan Oil, Gas and Metals National Corp.; Bunkyo, Tokyo 112-0002, Japan; ⁶) Petroleum Assoc. of Japan, Chiyoda, Tokyo 100-0004, Japan

Abstract

Acoustic emission (AE) testing based on database consisting of test procedures and evaluation criteria has been widely used in Europe for the evaluation of floor conditions (corrosion damage) in above-ground tanks. Since the test procedures were introduced to the Japanese industry in 1999, fundamental studies in laboratory and field applications have been made by several organizations. In performing AE field testing, various environmental noise caused by rain and wind are unavoidable. This paper discusses a method of AE signal/noise processing in corrosion damage evaluation of tank bottom, based on the field tests conducted on more than 70 tanks in Japan.

Keywords: Tank bottom testing, Corrosion damage, Noise

1. Introduction

In recent years, much attention has been paid to the possibility of applying AE test to evaluate corrosion damage of tank bottom, as an alternative in-service monitoring method [1]. In Europe, AE testing has been made for more than 1000 tanks per year as a cost-effective maintenance planning tool, based on the database [2] built by AE inspection of several thousands oil storage tanks. This technique was introduced to the Japanese industry in 1999. Since then AE field tests have been carried out on more than 70 tanks with different diameters by three research groups. Intensive works have been made of AE test procedures, data evaluation methods, and so forth [3].

This paper discusses about a method of AE signal/noise processing in corrosion damage evaluation of tank bottom, based on the tests conducted in Japan. It summarizes test results from the research project of High Pressure Institute of Japan (HPI), sponsored by the National Oil Corporation of Japan.

2. Case Studies - Noise in Tank

When applying AE testing to tank bottom evaluation, it is essential to discriminate valuable AE signals from other noise. However, since AE signals from corrosion are usually very weak, the AE testing system is set to very high sensitivity, resulting in data including possible noise. Moreover, since oil storage tanks are in the outdoors, various environmental noise due to rain, wind and, in addition, EMI are unavoidable.

Here, case studies, based on examples of AE data showing typical environmental noise, are demonstrated and a method of AE signal/noise processing is discussed.

2.1 Noise due to Wind

It has been demonstrated that the influence of wind generally appears at a wind speed of greater than 4 m/sec. Under the maximum wind speed of 10 m/sec, a source location result of wind noise is shown in Fig. 1. Event location exhibits a radial pattern, spreading from the center of the tank. Although it is possible to install a wind gauge and to record the output as an external parameter of AE measurement in order to monitor wind speed, the data might be different between tank circumference and the place where the gauge is installed. The wind speed is quite different around the tank, depending on the location where it is monitored. Because of this, it is often very difficult to filter wind noise by post-test analysis. However, the noise resulting from a sudden speed change can be filtered by post-test analysis, based on wind data monitored in real time. Figure 2 shows an example of such wind noise. The periods when wind speed exceeded 6 m/sec are indicated by the boxes, which show a good correlation with very high AE activities.

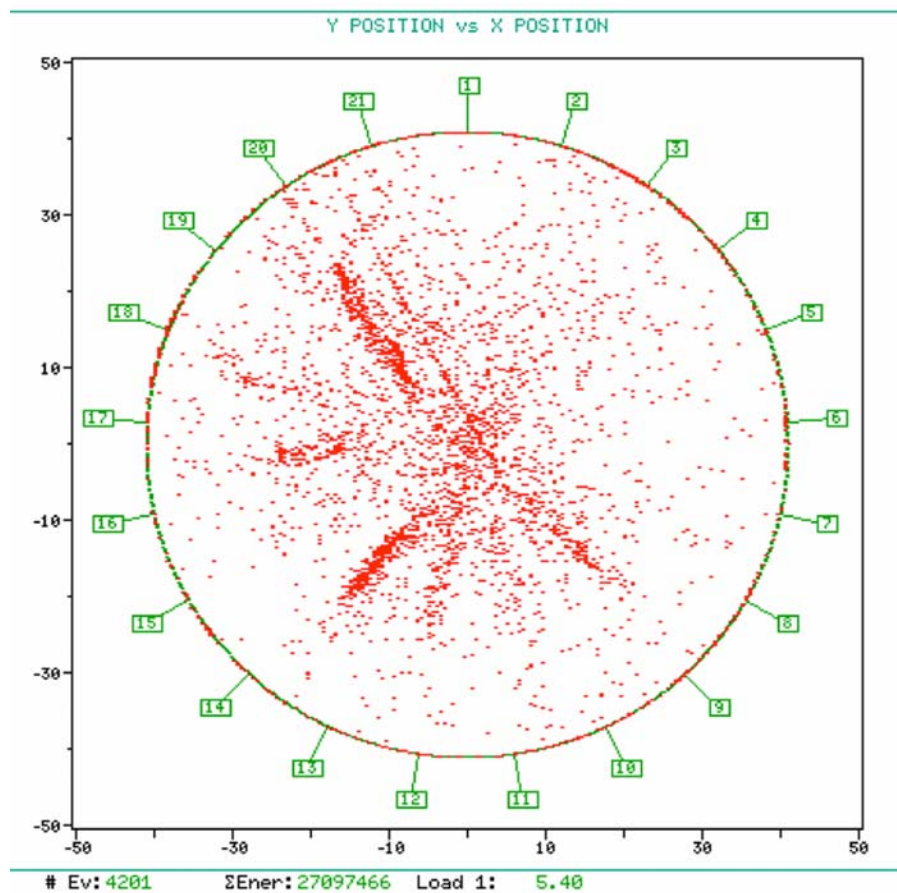


Fig. 1 AE source location based on TANKPAC procedure for AE data collected under strong wind (Crude oil tank, 82 m in diameter).

2.2 Noise due to Rain

As shown in Fig. 3, noise due to rain usually produces AE signals with large amplitudes over 80 dB. Source locations resulted from rain noise are spread evenly all over the whole region of

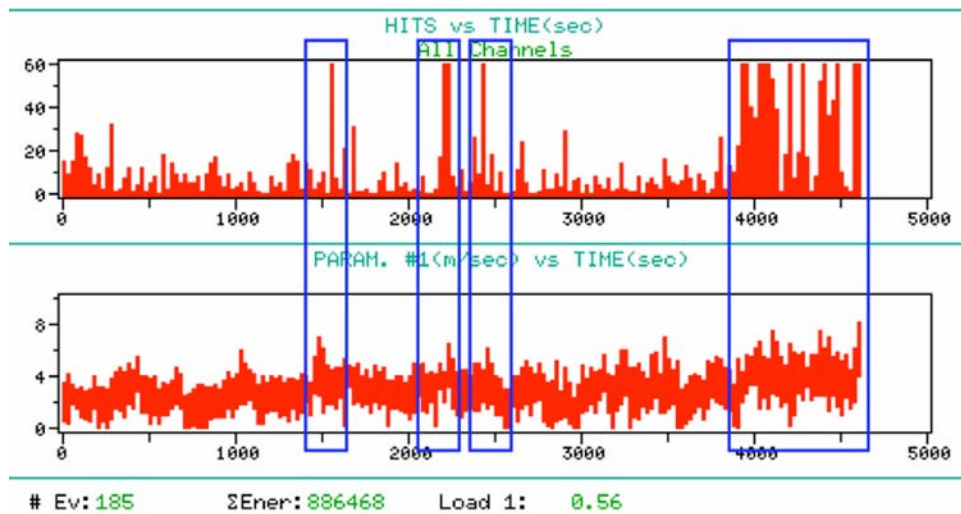


Fig. 2 History of AE hit rates (upper) and wind speed (lower), observed in a crude oil tank (83.3 m in diameter). High AE activities correspond to strong wind indicated by the boxes.

the tank bottom and clusters can be seen in some areas. Moreover, the noise does not stop until rainwater on the tank roof flows out completely. Especially, in a case of a large tank with a diameter of 80 m, the influence may remain for more than 24 hours. An example of rain noise, measured 24 hours after the rain had stopped, is given in Fig. 4. Source location indicates linearly spread cluster, which can be attributed to flow of rainwater in a drainpipe.

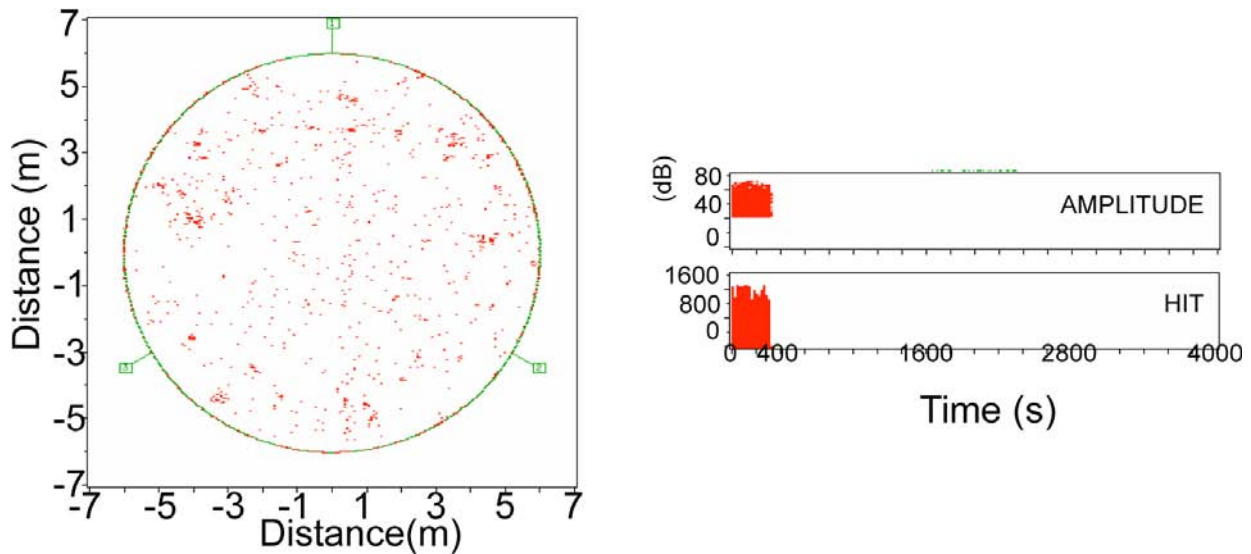


Fig. 3 Source location (left) of AE data collected in a product tank (12 m in diameter) under rain. Amplitude and hit rate history are also demonstrated.

2.3 Noise from Bird Movement on Tank Roof

As seen in Fig. 5, many signals were detected, showing high AE hit rates, for a period from 2600 seconds to 2700 seconds. Since several crows were seen to move on the tank roof during this period, the sudden increase of AE signals was attributed to the movement of the birds. Although most of such noise can be filtered by post-test analysis, it is important to pay attention to the situation around the tank to identify such noise in real time.

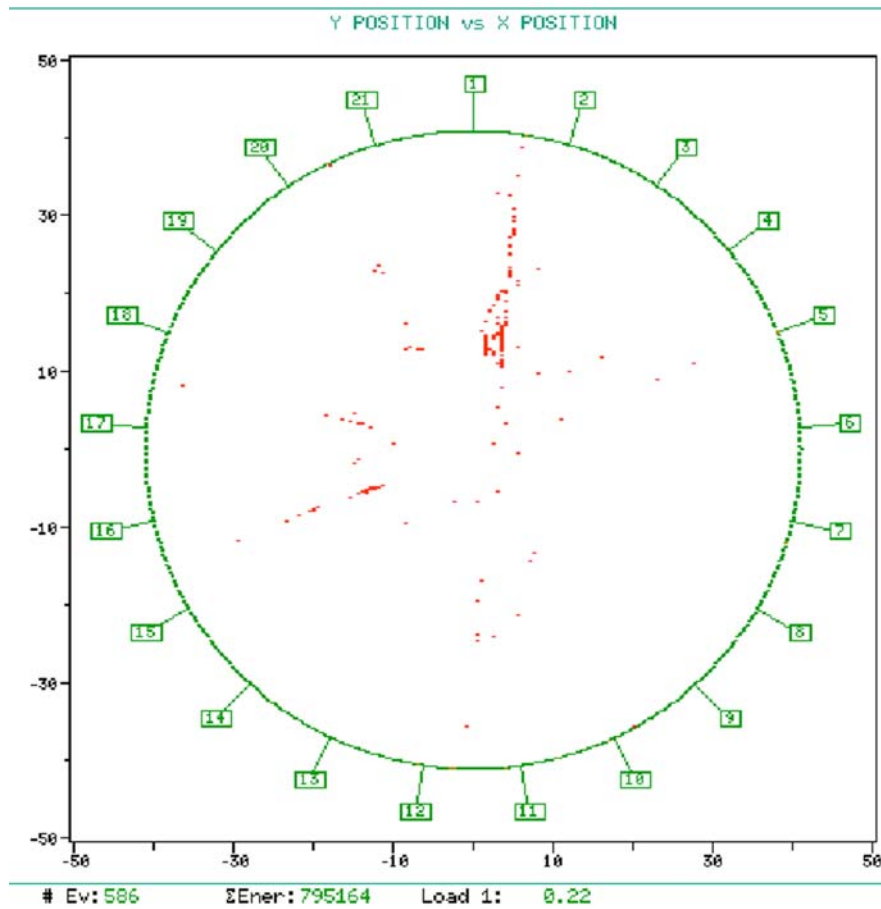


Fig. 4 Noise due to water flow in a drainpipe, observed 24 hours after rain stopped (Crude oil tank, 82 m in diameter).

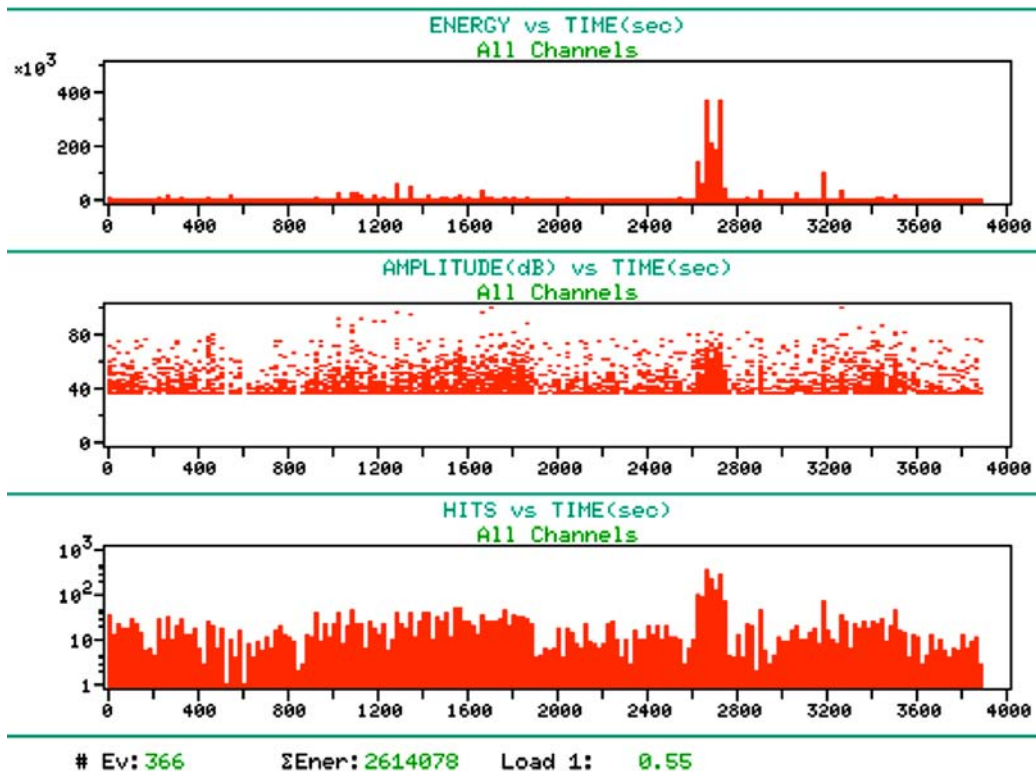


Fig. 5 Noise due to movement of birds on the tank roof (Crude oil tank, 61 m in diameter).

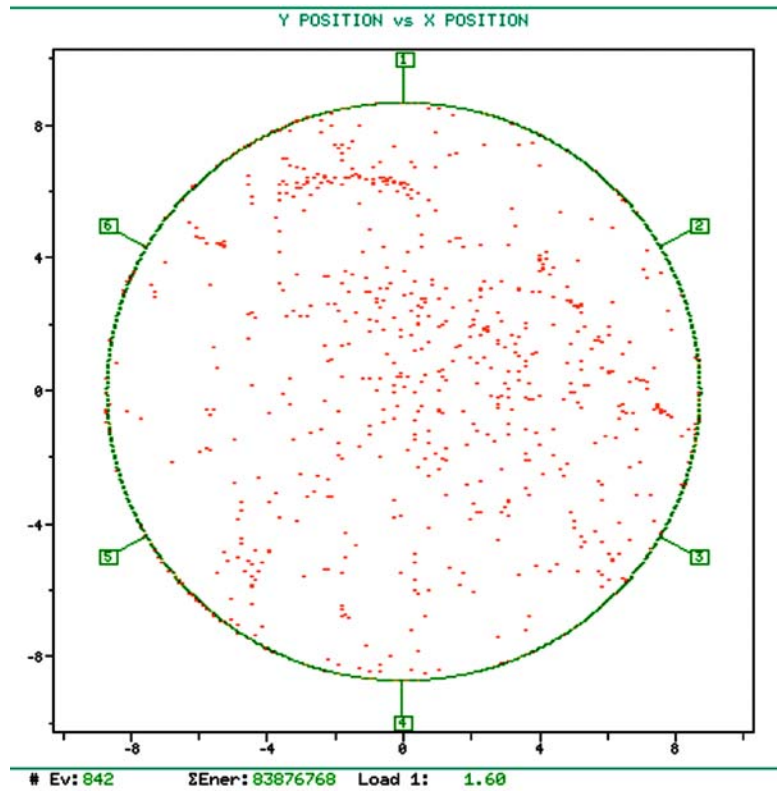


Fig. 6 Source location of AE data including signals due to water drops from the tank roof (water tank, 17 m in diameter) .

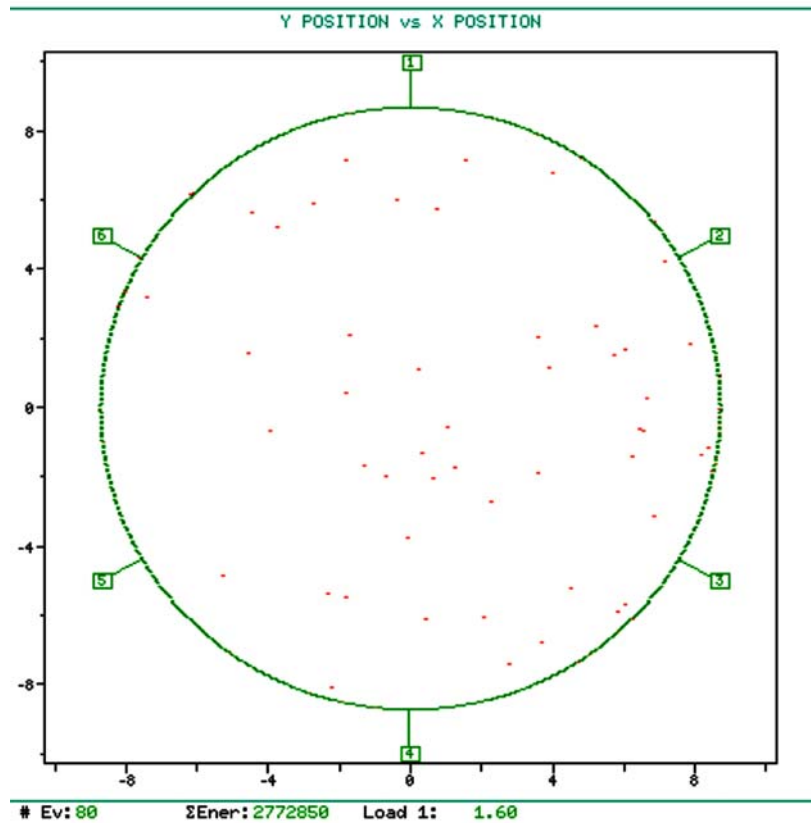


Fig. 7 Source location of filtered AE data excluding signals due to water drops from the tank roof (water tank, 17m in diameter).

2.4 Condensation Dripping in the Tank

Signals resulted from condensation dripping in the tank can be removed by using two rows of sensor array. Figure 6 indicates a source location result including condensation-dripping noise. 842 AE sources are detected and some clusters are observed. After signals attributable to condensation-dripping noise were filtered, only 80 AE sources remained and clusters disappeared, as seen in Fig. 7.

2.5 Pipe Vibration Noise due to Pump Operation

To perform AE testing properly, tanks must be set in quiet situation. Therefore, it is necessary to stop operation of pumps connected to the tank through pipes. Figure 8 shows amplitude and hit rate history indicating noise from strong pipe vibration. It should be noted that even if the threshold was set to 58 dB, many signals around 60 dB were detected, produced by pipe vibration. On the other hand, Fig. 9 gives results obtained under a threshold of 48 dB when pipe vibration was weaker than that of Fig. 8. It should be noted that all noise may not have been filtered due to continuous signals from the vibration. Therefore, in order to avoid such noise, it is necessary to stop pump operation near the tank during the test period.

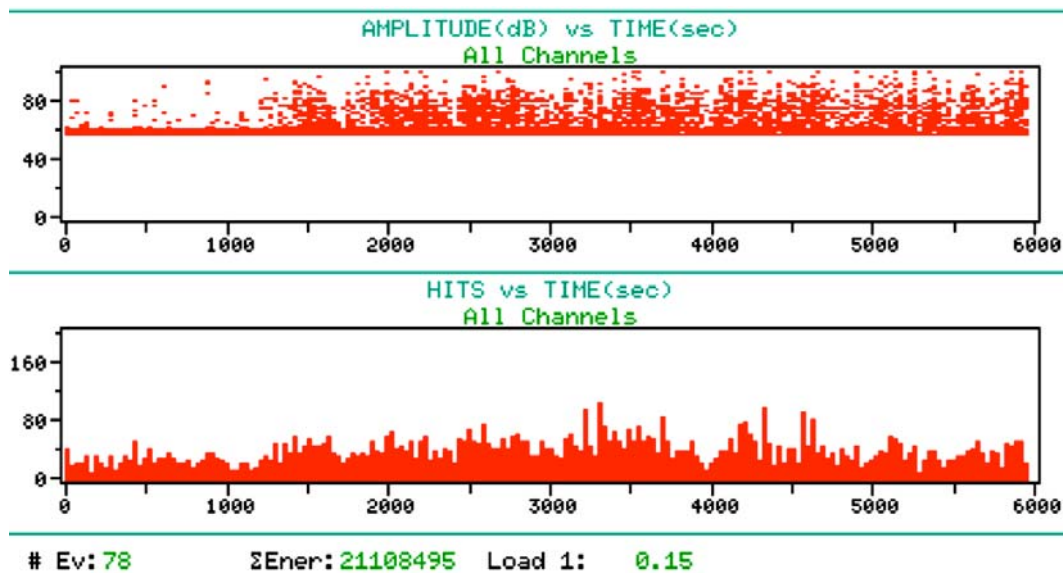


Fig. 8 Amplitude (upper) and hit rate (lower) history of noise due to vibration of pipes (Corn roof tank, 4.8 m in diameter).

2.6 Periodic Noise

In the case of a tank with dome roof, the inner pressure of the tank changes, depending on outside temperature. Nitrogen gas is charged or discharged in order to maintain a constant pressure. As shown in Fig. 10, the injection of nitrogen gas generates periodic extraneous noise. Note that nitrogen gas was charged at an interval of about 60 seconds and high noise continued for about 18 seconds. Such periodic noise can be identified by installing a guard sensor to detect signals beyond 90 dB in amplitude (Fig. 10) near the injection pipe of nitrogen gas. These noise can be filtered by post-test analysis. However, it is recommended that AE test should be carried out at a time when the atmospheric temperature is stable, so that the interval of gas injection becomes as long as possible.

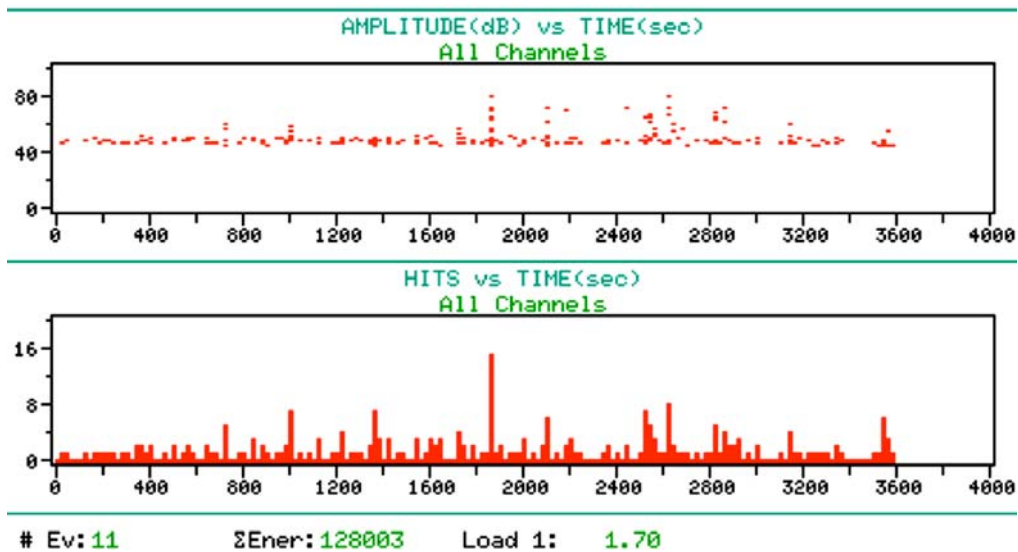


Fig. 9 Amplitude (upper) and hit rate (lower) history for the data after having filtered noise due to vibration of pipes by setting threshold at a high level (Corn roof tank, 11.6 m in diameter)

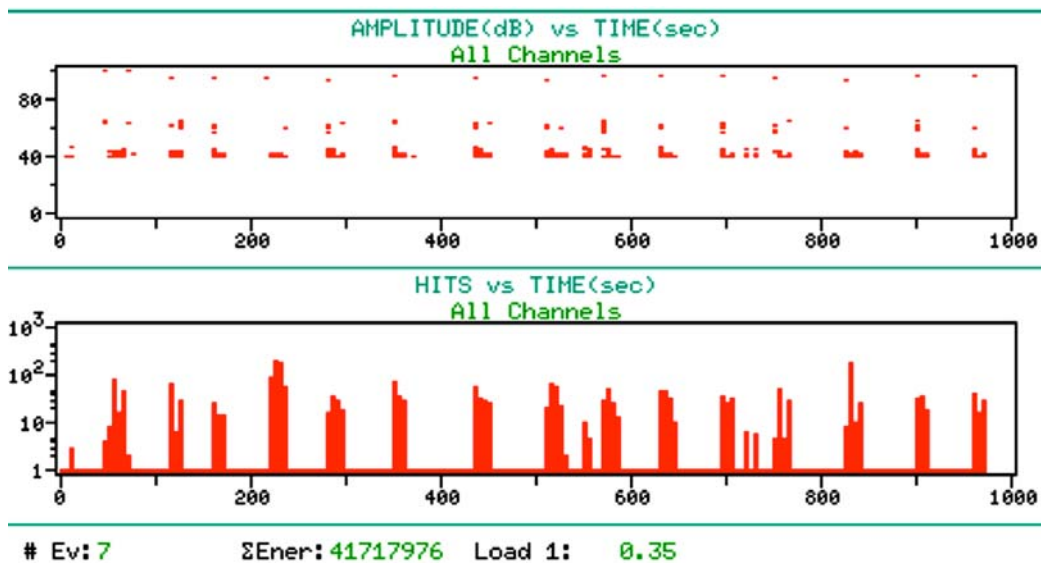


Fig. 10 Amplitude (upper) and hit rate (lower) histories, showing periodic noises due to pressure control by nitrogen gas injection (Dome roof tank, 13.5m in diameter).

2.7 Unidentified Noise (I)

When performing AE test, high AE activities are sometimes observed in a certain channel. One-hour monitoring was conducted three times in a crude-oil tank for two days. As shown in Fig. 11a to Fig. 11c, one of the three channels exhibits very high AE activities as compared to others. Although the source of these signals is not clear, it is very likely that they should be attributed to unidentified noise.

Although one hour monitoring is usually enough to perform tank bottom evaluation, it is necessary to extend testing time in order to obtain meaningful data when high AE activities are observed due to unidentified noise.

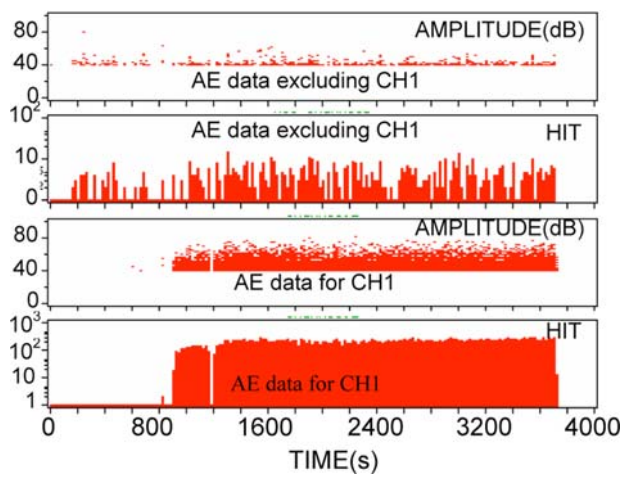


Fig. 11a Amplitude (upper) and hit rate (middle-upper) history of AE signals detected at other channels than CH-1 and the same for CH-1 during the first test (Crude oil tank, 82 m in diameter).

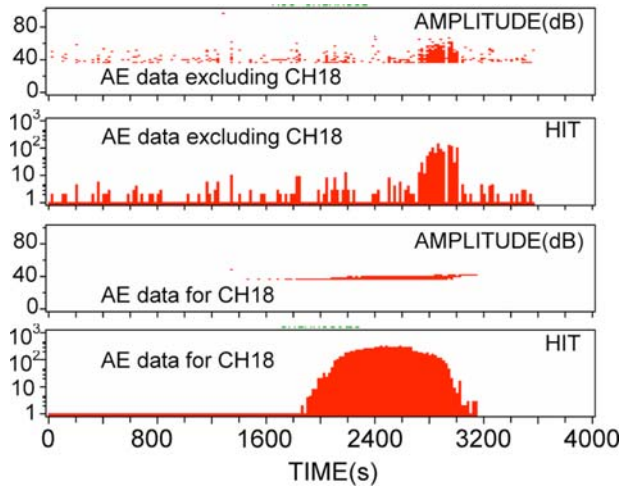


Fig. 11b Amplitude and hit rate history observed during the second test. High AE activities due to noise are observed at only CH-18 (Crude oil tank, 82 m in diameter).

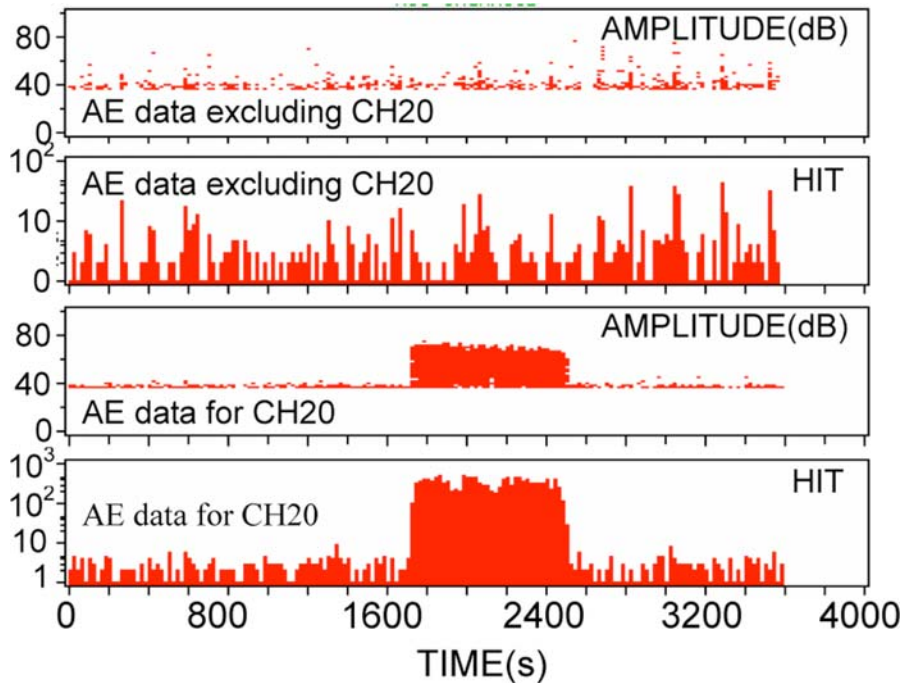


Fig. 11c Amplitude and hit rate histories observed during the third test. High AE activities due to noises are observed at only CH 20 (Crude oil tank, 82 m in diameter).

2.8 Unidentified noise (II)

Shown in Fig. 12 is discontinuous noise generated in more than two channels for certain periods. Although, many signals were detected for six periods (about 620 s to 680 s, 700 s to 1000 s, 1160 s to 1620 ss, 3860 s to 4030 s, 4180 s to 4230 s and 4380 s to 4503 s), the AE source that produced them could not be identified. Meanwhile, these signals were different from those resulted from condensation dripping. Furthermore, as shown in Fig. 13, source location showed no AE clusters in this case.

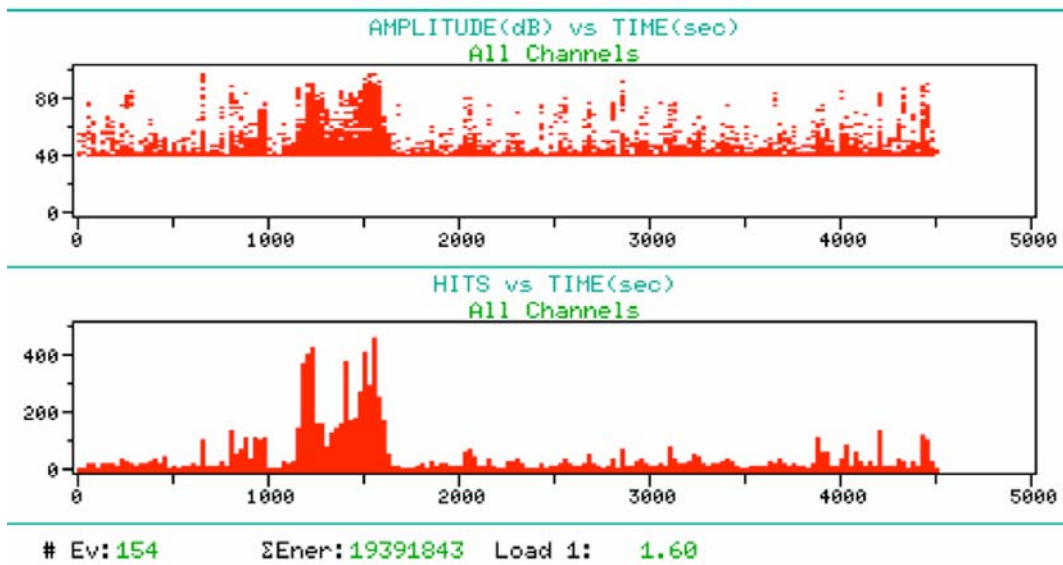


Fig. 12 Amplitude (upper) and hit rate (lower) history observed in a water tank (17 m in diameter). Strong noise detected during a certain period (1,160 -1,620 s) by multiple sensors.

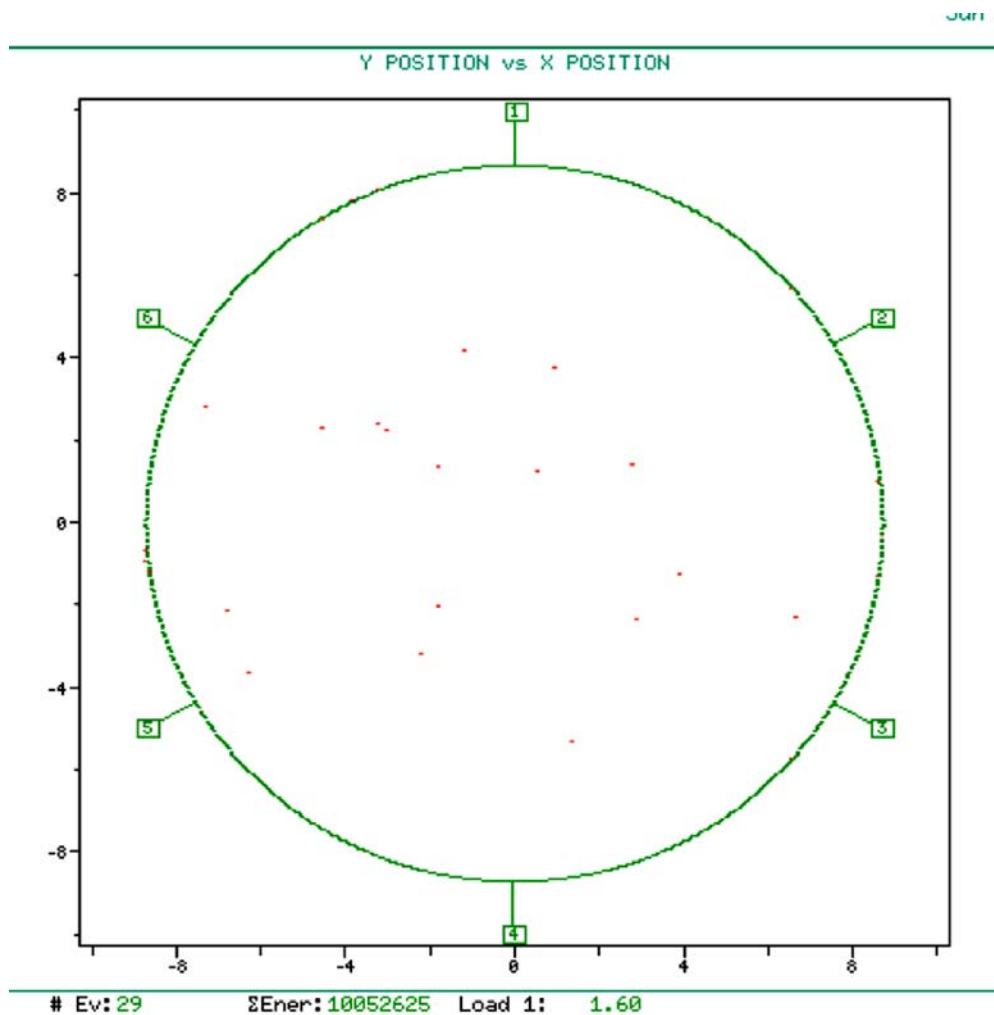


Fig. 13 Source location of AE data detected during 1160-1620 s in the water tank (17 m in diameter). No cluster observed in the figure.

The AE signals due to corrosion do not show such AE behavior. Therefore the above high AE activities were considered to be unidentified noise and meaningful AE signals observed in other periods were used for the evaluation.

3. Conclusion

Since AE signals due to corrosion are usually very weak, AE system is set to very high sensitivity, which very often results in detection of useless noise. Therefore, discrimination of meaningful signals from noise is essentially important in performing field test. Great care must be taken during AE tests by experienced inspectors to avoid unnecessary noise in real time.

References

- 1) S. Yuyama: *Inspection Engineering*, **26** (1997), 58.
- 2) P. T. Cole, P. J. Van de Loo: *Acoustic Emission-Beyond the Millennium*, Elsevier (2000), p. 169.
- 3) S. Yuyama, M. Yamada and K. Sekine: *Journal of High Pressure Institute of Japan*, **40** 4 (2002), 176.

EXAMINATION OF AE WAVE PROPAGATION ROUTES IN A SMALL MODEL TANK

HIDEYUKI NAKAMURA¹, TAKAHIRO ARAKAWA², MINORU YAMADA³

¹) System Divisions, Ishikawajima Inspection & Instrumentation Co., 1720 Kamai, Azuma, Inashiki, Ibaraki 300-0604, Japan. ²) R&D Divisions, Ishikawajima Inspection & Instrumentation Co., Yokohama 235-8501, Japan. ³) Fundamental Research Division, National Research Institute of Fire and Disaster, Mitaka, Tokyo 181-8633, Japan.

Abstract

This paper presents the results of a mock-up test executed to confirm accurate acoustic emission (AE) wave propagation routes. A 5-m diameter model tank was used and the propagation characteristics of the AE waves generated on the tank bottom plate were measured with sensors arranged at 100 mm intervals on the bottom plate and the wall plate in the test. It was confirmed that Lamb waves reached the wall plate, and the Lamb waves converted into other modes in water.

Keywords: Oil storage tank, Corrosion, Evaluation, Propagation route

1. Introduction

In evaluating the corrosion status of oil-storage tank bottom plates, acoustic emission (AE) waves that propagate in liquid are measured because AE attenuation is smaller in liquid than in steel. Although some studies up to 2002 have reported experimentally that the corrosion AE waves generated on the outside surface of the tank bottom plate propagate in water, no papers have conducted a detailed analysis of the results. It is important to accurately understand AE wave propagation routes. This is because locating the source of the AE wave generation requires the processing to be executed at a sound velocity that has been set to match the AE wave propagation route.

This study is aimed at confirming accurate AE wave propagation routes by conducting precision measurements (with densely located measuring points) of the pseudo AE waves generated on the tank bottom plate with a mock-up using a small model tank.

2. Experimental Procedures

2.1 Targets

This study was conducted under the following five test conditions (Points A, B and C are shown in Fig. 1).

- a. AE waves generated on the center (point B) of the inside surface: Confirm the propagation conditions of AE waves generated at point B on inside the tank bottom plate without large effects by detoured AE waves through the tank wall plate.
- b. AE waves generated on the quarter-point of the radius (point A) of the inside surface of the tank bottom plate: Confirm the propagation conditions of the AE waves that are propagated on the tank bottom and wall plates from point A on inside the tank bottom.

- c. AE waves generated on the opposite quarter-point of the radius (point C) of the inside the tank bottom plate: Same as above in b.
- d. AE waves generated in water 50 mm above point B: Confirm the propagation conditions of AE waves in water. In water sources are expected to be affected less by steel plates.
- e. AE waves generated at point B on the outside surface: Confirm the propagation conditions of AE waves generated at point B on the outside surface of the tank bottom plate. This simulates the corrosion AE waves generated on the outside surface of the tank bottom plate.

2.2 Test Procedure

On a small, indoor model tank, we installed the pseudo-AE sources inside and outside of the tank, as shown in Fig. 1. The sources generated AE waves at each position. We measured AE waves with 19 AE sensors attached to the wall and bottom plate of this tank (refer to Fig. 2). We measured AE waves at 19 locations at a time. The measurement positions are on the intersection of grids shown in Fig. 2. This test also used the waveguide shown in Fig. 3 in order to generate AE waves in contact with the bottom plate (conditions a, b, c) and in water for the condition d.

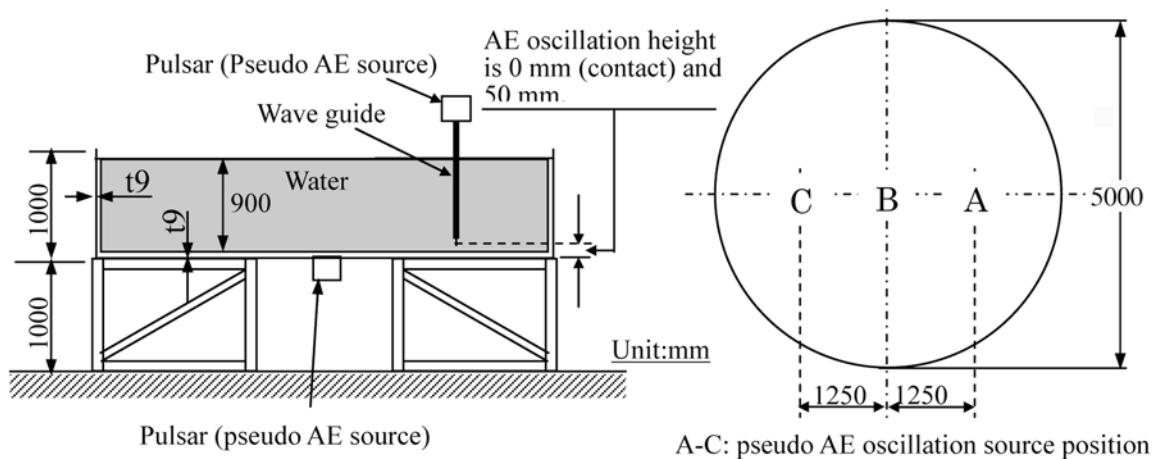
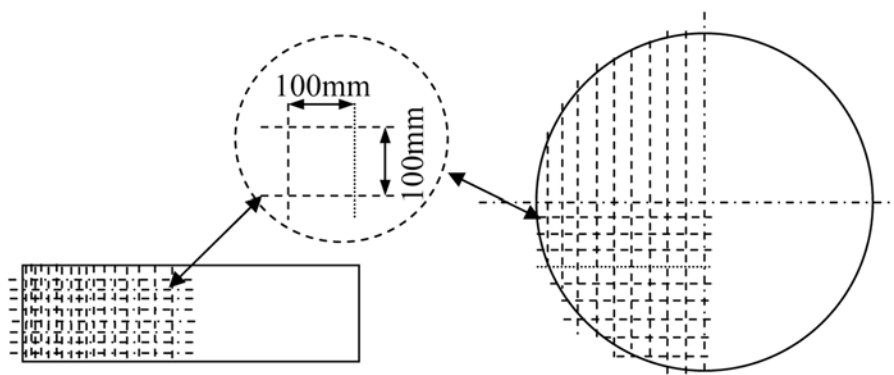


Fig. 1 The view of the model tank and the positions A, B and C on the tank bottom plate.



On a wall plate, sensors (30 kHz) are attached ranging in height from 0 to 800 mm with a 100 mm pitch over the range of 1/4 round.

For the tank bottom plate, sensors (30 kHz) are mounted in one fourth of the ranges of bottom plate with 100 mm pitch.

Fig. 2 Sensor mounting position and water surface height.

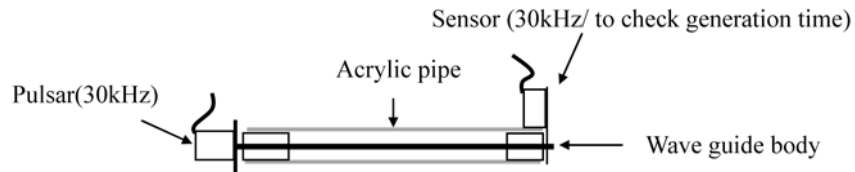


Fig. 3 Waveguide for in water AE source.

3. Results

A typical result of the AE wave propagation is shown in Fig. 4. The data are represented by a three dimensional graph, which corresponds to one fourth of the tank shown in Fig. 1 (oblique lines). The bar graph that projects from the bottom plate upward represents the intensity of the AE waves measured on the bottom plate. The amplitude is color-coded in 10 dB range; i.e., 0 dB or more in red, 0 to -10 dB in purple, etc. followed by yellow, blue and green. The bar graph that projects from the wall plate horizontally is the intensity of the AE waves measured on the wall plate. In this figure, the red, blue and green solid lines indicate the furthest reach of propagating waves on the bottom plate and up the wall (green only in this example). These represent the theoretical wave velocities (calculated values) of the AE waves. The slowest waves propagate through the liquid (red circle), next is A_0 -mode (blue circle) and the fastest S_0 -mode (green circle) Lamb waves that propagate through the steel, respectively. The respective velocities were calculated as 1480 m/s, 2400 m/s and 5460 m/s, respectively.

From the tip of the A_0 and S_0 waves, mode-converted waves are radiated into the liquid as “bow-waves”. The positions of these waves on the center-cross-section are marked by blue and green lines at angles, θ_2 and θ_1 . As shown in Note 1 and 2 in Fig. 4, these are 31.7° and 15.2° , respectively.

3.1 AE Wave Propagation Results

The propagation results in each test are as follow:

a. AE waves at the center of tank bottom plate (B point)

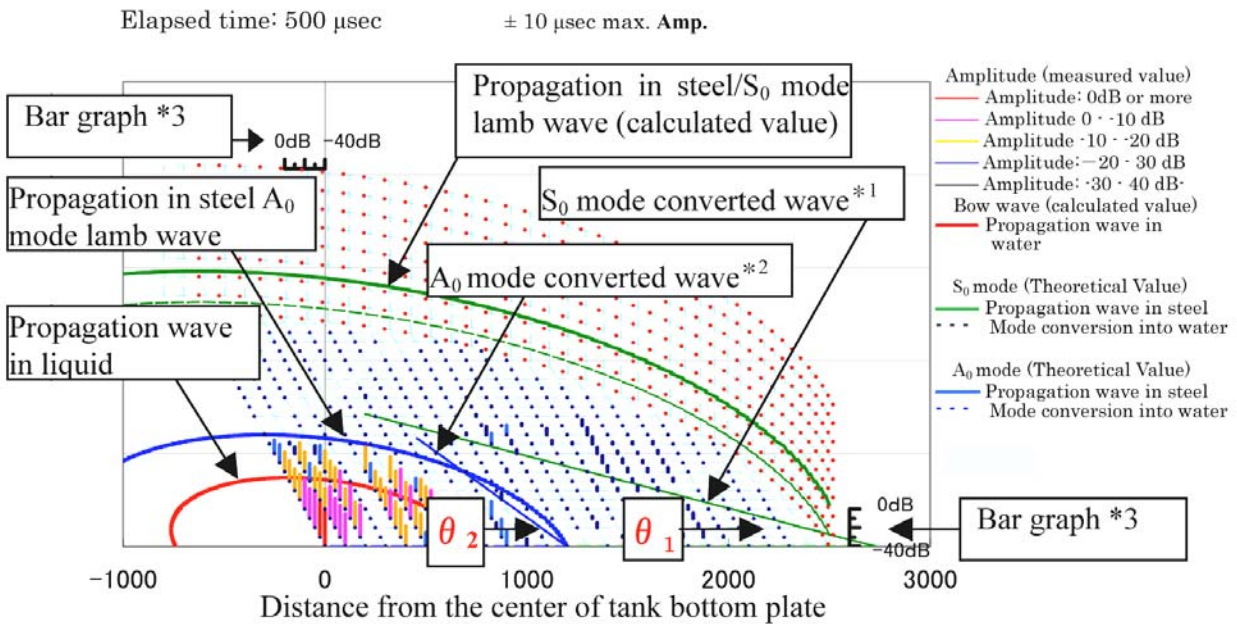
Results of this test are given in Fig. 5, and we confirmed that AE waves spread concentrically. AE waves with amplitude of -20 dB or less spread first, followed by stronger AE waves with the amplitude of -20 dB or more. These AE waves are Lamb waves that propagate in steel because of their faster sound velocities than liquid propagating waves. The first waves propagated are S_0 -mode Lamb waves and the second, higher amplitude waves are A_0 -mode Lamb waves. The sensors attached to the wall plates observed AE waves radiated into water from the bottom plate. When the Lamb waves spread in steel while radiating P-waves into water, the first AE waves that propagate in water with the inclination defined by the ratio of velocities of water and Lamb waves. As noted above, these are θ_1 and θ_2 .

b. AE waves from the quarter-point (A point)

We verified that AE waves of Lamb A_0 -mode propagated concentrically, centered at the quarter-point (A point), but S_0 -mode Lamb waves could not be measured. It appears that the tank frame support was directly under the AE generation point, and S_0 -mode waves were attenuated by the rubber board inserted between the support and bottom plate.

c. AE waves at the second quarter-point (C point)

We verified that AE waves at C point of the tank bottom plate propagated concentrically to the wall plate near the AE source before they reached the other sidewall.



- *1 S_0 mode-converted wave: Indicates the cross-section of AE waves (calculated value of bow wave) in which the S_0 mode lamb waves propagating in steel are converted into the mode in water. Velocity of water=app.1480m/s, Velocity of S_0 =app.5460m/s, $\theta_1 = \tan^{-1}(1480/5460)$
- *2 A_0 mode-converted wave: Indicates the cross-section of AE waves (calculated value of bow wave) in which the A_0 mode lamb waves in steel are converted into the mode in water. Velocity of A_0 =app.2400m/s, $\theta_2 = \tan^{-1}(1480/2400)$
- *3 The bar graph: The amplitude value in this data (dB) is the relative value with which the output voltage of a sensor (V) is expressed as $1V = 0 \text{ dB}$. It differs from the amplitude value ($10V = 100 \text{ dB}$ /reference voltage: 0.1 mV) usually used for AE measurement data.

Fig. 4 AE data example.

d. AE waves in water above the center of tank bottom plate (B point)

This test was intended originally to measure only the water propagating waves. The results, however, were similar to 'a' above in which AE waves were generated on the tank bottom plate. It appears that AE waves first entered into steel through water, then propagated in steel. This is because the distance between the AE source and the tank bottom plate was $\sim 50 \text{ mm}$ and waves through water are much slower than the Lamb waves.

e. AE waves at the back surface of B point

In this test, AE waves generated at the back surface of the center tank bottom plate were detected. The results were similar to AE waves generated on the face shown in 'a' above.

4. Discussion

The test results given in Fig. 5 indicate that, although the first AE waves generated on the center of the bottom plate is small with its amplitude less than -20 dB, it reached the bottom plate circumference 600 μ s after the generation. Using the relationship between the propagation distance and the arrival time, the sound velocity of the first arrival wave was calculated as 4,167 m/s. While this sound velocity was close to that of the Lamb waves in S_0 -mode (5460 m/s), it is about one-fourth slower. It is difficult to presume it to be the S_0 -mode Lamb wave. Since the Lamb waves radiate mode-converted AE waves in water moving at the slow P-wave velocity (1480 m/s), as shown in Fig. 4, the first waves reaching the wall plate are likely to be the mode-converted P-waves. If the first arrival waves propagate in the bottom steel plate 2/3 of the time

and the rest through water, the observed wave velocity is expected. In distance term, the waves propagate almost 90% in steel and 10% in water.

Next, we examined the state of propagation of the AE waves indicating high maximum amplitude (hereafter the maximum AE waves), shown by orange bars in Figs. 4 and 5. This indicates a large amplitude of -20 dB or higher. The maximum AE waves reached the circumference of tank bottom plate in 1,300 μ s. The sound velocity of the maximum AE waves was calculated to be 1,923 m/s. This is close to that of the A_0 -mode Lamb waves, but again it is slower, giving a high possibility that the maximum wave is mode-converted waves from the A_0 -mode Lamb waves.

We confirmed the propagation of the P-waves in water, shown in red in Figs. 4 and 5, which expand spherically. In this test, many of the sensors that were installed on the wall plate measured the maximum value at times between 1,600 to 1,700 μ s when the waves propagating through the water reached the wall plate.

In this study, we confirmed that, with a small tank of 5 m in diameter, the Lamb waves propagate through the steel and reach the sensors without much attenuation. It was also found that the AE waves, which have undergone a mode conversion from the Lamb waves entering from the bottom plate into the water, reached the wall plate. In actual tanks, the bottom plate contacts the ground, probably causing Lamb wave attenuation. In measuring AE waves in small tanks, however, it is essential to take into account the effect of the Lamb waves.

5. Conclusion

This study clarified the details of the propagation of AE waves on the bottom plate and the wall plate, and the following findings were obtained:

- 1) It was confirmed that the AE waves generated on the bottom plate propagate in the liquid and reach the wall plate.
- 2) For a small tank (5 m in diameter), the attenuation of the Lamb waves propagating in the steel is small, and the waves reach the wall plate with their signal intensities above the threshold of 40 dB_{AE} (-40 dB in the data of this test) as prescribed in corrosion evaluation by the AE method. Therefore, it is important to evaluate corrosion by taking into account the effect of the waves propagating in water.

Based on the results of this test, it was confirmed that, in applying the evaluation technology for tank bottom plate corrosion to large actual tanks according to the AE method, the AE waves that propagate in liquid with a little attenuation could be made the main measuring means. It was confirmed that, in applying the AE measurement to small tanks, it is necessary to set measuring conditions that take into account the effect of the Lamb waves that propagate in the steel plate.

References

- 1) A. Proust, J.C. Lenain, S. Yuyama: *Prog. in AE X*, Tokyo, 2000, p. 147
- 2) P.T. Cole, Van De Loo: *Acoustic Emission-Beyond the Millennium*, Tokyo, 2000, p. 169
- 3) S. Yuyama, M. Yamada, K. Sekine: *Proc. 2001 National Conf. on AE*, Kokura, 2001, p. 37.

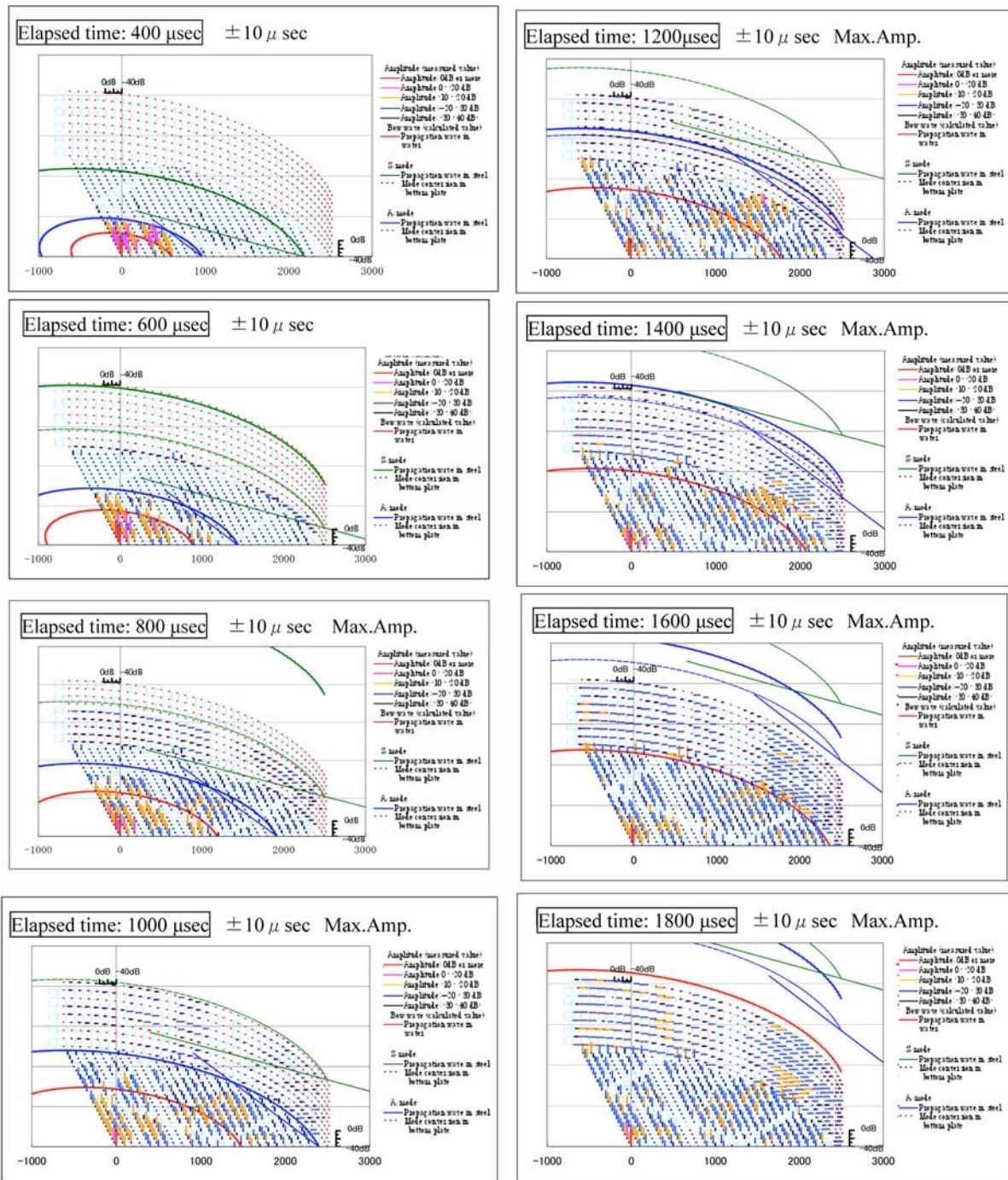


Fig. 5 AE waves generated at the tank bottom plate center (B point) surface.

INTEGRITY EVALUATION OF GLASS-FIBER REINFORCED PLASTIC VESSELS BY LAMB WAVE AE ANALYSIS

TAKASHI FUTATSUGI

Ajinomoto Co. Inc., 1-1 Suzuki, Kawasaki, Kawasaki 210-8681, Japan.

Abstract

Integrity evaluation of glass-fiber-reinforced plastic (GFRP) vessels has become an important problem with the long-term aging of in-service vessels in corrosive environments. We proposed a method for estimating the integrity of aged GFRP vessels utilizing the sheet velocities and developed a simple method for exciting and measuring the Lamb waves. Applying this method to GFRP vessels in service, the sheet velocity measured was found to correlate well to the bending strength of the aged members. We successfully utilized it for the health monitoring of the vessels. Next we monitored AEs during the bending test of the aged members and determined the threshold tensile stress to cause internal damage. We also monitored AEs from the manway located near the bottom of a vessel in service. AE activity was found to be closely correlated to the residual strength estimated by the sheet velocity.

Keywords: GFRP vessels, Integrity, Lamb waves, Sheet velocity, Residual strength

1. Introduction

Glass-fiber-reinforced plastic (GFRP) vessels have served well for over 30 years in various chemical industries because of their excellent corrosion resistance and low price. GFRP vessels, however, tend to lose their strength due to degradation, such as hydrolysis reaction, oxidization, environmental stress cracking and so on. Although the GFRP vessels are designed to have enough strength, with the safety margin of about 10, catastrophic disaster occurs if the degradation is severe. Figure 1 shows an example of failed FRP vessels in our company. We have several hundreds of GFRP vessels, which have been used for more than 20 years. Hence, the integrity evaluation of these GFRP vessels is becoming an important maintenance issue.



Fig. 1 An example of failed GFRP vessels, used as steam condensate tank. (left) overall view; (right) Cut-out GFRP wall part from around the failed side manway.

GFRP vessels have been examined by standards-based visual inspection [1]. However, the lifetime of GFRP vessels cannot be predicted by the visual inspection because sub-surface degradation tends to occur without remarkable change of the surface. In addition, deposits on the inside surface makes the visual inspection difficult.

Other inspection methods such as radiography or ultrasonic testing also have difficulty for GFRP inspection because it is not easy to separate the defect-induced reflection waves from those from fibers, filler and initial defects. GFRP vessels generally have own specifications about resins, thicknesses, service environment, laminated structures and fiber contents. Sometimes, even the vessel owners do not have the details of the specification, especially about the laminated structures. In addition, GFRP vessels have many initial defects caused during the construction. These make the prediction of residual strength and lifetime of GFRP vessels difficult.

The present author proposes to use the Lamb waves for estimating the residual strength of in-service GFRP vessels. We measured the sheet velocity of S_0 -mode excited by pencil-lead breaking on the vessel surface. The sheet velocity does not show any direct relationship with the strength of the GFRP, but can estimate the strength of composite materials. Seale *et al.* [2] reported a correlation between the damages of composites with sheet velocities. Toyama *et al.* [3] studied effect of density of transverse crack and delamination length on the sheet velocities. Hence, sheet velocity measurement has become an effective tool to predict damage of FRP materials. We measured the sheet velocities of many aged GFRP vessels in service and then studied the relation between the sheet velocity and residual strength estimated by bending test. We used AE technique to monitor the progression of internal damage of aged members of GFRP vessels during the bending tests. Advanced AE analysis for fracture-mode identification was used. [4, 5] Finally, we evaluated results of AE monitoring of two GFRP vessels in service. There observed a good correlation between the degradation predicted by sheet velocity and AE activities.

2. AE Monitoring and Sheet Velocity Measurement for the Aged Members

2.1 Test Specimens and Experimental Procedures

Test specimens were from the shell wall taken from a failed GFRP vessel. This vessel (Fig. 1) was used as steam condensate tank for 16 years. The structural layer of the vessel with the thickness of ~ 14 mm is produced by hoop filament winding with isophthalate unsaturated polyester resin. The interior corrosion layer of ~ 1 -mm thickness is constructed by Novolac vinyl ester with chopped E-glass mats (450 g/m^2). The vessel collapsed from cracks around the side manway. The cause of this accident is considered as the strength decrease by hydrolysis reaction of resin and by environmental stress cracking. New specimens, whose lamination structure is the same as the failed vessel, were prepared for comparison.

Bending strengths of these specimens σ_b were measured by three point bending tests based on JIS K7055. The sizes of bending test specimens are $30 \text{ mm}^w \times 245 \text{ mm}^l \times 15 \text{ mm}^t$. Outer span distance of three point bending is set as 208 mm. AEs were monitored by four resonant sensors (PAC, type PICO, center frequency 450 kHz) mounted on the specimen surface. Here the member was set so as the tensile stress by bending is on the inner surface. This member setup is based on the deformation pattern of GFRP vessel with internal fluid pressure.

For a vertical vessel with side manway, hoop stresses by liquid head concentrates around side manway. Figure 2 shows the deformation pattern analyzed by FEM. The upper portion of the

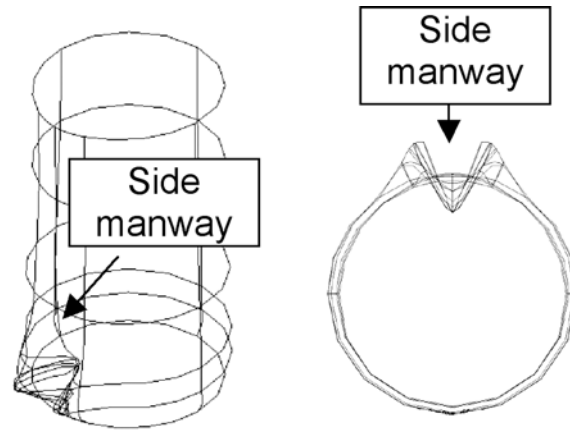


Fig. 2 Deformation of GFRP vessel with internal fluid pressure analyzed by FEM. (a) side view and (b) top view.

manway bends to the inside by liquid head. The tensile stress acts on the inside of the shell wall around the side manway and failure initiates from there. The failure of the actual vessel initiated from around the side manway shown in Fig. 1(b). Therefore the bending load must be applied so as to give the tensile stress on the inner surface of the member. Also the longitudinal directions of bending specimens must be circumferential so as the hoop fibers bear tensile stresses. Directions of Lamb wave propagation for sheet velocity measurement should be in the circumferential direction.

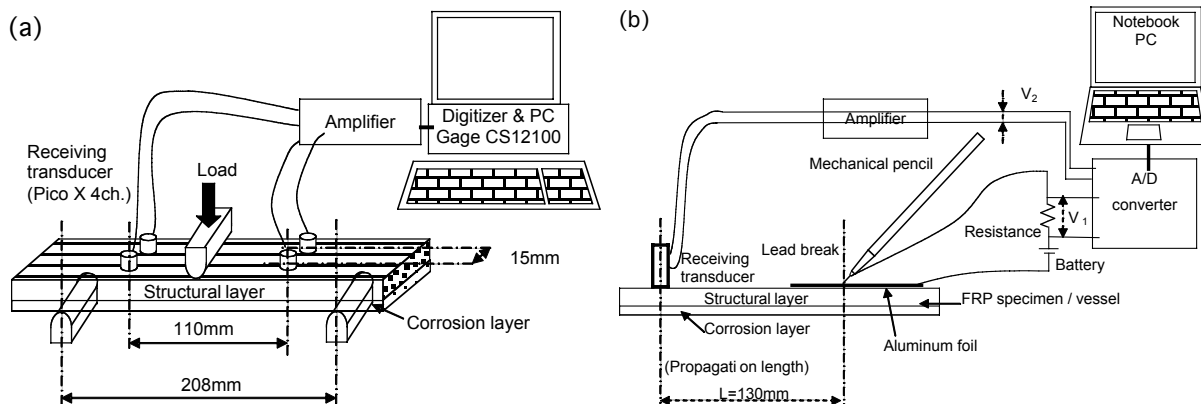


Fig. 3 Experimental arrangements (a) Bending test with AE monitoring (b) Lamb wave measurement

AE sensors were mounted on the upper or outer surface of the shell wall, as shown in Fig. 3(a). Sensor outputs were amplified 40 dB by a preamplifier (NF Corp. 9913), digitized (Gage CS-12100, 20 ns sampling interval), and fed to a personal computer. Figure 3(b) shows experimental setup for sheet velocity measurement. In order to measure the sheet velocities on site, we excited Lamb waves by breaking a pencil-lead. Here the lead breaking triggered the digitizer by a voltage change, which was applied between aluminum foil on the sample and the pencil lead via a 50-ohm resistor. The Lamb wave was detected by a PICO sensor mounted at distance $L = 130$ mm from the lead break. Both the voltage change and Lamb waves were recorded on digital oscilloscope (Adtek system science, AXP-DS01, 20 ns sampling interval). Figure 4 shows an example of detected Lamb waves. Sheet velocity was measured from the traveling time and distance.

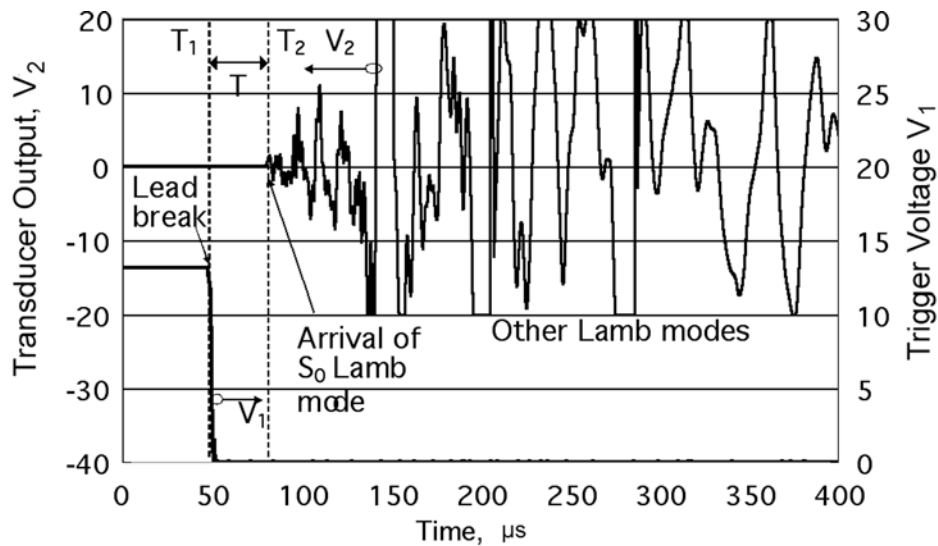


Fig. 4 Detected Lamb waves at distance of 130 mm for a GFRP sample.

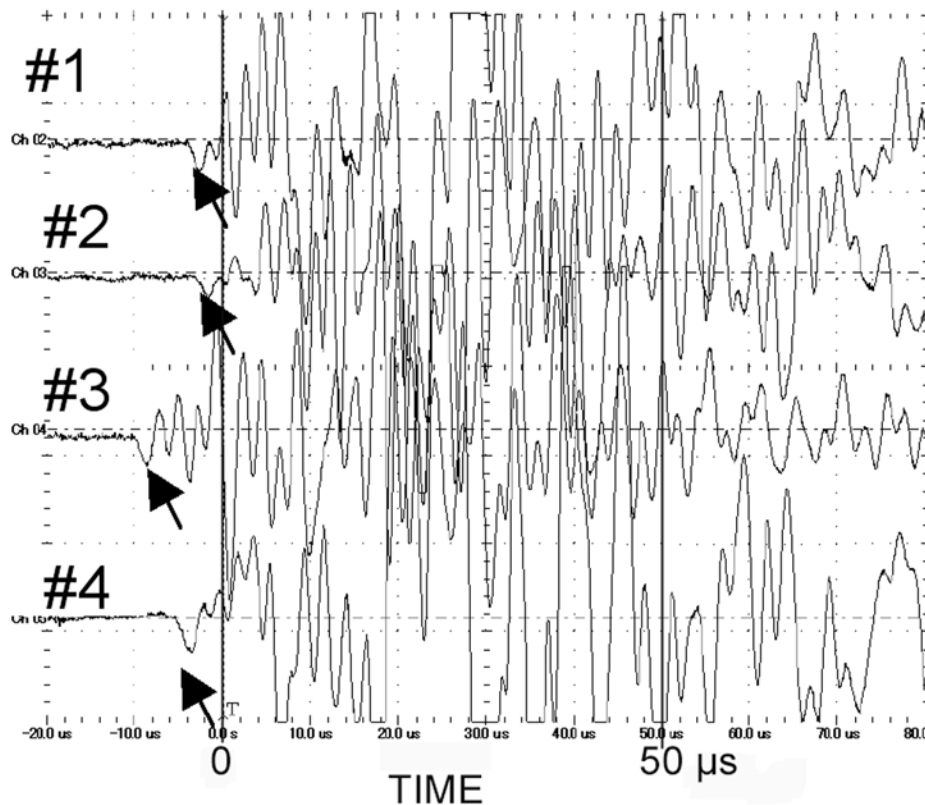


Fig. 5 Detected AE wave and its polarity distribution at bending test.

2.2 Test Result of Failed Vessel Samples

Figure 5 shows examples of AE waves detected during a bending test. These are typical Lamb waves AEs with weak S_0 -mode and trailing strong A_0 mode. We classified the fracture types by analyzing the polarity distribution of first arrival S_0 -waves. Two samples, i.e. (a) one from the failed vessel wall and (b) a new sample, were bent under the same condition. Figure 6 shows the load-deflection curves and cumulative AE events for samples (a) and (b). Upper two curves are the load-deflection curves and the lower two the cumulative AE counts. The new

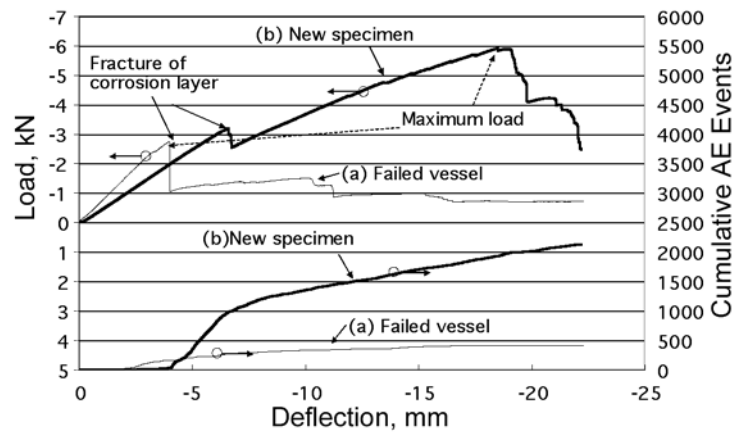


Fig. 6 Load-deflection curves and cumulative AE event counts.

specimen showed a pop-in at the load of 3.2 kN or ~50 % the maximum load. This pop-in is considered to be due to the fiber fracture in anti-corrosion layer. AEs were detected from 2 kN, and increased rapidly before the pop-in load. Above the pop-in stress, load increased almost linearly to 6 kN. For the failed vessel wall sample (a), the load-deflection curve showed many load drops. At the load of 2.7 kN, the first and largest load drop was observed. This is the ultimate bending load of the wall member. This value is less than a half that of the new specimen. Total AE event counts from the failed vessel wall is less than a quarter of those from the new sample. First AE was detected at the load approximately 50% of the maximum.

Figure 7 shows the separate plots of the cumulative AE counts from Mode-I and Mode-II fractures classified from the polarity distribution of first arrival S_0 waves. It is first noted that the number of Mode-I AEs is three times larger than that from Mode-II AEs for the new specimen (b). In contrast, the Mode-II AEs are one-third larger than Mode-I AEs for the failed vessel wall sample (a). It is also noted that Mode-I AEs from failed vessel wall is smaller than new specimen (b). Less Mode-I AEs from failed vessel wall is considered to be due to prior fiber breakage by environmental stress cracking. Fibers pull out due to weak interfacial strength between the fibers and matrix in the failed vessel wall appears to be the reason for higher Mode-II signals.

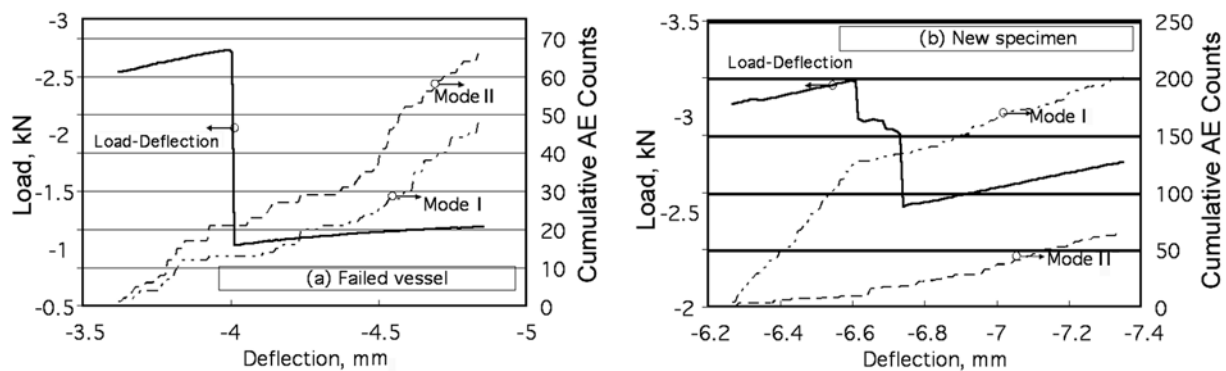


Fig. 7 Cumulative AE numbers identified by fracture mode about fracture of corrosion layer.

Next we measured the sheet velocity (C_e) of the two samples. They were measured as 3.87 km/s for failed vessel specimen (a) and 4.87 km/s for new specimen (b). The velocity is decreased by 1 km/s by the degradation in the failed vessel wall specimen. Thus, the sheet velocity can be used for estimating the degradation. To confirm this on a larger database, we measured the bending strength σ_b and sheet velocities C_e for 23 samples taken from various aged vessels.

Every specimen has different thickness and laminar structures, but their detail is unknown. Figure 8 shows the plot of the bending strength σ_b versus the sheet velocity C_e of these 23 samples. Relationship between C_e and σ_b can be represented by equation (1). Correlation coefficient $R = 0.86$ was obtained.

$$\sigma_b = 171C_e - 477 \quad (1)$$

The data points shown in an ellipse are the results from the failed vessel wall. The threshold of sheet velocity to estimate the critical degradation condition appears to be at 4.00 km/s.

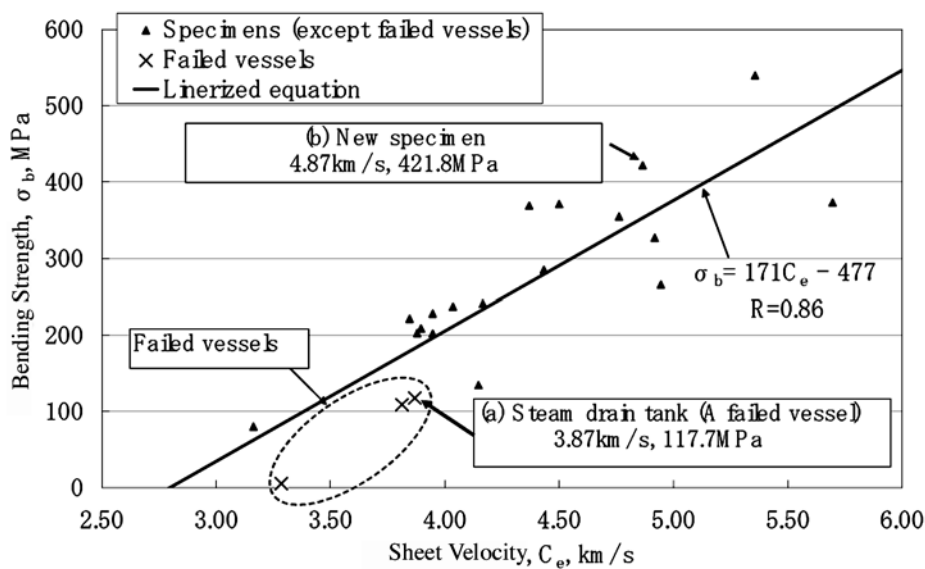


Fig. 8 Sheet velocities C_e vs. bending strengths σ_b of aged GFRP specimens.

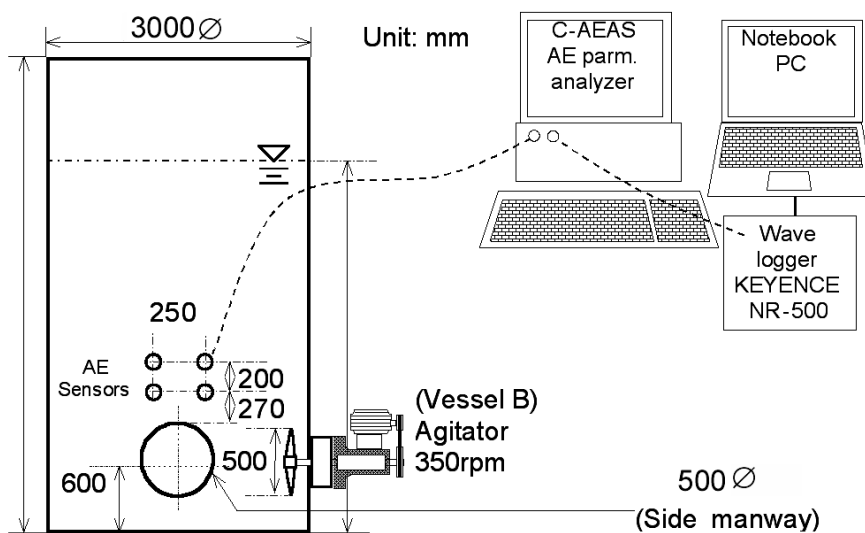


Fig. 9 Experimental arrangements for field AE monitoring.

3. Field Experiment for In-Service Vessels

From laboratory experiment presented above, Lamb-wave AE monitoring and sheet velocity measurements are expected to provide the residual stress or integrity of anti-corrosion layer of GFRP vessels. We monitored AEs of two GFRP vessels in service.

3.1 Test Vessels and Experimental Procedures

Two vessels were evaluated by AE and sheet velocity measurements. Dimensions of these vessels are almost identical. Capacity is 50 m³, with the inner diameters of 3000 mm, and 7900-mm height. Maximum thickness of the wall is 10 mm and the maximum liquid level is 7000 mm. Vessel A has been in service for 22 years. The stored liquid is a by-product of amino acid hydrochloride with pH = 0 at normal temperature. No agitator is installed in this vessel. During AE monitoring testing, the level of liquid is kept at 50 %. AE had been monitored for 3.2 x 10⁵ sec. Vessel B has been in service for 2 years. The stored liquid is a by-product of amino acid hydrochloride with pH = 0 at 60°C. An agitator with a diameter of 450 mm is installed from a side nozzle near the bottom. The agitator speed is 350 rpm. To keep the inside temperature at 60°C, a steam heat exchanger is installed from another side nozzle. During the AE monitoring, the level of liquid is increased from 0% to 84 %. AE had been monitored for 4.9 x 10⁵ sec.

Figure 9 shows the experimental setup for AE monitoring. AE monitoring system (Chiyoda Corp. C-AEAS 4ch monitoring system with total gain 60 dB amplifier and 100 kHz high-pass filter) is used. Four resonant type AE sensors with center frequency of 200 kHz and diameter of 5 mm were mounted on the upper surface of the bottom manway. Thresholds of all channels are set as 512 mV. To record AE waveforms, KEYENCE NR-500/HA-08 Wave Logger with 5 μs sampling interval is connected to signal output terminal of C-AEAS. Threshold of this wave logger is set as 2 V. Attenuation was measured as 1.7 dB/cm. The four AE sensors were mounted at the corners of a 250 mm × 200 mm rectangle.

3.2 Experimental Results

Table 1 shows the results of sheet velocity measurements and AE monitoring for vessel A and B. For vessel A, any degradation such as environmental stress cracking was not observed by visual inspection, in spite of 22 years service. Measured sheet velocity 4.61 km/s is higher than the threshold sheet velocity. No AE was monitored during approximately 4 days of measurement. For vessel B, overlap laminates between side plates and nozzles including the manway become white in color as shown in Fig. 10(a). In addition, pinholes were found over the whole anti-corrosion layer. Their color becomes black due to the permeation of liquid as shown in Fig. 10(b). These defects appear to be produced from shoddy fabrication. These defects were repaired by grinding and laminating before AE monitoring. No significant defects inside the vessel are observed at present. The sheet velocity of vessel B is measured as 3.46 km/s and is lower than that of the failed vessel. We detected a number of AE from this vessel.

Table 1 the results of sheet velocity measurements and AE monitoring for vessel A and B.

	Stored liquor Temperature	Agitator	Condition of corrosion layer	Sheet velocity Ce, km/s	Liquid level	AE
Vessel A	pH 0, Normal	None	No degradation	4.61	50% Constant	None
Vessel B	pH 0, 60°C	φ 500mm, 350 rpm,	Whitening. Pinholes (Already repaired)	3.46	0~84%	100,199,743 Events

Figure 11 shows the change of liquid level (a), AE event rates (b) and AE energy rates (c) of the events whose source location is in the sensors zone. As can be seen from (b), no AE was detected during feed pump operation since a high-pass filter was utilized.



Fig. 10 Inside defects on vessel B. (a) Overlapping of laminate around the side manway. (b) Pinholes with permeation of liquid into the corrosion layer.

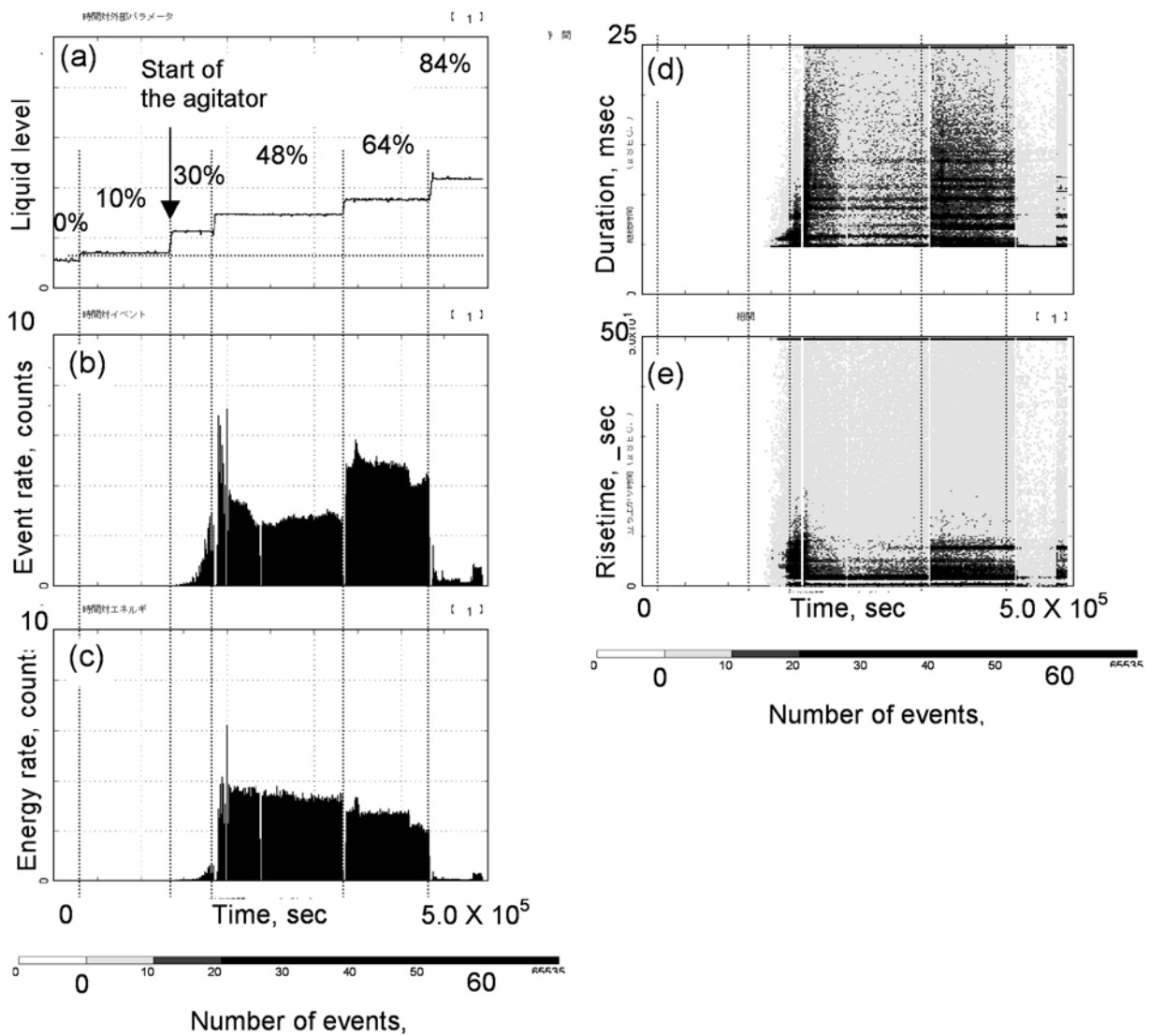
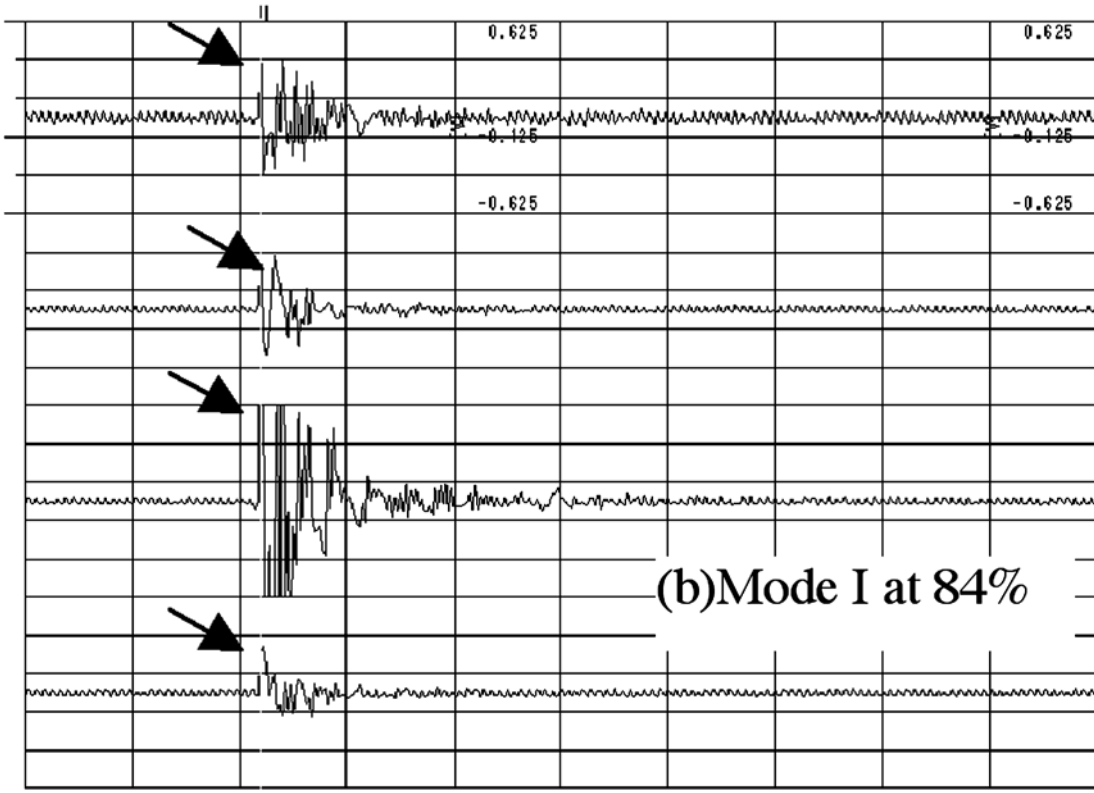
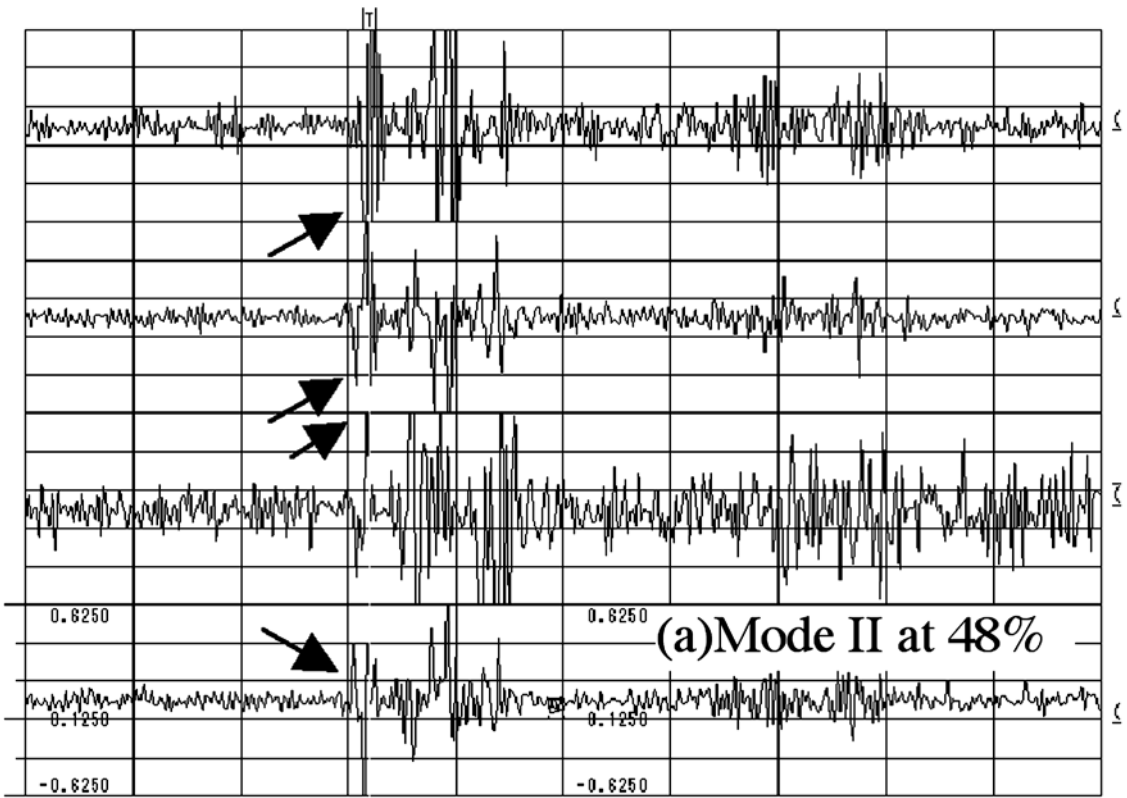


Fig. 11 AE parameters for vessel B monitored by the AE parametric analyzer.

The agitator of vessel B starts when the liquid level is higher than 30%. No AE events were detected when the liquid level was less than 30%. AE events and energy increased after the



0ms

20ms

Fig. 12 Typical AE waves for vessel B monitored. (a) Mode II signals at 48 % liquid level, (b) Mode I signals at 84 % liquid level.

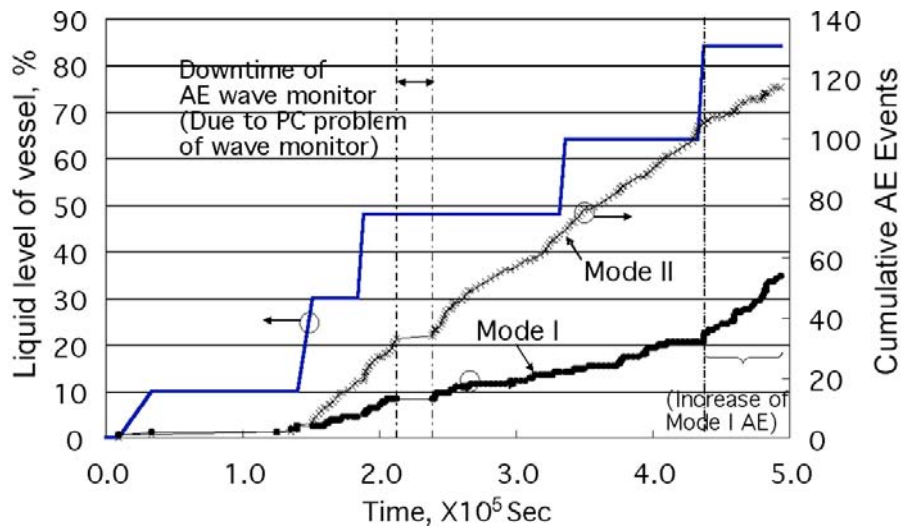


Fig. 13 Cumulative AE event counts for vessel B identified by fracture mode.

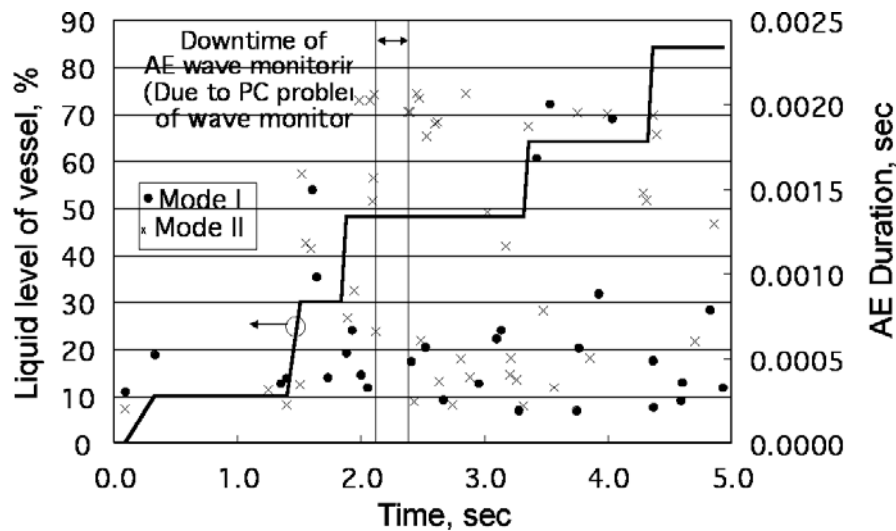


Fig. 14 Level dependence of AE duration identified by fracture modes.

liquid level reached 30% or the agitator was started. AE events and energy, however, decreased with an increase of the liquid level from 30 % to 84 %. As shown in Fig. 11(d) and (e), a large number of AE events with long duration and rise time were monitored during from 48 % to 64% liquid level. Some waveforms of Mode-I and Mode-II, detected at 48% and 84% liquid level respectively, are shown in Fig. 12. Fracture mode was classified from the polarity distribution of first arrival waves. Cumulative AEs from Mode-I and II are shown as a function of time and liquid level in Fig. 13. Waveforms, unfortunately, could not be recorded due to the capacity of the hard disk from 2.1×10^5 s to 2.4×10^5 s. Figure 14 shows effect of liquid level on the duration.

As shown in Figs. 13 and 14, a large number of Mode-II AEs with long duration were detected when the liquid level increased from 48 to 60 %. Mode-I AEs, however, increased after liquid level reached 84 %. Duration of AEs above 84% level became short. Figure 15 shows relation between AE duration and maximum amplitude of Mode-I and -II AEs. Mode-I events are in the area surrounded by dashed curve, but so as most of Mode-II AEs. The details of these results are now under investigation. It is now apparent that AEs are produced from not only the original defects but also agitation accelerated damages.

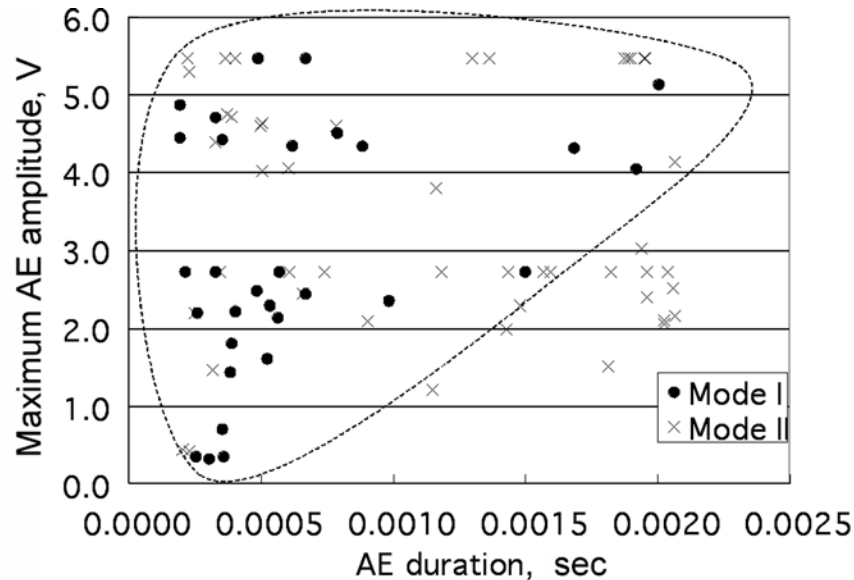


Fig. 15 Correlation between AE duration and AE maximum amplitude identified by fracture mode

4. Conclusion

The integrity of GFRP vessels was evaluated by means of AE monitoring and measurement of sheet velocities. AE monitoring during bending tests of aged and new GFRP plates and from vessels in service are attempted. Results are summarized below.

- (1) The sheet velocity is well correlated to the bending strength of aged members. It is successfully utilized for the diagnosis of the health condition of the GFRP vessels.
- (2) AE from aged GFRP during bending test was much less than that from new sample and emitted more Mode-II signals than Mode-I.
- (3) AE monitoring of new and aged vessel in service was performed. Old but undamaged vessel in service showed high sheet velocity and no AE was detected. Contrary to this, a new vessel with agitator with visible defects, showed low sheet velocity and emitted a number of AE signals. A relation between the sheet velocity and AE activity was observed. The details of these results are under further evaluation.

References

- 1) The Japan reinforced plastics society, FRPS C 002-1989: "Inspection guidelines for glass-fiber reinforced plastic vessels" (In Japanese).
- 2) M. Seale, B. T. Smith, W.H. Prosser: Lamb wave assessment of fatigue and thermal damage in composites, *J. Acoust. Soc. Am*, **103** (5), Pt. 1, 2416-2424, (1998).
- 3) N. Toyama, J. Noda, and T. Okabe: Quantitative damage detection in cross-ply laminates using Lamb wave method, *Composite Science and Technology*, **63** (10), 1473-1479, (2003).
- 4) T. Sato, M. Takemoto and K. Ono: Effect of fracture dynamics in thin plate on the waveform and radiation pattern of the Lamb waves, *Jpn. J. Appl. Phys.* **38** (1999, June) 3193-3200.
- 5) A. Yonezu, T. Ogawa, M. Takemoto: Fracture mechanism of toughened silicon Nitride studied by AE waveform simulation, *J. JSNDI*, **49**-12(2000, Dec.), 847-853.

EVALUATION OF REINFORCEMENT IN DAMAGED RAILWAY CONCRETE PIERS BY MEANS OF ACOUSTIC EMISSION

TOMOKI SHIOTANI¹, YASUHIRO NAKANISHI¹, KEISUKE IWAKI¹,
XIU LUO² and HIROSHI HAYA²

¹Research Inst. of Technology, Tobishima Corp., 5472 Kimagase, Noda, Chiba 270-0222, Japan.

²Railway Technical Research Institute, Hikari, Kokubunji, Tokyo 185-0034, Japan.

Abstract

We focus on a particular case of concrete piers, in which the damaged state and repaired state can both be investigated. In order to know the precise damage condition within the piers, boreholes are excavated, followed by internal wall observation with a borehole camera. Cracks within the retrieved core samples are examined with impregnation of fluorescent epoxy. In AE monitoring, active loads with train passage are utilized to induce AE signals. AE sources are only extracted from the detected raw AE data set using 3D source location. On the basis of the extracted AE events only, the damage quantification is performed along with an analysis of AE peak amplitude distribution. The AE monitoring is additionally performed in the structure after repair works have been completed, and the repair work is evaluated with AE activity. Through the AE monitoring in comparison with several observation techniques, it is concluded that the degree of damage can be quantified with the AE amplitude distribution reasonably well and the effectiveness of repair works can be evaluated with the distribution.

Keywords: Railway structures, Damage quantification, Fluorescent epoxy impregnation, Borehole observation, Reinforcement/Repair, Seismic prospecting

1. Introduction

In Japan the number of civil structures of older than 50 years will rapidly increase from 2005 on, and the maintenance and renewal cost is expected to exceed that of new construction in 2022. Determining the priority of structures to be maintained, for example, the damage assessment for the structures is essential. Thus, the damage quantification of civil structures to assess the structural integrity is in strong demand. In general, crack density as well as crack widths have been treated as damage indices so far; however, those cracks are conventionally evaluated visually and all information on cracks is based on the surface observation only. In evaluating damage degree the method, which can show the inside condition of the structures, is highly sought. An AE testing seems to give a reasonable resolution for such demand since active cracks only generate AE activity under in-service condition. Paying attention to the secondary AE activity, generated from existing cracks, the present authors have studied damage quantification in comparison with actual damage condition. In this paper, the AE testing is both applied for damaged and repaired state of railway concrete piers. Combining a variety of observation results with the findings of AE testing, damage degree as well as repair effect can be assessed.

2. Monitoring Site and Testing Procedure

Three railway concrete-piers, located in Chiba Prefecture, were examined in this study. Figure 1 shows the side view of the piers. The piers were made of plain concrete, have been used for

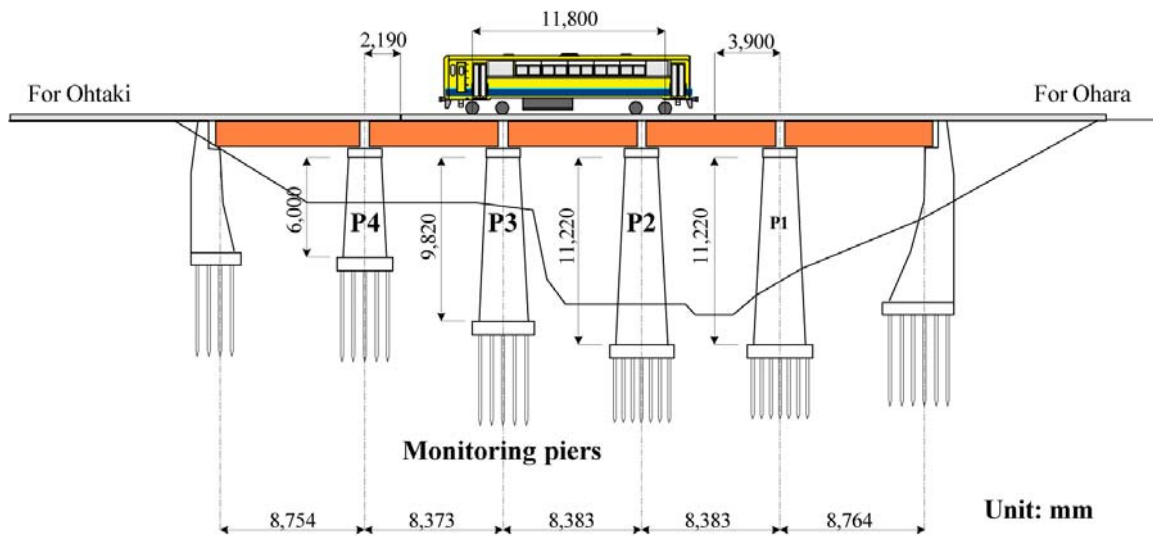


Fig. 1. Railway concrete piers to be tested.

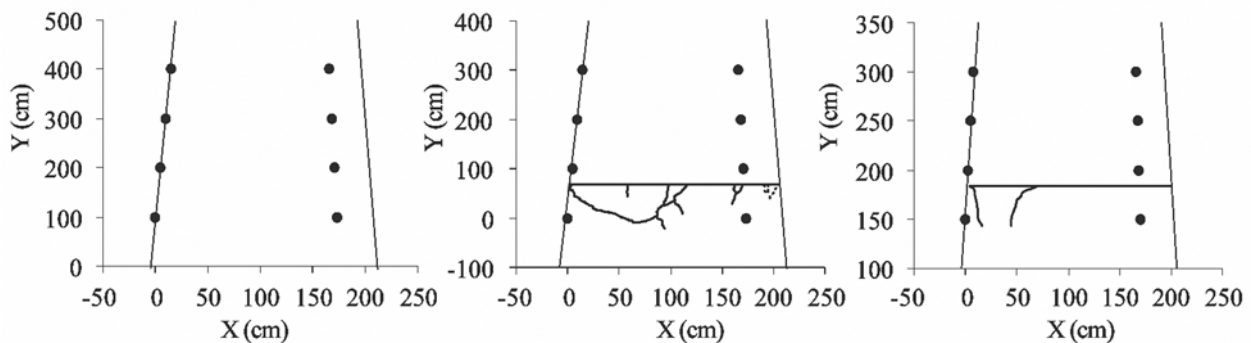


Fig. 2. Crack condition of the pier (from left to right P2, P3 and P4).

over 70 years, and have sustained, due to long-term weathering as well as earthquakes, a variety of damages. Degree of damage, severe (P3), intermediate (P4) and intact (P2), was each estimated by impact vibration tests [1, 2]. Figure 2 shows surface cracks observed. No visible cracks were found in P2, but a serious crack in a horizontal direction, which corresponds to the construction joint of concrete, was found in both P3 and P4. These cracks are generated by a recent earthquake. In P3 especially, a part of concrete was already separated from the stem of pier.

The monitoring protocol is shown in Fig. 3. Acoustic emission was carried out for three piers: two damaged and one intact, followed by seismic prospecting. In order to quantify the internal damage and cracking condition of the pier, three boreholes in a lateral direction and one borehole in a diagonal direction were made only in P3. This pier is employed as a representative of the piers. A borehole CCD camera was subsequently inserted into the boreholes to record the crack distribution precisely. In regard to the core retrieved, not only core observation but also impregnation of fluorescent epoxy [3] was performed. With impregnation of fluorescent epoxy, crack width smaller than 1 μm and air voids can be revealed under ultraviolet light.

3. Repair Works

The damaged piers, P3 and P4, were repaired using an injector specifically designed for repair work (Konishi Co.) under a constant pressure of 0.05-0.10 MPa with a pair of elastomer

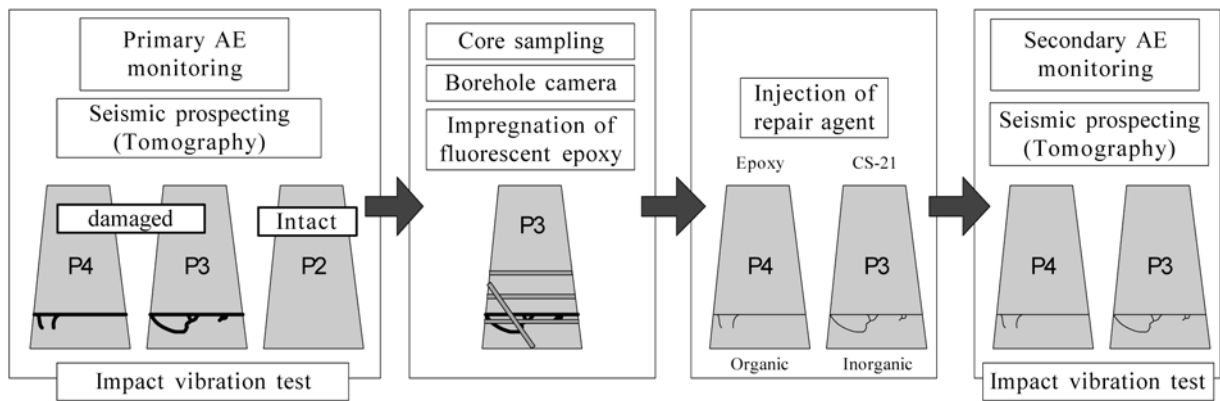


Fig. 3 Protocol of various testing methods.

band. The pressure varied depending on the amount of injection agent. In order to evaluate the repair agent, organic repair agent was used for P4 and inorganic agent with fine cement particles was selected for P3. Before injecting with the repair agent, all visible surface cracks on the piers were sealed with caulking material. Note that additional injection was made only for P3 using the borehole in a diagonal direction, where no pressure was given during the injection.

4. Damage Evaluation

Non-destructive techniques such as AE and seismic prospecting can provide rough locations of damaged/cracked areas; however, the details of crack geometry cannot be deduced through those tests. In contrast, destructive techniques with core retrieved, such as visual and microscopic crack observation, can give better insight in terms of crack distribution/geometry. In practice, however, applications with those destructive techniques are limited only to a part of the structures tested. Furthermore even when the destructive techniques were implemented, the findings are limited only to a partial condition of the structures. Thus, non-destructive techniques have been used as so-called *global health monitoring*, and the results of non-destructive techniques would be subsequently verified by the destructive techniques, which are locally conducted. Therefore, in this study, AE and seismic prospecting are performed in order to monitor the piers globally, whereas a variety of observation is conducted to follow up the findings obtained from the non-destructive techniques.

4.1 Acoustic Emission

12 AE sensors of 60 kHz resonance were placed on the pier surface as shown in Fig. 4. AE sensors were placed at four height levels in a set of three. The vertical spacing between AE sensors was 1 m for P2 and P3, and 0.5 m for P4 pier. AE monitoring was performed when passing trains pass over the bridge and AE signals are induced by the live load due to train passage. These were detected and amplified by 40 dB within the sensor. The AE signals over threshold of 40 dB (100 μ V at the amplifier input) were recorded for their AE parameters as well as AE waveforms with an AE monitoring system (Mistras, Physical Acoustics Corp.). Besides AE activity, acceleration with accelerometers (ASW-2A, max acceleration 2g, Kyowa Dengyo Corp), displacements with π -shaped displacement meters (PI-2-50, Kyowa Electronic Instruments) and strains with strain meters (PL-120, Kyowa Dengyo Corp) were each measured in the piers, where the data was sampled at 1 kHz and stored in a data logger (DRA-101B, Tokyo Sokki Kenkyujo).

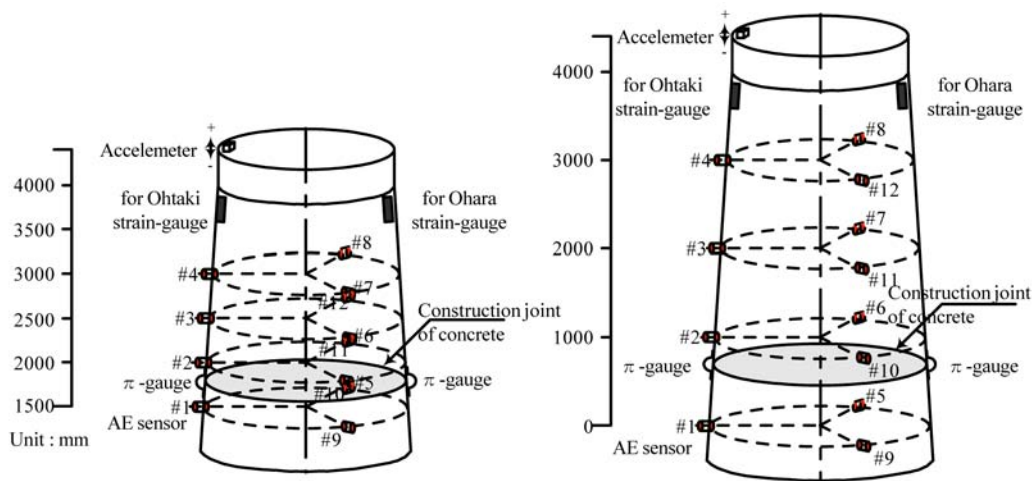


Fig. 4 Arrangement of AE sensors with other deformation-sensors. (left: P4 and right: P3)

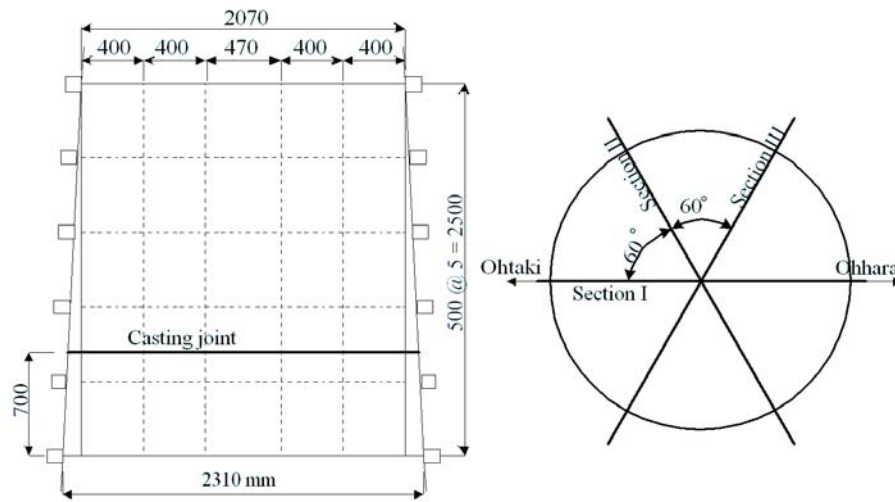


Fig. 5 Arrangement of accelerometers for seismic prospecting in P3. (left: side view, right: plan view)

4.2 Seismic Prospecting

Seismic prospecting was performed only in P3 for three sections as shown in Fig. 5. In each section, 12 piezoelectric accelerometers (SAF51, Fuji Ceramics Corp.), symmetrically arranged were placed onto the pier surface spaced by 50 cm. In the seismic prospecting, elastic waves were excited by impacting a steel ball of 5 cm in diameter. Elastic wave velocities in the section were estimated by means of ray-tracing and simultaneous iteration methods.

4.3 Observation of Boreholes and Sampled Cores

In order to better evaluate the crack condition, four boreholes were excavated as shown in Fig. 6. Three boreholes (No. 1-3) were made in the lateral direction and one (No. 4) in a diagonal direction. In particular, No. 1 and No. 4 boreholes were set so as to penetrate cracks observed on the surface. For the wall of boreholes excavated, optical images were recorded with BIPS (borehole image-processing system [4]). The BIPS enables us to obtain quantitative/qualitative results by projected/unfolded image data, along with valuable color data and oriented and non-disturbed borehole wall images. Besides the borehole image monitoring, cores retrieved were carefully observed visually to quantify the damage.

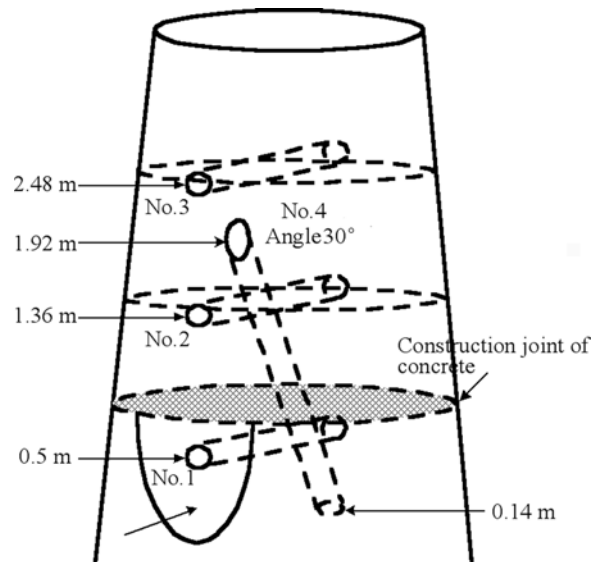


Fig. 6 Arrangement of boreholes in P3.

4.4 Impregnation of Fluorescent Epoxy

It is difficult to distinguish *real cracks* from *all of the observed cracks*, in the study of the damage/cracks of concrete material with various observation techniques. This arises due to the limitation of picture-resolution or disturbance of sampling and therefore it is essential to separate real cracks from apparent cracks. This is possible by means of impregnation technique with fluorescent epoxy. In this study, the bulk cores retrieved were placed into an impregnation chamber filled with fluorescent epoxy, under a reduced pressure (9.3 Pa) using a vacuum pump. By sectioning, cracks distributed within the core can be visualized under the ultraviolet light. Note that sectioning was conducted after the impregnation and no additional cracks are introduced.

5. Results

5.1 Observation in Damaged Condition

As a typical case the developed borehole image of No. 4 borehole is shown in Fig. 7. At 1.4 m depth, a crack smaller than 0.5 mm can be seen. Here, the depth of 1.4 m corresponds to that of the construction joint of concrete. Beside the observed crack and a void at 0.4 m depth, no other crack was found. Core samples retrieved at No. 4 borehole are also shown in the figure at right. A large number of ruptures, especially below 1.6 m depth, were obtained. Cracks corresponding to the depth of ruptures were not observed in the borehole image. These are likely to be produced by the excavation.

In order to study unidentified damage from the above observations, further examination was conducted by means of fluorescent epoxy impregnation. The core samples ranging from 1.1-1.6 m were subjected to the impregnation, and cuts were made at four locations representing 1-4 as shown in Fig. 7. Results are given in Fig. 8; one side of the cross-section at No. 1 and No. 4 are both shown. Under ultraviolet light, No. 1 section includes voids of large area. At No. 4, which is located close to the casting joint, a distinct macro-crack and branched cracks were detected. These findings imply that even for the bulk core/un-ruptured core, large scale of cracks and large area of voids existed, so that it is most likely that these critical cracks can readily generate AE activity due to a live load.

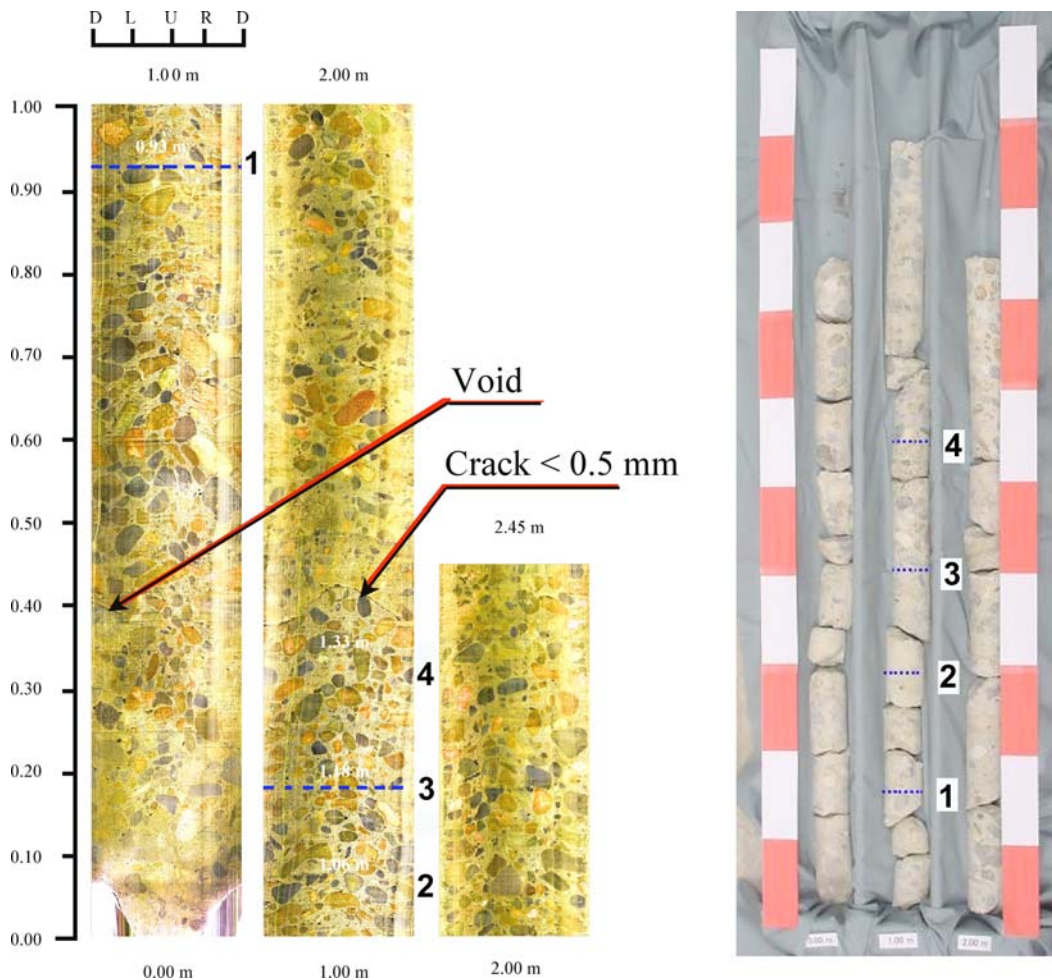


Fig. 7 Developed borehole image (left) and core retrieved (right).

5.2 Acoustic Emission

In the damaged condition, AE sources in three-dimension are shown in Fig. 9, where the diameter of AE source reflects the average of peak amplitude of AE hits contributing to the AE source/event. No significant AE sources were obtained in P2. In contrast to P2, substantial AE sources both in P3 and P4 were found, not only along the existing joints but within the whole monitoring area. These AE activities appear to agree well to the damage condition already evaluated from impact vibration tests and damage observation. Paying attention to the scale of AE sources in P3 and P4, AE sources ranging from small to large average peak amplitude were observed in P3, while in P4 such differences in peak amplitude among AE sources were small.

The same 3D sources after repair are shown in Fig. 10. Comparing to the damaged condition (see Fig. 9), generally, no significant decrease of the scale of AE sources as well as the number of AE sources could be found in repaired piers. In P3, however, not so many large scale sources were found in repaired condition. With regard to the average of peak amplitude, they were 39.24 (39.82) and 38.29 (38.63) in P3 and P4, respectively, where the value in parentheses denotes the average peak amplitude in the damaged condition (Fig. 9). Thus, notable change/improvement due to repair could not be obtained also from the average of peak amplitude.

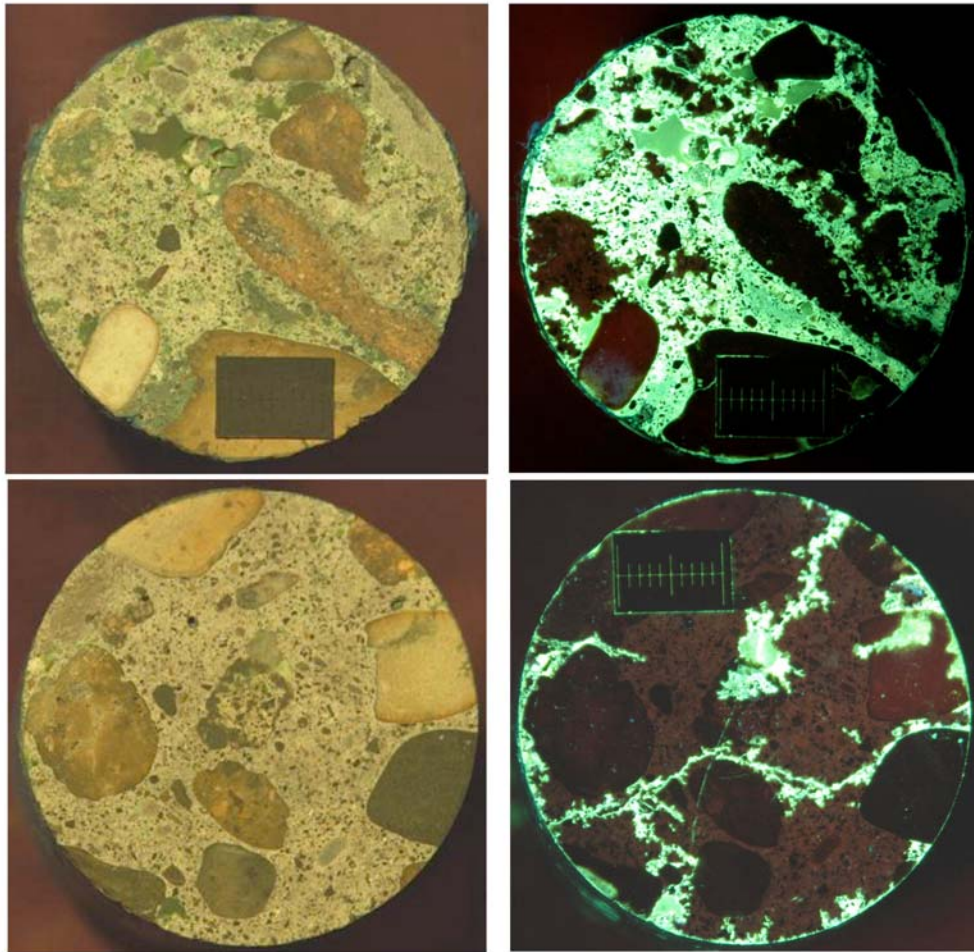


Fig. 8 Sections after the impregnation at No. 1 (top left) and No. 4 (bottom left), and the corresponding images under ultraviolet light. (No. 1: top right, No. 4: bottom right)

5.3 Seismic Prospecting

A typical distribution of elastic wave velocity on section II is shown in Figure 11 together with 3D AE sources projected to the section II. Comparison is made between damaged and repaired condition, where it is noted that the repair agent was poured into the borehole No. 4; i.e., no repair was performed in the range higher than 2.0 m since no pressure was applied when pouring. No improvement was observed at position higher than 2.0 m, which proves the accuracy of employed seismic prospecting. In the damaged condition, low velocity range of lower than 3000 m/s can be seen along the casting joint; however, after the repair work the elastic wave velocity in such low range becomes higher, suggesting the improvement of mechanical property in the pier. Effectiveness of repair work was thus verified with seismic prospecting. Note that the range of lower velocity could be found elsewhere except for the construction joint of concrete.

6. Discussion

6.1 Damage Condition Evaluated by Several Techniques

Except for P2, which was in the intact state, the predominantly evolved crack along the casting joint were found both in P3 and P4. These cracks could also be observed with borehole

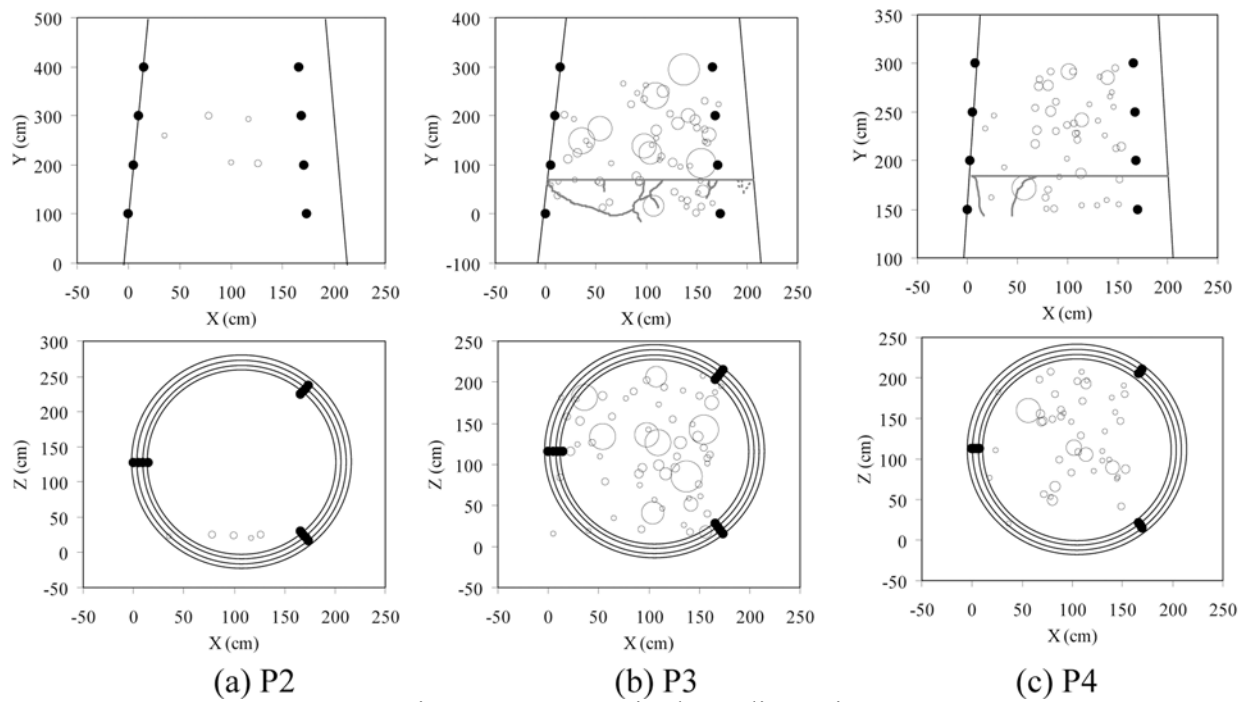


Fig. 9 AE sources in three-dimension.

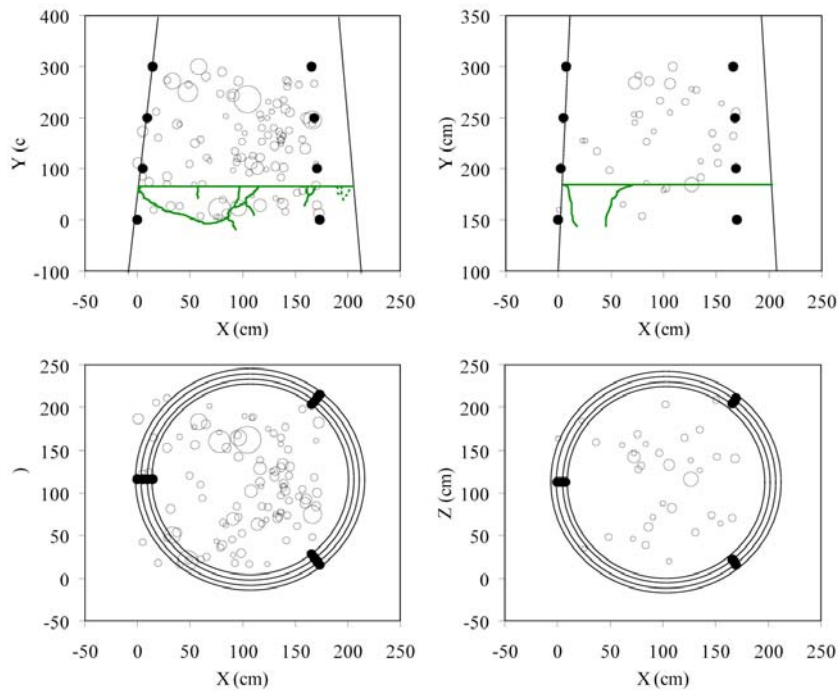


Fig. 10 AE sources after repair. (left: P3, right: P4)

observations. AE sources show, however, not only along the joint but in the range above the joint active AE sources were present. As shown in the core samples, many ruptures of core sample were obtained, implying that the numerous cracks obtained by the boring were generated when the pier was subjected to the torsion force due to the boring; i.e., the critical state of cracks as to grow macroscopic cracks with a slight stress had already existed within the pier. This fact was further verified by the observation results with fluorescent epoxy impregnation. Thus these findings lead to a conclusion that critical state of cracks had already been distributed within the

pier, although these could not be evaluated with conventional observations like borehole camera and unaided eyes, but could only be evaluated by AE activity.

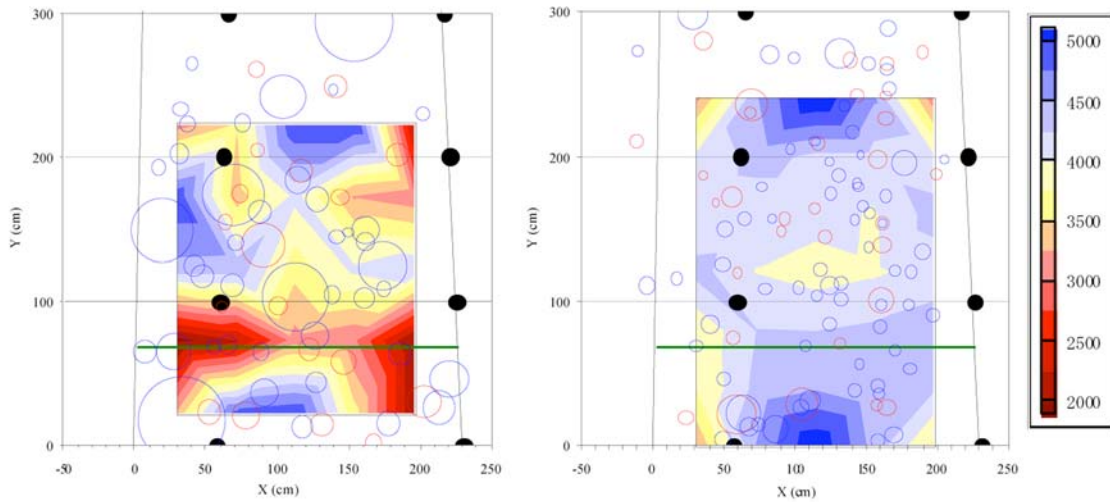


Fig. 11 Elastic wave velocities estimated by seismic prospecting in P3. (left: before repair, right: repaired)

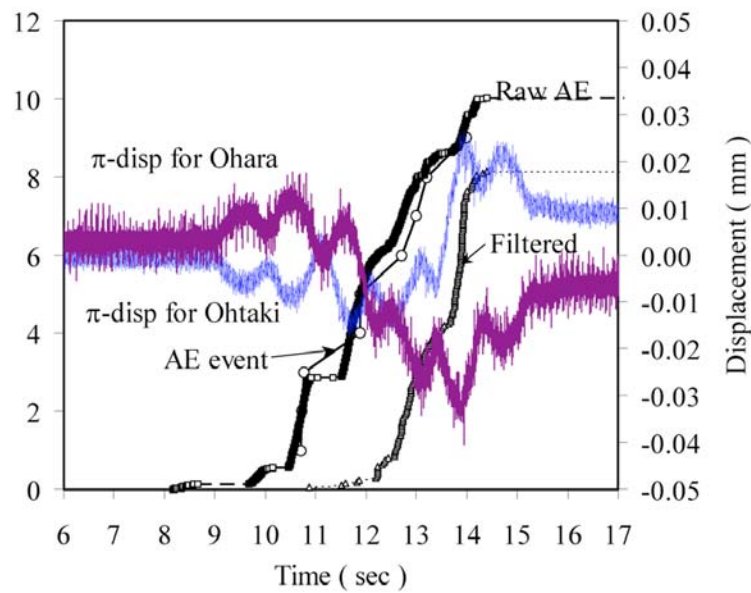


Fig. 12 Symmetric behavior of two π -shaped displacement meters along with AE activity due to train passage.

6.2 Quantification of Damage with AE Technique

In order to evaluate structural integrity, Calm ratio and RTRI have been proposed on the basis of train-induced AE activity, and they were successfully applied for damage evaluation of railway substructures [see 5]. When obtaining those two indices, structural behavior such as deformation is essentially incorporated with AE activity; i.e., a loading process as well as an unloading process should be defined when a train passes. As shown in Fig. 12, however, since the macroscopic crack had already existed in a horizontal direction along the casting joint and the pier showed rocking when a train passes. A variety of attempts to determine the processes were made, but no indices for the structures could be developed. AE amplitude distribution gives a unique

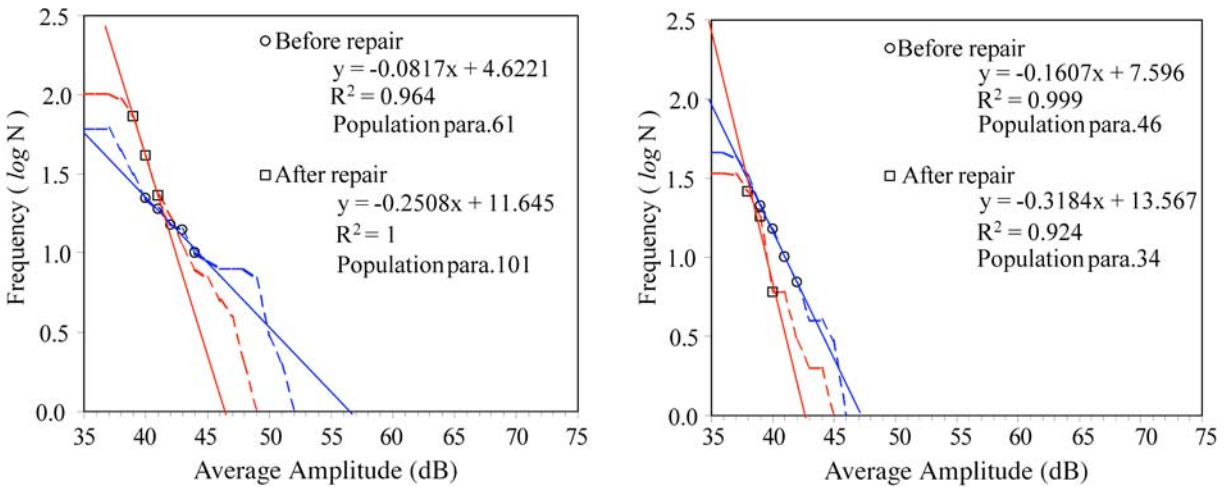


Fig. 13 Amplitude distributions in P3 (left) and P4 (right). The average amplitude of a set of AE hits contributing to an AE event is used to determine the distribution.

trend corresponding to the degree of damage and is used to quantify the damage. Cumulative amplitude distributions are shown in Fig. 13. To quantify the distribution, a gradient of the curve is extracted on the basis of improved *b*-value analysis [6, 7]. Note when comparing a seismic *b*-value, the improved *b*-value should be multiplied by a coefficient of 20.

As a typical result, the cumulative amplitude distribution in P3 is shown as in Fig. 13. In the state of *before repair*, or damaged condition, more AE events of large amplitude are generated, while in the *after repair* state, more small-amplitude events are generated. Such a difference of distribution can be seen in improved *b*-value; i.e., 0.0817 in the damaged condition and 0.2508 in the repaired condition. This difference is distinct enough to separate the two conditions. In Fig. 14, the *Ib*-values of the three piers are summarized in the left side along with the other results from I-site and K-site. In the present piers of P2, P3 and P4, damage recovery or repair effect can be illustrated by the variation of *Ib*-value. Considering other results, the degree of damage can be successfully classified with *Ib*-value;

serious damage	<i>Ib</i> -value of 0 - 0.1,
intermediate damage	<i>Ib</i> -value of 0.1 - 0.2, and
intact or minor damage	<i>Ib</i> -value of > 0.2.

Accordingly, damage quantification was successfully carried out using the improved *b*-value analysis. The improved *b*-value analysis has already been applied to several railway structures and was successful in quantifying the degree of damage.

7. Conclusions

Damaged railway concrete piers before and after repair were investigated with AE technique. Details of damage condition were also studied with several observation techniques. Through those studies following findings are obtained:

1. AE activity monitoring reflects the actual damage of structures. Using improved *b*-value, damage quantification is possible. However, more data with a variety of damage should be systematically collected and evaluated.

2. It is difficult to quantify the damage only from visual observations and from borehole wall observation. Critical damage assessment could only be done by means of fluorescent epoxy impregnation, but this is impractical in field.
3. Non-destructive techniques as AE and seismic prospecting showed reasonable results corresponding to the damage obtained from all observations. Seismic prospecting can give the effectiveness of repair works as an increase of the wave velocity. AE results failed to show substantial changes in terms of the number of AE events or the scale of amplitude. However, improved b -value demonstrated the possibility to quantify the damage.

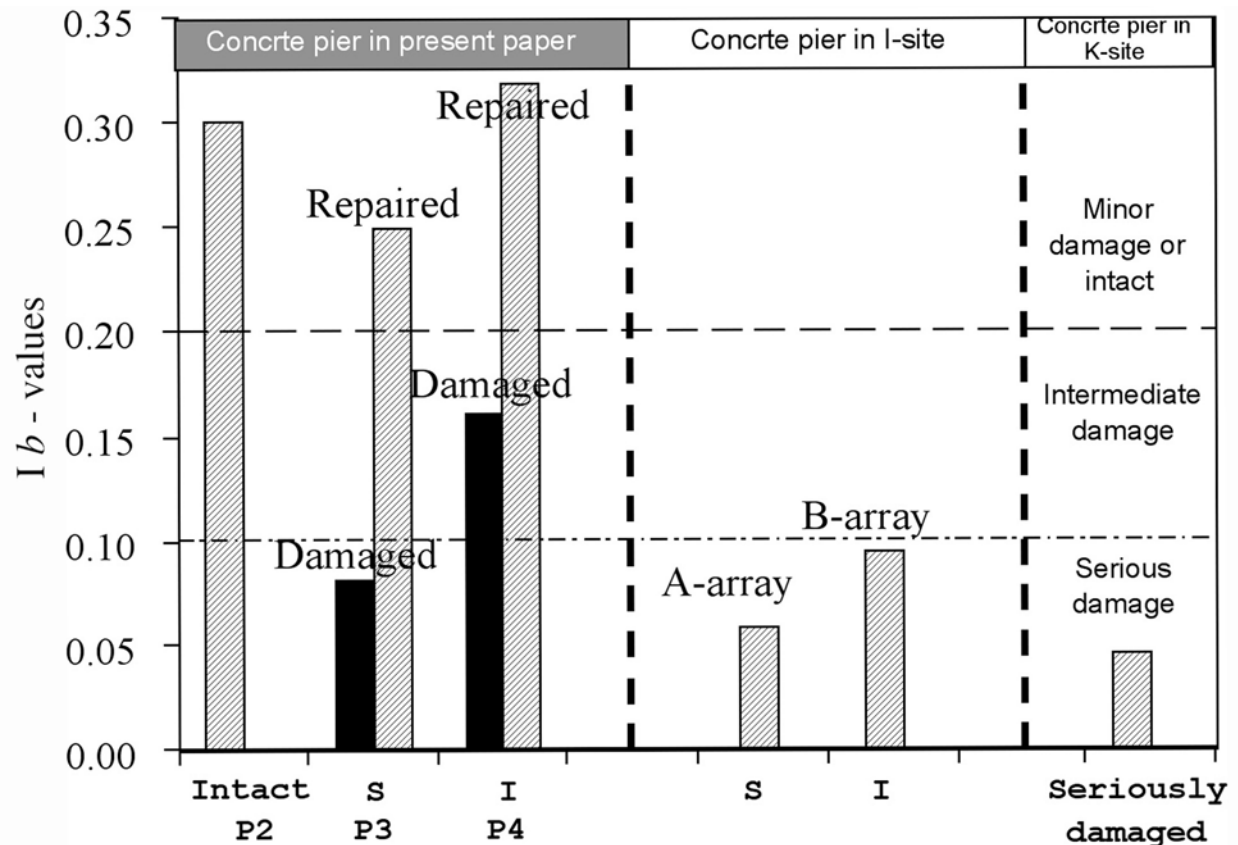


Fig. 14 Variations of improved b -value from various conditions of concrete piers.

References

- 1) Y. Kikuchi, A. Nishimura and M. Yamada, Investigation on the method of judging of integrity for the foundation of the bridge, The Proceeding of the 43rd JSCE Annual Meeting, Japan Society of Civil Engineering, pp. 250-251, 1988, in Japanese
- 2) A. Nishimura and H. Haya, Assessment of the structural integrity of bridge foundation by the impact vibration test, Proceedings of GEO-COAST '91, pp. 719-724, 1991.
- 3) T. Shiotani, J. Bisschop, J.G.M. van Mier, Drying Shrinkage Microcrack Measurements in Cementitious Composites Using AE and FLM, Society of Experimental Mechanics, Proceedings of the 2002 SEM Annual Conference & Exposition on Experimental and Applied Mechanics, Paper Number: 202 (CD-ROM), 2002.

- 4) T. Yasuda, S. Taniguchi, S. Kamewada and G. Okano, Crack evaluation system for analyzing the condition of superannuated tunnel, Proceedings of the international symposium on Fracture and Jointed Rock Masses, pp249-255, 1992.
- 5) X. Luo, H. Haya, T. Inaba, T. Shiotani and Y. Nakanishi, Damage evaluation of railway structures by using train-induced AE, Construction and Building Material, **18**, 215-223, 2004.
- 6) T. Shiotani, K. Fujii, T. Aoki and K. Amou, Evaluation of progressive failure using AE sources and improved b -value on slope model tests, *Progress in AE VII*, JSNDI, pp. 529-534, 1999.
- 7) T. Shiotani and Z. Li, S. Yuyama and M. Ohtsu, Application of the AE improved b -value to quantitative evaluation of fracture process in concrete-materials, Journal of Acoustic Emission, **19**, 118-133, 2001.
- 8) T. Shiotani, Y. Nakanishi, X. Luo and H. Haya, Damage assessment in railway sub-structures deteriorated using AE technique, 26th European Conference on Acoustic Emission Testing (EWGAE 2004), Vol. 1, p. 255.
- 9) T. Shiotani, X. Luo, H. Haya and M. Ohtsu, Damage quantification for concrete structures by improved b -value analysis of AE, 11th International Conference on Fracture (ICF11), CD-ROM (2005).

WATER-LEAK EVALUATION OF EXISTING PIPELINE BY ACOUSTIC EMISSION

TETSUYA SUZUKI, YUKIFUMI IKEDA, YUICHI TOMODA and MASAYASU OHTSU
Kumamoto University, 2-39-1 Kurokami, Kumamoto, Japan.

Abstract

Degradation of existing pipeline systems often leads to water leakage. In most cases, non-destructive tests, such as a water leak detection method and a ground probing radar method are applied to identify defects in pipeline. Although these methods are effective for surveying limited sections, further technical improvement is necessary for wide-range and long-term measurements for maintenance and management of the existing pipelines. In this study, an existing pipeline system is examined, applying AE method. It is found that AE behaviors in the pipeline are dependent on the degree of damage or water leakage, and can be evaluated by AE parameter analysis. AE activity in water-leak section is identified as tensile-type AE events. A relation between AE rate and the water leak is analyzed by the rate process theory and allows quantitative damage evaluation of water-leak in pipeline.

Keywords: Damaged pipeline, Water leak, AE parameter analysis, Rate-process theory

1. Introduction

In recent years, the maintenance for lifeline infrastructure has become a target of intensive research. The necessity for damage monitoring is growing, because it is difficult to conduct visual observation in buried pipeline systems.

Deterioration of existing pipeline systems often results in overt-through water leaks (Fig. 1) or inner pressure decrease. Conventionally, using a leak detection method or a leak survey method, the leakage has been identified. Damage to the pipelines results from not only the deterioration, but also water-hammer pressure. Wide-range and long-term measurements are needed for maintenance. Though the conventional methods are effective for intensive survey on a limited section, they are not effective for global and long-term measurements. In order to develop a new monitoring technique, acoustic emission (AE) method is applied to on-site measurement of pipelines. Based on a parameter analysis of AE results, water leaks are evaluated. AE activity is quantified by the rate process theory. Application of AE method to the detection of leakage and the evaluation of damage in the existing pipeline is studied.

2. AE Monitoring of Water Leakage

In this study, AE sensors detected AE generated due to water leakage in a pipeline. Based on AE characteristics, the degree of damage is evaluated. Compared to the conventional methods, AE method is promising, because results are not affected by the degree of deterioration in an existing pipeline. AE monitoring was conducted at Kasanohara main channel located in Kanoya, Kagoshima, Japan. The pipeline system was constructed 36 years ago. Water leak accidents occurred 92 times (2.6 leaks per year on average) from 1967 to 2002. 70% of water leaks occurred at joint sections.



Fig. 1 Water leakage in a joint section.

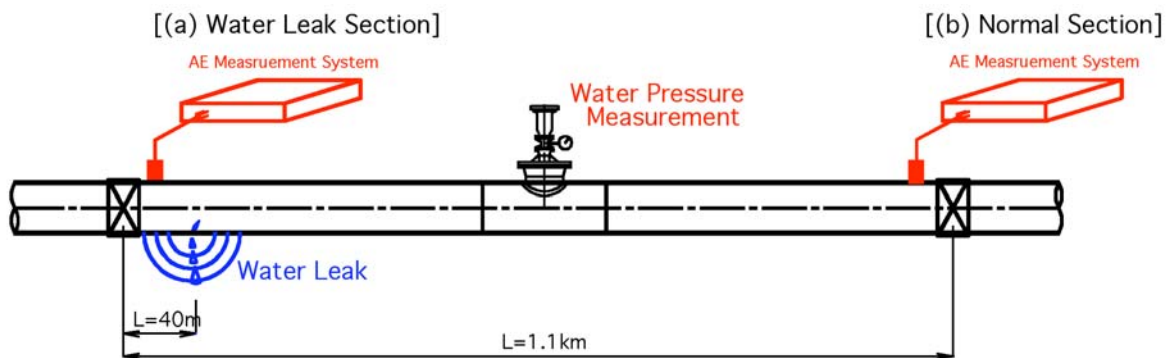


Fig. 2 Outline of AE Measurement on pipeline section.

A monitoring section of the length $L = 1.1$ km is illustrated in Fig. 2, consisting of a PC pipe with a diameter of 500 mm. Water leak was detected around a water-leak section in the figure. It is confirmed that a water leak is about $1.14 \text{ m}^3/\text{d} \cdot \text{cm} \cdot \text{km}$, which is ten times as much as the amount of allowable water leak in Japan ($0.1 \sim 0.15 \text{ m}^3/\text{d} \cdot \text{cm} \cdot \text{km}$) for a new PC pipeline [1]. Normal section in the figure corresponds to non-damaged line.

Three AE sensors were set on an exposed pipe at an existing manhole. Outline of the measurement system is illustrated in Fig. 3. DISP-AE system (manufactured by PAC) was employed. The duration of measurement was 30 minutes. AE hits were detected by using AE sensor (resonance frequency: approx. 150 kHz). To count the number of AE hits, the threshold level was set to 38 dB, with a total gain of 60 dB. AE measurement was conducted with a 3-channel system.

3. AE Parameter Analysis

AE behavior of a pipeline with leakage was associated with inner water pressure. AE hits were analyzed by using parameters of RA value (rise time/peak amplitude) and the average

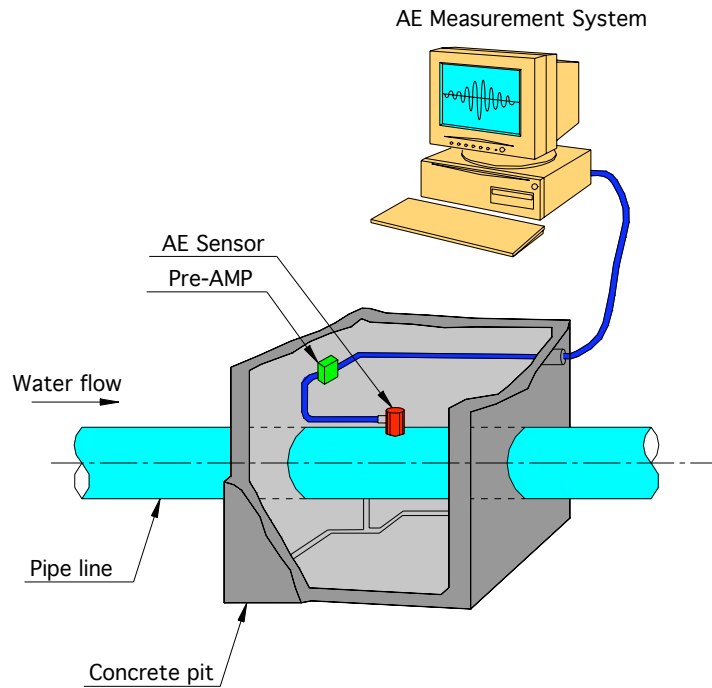


Fig. 3 AE measurement system in pipeline.

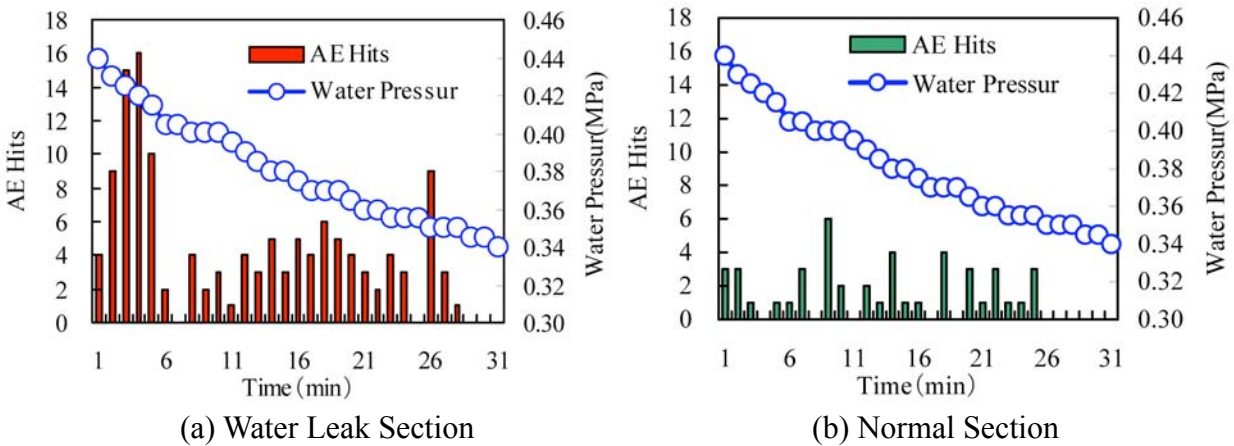


Fig. 4 Relations between AE hits and inner water pressure.

frequency (AE ring down counts/duration. [2] Inner water pressure was measured as 0.44 MPa under normal operation. AE monitoring was conducted after a gate valve had been closed. The inner water pressure dropped by 23% in 30 minutes, from 0.44 MPa to 0.34 MPa. Relations between AE hits and inner water pressure are shown in Fig. 4 (a) and (b).

At the leaked section, AE activity became stable about ten minutes after the inner water pressure started to decrease. It appears that high AE activity at the beginning is associated with water leak, caused by a high inner water pressure (Fig. 4(a)). On the other hand, at the normal section, AE activity is steady regardless of inner water pressure (Fig. 4(b)). Similar results were reported elsewhere in buried pipeline. [3]

AE generating behavior of the leaked section was compared with that of the normal section in terms of RA value and the average frequency. Results are shown in Fig. 5. Tensile-type AE events are mostly observed at the leak section, whereas shear-type AE events are active at the

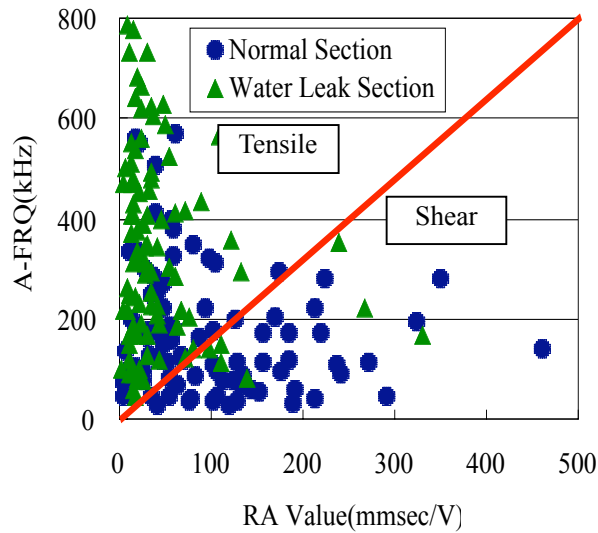


Fig. 5 Relations between A-FRQ and RA value.

normal section. It is expected that tensile-type AE events are generated by water leakage from the pipeline system as well as tension cracks of cover-coat mortar, while shear-type AE events are generated by the flow of water.

AE generating behavior observed in the existing pipeline system is closely related to inner water pressure. When water leakage occurs under high inner-water pressure, a large amount of tensile-type AE events were observed. Thus, for the evaluation of leakage and damage of existing pipeline systems, AE parameter analysis is effective.

4. Quantitative Evaluation by AE Rate-Process Analysis

The rate process theory has been applied to quantify AE generating behavior. AE activity in the existing pipeline with inner water pressure corresponds to the generation of micro-cracks and water leakage in pipelines. AE activities seem to increase in accelerated manner with variation in the inner water pressure. This process can be subject to stochastic process. (4)

Equation 1 represents the number of AE hits dN with an increment of inner water pressure from P to $P+dP$, where the total number of AE events is N and the rate of AE activity at the inner water pressure level P is $f(P)$:

$$f(P)dP = \frac{dN}{N} \quad (1)$$

The rates $f(P)$ estimated in AE rate-process analysis are shown in Fig. 6. The inner water pressure ratio, P/P_{max} , refers to the ratio of the inner water pressure P to the maximum inner-water pressure P_{max} . Results show the rate of AE activity under high inner water pressure is higher than that of the normal section. In the normal section, the rate of AE activity $f(P)$ remains always less than 0.04, without correlating to the decrease in the inner water pressure.

These results confirm that AE generating behavior in existing pipeline systems can be quantified by the rate process theory. Thus, it is possible to quantify the degree of damage in pipelines under different inner water pressures.

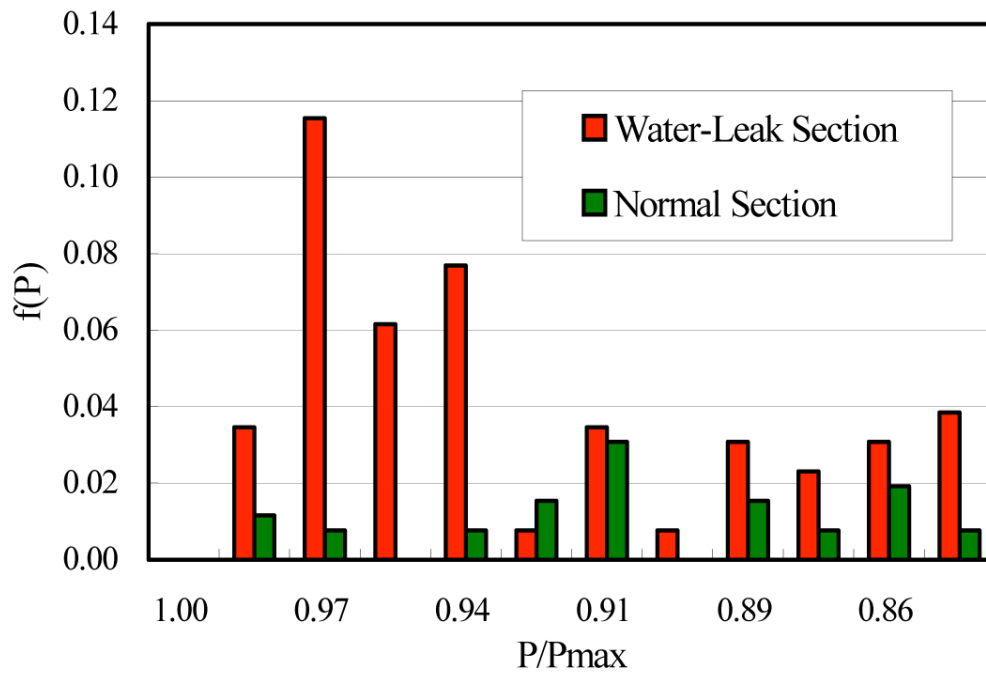


Fig. 6 AE rate-process analysis.

5. Conclusion

Leakage and damage of deteriorated pipeline are studied by AE method. AE activity is closely related with water leakage or damage of pipeline, and is analyzed by AE parameter analysis and the rate process theory. Thus, the degree of damage in existing pipeline is quantitatively evaluated. Conclusions are summarized, as follow:

- (1) AE generating behavior in pipeline with water leakage can be discriminated by applying AE parameter analysis.
- (2) The tensile-type AE hits are actively observed due to water leakage.
- (3) Quantitative damage evaluation of pipeline with water leakage can be performed by AE rate-process analysis.

References

- 1) N. Nawa, K. Sonoda, H. Iwata and T. Suzuki (2002), "Survey and Evaluation Method for Deteriorated Agricultural Pipeline Function", JSIDRE, **70** (12) 31-36.
- 2) JSCM-IIIB-5706 (2003), "Monitoring method for active cracks in concrete by acoustic emission".
- 3) S.J. Vahaviolos, R.K. Miller, D.J. Watts, V.V. Shemyakin and S.A. Strizkov (2001), "Detection and Location of Cracks and Leaks in Buried Pipelines using Acoustic Emission", J. Acoustic Emission, **19**, 172-183.
- 4) T. Suzuki, H. Watanabe and M. Ohtsu (2002), "Damage Evaluation in Concrete Using Acoustic Emission Method", *Proc. The 6th Far-East Conference on Non-Destructive Testing*, JSNDI, Tokyo, pp. 111-116.

ACOUSTIC EMISSION FOR FATIGUE DAMAGE DETECTION OF STAINLESS STEEL BELLOWS

KOJI KAGAYAMA, AKIO YONEZU, HIDEO CHO, TAKESHI OGAWA,
and MIKIO TAKEMOTO

Department of Mechanical Engineering, Aoyama Gakuin University,
Fuchinobe, Sagamihara, Kanagawa 229-8558, Japan

Abstract

We utilized acoustic emission technique to monitor crack progression of a formed 300 mm long stainless steel bellows subjected to cyclic axial loading with vibration amplitude of 15 mm. AEs from fatigue cracks in 0.12 mm thick bellow with 10 convolutions were monitored by three resonant type AE sensors mounted on the flange weld to the bellow ends. The bellows failed at 26770 cycles after producing three circumferential cracks near the upper jig and lower flange. First AE was detected at 21782 cycles. This timing was 1500 cycles earlier than the first circumferential crack near the upper jig observed by video camera. AE count increased after 24000 cycles at which large third circumferential cracks were produced near the lower flange. Wavelet analysis of AE signals showed largest amplitude at approximately 180 kHz at which the group velocity is measured as 3100 m/s. Three cracks in the axial direction were correctly located using this group velocity.

Keywords: Bellows, Fatigue crack, Wavelet analysis

1. Introduction

Bellows is a convoluted shell consisting of a series of toroidal shells, usually connected with annular plates called sidewalls [1, 2]. It provides additional flexibility for shell structures such as piping and heat exchanger. For these applications, fatigue fracture is important problem because vibration is inevitable. The critical fatigue damage is a crack initiation which allows fluid leakage. Therefore, fatigue crack initiation must be accurately monitored in the fatigue critical application.

In this study we evaluated fatigue strength of the bellows using AE technique. Crack initiation and propagation were successfully monitored by cylindrical wave AE [3, 4]. Source location estimated by quantitative analysis of cylindrical wave AE agreed well with the fatigue cracks.

2. Wave Propagation Characteristic and Source Location Method

Estimation of AE source location on the bellows is much more difficult due to complex shape of the bellows. We first studied propagation characteristics of elastic wave in the axial direction of the bellows. Shown in Fig. 1 is shape and size of the bellows tested. In the fatigue test, we monitored AEs by four AE sensors mounted on the one-end flange. For the source location in axial direction, we first studied cylindrical wave of the bellows. We excited elastic waves by lead breaking on the crown top of the bellows and monitored by two resonant-type AE sensors (PAC, Type PICO, center frequency 450 kHz) mounted on the crown top in Fig. 1.

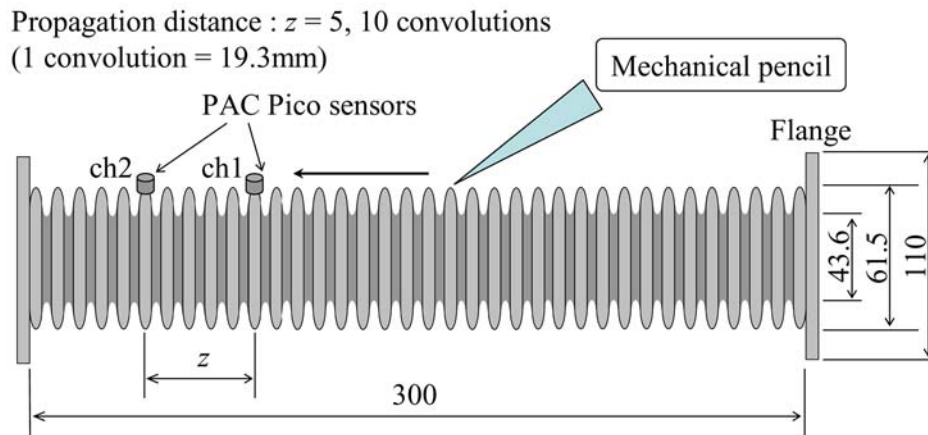


Fig. 1 Experimental setup and shape and size of bellows [mm].

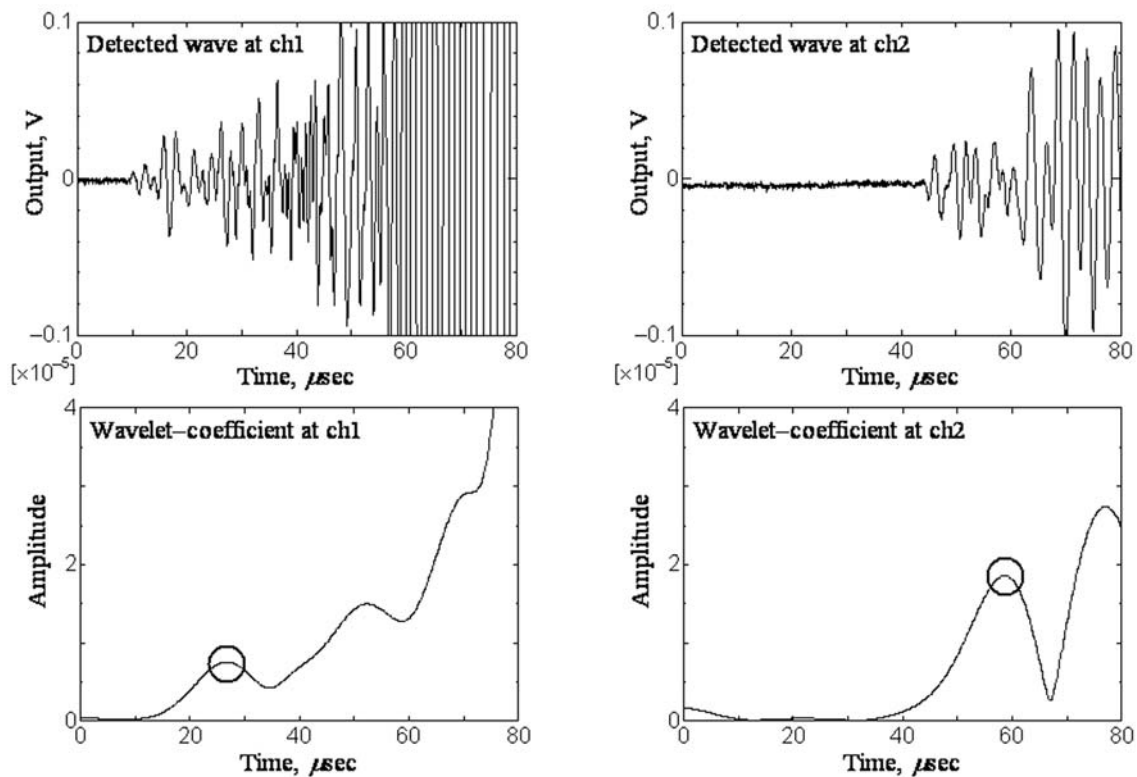


Fig. 2 Waveform (the upper) and wavelet coefficient of ch. 1 and ch. 2 at 180 kHz.

Distance of channel 1 and 2 sensors was changed from 5 convolutions (total zigzag propagation distance along 5 convolutions: 96.5 mm) to 10 convolutions (193 mm). Figure 2 shows typical AE signals from ch. 1 and ch. 2 sensors and their time transient of wavelet coefficients at 180 kHz. We utilized the first arrival component for the location analysis.

Group velocity of the first arrive wave was measured by the time differences of first peaks and determined as 3100 m/s. Figure 3 shows overlapping of theoretical velocity dispersion curves of $L(0, 1)$, $F(1, 1)$, $F(1, 2)$ and $F(1, 3)$ of a 52.6-mm diameter pipe of 0.12-mm wall thickness and the wavelet contour map of the wave measured for the bellows. Here the diameter 53 mm corresponds to an average diameter of inner and outer diameters of the bellows. The measured velocity of 3100 m/s at 180 kHz appears to coincide the group velocity

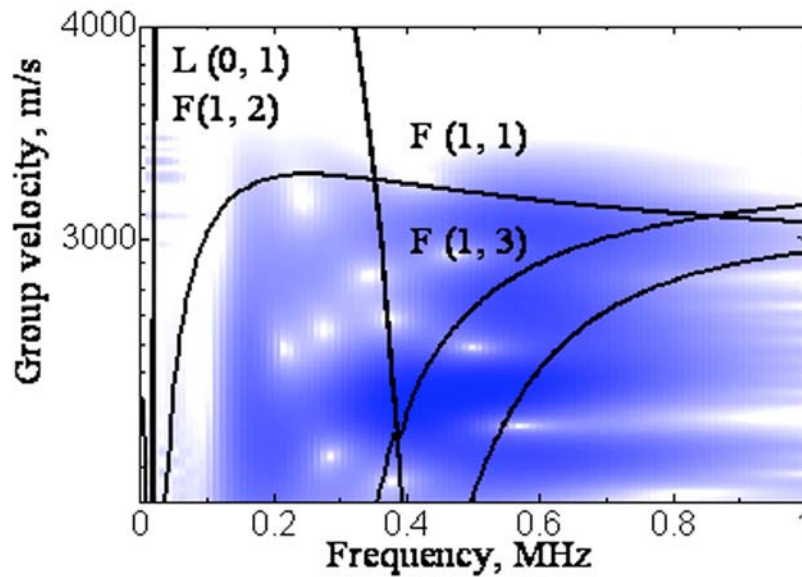


Fig. 3 Group velocity dispersion curves.

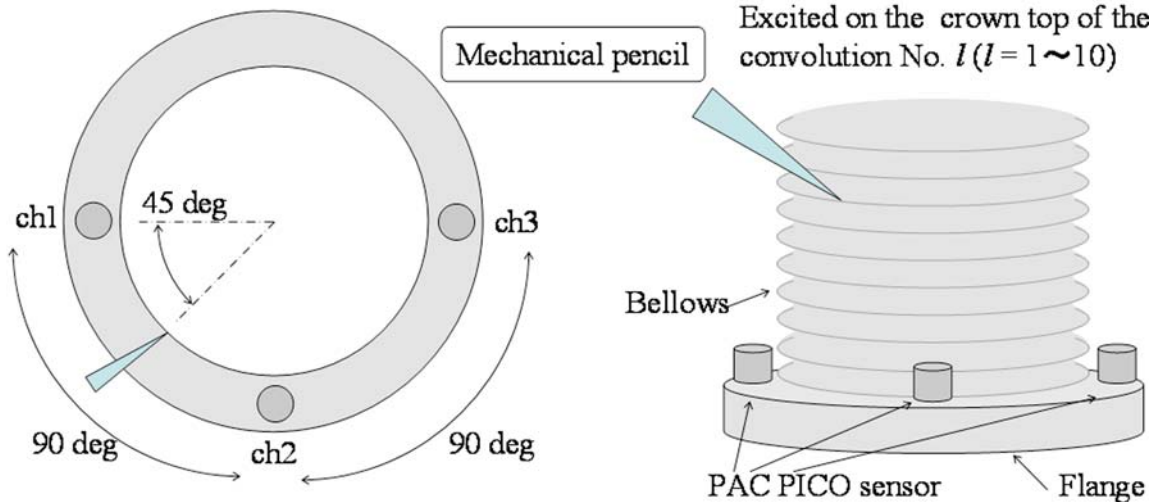


Fig.4 Setup for estimation for circumferential source location.

of F(1,1) mode. Source location in the axial direction was then estimated using the group velocity 3100 m/s and the equivalent diameter of 53 mm.

Next we attempted to determine the source location in the circumferential direction. Figure 4 shows an experimental setup for location determination. We excited elastic wave by breaking a pencil lead at the crown top of several convolutions from the flange. Here the convolution number l was changed from 1 to 10. AEs were monitored by three AE sensors (ch. 1 to ch. 3) mounted on the flange at 90° interval. Figure 5 shows AE signals from convolution of 1, together with their time transient of wavelet coefficient at 180 kHz. The sensors on the flange detects first packet of the wave with large enough amplitude for the source location. Then we estimated the circumferential locations using the arrival time difference of the first 180 kHz component and the group velocity of 3100 m/s. Figure 6 shows location results for $l = 1 \sim 10$. There observed a fairly good agreement between the given and estimated sources.

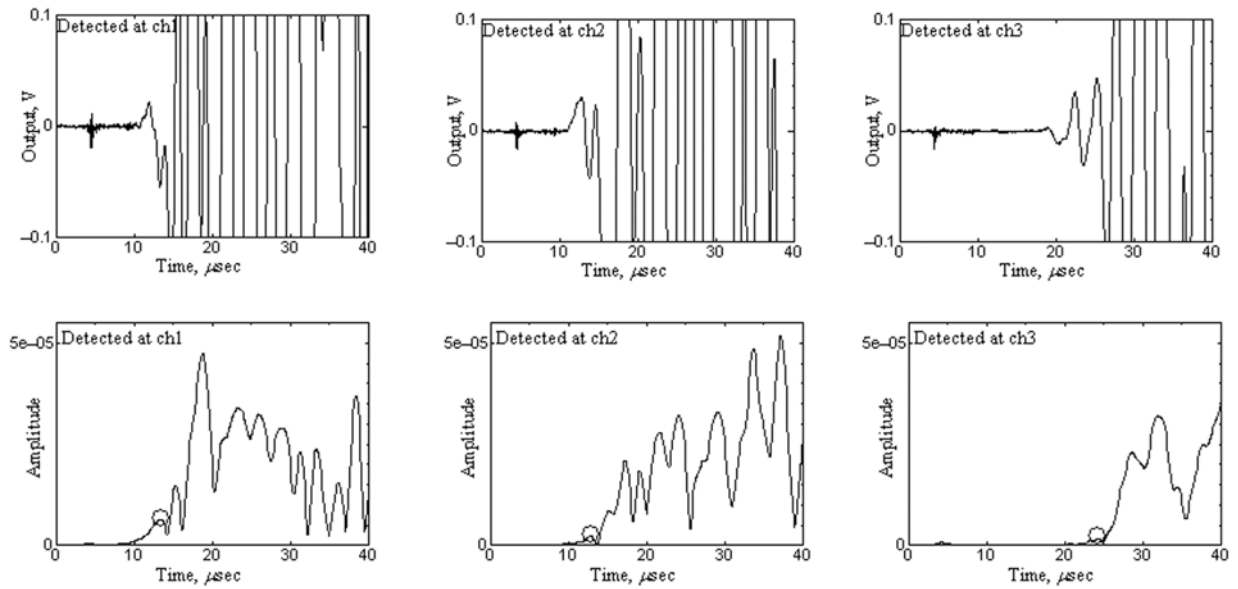


Fig. 5 Detected AE signals (upper) and their amplitude variations of wavelet coefficient (lower) at 180 kHz for $l = 1$.

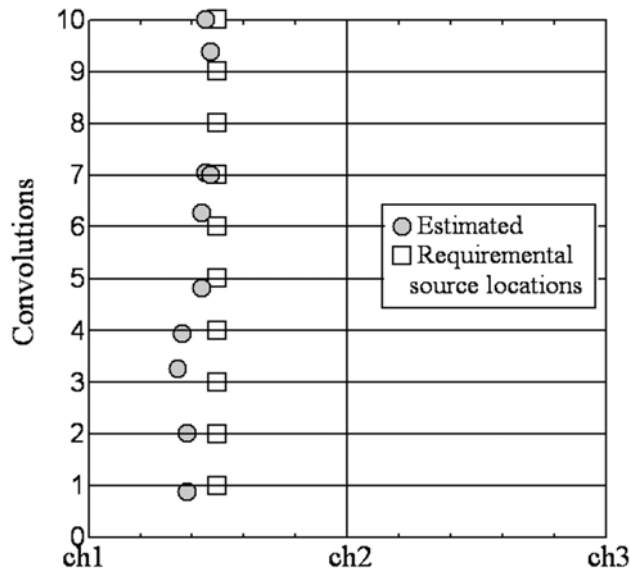


Fig. 6 Estimated source location.

3. Damage Detection on the Bellows

3.1 Experimental Setup

Experimental setup of fatigue test was shown in Fig. 7. A 300 mm long bellows was attached to jigs of fatigue machine as shown in Fig. 8. Lower jig was fixed and upper one was actuated at 1 cycle/s with a maximum displacement of 20 mm. Fatigue of upper 10 convolutions was, however, eliminated by attaching a special jig to give the lower ten convolutions large vibration displacement.

AEs from fatigue cracks in lower 10 convolutions were monitored by PICO sensors mounted on the lower 10-mm

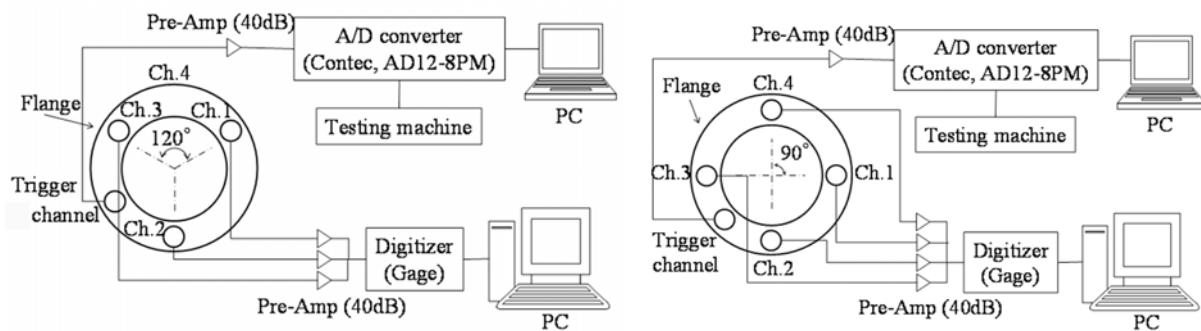


Fig. 7 Setup for AE monitoring during fatigue test of type-A (left), type-B (right).

thick flange as shown in Fig. 8. The bellows was welded to the flange. We utilized two-types of AE monitoring method shown in Fig. 7. One of four sensors (A) and five sensors (B) was used as a trigger signal to stop the fatigue test. Thus, AE signals were monitored by three (ch. 1, 2, 3) and four (ch. 1, 2, 3, 4) sensors in type-A and -B system, respectively. Sensor outputs were pre-amplified 40 dB, digitized at 200 ns interval, and fed to a computer. The trigger sensor signals were digitalized at 1 μ s interval. Type-A and -B systems were used for fatigue tests with 25 mm and 30 mm displacement, respectively.

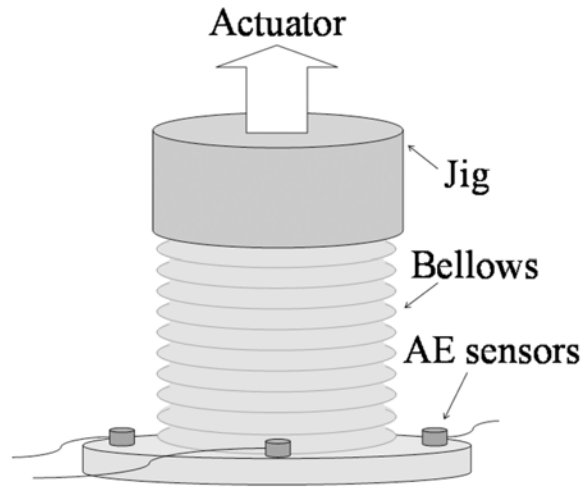


Fig. 8 Figure of specimens with jig.

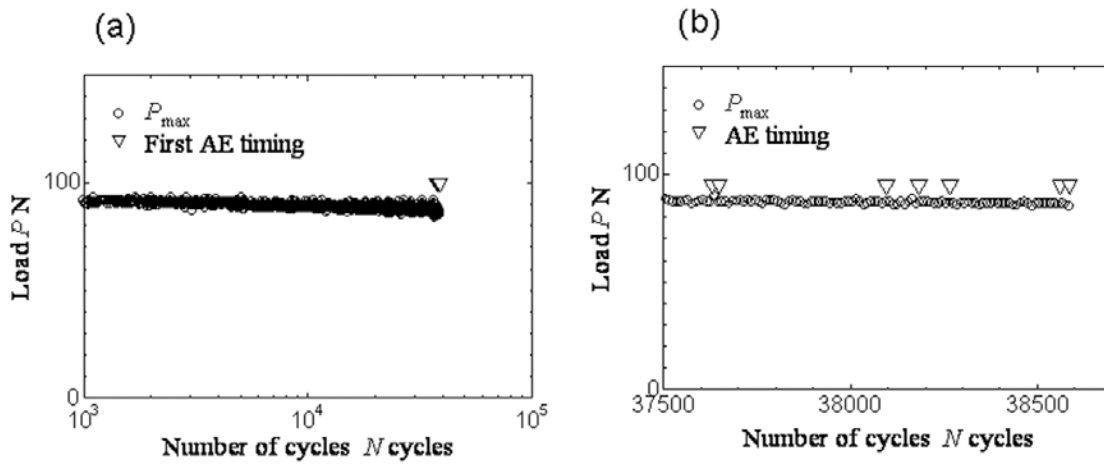


Fig. 9 Relationships between load P_{max} and AE timing at number of cycle N .

3.2 Results of Fatigue Tests

Figure 9 shows that load, P_{max} , changes with the number of cycles, N . Figure 9(a) represents P_{max} change and AE timing over entire cycles up to 38586, and Fig. 9(b) in expanded cycle number from 37500 to 38586. This bellows sustained cracks at the root of convolution near the lower flange between ch. 2 and ch. 3 sensors as shown in Fig. 10. Figure 9(b) shows that the first AE was detected at around 37630 cycles, 1000 cycles before the test finished at 38586 cycles. We detected 7 events before 38586 cycles. Figure 11 shows AE signals and their amplitude variations of wavelet coefficient at 180 kHz. We detected AEs with high S/N ratio and large S_0 component that are adequate for source location. In Fig. 12, damage areas are indicated by gray tone, and AE sources of 7 events were located close to the observed crack location.

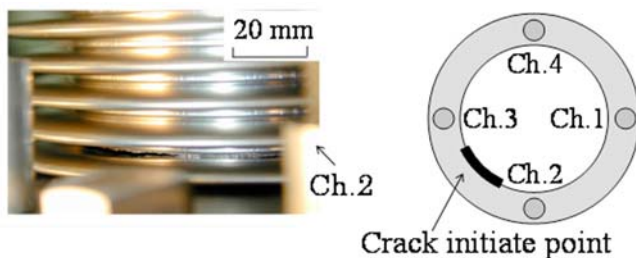


Fig. 10 Observation of fatigue crack.

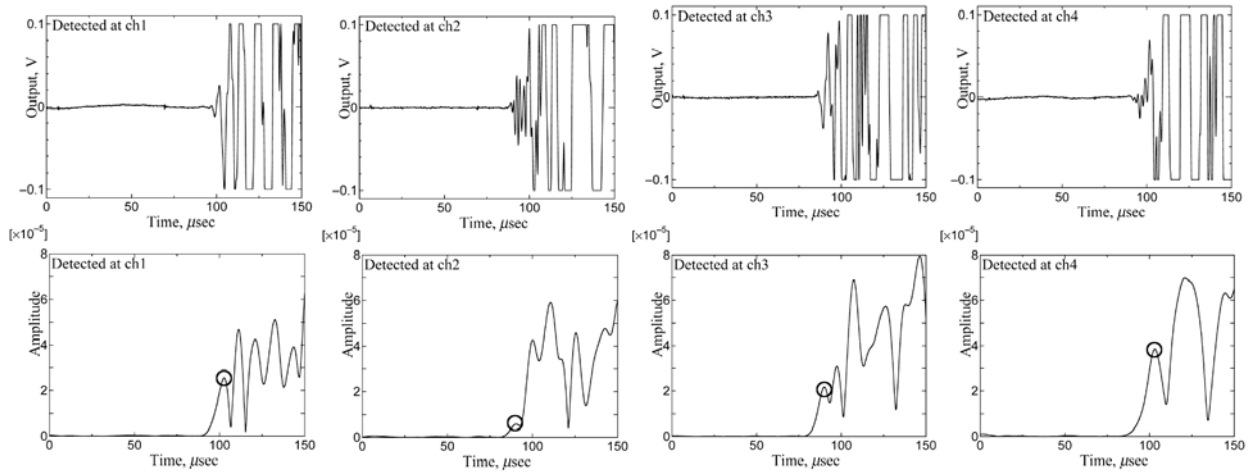


Fig. 11 Detected AE signals (upper) and their time transient of wavelet coefficient (lower) of type-A experiment.

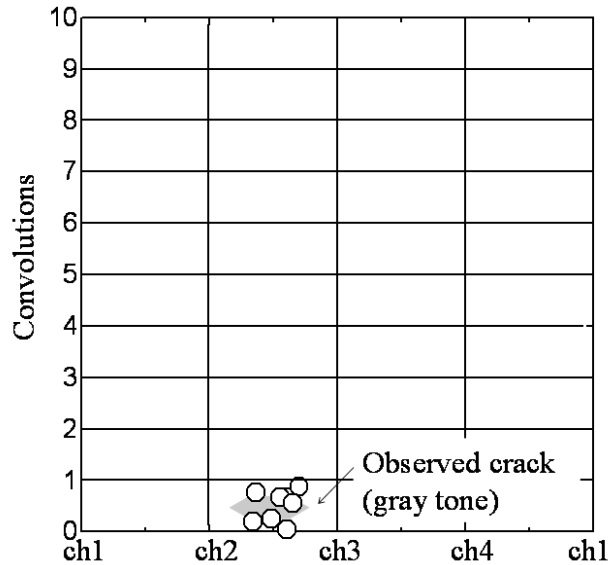


Fig. 12 Source location of type-A.

In the type-B test with 30 mm vibration displacement, we monitored crack initiation by one video camera. Figure 13 presents load and cumulative AE counts with N . We monitored the first AE at 21782 cycles, but no load reduction at this moment. AE increased continuously from 21782 to 2400 cycles and rapidly increased from 24000 cycles. Figure 14(a) shows the first circumferential fatigue crack near the upper jig at 22486 cycles. After this timing the load slowly decreased. Fatigue crack progressed in the circumferential direction and second crack started at around 22800 cycles when load decreased rapidly. This second crack could not be captured by the CCD camera since the crack occurred on the opposite side. At 24000 cycles at which sudden load drop and large event rate were observed, third circumferential crack was produced near the bottom flange, as shown in Fig. 14(b). Figure 15 shows the location result of type-B test, with damage areas indicated by gray tone. Source locations estimated after 24000 cycles were designated by open triangles. Location results agreed well with observed crack zone. Some of sources after 24000 cycles were located in upper gray tone. This is supposed to be due to noises by contacts of crack surface.

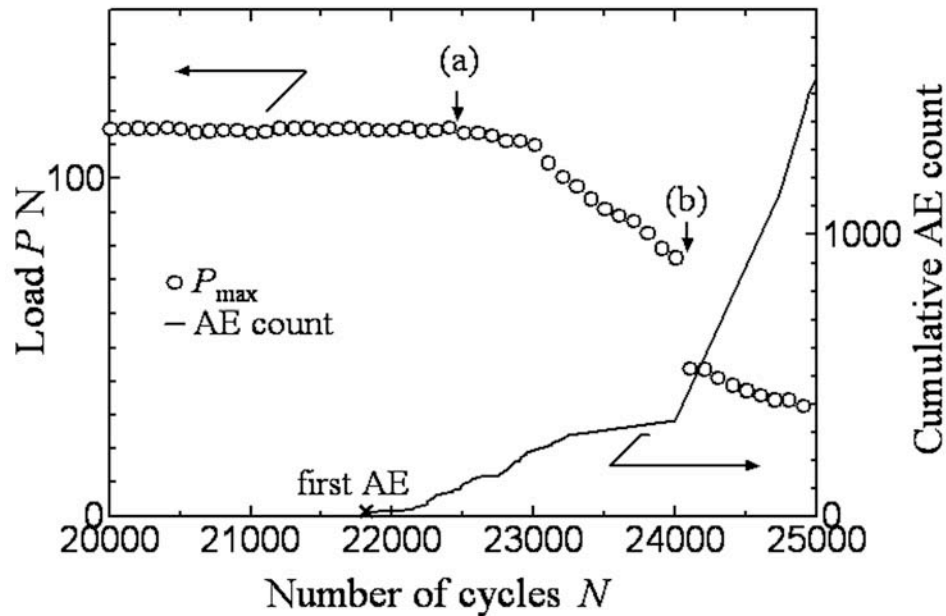


Fig. 13 Relationship between load P_{\max} and AE count at number of cycle N .

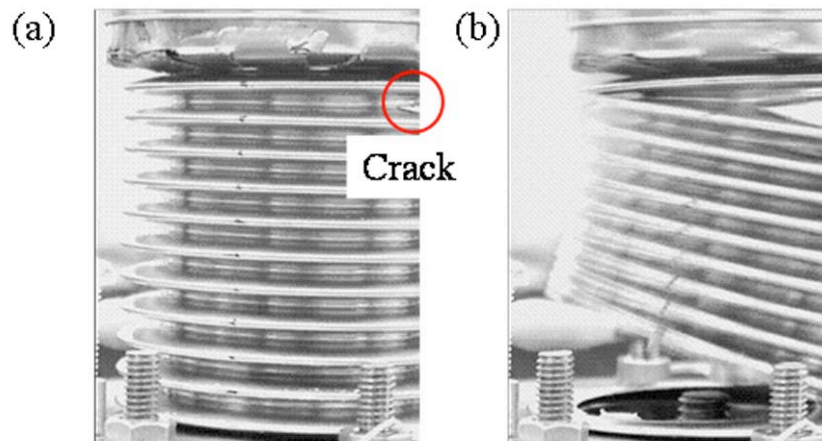


Fig. 14 Picture of video monitoring at 22486 cycles (a) and 24000 cycles (b), circled point is crack initiation.

4. Conclusion

We utilized AE technique to monitor the fatigue damage of formed bellows made of stainless steel. We monitored AE signals by sensors mounted on the weld flange, and utilized them for detecting the initiation and location of fatigue cracks.

- (1) Fatigue crack initiation of the bellows at vibration amplitude of 25 mm and 30 mm were correctly detected by AE at early time. AE technique was useful for detecting the fatigue crack initiation of complicated components such as formed bellows with weld flange. The flange can be successfully utilized for detecting the anti-symmetric-mode cylindrical AEs.
- (2) Source location of fatigue cracks were successfully performed utilizing the first arrival wave components. Locations of AE source, estimated by the group velocity of 3100 m/s at 180 kHz, agreed well with the fatigue cracks.

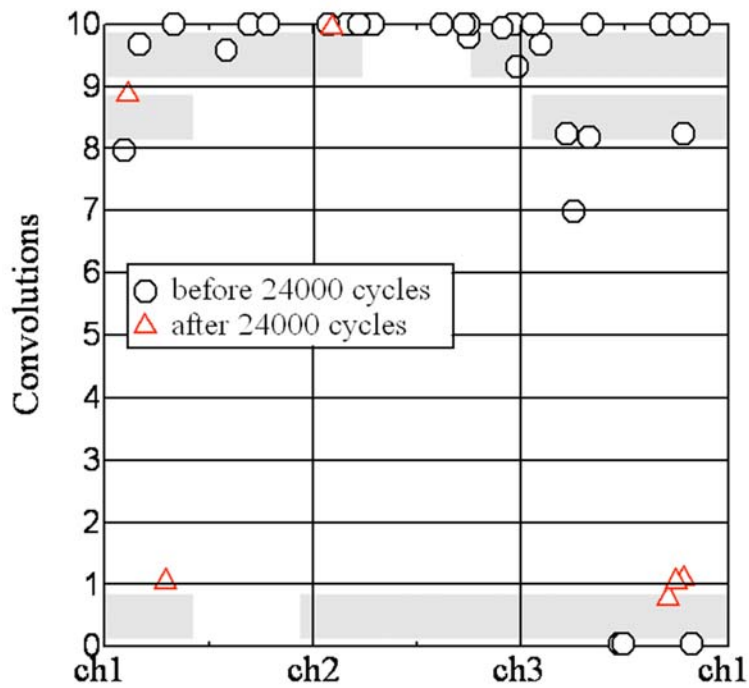


Fig. 15 Source location of type-B experiment.

References

- 1) C. Becht IV: International journal of pressure vessels and piping, **77** (2000), 843.
- 2) C. Becht IV: PVP, **388**, Fracture, Design Analysis of pressure vessels, heat exchangers, piping components, and fitness for service-1999 ASME (1999), p. 197.
- 3) H. Nishino, S. Takashina, F. Uchida, M. Takemoto and K. Ono: J. Jpn. Appl. Phys., **40** (2001), 1.
- 4) Hideo Nishino: J. Jpn. Soc. for Non-Destructive Inspection, **52-12** (2003), 654.
- 5) T. Hayashi: J. Jpn. Soc. for Non-Destructive Inspection, **52-12** (2003), 662.

PLASTIC REGION BOLT TIGHTENING CONTROLLED BY ACOUSTIC EMISSION MONITORING

TADASHI ONISHI, YOSHIHIRO MIZUTANI and MASAMI MAYUZUMI

2-12-1-11-70, O-okayama, Meguro, Tokyo 152-8552, Japan.

Abstract

Troubles related to bolt relaxation and fatigue have occurred in many fields. In the automotive industry, plastic-region tightening method is recognized as a good technique for preventing the relaxation and fatigue of bolts. However, this method requires a special torque wrench and involves a complicated procedure for stable tightening. Therefore, it is important that a new tightening method and a wrench that simplifies plastic region bolt tightening are developed. Two types of tensile tests using a torque wrench and a tensile tester were conducted for two different strength bolts. The Mahalanobis distance (MD) technique was utilized for discriminating acoustic emission (AE) signals from noise signals. We found that we can monitor the yield point of a high-strength bolt during loading by AE monitoring combined with the MD technique. Here, we conducted a feasibility study for controlling plastic-region tightening by AE techniques.

Keywords: Plastic region tightening method, Mahalanobis distance

1. Introduction

There have been many problems related to bolt relaxation and fatigue in many fields. For example, an accident involving a Nozomi express train in Japan from which a bolt fell off was caused by bolt relaxation [1]. Reliable bolt tightening is important to prevent problems and to maintain the efficiency of a machine. In the automotive industry, a plastic-region tightening method is known and used as a good method for preventing the relaxation and fatigue of bolts. There are three basic bolt-tightening methods for use at a work site; torque control, angle control and torque gradient control. The torque control method using a torque wrench is the most common method, although it cannot be applied to plastic-region tightening because of the relationship between the axial force and the torque of bolts is affected by a fluctuation of the friction coefficient of bearing surfaces. Both the angle control method and the torque gradient control method can be used for plastic-region tightening, although a special torque wrench is required and complicated procedures are involved. Thus, the applicability of the tightening method is limited. Therefore the development of a convenient plastic-region bolt tightening method is an important industrial necessity.

Table 1 Bolt specifications

	Nominal designation	Bolt length [mm]	Strength grade	Material	Surface finishing	Tensile strength [MPa]	Yield stress [MPa]	Thermal treatment after cold working
Bolt-A	M10	40	4.8	Carbon steel	Chromate treatment	420	340	×
Bolt-B	M10	40	10.9	SCM435	Oxide film treatment	1040	940	○

It is well known that some steels generate acoustic emission (AE) during plastic deformation. Therefore, there is a possibility to control plastic-region tightening by monitoring AE signals during tightening. Here, a feasibility study of a plastic-region tightening control using AE techniques is conducted.

2. Bolt Specifications and Experimental Procedures

2.1 Bolt Specifications

Two types of different strength bolts were tested. The specifications are shown in Table 1. Bolt-A, made of carbon steel, has a strength designation of 4.8; which, according to JIS B 1051-2000 [2], corresponds the tensile and yield strength of 420 MPa and 340 MPa, respectively. On the other hand, bolt-B, made of SCM435, has a strength designation of 10.9, indicating the tensile and yield strength of 1040 MPa and 940 MPa, respectively. In general, in the manufacturing process for high-strength bolts, thermal treatment is carried out after cold forging. Therefore, a thermal treatment was applied in the manufacturing process of bolt-B.

2.2 Experimental Procedures

The bolts were loaded in axial tension in two ways; using a torque wrench (experiment-1) and a tensile tester (experiment-2). Figure 1 shows the experimental setup for experiment-1. The bolt was set to a hydro-mechanical axial tension meter and an AE-sensor was mounted on the bolt head. An axial load was applied by a torque wrench, and AE signals and axial tension were monitored during the tightening. Detected AE signals were amplified 40 dB by a preamplifier and digitized by an A/D converter. To monitor just those AE signals produced by the plastic deformation of the bolts, a tensile test is conducted. Figure 2 shows the experimental setup for experiment-2. The sensor position and monitoring conditions are the same as in experiment-1. The bolt is loaded with axial tension in a constant stroke at 1 mm/min. Only bolt-A was tested in experiment-1; both bolt-A and -B were tested in experiment-2. Sampling conditions during the bolt tightening tests (both experiment-1 and -2) are shown in Table 2.

Table 2 Sampling conditions during bolt tightening test.

Sampling frequency [MHz]	Sampling points	Trigger level [V]	Measuring range [V]
25	8,192	0.02	± 4.5

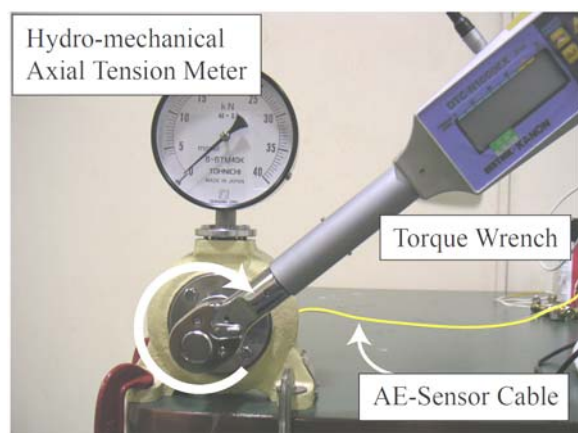


Fig. 1 Experimental setup for experiment-1.

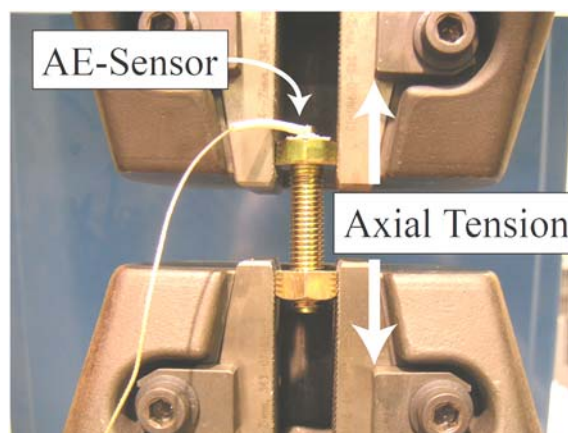


Fig. 2 Experimental setup for experiment-2.

3. Experimental Results

3.1 Result for Experiment-1

In this test, bolt-A shown in Table 1 was loaded using a torque wrench and axial tension and cumulative AE counts were monitored during the tightening. Figure 3 shows the relationship between cumulative AE counts and the axial tension on the bolt. Apparent electronic noise was manually excluded before analyzing the data. The yield load calculated for bolt-A is 19.7 kN, although changes were not observed at this load. As the AE signals were observed from early stage of the test, most of the AE signals detected seem to be friction noise.

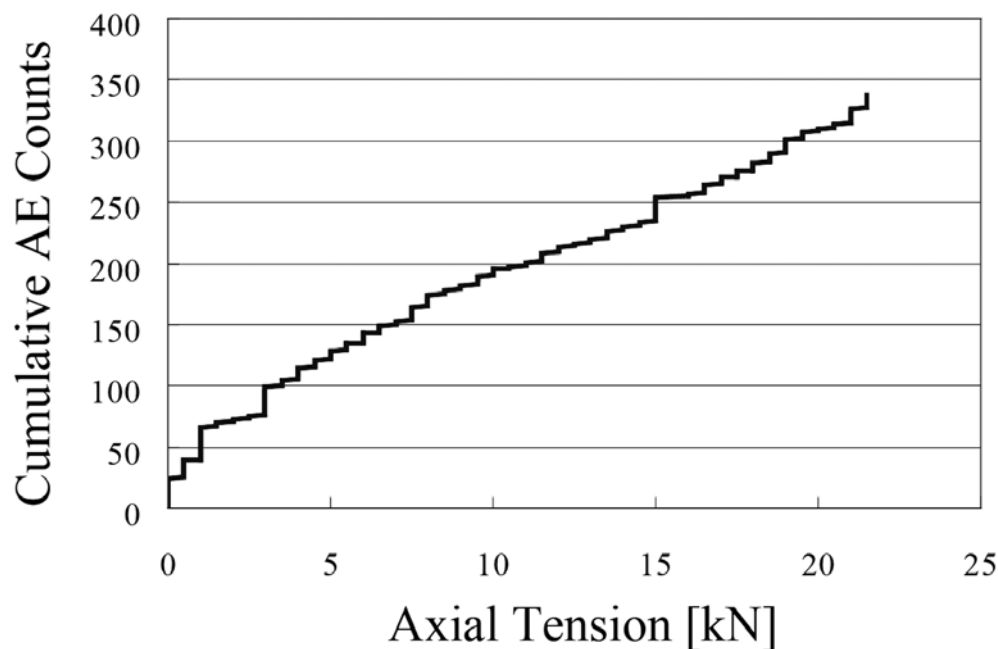


Fig. 3 Relationship between cumulative AE counts and axial tension

3.2 Results for Experiment-2

To remove the friction effect and to investigate the characteristics of AE signals due to bolt deformation, tensile tests of bolt-A and -B were conducted with a tensile tester. The results for bolt-A and -B are shown in Figs. 4 and 5, respectively. The relationship between the axial tension and elongation is also shown in these figures. The yield load estimated from the elongation-axial diagram (solid line in Fig. 4) for bolt-A is 23 kN. Although the authors expected that the cumulative AE counts increase simultaneously with the start of plastic deformation (23 kN), it rapidly increased only from 26 kN. On the other hand, the cumulative AE counts for the bolt-B test rapidly increased at around the expected yield load (56 kN), which is estimated from the load-elongation diagram (Fig. 5).

Figures 6 and 7 show examples of detected AE signals. Signal-(A) was monitored during the tightening of bolt-A at 27.5 kN. Signal-(B) was monitored during the tightening of bolt-B at 63.5 kN. The durations of the two signals are quite different. Total cumulative AE counts are also different between bolt-A and bolt-B. These differences may be caused by the existence of the heat treatment, because most of the AE may have already been produced during the manufacturing processes and few AE is observed without heat treatment.

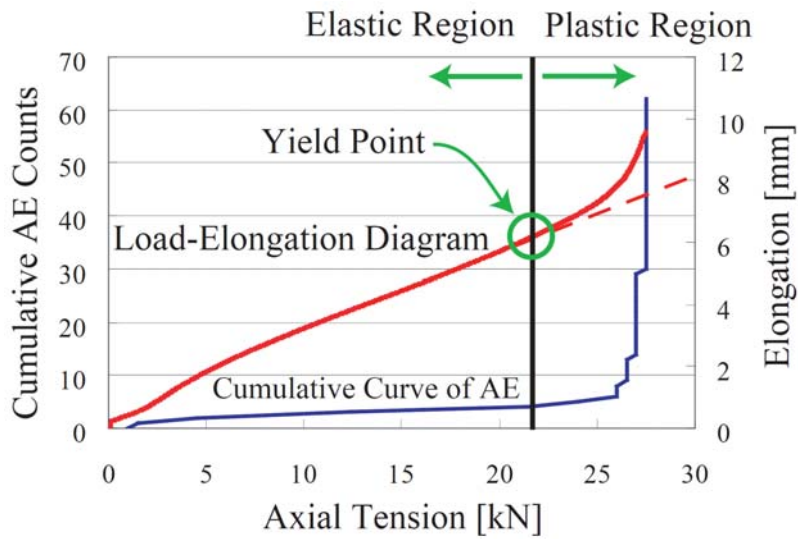


Fig. 4 Cumulative AE counts and elongation during a loading test for bolt-A. The yield point is indicated by an open circle.

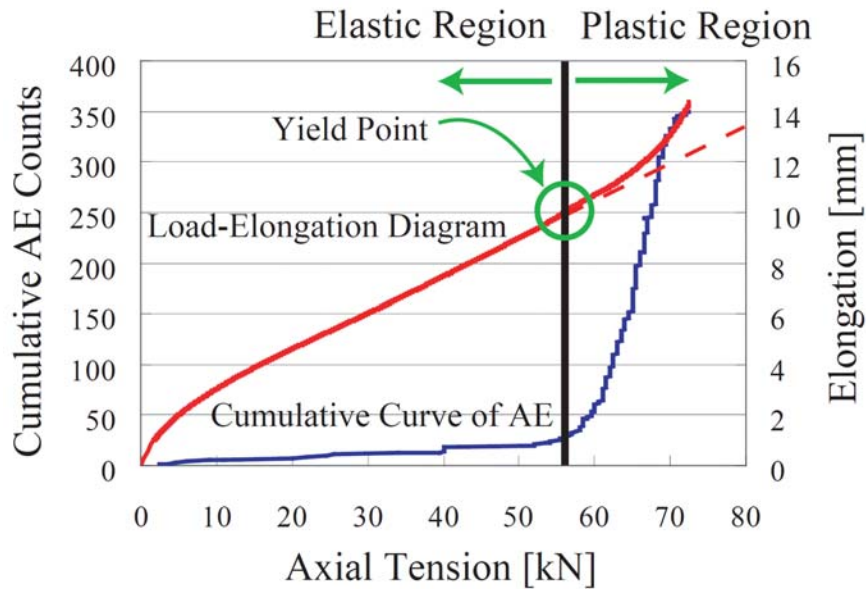


Fig. 5 Cumulative AE counts and elongation during a loading test for bolt-B. The yield point is indicated by an open circle.

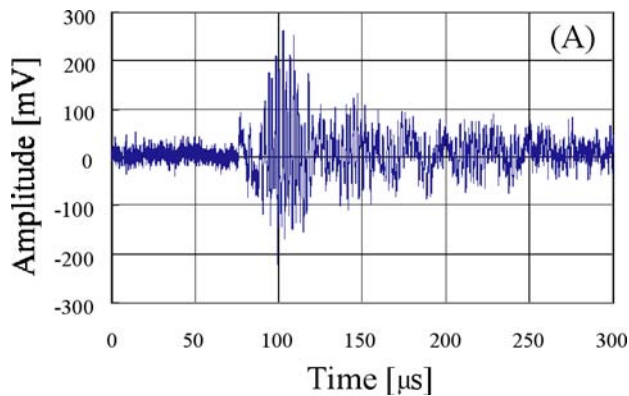


Fig. 6 AE signal observed during bolt-A test at 27.5 kN.

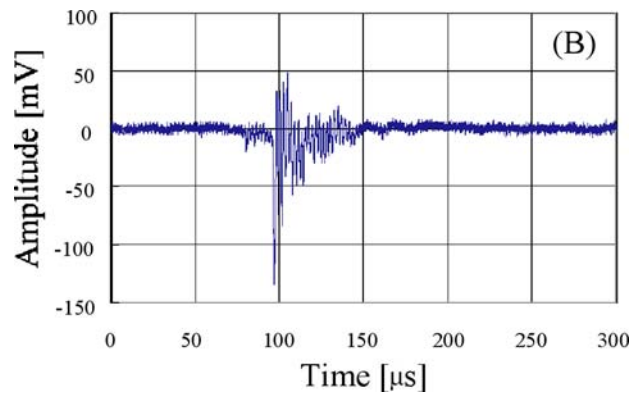


Fig. 7 AE signal observed during bolt-B test at 63.5 kN.

4. Discriminant Analysis

Many noise signals were monitored during the bolt loading tests; therefore, techniques that discriminate AE signals from noise signals are required. In this study, the Mahalanobis distance (MD) approach was examined to attain this objective.

4.1 Definition and Calculation of the Mahalanobis Distance (MD)

Formally, the MD is defined by equation (1),

$$D^2 = ((x - \bar{x})/s)' \cdot R^{-1} \cdot ((x - \bar{x})/s) \quad (1)$$

where $x = [x_1 \ x_2 \ \dots \ x_p]$ denotes a multivariate vector of the analyzed signal (AE and noise) parameters, $\bar{x} = [\bar{x}_1 \ \bar{x}_2 \ \dots \ \bar{x}_p]$ denotes the sample mean of the reference AE parameters, $s = [s_1 \ s_2 \ \dots \ s_p]$ denotes the sample variance of the reference data and R denotes the sample correlation coefficient matrix of the reference data [3, 4].

Figure 8 explains the method to distinguish AE signals and noise signals using MD. Here, two-dimensional representation of multi-dimensional space is shown. Group A is assumed to be AE signal group, Group B noise group, and it is assumed that the data of each group have distribution as shown. When the new AE data is obtained, the Mahalanobis distance between the data and each group (D_A and D_B) are calculated. When the D_A is smaller than D_B , a detected AE data is estimated as an AE signal (belonging to Group A). If $D_A > D_B$, the detected signal is noise, belonging to Group B.

In this study, eleven AE parameters were used for the calculation of MD. The following parameters are used (see also Fig. 9);

1. Mean and variance of amplitude (2 parameters).
2. Peak magnitude
3. AE signal rise time
4. The count using the threshold of half of the peak magnitude
5. Mean and standard deviations of a power spectrum calculated for every section of the analysis signal divided into three parts (6 parameters).

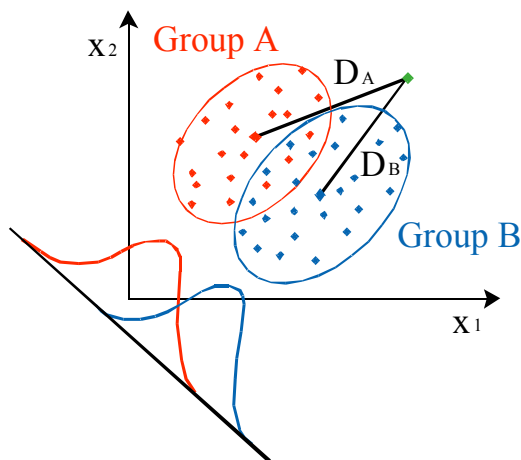


Fig. 8 Image of MD between groups A and B.

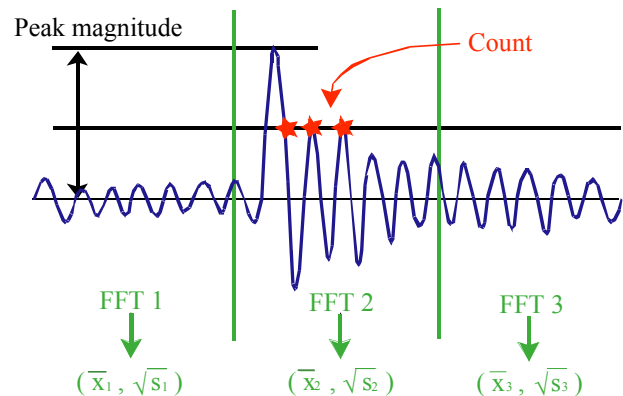


Fig. 9 AE signal parameters used for calculating MD.

4.2 Cluster Analysis for Deciding on Reference AE Data

Cluster analysis seeks similar samples by comparing sample parameters (in this study, 11 parameters were used) and by forming a homogeneous group. We used the Ward method for calculating similarity [3]. By conducting cluster analysis, the dendrogram as shown in Fig. 10 is obtained. We decided reference AE signals used for MD calculation by this cluster analysis.

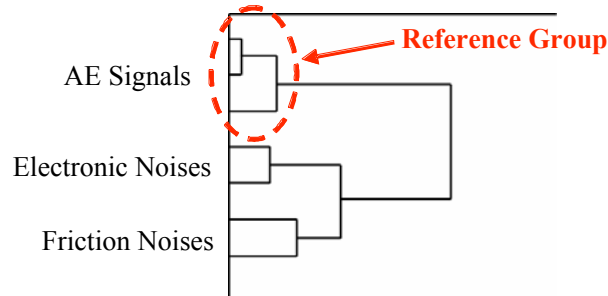


Fig. 10 Example of a dendrogram determined by cluster analysis.

4.3 Results of the Discriminant Analysis

Figures 11 and 12 show the relationship between the inverse of the MD and the cumulative count of AE for bolt-A and -B tests. To clearly show the results, the MD was changed into an inverse number. Twenty-two signals randomly selected from the AE group determined by cluster analysis were used to make a reference group. The starting point for plastic deformation is indicated by an arrow in the figures. For bolt-B testing (see Fig. 12), the highest $1/MD$ value is larger than 0.3 after the plastic deformation started. This shows the possibility that MD can be used for discriminating AE from noise. Furthermore, the result suggests that the plastic-region tightening of bolts can be controlled by monitoring AE and utilizing the MD technique. On the other hand, for bolt-A testing (see Fig. 11), the value of $1/MD$ is small even after the plastic deformation started. Considering the result together with that in Fig. 4, it appears difficult to control the plastic-region tightening of a bolt without undertaking thermal treatment in the manufacturing process by AE monitoring.

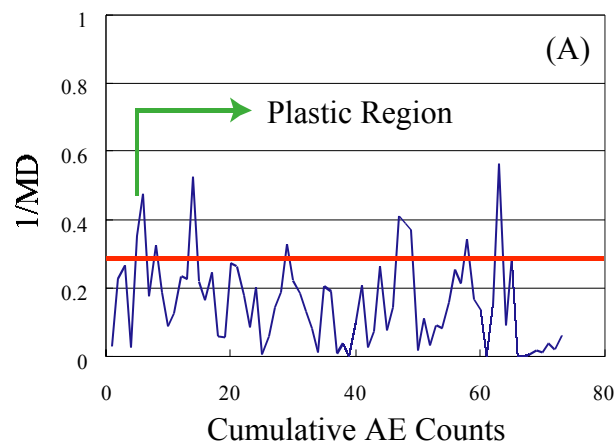


Fig. 11 Discrimination results

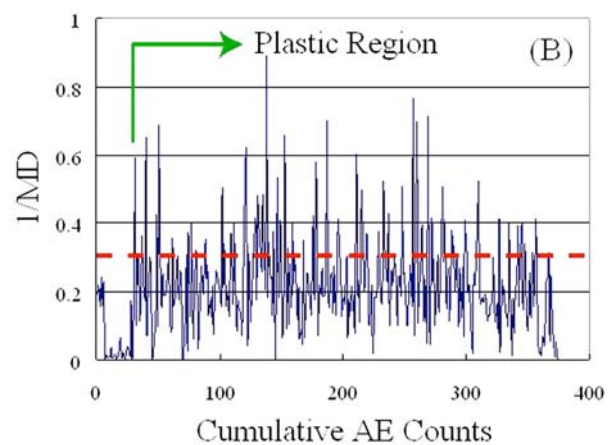


Fig. 12 Discrimination results

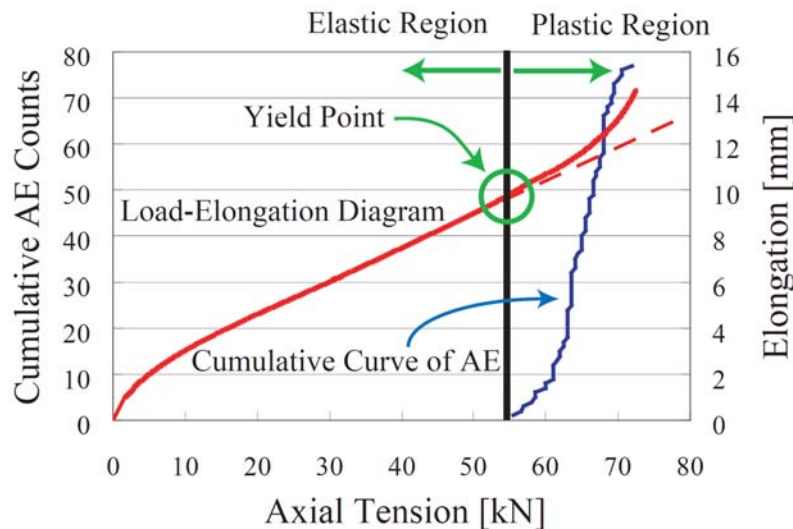


Fig. 13 Cumulative AE counts selected by MD and elongation during loading tests for bolt-B.

Figure 13 shows the relationship between the cumulative AE counts and tensile elongation during the loading test for bolt-B. The difference from Fig. 5 is that the noise data are separated from the AE signals by an MD technique. Figure 13 shows that the starting point for plastic deformation can be clearly determined by monitoring AE signals. Although not the subject of this report, there is the possibility for hydrogen induced cracking to occur, especially in the case of a high-strength bolt when plastic-region tightening is conducted. Therefore, special caution is required if there is a possibility of hydrogen induced cracking in the conditions that the bolts are used.

5. Conclusions

A feasibility study was conducted to control plastic-region tightening of bolts using AE techniques. The results can be summarized as follows;

- 1) Two types of tensile tests using a torque wrench and a tensile tester were conducted for two types of different strength bolts.
- 2) AE signals due to deformation were hardly observed for the low strength bolt since most of the AE signals had already been produced during the manufacturing process.
- 3) Cumulative AE counts of the high strength bolt increased rapidly near the yield load. This indicates the possibility of monitoring the initiation of plastic deformation by AE monitoring. Although the noise signals were monitored with AE signals.
- 4) The MD technique is utilized for discriminating AE signals from noise.
- 5) The yield point of a high-strength bolt during tensile load testing can be monitored by AE monitoring combined with MD technique.

References

- [1] T. Hattori, Failure analysis and prevention of mechanical, adhesive and welded joint, paper delivered at Study group on the accident/failure analysis method of JSME (2002).
- [2] JIS B 1083-1990 General rules for tightening of threaded fasteners.
- [3] Y. Tanaka, K. Wakimoto: *Methods of Multivariate Statistical Analysis*, (Japan, 1983) pp. 101-136, 229-244.
- [4] M. Miyagawa: *Technology for Getting Quality; What the Taguchi Method Has Brought Us*, (Japan, 2000), pp. 219-252.

ACOUSTIC EMISSION BEHAVIORS OF RECOVERY FOR Mg ALLOY AT ROOM TEMPERATURE

Y. P. LI and M. ENOKI

Department of Materials Engineering, The University of Tokyo, Hongo, Bunkyo, Tokyo, Japan.

Abstract

Traditionally, the recovery of materials was investigated by the evolution of microstructure, mechanical properties, electronic or magnetic properties. In present research, the recovery behavior of AZ31B alloy was investigated by acoustic emission (AE) at room temperature. After deformation, the specimen was attached to an AE sensor with broad response frequency. Considerable AE signals were observed and numerous AE signals appeared at the initial stage of the recovery process. Theoretical analysis was conducted on the origin and mechanisms of AE. AE signals appear to be from the dislocation annihilations driven by the internal stress of materials after deformation. The results also show that the cumulative AE counts are in good agreement with a non-linear relationship derived from the traditional recovery kinetics.

Keywords: AE count, Elastic energy, Recovery, Mg alloy

1. Introduction

Acoustic emission (AE) is the radiation of stress waves by materials, in which local dynamic restructuring of the internal structure occurs with the release of elastic energy. During the second half of the 20th century, AE from materials was studied extensively, especially in the AE from deformation and fracture of materials. More recently, the application of AE was extended greatly in fields such as thermal cycling, in which dislocation motion and microstructure damage are generally recognized to produce significant AE, martensitic transformation where the AE signal was thought to accompany the rapid variation in the shape of deforming volume, solidification of liquid, weld controlling, and fatigue, etc. Nearly all of the mechanisms of AE can be explained by one of these two approaches: dislocation motion or elastic stress release by micro-fracture of materials. In general, the model of AE source by dislocation motion is adequate in explaining and predicting the AE behavior. Schaarwachter et al. [1] successfully applied dislocation model of AE in the deformation of copper and its dilute alloys in explaining the relation between the dislocation motion and the behaviors of AE and later this results were applied by Moorthy et al. in explaining the AE behaviors of solution-annealed AISI type-316 austenitic stainless steel [2] in detecting micro- and macro-yielding of the materials and predicting the AE response frequency by dislocation model. All of the above have shown that dislocation motion and AE are closely related with each other. So AE is generated from the motion of dislocations, or we can suppose that wherever there is dislocation motion, there will be AE from materials no matter how weak the signal strength is. It is this supposition that paves the way for the present research.

The term of recovery denotes any modification of properties during annealing before the appearance of new strain-free recrystallized grains. Investigations performed on monocrystals have proved that recovery takes places by means of annihilation of dislocations with opposite Burgers vectors, tightening of dislocations loops, ordering of dislocation configurations, as well as by means of formation of subboundaries and their motions [3]. Recovery in polycrystals, apart from

intra-grain mechanism, can also take place by means of annihilation of dislocation, points defects on grain boundaries. From the above, we can conclude that recovery process is a source of dislocation motion and it is reasonable to expect that the recovery process should be accompanied with a release of elastic energy or acoustic emission. Traditionally, recovery behavior is characterized by the mechanical properties of materials such as strength, hardness, ductility or by the observation of microscopic mechanisms in dense dislocation tangles. The observation of microscopic mechanisms by electron microscopy is difficult for the large density of dislocations involved (between 10^{14} and $5 \times 10^{15}/\text{mm}^2$) and their heterogeneous distribution, which makes their energy density and their individual (cross-slip, climb, solute drag) or collective behavior difficult to handle either analytically using simple elementary dislocation models or by computer simulation. More recently, there is a growing interest in the characterization of microstructure by magnetic non-destructive techniques [4]. Structure sensitive magnetic macroscopic properties include coercive field, permeability, residual induction and power loss derived from a hysteresis loop. Recovery behavior of many materials can be evaluated properly by this method. However, like the method of mechanical properties, the detection of magnetic properties of materials is not so convenient for it has to be quenched each time after heat treatment in getting an instantaneous value of the property. That is to say, it is difficult to get continuous and synchronized behavior of recovery by this method. Furthermore, it is a time consuming and expensive process especially in some alloy containing noble metals because each datum shown in the recovery dynamic curve usually needs a specimen to be tested.

There has been much research about the recovery of Mg alloy [5, 6]. However, only few studies were specially conducted in the recovery of Mg alloy at room temperature. Koike et al. [7] reported that recovery can take place at room temperature by investigating the Kikuchi line and the deformation curve of the AZ31 Mg alloy. They analyzed the active role of dynamic recovery at room temperature to the deformation of Mg alloy. In fact, other researchers such as Miller in 1991 [8] and Conrad in 1957 [9] also proposed that the recovery of Mg alloy can take place at room temperature. The AE from phase transformation has been observed in many areas such as martensitic transformation, solidification of liquid, and so on. Many researches have shown that AE method is a powerful method in investigating the dynamic behavior of phase transformation [10, 11]. However, until now, no research of AE was performed upon diffusion-controlled (thermally activated) structural transformations – recovery and recrystallization. So it is the aim of this research to get the continuous and synchronized AE signal for a better and more convenient material evaluation method in understanding the recovery behavior of AZ31B alloy at room temperature.

2. Experimental Procedures

The materials system chosen was extruded bar of standard AZ31B Mg alloy from Osaka Fuji Magnesium Alloy Co.. Cylindrical samples with 15 mm in diameter and 15 mm in height were preliminarily subjected to annealing at 450°C for 1h. The samples were deformed to different strain levels at a deformation rate of 1.5×10^{-2} mm/min. As soon as deformation was finished, the specimen was attached to an AE sensor. AE sensor used in present study was low noise type (M304A, Fuji Ceramics, Japan). AE signals were measured by μDISP (PAC, USA) with a threshold of 40 dB and high-pass filter of 50 kHz effectively reducing the noise from environment. The RMS voltage of AE signal was also recorded by the AE discriminator system with a gain of 60 dB as shown in Fig. 1.

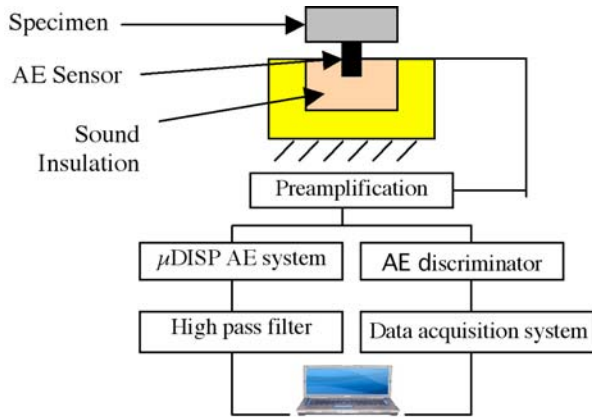


Fig. 1 AE system for evaluating the recovery behavior of AZ31B alloy.

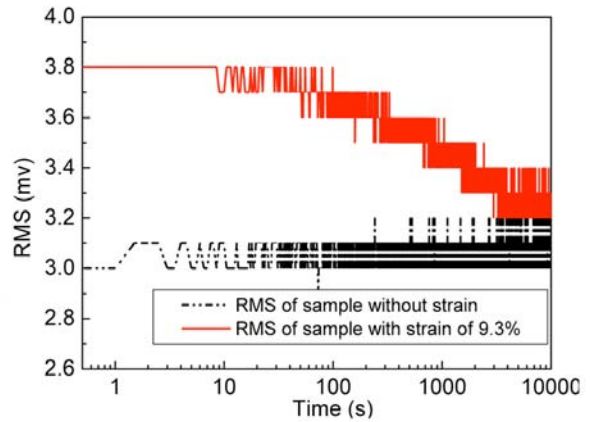


Fig. 2 RMS voltage of AE from recovery and noise level.

3. Results

Figure 2 shows the RMS voltages of AE signals during the recovery stage of AZ31B alloy at strain of 9.3% along with environmental noise level. Both the AE signals and noise were continuous waves. The RMS value of recovery decreased to the noise level eventually, which indicates that this AE system is effective in recording the AE signal from recovery.

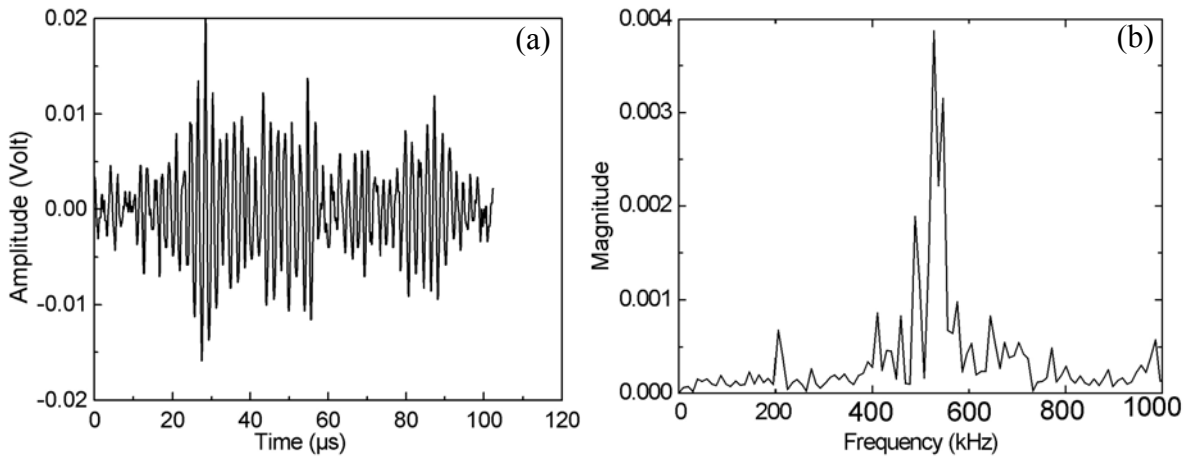


Fig. 3 (a) Typical AE waveform, (b) the frequency spectrum (FFT).

It is interesting to note that all of the AE waveforms are similar as shown in Fig. 3. They are of low level and some kind of continuous and the peak frequency is about 550 kHz. AE from recovery is similar to that from deformation process in Mg alloy [12]. With increasing recovery time, the amplitude or count of AE signal decreased gradually as shown in Fig. 4.

Figure 5 shows the cumulative AE event as a function of recovery time. It can be seen that most of the AE event occurred at the beginning of the recovery process where a steep slope in the initial section (<2000s) exists. Later, the cumulative AE event increased slowly and reached a horizontal stage during the final recovery stage (>4000s). It is found that no systematic relationship between the strain of AZ31B alloy and the overall AE events during the entire recovery process exists. Probably this is due to the difference in the time of specimen transfer from the compression jig to AE sensor since the initial AE event rate is so high that a little difference of

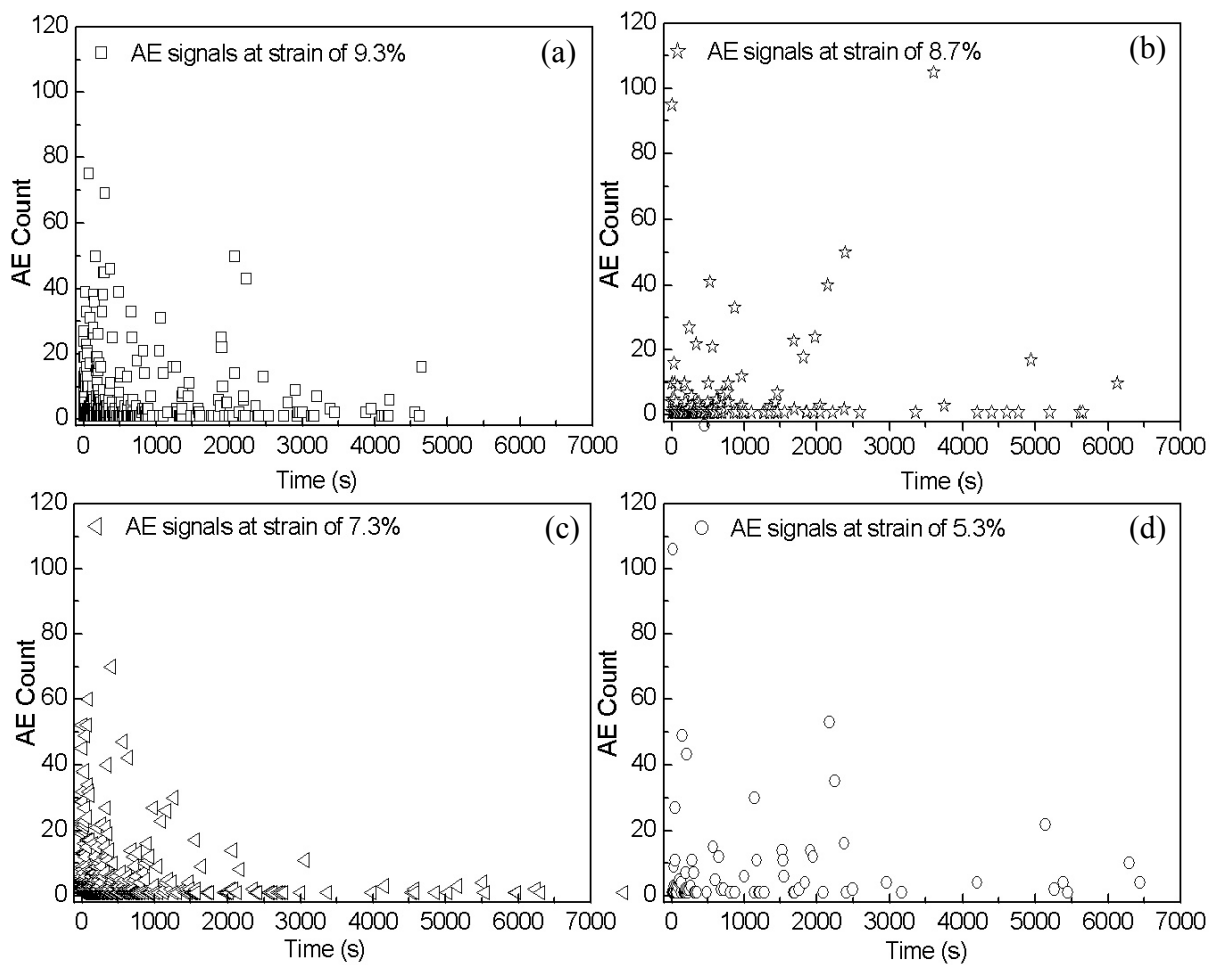


Fig. 4 AE signals during recovery at room temperature at strain of (a) 9.3%, (b) 8.7%, (c) 7.3%, and (d) 5.3%.

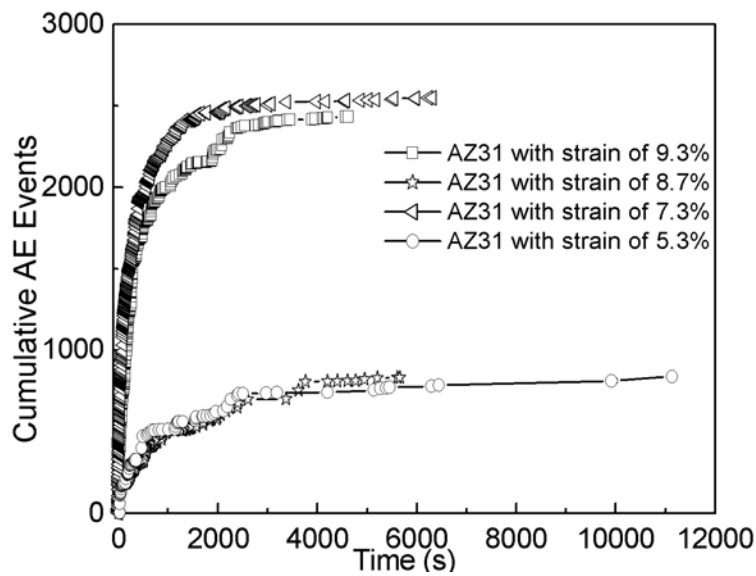


Fig. 5 Cumulative curve of AE event vs. the recovery time.

time can result in a large discrepancy in the overall AE events. We will discuss it later in detail.

4. Discussion

4.1 Theoretical Analysis of AE from Recovery

Only limited research has focused on the recovery of materials at room temperature [7, 8], even though recovery at room temperature is critical in affecting the deformation properties of materials. Some research focused on the evolution of yield stress during recovery stage [13, 14]. Friedel model [15] predicts a logarithmic decrease of the yield stress and assumes that applied stress is equal and opposite to the internal stress of the dislocation structure. If one assumes further that the relaxation rate of this structure, and that of the internal stress, occurs by thermally activated mechanism according to

$$d\sigma_i / dt = -K \exp(-U(\sigma_i) / kT) \quad (1)$$

where K is a constant, and that the activation energy decreases with stress $U = U_0 - \nu\sigma_i$, ν being the activation volume of the elementary recovery events, then a logarithmic time decay of the yield stress is

$$\sigma = \sigma_i = \sigma_{t=0} - (kT / \nu) \ln(1 + t / t_0) \quad (2)$$

and the plastic relaxation strain rate from recovery is

$$\dot{\epsilon}_p = \frac{\rho b^2 \nu_D}{M} \exp\left(-\frac{U_0}{kT}\right) \sinh\left(\frac{\sigma_i \nu}{kT}\right) \quad (3)$$

where ν_D is the Debye frequency, M the Taylor factor, and the U_0 and ν the parameters to be decided.

From above equations we can think the recovery process to be a deformation process, in which the force is applied opposite to the direction of deformation and decreases with increasing time, resulting into a plastic relaxation of materials. If we assume that the internal stress relaxation corresponds to dislocation annihilation and reorganization, and therefore to plastic relaxation strain, the AE activities from recovery process can also be thought as a result of dislocation motions and annihilations applied by the internal stress.

During the recovery stage, it is also assumed that the recovery is controlled mainly by the disappearance of the dislocations with opposite Burgers vectors (although many phenomena occurred in this process such as tightening of dislocations loops, ordering of dislocation configurations), and the disappearance of the dislocation will give rise to micro-slip in the slip plane and at the same time a certain strain energy will be released which results in AE signal (some of the strain energy will be released as a form of heat). During the AE generation process, it can be thought that the elastic wave was produced just as the origin of earthquake waves [16].

4.2 AE Behaviors and Recovery Kinetics

Theoretical considerations indicate that some properties of the materials are proportional to the square root of dislocation density during recovery process, e.g., the flow stress ($\sigma - \sigma_y$) [14]. Take R_y as the fraction of recovery at a certain temperature, then

$$R_y = (\sigma - \sigma_y) / (\sigma - \sigma_0) \propto k\sqrt{\rho} \quad (4)$$

where $(\sigma - \sigma_y)$ is the decrease of flow stress in recovery, and $(\sigma - \sigma_0)$ the overall decrease of flow stress after recovery. Then a general relation is satisfied to a specific property of materials at a fixed temperature [17] as follows:

$$R_y = a + b \ln(t) \quad (5)$$

where a and b are constants for the specific property at each given temperature at a fixed pre-strain. Figure 6 shows the relative cumulative AE counts curve of both the linear and logarithmic relationship with time. The relative cumulative AE counts increase with recovery time. In this figure we find a similar trend of AE at different pre-strain levels indicating the same mechanism of AE during recovery process.

Assuming the AE event counts proportional to the number of annihilated dislocation, the cumulative AE event (N_i) have the same relationship with dislocation density as event counts, and the relative cumulative event counts, N_i/N has the following relation with dislocation:

$$N_i/N \propto K(\rho - \rho_r) \quad (6)$$

where ρ is the dislocation density just after the deformation process, ρ_r is the dislocation density during recovery. From equations 4, 5 and 6, we can get

$$\frac{N_i}{N} = A[\ln(t)]^2 + B \ln(t) + C \quad (7)$$

Here A , B , C are constants. The exact meaning of these constants needs further research. The non-linear fit results of relative cumulative AE counts are shown in Fig. 7 at strains of 9.3% and 5.3%, respectively. It can be seen that the prediction of theory is in good agreement with the experimental data.

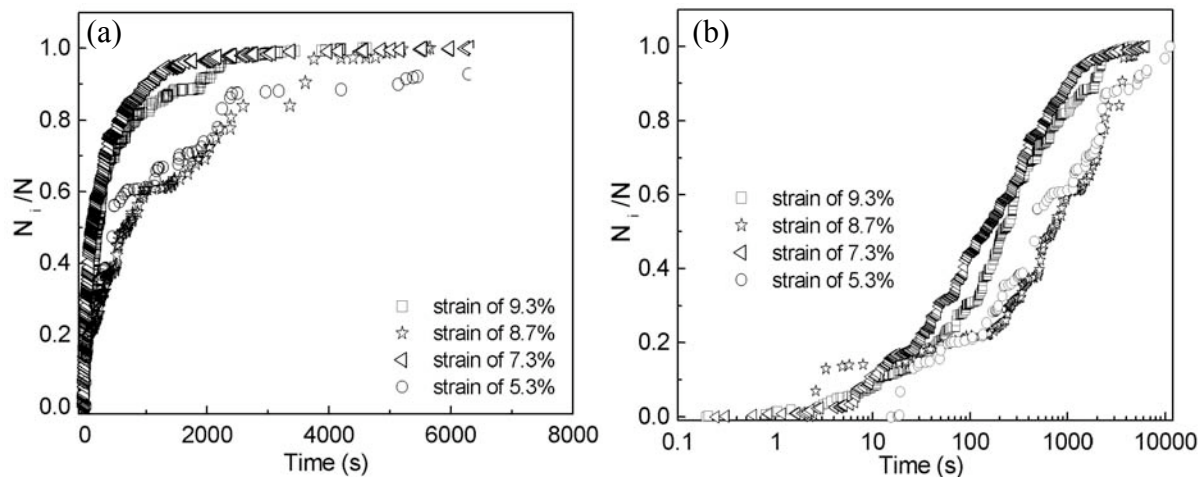


Fig. 6 Relative cumulative AE counts curve during recovery process in (a) a linear and (b) a logarithmic time scale.

5. Conclusions

1. AE signals were successfully detected in the recovery of AZ31B alloy at room temperature with a high pass filter of 50 kHz.
2. Cumulative AE events depend on the recovery time. Most of the AE events were recorded at the initial stage of recovery (<2000s), and AE event rate decreases gradually with the increase of recovery time.

3. The cumulative AE counts were assumed to be proportional to the dislocation density that decreases during recovery. A non-linear equation describes the relation between cumulative AE counts and the recovery time.

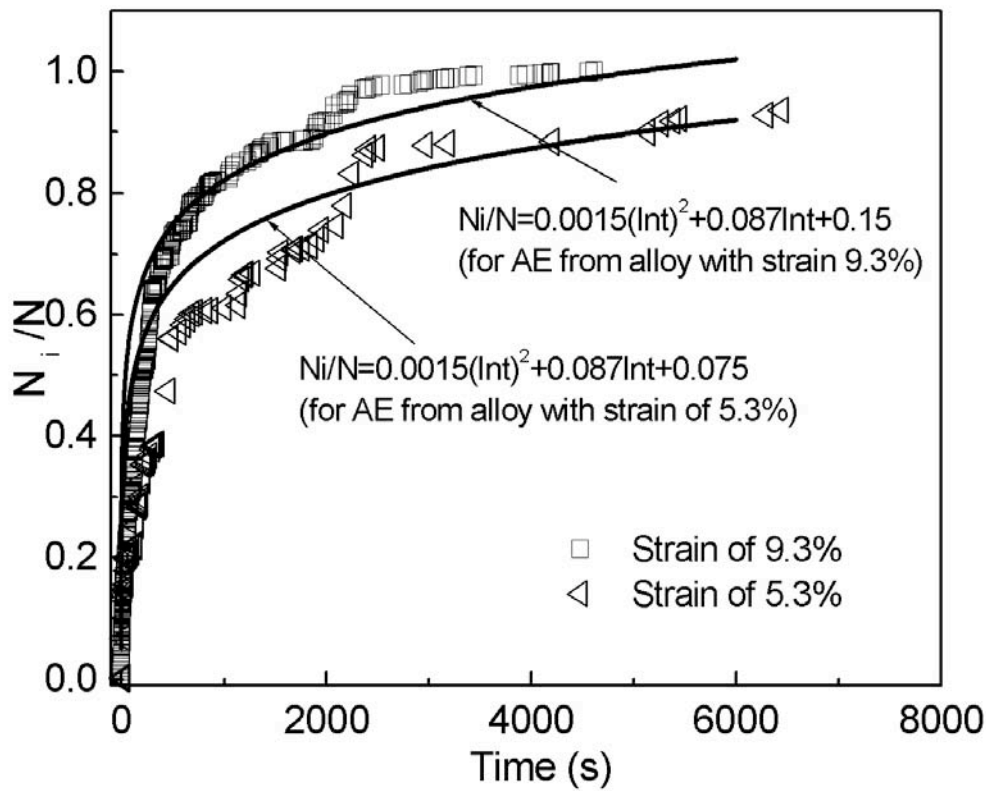


Fig. 7 Non-linear fit of the relative cumulative AE counts of Mg alloy with strain of 9.3% and 5.3%.

References

- 1) W. Schaarwächter, H. Ebener, *Acta metal. Mater.* **38** (1990), 195.
- 2) V. Moorthy, T. Jayakumar and Baldev Raj, *International J. of Pressure Vessels and Piping*, **64** (1995), 161.
- 3) T. Hasegawa and U. F. Kocks, *Acta metal.* **27** (1979), 1705.
- 4) A. Martinez-de-Guerenu, F. Arizti, et al., *Acta Materialia*, **52** (2004), 3657.
- 5) C. J. Beevers, *Acta Metal.*, **11** (1963), 1029.
- 6) J. V. Sharp, A. Mitchell, *Acta Metal.*, **13** (1963), 965.
- 7) J. Koike, T. Kobayashi, *Acta Materialia*, **51** (2003), 2055.
- 8) W.K. Miller. *Metall Trans A*, **22A** (1991), 873.
- 9) H. Conrad, W.D. Robertson, *J. Metals*, 1957, 503.
- 10) F. J. Perez-Reche, E. Vives, *J. Phys. IV France*, **112** (2003), 597.
- 11) J. Baram, J. Avissar, *Scripta Metallurgica*, **14** (1980), 1013.
- 12) K. Ono, *Acoustic Emission-Beyond the Millennium*, 2000, 57.
- 13) M. Verdier, Y. Brechet, *Acta Mater.* **47** (1999), 127.
- 14) E. Nes, *Acta Metall. Mater.*, **43** (1995), 2189.
- 15) J. Friedel, *Dislocation*. Pergamon Press, Oxford, 1964.
- 16) K. Aki, P. G. Richards, *Quantitative Seismology, theory and methods*, Volume **1**, 1980.
- 17) A. Martinez-de-Guerenu, F. Arizti, *Acta Materialia*, **52** (2004), 3667.

AN ACOUSTIC EMISSION TEST SYSTEM FOR AIRLINE STEEL OXYGEN CYLINDERS: SYSTEM DESIGN AND TEST PROGRAM

ALAN G. BEATTIE

Physical Acoustics Corporation, Princeton Junction, NJ 08550-5303, USA.

Abstract

An acoustic emission (AE) system, designed to perform pressure tests on steel airline oxygen cylinders, has been developed and tested. This system is similar in operation to the previously developed Halon Bottle AE Tester. The Halon tester source location algorithm was modified to locate events on the surface of cylinders with hemispherical end caps instead of on spheres. The proof load on the cylinder in this system is applied by gas pressurization instead of heating a hermetically sealed container as was done in the Halon System. A prototype of the AE Oxygen Cylinder Tester was built and used to test a random set of 72, 115 cubic-foot (3.26 m³) steel oxygen cylinders in a commercial oxygen bottle test facility. The bottles belonged to Federal Express (FedEx) and had been sent to the facility for their scheduled triennial hydrostatic tests. This testing program indicated that the cylinder test system works well and has adequate sensitivity to detect growing flaws in the cylinders. However, in contrast to Halon bottle tests, there was absolutely no indications of flaw growth in any of the cylinders at pressures up to 30 % above their normal fill pressure. The results suggest that the required 3-year cycle for pressure testing these bottles is excessive and that there is no reason to arbitrarily limit their service life to 24 years.

1. Introduction

Commercial airliners carry steel cylinders containing pressurized oxygen gas. This gas is used for emergency respiration of the passengers and crew in the event in the failure of the cabin pressurization at high altitudes. Many modern airliners have substituted short-term sources of chemically produced oxygen for the passengers but all carry oxygen cylinders for the crew. United States Department of Transportation regulations required an inspection of the pressure boundary of these cylinders every three years. The only currently accepted test is the hydrostatic test, where the cylinder is pressurized with water to twice its working pressure. The volumetric expansion of the bottle is measured and the bottle is then depressurized and the volume measured again. Any increase in bottle volume in the second zero pressure measurement over the first is attributed to inelastic expansion. Too high a value of inelastic expansion will result the cylinder failing the test.

Practically, steel airline oxygen cylinders are removed from service for several reasons. These are: obvious physical damage to the cylinder or its threaded connection for the valve, visual determination of excessive corrosion, inside or outside the bottle, and exceeding an arbitrary life span, currently set at 24 years. Failure of the hydrostatic test is extremely rare. Most apparent failures due to excess inelastic expansion have been determined to have been caused by operator errors during the test. The author has anecdotal knowledge of one cylinder, which blew up during pressurization. The failure of the hydrostatic test to find defective cylinders is not surprising. The test was designed over sixty years ago specifically to detect cylinders, which had experienced significant wall thinning due to excess corrosion. Better process control by the

manufacturers and better maintenance procedures by the airlines eliminated this problem many years ago.

This development program started with the goal of testing oxygen cylinders *in situ* in the airplane by over-pressurizing the cylinders with breathing oxygen. Real-time AE monitoring was to be performed during the pressurization. Three problems arose. First, to pressurize the cylinders in the plane with breathing oxygen requires a portable oxygen supply and oxygen booster pump. Second, access to the valve on the mounted oxygen bottles was sometimes difficult and the distribution plumbing in multiple bottle installations was not always easy to work with. Finally, there was little enthusiasm for introducing 15.9 to 18.6 MPa* oxygen gas into an airplane. Too many materials become highly flammable when subjected to pure oxygen at these pressures. A revised program was designed to test the system and develop failure criteria by testing a set of 200 oxygen cylinders in an airline bottle shop. This program was not implemented, partly from a misunderstanding over the requirements of the test procedure but primarily because of an increasing workload in the bottle shop. An agreement was finally reached with a commercial testing facility to test with AE cylinders sent to them by FedEx for their routine triennial inspection in return for an extra fee for each cylinder involved. In reaching this agreement, the decision was made to pressurize with nitrogen gas instead of oxygen since the bottles were received empty by the facility. This paper will cover the development of the AE oxygen cylinder test system and the testing of 72 oxygen cylinders just before they were subjected to a hydrostatic test. The testing program was ended when the AE system developed electronic problems. The test results from both this set of bottles and a dozen preliminary experiments did not find a single locatable AE event at pressures exceeding the 12.8-MPa fill pressure in any of the 84 bottles. (* 1000 psi gas pressure = 6.9 MPa)

2. System Design

The oxygen cylinder test system is based upon the previously developed AE Halon Bottle Test System [1]. The Halon bottle system uses a six-channel Physical Acoustics Corporation (PAC) Mistras system to monitor the spherical Halon bottles. This monitoring is performed as their internal gas pressure is raised by heating them to 62.8°C. The system locates AE sources using a nonlinear least-squares solution of an over-determined set of analytic equations in a spherical coordinate system. As each source is located, it is checked to determine whether it is a member of a cluster of AE events and each cluster, as it develops, is checked for its rate of growth as a function of temperature (pressure). There were three necessary changes to adapt this system for use with oxygen cylinders. First, the location algorithm had to be changed to calculate the shortest distance between any two points on a cylinder with spherical end caps. Second, a gas handling system had to be substituted for the industrial oven. Third, a new fixture to position and hold the sensors on the cylinder had to be designed. The whole system is shown in Fig. 1.

3. Location Program

The calculation of the shortest path length between any two points on a cylinder with spherical end caps is not a trivial problem. The coordinate system that was decided upon is a modified spherical coordinate system where each point is specified by the angles theta and phi and a radial vector and is constrained to lie either on the surface of the cylinder or on one of the hemispherical end caps. The cylinder surface is defined by the radius (cylinder and hemispheres), and the length of the cylindrical portion of the surface. The approach taken is to divide the path into up

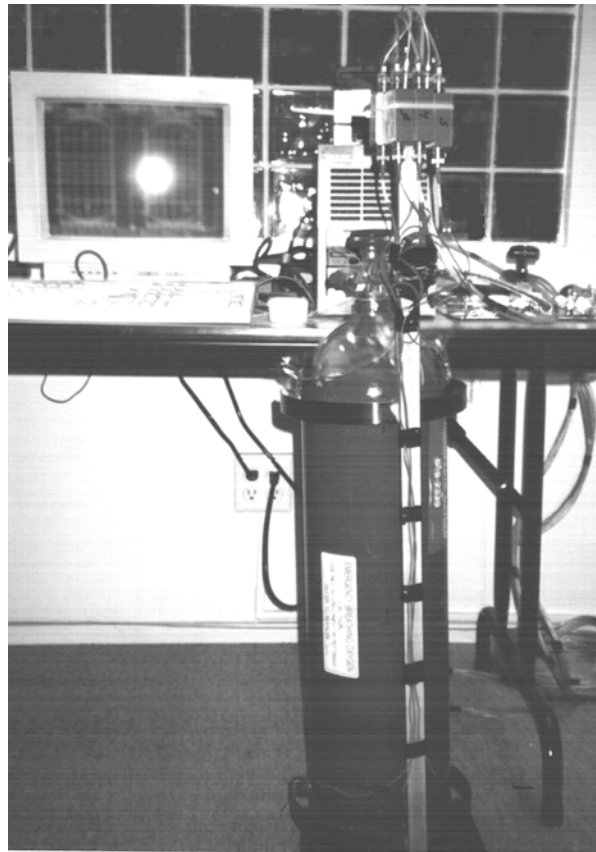


Fig. 1 Oxygen cylinder test system.

to a maximum of three separate pieces: the section on the top hemisphere, the section on the cylindrical surface and the section on the bottom hemisphere. The minimum distance on each surface is easily calculated. These paths are great circles on the hemispherical surfaces and a straight line on the unrolled cylindrical surface. The ends of the lines are joined at the junction of spherical and cylindrical surfaces. The shortest distance on the surface is defined when the phi derivatives of the great circles on the hemispheres and the spiral line on the cylinder are equal at the points of intersection. The resulting equation to be solved for the points of intersection is analytically complex (involving both the angle and trigonometric functions of the angle), so a numerical routine was written to solve for the coordinates of such points of intersection. The distances calculated between two specified points on the surface are then used by the same nonlinear least-squares fitting routine used in the Halon Bottle tester. The same clustering routine used in the Halon Bottle tester is also used to determine the severity of the located emission. Extensive testing with lead breaks on the surface of oxygen cylinders showed that the location and clustering programs worked well and that the actual deformation of the end caps of the oxygen cylinders from perfect hemispheres had only minor effects on the location accuracy. While the calculation of the source location can involve a very large number of steps, the program ran sufficiently fast on a 160-MHz computer to keep up with moderate data rates. With the increases in CPU speeds during the last few years, computation speed is no longer a problem for this type of program.

4. Gas Handling System

The proof load for the oxygen cylinders is provided by pressurized gas instead of the heating of a sealed sphere, used in the Halon Bottle system. The original intention was to pressurize the

cylinders using aviation-grade oxygen so that the cylinders would neither have to be emptied nor cleaned. This would still be a possibility if the system were installed in a hanger where cylinders were removed from the planes. However, the results of this series of tests along with extensive conversations with bottle shop personnel indicate that the major problem with oxygen cylinders is wear on the valve parts and not deterioration of the cylinder itself. Therefore if the valve is to be inspected, the bottle must be emptied and a cheaper and safer pressurizing medium than oxygen gas can be used.

The system was designed to use pressurized gas, originally introduced into the cylinder through the valve. The use of the standard valve for the cylinders presents some problems due to its incorporation of two sintered metal filters. These filters give some resistance to high gas flows. However, the main problem with these sintered filters is that they are acoustic noise generators during high gas flows. Thus, the fill rate had to be relatively slow to keep the noise level down. Even when using a valve without filters, there is a large amount of acoustic noise during the initial pressurization to about 3.5 MPa for pressurization rates between 0.7-1 MPa/min. This flow noise proved useful as an additional verification that all sensors were working satisfactorily during the test and did not produce locatable events.

The gas handling system, shown in Fig. 2, consists of a needle valve to control the input flow rate, two solenoid valves, a check valve to prevent cylinder gas from flowing into the gas source, and a pressure gauge. The needle valve is used to control the pressurization rate. One solenoid valve controls the input gas and the other is a dump valve which both reduces the pressure at the end of the test and acts as a safety valve to rapidly reduce the pressure in the cylinder if the system should detect a growing flaw in the cylinder. The computer constantly monitors the gas pressure and controls both solenoid valves. The dump solenoid valve can also be operated manually.

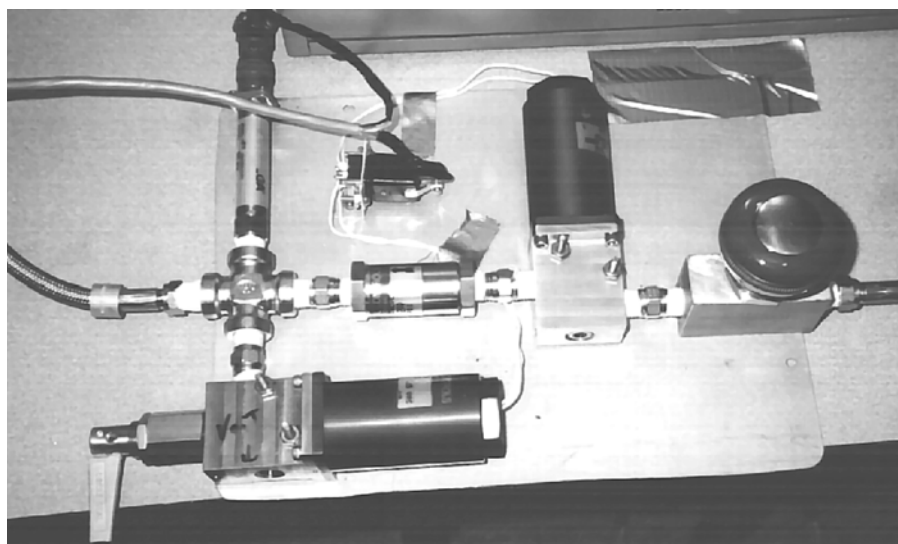


Fig. 2 Gas control system.

If the standard oxygen cylinder valve is used, the pressure gauge is separated from the cylinder itself by the two sintered filters when the valve is open. The actual pressure drop across the entire valve assembly when gas is flowing at the desired rate is less than 35 kPa, and this drop moves toward zero as the pressure inside the cylinder approaches the test pressure. The use of dry nitrogen gas as the pressure medium allows the use of a valve without the sintered filters and removes any detectable pressure drop across the valve assembly.

5. Sensor Fixture

The sensor fixture both positions the sensors on the oxygen cylinder and holds them in spring-loaded contact with the cylinder. Many possible sensor configurations were tried. The configuration which gave the best results with the non-linear least squares location program consisted of two rows of sensors around the circumference of the cylinder portion just adjacent to the cylinder-hemisphere junction. The sensors are spaced at 120° intervals. Studies showed slightly better location when both rows had the same phi angles instead of one row displaced by 60° from the other. Using the same phi positions for both rows made for a much simpler portable fixture so this lay out was used in the fixture, shown in Fig. 3. The PAC Nano-30 sensors are contained in magnetic hold-downs, which are mounted on about 260° arcs of spring steel.

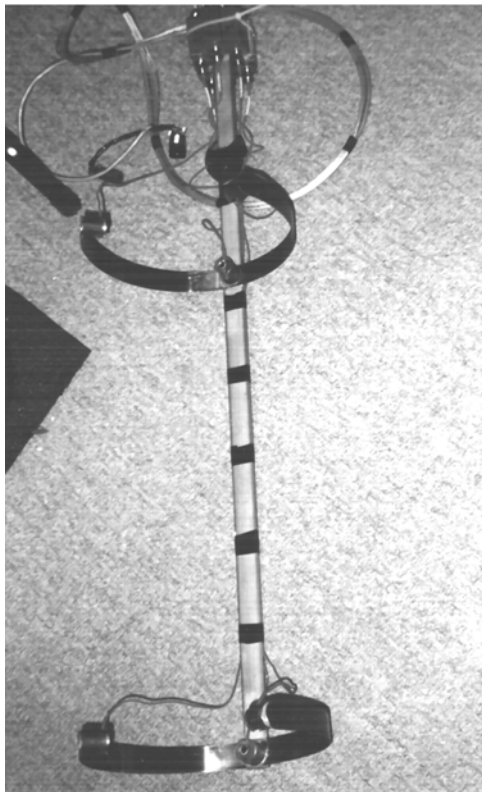


Fig. 3 Sensor mounting fixture.

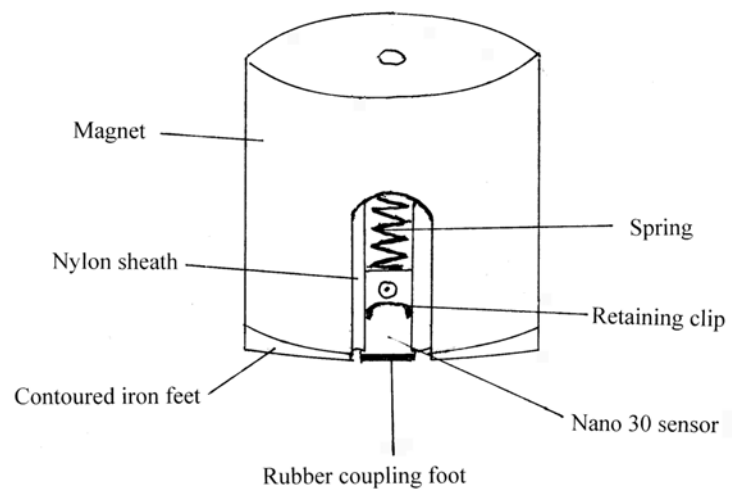


Fig. 4 Sensor holder.

The arcs are attached to a stainless steel bar at the correct spacing for the cylinders under test (this design requires a different fixture for each size of oxygen cylinder. It was dictated by the original requirement for the capability of testing the cylinders while mounted in the aircraft). The six PAC 110-5015 preamplifiers are mounted on the end of the stainless bar. They have a gain of 40 dB and a band pass of 250 to 500 kHz. The 300-kHz center frequency of the sensor-preamplifier combination was designed to be relatively insensitive to the gas flow noise.

The magnetic sensor hold-downs are diagramed in Fig. 4. The magnet has a diameter and height of 22.2 mm with a holding force of 40 N. This was a compromise between relatively easy handling of the fixture and sufficient force to have a strong spring for adequate coupling. A holding force of 90 N would have been more satisfactory from a coupling point of view. However, trying to change position of the fixture or detach all six magnets at once would have been quite difficult. A nylon sleeve glued inside the magnet and a compression spring inside the sleeve completed the assembly. The sensor is slipped inside the nylon sleeve, compressing the

spring and a retaining clip placed under the coaxial cable. The hard rubber disk glued onto the sensor is about one mm thick and aids in the acoustic coupling to the cylinder. A thin film of silicone grease is also used as the spring and magnet are not strong enough to insure effective dry coupling.

6. Autosensor Test

A successful AE test is a negative test. One looks for the absence of AE in a good test specimen. For an automatic AE test, it is essential that the system is known to be working. In this program, the first step after the operator starts the test is to perform an Auto Sensor Test (AST). The program will not start the pressurization until this test is passed. The AST test consists of each sensor being excited with twenty sequential electrical pulses. These pulses generate strong acoustic signals in the specimen, which are detected by each of the other sensors. The detected signals have their AE parameters at each detecting sensor averaged over the twenty pulses. The oxygen bottle test program uses only the signal peak amplitude, which is measured in decibels, to determine whether the AST test is passed. The averaged peak amplitudes received by all the sensors from each pulsed sensor are themselves averaged (six sensors times five transmitted signals equal 30) and then the five signals received by each individual sensor are averaged. To pass the AST test, the average from each individual sensor has to be within ± 4 dB of the overall average. This states that the average sensor peak amplitude has to be within ± 60 % of the overall average. This is a fairly stringent requirement when differing path lengths, coupling efficiencies and minor variations in sensor calibrations are considered. The Mistras system has a dynamic range of over 80 dB and many AE tests show signal strength variations of over 60 dB. Extensive testing with pencil-lead breaks on the surface of these cylinders have shown that the location accuracy with a system, which passes this AST test, will locate the signal source with an accuracy of about ± 4 mm.

7. Total AE System

A block diagram of the system is shown in Fig. 5. The AE system is a standard six-channel PAC Mistras system. The computer and three Mistras cards are mounted in an industrial case. An Iomega pressure readout feeds the computer and electric signals from a Mistras card operate two solid state relays which control the solenoid valves. In accordance with the original design specifications, the relays, Mistras cards and pressure readout are connected to the solenoid valves, preamplifiers and pressure gauge through a 15-m umbilical cord. This cord consists of six UG-316 coaxial cables and wiring to carry the 115V ac to the solenoids as well as the excitation and output voltages of the pressure gauge. If the system had been used inside an aircraft, a 15-m flexible pressure hose would also have been included in this umbilical cord. The preamplifiers are powered by the Mistras cards through the signal coaxial cables.

8. Pressurization System:

Arrangements were made with AV-OX Co. in Louisville KY to operate the Oxygen Bottle Tester on one hundred 115 cubic-foot oxygen cylinders owned by FedEx, which were sent to AV-OX for their normal triennial hydrostatic test. The cylinders are delivered to the company empty so there was no compelling reason to use oxygen as the pressurizing medium. Therefore dry nitrogen gas was used instead. This decreased the cost of the tests and increased their safety. A booster pump and containment cage was installed at AV-OX. The booster pump allowed the use of most of the gas in the commercial nitrogen cylinders. A valve without sintered

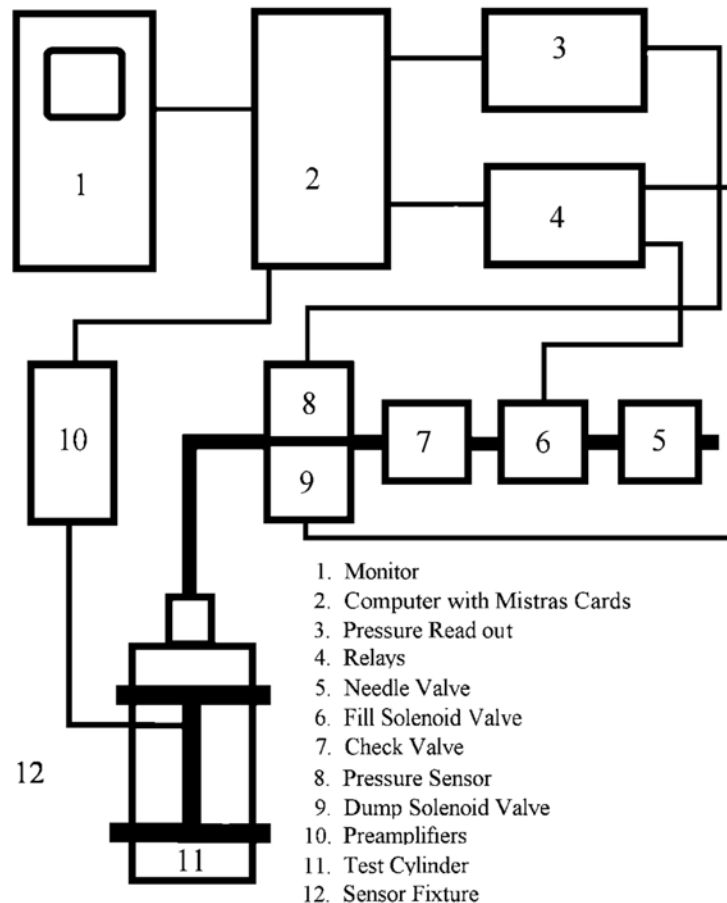


Fig. 5 A block diagram of the test system.

filters was installed in each cylinder under test and the pressurized gas fed in through it. This valve was fully open during the testing. All gas flow adjustments were made with the needle valve in the gas control fixture. This needle valve proved more sensitive than anticipated so once set, it was left alone. At the end of the test, the cylinder was bled down to atmospheric pressure. No attempt was made to recycle the nitrogen gas. Gas pressure was monitored by a Heise gauge on the supply line and the pressure gauge in the gas handling fixture. In operation, the supply pressure was set to 17.9 MPa to insure a steady pressurization rate.

9. System Operation

The duties of the test operator were to install the nitrogen valve in the test cylinder, place the cylinder in the safety cage and connect the gas line from the gas handling fixture. The sensor fixture was then placed on the cylinder and all sensors checked to insure that they were properly seated. To produce the best coupling of the sensor to the cylinder, a light coating of silicone grease was applied to the rubber disk on the sensor face. This would not have been necessary with stronger magnets and coupling springs. Finally the operator enters the cylinder serial number into the computer on the table shown in Fig. 6. The entries in italics were the only information entered by the operator.

After checking to make sure the pressurization system is working and all the valves are in the correct position, the operator starts the computer program. The first operation is the AST test. If it is not passed, the computer asks the operator to check the sensors and try again. It should be

noted that an AST test failure will be caused by any type of operational failure in the system as well as by poor acoustic coupling of the sensors. Once the AST test is passed, the computer opens the solenoid fill valve.

1	Airline	<i>Federal Express</i>
2	Part Number	<i>ABC-01234</i>
3	Cylinder Size	E – 115 ft ³
4	Final Pressure (psi)	1600
5	Cylinder Serial #	<i>09333</i>
6	Hold Pressure (psi)	2400
7	Hold Time (sec)	120
8	FAA Center	QX3D80SL
9	Test Facility	AV-OX

Fig. 6 Computer entry table.

During the pressurization, the initial gas flow produces a large amount of low amplitude AE. This flow-produced emission usually falls below the detectable threshold of 30 dB by the time the internal pressure of the cylinder reaches 2.8 MPa. This creates a moderately large data file but has the advantage of showing that AE system was actually working during the fill. Once started, the system is constantly searching for locatable emission sources. However despite many hundreds of detected emissions during the initial fill stage in each of the tested cylinders, the arrival sequences of gas-flow-produced AE signals have never produced a located emission source.

The AE test continues until the internal pressure of the cylinder reaches 16.56 MPa (2400 psi). Then the computer closes the fill valve. AE monitoring is continued for another two minutes. The program then evaluates the entire test and decides whether the cylinder has passed or failed the test. The operator is asked to print out the report and the program then opens the dump valve until the internal pressure falls below the normal operating pressure of 12.8 MPa (1850 psi). At this point, the test is over and the operator can either manually open the dump valve to drain the remaining gas or shut the cylinder valve, disconnect the cylinder from the sensor and gas control fixtures remove it from the protective cage and drain the remaining gas from the cylinder in another location.

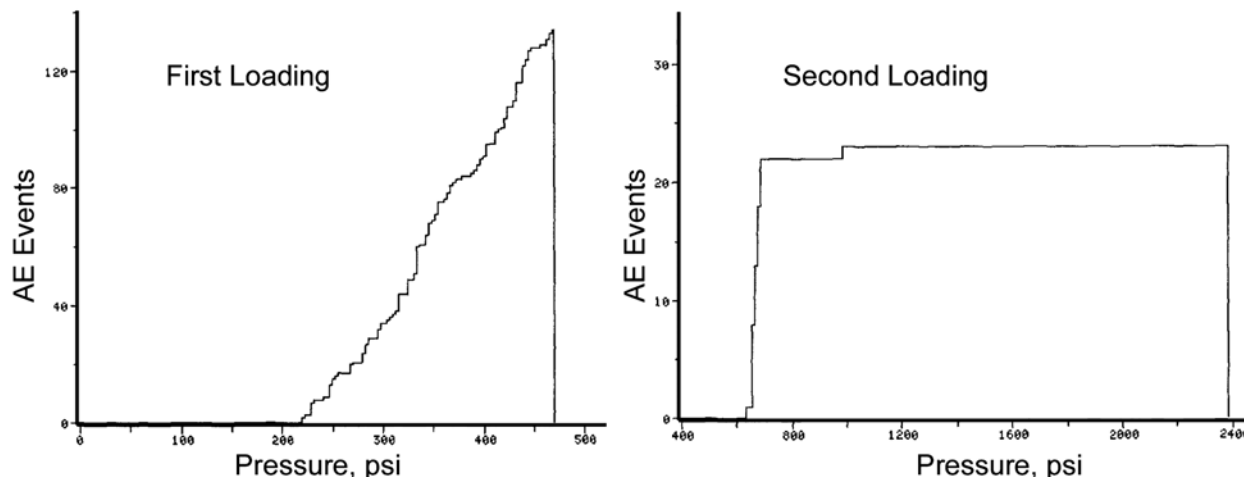


Fig. 7 First and second pressurization of a corroded cylinder. Located AE events vs. pressure.

10. Experimental Results

Seventy-one FedEx cylinders were tested as they arrived at AV-OX for their triennial hydrostatic tests. One cylinder from another airline, which had been mistreated (probably exposed to salt water) during the removal and shipping process, was added to this test set. This cylinder had visually identifiable corrosion spots on the inside surface and was scheduled to be returned to the cylinder manufacturer to have its inside surface reworked. It was the closest thing to a bad cylinder, which was available for testing. The prototype system was operated primarily by one employee of AV-OX. The testing was on a sporadic basis, being carried out whenever FedEx cylinders arrived for their scheduled hydrostatic test. The only cylinder, which was deliberately selected for testing, was the corroded one.

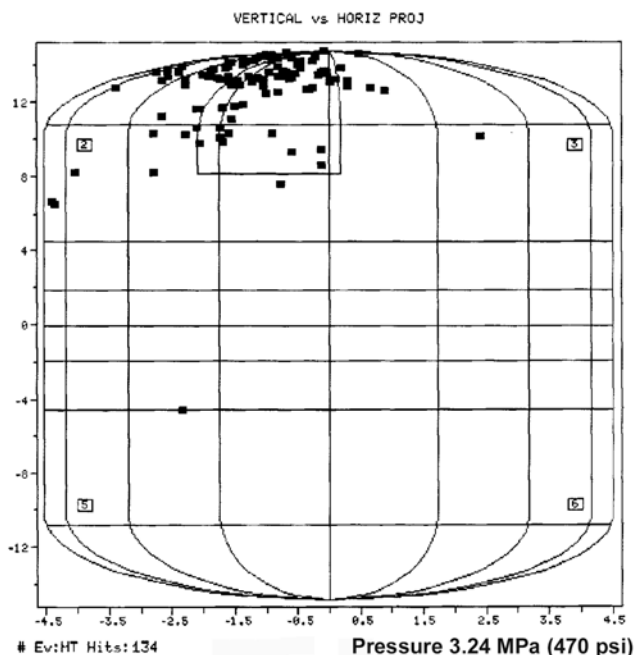


Fig. 8 Locations of AE sources on the corroded cylinder. First pressurization.

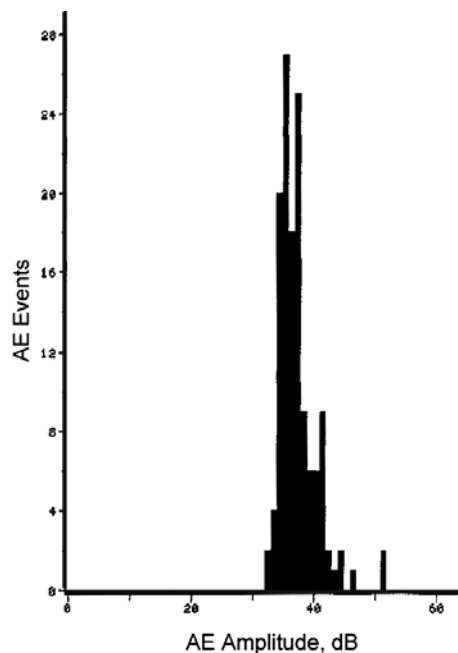


Fig. 9 Peak amplitude distribution of located AE at the first hit sensor.

At the beginning of the pressurization all of the cylinders produced low-level AE. This emission decreased in amplitude to below the 30 dB threshold below 4.2 MPa. All sensors were excited by this flow noise. However these randomly occurring signals never generated a sensor hit sequence with delta times which would locate on the surface of the cylinder. Two bottles showed a small gas leak in the piping connection to the valve at ~16 MPa. Again no locatable emission was produced by these leakage signals. Very few AE hits were seen above the pressures where the flow noise ended.

The final result of this testing was that none of the FedEx bottles produced any locatable emission at any pressure. During set up of the system, several pencil-lead breaks were done at the cylinders at 16.6 MPa (2400 psi) and all were located by the system. The results for the corroded cylinder were quite different. Locatable emission started occurring at 1.5 MPa (220 psi). The arbitrary safety limit written into the program was reached at 3.3 MPa (470 psi) and the program terminated the test automatically. In order to determine how badly the corrosion affected this cylinder, the pressure was released and the test was restarted. Locatable emission returned at 4.5 MPa (620 psi) and continued at a lower level until the last locatable emission occurred near 7

MPa. This cylinder was then quiet up to the maximum pressure of 16.6 MPa (2400 psi). Figure 7 shows the located emissions plotted against pressure for the first and second pressurization of this cylinder. Figure 8 shows the location of emission sources on one view of the cylinder. Visual observation of the interior of the cylinder had shown most of the corrosion to be near the top, in agreement with Fig. 8.

11. Discussion:

The locatable emission in the test of the corroded cylinder is attributable to corrosion particles fracturing or flaking off as the metal wall of the cylinder elastically expanded with increasing pressure. Once all of the particles which could be affected by the expansion of the cylinder had been affected, emission ceased. It is apparent that the corroded spots had no measurable effect on the strength of the cylinder. The test of this cylinder is important as it demonstrated that system is capable of detecting and locating AE produced by a cylinder. Figure 9 shows the distribution of peak amplitudes of the first hit sensor for these located events. The large majority have peak amplitudes which lie between 32 and 40 dB. It should be noted that 40 dB corresponds to peak amplitude out of the sensor of 100 μV . Therefore the system is locating well on signals with peak amplitudes between 30 and 100 μV . For a comparison, a pencil-lead break on one of these bottles generates a signal with a peak amplitude of approximately 70 dB or 3000 μV .

It is assumed that these cylinders are normally filled to a pressure of 12.8 MPa at 21°C. It is further assumed that these bottles will not exceed a temperature of 43.5°C in normal usage. The test pressure of 16.6 MPa is then 21% greater than the 13.7 MPa, which one of these bottles might reach at 43.5°C. It can be concluded from these tests that there was no microscopic crack initiation or growth in these cylinders at a pressure of 20% above the maximum pressure that the cylinder could have experienced in normal operation.

During the preliminary experiments on the development of the AE Oxygen Cylinder Tester, 7 cylinders, which had been retired from service because they had exceeded the DOT mandated life span of 24 years, were hydrostatically pressurized to 18.6 MPa. No emission was seen which could be attributed to the cylinder itself. One cylinder then had a depression etched in its side approximately 6.4 mm wide by 51 mm long by 2.5 mm deep. This cylinder was hydrostatically pressurized to 26.2 MPa. Again, no emission was detected from the cylinder. These preliminary tests support the conclusion that no evidence of any flaw growth was seen in these cylinders as well as the conclusion that these cylinders are quite conservatively designed.

12. Conclusions

1. The AE Oxygen Cylinder Tester will detect and locate AE signals from flaw growth in airline steel oxygen cylinders. The level of detection appears more than adequate to detect flaw growth long before there is any danger of rupture. A reproof test by an AE tester would give a greater margin of safety than a hydrostatic test.
- 2: The original premise of having the cylinders tested *in situ* in the airplane is impractical and probably not cost effective.

3. There was no indication at all of detectable flaws in any of the cylinders tested. Normal handling procedures in the airline industry appear adequate to prevent damage to these cylinders.
4. The three year inspection cycle for these cylinders does not appear necessary. Visual inspection of the cylinders when the valve is serviced should be more than sufficient to insure safety of the cylinders.
5. The arbitrary 24 year service life for these cylinders does not appear justified. A well maintained cylinder should have an indefinite life span.

Acknowledgement

The author would like to thank Kamran Ghaemmaghami of Federal Express for his counsel, encouragement and aide during the course of this program. Richard W. Anderson of the ATA has helped keep the program going despite setbacks. Paula and Ed Wilden were instrumental in setting up and conducting the testing program at AV-OX Inc. and David Croan of AV-OX did most of the actual testing.

The development of the Oxygen Bottle Tester was funded by the Air Transport Association. AV-OX Company provided space, materials and labor and were recompensed in part by Federal Express, which provided an extra fee to them for each cylinder tested.

Reference

1. Alan G. Beattie "An Acoustic Emission Tester for Aircraft Halon-1301 Fire Extinguisher Bottles," *Journal of Acoustic Emission*, **15** (1-4) 1997, 63-68.

DEVELOPMENT OF IN-SITU MONITORING SYSTEM FOR SINTERING OF CERAMICS USING LASER AE TECHNIQUE

S. NISHINOIRI and M. ENOKI

Department of Materials Engineering, The University of Tokyo,
7-3-1, Hongo, Bunkyo, Tokyo 113-8656, Japan.

Abstract

Acoustic emission (AE) technique is useful for in-situ detection of micro-fracture in materials. However, a piezoelectric sensor has a limitation in application at elevated temperatures because PZT has Curie point. We have investigated a non-contact AE technique using laser interferometer as a sensor. Cracking in firing of structural ceramics presents serious fabrication problems. Cracks form in the heating, sintering or cooling step of firing, and their initiation is strongly affected by shape, density, particle size and firing pattern. It is important to investigate when cracks occur for the optimization of firing condition. In this study, we firstly developed a non-contact in-situ monitoring system for firing of ceramics. We tried to monitor the cracking in firing of alumina (Al_2O_3) with the maximum temperature of 1600°C . A sample was heated in electrical furnace and probe beam was irradiated on surface of SiC disc inserted between the sample and the furnace through small opening. Developed monitoring system could successfully detect cracking in firing. This system can be applied to AE measurement of samples above 1500°C . It was demonstrated that laser AE system could detect internal cracks, which did not reach to surface of sample in firing process. This means that integrity of sintered ceramics may be ensured based on non-contact AE measurement.

Keywords: In-process monitoring, Laser AE technique, Firing, Ceramics, Alumina

1. Introduction

In recent years, the production of large advanced engineering ceramic parts has been needed for industries. It is very important to inhibit the generation of surface or internal cracks during firing of these ceramic components. These cracks are caused by several factors: one is a thermal stress due to uneven temperature distribution of a sample during heating or cooling. The other is the difference in shrinkage rates between the surface and interior of a sample during sintering. Therefore, it is difficult to optimize the firing of complicated ceramic parts from empirical findings. Our co-workers have investigated the strength and toughness of partially sintered alumina during firing [1]. It was reported that the strength and deformation behavior of alumina change dynamically during firing. Thus, it is difficult to predict cracking during firing. There are some references about the simulation for shrinkage of alumina during firing [2]. As actual cracking condition is complicated, in-situ detection of micro-cracks is useful in evaluating the failure of ceramics.

Acoustic emission (AE) technique is useful for in-situ detection of micro-fracture in materials. However, piezoelectric sensor has a limitation in application at elevated temperature because PZT has Curie point. Many studies have detected micro-fracture at elevated temperatures using waveguide and cooling of specimen near sensor for such experiments. However, the use of waveguide causes distortion of propagating waveforms and quantitative analysis of AE using

such modulated waveforms is difficult. In addition, contact of sensor may damage brittle or soft samples. Therefore direct detection technique applicable even at elevated temperatures is needed.

We have investigated a non-contact AE technique using laser interferometer as a sensor [3, 4]. Surface vibration can be detected as frequency shift of laser beam based on Doppler effect of light. The intensity of beat signal detected using photo diode is converted into velocity by modulator. Laser AE technique has some advantages: such as absolute measurement, applicability for measurement under severe environment and measurement at small areas. We applied this technique to monitoring of various failure processes and in-process monitoring of fabrication [5-7].

The first objective of this study is to develop a non-contact in-situ monitoring system for firing of ceramics. Then we monitor the cracking in firing of alumina with the maximum temperature of 1600°C, and investigate the cracking process of alumina during firing based on detected AE signals with single-channel inverse analysis of waveforms.

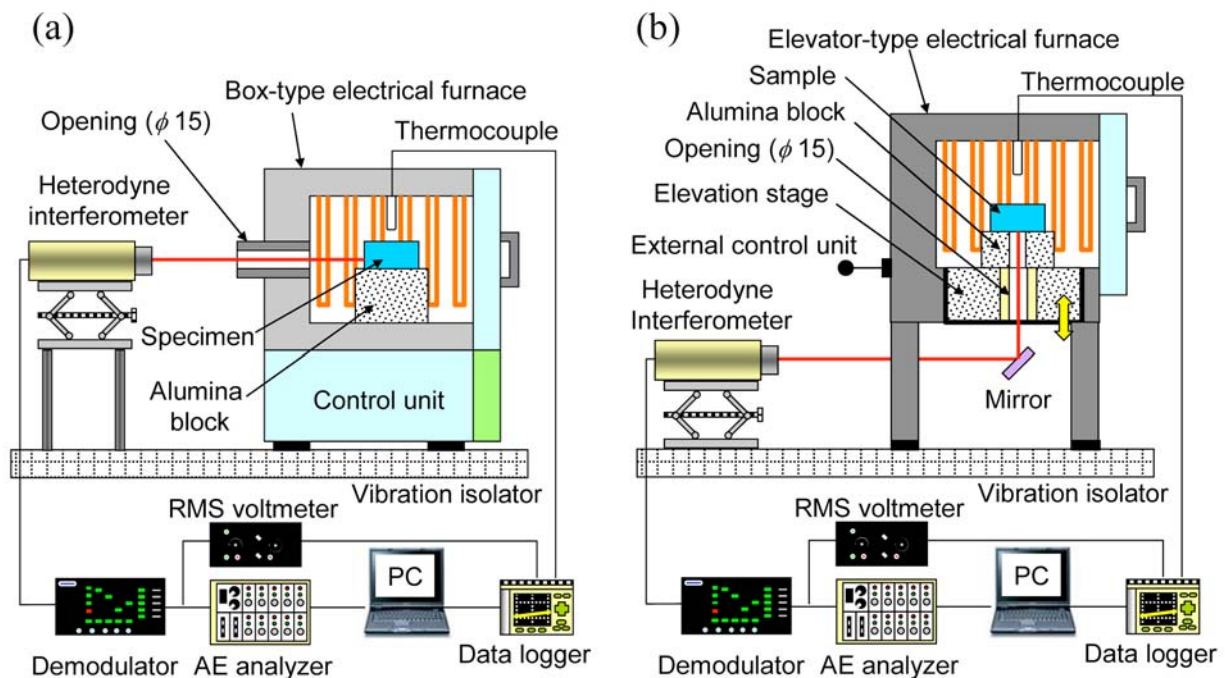


Fig. 1 Experimental setup for in-process monitoring of firing of ceramics using laser AE technique: (a) a side-detection system, (b) a bottom-detection system.

2. Development of Measuring System

2.1 Configuration of Measuring System

Figure 1(a) illustrates a side detection type system. Alumina compact was fired in a box-type electric furnace (KBF524N, Koyo Thermo System Corp.). Temperature control and measurement of the furnace were carried out using B-type thermocouples. Probe beam is irradiated to the side surface of a sample through a small opening (15-mm diameter) on a side of the furnace. AE events during the firing were detected using a heterodyne-type interferometer (AT-0022, Graphtec Corp.) as a non-contact AE sensor. Low-noise demodulator (AT-3600S, Graphtec Corp.) was used for the measurement of out-of-plane surface velocity with 1 mm/s/V sensitivity. In order to

reduce the noise level, output signals were filtered with a high-pass filter (HPF) of 500 Hz and low-pass filter (LPF) of 200 kHz. Detected AE waveforms were recorded by AE analyzer (DCM-140, JT-Toshi Corp.) with the velocity threshold of 0.15 mm/s. Filtered signals were also fed to a discriminator and then averaged signal (root-mean-square value (RMS) of the surface velocities) were recorded using a data logger (NR-1000, Keyence Corp.) with temperature inside the furnace.

We also developed bottom detection type system as shown in Fig. 1(b). Alumina compact was sintered in an elevator type electric furnace (NHV-1515D-SP, Motoyama Corp.), placed on an alumina block and on the bottom plane of the furnace. Probe beam is irradiated to the bottom surface of sample through an opening of 15-mm diameter. Other AE measurements and measuring conditions are identical to the side-detection system.

2.2 Evaluation of AE Detectability

Figure 2(a) shows the change in noise with temperature measured on the mirror-polished SiC plate using the side-detection system. Because of convection in the firing chamber and opening, noise increased with temperature. Periodic variation due to mechanical or electric noise was also observed. In addition, large deformation due to sintering may cause the defocusing of probe beam.

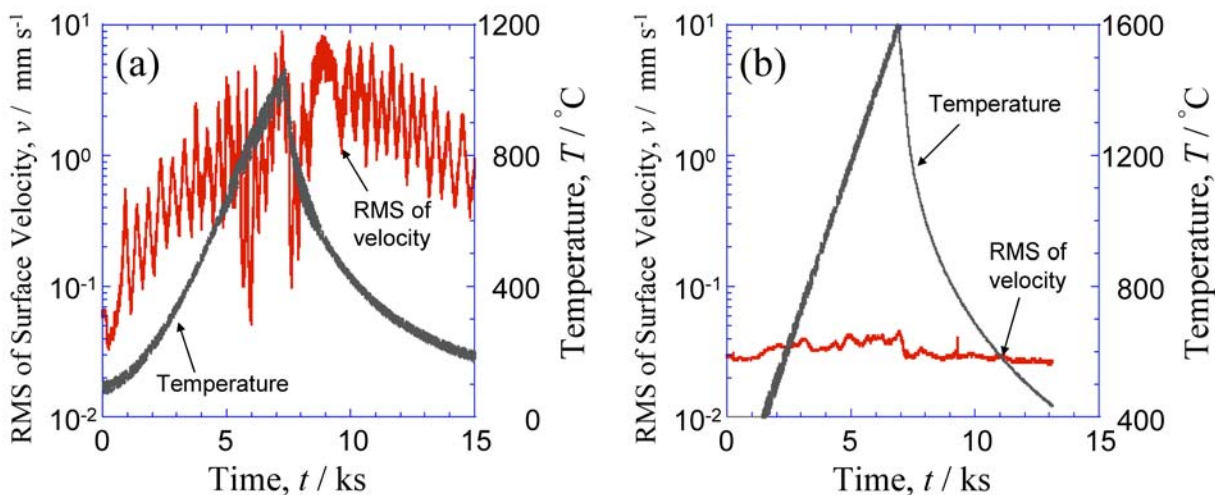


Fig. 2 RMS of surface velocity on measuring plane as a function of temperature in the furnace, (a) side-detection type, (b) bottom-detection type.

Figure 2(b) shows the change in noise with temperature measured on SiC plate using the bottom-detection system. This result is different from the RMS value of the side-detection system. There is no increase of noise even at elevated temperatures, and the periodic variation in noise disappeared. This means that the convection in the furnace does not affect AE measurement. In addition, defocusing of probe beam due to deformation during firing may be suppressed. Thus it was expected that directly detected AE signals at elevated temperatures with a lower threshold of recording was possible.

2.3 Final Setup for In-process Monitoring of Firing

There was still a serious problem in direct detection on alumina surface with the bottom-detection system. That is the warping of a sintered sample. The cause of warping was local

temperature distribution of the sample. We carried out several additional improvements of the system to reduce the temperature variation around the opening. SiC plate of 5-mm thickness was inserted between the sample and furnace, and the size of opening in contact to the SiC plate was reduced. From these improvements, the warping of a sample was successfully inhibited. Therefore, in-situ noncontact AE measurement in firing was conducted with this improved bottom-detection system.

3. AE Measurement during Firing

3.1 Preparation of Specimens and Firing Conditions

Two types of alumina, fine grain powders and mixed grain powders, were prepared as raw materials. The purity of each powder was 99.9 % and 99.5 %, respectively. Green compacts were formed by uniaxial press and cold isostatic press (CIP). All compacts were heated up to 500°C to remove binder. Then rectangular samples of 35 x 35 x 20 mm were cut out. Surface of samples were polished to surface roughness Ra of 0.8 μm. Unless otherwise noted, tested samples are smooth. In some samples a center notch of depth of 15 mm by a blade of thickness of 0.1 mm was machined.

Samples were fired in the elevator-type electric furnace. Maximum temperature was 1600°C. Heating rates were 800 K/h or 1600 K/h. After holding at 1600°C, samples were air cooled until room temperature. Holding time was 0, 30, 60 or 120 min.

3.2 Estimation of Microcrack Size

Single-channel inverse analysis was applied to estimate the microcrack size using a deconvolution method. In this study, the breaking of a pencil lead was used as the simulated AE signal source. With assumption of mode-I type penny-shaped cracking, the Green's function of the media was calculated from the simulated AE signal by the response waveform detected at the epicenter of the media and converted numerically to a dipole from the monopole source. The crack radius, a , was estimated as follows [3]:

$$a = \left(\frac{3(1-2\nu)D_0}{16(1-\nu^2)\sigma_0} \right)^{\frac{1}{3}} \quad (1)$$

where D_0 is the first peak of source function, σ_0 is the strength for microfracture and ν is the Poisson's ratio, respectively. Properties used in calculation were that of fully-sintered alumina ($\nu=0.23$, $\sigma_0=340$ MPa).

4. Results

3.1 Observation of Fracture

Figure 3(a) shows a fractured smooth sample after firing. Observation shows that cracks were initiated at the center of the sample and then propagated in a radial pattern toward edges. Figure 3(b) shows a fractured notched sample after firing. Cracks propagated to the bottom surface of the sample from the notch tip.

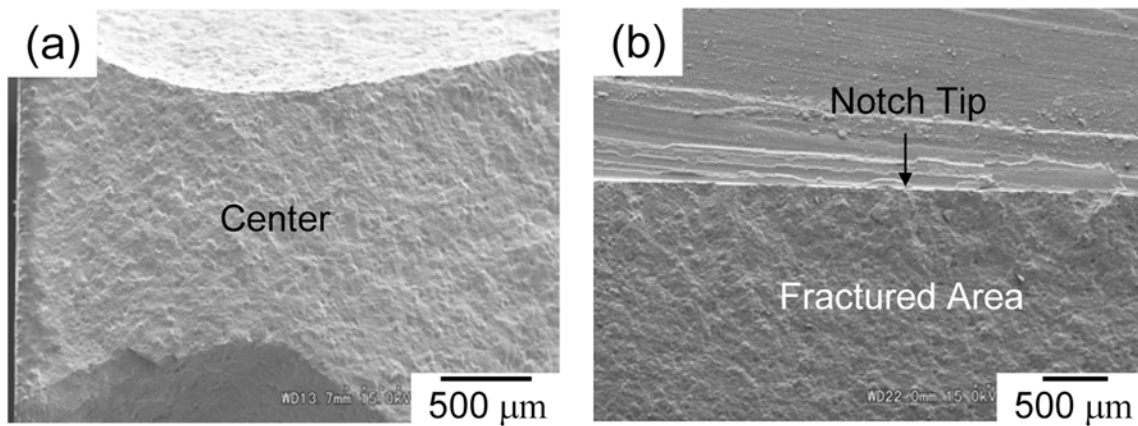


Fig. 3 Observation of fractured samples after firing; (a) a smooth sample, (b) a notched sample.

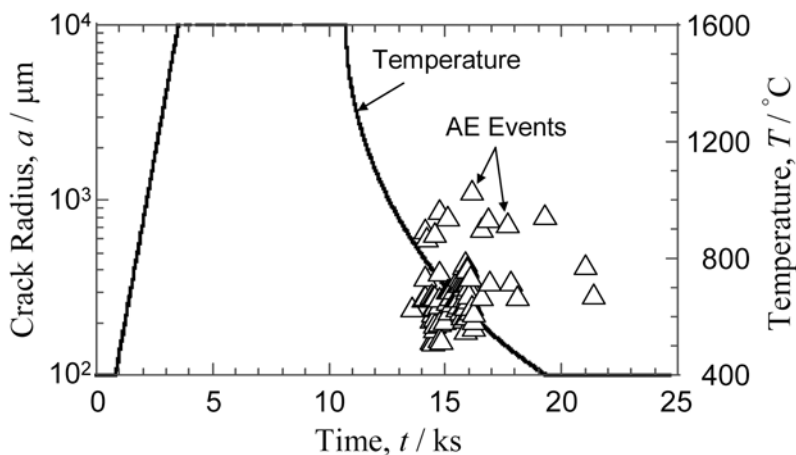


Fig. 4 Temperature history and crack radii as a function of temperature and time. The mixed-grain sample was fired with heating rate of 1600 K/h, holding time of 120 min.

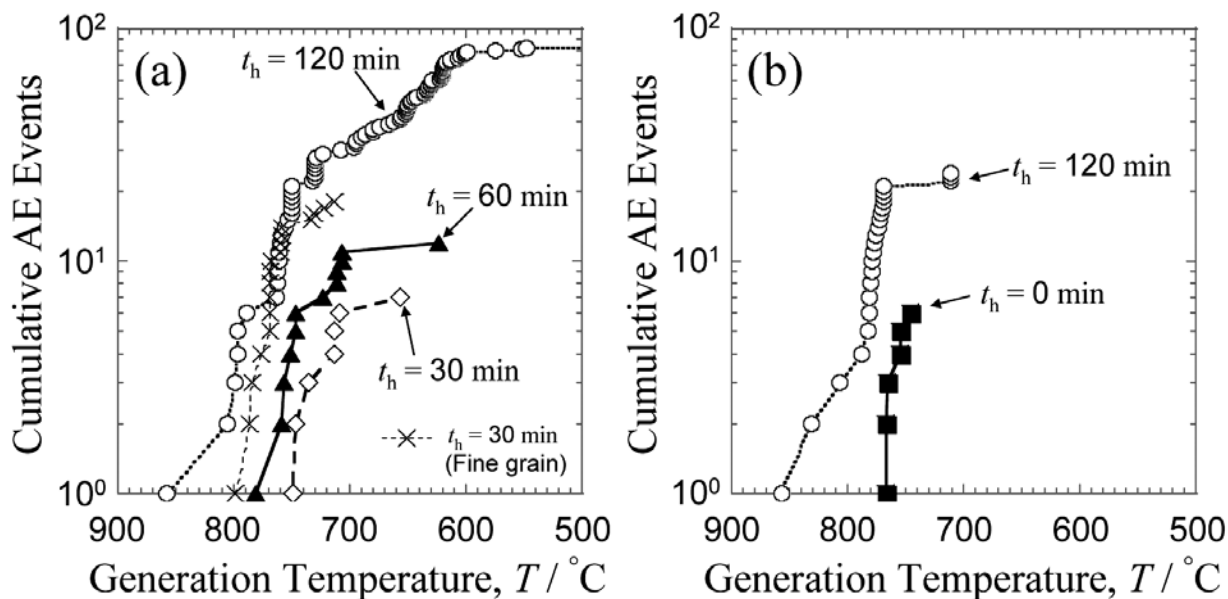


Fig. 5 Cumulative AE events as a function of generation temperature with different t_h ; (a) results of mixed-grain samples with heating rate of 1600 K/h, (b) results of fine-grain samples with heating rate of 800 K/h.

4.2 AE Behavior

Figure 4 shows a typical AE behavior during firing. AE events were detected only in brittle region (below 900°C) during cooling. Within tested firing conditions, no AE signal was detected during heating or sintering period of firing.

Figure 5 shows the change in cumulative AE events as a function of cooling temperature (AE generation temperature) for various holding time, t_h , at the maximum temperature. Generation temperature of the first AE event increased with the increase in holding time regardless of heating rate. Cumulative AE events also increased with the increase in holding time. Although AE signals were detected in samples fired with heating rate of 800 K/h and holding time of over 60 min, no surface crack was observed. Some of these samples cracked a few days later.

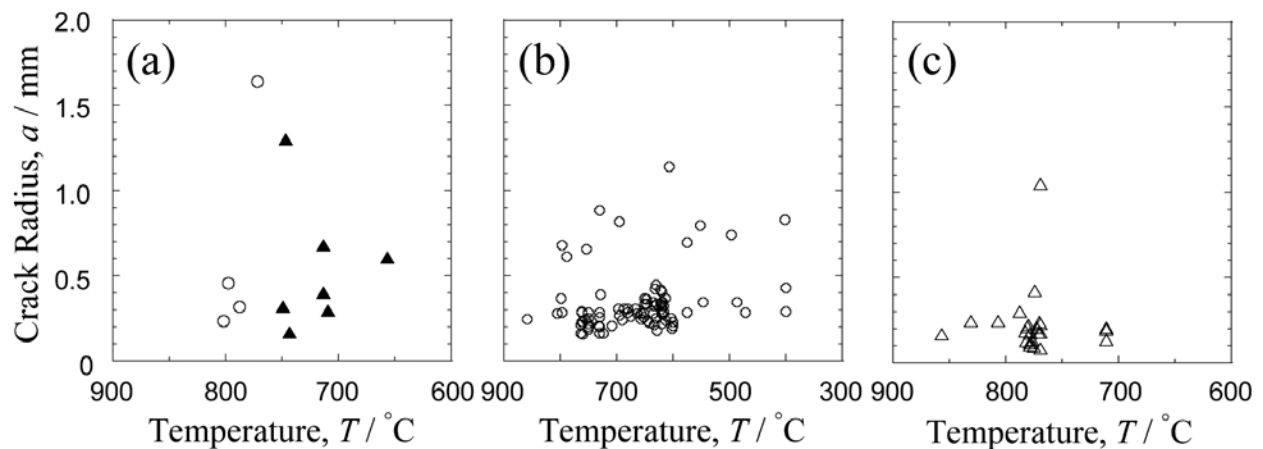


Fig. 6 Crack radius as a function of generation temperature of samples with different grain, heating rate, holding time and notch type; (a) mixed grain, 1600 K/h, 30 min, both notched (\circ) and smooth (triangles), (b) fine grain, 1600 K/h, 120 min, smooth, (c) mixed grain, 800 K/h, 120 min, smooth.

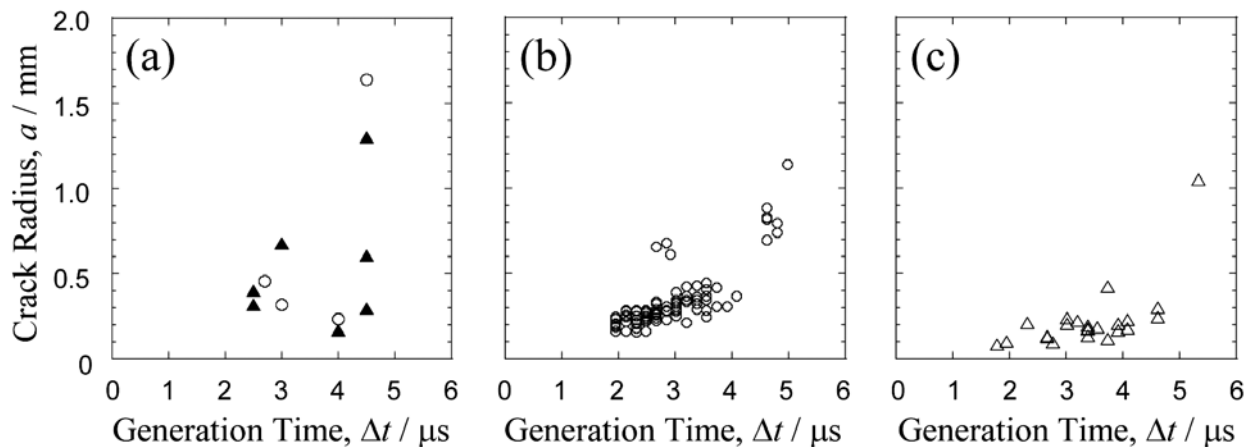


Fig. 7 Crack radius as a function of generation time. Firing conditions of the samples were same as indicated in Fig. 6(a-c).

Figure 6 shows the relation between generation temperatures of AE signals and crack radii estimated by the inverse analysis of AE. The generation temperature of the first AE of notched sample was higher than that of smooth one, shown in Fig. 6(a). No AE signal was detected in the notched sample after generation of the microcrack radius of over 1 mm, while some AE events

were detected in the smooth sample. Smooth samples with 120-min holding time in Fig. 6(b) and (c) also demonstrated a similar behavior, and many AE events with relatively small microcracks were detected compared with the case of 30 min. Most frequent crack size in Fig. 6(b) and (c) was about 250 and 300 μm , respectively. No visible surface crack was found in the mixed-grain, smooth sample (Fig. 6(c)) after firing, while the other samples were cracked after firing. Figure 7 shows the relation between crack generation time and crack radii. Microcracks with generation time of 1.5-5.5 μs were found, and larger cracks had relatively longer generation time.

5. Discussion

5.1 AE Detectability during Firing

As shown in Fig. 4, AE signals during cooling were successfully detected with the developed in-process monitoring system. Although the temperature of measuring plane of SiC plate reached approximately 1500°C during firing, it was demonstrated that AE signals could be detected even at elevated temperature using non-contact laser AE technique. As shown in Fig. 2(b), the change in noise level at the measuring plane through firing is small. If microcracks generate during heating or sintering period, they will be detected as well as microcracks during cooling period. As shown in Figs. 6 and 7, microcracks with radius of 150-1500 μm and generation time of 1.5-5.5 μs could be detected using the measuring conditions for long-term stable recording. Because observed surface cracks after firing were of the mm-order, the initiation and growth of microcracks seems to be detectable using this technique within tested firing conditions and geometry of the sample. Applicability for larger samples remains to be solved. As described above, AE signals were also detected when no surface crack was observed on samples fired with lower heating rates and longer holding times. This means that internal microcracks during firing can be detected using this technique.

5.2 Firing Conditions and Cracking Behavior

Because of stress concentration at the notch tip, the notched samples will be easily cracked. Therefore generation temperature of the first AE of the notched sample (shown by circles) was higher than that of the smooth sample (triangles), as shown in Fig. 7(a). In addition, only a few AE events were detected and no AE event was detected after the generation of larger microcracks in the case of notched sample. The difference in crack path of samples as shown in Fig. 3 can be described based on the difference in these AE behaviors. Several microcracks generated near the notch in the notched sample and then a main crack from the notch propagated through the specimen. Microcracks initiate in the center of specimen in the smooth samples and a crack gradually propagates toward the surface. Visible cracks on the surface may not be found in some sintering conditions because a crack does not reach the surface. Samples show a brittle behavior below the first AE event temperature because sintering of alumina occurs in ductile region above 1400°C. All samples, especially notched samples, fractured in brittle manner. This means that internal temperature distribution of samples is the dominant factor of cracking within tested firing conditions and geometry.

As the progress of densification during holding affects cracking behavior, AE behavior can be used to understand the relation between densification and fracture process. Shrinkage after firing increased with the increase in holding time, especially in the early stage of holding. As shown in Fig. 5, cumulative AE events and generation temperature of the first AE increased with the increase in holding time. The increase of densification causes the loss of stress relaxation in

relatively low densification range. However, the specimens were not fractured in the samples fired with heating rate of 800 K/h and holding time over 60 min, although AE signals were detected. Many AE signals were observed in the sample of Fig. 6(b) where a crack from the center reached the surface. A relatively small number of AE signals were found in the sample of Fig. 6(c) where no visible crack was observed on the specimen surface. AE signals corresponding to a crack size of around 250-300 μm were detected around 750°C in both samples. The further densification increases the fracture resistance and arrests the propagation of cracks to the surface. This laser AE technique is expected to find practical applications in detecting internal cracks, which cannot be observed in the surface.

6. Summary

- (1) In-situ monitoring system of firing of ceramics using a laser AE technique was developed and cracking in firing was successfully detected. This system can be applied to AE measurement of samples above 1500°C.
- (2) In the case of heating rate of 800 and 1600 K/h, micro-cracks due to non-uniform temperature distribution in a sample occurred during cooling period where the sample showed brittle behavior.
- (3) As the results of the inverse analysis of AE waveforms, it was demonstrated that cracking with radius of 150-1500 μm and generation time of 1.5-5.5 μs occurred in firing. Most frequent crack size was 250-300 μm .
- (4) It was demonstrated that the laser AE system can detect internal cracks, which did not reach the surface of the sample in firing process. This means that the integrity of sintered ceramics may be ensured based on non-contact AE measurement.

Acknowledgment

This work is supported in part by a Grant for 21st Century COE Program "Human-Friendly Materials based on Chemistry" from the Ministry of Education, Culture, Sports, Science, and Technology of Japan.

References

- 1) S. Nambu and M. Enoki: Key Engineering Materials, submitted.
- 2) N. Miyata, T. Shiogai, C. Yamagishi and Y. Matsuo: J. Ceram. Soc. Jpn., **106** (1998), 665.
- 3) M. Enoki, M. Watanabe, P. Chivavibul and T. Kishi: Sci. Technol. Adv. Mater., **1** (2000), 157.
- 4) M. Watanabe, M. Enoki and T. Kishi: Mater. Sci. Eng. A., **359** (2003), 368.
- 5) S. Nishinoiri, M. Enoki and K. Tomita: Sci. Technol. Adv. Mater. **4** (2003), 623.
- 6) S. Nishinoiri, M. Enoki, T. Mochizuki and H. Asanuma: Mater. Trans., **45** (2004), 257.
- 7) M. Enoki, S. Nishinoiri, T. Seki and A. Kishimoto: Key Engineering Materials, **270-273** (2004), 485-490.

PATTERN RECOGNITION TECHNIQUES FOR ACOUSTIC EMISSION BASED CONDITION ASSESSMENT OF UNFIRED PRESSURE VESSELS

ATHANASIOS ANASTASOPOULOS

Envirocoustics S.A., El. Venizelou 7 & Delfon, 144 52 Athens, Greece.

Abstract

The basic principles of supervised and unsupervised pattern recognition (PR) techniques for classification of acoustic emission (AE) data are presented herein together with successful applications of the techniques, for AE condition-assessment of unfired pressure vessels. The paper discusses the basic principles of supervised classification, consisting of a learning process, where representative AE data are used as examples to train a classifier for subsequent classification and automatic evaluation of unknown AE data. It also discusses the use of unsupervised PR, as a multidimensional sorting technique aiming to identify and separate noise-related AE (EMI, friction, mechanical impacts, flow noise) from legitimate AE. Strategies for validating the unsupervised PR outputs, as a mean to define the required training examples for supervised pattern recognitions, are investigated. Case studies from AE testing and PR analysis applied for the evaluation of pressurized vessels and reactors are presented. The advantages and limitations of the entire methodology are discussed in relation with conventional evaluation techniques. The feasibility of real time classification is considered.

Keywords: Pattern recognition, Structural integrity, Health monitoring

1. Introduction

Acoustic emission (AE) testing of unfired pressure vessels is usually performed during controlled stimulation [1] where mechanical or thermal stresses give rise to AE signals from active discontinuities. Most of the times, empirical techniques are used for noise identification and filtering, while evaluation of genuine emissions from filtered data is performed by means of codes and standards and in association with knowledge based systems [2, 3]. None of the codes and standards discusses in depth filtering process and in most cases the quality of AE data and noise filtering strongly depends on operator experience. Pattern recognition (PR) techniques are presented as an alternative and/or complementary AE data processing technique, to the well established knowledge based systems, aiming to help operators in noise identification and/or filtering as well as assisting the overall AE based evaluation of unfired pressure vessels.

The use of pattern recognition techniques for the analysis of AE data has been proposed the past decade in order to overcome limitations of conventional analysis techniques using single AE feature, such as amplitude, or using two-dimensional correlation plots. The initial applications of PR were limited to laboratory AE tests and research applications. Since then, the use of PR for AE data analysis in industrial applications has increased drastically [4-8]. The present paper outlines the basic principles of both unsupervised and supervised pattern recognition for AE data analysis and reports on some successful application examples of the technique, for AE condition assessment of unfired pressure vessels. Case studies from AE testing and pattern recognition

analysis applied for the evaluation of AE data from pressurized vessel [9, 10] and reactors are presented.

2. Acoustic Emission Patterns & Pattern Recognition Implementations

Pattern Recognition (PR) [11, 12] is the process, by which similarities between objects are recognized and weighted so as to distinguish alike objects. Recognition is a basic attribute of living organisms and mainly of human beings. Our everyday life involves the recognition of sounds, voices, faces, and any kind of objects around us. This is a complicated task based on sensory information acquisition (eyes, ears, etc), information processing and memory recall and finally comparisons, classification and recognition. Pattern recognition, as a branch of Artificial Intelligence, aims to develop theories and techniques, particularly suited for computer implementation, in order to transfer some of the human's intelligence on a machine. Speech analysis and recognition and ultrasonic signals classifications, for medical or NDT needs, are typical applications closely related with those of Pattern Recognition of AE signals.

The first, and very crucial, step in any pattern recognition application is the collection of the appropriate and good quality data to describe the objects. Any object can be described using a number of its characteristics (features). If the features used are not descriptive of the specific object, then, no matter how elaborate the applied pattern recognition scheme is, the result will be poor.

For most practical application, a pattern is a vector \mathbf{X} in a feature space. By this process of feature measurement and representation, we can think of an object or event abstractly as a point in an n-dimensional feature space as shown in Fig. 1. The collection of all the vectors (AE Hits or data points in general) forms the *Pattern Matrix*. Thus the *Pattern Matrix* contains the whole data set and is easily viewed in a data table format. The concept of the *Pattern Matrix* is shown in Fig. 2 where each row represents one *AE Hit (record, pattern vector)* composed of extracted features from the corresponding waveform.

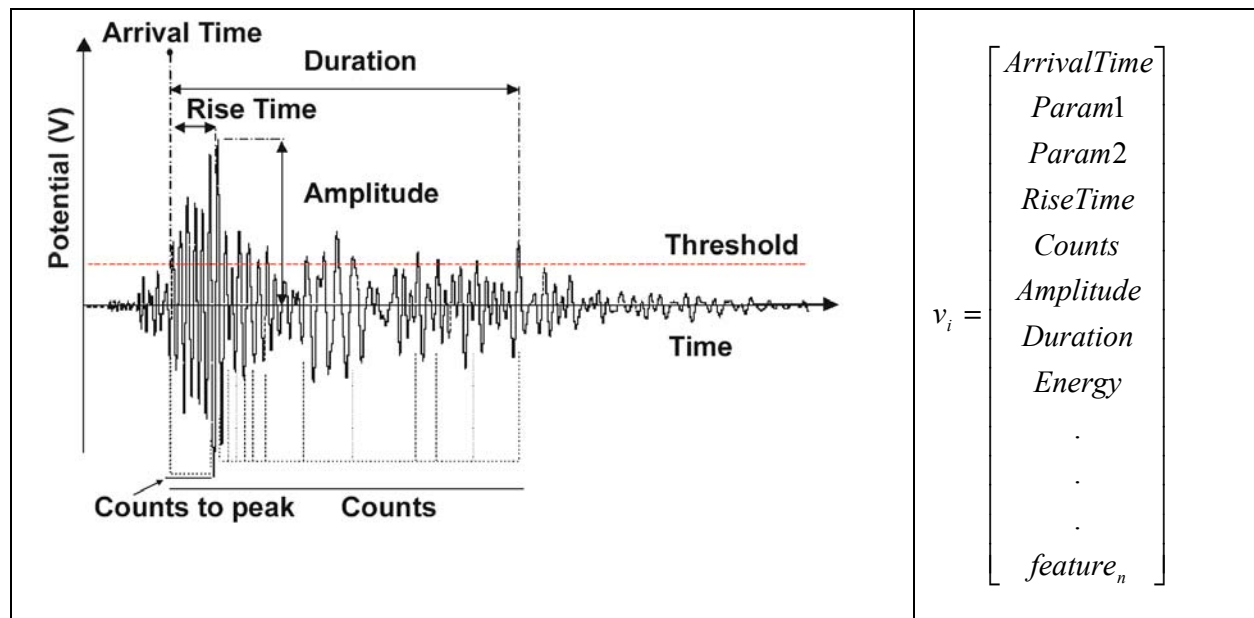


Fig. 1: Typical AE signal. Some of the features extracted are shown. The Features Vector for each AE hit (record) is the representation of that hit as a vector in n-dimensional space.

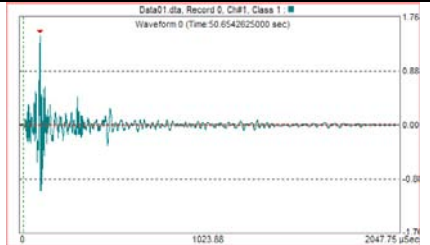
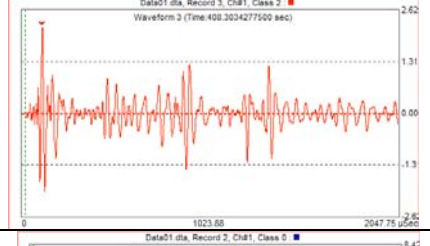
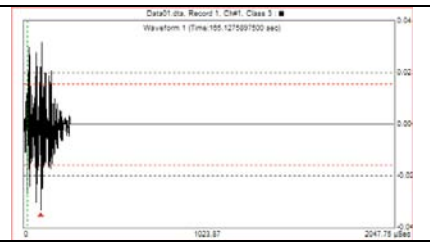
	Waveform ⇒	Feature 1 (Rise Time)	Feature 2 (Amp dB)	Feature 3 (counts)	...	Feature k (MARSE)
R1		89	83	79	...	157
R2		93	87	92	...	994
R3		249	97	19	...	155
...
Rn		76	52	11	...	2

Fig. 2: Pattern matrix of a typical set of AE data. Data No. = n, Feature No. = k.

Upon features extraction, the next step is pre-processing, i.e. to process the data in a usable form to compare with known data. Pre-processing includes additional features calculation (e.g. as a combination of extracted features), features selection (e.g. removal of confusing features or highly correlated features) and features transformation. Features normalization, is an important part of classifier design and pattern recognition in general. Normalization aims to scale features to the same range. Other transforms, such as zero mean or unit variance are also commonly used during normalization phase. Simple normalization actions (e.g. scaling) stretches or shrinks the axes in feature space (e.g. amplitude and counts will both range from zero to one instead of 40 dB to 100 dB and 1 to 65000, respectively) and might distort their geometrical shape (e.g. a spherical clusters of data points might get stretched into ellipsoid and vice versa). Within the framework of pre-processing, principal component projections might be used as well.

The next step in developing pattern recognition process for AE application, is the inter-comparison of the collected data to sort unknown objects in groups by similarity, or the comparison against a data base trying to match the object(s) with known. For the needs of applying pattern recognition during AE testing of unfired pressure vessels, pattern recognition is treated as pure classification process - assigning an input to a category called class - where:

- AE hits (Patterns) in the same class exhibit similar properties, and they are SIMILAR.
- AE hits (Patterns) in different classes, exhibit different properties, and they are NOT SIMILAR, they are DISSIMILAR.

Classification can be performed by two main methodologies:

- *Unsupervised Pattern Recognition* is the process by which objects are classified in general groups according to their similarity. This process does not require any previous knowledge or database. Objects are classified into groups by comparing their features and deciding upon their similarity. In such cases, the number of classes/categories must be estimated as well as a meaningful grouping of the data for further use as a training set during the classifier design.

The nature of AE (non-stationary signals, irreversible phenomena, such as crack propagation) implies the absence of *a priori* knowledge about recognition problem and "Unsupervised Pattern Recognition" techniques are usually employed [5-6, 12, 15].

- *Supervised Pattern Recognition*, which involves a learning process and where each new (unknown) set of data is processed and classified to one of the previously known and pre-defined groups by comparing its features to a database or using rules derived from the learning process. In this case, the Classifier design is a process of "Learning from Examples" and is called Supervised Pattern Recognition.

Applying Supervised Pattern Recognition in AE implies previous knowledge about the number of classes as well as a set of known examples from different AE sources (called also training set) to be used in the classifier design. Different Supervised Algorithms might be used, depending on the complexity of the problem as well as the required speed performance of the classifier. Among the different classifiers the simple minimum distance classifier, the linear classifier and the complex Neural Networks have been used for the classification of AE data [12-15].

Classification is a very elaborate step as the measure of similarity has to be chosen, the significance of each feature must be taken into account and ways to measure the effectiveness of classification have to be defined.

The case of Supervised PR, is relatively easier compared with Unsupervised, since it assumes that *a priori* knowledge exists in the form of representative AE hits from each signal class (training set). In this case, three general types of classifiers, able to realize a wide range of decision surfaces, are considered [12-14] named k-Nearest Neighbor Classifier (k-NNC), Linear Classifier and Back Propagation (BP) Neural Network.

- The first algorithm k-NNC, base its decision on direct distance measurements. The Euclidean distance D_{ij} of a test pattern \mathbf{X} from the j^{th} training pattern of the i^{th} class serves as a measure of similarity between patterns (where $\mathbf{X}^{(i)}$, $i = 1, \dots, N$, denotes a set of N training samples distributed in c classes, C_1, \dots, C_c). The k-NNC algorithm classifies the unknown pattern vector \mathbf{X} by assigning it to the class label most frequently occurring among the k nearest samples.
- In the second class of algorithms, multi-class *Linear Classifiers*, "c" linear discriminant functions, one for each class, are defined. The unknown pattern \mathbf{X} is classified to the class scoring the highest value among the c discriminant functions [11-14]. The weights involved in the linear discriminant functions are estimated during the training process using previously known examples.

- Finally, the *BP Neural Network* or artificial neural system (ANS) is characterized by its multilayer Perceptron topology where connection weights and processing element biases are modified using the generalized delta rule. The BP learning (or otherwise encoding) process is an iterative one and thus needs to be repeated until a satisfactory output is attained. Upon training completion, BP classification (recall) is done simply by introducing the new input vector to the ANS's input layer and computing the values towards the ANS's output layer. A complete description of the “plain” BP model used here is given by Simpson [16].

Concerning Unsupervised PR, data partition is performed by means of cluster analysis, which aims to separate the AE hits (pattern vectors) in a limited number of clusters characterized mainly by their mean pattern vector. Different clustering algorithms have been proposed to deal with the needs of various AE data structures and signatures [5, 12, 15]:

- a) Cluster Seeking/Wish,
- b) Max-Min distance,
- c) K-Means/Forgy,
- d) Isodata.

All the above mentioned algorithms use Euclidean distance as a measure of dissimilarity between pattern classes. The first two algorithms are heuristic and are based on the selection of a representative distance threshold by which the bound of each class is defined in the multidimensional space. The remaining two algorithms aim to minimize the square error for a given number of clusters based on an iterative procedure. From the different clustering algorithms, Wish, Forgy and Isodata implement heuristic procedures for creating new clusters and/or deleting small ones.

All the above algorithms clustering as well as conventional Unsupervised Neural Net algorithms [15] are influenced by the initial cluster selection and require multiple runs for the selection of the optimum clustering. Such instabilities are avoided by the proposed methodology [5, 12], which is based on the interactive coupling of Max-Min distance and Forgy algorithm. The modified Max-Min Distance algorithm implemented uses two starting clusters, which are selected as the point furthest to the mass center and the point furthest to the previous one. A new cluster center is created if : $D_{mi} > T_m D_{av}$, where D_{mi} is the maximum of the minimum distances between each pattern/AE hit to the existing cluster centers, D_{av} is the average between clusters distance and T_m a user specified parameter in the range [0,1]. The algorithm identifies cluster regions, which are farthest apart and therefore is particularly useful either for extreme noise condition identification or for the first approximation of initial clusters centers to be refined by Forgy algorithm. Forgy algorithm is an iterative procedure aiming to minimize the sum of squared error for a given number of classes. In the present study, the algorithm starts from the initial cluster centers previously established by Max-Min Distance algorithm. Nearest neighbor classification is applied to reclassify all the patterns followed by update of the cluster centers by calculating the mean vector of the resulting classes. The above procedure is repeated until convergence. In addition to that, heuristic procedures are implemented for controlling the number of classes:

- a. A new cluster is created if $|D_{avi} - D_{mi}| < T_f D_{mi}$, where D_{avi} denotes the average distance of pattern i to the existing cluster centers, D_{mi} is the distance of pattern i to the nearest cluster centre and T_f a user specified parameter in the range (0,1),
- b. An existing cluster is omitted if it is sufficiently small and composing with less than N_{min} patterns. This is the only way to decrease the number of clusters.

Further details on implementation of the clustering algorithms as well as on the estimation of the number of classes and the selection of optimum clustering the can be found in references [5, 12].

3. Limitations, Errors and Classifier Validation

What makes pattern recognition problems difficult is that there can be a large degree of variability of inputs that belong in the same class, relative to the differences between patterns in different classes; i.e. data is not really separable. Prior to deciding on the efficiency of PR methodology and validating the results, the following items should be clarified: “What does a class really mean?”, “Which clustering is valid?” and furthermore, “How many classes do we expect?” From the AE point of view one may expect the number of classes to be equal to the active failure mechanisms plus the detected noise sources. On the other hand, two failure mechanisms may be indistinguishable if they result in similar AE signatures, or one failure mechanism might result in two clusters. From the PR point of view, valid is any clustering identifying the structure of the data, while optimum might be considered the one maximizing the separability between classes. From the engineering point of view, valid is the methodology, which results in partitions that represent the physical phenomena. In any case, further validation should be performed by detailed evaluation of the respective cumulative hits of each class and comparison with conventional NDT methods and/or stress analysis.

For the needs of supervised PR analysis, the results are validated by means of overall classifier error or within-class error as revealed from the trial of the classification process in previously known examples. Universal classifier design rules do not exist and the entire PR methodology should be seen as an iterative procedure where each step; i.e., features selection, pre-processing, definition of training and test set, algorithm selection, is repeated and the overall performance is evaluated. In other words, a trial-and-error investigation should be scheduled. Causes of errors include inadequate or correlated features, complicated class boundaries or insufficient training set. In the first case, if the features do not contain the information needed to separate the classes, a different feature set should be investigated. For example it is a common practice to start the classifier design using well-known features such as hit amplitude, duration and energy. However, in case of poor results, alternative features from the frequency domain, such as frequency centroid or partial powers, might be investigated. The classifier design is complicated and its performance degrades in case two features are highly correlated, as it is often the case for AE counts and durations. On the other hand, the piece-wise linear decision surface produced by the linear classifier may not be sufficient for some problems necessitating the use of neural network, which in principle performs better in complex problems. However, when using neural networks, the size and the quality of training data will play an important role on the classifier design.

For the needs of unsupervised PR analysis of AE data (or for the definition of training set during unsupervised PR analysis), multiple runs of clustering algorithms are performed and the results are ranked in terms of separability and compactness of the resulting classes by means of numerical indices based on the within-class scatter matrix and the overall scatter matrix. Since unsupervised PR partitions are not uniquely defined resulting in multiple solutions [5], extensive validity studies should be scheduled.

Understanding that pattern recognition is not a panacea, the users should realize that the algorithms and respective software [15] offers all the necessary tools for evaluating the complexity of the problem and proceed with classifier design. However, measurement set-up and data quality are always the key issues.

4. AE Classifier Design - Demonstration Case Study

Three resonant frequency sensors (PAC-R15I, 150 kHz) were mounted on a thick metallic plate in a triangular pattern (320 mm X 540 mm). Four channels PAC-DiSP board was used for real-time data acquisition and NOESIS [15] PR software for the analysis and PR studies. Simulated AE signals produced by mechanical pencil-lead breaks (0.3 mm, 2H) at various positions on the plate. Mechanical friction simulated signals produced by sliding a small metal piece across the surface of the plate. Finally, electromagnetic interference (EMI) signals were generated by unplugging the sensor cable during acquisition.

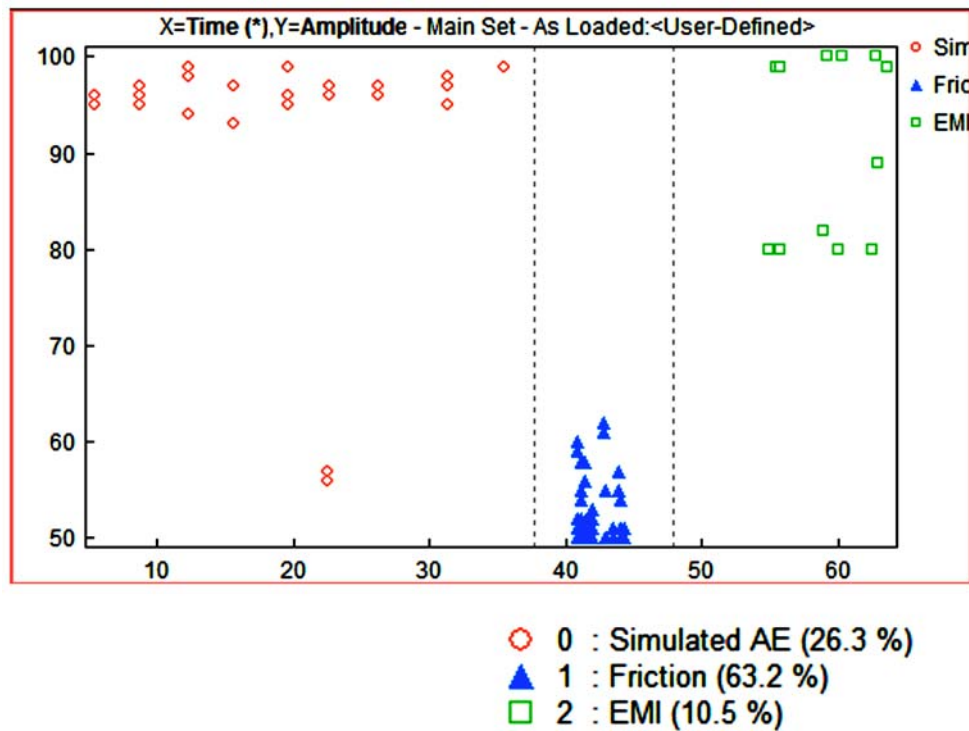


Fig. 3: Simulated AE used for Supervised PR example.

The time-amplitude plot of Fig. 3 presents the sequence of experimentation. Since the experiment was performed in a controlled way and representative AE hits – examples – from each signal class are available, the associated pattern matrix can be used for Supervised PR. In order to demonstrate a classifier design, the available data divided in two parts (at random) in training and testing set, are used to train and test the classifier. The various supervised algorithms available have both advantages and disadvantages [14].

For the demonstration needs of the present study a Back Propagation Neural Network was trained. The network topology is presented in Fig. 4. As can be seen the input layer contained ten nodes, representing the dimension of the pattern vectors, i.e., the 10 features used (Rise Time, Counts to Peak, Counts, MARSE, Duration, Amplitude, Absolute Energy, Frequency Centroid and Peak Frequency), the hidden layer contained three nodes, the same with the output layer. The three nodes of the output layer represent the three different classes of interest, i.e., Simulated AE, Friction and EMI. The network successfully trained, resulting 1.8% overall error, which represent 1 misclassified point (from AE class to friction class). The error is due to pure definition of the training set. More specifically the two low amplitude hits at time 22.5 sec (Fig. 3), were labeled and used in both training and test sets as simulated AE, although it represents a type of

friction at the time just before the pencil break. Deleting those two hits from the training and test set, a 100% recognition (0% error) was achieved.

Further optimization of classifier performance, aiming to improve classification speed without sacrificing accuracy, can be performed by reducing the size of pattern vector, i.e. removing features. A step-by-step approach of reducing the size of the pattern vector by one (using 9 features), repeating training and evaluating the overall and within-class error might be adopted. In any case, classifier stability should be evaluated by evaluating the classifier performance using different training-test sets.

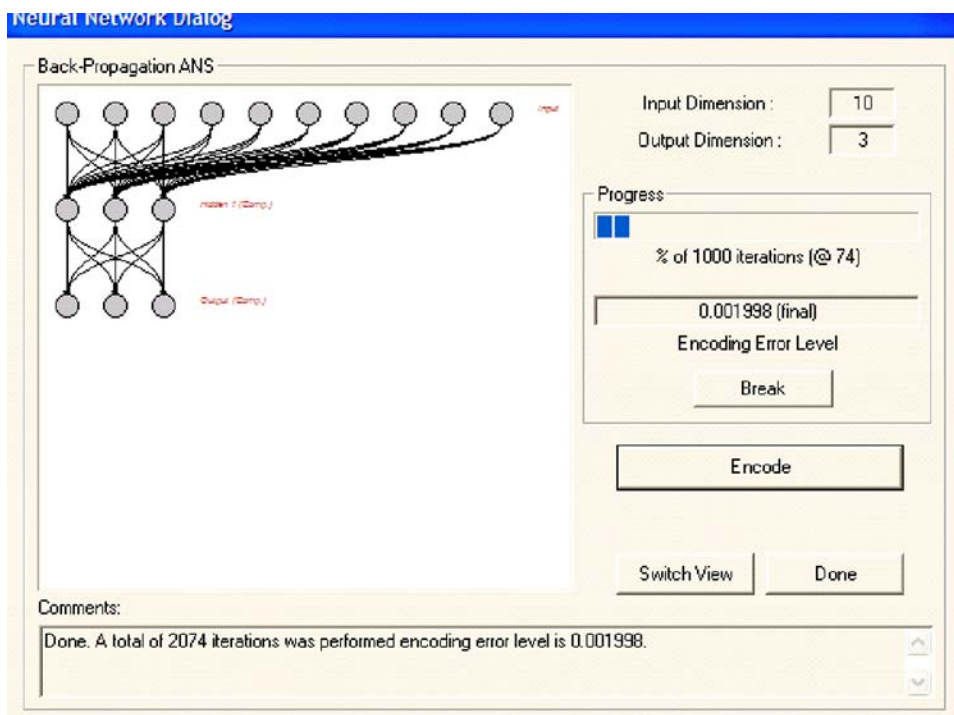


Fig. 4: Back Propagation Neural Network topology.

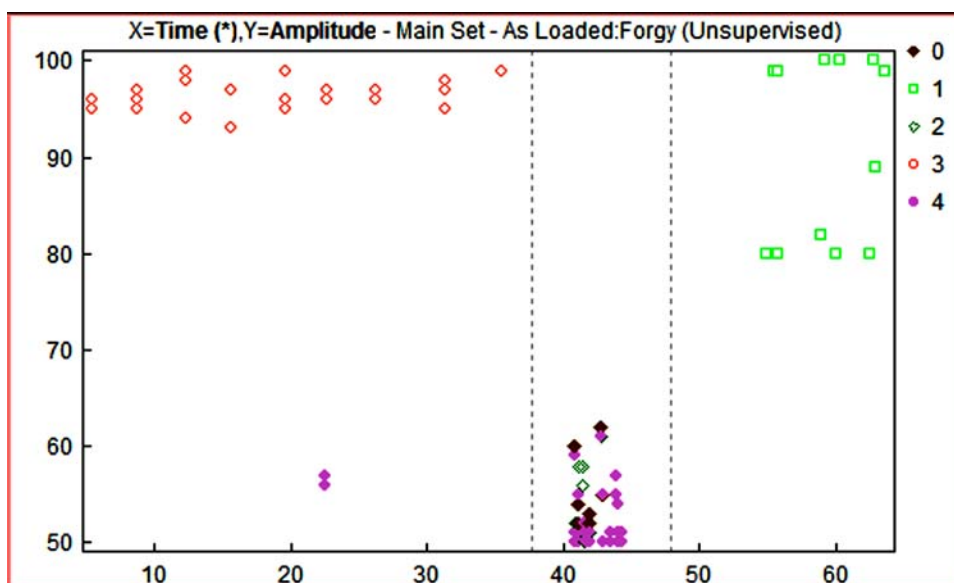


Fig. 5: Results of unsupervised PR applied on data of Fig. 3.

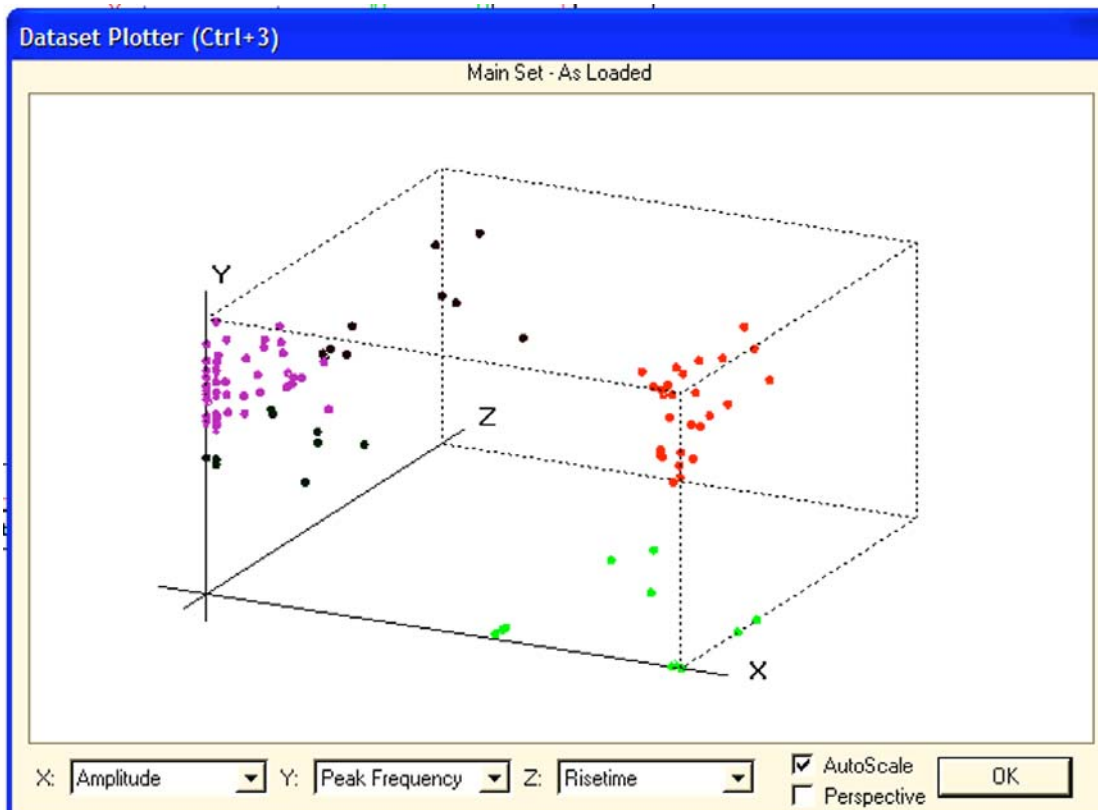


Fig. 6: 3D Scatter plot of unsupervised PR results.

Presuming that *a priori* knowledge about the data of Fig. 3 is unavailable, Unsupervised PR techniques are used in order to demonstrate the classification sequence. Following the unsupervised PR methodology, discussed in previous paragraph and presented in depth elsewhere [5, 12], the interactive coupling of Max-Min distance and Forgy algorithms resulted in the five different classes, as presented in Fig. 5. Close observation of the resulting partition indicates that all the data from pencil breaks were grouped together (named class 3 – red circles in this case) resulting in 100% recognition. Similarly the EMI data recorded from times greater than 50 sec, were all grouped together (named class 1 – green boxes in this case) resulting in 100% recognition. However, the AE data, due to friction – between 37 sec and 47 sec, were grouped in three different classes (named 0, 2 and 4 in Fig. 5). Close investigation of the 3D scatter plot of Fig. 6 indicates the wide scatter of friction-like AE hits when viewed in the rise time vs. peak frequency plane. In other words, grouping of these data in 3 different classes reflects hidden correlations, not expected from the pure AE point of view. It is worth noting that different results should be expected if a subset of the 10 features was used (for example using only Counts, Amplitude and Duration).

Validating the results is a complicated task and requires a great deal of intuition and experimentation. However, validity studies concerning the result of clustering algorithms are necessary in order to increase our confidence on the estimated number of clusters and to decide for the best partition of the data.

Once a desired clustering scheme has been achieved, the resulting partitioning can be used to automate the classification process on other data sets of similar-in-nature AE testing. This is by design a classifier, and we then have supervised PR.

5. Pressure Spheres–AE/PR Case Study

SPR was applied [10] on data acquired during hydrostatic pressure tests of three 19.7-m diameter, spherical pressure vessels. The tests were conducted per MONPAC procedure to a maximum test pressure of 16.5 bar. 49 PAC R15I sensors were mounted at the locations shown in Fig. 7. From the three hydrostatic pressure tests, AE data were acquired for two loading cycles. Additional data were collected; such as simulated AE sources at various locations around the vessels as well as impact noise data. Various noise sources appeared during each test (sliding of the fire-line supports on the vessels and the mechanical noise from bolts in new blinds and manholes). These AE data were mixed to provide a data set including all representative data types found in these tests.

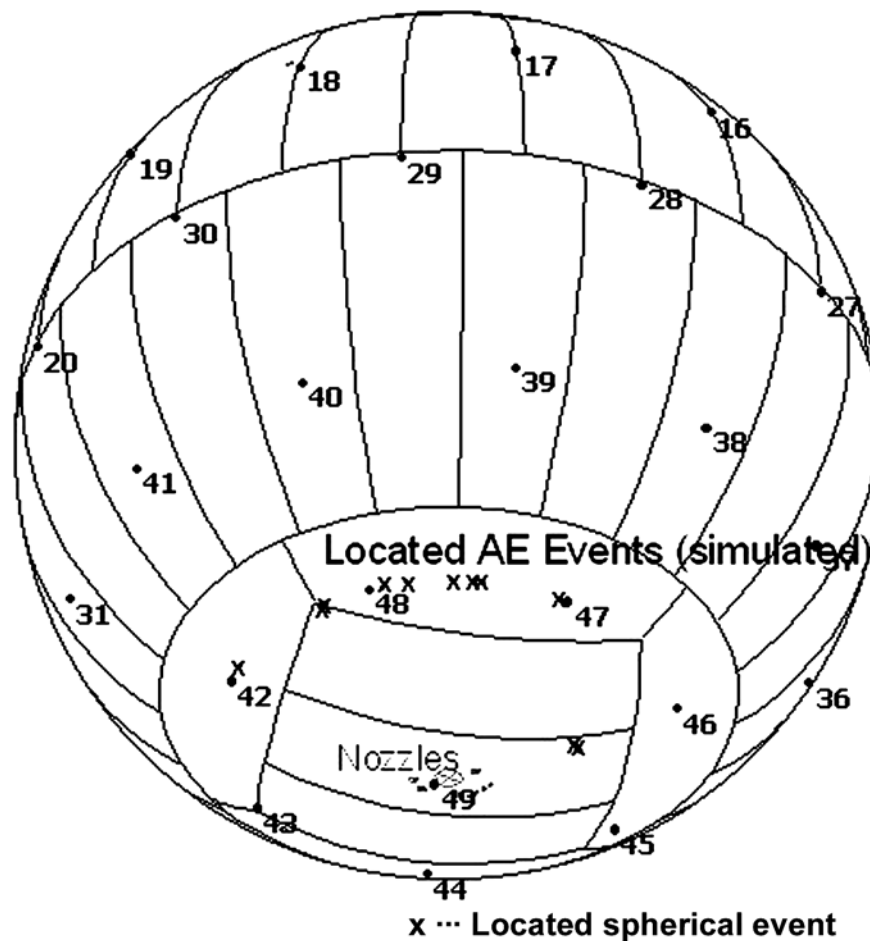


Fig. 7: Located AE events from the classifier output of the simulated and AE classes for sphere simulated AE sources data.

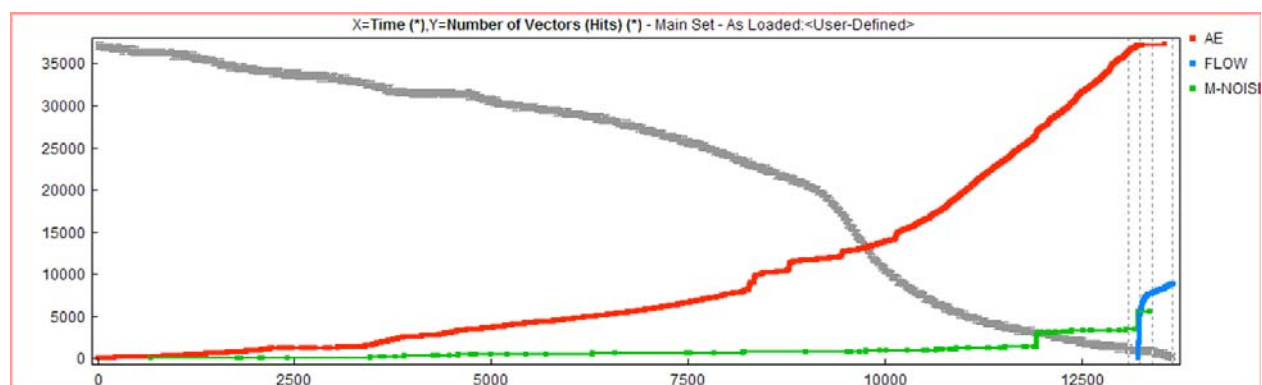
The data set created contained 3 classes:

- simulated sources and real AE,
- debris noise,
- impact and mechanical noise.

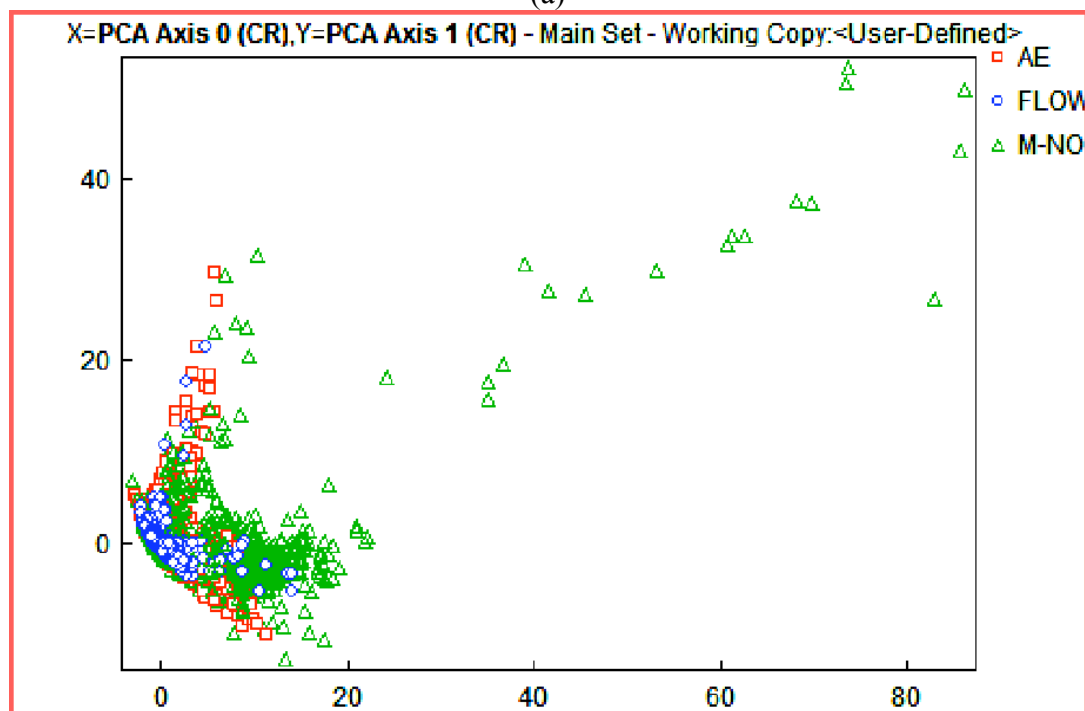
A k-NNC was trained to separate the data. A random half of the data was used to train the classifier and the rest were used to test the classifier. The testing classification error was 2.95% (87/2951 hits). It is worth noting, that statistical analysis showed that even in 7D space (7 features), it would not be mathematically efficient to separate the various types of data due to data

concentration at low feature values. To improve this, all features were converted by logarithmic functions and projected based on principal component covariance analysis.

Further analysis using spherical location techniques confirmed classifier performance as for example for sphere B, where debris noise existed while performing pencil breaks (simulated AE), the classifier recognized in the data all three classes. The data classified as Simulated AE gave good spherical location with 16% first hits, and 6.7% spherical events (required 3 hits for each spherical event) concentrated in the bottom section of the sphere where the simulated sources were introduced (see Fig. 7). Spherical location on the data classified as Debris Noise provided 65.9% first hits but only 1.5% spherical events. Most of the first hits were observed in channels from the top section of the sphere where the debris problem was encountered. Further application of the classifier to the actual test data showed similar results to the traditional analysis techniques for spheres C and D. For the case of sphere B it was the only method that provided meaningful results as attempts to analyze the data via traditional techniques failed to produce good results due to the complexity of the problem.



(a)



(b)

Fig. 8: a) Cumulative AE hits from three different hit categories Temperature variation superimposed. b) Principal components projection of reactor data.

6. Reactor Cool-Down – AE/PR Case Study

Eighteen PAC-R15I AE sensors were mounted on waveguides, on a triangular set-up, on a reactor vessel (O.D. = 3.3 m, L = 5.7 m, thickness 42 mm). AE was monitored during partial cooling down from 260°C to 170°C. AE data were originally analyzed by means of standard MONPAC practices. The results of conventional analysis using AE signatures are presented in Fig. 8a together with temperature variation (decreasing as a function of time – grey line). Among the three cumulative hits lines plotted in Fig. 8a, genuine AE (red line) can be seen well correlated with temperature variation while the remaining two categories not. The green line, active from the beginning of the test, corresponds to friction and mechanical noise, while the light blue line of cumulative hits, corresponds to flow noise at the end of the cool down, as confirmed by the operation department of the plant. The AE data were further analyzed by means of supervised PR using NOESIS [15] software.

During preprocessing stage, rise angle, initiation and reverberation frequencies were calculated [5, 12] and used as part of the pattern vector. Principal component projection (scatter plot of the 1st and 2nd principal components is presented in Fig. 8b) performed before the training of the k-NNC classifier. The overall error (misclassified hits over the total number of hits) was below 5%. However, an increase of within-class error, up to 19%, was encountered in some cases, depending on the training and test set used. In most of the cases of increased within-class error, flow noise signals were recognized as genuine AE. Confusion found also between friction and AE where friction and mechanical noise signals were classified as AE. Closer investigation on the classifier performance and the misclassified hits, indicated that the confusion was due to the secondary hits and reverberated signals, since the first hit (as revealed by zonal analysis) were classified successfully). Therefore, first hit analysis was applied as a preprocessing step. In this way, only the first hits were presented to the classifier resulting in overall error of less than 4% and within-class error of less than 7.5%. Overall the results show that supervised PR can be applied effectively for the classification of AE data during cool-down of thick-wall vessels.

7. Discussion

Pattern recognition techniques have proven as a fast and effective tool for AE data analysis from pressure vessels and reactors. Care, though, must be taken to understand the limitations of the technique so as to use it properly. Pre-processing should be considered as an important step in classifier design as well as the use of AE hits versus AE events (first hit only).

A generalized classifier applicable in all types of vessels cannot be designed. A number of reasons (e.g., sensors spacing or the use of waveguides, a variety of noise sources for test type, different source mechanisms etc.) limit such generalization. However, once a large database from similar tests is established, and once PR results are validated, the technique can be used for real time interpretation of AE data. Optimizing the speed performance of the classifier should be considered when attempting to use PR for real time data classification.

References

- 1) ASTM E569-02, “Standard Practice for Acoustic Emission Monitoring of Structures During Controlled Stimulation”
- 2) ASME, Section V, Article 12, “Acoustic Emission Examination of Metallic Vessels During Pressure Testing”, 1988.

- 3) Journal of Acoustic Emission, **8** (3) July-September 1989, 1-33, "Selection of 5 papers on MONPAC technology and applications".
- 4) R. W. Chan et al., J. of Acoustic Emission, **4** (4), 1985, 115-123.
- 5) A. Anastopoulos, T. Philippidis, J. of Acoustic Emission, **13** (1/2), 1995, 11-21.
- 6) T. Philippidis, V. Nikolaidis, A. Anastopoulos, NDT&E, **31** (5), 1998, 329-340.
- 7) D. Kouroussis et al., J. of Acoustic Emission, **18**, 2000, 217-223.
- 8) A. Anastopoulos et al., J. of Acoustic Emission, **18**, 2000, 224-230.
- 9) A. Tsimogiannis et al., NDT.net, Sept. 2002, **7** (09), www.ndt.net/v07n09.htm
- 10) A. A. Anastopoulos, A. N. Tsimogiannis, D. A. Kouroussis, *Proc. EWGAE 2002*, Vol. I, pp. 29.
- 11) J. T. Tou, R. C. Gonzalez, *Pattern Recognition Principles*, 1974, Addison-Wesley, Reading, Massachusetts.
- 12) A. Anastopoulos, PhD Thesis, University of Patras, 1995.
- 13) L. Schilemans et al., *Advanced Composite Materials*, 1993, **3** (1), 57-91.
- 14) A. Anastopoulos, et al., *Neural Computing & Applications*, 1999, **8**, 53-61.
- 15) NOESIS V 4.1, *Overview & Reference Manuals*, Envirocoustics S.A., 2004.
- 16) Simpson, P. K. *Artificial Neural Systems*, Pergamon Press (1990).

THE ACOUSTIC EMISSION HALON 1301 FIRE EXTINGUISHER BOTTLE TESTER: RESULTS OF TESTS ON 649 BOTTLES

A. G. BEATTIE¹ and D. D. THORNTON²

¹) Physical Acoustics Corporation, Princeton Junction, NJ 08550-5303, USA.

²) American Airlines Maintenance and Engineering Center, Tulsa, OK 74158-2809, USA.

Abstract:

The first commercial model of the acoustic emission Halon Bottle Tester has been in operation at the American Airlines Maintenance Facility, Tulsa OK for about two years. A data set of 649 bottle tests was reanalyzed with a FORTRAN program including all recent tester program modifications. Thirty-four bottles, 5.2%, failed the test. The analysis showed no reasons to modify the pass-fail criteria given in DOT-E 11850. Metallographic studies of some of the failed American bottles showed that the detected acoustic emission attributed to corrosion came from corroded regions on the interior of the bottles. The cause of the corrosion appears to be the deterioration of Halon 1301 in the presence of small amounts of water.

1. Introduction:

An acoustic emission (AE) tester for airline Halon 1301 (CBrF₃) fire extinguisher bottles was developed at Sandia National Laboratory under the sponsorship of the Federal Aviation Administration (FAA) and the Air Transport Association (ATA). After extensive testing at two bottle manufacturers' testing and repair facilities, an exemption to allow its use on commercial aviation bottles was given to the ATA by the Department of Transportation. Physical Acoustics Corporation (PAC) produced a commercial version of the tester and sold the first machine to American Airlines, which had it installed in its Tulsa Maintenance Facility. This machine has been in operation for about two years and, despite several unexpected problems characteristic of new technology, has tested almost 500 Halon bottles to date. The original pass-fail criteria built into the tester and the DOT Exemption were based upon a data set of 208 bottle tests. To this original data set, the tests of about 475 bottles by American Airlines were added. This combined data set was then examined and slightly culled to arrive at a data set covering 649 tests.

The Halon Bottle Tester writes a data file for each test containing the raw data before any analysis by the AE system. All of these files are stored on compact disks. This allows post-test analysis using any desired methodology. During the commercialization of the test system, a series of minor modifications to the original Halon Bottle test program have been made. To assure that all data was treated equally, an analysis program was written in FORTRAN, which included a series of small changes incorporated in recent commercial version of the tester program. This FORTRAN program was used to analyze all data sets. Because of this accumulation of minor program changes during the commercialization of the tester, the classification of three of the bottles, whose test results placed them right at the pass-fail boundary, changed, one from pass to fail and two from fail to pass. Such a discrepancy can be expected any time arbitrary criteria are used. The original criteria were set at a level where it was expected that all bad bottles would fail and a few good bottles would be rejected. All indications are that these expectations have been met.

2. Test System

The AE Halon Bottle test system has been described in some detail [1]. It is based on a PAC six-channel Mistras AE system. The program is unique to the Halon tester. It controls the loading, collects and analyzes the AE data and evaluates the results, giving a pass or fail grade to the bottle at the end of the test. The test load is applied to the bottle by heating it in an industrial oven up to a surface temperature of 65.6°C. This temperature produces a pressure, which is roughly twice the fill pressure and is more than 140% of the pressure at a maximum expected operating temperature of 43.5°C. After the oven heaters and fan are shut off, the bottles are held for five minutes to allow the temperature of the contained Halon to reach equilibrium with the bottle surface. The final temperature of the Halon is between 64° and 65°C. At the end of the test, the system prints a report grading the bottle and giving the locations with respect to the sensor locations of the suspect regions if the bottle has failed the test.

All AE signals during the heating cycle and hold period are detected down to a threshold of 25 dB (18 μ V from the sensor). The AE system records the signal arrival time (to an accuracy of 0.25 μ s) and several signal parameters for each AE signal detected by a sensor. Each sensor can detect up to about 500 signals per second, depending upon the signal length. The waveform of each emission is also recorded. The computer program then looks for groupings in time of the detected signals. All signals detected within a time period equal to 120% of the time that it takes for a flexural-mode AE signal to travel half way around the sphere are grouped into an event data set. If the data set meets certain criteria, such as each sensor only being excited once and at least four of the six sensors being excited, a nonlinear least-squares fitting routine attempts to calculate the location of the signal source on the sphere. The use of an over-determined data set (mathematically only three sensors have to be hit for exact location) results in the calculation of the most probable location for that set of data. The accuracy of the location is dependent upon many factors. The two which have the most influence on when the system triggers for each arriving AE signal are the initial amplitude and the physical conditions in the bottle wall along the shortest paths to each sensor. Doubler plates, tack welded on the external surface containing attachment fixtures and ports for gas fill or exhaust will distort the waveform of AE signals passing under or near them. This can result in the system triggering on different points of the waveform at different sensors. The program uses both the over-determined data set and other features such as weighting the data points based upon signal characteristics to overcome some of these problems but there is always some ambiguity in the location accuracy. On a test specimen without attached surface features, such as a gas cylinder, the location accuracy can routinely be ± 1.6 mm, but on Halon Bottles the location accuracy is partially dependent upon the relationship between the position of the source and that of the surface features. The accuracy usually falls between ± 6.4 and ± 18 mm. The location routine succeeds in finding a location on the surface of the sphere for between 70 to 90% of the signal groupings. The main reason for failing to locate a source on the surface is triggering at quite different places on the waveform at the different sensors, resulting in either totally wrong arrival times or the determination of arrival times at different sensors from different acoustic modes.

The analysis program is not based on the individual AE signals but on the located AE events. A basic assumption is that AE signals produced by the same growing flaw will have their sources all located in the same region on a specimen. Therefore, one should search for a spatial clustering of the emissions. In this program, as each event is located, it is checked to determine whether it is a member of a cluster of events. A cluster is defined in the program as two or more events located within a circle on the surface of the sphere, whose radius is 15° of arc (0.26 times the

radius of the sphere). This definition of a cluster removes the influence of sphere size from the analysis. The program tracks how many events are included in each cluster and the temperature, at which each event occurred. The slope of the curve for the number of events as a function of temperature is monitored for each cluster. The pass-fail criteria are based upon the number of events contained in a cluster and the behavior of the slope of the events vs. temperature curve for the cluster.

3. Rejection Criteria

Acoustic emission can be generated by a wide variety of mechanisms. For aircraft Halon bottles, the two most likely mechanisms are crack growth and corrosion. These two mechanisms show somewhat different patterns in the generation of the emission. In crack growth a crack tip advances in discrete jumps when the local stress field exceeds the level necessary for crack advance. These jumps are small, usually involving one or two metal grains to start with but they produce detectable bursts of AE. In stable crack growth, each jump decreases the local stress field enough so that the crack arrests until a further increase in the applied load brings the local stress field back to a level sufficient to produce another crack jump. This behavior appears as an apparent steady AE event rate as a function of increasing load. As the crack grows, it will reach a point where each jump not only decreases the local stress field but also decreases the strength of the surrounding material. At this point, the jump rate and thus the emission rate starts to increase in an exponential manner. This condition is unstable crack growth and will result in fracture of the specimen if the loading is not reduced or stopped. If the increase in the external load is slow, the exponential increase in the AE rate can usually be detected long before failure occurs. Thus an AE rate, which is constant with load increase, is indicative of stable crack growth while an increasing rate with load increase is a sign of unstable crack propagation.

The term corrosion, as one might expect, covers a large variety of conditions. For steel bottles there are at least two different types of corrosion. In alloy steels such as AISI4130, small patches of corrosion can form on the interior surface of the bottles. When the bottle wall is strained by pressure loading, the corrosion product can either fracture or pop off of the surface. Either process produces large bursts of emission. A characteristic of this type of corrosion is a high initial emission rate, which decreases as an increasing percentage of the corrosion products are affected by the strain. After a certain load level is reached, all emission will cease. This type of corrosion is usually not seen in stainless steels. However, these steels can be etched by an acid attack. If the acid attacks the grains preferentially, either with respect to composition or orientation, one will end up with a rough surface and possible pitting as the acid follows either the grain surface boundary or the grain itself down into the base metal. The application of a strain to such a surface may cause many small fractures at weakened grain boundaries or dissolved pits in the surface. These fractures produce detectable AE. Again, the probability of fracture of any defect will depend on the local stress field. The difference between controlled crack growth and the etching corrosion is the larger number of potential fracture sites produced by the corrosion. The emission rate from this type of corrosion will be proportional to the strain and thus the applied load. This should produce a roughly constant emission rate for a constant loading rate. Another possibility for this surface corrosion is that there may be coalescence of the small surface cracks, which can lead to unstable crack growth.

This discussion predicts three types of characteristic emission behavior for three different sources of the emission. Small patches of surface corrosion produce an emission rate, which may be high initially but falls off with an increasing load. Such surface corrosion has little effect

on the strength of a bottle. Etching corrosion and controlled crack growth produce an emission rate linearly proportional to the loading rate. Small amounts of either are relatively innocuous to the bottle. Unstable crack growth will produce an emission rate, which can increase exponentially with respect to the loading rate. Such a crack will inevitably lead to failure of the bottle if the load is not reduced or removed. However, the AE rate usually predicts imminent fracture far enough in advance to enable a test to be stopped before catastrophic failure occurs.

By locating the source of each burst of emission, the growth rate of the individual flaws can be estimated. The decreases in the local stress field with crack advance will often restrict activity to a single crack in a local region. The amplitude of each emission is related to the volume of the growing crack. However, by the time an AE signal reaches a sensor and is detected, the exact waveform is determined by the characteristics of both its source and the details of the path it travels to the sensor. A study of the characteristics of all waveforms detected by sensors from a single event can give information about the event but this is not a process easily automated, especially for a wide variety of waveforms. Therefore, the information that is used in the grading of a Halon Bottle in this tester is the existence of located events; whether they form local clusters with other events; what is the number of events contained in a cluster and what is the event rate as a function of load for the cluster. By focusing only on located events, the effect of the fine details of the waveforms at different sensors is minimized and external noise becomes a nuisance instead of a severely limiting factor.

Two concepts are used in setting the failure criteria for the Halon Bottle Tester. First: the size of a flaw is roughly proportional to the number of emission bursts produced. Second: the severity of a flaw is proportional to the rate of increase of the number emission bursts in the cluster with increase in load. A simple method is used to determine when the rate of bursts versus load is increasing as a function of load. The number of cluster events occurring above 54°C is divided by the number of events occurring between 43° and 54°C. If this rate ratio reaches 3.0 or higher, it indicates that the burst rate is undergoing an exponential increase and that uncontrolled crack growth is occurring. By applying these concepts to the original set data set of 208 tests, a failure criterion for growing cracks was set. It is that a cluster of AE events having 18 or more members and a rate ratio of 3.0 or higher has failed the test. The failure criterion for controlled crack growth and corrosion is based only on the number of located events in the cluster. Any cluster containing 35 or more members irrespective of the value of the rate ratio fails the test. It must be stressed that these criteria are arbitrary and are based upon the experimental results from 208 bottle tests by the prototype system. They were in no way meant to apply to any other type of test or AE system. Any major change in the Halon Bottle Tester or its software would require a new set of pass-fail criteria.

4. Data Sets

Two separate data sets were combined for this study. The first is the original data obtained during the development of the system and used in setting the pass-fail criteria quoted in the Department of Transportation exemption DOT E-11850. The second set is data obtained between February 2002 and October 2003 from the commercial Halon Bottle system at the American Airlines Bottle Shop, Tulsa OK. The original data set was obtained at the Halon Bottle repair facilities of Walter Kidde Aerospace in Wilson NC and Pacific Scientific Company in Duarte CA. These sets were combined and the data then culled in the following manner. First: a test had to either complete the full temperature cycle, 66°C plus a five minute hold, or had to continue until an automatic safety provision stopped the test due to excess emission in a cluster.

Second: any test, which did not detect a single emission was rejected. There were only eight such tests, most in the original data set. Despite an Automatic Sensor Test, which had to be passed before any bottle test could start, the absence of any AE raised a question as to whether the system was working correctly. Third: only data from steel bottles was included. Both of the sets contained data from some titanium bottles. However, recent testing at American has raised questions about the results of tests on titanium bottles. Therefore, only data from bottles made of various steels was included.

Most Halon bottles are spheres but there are three models of elliptical Halon bottles. They consist of two hemispheres with a short cylindrical section centered between them. It had been determined that the elliptical bottles with a 38-mm-wide center section could be tested successfully in the spherical fixture with the spherical program. Nineteen of these tests are included in the data set (three of them failed the test). However, 12 data sets from bottles, which had 76-mm and 127-mm cylindrical sections, were excluded because they required a different fixture and program to analyze them. The sizes of the Halon spheres included in the data set ranged from 170 to 356 mm in diameter. The elliptical bottles had a diameter of 356 mm. Most of the bottles were made of Nitronic stainless steel (21-6-9). Some of the older bottles were made of Almar, some of 4130 steel and a few bottles of unknown stainless steel. No significant differences in the test results were seen between these materials.

No AE testing has been done on new Halon Bottles. All tested bottles had either been removed from an aircraft or had been warehoused as a spare part for many years. No attempt was made to determine the age of these bottles. The majority of the bottles is currently owned by either FedEx or American Airlines but bottles, which were or are owned by other airlines, were included in the data set. Most of the bottles were manufactured by either Walter Kidde or Pacific Scientific but some of the older bottles were made by companies which have been sold or are no longer in business.

Table 1 Distribution of located events per bottle.

Number of located events per bottle	Number of bottles	Percent of total bottles
0	160	24.7
1 - 10	345	53.2
11 - 20	45	6.9
21 - 30	31	4.8
31 - 40	11	1.7
41 +	57	8.8

5. Analysis

The failure criteria are based only on the located events. Table 1 shows a rough distribution of the number of events per bottle without considering their location. Almost one fourth of the bottles had no locatable events and half the bottles had between one and ten locatable events. After 30 events per bottle, the distribution drops off to along tail with an upper end at 588 events for a bottle. The number of located events per bottle could be used as a simple pass-fail criterion but with the locations of the sources available, better criteria can be developed.

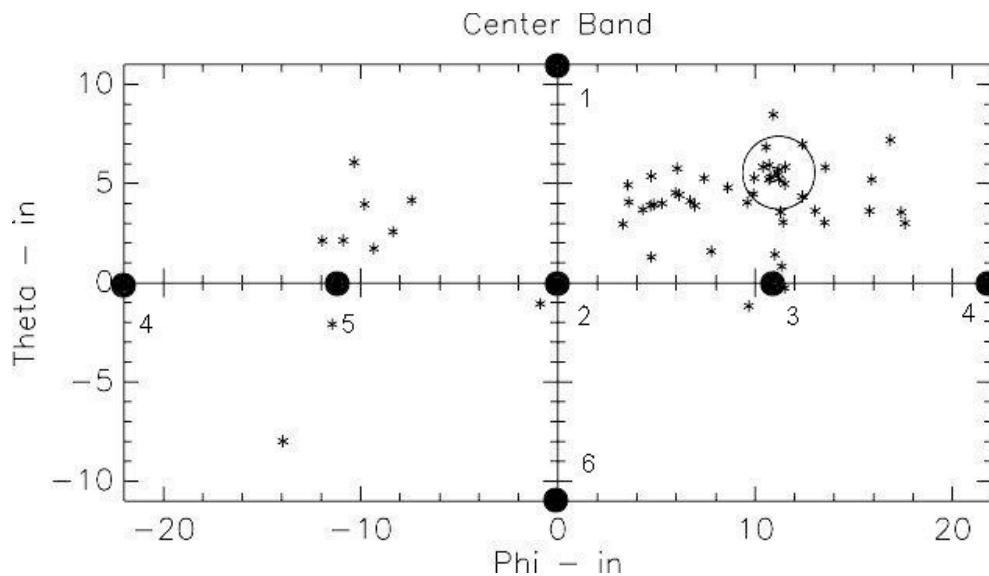


Fig. 1 Location of sources on Bottle HTAL0875.

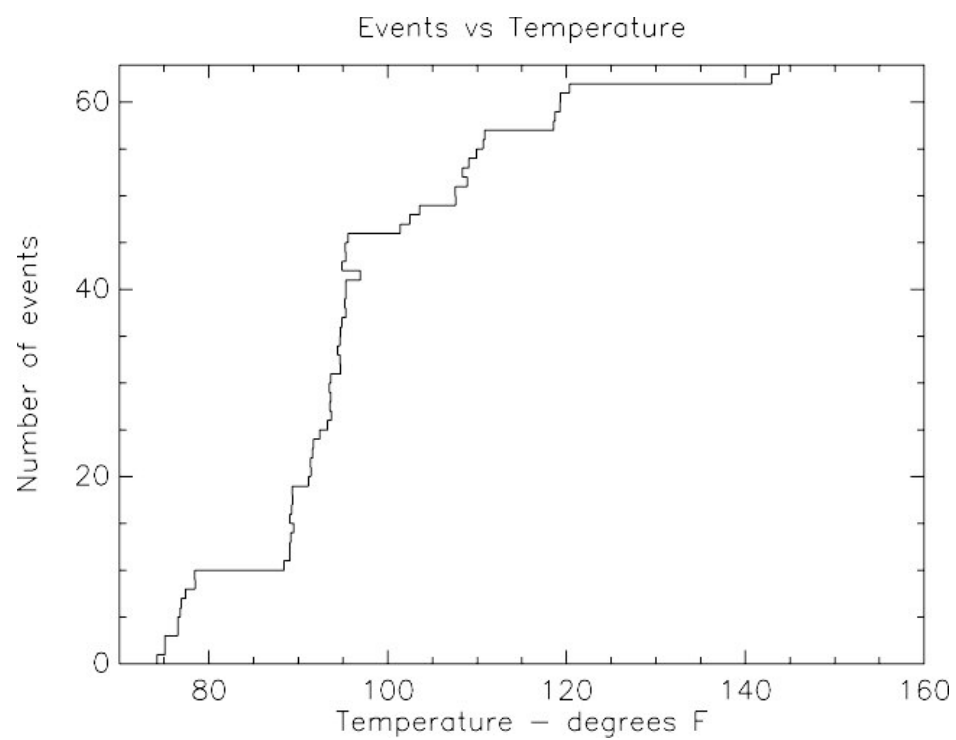


Fig. 2 Number of located events as a function of temperature for HTAI 9828.

When the distribution of the sources over the surface of the bottles is examined, the idea of grouping these sources in clusters becomes obvious. Figure 1 shows a location graph of the sources from a test. For simplicity of display, the surface of the sphere has been distorted to that of a cylinder with the poles of the sphere at the top and bottom of the cylinder. This will show reasonably accurate relationships for the center band around the equator with extreme distortion only near the poles. The sensor positions are shown and numbered with #1 being at the north-pole (arbitrarily defined on the sphere) and #6 at the south-pole. This bottle had 15 emission sources contained in the cluster defined by the circle with the rest of the 63 located sources scattered over much of the bottle. Figure 2 shows a running sum of all located events as a function

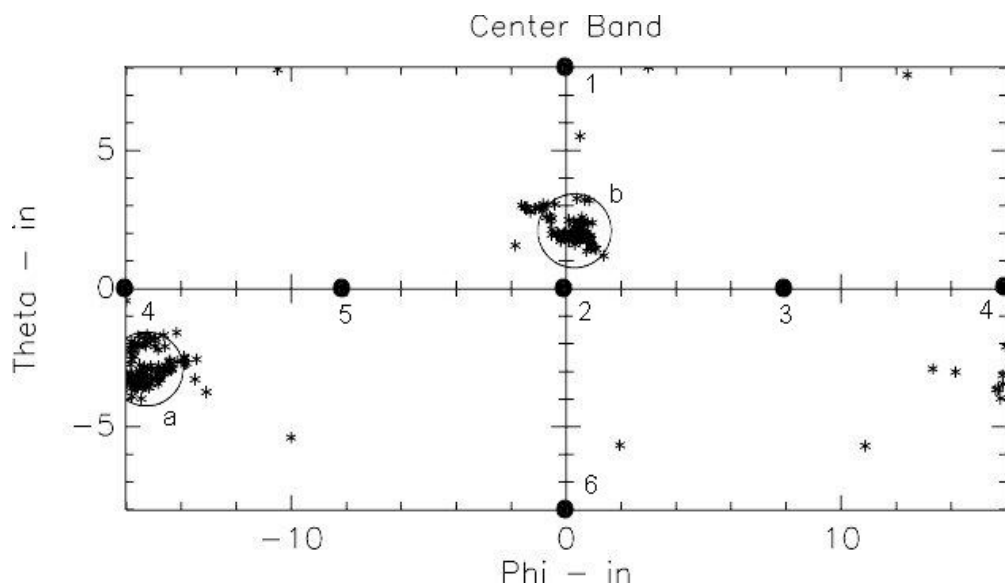


Fig. 3 Distribution of located events on bottle HTAH1254

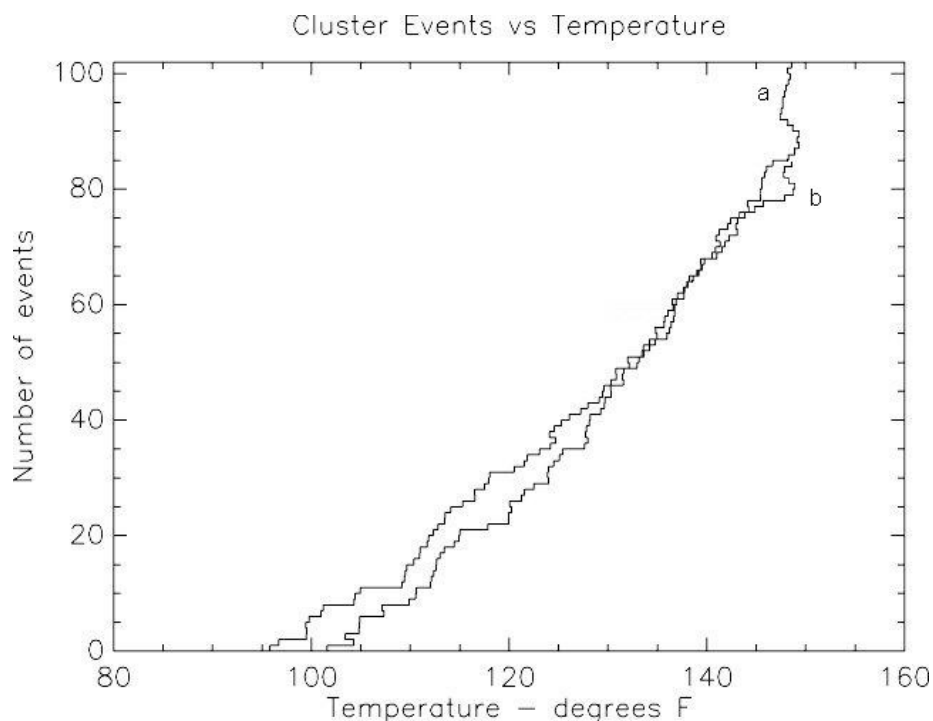


Fig. 4 Number of located events vs. temperature for two clusters seen on bottle HTAH1254.

of temperature. This curve shows the behavior for mild corrosion on the inside of the bottle. As the strain in the bottle wall increases, the number of corrosion products left unaffected on the wall surface decreases and emission rate approaches zero. This bottle appears to have random corrosion with only a small amount of localization. The conclusion is that this amount of corrosion has only a minor effect on the integrity of the bottle.

In Fig. 3, a bottle is shown with 217 located emissions. This bottle has almost all of the emissions located in two clusters, one containing 85 events and the other, 102. It appears that the

bottle has two obvious problems. The question here is not whether these clusters are serious or not but, rather, is the bottle in imminent danger of failing during the test. Figure 4 shows a graph of the running sum of events in each cluster as a function of bottle temperature. Both clusters show a constant rate of emission as a function of temperature. There is a slight indication of a rate increase for cluster “a” above 63°C (145 F), but it is not definitive. The best scenario is that these both show controlled crack growth. There is no question that they appear serious but there is also no indication impending failure. Under the pass-fail criteria currently in place, the system declared them as corrosion and failed the bottle.

The next bottle test to be presented is show in Fig. 5. This bottle did not just fail the test, it ruptured a burst disk inside the oven at a temperature of 65°C (one degree before the computer would have turned off the fan and heater). The result was spectacular although the resulting damage was rather easily repaired. Two tight clusters are seen in the figure. There is no question that these are the exit ports containing the burst disks.

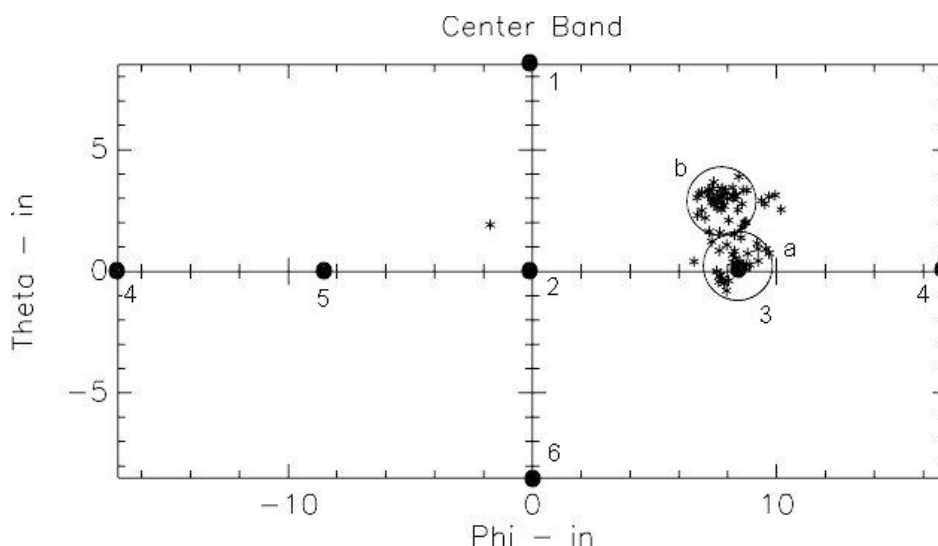


Fig. 5 Located events on bottle HTAI6427

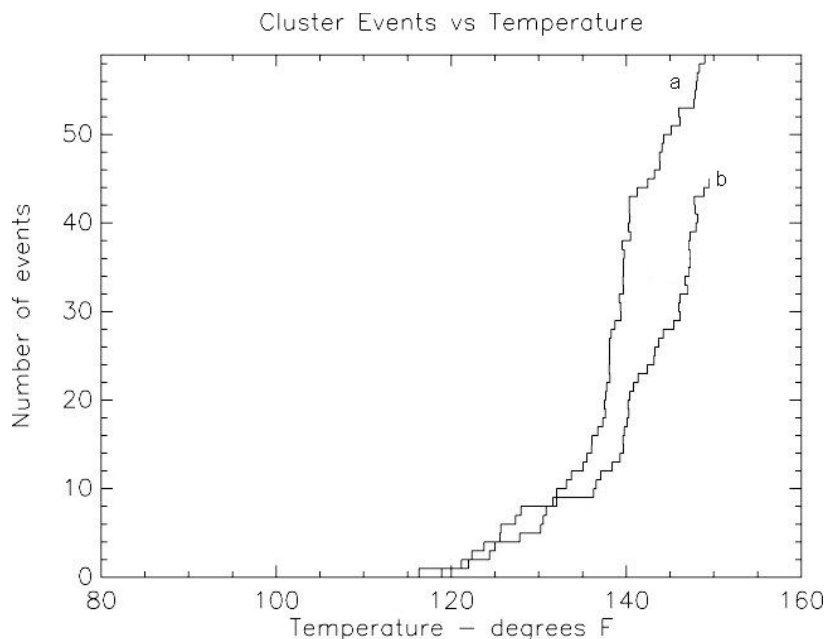


Fig. 6 Number of events vs. temperature for two clusters on bottle HTAI6427.

The spacing between the clusters on the graph is about an inch less than the actual spacing on the bottle. A discrepancy could be expected as the events occurred on the top of the ports and the acoustic waves had to travel about two inches down the ports before they reached the surface of the sphere. Figure 6 shows the number of events as a function of temperature for the two clusters. The shows that the burst disk on “b” was the disk, which fractured. The last emission from “a” occurred about one minute and 0.8°C before the last event seen on “b”. However, from these curves, it is apparent that both disks were well on their way to fracture. The curves indicate that the transition to uncontrolled crack growth occurred at about 56°C (130 F) for “a” and 58°C (137 F) for “b”. This is in contrast to Fig. 3 where the first indication of an upturn in the rate was at 63°C. These curves also illustrate that the growth of each crack depends strictly on local conditions. With several cracks growing on a structure, it is impossible to predict which one will result in failure of the structure.

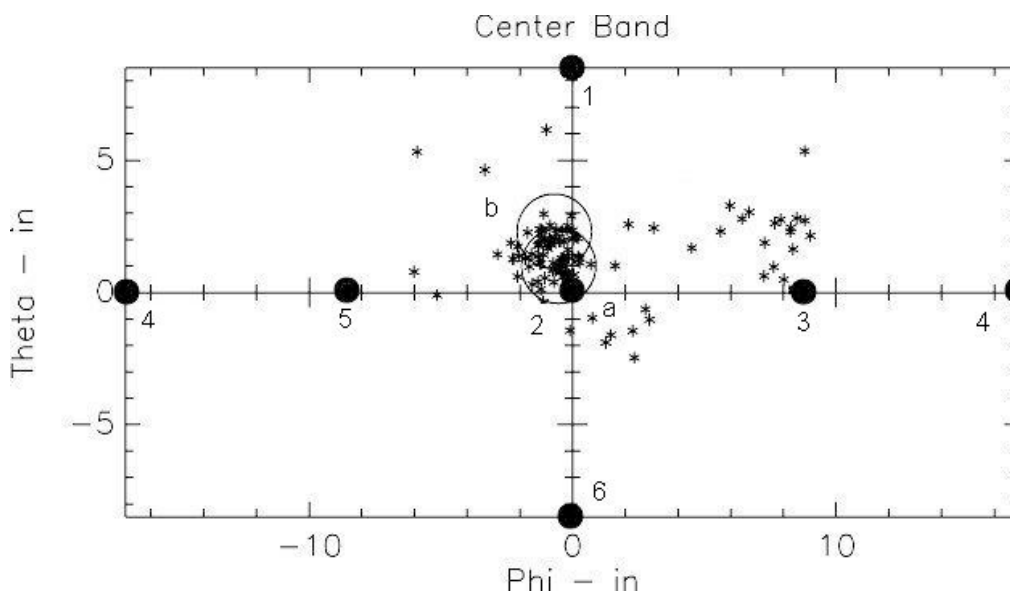


Fig. 7 Located events on bottle HTAI9828.

The data from this unexpected failure made several important points. First the significance of the increasing slope of the AE versus load curves is quite real. Second, the choice of the number of events in a serious cluster is certainly realistic and is of the correct order of magnitude. Third, the safety criteria for shutting down the system before a failure occurs needs to be reviewed and revised.

The question of whether corrosion was producing some of the emission or not, was resolved when American [2] sectioned and examined the inside of several of the bottles, which had failed the corrosion criteria. All of the sectioned bottles showed corrosion stains at the apparent low point, during storage, of the spheres. These stains were between 51 and 63.5 mm diameter circles. Micrographs showed corrosion and wall thickness measurements revealed thinning up to 25% of the wall thickness. Figure 7 shows the emission locations seen during the test of bottle HTAI9828, one of the sectioned bottles. The emission rates, seen in Fig. 8, suggested unstable crack growth for cluster “a” and stable crack growth for cluster “b”. A micrograph of a stained region on the interior wall is shown in Fig. 9. The etching of the surface is clearly visible as tool marks that remain on the original portions of the surface.

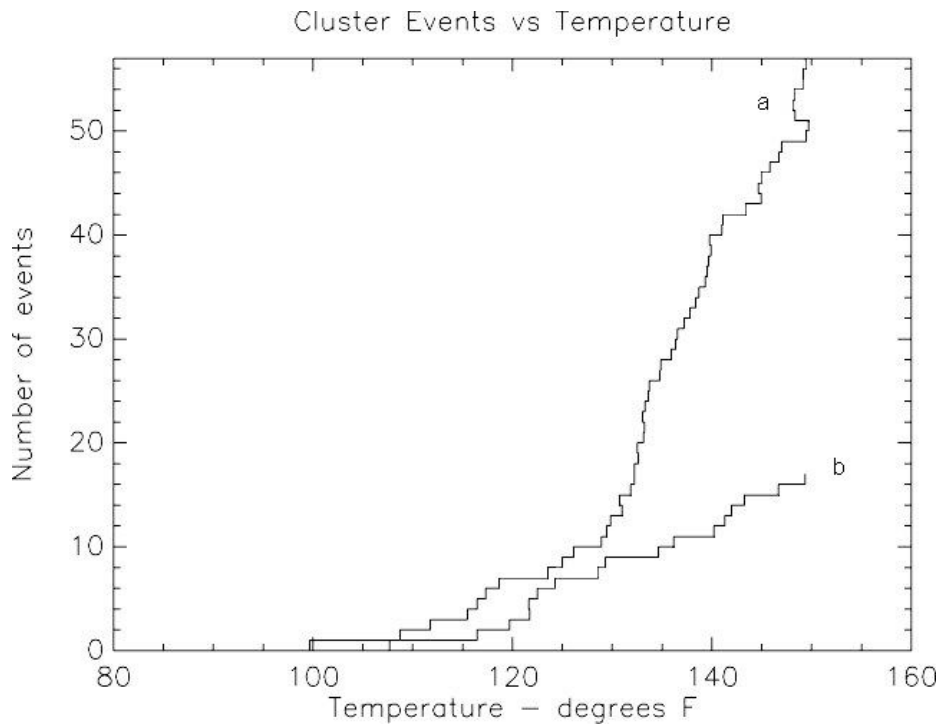


Fig. 8 Number of events as a function of temperature for clusters on bottle HTAI9828.



Fig. 9 Corrosion on inside of bottle HTAI9828. Magnification 31x.

Thirty-four of the bottles in the data set of 649 bottles failed the AE test. Eighteen, 2.8%, failed the test based on the unstable crack growth criterion and 16, 2.5%, failed the test based upon the corrosion or stable crack growth criterion. Of the 16, 11 had curves characteristic of stable crack growth, some with hints of transition to unstable crack growth near the end of the test and five were more characteristic of corrosion with the emission rate slowing down near the end of the test. One of the failures in the original data from Walter Kidde was due to a replaced pressure switch protective housing, which was mounted with screws instead of being welded.

This test is included as the system definitely failed the bottle although there was probably nothing wrong with the actual structure of the bottle

6. Discussion

The pass-fail criteria established for the prototype Halon Bottle Tester have held up remarkably well for this expanded data set. Changing the required number of events in a cluster necessary to fail the test due to unstable crack growth would have only minor effect on the number of bottles failed. Decreasing the number from 18 to 15 would have failed one more bottle while increasing it to 30 would have passed four more bottles. However, two of those bottles had identified flaws. The definition of the critical number for the ratio test of 3.0 is supported by catastrophic failure of Bottle HTAI6247. The final ratios of the two clusters at failure were 10.8 for the burst disk that appears to have survived and 4.63 for the burst disk that failed. Lowering the ratio to 2.5 would have failed two more bottles while raising it to 4.0 would come close to missing the unstable crack, which caused the failure of HTAI6247. The best compromise is approximately the original pass-fail ratio and there appears little reason to change it.

When the original pass-fail criteria were being developed, the primary problem was thought to be unstable crack growth. Then several bottles appeared that had clusters containing large numbers of locatable events but a constant emission rate as the pressure increased so another mechanism was suspected. Experience had shown that a corroded piece of metal, when strained, produced emission, whose rate decreased as the finite supply of corrosion products was used up. When several bottles showed clusters with either steady or decreasing emission rates as the temperature increased, it was recognized that while failure of the bottle was not imminent, the larger clusters did indicate a problem with the bottles. Corrosion was thought to be the most likely cause and thus it was labeled. This was confirmed by corrosion stains with accompanying wall thinning, found when American sectioned some of the bottles, which had failed the corrosion criteria. However, it is not clear that many of the bottles contain brittle corrosion products in the stained areas. Only 5 bottles show the decreasing emission rate characteristic of fracturing corrosion byproducts. Most bottles that failed the corrosion criteria had a constant emission rate and a few even had a noticeable rate increase above 60°C. Some of the micrographs show pitting in the corroded area but few flakes of corrosion byproducts are seen. What is postulated as a mechanism for generating the AE is the formation of microcracks associated with the pits. As the load is increased, not only do more fractures occur but some propagate into the surface. Some of these microcracks may coalesce into larger cracks and eventually start to show unstable crack growth. This scenario would tend to produce the emission curves seen in these bottles.

This explanation leaves one problem. Halon 1301 is supposed to be stable. However, in the presence of water, fluorocarbons can react very slowly with water. Products of such a reaction for Halon 1301 (CBrF₃) will include hydrogen fluoride HF and hydrogen bromide HBr. Water and Halon 1301 are not miscible with Halon being the denser liquid (the density is 1.57). Any free water would float on top of the liquid Halon. Most but not all of the corrosion stains in the examined bottles appear to be positioned at the bottom of the bottle as it is mounted in the aircraft. HF and HBr appear to be able to dissolve in Halon and sink to the bottom, where they produce the observed puddle shaped corrosion stains. These puddles are between 38 and 64 mm in diameter. The sizes of these puddles agree with the sizes of the AE clusters shown in Figs. 3 and 7. Both micrographs and wall thickness measurements show that these stains are corrosion puddles. A wall thinning of 27% has been measured at the low point of one of the puddles.

The sectioning studies of the failed bottles show that the corrosion puddles found by AE may have a significant effect on the integrity of the Halon bottles and justifies the inclusion of the corrosion criteria in the original Halon bottle test program. Examination of the cluster curves for all 30 bottles with 20 or more events per cluster and rate ratios less than 3.0 shows that 6 have corrosion-type curves and the rest have emission rates, which are relatively constant and independent of the temperature. Sixteen failed the current criteria with 2 bottles having between 35 and 40 events in the cluster. Five more bottles had between 30 and 34 events. None of these 5 showed any indication of unstable crack growth at the higher temperatures. Changing the current corrosion criterion to 40 events per cluster would have passed two more bottles, while the criterion of 30 or more events would have failed five more bottles. The bottles that failed the corrosion criteria averaged 64 ± 20 events in the largest cluster. Because of the reported wall thinning in several of the sectioned bottles, the corrosion criteria should not be raised very far and there seems no compelling reason to lower it. Therefore, it is recommended that neither failure criteria should be changed from the current values.

7. Conclusions

The original pass-fail criteria for the AE Halon Bottle Tester were based upon 208 bottle tests. The addition of another 475 bottle tests from the American Airlines Halon Bottle Tester in its Tulsa Bottle shop gave no reason to change these criteria. The combined data set of 649 bottles included 34 bottles, which failed the criteria. Metallographic studies of some of the failed bottles at American showed that the AE tester detected the corrosion on the interior of the bottle. This corrosion included significant wall thinning. The cause of the corrosion is thought to be the decomposition of Halon 1301 in the presence of water. The most likely decomposition products are HF and HBr.

Acknowledgements

The authors would like to thank Kamran Ghaemmaghami of Federal Express for support and aide throughout the Halon Bottle tester program. Fred Munkholm and Randy Attebury in the American Airlines bottle shop were unwavering in their support of the tester despite a series of “teething” problems and Tom Forsberg both performed and interpreted many of the metallographic examinations. We would also like to thank Ric Anderson of the Air Transport Association and Dr. Mark Toughiry of the DOT for their interest and support.

Reference

1. A.G. Beattie, “An Acoustic Emission Test for Aircraft Halon 1301 Fire Extinguisher Bottles” DOT/FAA/AR-97/9, Apr 1998. *Journal of Acoustic Emission*, **15**, 1997, 63-68.